Transactions of the ASME

Journal of Fluids Engineering

Published Quarterly by The American Society of Mechanical Engineers

VOLUME 112 • NUMBER 4 • DECEMBER 1990

Contents (continued)

W. H. Schofield

Defence Science and Technology
Organization,
Aeronautical Research Laboratory,
Melbourne, Australia
Mem. ASME

E. Logan

Department of Mechanical and Aerospace
Engineering,
Arizona State University,
Tempe, Ariz. 85287
Fellow ASME

Turbulent Shear Flow Over Surface Mounted Obstacles

The mean flow field surrounding obstacles attached to a wall under a turbulent boundary layer is analyzed. The analysis concentrates on how major features of the flow are influenced by model geometry and the incident shear flow. Experimental data are analyzed in terms of nondimensionalized variables chosen on the basis that their effect on major flow features can be simply appreciated. The data are restricted to high Reynolds number shear layers thicker than the attached obstacle. The work shows that data from a wide range of flows can be collapsed if appropriate nondimensional scales are used.

Introduction

The mean flow around a sharp edged obstacle in unsheared flow is relatively simple to analyze because regions of separated flow do not vary in relative size or shape with velocity or scale. Thus the mean flow field around the obstacle is constant implying a constant coefficient. However, if the obstacle is attached to a wall and submerged in the boundary layer on that wall the flow over the obstacle is no longer simple and now depends on a range of variables. As this class of flow is important in many practical flows, such as lift spoilers on aircraft, behavior of VSTOL aircraft near buildings and in meteorology, it has been the subject of much previous work.

Initially authors (e.g., Hoerner [1]) tried to describe the sheared flow case in terms of a simple drag coefficient as in unsheared flow, i.e., they tried to define velocity and length scales which would yield a constant drag coefficient over a range of flow conditions. It is now well-established that this simple approach does not work.

A large number of parameters affect the drag or flow around a wall mounted prism; viz. $C_D = f_1(h, \delta, \tau_0, z, U_1, \rho, \nu, W, L, S)$ or

$$C_D = f_1(h/\delta, u_\tau/U_1, z/h, W/h, L/h, U_1 h/\nu, S/h) \qquad (1)$$

There are many studies reporting work in which some of these nondimensional groups defining the geometry of the obstacle are held constant and data collected to demonstrate how C_D varies in terms of the remaining nondimensional group(s). Thus we have results, among others, which show

$$C_D = f_2\left(\frac{hu_\tau}{\nu}, \frac{h}{\delta}\right) \text{ (Good and Joubert [2]);}$$

$$C_D = f_3\left(\frac{hU_h}{\nu}\right) \text{ (Castro [3]);}$$

$$C_D = f_4\left(\frac{h}{z}, \frac{u_\tau}{U_1}\right) \text{ (Raju, Loeser, and Plate [4]).}$$
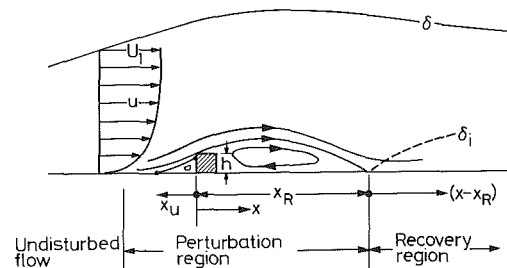
Fig. 1 Schematic of flow features over a wall mounted obstacle

These results demonstrate that flow around surface-mounted prisms is mainly influenced by the parameters; h, δ, u_τ.[1] This approach, however, has not led to any understanding of the physical mechanisms that determine these flows.

The present study analyzes the data from a slightly different viewpoint. It concentrates on how major features of the flow (separation position, internal layers, shed vortices) are influenced by model geometry and overall flow parameters. Data are presented in terms of nondimensional variables chosen on the basis that their effect on major flow features can be simply appreciated. Although this paper presents some new data it mainly reanalyzes or reinterprets previously published data, some of which was inaccessible or in a form that made it difficult to interpret. The reanalysis leads to a unified description of a wide collation of data. The only restriction applied to data selection, apart from high Reynolds number, was that the prism height was to be less than the shear layer thickness.

Flow Over a Two-Dimensional Obstacle

Flow over a two-dimensional obstacle is the most commonly treated case in the literature and much good quality data have been published. However, there is little published data on the flow development in front of the obstacle and it can be demonstrated that flow upstream of the obstacle sets the initial conditions for the development of the downstream flow.

As the undisturbed flow approaches an obstacle, the pressure field created by the obstacle retards the boundary layer until

[1] u_τ and z are simply and directly related (for a smooth wall as shown later.)
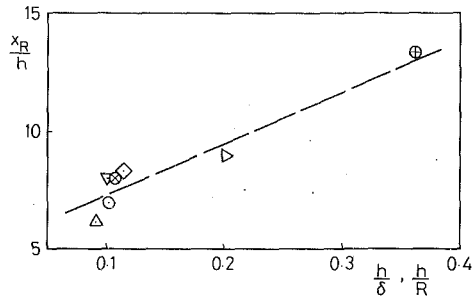
Fig. 2 Length of separated flow behind a two-dimensional obstacle.
⊙, Phataraphruk [15] pipe flow, flow A; ▷, Phataraphruk [15] pipe flow, flow F; ⊕, Tillmann [14] boundary layer flow; ⊗, Chang [16] pipe flow; △, Siuru and Logan [17] pipe flow; ▽, Robins unpublished, boundary layer flow; ◇, Schofield et al. [18], boundary layer flow.

the flow near the wall separates (see Fig. 1). Results of Good and Joubert [2] show that the form of the pressure distribution over the front face of an obstacle changes little with the relative obstacle height, i.e., the ratio of height to layer thickness, h/δ. This means that the relative position of the stagnation streamline on the front face of the obstacle varies little with the ratio h/δ. Now if the obstacle is small relative to the layer (small h/δ) then the pressure field generated by the obstacle acts on the innermost, low momentum portion of the boundary layer causing the layer to separate relatively early in the upstream pressure field. If, on the other hand, the obstacle is large relative to the layer thickness (large h/δ) then the pressure field due to the obstacle acts on flow with a higher average momentum and therefore separates relatively closer to the obstacle. It follows that the slope of the separation streamline in front of an obstacle will vary with relative obstacle height (i.e., with h/δ) because the separation streamline's position on the block face is fixed but its relative position on the upstream wall varies with h/δ. The slope of the separation streamline determines the size and shape of the separation bubble over and downstream of the obstacle.

Relative obstacle height is not of course the only factor that affects the position of the upstream boundary layer separation; any agency that degrades or changes the condition of the boundary layer entering the upstream pressure field of the obstacle will affect the position of the upstream separation. Such agencies could include: distributed roughness on the upstream walls, another upstream obstacle, or large changes in the Reynolds number of the layer. The Reynolds number effect comes in two parts; change in mean profile shape and layer thickness. As can be seen from the argument above both of these affect the (relative) position of the upstream separation. In the Reynolds number regime of practical flows these effects

are weak; they require large changes in Reynolds number for small changes in flow around an obstacle.

This description of the flow implies that the perturbation region near the block is governed by the variables h, δ, U_1, and u_τ. This explains the various nondimensional groupings that many authors have found to correlate their results: $\frac{h}{z}$, $\frac{u_\tau}{U_1}$, $\frac{hU_1}{\nu}$, $\frac{zu_\tau}{\nu}$, $\frac{hu_\tau}{\nu}$. The data considered below are all in the high Reynolds number regime that is of most practical interest and within this regime effects due to changes in Reynolds number will be secondary.

Perturbation Flow

Good and Joubert's [2] measurements of wall pressure upstream of a two-dimensional plate showed that the relative extent of the upstream influence[2] decreased rapidly as the ratio h/δ increased. Their results (for high Reynolds number flow) are correlated by: $x_u/h = 15.0(h/\delta)^{-0.7}$. This equation gives that as h/δ increases from 0.1 to 1.0 the extent of the plate's upstream pressure gradient moves from 75h to 15h. This large relative movement will of course be accompanied by a large relative movement in the position of the upstream separation and a corresponding change in the shape of the streamlines over the obstacle and thus in the length of separated flow behind the obstacle. This suggests that the streamwise length of separated flow behind a two-dimensional obstacle should be simply related to its relative height. Figure 2 shows data which support this proposition. These data include both boundary layer and pipe flow results. There are large differences in Reynolds number within these data which probably accounts for the small scatter in the data. Data for flows over relatively large obstacles in pipes will not follow this distribution because the proximity of the opposite pipe wall will restrict the development of the separated region.

Useful data on the effect of upstream wall shear stress and the flow around an obstacle are sparse. Good and Joubert's data showed that for constant h/δ the drag coefficient of a two-dimensional plate was a weak function of the wall stress in the upstream boundary layer. They also showed that this effect decreased as h/δ increased until at $h/\delta > 0.8$ the drag coefficient was insensitive to upstream shear. The reason for this change of behavior at large h/δ is that as the plate height approaches the boundary layer thickness, the average momentum of the flow deflected by the plate approaches the freestream value and small differences to the flow near the wall (as indicated by the wall shear) have a very small and

---

[2]Defined as the first detectable increase in pressure on the upstream wall.

Nomenclature

A, B = constants in the logarithmic law of the wall
c_f' = skin friction coefficient ($= 2u_\tau^2/U_1^2$)
C_D = drag coefficient
G = Clauser's profile parameter
h = height of prism
k = height of distributed roughness elements
L = width of prism (lateral to main flow direction)
R = pipe radius
S = spacing between prisms in main flow direction
u = mean velocity in main flow direction

U_1 = freestream velocity
u_τ = wall shear velocity $\left(= \left(\frac{\tau_0}{\rho}\right)^{1/2} \right)$
Δu = velocity deficit (maximum difference between relaxing profile and equilibrium profile)
W = length of prism in main flow direction
x = distance in main flow direction
y = distance normal to wall
z = length scale of the wall flow
δ = boundary layer thickness

ρ = fluid density
μ = fluid viscosity
ν = fluid kinematic viscosity
κ = constant in the logarithmic law of the wall
τ = shear stress

Subscripts

eq = equilibrium value
h = at the height of the prism
i = internal layer
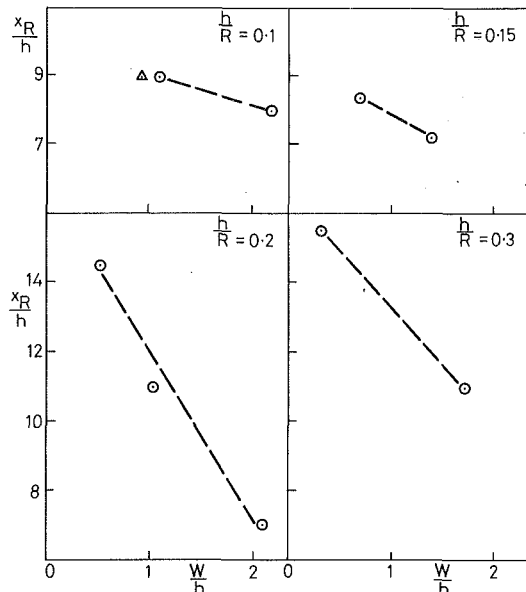0 = at the wall
R = reattachment
u = upstream

Fig. 3 Effect of streamwise length of obstacle on length of separated flow. Pipe flow; ⊙, Phataraphruk [15]; △, Chang [16].

diminishing effect on the average momentum deflected by the plate.

Castro [3] measured flow recoveries downstream of two-dimensional blocks on walls with distributed roughness where the height of the distributed roughness varied between tests. The length of separated flow behind the block on the rougher surface was smaller than the separated length behind the block on the less rough surface (see data presented in Schofield and Logan [5]). The rougher wall produced a mean velocity profile with low momentum near the wall which separates early giving rise to low angles of separation at the top of the block which in turn leads to early reattachment of the flow downstream. Similar results are presented by Sami and Lui [6] in which large increases in Reynolds number over a smooth wall produce small changes in wall shear giving very modest increases in the length of separated flow downstream of the obstacle.

The size of the downstream separation is not, of course, solely determined by the upstream flow. Other factors, include: the shape of the prism downstream of its leading face, proximity of walls that limit the vertical development of the separation bubble, and the presence of a longitudinal pressure gradient.

The shape of an obstacle downstream of its leading edge can have a pronounced effect on the size of the separated flow over the obstacle. The (internal) shear layer generated at the top of a thin plate (see Fig. 1) can grow in an unrestricted way to its reattachment point on the downstream wall. However the same internal shear layer generated at the leading edge of a block with a large streamwise dimension will be quite different. Entrainment into the internal shear layer will be restricted over the top of the block due to the small flow area between the block and the shear layer; this restriction will lead to a reduction in pressure on top of the block and the shear layer moving downwards towards the block. The downstream effect of this movement of the shear layer is a reduction of separated length x_R, as shown in Fig. 3. The limiting case of this process is obviously where the shear layer reattaches to the top of the block and separates from the trailing edge horizontally (see Schofield and Logan [5]).

The geometrical shape of the roof of a prism also affects the size of the downstream separation bubble through its effect on shear layer entrainment. Durst and Rastogi [7] investigating flow over a thin plate found that by simply sharpening the top edge of the plate they increased the length of the downstream
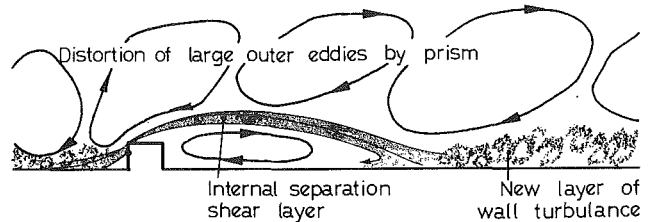
Fig. 4 Structure of a turbulent boundary layer over a two-dimensional obstacle

separation region by one obstacle height. An early study by Holdredge and Reed [8] gives further data on the effect of the roof shape on the length of separated flow.

Recovery Length Scales

The recovery of a turbulent boundary layer downstream of an obstacle is different in the wall and outer regions of the layer. This difference is a consequence of the turbulence structure of a wall shear layer, shown in Fig. 4. The outer region contains large roller eddies, whereas fine scale turbulence is generated near the wall. The outer large scale eddies have a length scale comparable with the total layer thickness and hence flow behavior can be described in terms of δ or R (e.g., the Universal Defect Law, [9]). It follows that parameters describing outer flow recovery will scale with δ or R.

The fine scale turbulence of the inner flow of a layer has a length scale related to the size of the wall generated eddies, which differs depending on whether the wall is smooth or covered with distributed roughness. This flow behavior is described in terms of the wall length scale z in the universal law of the wall [9], which for a smooth wall is;

$$\frac{u}{u_\tau} = \frac{1}{\kappa} \log_e \frac{y u_\tau}{\nu} + A = \frac{1}{\kappa} \log_e y/z \qquad (2a)$$

whence $z = \nu/[u_\tau \exp\kappa A]$. For a wall with distributed roughness it is;

$$\frac{u}{u_\tau} = \frac{1}{\kappa} \log k + B = \frac{1}{\kappa} \log_e y/z \qquad (2b)$$

whence $z = k/\exp\kappa B$ and is thus independent of viscosity (for a rough wall). Parameters describing inner flow recovery will scale on z determined from one of the above two equations depending on whether the recovery takes place on a smooth wall or on a wall with distributed roughness.

The development length for the wall recovery must have as its origin the point at which the new attached wall turbulence is initiated. The development length $(x - x_R)$ is also the most appropriate length for the outer flow because the distortion of the outer eddies by the obstacles has been completed at the distance x_R and the recovery of the (long lived) outer eddies commences with an origin near $(x - x_R)$.

It should be noted that several previous authors have tried to correlate data downstream of an obstacle using simply h and x. Both these length scales are only appropriate to the perturbation flow; h determines the size of the perturbation to the flow but is not related to how the flow relaxes back to its undisturbed state and using x to measure the length of recovery flow is simply in error by x_R.

Wall Recovery. Equation (2) has been shown by many authors to be remarkably resilient in giving an accurate description of mean velocity near the wall for both perturbed and unperturbed flows. Bradshaw and Wong [10] and Schofield [11] have shown that equation (2) is valid and can be used to find accurate values of the wall shear in flows very close to separation[3]. However, the vertical extent of the wall flow that

---

[3]The criterion appears to be that the flow at that station has no periods of intermittent flow reversal (the 99 percent flow attachment condition, see Simpson et al. [12]).
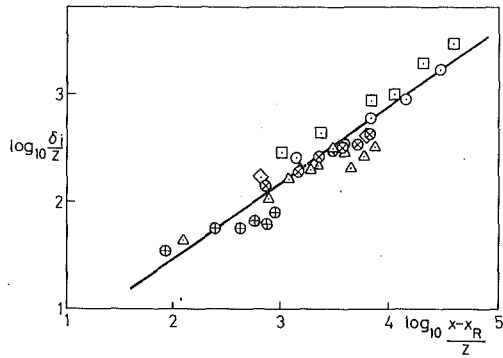
Fig. 5   Depth of internal layer downstream of reattachment. ⊙, Tillmann [14]; ⊡, Siuru & Logan [17]; ◇, Phataraphruk [15]; △, Castro [3] flow F1S; ▽, Chang [16]; ⊕, Castro [3] flow F2L; ⊗, Castro [3] flow F1L. ———, Regression line.
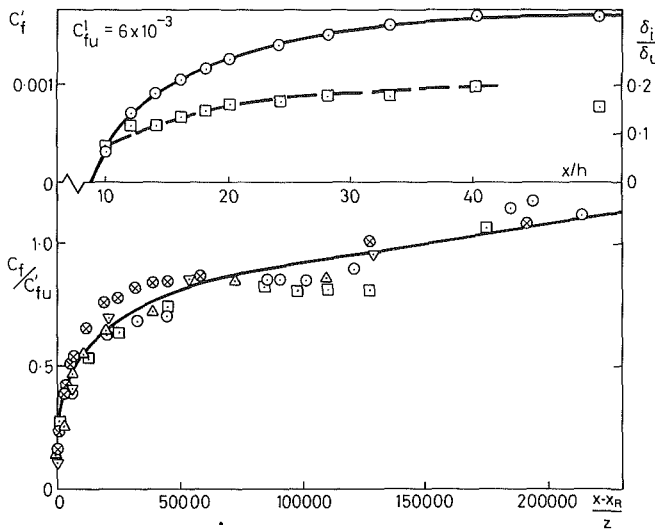
Fig. 6   Skin friction recovery downstream of reattachment (a) Data of Castro [3], ⊙, c_f'; ⊡, δ_i. (b) Pipe and Boundary Layer data; ⊙, Phataraphruk [15], flow A; ⊡, Phataraphruk [15], flow B; ⊗, Chang [16]; ▽, Schofield et al. [18]; △, Siuru & Logan [17].

Fig. 7   Skin friction downstream of reattachment. Rough wall flow. Data of Castro [3], ⊗, flow F1S rough wall; —·—, line of best fit for smooth wall data ($h/\delta = 0.081$).
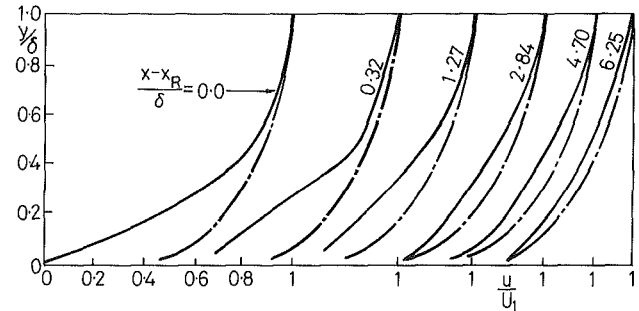
Fig. 8   Relaxation of mean velocity profiles downstream of reattachment. Data of Castro [3] flow F1L, $h/\delta = 0.16$; —·—, upstream undisturbed profile.
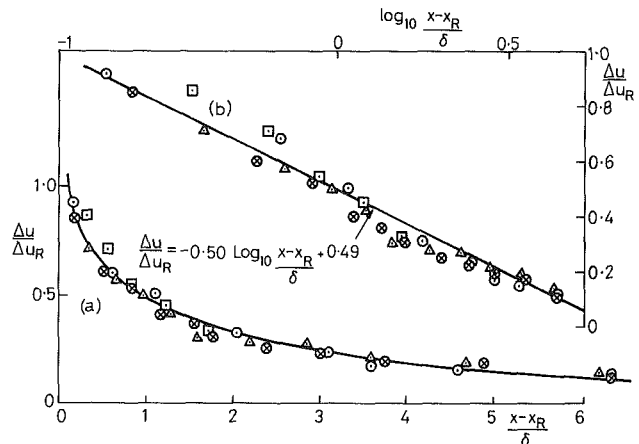
Fig. 9   Decay of maximum deficit in mean velocity downstream of reattachment. ⊙, Robins (unpublished) $h/\delta = 0.1$; △, Castro [3] flow F1L $h/\delta = 0.16$; ⊗, Castro [3] flow F2L, $h/\delta = 0.16$; ⊡, Counihan [19], $h/\delta = 0.13$.

can be accurately described by equation (2) is strongly affected by proximity to separated flow [10,11]. The vertical extent of wall flow correlating with equation (2) is related to the depth of new wall turbulence generated downstream of reattachment and the recovery of the wall layer after the perturbation.

Figure 5 presents data showing that this depth of new wall turbulence scales simply with the length scales $x - x_R$ and z. The regression line that correlates the data over nearly three decades of $\dfrac{x - x_R}{z}$ is;

$$\log_{10} \frac{\delta_i}{z} = 0.69 \log_{10} \frac{x - x_R}{z} + 0.11; \ \frac{\delta_i}{z} = 1.29 \left(\frac{x - x_R}{z} \right)^{0.69} \quad (3)$$

The collapsed data of Fig. 5 are for both pipe and boundary layer flow and cover a large range of perturbation strengths (h/δ) and a reasonably wide range of Reynolds numbers. This shows the nondimensional growth rate of the new wall turbulence is not strongly affected by the flow upstream of the obstacle nor by the nature of the outer flow. The fact that the logarithmic law (equation (2)) is valid does not mean however that equilibrium flow has been re-established in the wall region. Figure (6a) shows that the wall shear has not regained its undisturbed value by the time the depth of the logarithmic region had reached the equilibrium value ($\sim 0.2 \delta$). Figure 6(b) shows a collation of skin friction recovery data, from both

pipe and boundary layer flow, which collapse using the present scaling.

Finally, Fig. 7 shows the rate of wall shear recovery does not appear to be affected significantly by distributed wall roughness.

Outer Flow Recovery.   At reattachment the mean velocity profile is severely distorted compared with the upstream equilibrium profile (Fig. 8). The large strain near the wall relaxes outwards through the profile as the layer recovers downstream of reattachment. The mean velocity difference between the relaxing and equilibrium profile is initially larger near the wall but the short time-scale of wall turbulence means that the return to equilibrium proceeds much more rapidly near the wall than in the outer layer. Thus shortly after reattachment the maximum deficit in the mean profile moves away from the wall into the outer flow. Because the large eddies in the outer flow scale on δ, the decay of the maximum velocity deficit should also scale on δ. Data presented in Fig. 9(a) show that this scaling does correlate the data and the form of the correlation
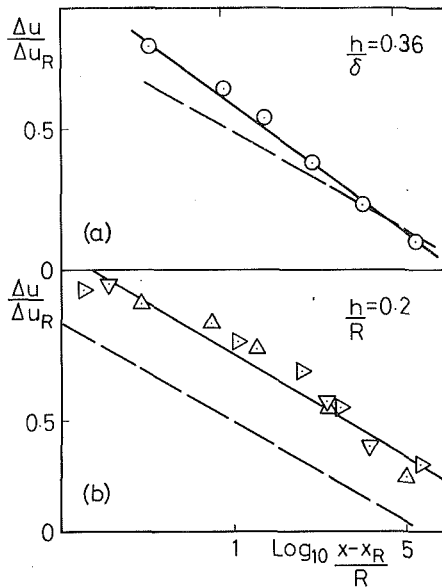
Fig. 10 Decay of maximum deficit in mean velocity for several types of flow. ⊙, Tillmann [14], ▷, Phataraphruk [15] flow G; ▽, Phataraphruk [17] flow E; △, Phataraphruk [15] flow F; ——, regression line from Fig. 9.

Fig. 11 Relaxation of mean profiles downstream of reattachment. —·—, undisturbed profile; (a) Tillmann [14], $h/\delta = 0.36$, boundary layer flow; (b) Phataraphruk [15] flow E, $h/R = 0.20$, pipe flow.

suggests a logarithmic dependence which is confirmed in Fig. 9(b).

The data for Fig. 9 are for small perturbations ($h/\delta < 0.15$) in pipe or boundary layer flow. Data for other flows are given in Fig. 10. As noted previously the lack of restraint to vertical deflection in boundary layer flows results in little distortion to the large eddies. Thus, the relaxation rate of the maximum velocity deficit in a boundary layer over a large prism ($h/\delta = 0.36$, Fig. 10(a)) is little different from the small perturbation case. This does not apply where the large eddies are severely elongated by large (annular) obstacles in a pipe. Figure 10(b) shows the corresponding relaxation for pipe flow after large perturbations and it differs substantially from the result for small prisms.

Data presented in Fig. 11 illustrate that the readjustment back to equilibrium conditions is not usually monotonic. As the outer profile approaches an equilibrium distribution, the flow near the wall continues to accelerate and moves the mean wall profile past the equilibrium distribution. Such behavior

Fig. 12 Distributions of G downstream of reattachment. Boundary layer data.
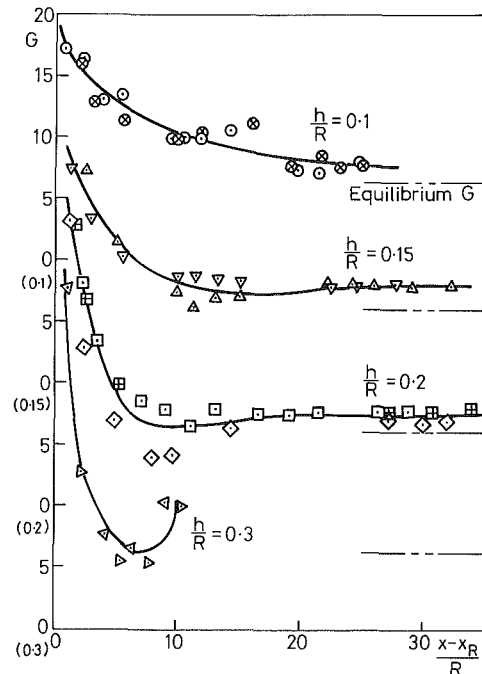
Fig. 13 Distributions of G downstream of reattachment. Pipe Flow Data of Phataraphruk [15].

was implied by the overshoot in the skin friction data of Fig. 6.

The most commonly used technique for judging a flow's equilibrium, or lack of it, is to evaluate Clauser's [9] mean velocity profile shape parameter defined as;

$$G = \int_0^1 \left\{\frac{U_1 - u}{u_\tau}\right\}^2 d(y/\delta) \bigg/ \int_0^1 \left\{\frac{U_1 - u}{u_\tau}\right\} d(y/\delta)$$

and compare it with the equilibrium value for that flow. G has a value near 6.2 for pipe flow profiles in equilibrium and 6.8 for equilibrium boundary layer profiles in zero pressure

(a) Centreline cross-section

(b) Vortices and induced flow
behind a prism

(c) Positions of major vortices downstream (x = 7h)
of a prism

Fig. 14   Schematic of mean flow around a three-dimensional prism

Fig. 15   Length of separation on the flow centerline downstream of cuboids of different widths. Data of Logan and Lin [25]; $h/\delta = 0.11$; ⊙, single prism; ▫, double prism $s/h = 2$.

imum value of G decreases and this minimum occurs later in the relaxation process.

Similar, but more pronounced, behavior occurs in pipe flow (Fig. 13) where the minimum value of G changes much more rapidly with prism height than in the boundary layer case. This is consistent with the large distortion in pipe flow caused by large (annular) prisms. Such an explanation is supported by the fact that pipe and boundary layer recovery for h/R, $h/\delta = 0.1$ flows are identical [5].

Flow Over a Three-Dimensional Obstacle

The flows around wall mounted three-dimensional obstacles are inherently more complex than the two-dimensional case because sets of streamwise vortices are generated within the shear layer. These vortices radically change the flow field near the prism and the downstream recovery of the flow.

Flow in the Perturbation Region.   Although the main features of flow around a three-dimensional prism have been the subject of several studies (Hunt, Abell, Peterka, and Woo [21], Werle and Gallon [22], Perry and Hornung [23], and Fairlie [24]), there remain many unresolved points of detail. It should also be noted that practically no measurements of three-dimensional flow components exist and thus all proposed flow patterns are based on flow visualization studies (mainly wall flow patterns), and as yet there is insufficient evidence to fully evaluate the effect of Reynolds number on the number and position of vortices in geometrically similar flow fields.

The flow field sketched in Fig. 14 is consistent with the data of the four studies cited above and the surface flow patterns observed by Fairlie.[6] It has the following features. First, there are no closed separation bubbles; it is now well-established that closed separation bubbles do not form around any three-dimensional obstacle on a wall (Hunt et al. [21]). Instead the separated regions have fluid passing through them and are the origins of line vortices that are shed into the downstream flow. Mean streamline flow near these vortices is often complex and can be difficult to map out from surface streamlines. Second, upstream of the prism, four vortices form near the junction of the wall and the prism, see Fig. 14(a). These vortices are shed around the edges of the prism into the downstream flow. At low Reynolds numbers more vortices form; the frontispiece in Thwaites [26] shows five vortices at a low Reynolds number. The third feature to note is that the mean flow reattaches to the top of three-dimensional obstacles at streamwise lengths much shorter than for two-dimensional obstacles. The separated region formed on top of the prism is not closed and vortices are shed into the downstream flow at about prism height. More complex reattachment patterns on top of a prism involving multiple vortices have been reported (see the results of Woo et al. [27] as analyzed in Hunt et al. [21]). Castro and

gradient.[4] Previous attempts to evaluate relaxation behaviors downstream of a prism by using distributions of G have not been successful (e.g., Bradshaw and Wong [10]) due to poor choices of scaling lengths. Although it is obviously attractive to use a single parameter to judge the degree of departure from equilibrium, values of G downstream of a wall-mounted prism require careful interpretation. As shown in Fig. 11 the mean profile adjusts unevenly with inner and outer regions reaching the equilibrium distribution at different distances downstream. This combined with the overshooting of the equilibrium distribution by the wall profile means the attainment of an equilibrium value of G by a relaxing layer does not necessarily imply that the profile is in equilibrium. For instance the profile at $x - x_R/R = 7.1$ in Fig. 11(b) has a value of G near 6.2 but the profile shape is far from equilibrium and continues to be so for a considerable distance downstream.

Another problem in comparing data from different flows is to decide which parameter should be used to nondimensionalize the recovery distance $(x - x_R)$. The initial relaxation occurs quickly in the wall layer while the overall relaxation takes a much longer time and occurs mainly in the outer layer. As the prime interest is in the final return to equilibrium conditions the outer length scale δ is more appropriate.[5] Using these length scales boundary layer data (Fig. 12) form a progressive ordered set. These data show that as prism height increases, the min-

---

[4]As G involves u_τ its value depends on the accuracy of c_f. In flow regions near separation and attachment where the depth of equilibrium wall flow is small the uncertainty in the value of c_f and hence G will be large.

[5]Inaccuracies in c_f and hence G decrease rapidly downstream of reattachment and are small at a distance of 10δ downstream of reattachment.

---

[6]It does however differ in detail from the pattern observed by Logan and Lim [25] at a lower Reynolds number.

Fig. 16 Recovery of centerline skin friction downstream of three-dimensional prisms on smooth walls. Data of Logan and Lin [25]; $\otimes$, $L/h = 3$; ∇, $L/h = 6$; $\odot$, $L/h = 9$; $\triangle$, two-dimensional data of Schofield et al. [32]. Solid symbols are for two three-dimensional prisms aligned in the flow direction.
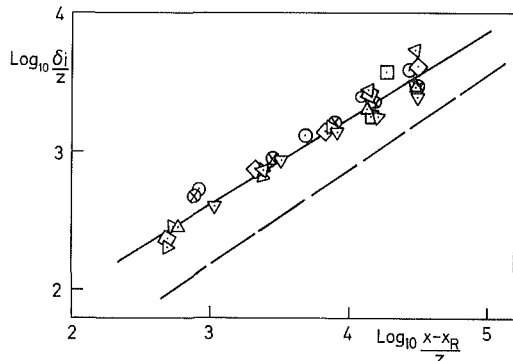
Fig. 17 Internal layer growth downstream of reattachment. — — — regression line for two-dimensional data. Three-dimensional data of Logan and Lin [25]. $\otimes$, $L = 3h$; $\odot$, $L = 6h$; $\lhd$, $L = 9h$. Data for two three-dimensional prisms in line: $\boxdot$, $L = 6h$, $S = 2h$; ∇, $L = 6h$, $S = 3h$; $\rhd$, $L = 6h$, $S = 6h$; $\Diamond$, $L = 6h$, $S = 9h$; —regression line for all three-dimensional data.

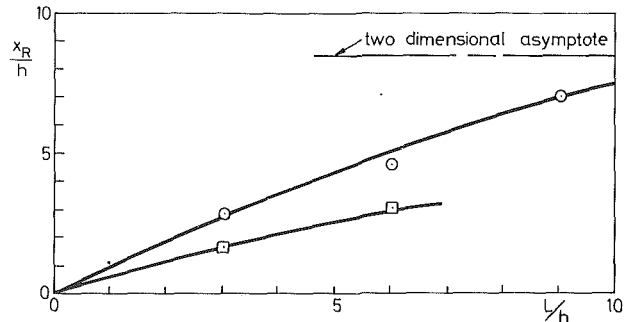Fig. 18 Mean flow recovery downstream of reattachment (a) three-dimensional flow, data of Logan and Lin [25]; $h/\delta = 0.11$, $L/h = 3$; (b) two-dimensional block, Schofield et al. [32]; $h/\delta = 0.11$.

Robins [28] present evidence of strong vorticity shed from the upper edge of a cube set at 45 deg to the flow. These delta-wing-type vortices were much stronger than the vortices formed with the cube set square on to the flow.

The flow immediately behind a three-dimensional prism is not simple. The flow sketched in Fig. 14(b) relies heavily on data presented by Hunt et al. [21] and the theoretical analysis of three-dimensional separation developed by Hornung and Perry [29]. The downstream flow is driven by a pair of vortices originating on the wall (number 8 in the figure) and a horseshoe vortex held in the flow behind the prism (number 7). Between them they produce the wall flow pattern that Perry and Hornung have named as "owl face of the second kind." The vortices nearest the wall (number 7) produce a mean flow along the centerline plane that flows down the centerline streamsurface into the wall. However, further away from the wall mean flow in the centerline streamsurface deflects upwards, away from a separation line (S_4) under the influence of vortex pair number 8. Thus downstream of a three-dimensional prism it should be possible to measure both upwash and downwash on the centerline, depending on where the measurement is taken. Significant swirl has been measured by Peterka and Cermak [30] at $x/h = 80$ downstream of a three-dimensional prism and Colmer [31] measured mean upwash on the centerline downstream of an aircraft hangar. Laterally outside the separation streamsurface S_3 is the vortex system emanating from in front of the prism. Estimated relative lateral positions of all vortices (at a distance 7h downstream of a prism) are shown in Fig. 14(c). These positions have been inferred from the swirl measurements of Castro and Robins [28] and the position of the
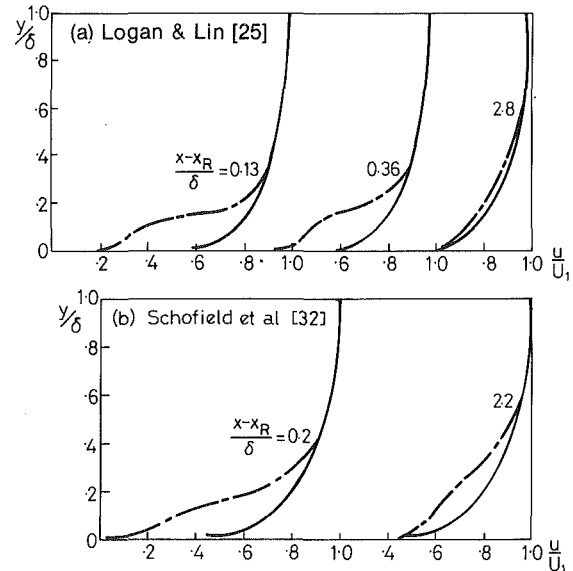
attachment line A_1 in their surface flow visualization patterns. There are no published data on the behavior of the two small corner vortices 4 and 6 (Fig. 14(a)),[7] and because of this the position shown for vortex 3 in Fig. 14(c) is rather speculative.

The length of separated flow behind a three-dimensional obstacle is much smaller than the length behind a similar two-dimensional obstacle of the same relative height. This is because a large proportion of the upstream flow goes around a three-dimensional object rather than over it. Also the complex eddy structure that forms in front of a three-dimensional prism is relatively large (Fig. 14(a)) which puts the stagnation streamline high up on the front face. Only the flow above the stagnation streamline can go over the prism and because the streamline deflections required in this case are small, the flow quickly reattaches to the roof of the prism. Reattachment occurs even on the roof of a cube which contrasts strongly with the two-dimensional case where a significantly longer streamwise length is required for flow reattachment to the roof. Thus for flow over nearly all three-dimensional prisms a streamline will separate horizontally from the trailing edge of the prism's roof and, as discussed previously, this results in a small length of separated flow behind the prism. The actual separated length (say along the centerline) will be determined by the interaction between the flow over the prism and the flow around the prism. Limited data for length of separated flow along the centerline as a function of aspect ratio are presented in Fig. 15. As the aspect ratio increases the vortex system around the prism moves laterally away from the centerline and the separated length on the centerline increases.

Wall Flow Recovery. Figure 16 compares centerline wall shear recovery for three-dimensional prisms of different aspect ratios with the corresponding recovery for the two-dimensional case. They form an ordered set with expected characteristics. The wall shear recovers more quickly behind a three-dimensional obstacle due to the additional mixing induced by the streamwise vortices. As the aspect ratio of a prism increases the streamwise vortices move away from the centerline decreasing the mixing along it, which results in a slower recovery rate for the skin friction.

The rate at which the depth of new wall turbulence is generated on the centerline downstream of reattachment is shown in Fig. 17. The data correlate with:

---

[7]And therefore they have not been shown on Fig. 14(c).
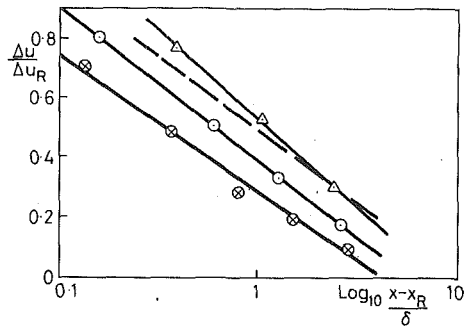
Fig. 19 Decay of maximum deficit in mean velocity. Data of Logan and Lin [25]; $\otimes$, $L=3h$, $\dfrac{\Delta\mu}{\Delta\mu_R} = -0.46\,\mathrm{Log}\,\dfrac{x-x_R}{\delta} +.28$; $\odot$, $L=6h$, $\dfrac{\Delta\mu}{\Delta\mu_R} = -0.52\,\mathrm{Log}\,\dfrac{x-x_R}{\delta} +0.39$; $\triangle$, $L=9h$, $\dfrac{\Delta\mu}{\Delta\mu_R} = -0.59\,\mathrm{Log}\,\dfrac{x-x_R}{\delta} +0.54$; — — —two-dimensional rate of decay.
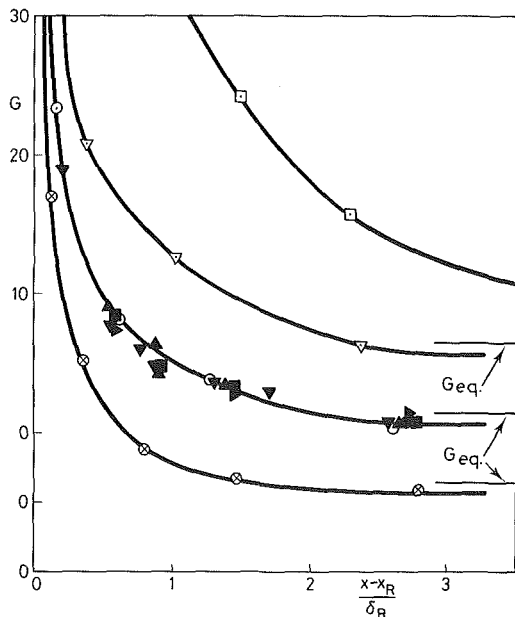
Fig. 20 Distributions of G on the centerline downstream of reattach-ment. Data of Logan and Lin [25]; h/δ = 0.11; $\otimes$**, L/h = 3;** $\odot$**, L/h = 6;** ∇**, L/h = 9;** $\Box$**, two-dimensional data (Schofield et al. [17]). Solid symbols for flow behind two prisms in line.**

$$\log_{10} \delta i/z = 0.63\,\log_{10}\,(x-x_R/z)+0.74; \quad \delta i/z = 5.5(x-x_R/z)^{0.63}$$

$$(4)$$

which is compared in Fig. 17 with equation (3). These two equations imply that the depth of new wall turbulence grows about four times faster (i.e., 5.5/1.29) downstream of a three-dimensional prism than in the two-dimensional flow.

Outer Flow Recovery. The rates at which mean profiles in two and three-dimensional flows return to equilibrium conditions differ greatly due to the presence of streamwise vortices in the three-dimensional flow. Figure 18 compares mean profiles downstream of a narrow three-dimensional prism with those downstream of a corresponding two-dimensional block. At $(x-x_R/\delta) = 2.8$ downstream of the three-dimensional prism the recovery of the mean velocity profile is well advanced over the whole profile, whereas the corresponding profile for the two-dimensional flow is still badly distorted. A broader view of relative recoveries is given by the rate of decay of the maximum deficit in mean velocity, Fig. 19. The decay rates for three-dimensional prisms are again semi-logarithmic and the rates increase as the aspect ratio of the prism decreases. Note that the centerline decay rate for a prism 9h wide is little different from the two-dimensional rate.

These limited three-dimensional data have been reduced to
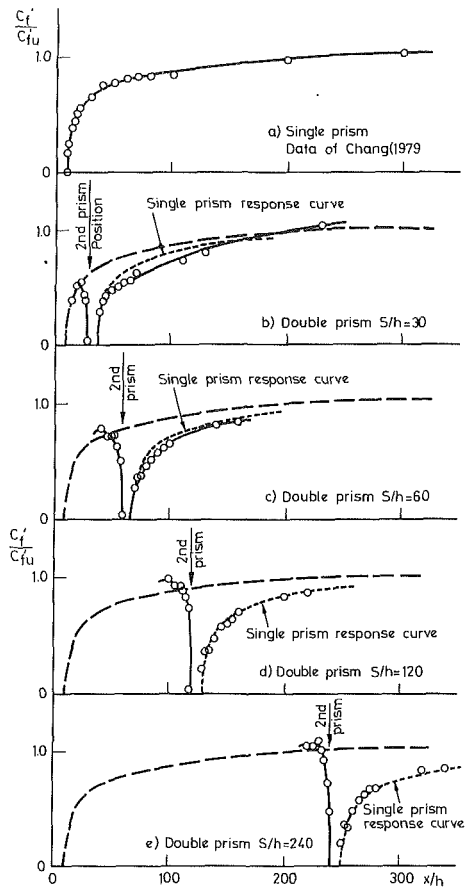
Fig. 21 Skin friction recovery downstream of a pair of two-dimensional obstacles. Pipe flow data of Chang [32,33], h/R = 0.105.
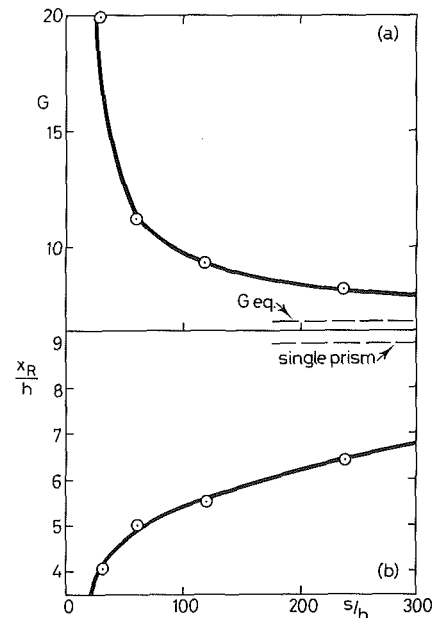
Fig. 22 Length of separated flow behind the second of a pair of two-dimensional obstacles. Pipe flow data of Chang [32,33], h/R = 0.105.

yield the integral parameter G, Fig. 20. The recovery rate of the full velocity profile downstream of three-dimensional prisms is seen to be much faster than for the two-dimensional case. Note that G also undershoots the equilibrium value but again does it much earlier than in the two-dimensional case.

Flow Over Multiple Objects

The factors determining the development of a shear layer

over a multiple array are the same as those for single prisms with the additional complication of flow interaction around and between prisms. The limited data available are sufficient to illustrate the nature and degree of these interactions.

Two-Dimensional Prisms. For the simple case of a pair of two-dimensional objects in line, the recovery of the flow after each obstacle depends solely on the normal mixing processes of a turbulent boundary layer. Figure 21 shows wall shear recoveries for increasing spacings between a pair of two-dimensional obstacles. For the two smaller spacings the flow distortion caused by the first obstacle modifies the shear stress recovery after the second obstacle. The difference in recovery rate is quite small[8] and decreases as the spacing between the obstacles increases, disappearing completely at a spacing of about 120h. This result implies that the distortion in the large scale eddies in the outer boundary layer is no longer important (at least to wall shear recovery) ten layer thicknesses downstream of the perturbation. The shear stress overshoot that can be noted in front of the second obstacle results from a reduction in flow area, and consequent flow acceleration, caused by the axisymmetric prism on the wall of the pipe.

Figure 22 shows the variation in separated length behind the second obstacle and compares this with the value for G of the boundary layer at the position of the second obstacle. The data suggest that quite small distortions cause quite large

---

[8]This behavior is similar to the measured decay of turbulence intensity for these flows (see Chang et al. [33]).
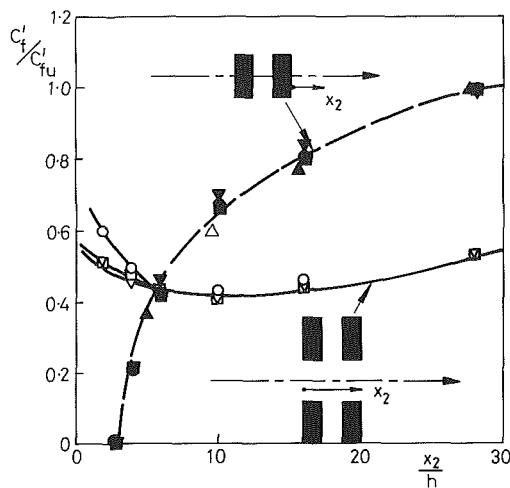
Fig. 23 Skin friction recovery around arrays of three-dimensional prisms. Results of Logan and Lin [25]; four prism array: ⊙, S/h = 3; ▽, S/h = 6; ▣, S/h = 9; — — —two prism array.

changes in the length of downstream separated flow. At a spacing of 240h the separated length behind the second obstacle is considerably different from the single prism length and yet the profile distortion as measured by G is quite small.

Three-Dimensional Prisms. The results for two three-dimensional prisms separated in the main flow direction are quite different from the two-dimensional results. The centerline recovery downstream of the second three-dimensional prism is quite unaffected by the presence of the first prism, as shown by the inner flow recovery, plotted on Figs. 16 and 23 and the overall flow recovery, plotted on Fig. 20. The invariance of these recoveries implies that outer flow distortion caused by the upstream obstacle has a negligible effect on centerline recovery downstream of the second obstacle. Second, it shows that there has been no important interaction between the streamwise vortices shed from the upstream prism with those shed from the downstream prism. The effect of prism width on the recovery rates behind pairs of three-dimensional prisms is the same as the isolated case (see Schofield and Logan [5]). Recovery rates at points well removed laterally from the centerline of the flow could be quite different from single prism results due to the presence of the additional vortices shed from the upstream prism. There is, however, no published data for this region.

Complex Arrays. Figure 23 shows skin friction distributions for flow between two similar pairs of prisms. Surface oil flow patterns show (see Schofield and Logan [5]) that at large streamwise spacings of the obstacles the wall flow spreads laterally into the region between the prisms whereas at small spacings it cannot. The difference causes variations in skin friction distribution upstream of the second row of prisms as shown in Fig. 23. However, downstream of the second line of prisms in all three cases the centerline flow is governed by the same set of vortices and the skin friction distributions are identical. The form of the recovery is quite different from the recovery on the prism centerline and arises from the different vortex spacings and origins driving each recovery. The recovery behind the single pair of prisms is dictated by the four vortices generated immediately behind the second prism whereas the recovery between a double pair is affected by many vortices including those shed from in front of the prisms.

Figure 24 shows the wall recovery behind a prism downstream of a gap[9] in a two-dimensional wall of the same height. It is obvious that compared with an isolated prism the upstream gap retards the wall recovery downstream of a prism. However, the spacing between the prism and gap has a negligible effect on this recovery. Figure 25 shows that the distortion to the

---

[9]Photographs of the wall flow patterns are shown in Schofield and Logan [5].
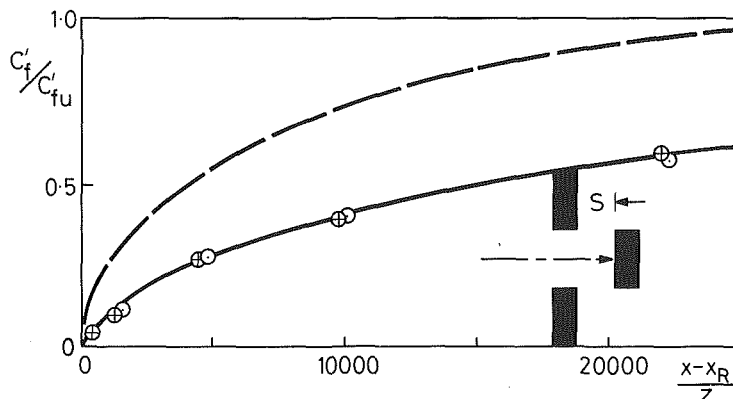
Fig. 24 Wall recovery downstream of a prism behind a gap. Data of Logan and Lin [25]; h/δ = 0.11, L/h = 6, gap = 6h; ⊙, S/h = 3; △, S/h = 6; — — —recovery downstream of a similar isolated prism.
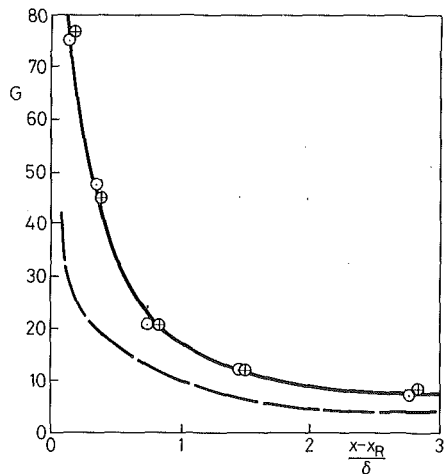
Fig. 25 Outer flow recovery downstream of a prism behind a gap. Data as for Fig. 24.

centerline mean profile, as measured by G, has been significantly increased by the presence of an upstream gap and the spacing between the gap and the prism again has little effect. These results suggest that the effect of the upstream gap is mainly attributable to vortices shed from the upstream gap edges flowing over the downstream prism.

Conclusions

The responses of a wide range of turbulent shear layers to an obstacle attached to a wall can be collapsed if appropriate non-dimensionalizing length scales are used. Different scales apply to the perturbation and recovery region of the flow and to the inner and outer portions of the layers.

Recovery after a two-dimensional obstacle relies on the usual turbulent mixing processes in a shear flow, and this is intrinsically slower than the recovery after a three-dimensional obstacle, which is driven by streamwise vortices generated by the obstacle.

The data available for flow around multiple objects demonstrate that interaction between a pair of two-dimensional objects has a second order effect on the downstream recovery. Recovery at any point downstream of a pair of three-dimensional prisms depends critically on the relative proximity to streamwise vortices in the flow.

References

1 Hoerner, S., *Fluid-Dynamic Drag*, Published by the author, 1958.

2 Good, M. C., and Joubert, P. N., "The Form Drag of Two-Dimensional Bluff-Plates Immersed in Turbulent Boundary Layers," *J. Fluid Mech.*, Vol. 31, 1968, pp. 547–582.

3 Castro, I. P., "Relaxing Wakes Behind Surface-Mounted Obstacles in Rough Wall Boundary Layers," *J. Fluid Mech.*, Vol. 93, 1979.

4 Ranga-Raju, K. G., Loeser, J., and Plate, E. J., "Velocity Profiles and Fence Drag for a Turbulent Boundary Layer Along Smooth and Rough Flat Plates," *J. Fluid Mech.*, Vol. 76, 1976, pp. 383–399.

5 Schofield, W. H., and Logan, E., "Viscous Flow Around Wall Mounted Obstacles," Aeronautical Research Laboratories, Aero Propulsion Report 172, Australian Department of Defence, 1987.

6 Sami, S., and Lui, W. H., "Confined Shear Layer Approaching a Stagnation Point," *Proc. 14th Midwestern Mechanics Conference*, Vol. 8, 1975, p. 497.

7 Durst, F., and Rastogi, A. K., "Turbulent Flow Over Two-Dimensional Fences," *Proc. 2nd Symp. on Turb. Shear Flows*, London, 1979, pp. 16–30.

8 Holdredge, E. S., and Reed, B. H., "Wind Tunnel Studies of Pressure and Velocity Distribution," Summary Report No. 2 to the Dept. of the Army from Texas Agricultural and Mech. College System. Contract No. DA-18-1064-404-CML-189, 1956.

9 Clauser, F. J., "Turbulent Boundary Layers in Adverse Pressure Gradients," *J. Aero. Sci.*, Vol. 21, 1954, pp. 91–108.

10 Bradshaw, P., and Wong, F. Y. F., "The Reattachment and Relaxation of a Turbulent Shear Layer," *J. Fluid Mech.*, Vol. 52, 1972, pp. 113–135.

11 Schofield, W. H., "Two-Dimensional Separating Turbulent Boundary Layers," *AIAA J.*, Vol. 24, No. 10, pp. 1611–1621.

12 Simpson, R. L., ASME JOURNAL OF FLUIDS ENGINEERING, Vol. 103, 1981, p. 521.

13 Petryk, S., and Brundrett, E., "Recovery of a Turbulent Boundary Layer Disturbed by a Single Roughness Element," University of Waterloo, Mech. Eng. Res. Report. No. 4, 1967.

14 Tillmann, W., "Investigations of Some Particularities of Turbulent Boundary Layers on Plates," *U & M* 6627, 1945. Translation; British Rep. and Transl. CGD-497, MAP-VG 34-T, 1946.

15 Phataraphruk, P., "Measurement and Prediction of Flow Past a Single Roughness Element in Turbulent Pipe Flow," M.Sc. thesis Arizona State University, 1976. See also Phataraphruk, P., and Logan, E., *Proc. ASME–CSME Appl. Mech. Conf.* (1979), pp. 187–196.

16 Chang, J. E., "Perturbation of Turbulent Pipe-Flow by Roughness Elements," M.Sc. thesis, 1978, Arizona State University

17 Siuru, W. D., and Logan, E., "Response of a Turbulent Pipe Flow to a Change in Roughness," ASME J. FLUIDS ENGINEERING, Vol. 99, 1977, pp. 548–555.

18 Schofield, W. H., Barber, D. S., and Logan, E., "Turbulent Boundary Layer Flow Through a Gap in a Wall Mounted Roughness Element," ASME J. FLUIDS ENGINEERING, Vol. 103, 1981, pp. 97–103.

19 Connihan, J., "An Experimental Investigation of the Wake Behind a Two-Dimensional Block and Behind a Cube in a Simulated Boundary Layer Flow," Central Electricity Research Laboratories (UK) Lab. Note RD/L/N 115/71, 1971.

20 Nigim, H. H., and Cockrell, D. J., "Effects Caused by Small Discrete Two-Dimensional Roughness Elements Immersed in Turbulent Boundary Layers," *J. Fluid Mech.*, 1985, Vol. 153, pp. 17–30.

21 Hunt, J. C. R., Abell, C. J., Peterka, J. A., and Woo, H., "Kinematical Studies of the Flows Around Free or Surface-Mounted Obstacles, Applying Topology to Flow Visualization," *J. Fluid Mech.*, Vol. 86, 1977, pp. 179–200.

22 Werle, H., and Gallon, M., "Sillages de Cheminees, Faisceaux Turbulaires, Grilles et Turbomachines. Quelques Exemples de Visualisations Bases sur l'Amalogie Hydraulique," *La Houille Blanche*, No. 4, 1973, pp. 339–360.

23 Perry, A. E., and Hornung, H., "Some Aspects of Three-Dimensional Separation, Part II: Vortex Skeletons," *Z. Flugwiss. Weltraumforsch*, 8, Heft 3, 1984, pp. 155–160.

24 Fairlie, B. D., "Flow Separation on Bodies of Revolution at Incidence," *Proc. 7th Australasian Conference on Hydraulics and Fluid Mechanics*, Brisbane, 1980, p. 338.

25 Logan, E., and Lin, S-H., "Wakes from Arrays of Buildings," *NASA Cr-170666*, 1982.

26 Thwaites, B. (ed.), *Incompressible Aerodynamics*, O.U.P., 1960.

27 Woo, H. G. C., Peterka, J., and Cermak, J. E., "Wind Tunnel Measurements in Wakes of Structures," Colorado State Univ. Rept. CER7575-76 HGCW-JAP-JEC40, 1976.

28 Castro, I. P., and Robins, A. G., "The Flow Around a Surface-Mounted Cube in Uniform and Turbulent Streams," *J. Fluid Mech.*, Vol. 79, 1977, pp. 307–335.

29 Hornung, H., and Perry, A. E., "Some Aspects of Three-Dimensional Separation, Part 1: Stream Surface Bifurcations," *Z. Flugwiss. Weltraumforsch.* 8, Heft 2, 1984, 1984, pp. 77–87.

30 Peterka, J. A., and Cermak, J. F., "Turbulence in Building Wakes," *Proc. 4th Int. Conf. on Wind Effects on Buildings and Structures*, Heathrow, 1979, C.U.P.

31 Colmer, M. J., "Some Full Scale Measurements of the Flow in the Wake of a Hangar," R. A. E. TR70202, 1970.

32 Schofield, W. H., Barber, D. S., and Logan, E., 1981, "Turbulent Boundary Layer Flow Through a Gap in a Wall Mounted Roughness Element," ASME JOURNAL OF FLUIDS ENGINEERING, Vol. 103, pp. 97–103.

33 Chang, J. E., "Perturbation of Turbulent Pipe Flow by Roughness Elements," M.Sc. thesis 1978, Arizona State University.

34 Chang, J. E., Logan, E., Alexander, M. B., and Camp, D. W., "The Response of a Disturbed Pipe Flow to an Upstanding Roughness Element," *Proc. 2nd Symp. on Turb. Shear Flows*, Long. 1979, pp. 6–18.

A Study on Vortex Shedding From Spheres in a Uniform Flow

H. Sakamoto

H. Haniu

Department of Mechanical Engineering,
Kitami Institute of Technology,
Hokkaido, 090 Japan

Vortex shedding from spheres at Reynolds numbers from 3×10^2 to 4×10^4 in a uniform flow was investigated experimentally. Standard hot-wire technique were used to measure the vortex shedding frequency from spheres in a low-speed wind tunnel. Flow-visualization experiments were carried out in a water channel. Important results from the investigation were that (i) the variation of the Strouhal number $St (= fD/U_0,$ U_0: freestream velocity, D: diameter of the sphere, f: vortex shedding frequency) with the Reynolds number ($= U_0 D/\nu$, ν: kinematic viscosity) can be classified into four regions, (ii) the Reynolds number at which the hairpin-shaped vortices begin to change from laminar to turbulent vortices so that the wake structure behind the sphere is not shown clearly when a Reynolds number of about 800 is reached, and (vi) at Reynolds numbers ranging from 8×10^2 to 1.5×10^4, the higher and lower frequency modes of the Strouhal number coexist.

1 Introduction

Wakes behind a sphere are encountered so frequently in engineering applications that large amounts of research have been conducted and massive amounts of data have been accumulated. Many reports which concern only the vortex shedding frequency from a sphere have been published. Möller (1938) has measured the frequency of vortex shedding from a sphere by flow-visualization in the Reynolds number range of $10^3 < Re < 10^4$. He demonstrated that there are two Strouhal numbers in this Reynolds number range, i.e., a high-mode and a low-mode Strouhal number. Cometta (1957) measured the Strouhal number in the ranges of $10^3 < Re < 4 \times 10^4$ using a hot-wire technique, and also found the same phenomenon. However, his conclusion that the two Strouhal numbers exist only when the sphere has a certain diameter is not very convincing from a hydrodynamic viewpoint. Achenbach (1974) experimentally investigated on the Strouhal number by means of both the flow-visualization and hot-wire techniques, and demonstrated that the values for the higher frequency mode of Strouhal numbers showed the same results as those obtained by Möller at Reynolds numbers lower than $Re = 3 \times 10^3$. He also clarified that, when the Reynolds number is above 6×10^3, the vortices with the lower frequency mode are periodically shed from the sphere, and this phenomenon could be observed as far as the upper critical Reynolds number of 3.7×10^5. However, his measurement which used a hot-wire probe attached to the surface of the sphere failed to detect any low-mode Strouhal number in the range of the Reynolds numbers lower than $Re = 6 \times 10^3$. In other words, he did not succeed in confirming the existence of two Strouhal numbers in the ranges of $10^3 < Re < 10^4$, as was reported by Möller and Cometta. Recently, Kim and Durbin (1988) performed experiments in

the wakes of spheres for the Reynolds number range of $5 \times 10^2 < Re < 6 \times 10^4$, and they found two distinct modes of unsteadiness which were associated with the small scale instability of the separating shear layer and with the large scale instability of the wake. In particular, they demonstrated that the higher frequency was detected only in the region of the wake immediately downstream of the sphere when the Reynolds number exceeded 800. Taneda (1978) examined the wake configuration formed behind a sphere in the range of $10^4 < Re < 10^6$ by means of the flow-visualization methods. He clarified that the Strouhal number which was based on the wavelength caused by the alternate fluctuations of the wake was about 0.2 in the ranges of $10^4 < Re < 3 \times 10^5$. Majumdar and Douglas (1970), Calvert (1972), Magarvey and Bishop (1961), and Pao and Kao (1977) also have measured the frequency of the vortex shedding from the sphere. However, they only measured in some limited ranges for the Reynolds number, and their results did not always coincide with one another.

Thus, many reports have been made concerning the vortex shedding from a sphere. The results, however, are fairly different from report to report. Therefore, it must be pointed out that reliable values for the Strouhal number in a wide range of the Reynolds numbers have not yet been found. This is due to the fact that the formation mechanism of the vortex for the change of the Reynolds number has not been properly clarified. Considering these facts described above, the present study is intended to measure the Strouhal number of a sphere by means of the hot-wire measurement for a wide range of the Reynolds numbers, including a low Reynolds number with a very low stream velocity. In particular, it closely examines the relationship between the wake configuration behind the sphere and the frequency of vortex shedding, observing its form through the flow visualization and concentrating on the high-mode and low-mode Strouhal numbers in the range of the Reynolds number of $10^3 < Re < 10^4$.
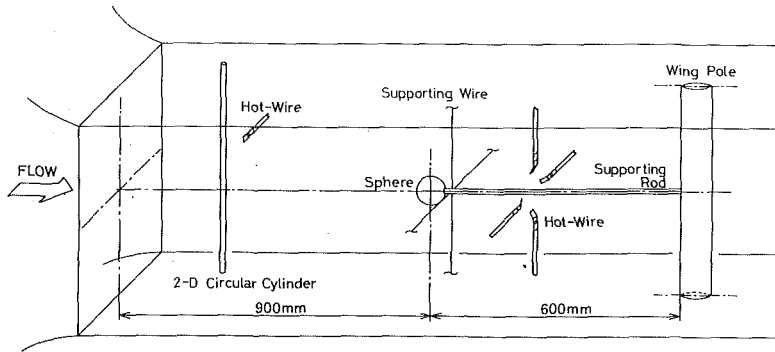
Fig. 1 Sketch of sphere placed in test section
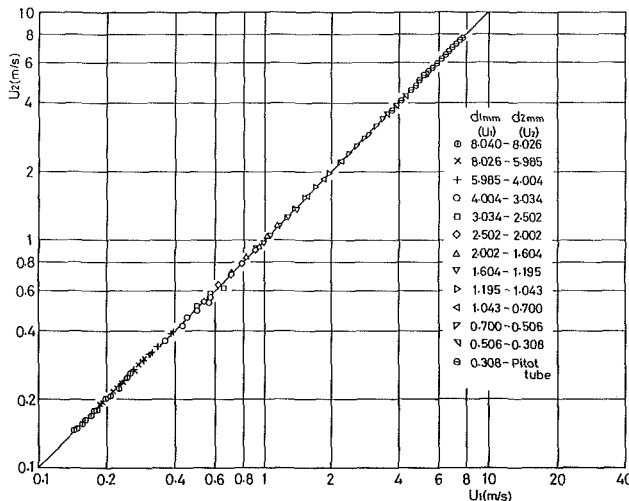
Fig. 2 Calibration curve for velocity estimated from vortex shedding frequency of 2-D circular cylinder. (Uncertainty in U_1 and U_2: Less than ±2 percent.)

2 Experimental Apparatus and Procedure

2.1 Experimental Apparatus. The experiments were carried out in a suction-type wind tunnel with a 30cm by 30cm, 4m long working section and in a recirculating water channel whose test section had dimensions of 30cm in width, 40cm in depth, and 1.5m in length. Measurements for the frequency of the vortex shedding from the sphere were made by means of a hot-wire technique in the wind tunnel. The observation of the wake configuration for the sphere and a part of the measurements for the vortex shedding frequency were made in the water channel. The diameters, D, of the spheres selected for measurement were 20, 30, 40, and 60mm. The Reynolds number, $Re(= U_0D/\nu)$, was varied not only by varying the freestream velocity, U_0, but also by using spheres of different diameters. Thus, the upper Reynolds number obtained in the present experiment was 5.5×10^3 in the water channel and 4×10^4 in the wind tunnel, respectively. In order to avoid interference by the support system, the sphere was supported at its rear by a small steel rod 3mm in diameter and 0.6m in length. The rod was fixed horizontally on the centerline of the test section by four fine cross-wires, 0.2mm in diameter, and a wing pole as shown in Fig. 1. The turbulence level in the freestream was below 0.2 percent at the wind tunnel and 0.1

percent at the water channel, and they did not vary noticeably with the change of the free-stream velocity.

2.2 Measurement of Freestream Velocity. In the wind tunnel test, it was difficult to measure the freestream velocity using a pitot tube or hot-wire anemometer when the velocity was lower than about 3 m/s. Therefore, when the free-stream velocity was lower than 3 m/s, it was estimated by using Roshko's formula (Roshko, 1956) based on the vortex shedding frequency of the regular mode from a two-dimensional circular cylinder mounted at the upstream of the test section. Since the vortex shedding of the regular mode from a two-dimensional circular cylinder is generated only in the limited range of the Reynolds numbers of $40 < Re < 160$, thirteen cylinders whose diameters ranged from 0.3mm to 8mm were employed in accordance with the change in the freestream velocity. Also, in order to avoid the effect of the boundary layer along the tunnel wall on the frequency of vortex shedding from the circular cylinders, disks which were 7 to 10 times larger than the diameter of the cylinder were attached on both ends. Figure 2 shows a calibration curve for the velocity estimated from the vortex shedding frequency of the cylinder for each diameter. The calibration curve was produced using the following method: first, a relation between the reference velocity, U_2, measured by a pitot tube and U_1 obtained using the cylinder with a diameter of 0.308mm was found, secondly, a relation between the reference velocity, U_2, using the cylinder with the diameter of 0.308mm and U_1 using the cylinder with a diameter of 0.506mm was found, and then the relations between the reference velocity, U_2, and U_1 obtained using each cylinder were successively found in the same manner. Also, the circular cylinder which had been placed upstream of the sphere was removed from the test section during the measurement for the vortex shedding frequency of the sphere to avoid any influence on the flow characteristics. Furthermore, the freestream velocity in the test section of the water channel was obtained by measuring the time of travel for hydrogen bubbles passing a distance of 1m.

2.3 Flow Visualization. Flow around the spheres in the water channel were visualized using uranine dye. The injection of the uranine dye into the water channel was performed using a stainless tube with a diameter of 1mm. After the uranine dye was injected for specified period of time, the stainless tube was removed from the test section in order to avoid any disturbance generated by it.

————— **Nomenclature** —————

D = diameter of sphere
F = nondimensional frequency of vortex shedding $= fD^2/\nu$

Re = Reynolds number $= U_0D/\nu$
St = Strouhal number $= fD/U_0$
T = taking time for shedding of one hairpin-shaped vortex

U_0 = free stream velocity
f = frequency of vortex shedding
ν = kinematic viscosity of fluid
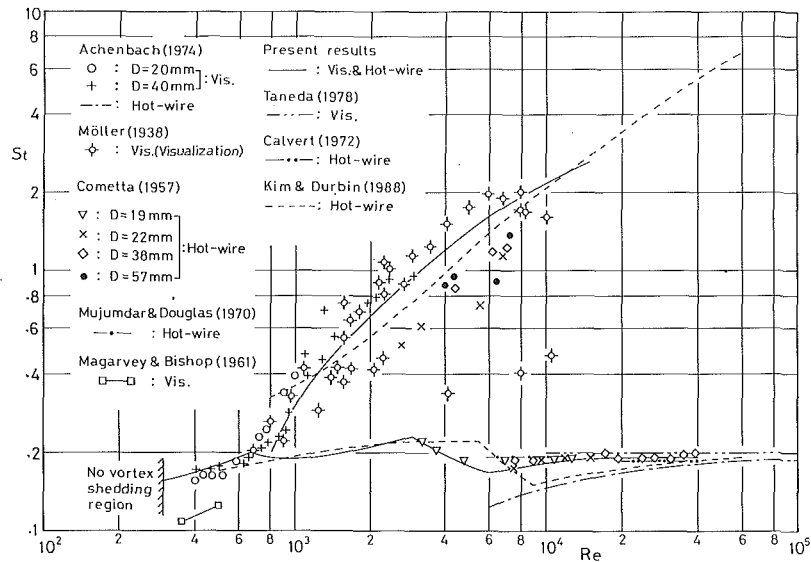
Fig. 3 Various data for Strouhal number of sphere [1-8]
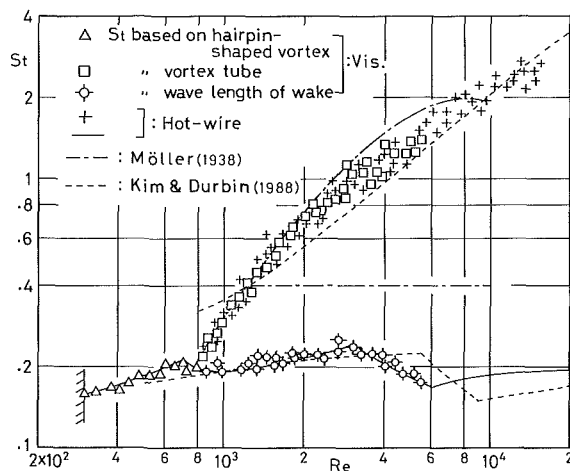
Fig. 4 Distribution of low-mode and high-mode Strouhal number versus Reynolds number. (Uncertainty in St: less than ±3.5 percent, in Re: less than ±2 percent.)

2.4 Measurement of Frequency. The frequency of vortex shedding from the sphere placed in the wind tunnel was determined on the basis of the power spectrum analysis of the fluctuating velocity detected by a hot-wire probe mounted in the wake behind the sphere. The position of the hot-wire probe (which was somewhat dependent on the Reynolds number) was determined by observing visualized patterns in the wake; it was in the range of (3 to 4)D from the rear surface of the sphere. In order to avoid any influence from the hot-wire probe on the wake characteristics of the sphere, the prongs were made of pino-wire with a tip diameter of about 0.1mm and a length of 60mm; they were bent to a 135 degree angle and both ends of the hot wire were soldered of them. Also, the vortex shedding frequency of the sphere mounted in the water channel was determined by measuring the time necessary for a sequence of fifty vortices to be shed.

3 Results and Discussions

Figure 3 shows the main results that have been reported concerning the Strouhal number of a sphere St($=fD/U_0$, where f is the frequency of the vortex shedding, and D the diameter of the sphere). The hairpin-shaped vortices begin to be periodically shed when the Reynolds number reaches about

Re = 350 ~ 400 (about Re = 300 in the present experiment). The values of these Strouhal numbers up to Re = 10^3 are almost the same as those previously recorded except for those obtained by Magarvey and Bishop (1961). In the range of the Reynolds numbers between 10^3 and 10^4, two Strouhal numbers exist, namely, the high-mode and low-mode Strouhal number. The high-mode Strouhal number obtained by Möller (1938) exists up to Re = 10^4, but Cometta's result (Cometta, 1957) exists only up to Re = 7.4×10^3; these values are somewhat lower than those given by Möller. On the other hand, results obtained by Kim and Durbin (1988) show clearly that the two distinct modes exist simultaneously in the Reynolds number ranges of $8 \times 10^2 <$ Re $< 6 \times 10^4$. In particular, it is noticeable that the high-mode St exists up to Re = 6×10^4. However, those values are somewhat lower than those obtained by Möller (1938) in the Reynolds number range of $10^3 <$ Re $< 10^4$. Also, the value for the low-mode St obtained by Möller is a constant value of 0.4 in this range. When the Reynolds number is higher than about 10^4, Mujumdar and Douglas (1970), Taneda (1978), and Calvert (1972) have reported that there exists only the low-mode St and it is a constant value of approximately St = $0.19 \sim 0.2$, although the results of Kim and Durbin (1988), and Achenback (1974) are a little different. Thus, in a range where Re is comparably small (Re $< 10^3$) or large (Re $> 10^4$), the Strouhal number obtained by the above researchers are mostly similar, while in the intermediate range of $10^3 <$ Re $< 10^4$, the values differ considerably from researcher to researcher.

Figure 4 shows the values for the Strouhal number, St, obtained by the flow-visualization and hot-wire measurements in the present experiment at the range of the Reynolds numbers lower than Re = 1.5×10^4, in which there exist two Strouhal numbers, namely, the high-mode and low-mode St. When a Re of 300 is reached, the hairpin-shaped vortices begin to be periodically shed from the sphere, forming a laminar wake as shown in Fig. 8(b). When the Re is further increased to 800, the wake flow becomes turbulent with alternate fluctuations so that the configuration of the vortices is not clearly discernible as is shown in Fig. 8(d). In the Reynolds number range of 800 < Re < 10^4, the Strouhal number determined on the basis of the wave length and velocity of the turbulent wake estimated from visual observation shows almost the same low-mode St as that which was obtained by the hot-wire measurements. This suggests that the low-mode St is caused by the progressive wave motion of the wake with alternate fluctuations. Moreover, when the Re is greater than 800, the pulsation is seen on

the vortex sheet separated from the sphere surface, and in accordance with its pulsation, the cylindrical vortices (defined as vortex tube in the present study) begin to be periodically shed, covering the vortex formation region as shown in Fig. 6(a). The values for the Strouhal number determined based on the frequency of the vortex tube shedding estimated from the visual observation are very similar to the high-mode St obtained by Möller (1938) and Achenbach (1974). This suggests
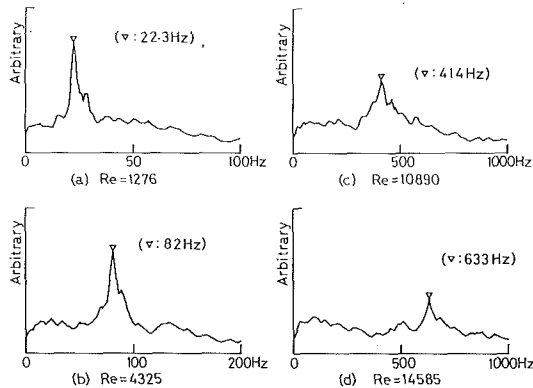
Fig. 5 Power spectrum of fluctuating velocity based on vortex tube shedding (Uncertainty in Re: less than ±2 percent.)
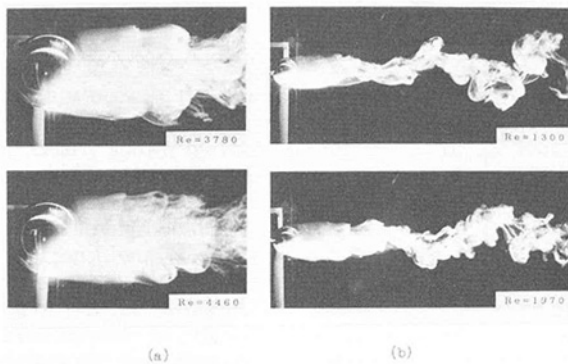
Fig. 6 Visualized observation for wake behind sphere (a) Vortex tubes, (b) large-scale vortices. (Uncertainty in Re: less than ±2 percent.)

that the high-mode St is based on the shedding of the vortex tube generated by the pulsations of the vortex sheet. Also, when a hot-wire is placed in the extreme neighborhood of the sphere, the frequency of the vortex tubes shed from the sphere could be detected by the spectrum analysis of the fluctuating velocity as shown in Fig. 5. On this spectrum analysis of the fluctuating velocity, the frequency of the large-scale vortex shedding which is considerably lower compared with that of the vortex tube is cut off by an analogue high-pass filter in order to appear only as a prevailing frequency based on the vortex tube. However, when the Re is larger than 1.5×10^4 in the present experiment, no clear peak is observed by the spectrum analysis because the fluctuation energy becomes extremely small. Furthermore, the energy level of the fluctuating velocity based on the shedding of the vortex tubes is much smaller than that based on wave motion of the wake with alternate fluctuations as shown in Fig. 6(b). Accordingly, it would be safe to consider that the unsteady flow around the sphere is mainly caused by the wave motion of the wake with alternate fluctuations when the Re is larger than about 800. On the other hand, Kim and Durbin (1988) have found that the high-mode St exists in the wide range of the Reynolds numbers between 8×10^2 and 6×10^4, and then it is associated with the small scale instability of the separating shear layer. However, they did not make clarifications concerning the structure of the small scale instability of the separating shear layer. Perhaps, it could be concluded that the vortex tube is formed by the small scale instability of the separating shear layer.

Figure 7 shows the Strouhal number based on the hairpin-shaped vortex and the large-scale vortex shedding obtained by the hot-wire measurement, namely the low-mode St, with the Reynolds number. We classified these results into regions I ~ VI and transitional regions A ~ C, taking into account the change in the Strouhal number corresponding to the Reynolds number. The following is a rough description of each region in terms of the relationship between its St and the configuration of the wake.

(i)Region I(300 < Re < 420)

According to Taneda's flow-visualization experiment in the range of 5 < Re < 300 (Taneda, 1956), when the Re is over 130, faint periodic pulsative motion with a very long period occurs at the rear of the vortex-ring formed behind the sphere, forming
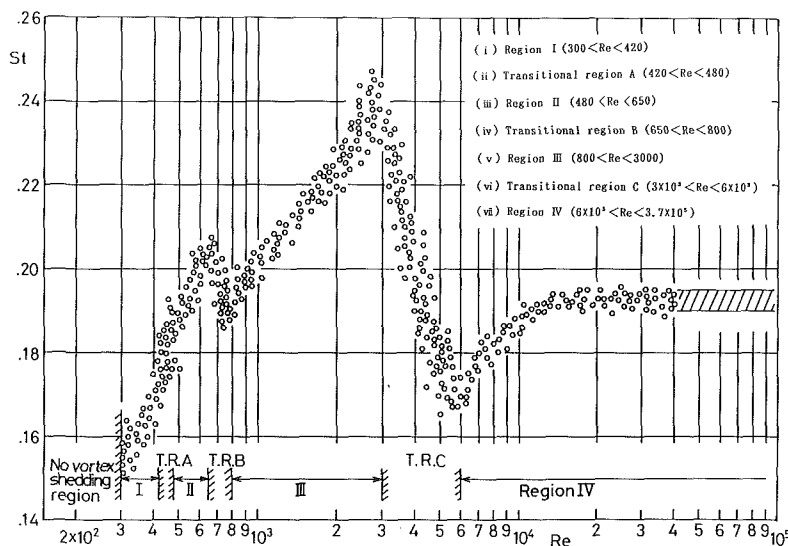
Fig. 7 Strouhal number based on hairpin-shaped vortex and large-scale vortex shedding versus Reynolds number. For further information, see the caption of Fig. 4.
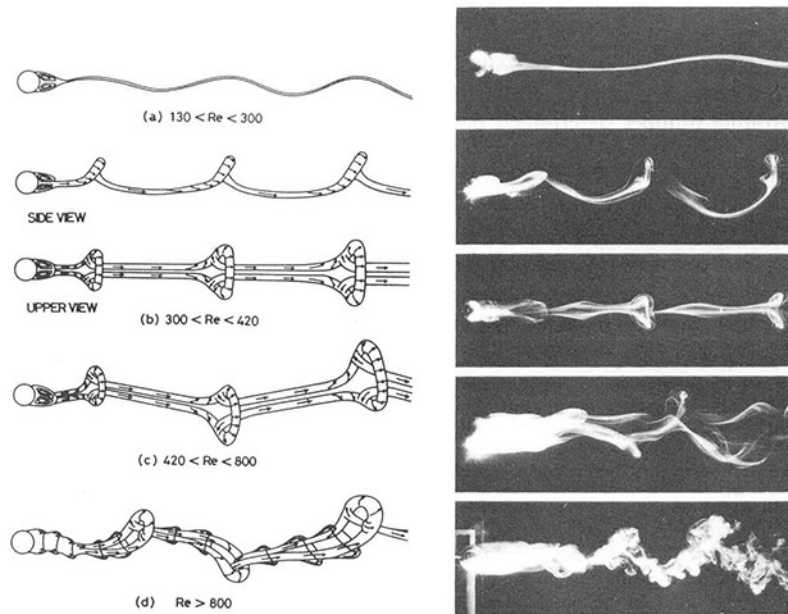
Fig. 8   Patterns of vortex shedding in wake at each region. For further information, see the caption of Fig. 6.
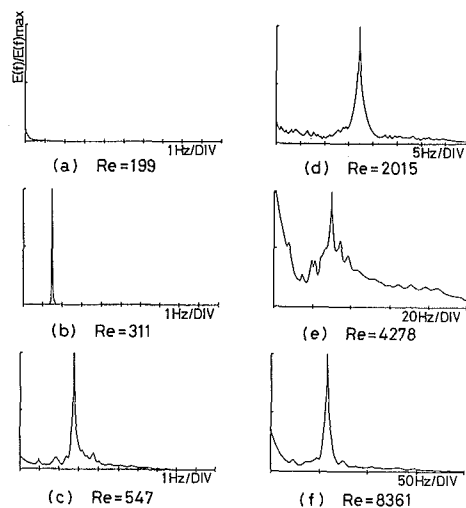
Fig. 9   Power spectrum of fluctuating velocity based on hairpin-shaped vortex and large-scale vortex shedding at each region. For further information, see the caption of Fig. 5.

a wavelike wake as shown in Fig. 8(a). Taneda also has reported that this phenomenon continues until a Reynolds number of about 300 is reached. Achenbach (1974), on the other hand, has reported that the wavelike wake turns into a so-called hairpin-shaped vortex when a Reynolds number of about 400 is reached. But, the present results which were measured by means of visual observation and spectrum analysis of the fluctuating velocity, as shown in Fig. 9 show that the hairpin-shaped vortex begins to be shed when the Re exceeds 300 (as shown in Fig. 9(a), there is no spectral peak in the power spectrum distribution when the Re is lower than 300). Taneda's report that a wavelike wake continues to be seen as far as the range of Re = 300 justifies the present results in which the hairpin-shaped vortices begin to be shed at Re = 300.

Figure 10 shows the waveform of the fluctuating velocity which was detected by the four hot-wire probes (CH 1~4) set at intervals of 90° on the circumference of a circular facet at a right angle in the wake behind the sphere. As the figure clearly shows, the amplitude of the waveform of the fluctuating
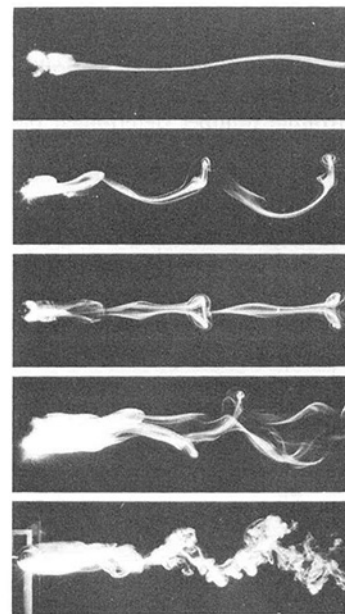
Fig. 10   Waveform of fluctuating velocity detected by four hot-wires equally spaced on circumference of a circle. (Uncertainty in bias error: less than ±3 percent.)
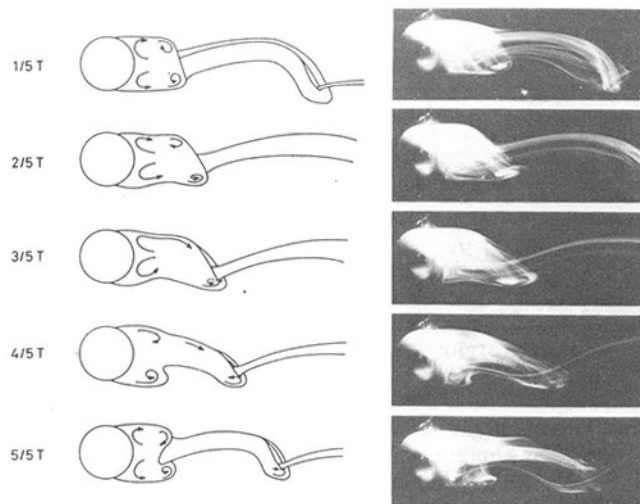
Fig. 11 Shedding pattern of hairpin-shaped vortex with respect to one period

Fig. 12 Non-dimensional frequency versus Reynolds number. (Uncertainty in F: less than ± 3.5 percent, in Re: ± 2 percent.)

velocity detected by CH 4 is much larger than the others; this suggests that the hairpin-shaped vortices flow out in one direction from the point near where CH 4 is set. Moreover, the power spectrum as shown in Fig. 9(b) and the waveform of the fluctuating velocity as shown in Fig. 10(a) suggest that the hairpin-shaped vortices are periodically shed in what is called a regular mode with regularity in strength and frequency. This is perhaps because the energy entraining into the vortex formation region is very regularly supplied, stored and emitted, as is clearly shown by the shedding system of the vortex as shown in Fig. 11 (where T is the time when one vortex is shed). This also explains why the vortices shed in succession are of the same strength and frequency.

(ii) Transitional Region A (420 < Re < 480)

When the Re is greater than 420, the amplitude and waveform of the fluctuating velocity based on the shedding of the hairpin-shaped vortices begin to be generated with irregularity, and their shedding direction oscillates intermittently from left to right. The vortex shedding of the regular mode which existed in the previous region is also seen intermittently. Perhaps, regular and irregular modes appear alternately and last for a certain period of time in this region.

(iii) Region II (480 < Re < 650)

When the Re exceeds 480, the waveform of the fluctuating velocity based on the shedding of the hairpin-shaped vortices becomes irregular as shown in Fig. 10 (b). In other words, the shedding pattern of the vortex is always in the irregular mode. This is perhaps because the supply, storage, and emission of energy within the vortex formation region becomes imbalanced so that the strength of the vortices shed from the formation region differs from one another. Furthermore, as is shown in Fig. 10(b), the amplitude of the fluctuating velocity differs from CH 1~4 as time passes; this suggests a change in the shedding point of the hairpin-shaped vortices. Accordingly, as Taneda (1978) has pointed out, the vortices are shed as if the facet including the vortices are rotating slowly and irregularly about an axis through the center of the sphere in the direction of the undisturbed flow.

Figure 12 shows the nondimensional frequency $F(=fD^2/\nu)$ in terms of the frequency, f, of the hairpin-shaped vortex shedding. According to Roshko (1974), Karman's vortex streets begin to be shed with regularity from a two-dimensional circular cylinder when a Re of about 40 is reached, and the shedding pattern becomes irregular when the Re approaches 160. Roshko has also reported that the non-dimensional frequency $F(=fd^2/\nu$, where d is the diameter of the cylinder) is distributed on different straight lines in the regular and irreg-

ular modes with the Reynolds number. The nondimensional frequency, F, of the vortices shed from the sphere shows a similar property, i.e., it is regular in region I and irregular in region II, while the transitional region A is somewhere between the two regions. Furthermore, when the Re exceeds 650, the shedding pattern of the vortices is fairly different from that region II so that the non-dimensional frequency is distributed on a different straight line as shown in Fig. 12.
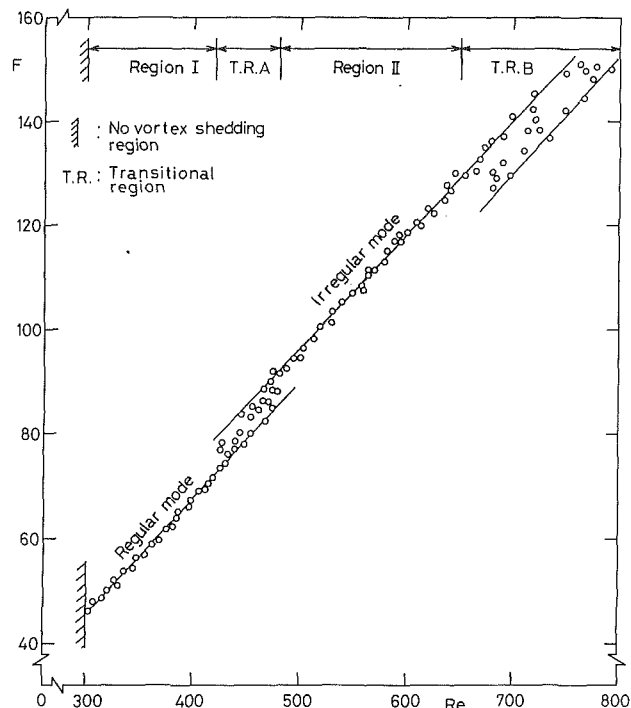
(iv) Transitional Region B (650 < Re < 800)

As has already been previously described, when the Re exceeds 650, the cylindrical vortex sheet separated from the sphere surface shows pulsation, and the vortex tubes begin to be periodically shed in accordance with the pulsation as if covering the vortex formation region. These vortices diffuse near the sphere without retaining a cylindrical form. Also, the large-scale vortices flowing out from the formation region begin to change from laminar to turbulent vortices, thus obscuring their form.

(v) Region III (800 < Re < 3000)

When the Re exceeds 800, some of the vortex tubes formed by the vortex sheet separating from the sphere surface flow into the vortex formation region at its rear end, while others are shed in small vortex loops. Some of the small vortex loops move downstream, intricately intertwining with the large-scale vortices which alternatingly flow out from the formation region as is shown in Fig. 6(b). As is clearly shown by the fluctuating waveform of Fig. 10(c), the point where the large-scale vortices are shed rotates slowly and irregularly since the amplitude detected by each hot-wire probe CH differs as the time elapses. And the large-scale vortices move away from the sphere rotating at random about an axis parallel to the flow through the center of the sphere; this has already been pointed out by Taneda (1978). The shape of the large-scale vortex has not yet been clarified. However, Perry et al. (1981) investigated the structure of turbulent wake behind an axis-symmetrical blunt body using a flying hot-wire apparatus, and clarified that it has the same structure as a hairpin-shaped vortex that is formed behind the blunt body in the low Reynolds numbers. Therefore, the large-scale vortex that flows out with alternate fluctuations away from the sphere may have the same structure as the

Table 1 Classification of vortex shedding pattern with respect to change of Reynolds number

	No vortex shedding	Periodic vortex shedding							No periodic vortex shedding
Vortex shedding	No vortex shedding	Periodic vortex shedding							No periodic vortex shedding
Orientation of the wake		One way	Rolling	Irregular rotation of the plane containing the wake					Rotation about streamwise axis
Configuration of the wake	Fixed vortex ring	Vortex loop		Vortex tube / Waving wake					Ω-shaped vortex
Region	No vortex shedding region	1	A	II	B	III	C	IV	V
Reynolds number	10^2 2 3	4 5 6 7 8 9 10^3		2	3	4 5 6 7 8 9 10^4	2	3	4 5 6 7 8 9 10^6	

hairpin-shaped vortex observed in the low Reynolds number region ($Re < 800$) whose model is shown in Fig. 8(d). Its structure has not yet been sufficiently clarified through detailed measurement concerning the structure of the turbulent wake behind the sphere. Therefore, it would be desirable to continue the investigation of the structure of the turbulent wake behind the sphere.

(vi) Transitional Region C ($3 \times 10^3 < Re < 6 \times 10^3$)

As is shown in Fig. 7, the Strouhal number decreases rapidly when the Re exceeds 3×10^3. In this region no evident peak is seen in the power spectrum distribution which has widely scattered values as shown in Fig. 9(e). This is perhaps because the vortex sheet which separates from the sphere surface changes from laminar to turbulent flow. The Strouhal number becomes smaller perhaps because it takes a longer time to store the necessary energy for the shedding of large-scale vortices since the dissipation of the energy increases in the turbulent vortex sheet so that the energy entraining into the vortex formation region decreases.

(vii) Region IV ($6 \times 10^3 < Re < 3.7 \times 10^5$)

When the Re exceeds 6×10^3, the vortex sheet separating from the surface of the sphere becomes completely turbulent. As is the case with the Karman vortex streets formed behind a two-dimensional body, the vortices shed from the formation region become stabilized when transition from laminar to turbulent flow occurs in the separated shear layer. Therefore, the alternate shedding of the large-scale vortices from the formation region also shows the pseudoregularity as is seen in the power spectrum distribution of Fig. 9(f). The Strouhal number based on the frequency of vortex shedding increases again with an increase in the Reynolds number until it becomes constant at $0.19 \sim 0.195$ when the Re exceeds 2×10^4. For the Strouhal number in the region where the Re is over the upper value of 4×10^4 studied in the present experiment, Achenbach has already reported that the Strouhal number which has a constant value of 0.19 exists as far as the region of $Re = 3.7 \times 10^5$; this is called the upper critical Reynolds number. Further, Taneda (1978) has clarified that when the Re exceeds the upper critical Reynolds number, the vortex sheets separating from the sphere flow out and roll up to form a pair of streamwise vortices without the periodic vortex shedding.

Table 1 shows the results of the present experiment for Reynolds numbers ranging from 10^2 to 4×10^4, together with those obtained by Achenbach (1974), Kim and Durbin (1988), and Taneda (1978) at Reynolds numbers higher than $Re = 4 \times 10^4$. The table shows the change in the shape of vortices formed behind a sphere, the change in the direction of vortex shedding, and the existence or non-existence of the periodic vortex shedding in accordance with the change in the Reynolds number.

4 Conclusions

The present study has described an experimental investigation of the Strouhal number of the spheres by means of both the flow-visualization and hot-wire measurements in a wide range of the Reynolds number including the very low freestream velocity. The results led to be the following conclusions.

(1) The variation of the Strouhal number with the Reynolds number can be classified into four regions, and the relationship between the Strouhal number and the configuration of the wake in each region is clarified.

(2) When a Reynolds number exceeds about 300, the hairpin-shaped vortices begin to be periodically shed with regularity in its strength and frequency, forming laminar vortices until a Reynolds number is about 800.

(3) When a Reynolds number exceeds about 800, the hairpin-shaped vortices begin to change from the laminar to turbulent vortices with alternate fluctuations, this pattern of vortex shedding continues as far as the region of $Re = 3.7 \times 10^5$, which is called the upper critical Reynolds number.

(4) When a Reynolds number exceeds 800, the vortex tubes begin to be periodically shed covering the vortex formation region, in accordance with the pulsation of the vortex sheet separated from the surface of the sphere.

(5) At the Reynolds number ranging from 8×10^2 to 1.5×10^4 (which is some lower than that obtained by Kim and Durbin, 1988), the higher and lower frequency modes of the Strouhal number, which are caused by the periodic fluctuation in the vortex tube formed by the pulsation of the vortex sheet separated from the surface of the sphere and in the turbulent wake with progressive wave motion respectively, are coexisted.

References

Achenbach, E., 1974, "Vortex Shedding from Spheres," J. Fluid Mech., Vol. 62, Part 2, pp. 209-221.

Calvert, J. R., 1972, "Some Experiments on the Flow Past a Sphere," Aero. J. Roy. Aero. Soc., Vol. 76, pp. 248-250.

Cometta, C., 1957, "An Investigation of the Unsteady Flow Pattern in the Wake of Cylinders and Spheres Using a Hot Wire Probe," Div. Engng, Brown University, Tech.Rep. WT-21.

Kim, K. J., and Durbin, P. A., 1988, "Observation of the Frequencies in a Sphere Wake and Drag Increase by Acoustic Excitation," Phys. Fluids, Vol. 31, No. 11, pp. 3260-3265.

Magarvey, R. H., and Bishop, R. L., 1961, "Wakes in Liquid-Liquid Systems," Phys. Fluids, Vol. 4, No. 7, pp. 800-805.

Möller, W., 1938, "Experimentelle Untersuchung zur Hydromechanik der Kugel," Phys. Zeitschrift, Vol. 39, No. 2, pp. 57-80.

Mujumdar, A. S., and Douglas, W. J. M., 1970, "Eddy Shedding from a Sphere in Turbulent Free Streams," Int. J. Heat Mass Transfer, Vol. 13, pp. 1627-1629.

Pao, H. P., and Kao, T. W., 1977, "Vortex Structure in the Wake of a Sphere," Phys. Fluids, Vol. 20, No. 2, pp. 187-191.

Perry, A. E., and Watmuff, J. F., 1981, "The Phase-Averaged Large-Scale Structures in Three-Dimensional Turbulent Wakes," J. Fluid Mech., Vol. 103, pp. 33-51.

Roshko, A., 1956, "On the Development of Turbulent Wakes from Vortex Streets," N.A.C.A Report, No. 1191.

Taneda, S., 1978, "Visual Observations of the Flow Past a Sphere at Reynolds Numbers Between 10^4 and 10^6," J. Fluid Mech., Vol. 85, Part 1, pp. 187-192.

Taneda, S., 1956, "Studies on the Wake Vortices (III). Experimental Investigations of the Wake Behind a Sphere at Low Reynolds number," Res. Inst. Appl. Mech., Kyushu University, Fukuoka, Japan, Report No. 4, pp. 99-105.

An Experimental Study of the Flow Downstream of a Circular and Tapered Cylinder

P. A. Eibeck

Assistant Professor,
Mechanical Engineering Department,
University of California at Berkeley,
Berkeley, CA 94720

The flow downstream of the intersection of both a circular and a tapered cylinder with a flat plate was examined at $Re_D = 1.3 \times 10^5$ using surface visualization, five-hole-probe anemometry, and flow visualization. A pair of large, counter-rotating swirls with common flow away from the wall and with centers over one diameter away from the wall was present downstream of both obstacles. It is suggested that the large, swirling pair are formed in the near wake of an obstacle that is exposed to symmetrical channel flow. A pair of smaller counter-rotating vortices with common flow toward the wall was observed embedded in the wall-shear flow eight diameters downstream of the tapered cylinder. This implies that the legs of the horseshoe vortex system only propagate downstream behind the streamlined obstacle shape.

Introduction

An experimental investigation of the flow downstream of a circular and a tapered cylinder has been performed to determine the extent that flow features are modified by the shape of the obstacle. At the junction of an obstacle and a flat plate, a horseshoe vortex system is formed and may propagate downstream, thereby influencing wall properties such as heat transfer and skin friction for considerable streamwise distances. Fisher and Eibeck [1] have shown that the heat transfer along the flat plate downstream of a nominally two-dimensional tapered cylinder is increased by as much as 50 percent at a Reynolds number (Re_D) of 7.7×10^4, whereas a circular cylinder augments heat transfer at most by 32 percent. The current study was undertaken to determine whether a vortex pair from the horseshoe vortex propagates downstream and, hence, could influence the heat transfer in one or both of the obstacle configurations.

The physical mechanism responsible for the formation of a horseshoe vortex is the adverse pressure-gradient present at the leading edge of an obstacle. The mean shear within the approaching boundary layer is skewed, or deflected, by the transverse pressure gradient. The boundary layer separates and rolls up to form the primary, or root, vortex along with multiple smaller vortices at the leading edge. The fluid away from the junction is undisturbed and wraps the vortex system around the obstacle, resulting in streamwise vortex legs. The resulting vortex pattern resembles that of a horseshoe, hence the name horseshoe vortex. The primary parameters that govern the dimension and number of vortices in the leading edge are the

Reynolds number based on obstacle diameter, Re_D, and the ratio of the boundary-layer-thickness to the obstacle-dimension (δ_{99}/D). Other parameters that influence the horseshoe-vortex system include the approach boundary-layer shape, the obstacle's geometry, and the angle-of-attack of the obstacle.

The horseshoe vortex system consists of four distinct regions: the leading edge, the junction, the trailing edge, and the region downstream of the obstacle. The flow in the leading edge is dominated by the strong pressure gradient and may contain multiple vortices that are unsteady and cyclic in nature [2-4]. As the vortex legs wrap around the sides of the obstacle, they enter the junction region. At this point the root vortex is growing in size, and depending on the length of the obstacle, it may be influenced by the stress-induced streamwise vorticity present in a streamwise corner. The third region, which occurs at the trailing edge of the obstacle, is where the vortex legs separate from the obstacle and interact with the obstacle's wake. The flow in the final region, downstream of the obstacle, includes the interactions of the vortex trailing legs with the wall and the obstacle's wake. This region is not well understood, and is the subject of this investigation.

The objective of this research has been to illuminate the general features of the horseshoe vortex system downstream of a nominally two-dimensional obstacle in a turbulent boundary layer, contrasting the flow structure produced by a circular cylinder to that associated with a streamlined cylinder. In addition, the presence of a dominant vortex pair located above the wall with opposite vorticity to the horseshoe vortex legs is also investigated. This paper reports surface visualization and mean velocity measurements behind two-dimensional obstacles placed in a wind-tunnel at $Re_D = 1.3 \times 10^5$ and $\delta_{99}/D = .63$. In addition, flow visualization performed in a water channel at $Re_D = 615$ are presented to highlight the flow structure in the near wake.

Background

Flow visualization studies have been performed in an effort to understand the formation process of horseshoe-vortex systems, primarily focusing on the leading edge of an obstacle. Schwind [2], Peake and Galway [3], and Peake et al. [4] demonstrated that the flow is unsteady and cyclic in the leading edge region under laminar boundary-layer conditions. If the approaching boundary layer is turbulent, East and Hoxey [5] show that the leading edge flow is likely to be steady. Belik [6] found that the turbulent flow separation region can be characterized by the Reynolds number based on boundary layer thickness, enabling predictions of the position of the separation line upstream of the cylinder. Baker studied the leading edge region of cylinders interacting with both laminar [7] and turbulent boundary layers [8] in detail, and postulated that four counter-rotating vortices are formed at the intersection of a turbulent boundary layer and a cylinder. Goldstein and Karni [9] postulate that a large vortex with a diameter roughly equal to the boundary layer thickness is present, as well as smaller, more vigorous, vortices. Surface visualization of the flow downstream of a cylinder that spans the height of a fully-developed channel was performed by Ichimiya et al. [10]. At low Reynolds numbers ($Re_D < 750$), stable laminar twin vortices were observed trailing from the obstacle, whereas at higher Reynolds numbers the vortices became irregular.

Detailed experimental measurements have been made within the junction flow region of a semi-infinite body. Moore and Forlini [11] observed secondary flow velocities downstream of the leading edge of a Rankine half-body showing the streamwise vorticity associated with the horseshoe vortex. Extensive mean-velocity and turbulence measurements were made in cross-planes at a number of streamwise locations along a semi-infinite body by Shabaka and Bradshaw [12], McMahon et al. [13, 14], and Hsing and Teng [15]. The flows have well-defined longitudinal vortices with maximum spanwise velocities equal to 10 to 15 percent of the freestream. Mehta [16] notes that the strength and size of the secondary flow in the junction flow of a semi-infinite body depends on the leading-edge shape, with blunter shapes resulting in stronger vortices.

Experimental studies of the flow around finite chord obstacles have also been conducted. Dickinson [17] observed separated flow caused by the vortex secondary flow using oil dot and oil film visualization on the endwall around and downstream of an airfoil. Velocity profiles in the region of the appendage did not reveal the expected horseshoe vortex and the author suggests the vortex is flattened in the forward region of the appendage and expects the vortex to move up in the boundary layer and become rounded in the aft portion of the appendage and in the wake. Merati et al. [18] measured mean velocities and turbulence quantities near the leading edge, in the junction region, and three chord lengths downstream of a modified NACA 0020 airfoil at a chord Reynolds number of 3.07×10^5. A strong secondary flow was observed which was dominated by a horseshoe root vortex and persisted downstream.

Mean-flow measurements of surface pressure and velocity distributions around the base of a streamlined cylinder were made by Pierce and Harsh [19] at test conditions of $Re_D = 1.8 \times 10^5$ and $\delta_{99}/D = 0.64$, similar to the conditions of the current experiment. Secondary flow in the 100 percent chord transverse plane reveals a horseshoe vortex leg with an approximate size of $0.3D$ positioned at roughly $z/D = 0.8$. Vorticity calculations show that the vortex decreased in strength from $120s^{-1}$ at 43 percent chord to $45s^{-1}$ at 100 percent chord. Pierce and Harsh suspect that two additional smaller vortices exist closer to the floor, but the vortices could not be resolved by the measurement grid.

Experimental Methods

Wind Tunnel Measurements. Measurements of velocity vectors and surface flow visualization were made in an open-circuit, subsonic wind tunnel located in the Fluid Mechanics Research Laboratory at UC Berkeley. The wind tunnel consists of a centrifugal blower and diffuser, a stagnation chamber followed by multiple screens, a contraction section, a test section, and a discharge duct. The test section is 347 cm long, with an 81.3 cm by 81.3 cm square cross-section. The boundary layer, which develops along the polished wooden floor of the test section, is tripped by a 0.1 cm-high and 1 cm-wide phenolic strip. Reference velocity was measured 25 cm from the tunnel entrance, and due to the displacement of the boundary layer development in the constant cross-section tunnel, the free stream velocity increased from nominally 25 m/s at the reference position to 28 m/s at the exit of the wind tunnel. The velocity only varied by 3 percent between the reference location and the leading edge of the obstacles.

Two different flow obstacles were used in the experiments; a circular cylinder and a tapered cylinder. The tapered cylinder consists of a circular leading edge with two tangential flat sides that terminate in a sharp trailing edge. The tapered cylinder has a chord of 19.4 cm, with the diameter of the circular section identical to that of the cylindrical obstacle, which is 8.3 cm. Both obstacles span the height of the tunnel, have an aspect ratio (H/D) of 10, and are positioned on the centerline with their leading edge 231 cm downstream of the boundary-layer trip. The dimensions of the obstacles and their position in the wind tunnel were chosen to achieve, as closely as possible, geometric and dynamic scaling with the experiments conducted by Pierce and Harsh [19].

Figure 1 is a schematic of the test section, showing the reference coordinate system and the location of the obstacles and the measurement stations. The origin of the streamwise coordinate (i.e., $x=0$) occurs at the leading edge of the obstacle.

Experiments were conducted at a Reynolds number based on cylinder diameter (Re_D) of 1.3×10^5. Two dimensional boundary-layer characteristics were determined by making velocity profile measurements with a pitot probe at $x = 25$ cm with no obstacle present. A slight non-uniformity in the spanwise profile of the boundary layer was observed. In the vicinity of $z/D = 0.5$, a localized momentum deficit was present, with the boundary layer thickness roughly 25 percent greater than the rest of the boundary layer. Measurement of the velocity vectors with the five-hole probe in the cross-sectional plane of

---

————— Nomenclature ———————————

D = obstacle diameter, or maximum width

H = height of test section and obstacle

P_i = pressures measured from five-hole probe; $i = 1, 5$

Re_D = Reynolds number based on obstacle diameter: $\dfrac{U_{ref}D}{\nu}$

Re_θ = Reynolds number based on boundary layer momentum thickness: $\dfrac{U_{ref}\theta}{\nu}$

U_{ref} = reference free-stream velocity

x = streamwise direction

y = normal distance

z = spanwise distance

α = pitch angle

β = yaw angle

δ_{99} = boundary layer thickness

θ = boundary-layer momentum thickness

ν = kinematic viscosity

Fig. 1 Schematic of the wind-tunnel's test section

Fig. 2 Five-hole probe used to measure mean velocity vectors

Fig. 3 Schematic of water channel facility

the flat plate flow revealed secondary velocities less than 3 percent of the free-stream velocity, which is within the measurement uncertainty of the probe. There was no evidence of any organized flow structure that would be causing the local momentum deficit.

The boundary-layer thickness at the centerline was 5.7 cm with a momentum thickness Reynolds number (Re_θ) of 9700, a shape factor of 1.35, and a flat-plate velocity profile that matches the familiar law-of-the-wall and law-of-the-wake. Assuming the standard growth rate of a turbulent boundary layer, $\delta/x \propto Re_x^{-1/7}$, the boundary layer thickness at $x=0$ was estimated, giving a δ_{99}/D of 0.63 at the leading edge of the obstacle.

The surface flow downstream of the obstacles was visualized using the ink-trace/oil-of-wintergreen technique developed by Langston and Boyle [20]. Drafting film with an array of ink dots is attached to the floor of the wind-tunnel. Just prior to turning on the flow, a thin film of oil-of-wintergreen is sprayed over the surface to dissolve the ink dots. Once the flow begins, the dissolved ink flows in response to the wall-shear forces as the oil-of-wintergreen rapidly evaporates. Assuming the displacement of the ink particles is locally parallel to the mean velocity vector of the air just above the surface, the final ink traces represent the local velocity and wall-shear direction along the surface.

The distribution of velocity vectors, static pressure, and total pressure was measured at three streamwise locations, $x/D = 4, 6,$ and 8 (see Fig. 1), using a United States Sensor directional five-hole probe shown in Fig. 2. The 0.32 cm diameter probe was calibrated in a jet calibration facility following the method recommended by Treaster and Yocum [21]. The calibration was performed over a velocity range of 8 to 30 m/s and for pitch (α) an yaw (β) angles between $-30°$ and $20°$. The pressure differences $P_1 - P_2$, $P_1 - P_3$, $P_1 - P_4$, $P_1 - P_5$, $P_1 - P_{atm}$, and $P_1 - P_{static}$ were measured using a pressure transducer (Validyne, Model DP45) sampled by an IBM PC/AT and a scanivalve (Scanivalve, Model JS4-48). The following coefficients were then calculated:

$$C_{yaw} = (P_2 - P_3)/(P_1 - P_{avg}) \qquad (1)$$

$$C_{pitch} = (P_4 - P_5)/(P_1 - P_{avg}) \qquad (2)$$

$$C_{static} = (P_1 - P_{static})/(P_1 - P_{avg}) \qquad (3)$$

$$C_{total} = (P_1 - P_{total})/(P_1 - P_{avg}) \qquad (4)$$

where

$$P_{avg} = (P_2 + P_3 + P_4 + P_5)/4 \qquad (5)$$
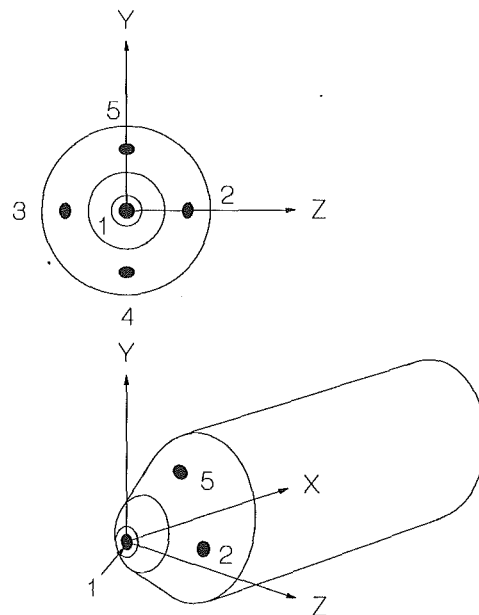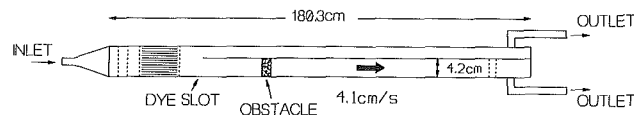
Plots of C_{yaw} versus C_{pitch}, C_{total} versus α, and C_{static} versus α, were generated using a spline-fit routine to produce continuous curves. These calibration curves were then stored in the form of a look-up table for use during data acquisition.

Measurements using the five-hole pressure probe in the wind-tunnel were automated. The data acquisition system consisted of four Validyne pressure transducers (Models DP45 and DP15) sampled by the IBM PC/AT. Each pressure signal was sampled at 800 Hz over a period of 10 seconds. The probe's position was controlled by two driving stepper-motors with a minimum spanwise motion of 0.16 μm, and vertical motion of 3.2 μm. The probe's traverse was limited to distances less than 20 cm from the wall due to restraints of the probe. No measurements were made closer than 0.5 cm to the wall to avoid wall-interference effects on the signal.

Velocity measurements were normalized by U_{ref}, which is the free-stream velocity measured near the entrance of the test section ($x/D = -25$). The probe can measure flow angle with an uncertainty of ±5 deg and magnitude of velocity within ±6 percent. Velocity measurements made by a pitot probe and the five-hole probe within the undisturbed two-dimensional boundary-layer match within the uncertainty.

Water Channel Visualization. Flow visualization using dye and hydrogen bubbles was performed in a water channel to better observe the flow in the separated region. The water channel, shown in Fig. 3, has a 36.6 cm by 6.7 cm cross section and a total length of 180.3 cm. An overhead tank provides a constant head for the gravity-fed water supply into the flow channel. Water enters the horizontal channel through a 5 cm ID pipe and is smoothly expanded to the full channel cross-section in a diverging section that has side walls machined to a fifth-order polynominal shape designed to minimize separation. A combination of five screens and a 7.6 cm length of honeycomb are located downstream of the diverging section to produce a uniform flow across the channel cross-section.
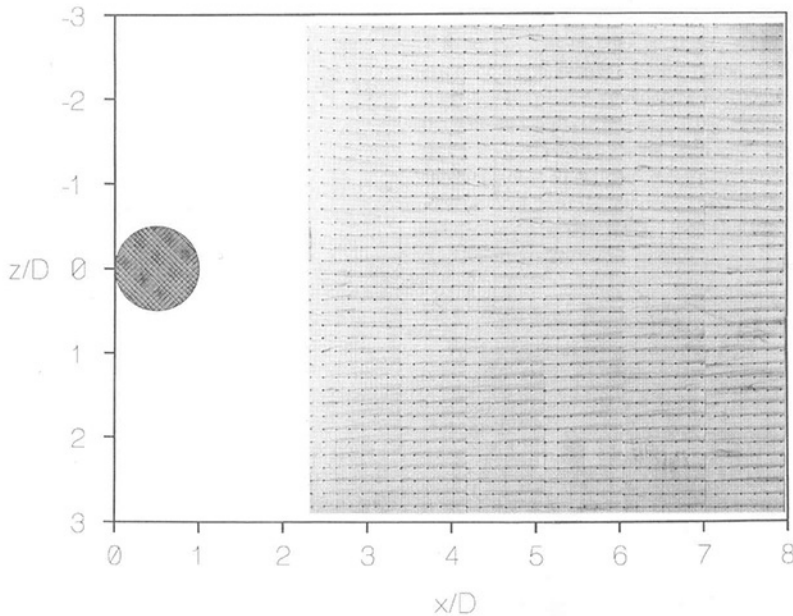
Fig. 4 Surface visualization downstream of the circular cylinder using the ink-dot technique, $Re_D = 1.3 \times 10^5$

All walls of the channel are fabricated from 1.9 cm thick plexiglass. The aspect ratio of the test section can be varied using a splitter plate, which was positioned 4.2 cm from the floor for these tests. Hydrogen bubbles and dye sheets were used to establish the uniformity of flow entering the test section and passing over the splitter plate.

Dye or hydrogen bubbles were introduced to observe the flow past two different obstacles with cross-sections geometrically scaled to those used in the wind-tunnel experiments. The diameter of the circular cylinder and the maximum width of the tapered cylinder are 1.5 cm. Both obstacles have a height of 4.2 cm, and hence, an aspect ratio of 3. Uniform sheets of neutrally buoyant dye were produced by dye wells equipped with slits spanning the width of the channel. In addition, small dye ports were used to introduce localized sources of dye. Hydrogen bubbles were generated by a 25 μm nichrome wire strung spanwise between two support rods of variable height projecting from the floor.

Results

Wind Tunnel Tests. Visualization of the surface shear direction behind both the blunt and the tapered obstacle was performed to find evidence of the horseshoe vortex legs. Reynolds number was $Re_D = 1.3 \times 10^5$, and the visualization was made over the region $2.3 \leq x/D \leq 7.8$ and over a spanwise extent of $-2.9 \leq z/D \leq 2.9$, as indicated in Fig. 1.

Figure 4 shows the ink streaks produced by the circular cylinder. The surface direction of the flow on most of the plate is toward the centerline, with a more pronounced effect as streamwise distance increases. Note that little evidence of a recirculation region can be observed since the beginning of the visualized region at $x/D = 2.3$ is downstream of the separation region behind the cylinder. The shear direction observed in Fig. 4 is consistent with the oil flow surface visualization of a circular cylinder in the subcritical regime at $Re_D = 2.0 \times 10^5$ shown by Schewe [22]. Figure 2 of [22] reveals a separation line at approximately $z/D = 0.6$ which is not revealed by our ink-dot technique.

If the primary root vortex of the horseshoe vortex system remains near the wall downstream of the obstacle, the two legs would form a counter-rotating vortex pair with surface shear vectors pointing away from the centerline. Therefore, the surface shear directions indicated in Fig. 4 do not reveal any

evidence of the horseshoe vortex pair near the wall downstream of the circular cylinder.

Figure 5(a) presents the ink streaks observed downstream of the tapered cylinder. The beginning of the visualization region is just downstream of the obstacle's trailing edge and a small recirculating region can be seen. On the centerline after the near wake is a source point, indicating a location of flow downward toward the wall and then outward in all directions. Downstream of this point is a growing region in which the surface flow direction is away from the centerline. This indicates a strong downflow toward the wall which attaches along the centerline and is swept outward. Two symmetric and diverging separation lines are indicated which divide the central region of flow away from the centerline and the outer flow which is oriented toward the centerline. Figure 5(b) is a schematic of the surface topology inferred from the ink-dot streaks.

The ink-dot visualization downstream of the tapered cylinder suggests that the horseshoe vortex legs do remain near the wall. The shear direction near the centerline is consistent with a counter-rotating vortex pair positioned near the wall, and the two separation lines could correspond to the lateral extent of the vortex pair. Figure 5(c) is a flow schematic that associates the topology indicated in Fig. 5(b) with the horseshoe vortex legs formed around the tapered obstacle.

Secondary flow vectors in cross-sectional planes downstream of the circular and tapered obstacles are shown in Figs. 6 and 7, respectively. Measurements were made at three streamwise locations, but only the results at $x/D = 4$ and $x/D = 8$ are presented. The profiles extend over a spanwise distance of ±3 obstacle-diameters, and a height of 1.2 diameters. The profiles are plotted in non-dimensional spatial coordinates, z/D and y/D. The secondary velocity vectors are normalized on the reference free-stream velocity, U_{ref}, which was approximately 25 m/s.

Figures 6(a) and 6(b) present the secondary velocity vectors downstream of the circular cylinder at $x/D = 4$ and $x/D = 8$, respectively. The most prominent feature of the flow in both figures is the central upwash region directly behind the obstacle along the centerline, and the downwash flow at $z/D > \pm 1$. Only a slight decay occurs in the magnitude of the velocity vectors with streamwise distance from a peak of 12 percent U_{ref} at $x/D = 4$ to a peak of 10 percent U_{ref} at $x/D = 8$. (Note the change in calibration of vector-length between Figs. 6(a)
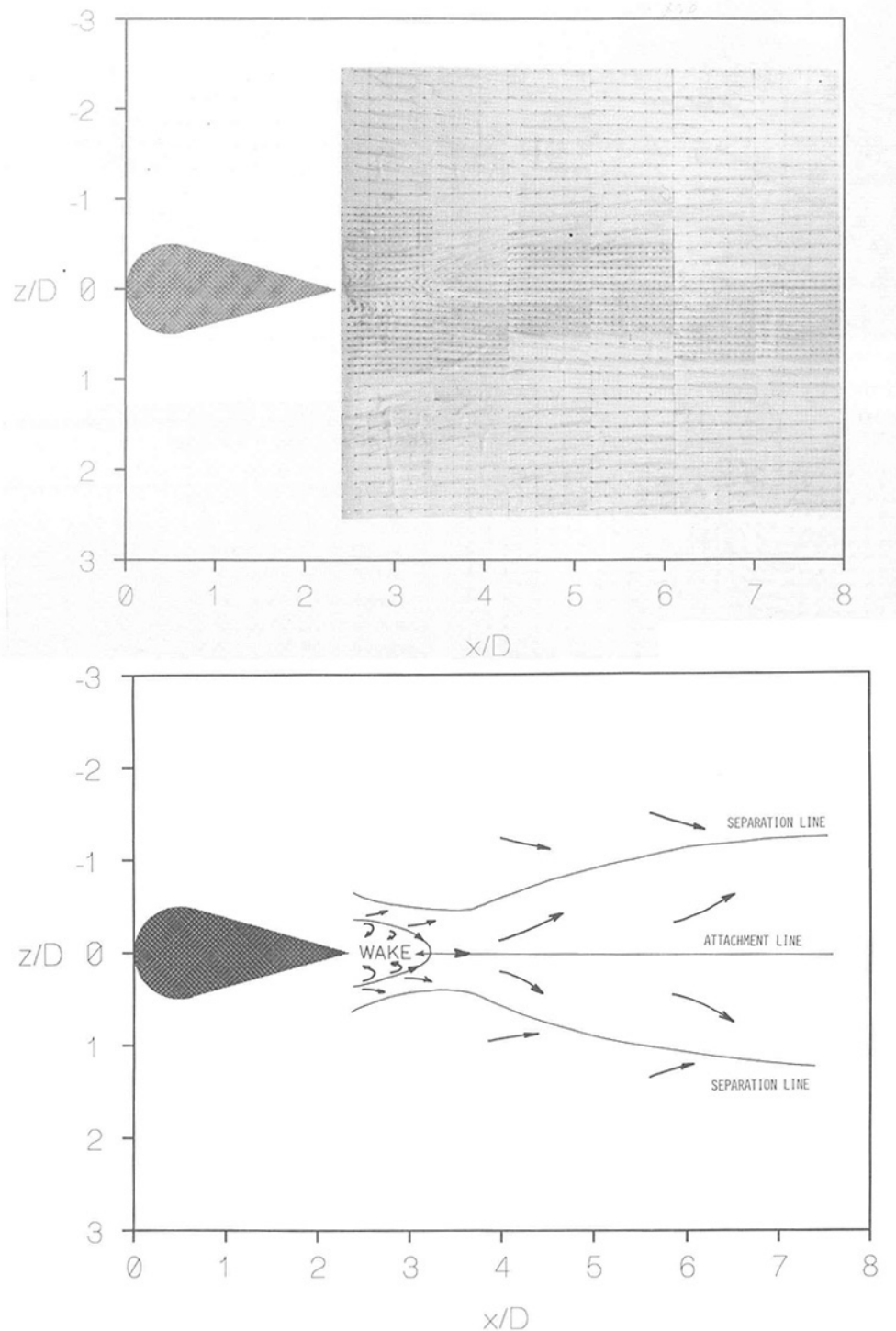
and 6(b)). This secondary flow seems to be a segment of a counter-rotating, swirling pair with a length scale approximately half of the wind tunnel height. The rotational direction of the swirling pair is opposite to that of the horseshoe vortex legs if they were present.

There is no clear evidence of the horseshoe vortex legs behind the circular cylinder in Figs. 6(a) and 6(b). At the centerline, a saddle point at $y/D = 0.14$ can be seen at both streamwise locations. Below the saddle point, the flow is oriented toward the wall producing vorticity of the opposite sign of the swirling pair, possibly corresponding to the horseshoe vortex system. However, no mean secondary motion that could be attributed to the horseshoe vortex legs was resolved.

The lack of horseshoe vortex legs behind the circular cylinder is supported by Eckerle and Langston [23]. They show that the horseshoe vortex legs had dissipated by 90 deg from the leading edge at a Reynolds number of 5×10^5.

The mean secondary flow behind the tapered cylinder at $x/D = 4$ (Fig. 7(a)) is similar to that of the circular cylinder at the same location. The dominant swirl flow is present, and a saddle point can be identified at $y/D = 0.17$. By $x/D = 8$ (Fig. 7(b)) the saddle point has moved to $y/D = 0.46$, lifting the large swirling pair away from the wall. Near the wall, secondary flow vectors are in the opposite sense of rotation from the upper swirling pair, showing streamwise vorticity associated with the horseshoe vortex legs. The approximate
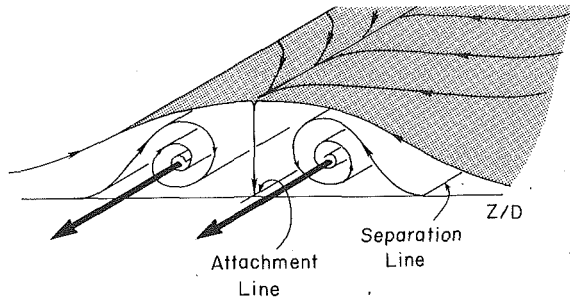
Fig. 5 Flow downstream of the tapered cylinder. (a) Surface visualization using the ink-dot technique, $Re_D = 1.3 \times 10^5$; (b) Schematic of surface topology; (c) Schematic of flow associated with surface topology.
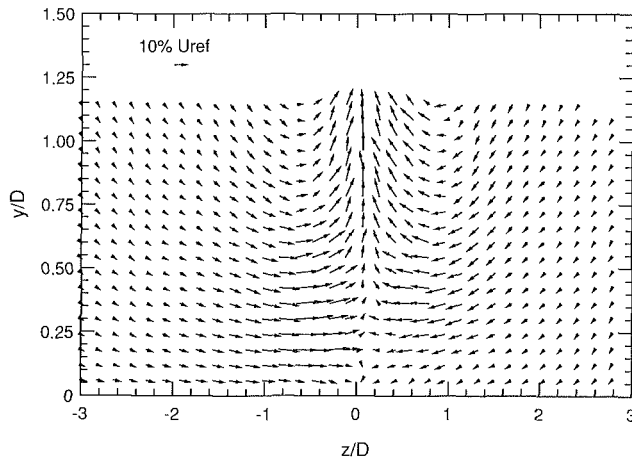
Fig. 6(a) Secondary velocity vectors downstream of the circular cylinder, $x/D = 4$, $Re_D = 1.3 \times 10^5$

Fig. 6(b) Secondary velocity vectors downstream of the circular cylinder, $x/D = 8$, $Re_D = 1.3 \times 10^5$

Fig. 7(a) Secondary velocity vectors downstream of the tapered cylinder, $x/D = 4$, $Re_D = 1.3 \times 10^5$
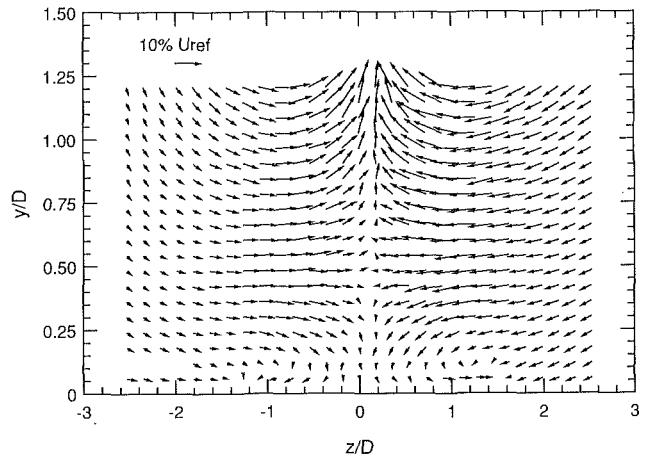
Fig. 7(b) Secondary velocity vectors downstream of the tapered cylinder, $x/D = 8$, $Re_D = 1.3 \times 10^5$

Fig. 8 Contours of constant streamwise velocity downstream of the circular cylinder, $x/D = 8$, $Re_D = 1.3 \times 10^5$

center of the horseshoe vortex legs is $y/D = 0.1$ and $z/D = \pm 1.25$. The vortex located at $z/D = +1.25$ is slightly larger than its counterpart at $z/D = -1.25$, which may be due to the slight asymmetry of the approach boundary-layer. The vortex pair near the wall has a maximum velocity of roughly 5 percent U_{ref}.

There is greater decay of the secondary flow between $x/D = 4$ and 8 for the tapered cylinder than the circular cylinder. The peak secondary flow behind the tapered cylinder is 45 percent U_{ref} at $x/D = 4$, and it decreases to 10 percent U_{ref} by $x/D = 8$. The greater magnitude of the secondary flow associated with the tapered cylinder at $x/D = 4$ may be due to a shorter development length behind the tapered cylinder,

whose trailing edge is at $x/D = 2.3$ compared with the circular cylinder's trailing edge at $x/D = 1$.

Figures 8 and 9 show the contours of constant streamwise velocity at $x/D = 8$ for the circular cylinder and tapered cylinder, respectively. Data are normalized on the local free-stream velocity, measured by the five-hole probe. The wake associated with the circular cylinder (Fig. 8) is relatively symmetric, with a central momentum deficit region where the flow is less than 95 percent U_{inf} that is approximately 2 diameters
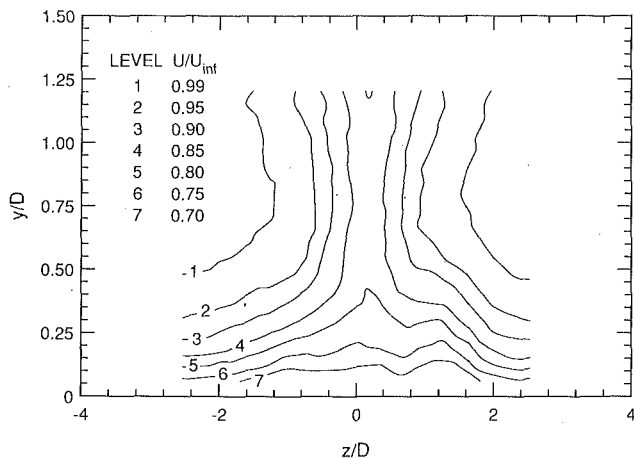
Fig. 9 Contours of constant streamwise velocity downstream of the tapered cylinder, $x/D = 8$, $Re_D = 1.3 \times 10^5$

Fig. 10 Visualization of the recirculation region behind the circular cylinder using hydrogen bubbles, $Re_D = 615$

Fig. 11 Visualization of the recirculation region behind the tapered cylinder using dye injection, $Re_D = 615$

wide. Away from the centerline at $z/D > \pm 2$, the wall-shear region becomes relatively uniform, implying that the wall boundary-layer may regain its two-dimensional characteristics. The boundary layer thickness at large transverse locations approaches 0.40 diameters, less than the boundary layer thickness at the leading edge of the obstacle, which is 0.63 diameters. The boundary layer may thin as it flows around the obstacle due to the acceleration of the free stream.

The streamwise velocity behind the tapered cylinder (Fig. 9) exhibits a greater momentum deficit along the centerline. The width of the wake is slightly less than the wake associated with the circular cylinder since the 95 percent U_{inf} region extends only 1.5 diameters in width. This may be due to the shorter development length or to a difference in the mixing characteristics in the wake of the streamlined obstacle.

The streamwise velocity contours in the wall-shear region of the tapered cylinder are less uniform than those of the circular cylinder, indicating redistributions of momentum near the wall introduced by the horseshoe vortex legs. A comparison of Figs. 7 and 9 shows that the vortex legs are close to the wall, embedded within the wall-shear region behind the tapered cylinder. The effect of the asymmetry in the vortex pair near the wall can be seen, since the perturbations of the wall-shear region is greatest at $z/D = +1.25$ where the stronger of the two vortices is located. Within the range of our measurements ($z/D < \pm 2.5$), the nonuniform streamwise velocity contours near the wall imply that the wall boundary-layer remains three-dimensional in nature.

In summary, the measurements in the wind-tunnel suggest that the horseshoe vortex legs are present downstream of the tapered cylinder, but not behind the circular cylinder. In the case of the tapered cylinder, the legs remain very close to the wall at the trailing edge of the cylinder, and then lift away from the wall with streamwise development. This is confirmed by the surface-shear vectors which indicate a vortex pair interacting with the wall behind the tapered cylinder, and by the secondary flow vectors that show a vortex pair near the wall with the same rotational direction as the primary horseshoe vortex. Both the surface visualization and the mean velocity measurements behind the circular cylinder show no indication of the horseshoe vortex legs near the wall at any of the streamwise locations studied.

Water Channel Visualization. Flow visualization was performed in water behind circular and tapered cylinders to observe the formation of the large swirling pair. Note that the two experiments do not have exact kinematic and dynamic scaling since the obstacles in the water channel have an aspect ratio of 3 compared with an aspect ratio of 10 for the wind
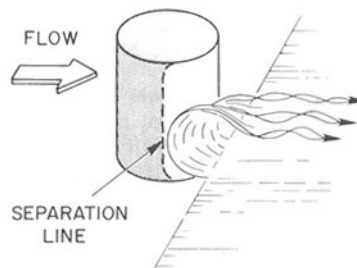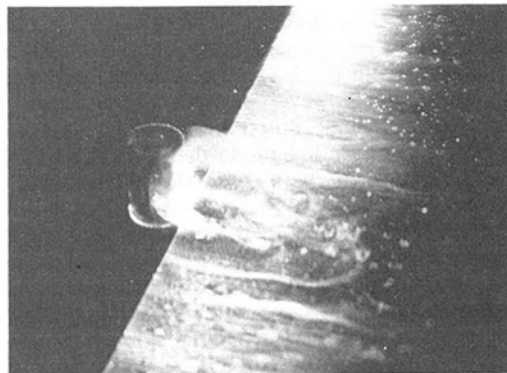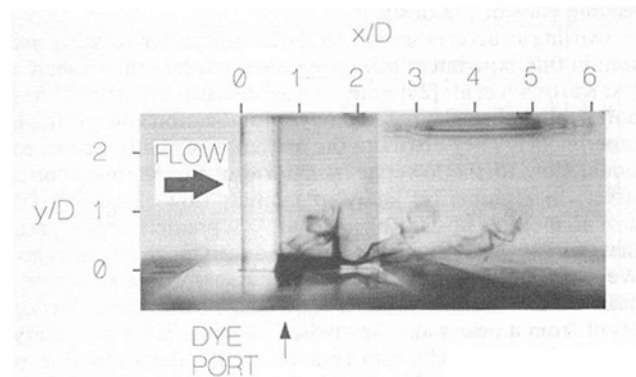
tunnel experiments, and the water visualizations were conducted at a Reynolds number of $Re_D = 615$ compared with $Re_D = 1.3 \times 10^5$ in the wind-tunnel. However, since the Strouhal number is independent of Reynolds number throughout this range, the global features of the wake at the lower Reynolds number should provide some insight into the flow's behavior at the higher Reynolds number.

Figures 10 and 11 present dye visualization of the recirculation region directly behind the two obstacles. For both cases, a strong upwash of the flow near the wall toward the channel's midheight occurred in the separated region behind the obstacles. Two types of visualization were used in this region; hydrogen bubbles and dye injection.

In Fig. 10, a hydrogen bubble wire was placed behind the circular cylinder, parallel with the channel floor and approximately $0.2D$ above the floor at the trailing edge. (Note that an opaque film of extremely small bubbles accumulated on the top wall of the channel in the recirculation region of the cylinder, slightly obscuring the visualization.) In the separated region behind the obstacle, the bubbles are lifted away from the channel floor toward the midheight of the channel. Some bubbles travel upstream to the separation line on the cylinder body, lift up along the cylinder surface, and then continue to

flow downstream along the channel's midheight. The hydrogen bubbles indicate that the separation line occurs at approximately 110 deg from the leading edge of the cylinder at the channel midheight. However, separation is delayed near the intersection of the cylinder and floor, as indicated by the curved shape of the separation line along the cylinder's height.

Dye visualization of the upwash flow behind the tapered cylinder is presented in Fig. 11. Dye was injected from a small hole in the wall at the edge of the obstacle. The dye traveled downstream until it reached the separation line, where most of the dye was lifted up along the obstacle's surface before progressing downstream near the channel's midheight. Note that the separation line on the tapered cylinder occurs significantly farther downstream on the body than was the case for the circular cylinder due to the streamlined nature of the tapered cylinder.

Discussion

The experimental results indicate that there are time-averaged, vortical flow structures that remain intact for at least eight diameters downstream of a nominally two-dimensional obstacle. Two different swirling flows were observed in this study. The dominant structure is a streamwise counter-rotating swirling pair that were observed behind both the blunt and the tapered obstacles. A second smaller counter-rotating vortex pair of opposite vorticity was observed near the wall behind the tapered cylinder. This smaller vortex pair is most likely associated with the horseshoe vortex system generated at the leading edge of the obstacle.

Swirling structures similar to the large counter-rotating pair seen in this experiment have been observed by other researchers. Kurosaka et al. [24] noted the existence of crossflow transport behind obstacles based on dye visualization and gas tracer experiments. They attribute the existence of the three-dimensional flow to the lower pressure within the Karman vortex street. In a numerical study of laminar flow ($Re_D = 1000$) around multiple posts, Rogers, et al. [25] predict particle paths that swirl upward behind the posts and then move downstream. Wei and Smith [26] observed streamwise vortices in the very near wake of circular cylinders and suggest that these vortices result from a near wake, spanwise free-shear layer instability.

The physical mechanism responsible for the formation of the swirling pair is difficult to isolate in such a complex flow. The flow visualization reported in this study reveal upward flow in the near wake that then propagates downstream, suggesting the swirling pair originates in the near wake of the obstacles. It is interesting to note that Pierce and Harsh [19] and Merati et al. [18] did not observe this upper vortex pair in their measurements both in the 100 percent chord plane and in planes multiple chord lengths downstream. In both experiments, finite height obstacles were studied; Pierce and Harsh had an obstacle that spanned one-half of the channel height, while Merati, McMahon and Yoo placed their obstacle outside of the exit plane of the wind tunnel. Hence, it seems the formation of the streamwise vortex pair requires symmetrical channel flow about an obstacle.

The longitudinal swirling pair may be related to the twin tornado-like vortices observed in the lee of obstacles [27]. In the case of a two-dimensional obstacle, the tornado-like vortices may impinge at the obstacle's midheight with the mirror vortices formed on the upper surface, then turn and propagate downstream. If the obstacle is of finite height, the twin vortices may remain vertical until they are entrained by the flow passing over the obstacle. Hence, the longitudinal swirling flow would be formed from the tornado vortices only for the case of the symmetrical channel flow.

The distinction between the flow structure behind the tapered and the circular cylinder is the lack of a second vortical pair close to the wall for the case of the circular cylinder.

The distinct flows behind the two obstacles may be a result of the flow Reynolds number of $Re_D = 1.3 \times 10^5$, which is close to a transitional regime for flow around circular cylinders. Dallmann and Schewe [28] point out the sensitivity to Reynolds number of the global three-dimensional flow structure that separates from a circular cylinder in crossflow. Near the transition Reynolds number, $Re_D \approx 3.5 \times 10^5$, drastic changes in drag, lift and vortex shedding frequency have been observed for nominally two-dimensional cylinders. The transition Reynolds number separates the subcritical flow, in which laminar separation from the cylinder occurs with transition to turbulence occurring in the wake, from the supercritical flow regime, where separation of a turbulent boundary layer occurs.

In this experiment, both the circular cylinder and the tapered cylinder were exposed to the same Reynolds number of $Re_D = 1.3 \times 10^5$, which should be below the critical Reynolds number, and hence, a laminar separation should occur from the cylinder. However, the streamlined shape of the tapered cylinder may delay separation until a turbulent boundary layer is formed on the surface. (Pierce and Harsh [19] estimate the boundary layer is turbulent on the tapered cylinder at $Re_D = 1.8 \times 10^5$.) This difference in separation characteristics, even at the same flow Reynolds number, may induce different global flow structures downstream of the obstacles. This implies that the presence, or lack thereof, of the horseshoe vortex legs behind the circular and tapered cylinder may be sensitive to Reynolds number.

Alternately, the lack of horseshoe vortex legs downstream of the circular cylinder may be due to the vigorous wake associated with the blunt obstacle. The large flow oscillations of the Karman vortex street may entrain the legs and rapidly dissipate their vorticity. The streamlined cylinder, on the other hand, produces a milder wake with a smaller spanwise extent, thereby permitting the propagation of the horseshoe vortex legs downstream of the obstacle.

The different behavior of the vortex legs for the tapered and the circular cylinder imply that the vortex legs are not the governing mechanism influencing local convective heat transfer. The heat transfer results in Fisher and Eibeck [1] show a single peak in Stanton number near the centerline for the tapered cylinder and an increase in Stanton number of lower magnitude spread over $z/D = \pm 1$ for the circular cylinder. If the convection was governed by the horseshoe vortex legs, one would expect legs present near the wall for both cases, with the tapered cylinder's legs in close proximity at the centerline and the circular cylinder's vortex legs positioned farther apart. Since no vortex legs were resolved in the case of the circular cylinder, the convective heat transfer is most likely governed by the highly turbulent oscillating wake flow which has greater spanwise extent in the case of the circular cylinder.

Conclusions

The flow downstream of the intersection of both a circular and a tapered cylinder with a wall was examined using surface visualization, five-hole-probe anemometry, and flow visualization. An evaluation of the results of these measurements lead to the following conclusions:

1. A pair of large, counter-rotating swirls with common flow away from the wall and with centers over one diameter away from the wall are present downstream of both obstacles.

2. A pair of smaller counter-rotating vortices with common flow toward the wall were observed embedded within the wall-shear flow eight diameters downstream of the tapered cylinder, but not downstream of the circular cylinder. This implies that the horseshoe vortex legs only propagate downstream behind the streamlined obstacle shape.

3. The large swirling pair appears to be formed in the near

wake of the obstacles that are exposed to symmetrical channel flow.

4. The augmentation of heat transfer downstream of the circular and tapered cylinders presented in [1] is most likely governed by the highly turbulent wake behind the obstacles, rather than by the horseshoe vortex legs.

Acknowledgments

References

1 Fisher, E. M., and Eibeck, P. A., "The Influence of a Horseshoe Vortex on Local Convective Heat Transfer," ASME *Journal of Heat Transfer*, Vol. 112, No. 2, pp. 329–335, 1990.

2 Schwind, R. G., "The Three-Dimensional Boundary Layer Near a Strut," Gas Turbine Laboratory Report No. 57, Massachusetts Institute of Technology, Cambridge, MA, 1962.

3 Peake, D. J., and Galway, R. D., "Three-Dimensional Separation of a Plane Incompressible Laminar Boundary Layer Produced by a Circular Cylinder Mounted Normal to a Flat Plate," *Recent Developments in Boundary Layer Research*, Part II, NATO Agardograph No. 97, 1965, pp. 1049–1080.

4 Peake, D. J., Galway, R. D., and Rainbird, W. J., "The Three-Dimensional Separation of a Plane, Incompressible, Laminar Boundary Layer Produced by a Rankine Oval Mounted Normal to a Flat Plate," Report No. LR-446, National Aeronautical Establishment, Ottowa, Ontario, Canada, 1965.

5 East, L. F., and Hoxey, R. P., "Boundary Layer Effects in an Idealized Wing-Body Junction at Low Speed," RAE TR 68161, July 1968.

6 Belik, L., "The Secondary Flow About Circular Cylinders Mounted Normal to a Flat Plate," *Aeronautical Quarterly*, Vol. 26, 1973, pp. 47–54.

7 Baker, C. J., "The Laminar Horseshoe Vortex, " *Journal of Fluid Mechanics*, Vol. 95, Part 2, 1979, pp. 347–368.

8 Baker, C. J., "The Turbulent Horseshoe Vortex," *Journal of Wind Engineering and Industrial Aerodynamics*, Vol. 6, 1980, pp. 9–23.

9 Goldstein, R. J., and Karni, J., "The Effect of a Wall Boundary Layer on Local Mass Transfer from a Cylinder in Crossflow," ASME *Journal of Heat Transfer*, Vol. 106, 1984, pp. 260–267.

10 Ichimiya, K., Akino, N., Kunugi, T., and Mitsushiro, K., "Fundamental Study of Heat Transfer and Flow Situation Around a Spacer (in the Case of a Cylindrical Rod as a Spacer)," *Intl. J. of Heat Mass Transfer*, Vol. 31, No. 11, 1988, pp. 2215–2225.

11 Moore, J., and Forlini, T. J., "A Horseshoe Vortex in a Duct," ASME Paper No. 84-GT-202, presented at the ASME 29th International Gas Turbine Conference and Exhibit, Amsterdam, The Netherlands, June 4–7, 1984.

12 Shabaka, I. M. M. A., and Bradshaw, P., "Turbulent Flow Measurements in an Idealized Wing/Body Junction," *AIAA Journal*, Vol. 19, No. 12, 1981, pp. 131–132.

13 McMahon, H., Hubbartt, J., and Kubendran, L., "Mean Velocities and Reynolds Stresses in a Juncture Flow," NASA Contractor Report No. 3605, NASA-Langley Research Center, Hampton, VA; 1982.

14 McMahon, H., Hubbartt, J., and Kubendran, L., "Mean Velocities and Reynolds Stresses Upstream of a Simulated Wing Fuselage Juncture," NASA Contractor Report No. 3695, NASA-Langley Research Center, Hampton, VA, 1983.

15 Hsing, T., and Teng, H., "Experimental Study of the Behavior of 3-D Turbulent Boundary Layer in a Simplified Wing/Body Junction," AIAA Report No. 84-1529, 1984.

16 Mehta, R. D., "Effect of Wing Nose Shape on the Flow in a Wing/Body Junction," *Aeronautical Journal*, Vol. 88, No. 880, 1984, pp. 456–460.

17 Dickinson, S. C., "Flow Visualization and Velocity Measurements in the Separated Region of an Appendage-Flat Plate Junction," *Proceedings of the Ninth Biennial Symposium on Turbulence*, Univ. of Missouri-Rolla, Rolla, MO, Oct. 1–3, 1984.

18 Merati, P., McMahon, H. M., and Yoo, K. M., "Experimental Modeling of a Turbulent Flow in the Junction and Wake of an Appendage Flat Plate," AIAA/ASME/SIAM/APS 1st National Fluid Dynamics Congress, July 25–28, 1988, Cincinnati, Ohio, pp. 1255–1264.

19 Pierce, F. J., and Harsh, M. D., "The Mean Flow Structure Around and Within a Turbulent Junction or Horseshoe Vortex—Part II. The Separated and Junction Vortex Flow," ASME JOURNAL OF FLUIDS ENGINEERING, Vol. 110, 1988, pp. 415–423.

20 Langston, L. S., and Boyle, M. T., "A New Surface-Streamline Flow-Visualization Technique," *J. of Fluid Mechanics*, Vol. 125, pp. 53–57.

21 Treaster, A. L., and Yocum, A. M., "The Calibration and Application of Five-hole Probes," *ISA Transactions*, Vol. 18, No. 3, pp. 23–24.

22 Schewe, G., "Sensitivity of Transition Phenomena to Small Perturbations in Flow Round a Circular Cylinder," *J. Fluid Mechanics*, Vol. 172, 1986, pp. 33–46.

23 Eckerle, W. A., and Langston, L. S., "Horseshoe Vortex Formation Around a Cylinder," ASME *Journal of Turbomachinery*, Vol. 109, April, 1987, pp. 278–285.

24 Kurosaka, M., Christiansen, W. H., Goodman, J. R., Tirres, L., and Wohlman, R. A., "Crossflow Transport Induced by Vortices," *AIAA Journal*, Vol. 26, No. 11, 1988, pp. 1403–1405.

25 Rogers, S. E., Kwak, D., and Kaul, U. K., "A Numerical Study of Three-Dimensional Incompressible Flow Around Multiple Posts," presented at the AIAA 24th Aerospace Sciences Meeting, Reno, NV, Paper No. AIAA-86-0353, 1986.

26 Wei, T., and Smith, C. R., "Secondary Vortices in the Wake of Circular Cylinders," *J. Fluid Mech.*, Vol. 169, 1986, pp. 513–533.

27 Sedney, R., and Kitchens, C. W., "The Structure of Three-Dimensional Separated Flows in Obstacle, Boundary Layer Interactions," *Flow Separation*, AGARD CP-168, May 1975, pp. 37.1–37.15.

28 Dallmann, U., and Schewe, G., "On Topological Changes of Separating Flow Structures at Transition Reynolds Numbers," presented at the AIAA 19th Fluid Dynamics, Plasma Dynamics and Lasers Conference, Honolulu, Hawaii, AIAA Paper No. AIAA-87-1266, 1987.

H. S. Govinda Ram

V. H. Arakeri

Department of Mechanical Engineering.

Department of Civil Engineering,
Indian Institute of Science,
Bangalore 560 012, India

Studies on Unsteady Pressure Fields in the Region of Separating and Reattaching Flows

Experimental studies on the measurement of pressure fields in the region of separating and reattaching flows behind several two-dimensional fore-bodies and one axisymmetric body are reported. In particular, extensive measurements of mean pressure, surface pressure fluctuation, and pressure fluctuation within the flow were made for a series of two-dimensional fore-body shapes consisting of triangular nose with varying included angle. The measurements from different bodies are compared and one of the important findings is that the maximum values of rms pressure fluctuation levels in the shear layer approaching reattachment are almost equal to the maximum value of the surface fluctuation levels.

1 Introduction

Pressure fluctuations are of common occurrence in unsteady fluid flows. A need to measure these has been a long felt need with reference to aerodynamic applications like jet noise, aircraft cabin noise etc. Similarly, knowledge of the pressure fluctuation characteristics is an essential ingredient of predicting and understanding of "sonar" self-noise, Blake [1], in underwater applications. The possible role of pressure fluctuations in the problem of cavitation inception has been realized for some time, but, perhaps the first systematic study in this direction has been due to Arndt and Ippen [2]. These studies were limited to wall bounded turbulent flows. Subsequent studies by Arakeri [3] and Huang and Hannan [4] have shown that the role of turbulent pressure fluctuations can be even more dramatic for certain class of flows like separating shear layers. Substantially stronger magnitude pressure fluctuation levels have been measured in certain regions of such flows than those existing in attached fully developed turbulent boundary layers. Recently, Katz [5] has carried out extensive pressure fluctuation measurements in flows with laminar separation and subsequent turbulent reattachment. However, one of the questions which remained unanswered was, whether the fluctuation levels could be even higher in the developing shear layer away from the surface than those measured at the surface itself. It is of interest to note that Katz [5] measured surface rms pressure fluctuation levels as high as 19 percent of the dynamic head on a blunt cylindrical nose model. A natural question which arises is, whether there is an upper limit for the rms pressure fluctuation levels either in the flow or at the surface. This is relevant from the point of view, that, cavitation inception index for flow past a sharp edged disk does not seem to show an upper bound with increase in Reynolds number, Kermeen and Parkin [6]. The problem of cavitation inception
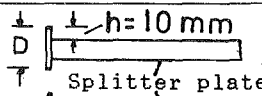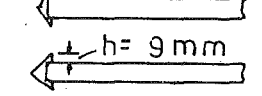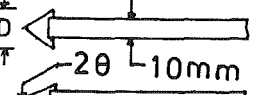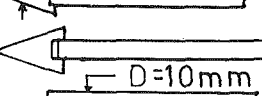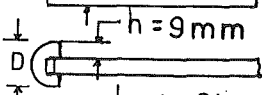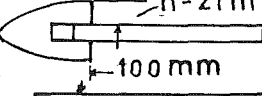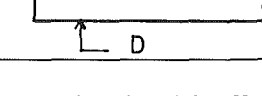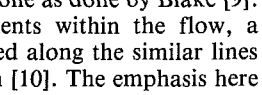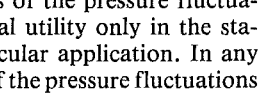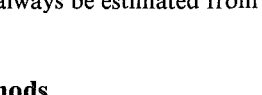
is, however, compounded by the "nuclei" supply conditions and hence one must be cautious in interpreting cavitation inception observations in relation to the level of turbulent pressure fluctuations occurring in the flow.

In the past, basically, two types of pressure fluctuation measurement in turbulent flows have been attempted, namely, surface and within the flow. The former are much more numerous than the latter; the majority of the former and to the best of our knowledge all the latter have been carried out using wind tunnel facility rather than water tunnels. Some specific references directly relevant to the present studies will be cited in later sections; however, two review articles on the subject by Willmarth [7] and George et al. [8] may be mentioned here. From these articles one can gather that pressure fluctuation measurements, in general, pose experimental difficulties and in particular, for pressure fluctuation measurements within the flow. In the earlier days, spatial resolution as well as vibration isolation were significant problems; however, presently the availability of highly sensitive miniature pressure transducers with acceleration compensation have made the task of pressure fluctuation measurements much simpler and more reliable. In particular, very fine spatial resolution is possible by communicating the pressure fluctuations through a small hole at the surface to a relatively much larger transducer as done by Blake [9]. The Helmholtz resonance frequency of such a configuration can be made sufficiently high as compared to the dominant frequencies associated with the turbulent pressure fluctuations.

The present study is aimed at fulfilling certain gaps in the measurement of pressure fluctuations in one class of flows where the boundary layer at separation from a forebody is laminar and the flow reattaches on a splitter plate turbulently. In particular, attempts for the first time have been made to measure both the surface pressure fluctuations and pressure fluctuations within the flow in the region of separation and reattachment. The surface pressure fluctuations have been measured by communicating them through a small hole in the

Table 1 Some details of the models used in the experiments

Model	Shape	Aspect ratio	blockage	X_R/D	X_R/h
Triangular (2θ = 180 deg) "normal plate"	$h = 10$ mm, Splitter plate	61	4.9	8.8	26.5
Triangular (2θ = 140 deg)		67	4.6	7.9	24.4
Triangular (2θ = 127 deg)	$h = 9$ mm	67	4.6	7.5	23.3
Triangular (2θ = 90 deg)		67	4.6	5.5	17.2
Triangular (2θ = 60 deg)	2θ 10 mm	67	4.6	4.8	15.0
Triangular (2θ = 30 deg)		67	4.6	3.6	11.1
Right angle corner blunt edge plate	$D = 10$ mm, $h = 9$ mm	61 (W/D)	1.6	4.8	—
Semicircular nose	$h = 21$ mm	67	4.6	4.8	15.0
Elliptical nose	100 mm	30	8.0	2.4	6.0
Blunt nose circular cylinder	D	—	1.5	1.7	—

splitter plate to a condenser microphone as done by Blake [9]. For pressure fluctuation measurements within the flow, a "probe microphone" was constructed along the similar lines of a probe used by Arndt and Nilsen [10]. The emphasis here is on the measurement of rms values of the pressure fluctuations since peak values have practical utility only in the statistical sense depending on the particular application. In any case, if the statistical characteristics of the pressure fluctuations are known then the peak values can always be estimated from the measured rms values.

2 Experimental Setup and Methods

2.1 Facility and Models. The facility used for the present experimental study is a suction type low speed wind tunnel driven by a 4 bladed fan connected to a 15 HP motor. The cross-sectional area of the test section is 610 mm × 610 mm and the total length is 2100 mm. The tunnel contraction ratio is 9:1, several screens and a honeycomb are provided in the upstream settling chamber with a fine mull cloth cover at the bell mouth entry. A velocity survey in the test section showed that it was uniform within two percent of the centerline velocity except for the boundary layer regions and the turbulence level u'_{rms}/U_∞ was measured to be about 0.3 percent within the present experimental velocity range of 8.5 m/s to 20 m/s. At a distance of 500 mm from the entry location of the test section, the tunnel wall boundary layer thickness was found to be about 1.5 percent of the tunnel height. To provide as quiet an environment as possible for pressure fluctuation measurements, the transmission of the diffuser vibration was minimized by providing a flexible attachment between the diffuser and the test section.

Different nose model shapes were used in the present study. The first set of models selected were isosceles two-dimensional triangular cylinders of 28 mm base height and different vertex angle. The vertex or included angle, 2θ varied from $2\theta = 30$ to 180 deg. The model with $2\theta = 180$ deg is termed as a normal plate here. The second set of models, also two-dimensional, consisted of 1:2 ratio elliptical nose, semi-circular nose with a step at the tangent point and finally right-angle corner blunt

—————— **Nomenclature** ——————

C_p = mean pressure coefficient, $(p - p_\infty)/\frac{1}{2}\rho U_\infty^2$

C_{pb} = base pressure coefficient, $(p_b - p_\infty)/\frac{1}{2}\rho U_\infty^2$

C_p' = fluctuating pressure coefficient, $p'_{rms}/\frac{1}{2}\rho U_\infty^2$

$C_{p'\,max}$ = maximum value of fluctuating pressure coefficient

C_p^* = modified pressure coefficient, $(C_p - C_{pb})/(1 - C_{pb})$

D = bluff body diameter or the width of the two-dimensional body

h = step height

k = constant

p = mean static pressure

p_b = mean base static pressure

p' = fluctuating pressure

p'_{rms} = root-mean-square (rms) value of the fluctuating pressure, $\sqrt{\overline{p'^2}}$

$\overline{p'^2}$ = mean square value of the fluctuating pressure

p_∞ = freestream pressure

Re_h = Reynolds number based on step height, $U_\infty h/\nu$

Re_d = Reynolds number based on body width or diameter, $U_\infty D/\nu$

U_∞ = freestream velocity

u' = fluctuating component of streamwise velocity

u'_{rms} = root-mean-square (rms)

value of the fluctuating velocity, $\sqrt{\overline{u'^2}}$

$\overline{u'^2}$ = mean square value of the fluctuating velocity

W = tunnel width

x = axial distance downstream of shoulder (also the point of separation)

X_R = reattachment length

y = distance normal to surface

ν = kinematic viscosity of the fluid

ρ = density of the fluid

2θ = included angle of the triangular nose
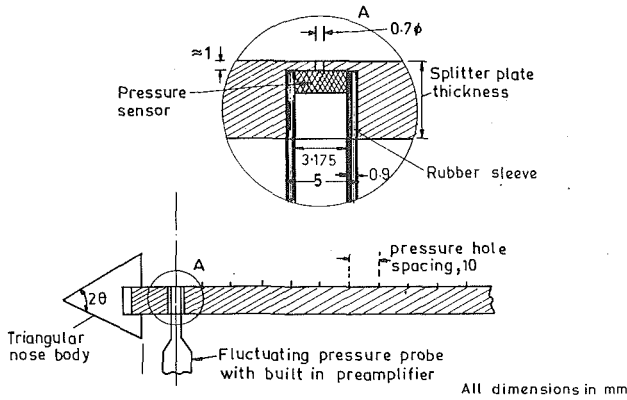
Fig. 1 Mounting details of the fluctuating pressure sensing probe and its location in the splitter plate
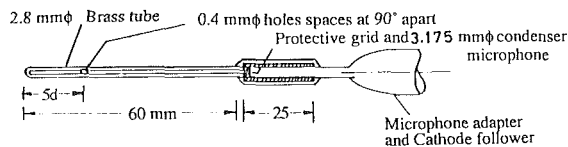
Fig. 2 Geometry of the "probe microphone" used in the separated flow region

edge plate. All these models were provided with a 10 mm groove to accommodate a perspex splitter plate which was more than 610 mm in length. The two-dimensional models were mounted spanning the test section. In addition to the two-dimensional models mentioned, two axisymmetric blunt cylindrical models having diameters of 85 mm and 105 mm were also used in the present study. These were mounted with a vertical strut support with its location being quite downstream from the leading edge of the models. A summary of the geometric and some other features of the models is given in Table 1. No attempts were made to measure the boundary layer thickness at separation; however, it is expected that it will be quite small except for the elliptical nose body. For example, Cherry et al. [11] have estimated the momentum thickness at separation to be $0.004D$ for the right angle corner blunt edge plate.

2.2 Mean Pressure Measurements. The mean pressure measurements were made with the help of pressure tappings provided along the center line of the splitter plate. In a few cases, three rows at different spanwise location were used to check on the two-dimensionality of the flow. The static pressure was measured using an alcohol projection manometer and the free-stream velocity was monitored simultaneously with the help of a standard pitot tube and a second projection manometer. All the pressure measurements mentioned above were made with respect to the freestream pressure, the pressure tapping for which was provided at the entry of the test section.

2.3 Fluctuating Pressure Measurements. The surface static pressure fluctuations were measured with a 3.175 mm diameter B and K condenser microphone (model No. 4138) mounted close to the surface of the splitter plate. Figure 1 shows the geometric details of the fluctuating pressure sensing probe and its mounting in the splitter plate. As shown in the figure, 0.7 mm diameter holes to a depth of within 1 mm are drilled in the splitter plate, at its midspan location. Spacing between the holes was 10 mm, but measurements for any closer spacing was possible by moving the splitter plate inside the groove provided in the model nose. The microphone was mounted in a soft rubber sleeving to isolate it from plate vibration and prevent damage to it. The output of the microphone was fed into a B and K model 2462 cathode follower built-in pream-

Table 2 Statement of experimental uncertainty in the present experimental studies

Parameter	estimated uncertainty	main source of error
x	± 0.5 mm	—
y, h, D	± 0.1 mm	—
X_R	± 2 percent for all bodies except large included angle triangular shaped bodies. ± 8 percent for triangular shaped bodies with $2\theta = 127, 140$ and 180 deg	Locating the reattachment line from flow visualization studies. The smaller error is for cases where the reattachment was relatively steady and fixed.
U_∞	± 1.5 percent	Inaccuracies in reading the height of the meniscus in projection manometer.
C_p	± 6.0 percent	Inaccuracies in reading from projection manometer and day-to-day reproducibility.
$C_{p'}$	± 4.5 percent	Inaccuracy in the measurement of velocity and dB value from the measuring amplifier.
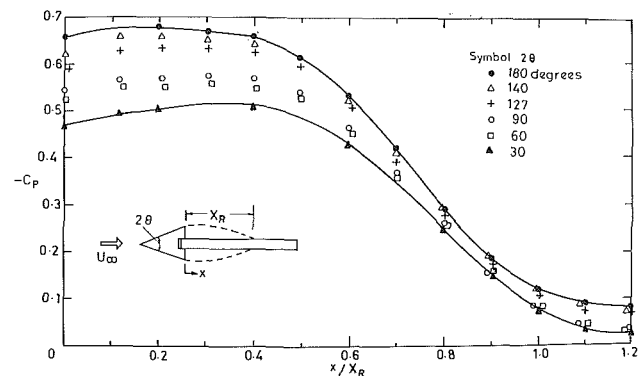
Fig. 3 Mean pressure distribution along the surface of the splitter plate for different triangular nose models (U_∞ = 12.9 m/s)

plifier and the root-mean-square (rms) values of the fluctuating signal were measured with a B and K model 2120 measuring amplifier/frequency analyzer. The condenser microphone was supplied with a calibration chart by the manufacturer; however, its quoted sensitivity was verified with B and K model 4220 piston phone calibrator.

Measurement of pressure fluctuations within the flow was made with a probe very similar to the one used by Arndt and Nilsen [10] and also briefly described in George et al. [8]. The geometric details of this probe are shown in Fig. 2 and it was calibrated against a standard microphone in an "anechoic" chamber. Preliminary calibration runs of the "probe microphone" clearly showed a peak in the response at about 1500 Hz. This frequency agrees well with the predicted resonance frequency for organ type of resonance of the probe tube. Following Arndt and Nilsen [10], the resonance peak was reduced by placing glass wool as damping material. This material was placed between the face of the transducer and the static pressure sensing holes. The response of the probe with modifications was found to agree well with the standard microphone and was found to be flat within 2 dB over a frequency range of 20 Hz to 1500 Hz. The directional sensitivity of the probe microphone with respect to the sound source was also checked and up to 15 to 20 deg tilt very small changes in the readings were observed and this is consistent with the findings of George et al. [8] with a similar probe.
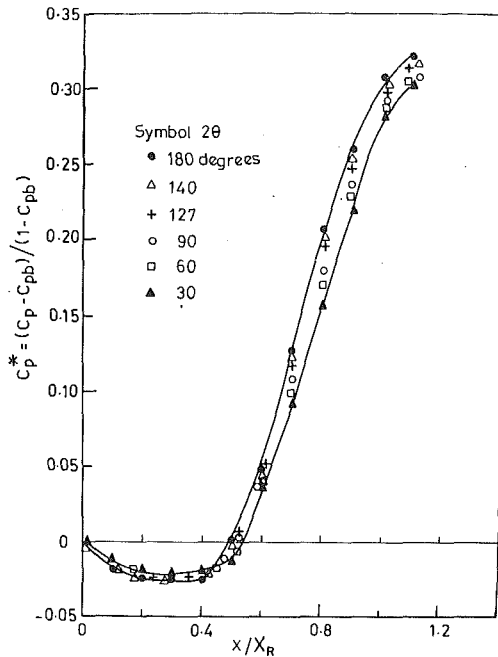
Fig. 4 Pressure distribution in reduced form for different triangular nose models
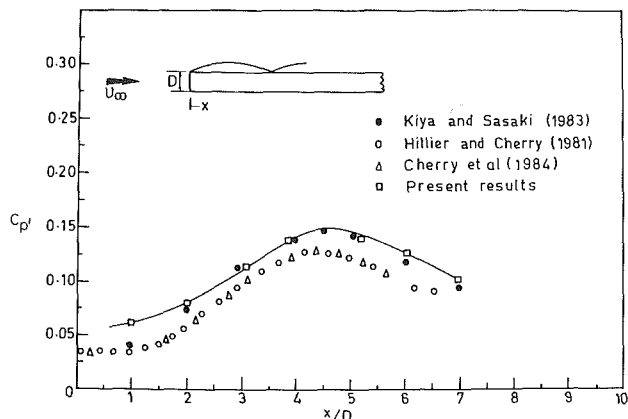
Fig. 5 Distribution of rms pressure fluctuation on the surface of the right angle corner blunt edge nose body ($X_R/D = 4.8$, $R_{ed} = 1 \times 10^4$)

Fig. 6 Distribution of rms pressure fluctuation along the splitter plate for an elliptic nose model ($X_R/h = 6.0$, $U_\infty = 12.9$ m/s)
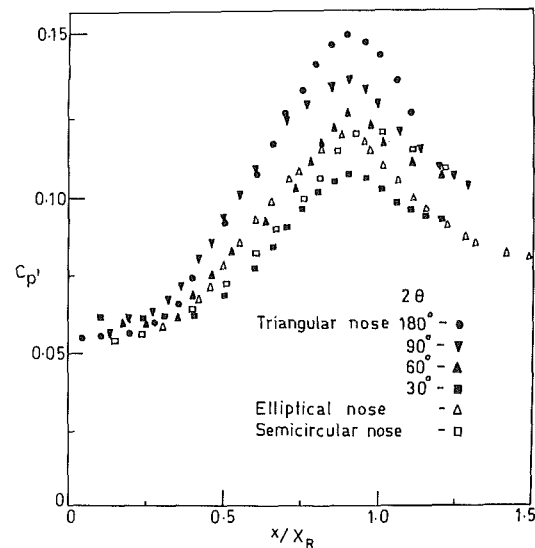
Fig. 7 Distribution of rms pressure fluctuation on the splitter plate for different two-dimensional fore-bodies ($U_\infty = 12.9$ m/s)

3 Experimental Results and Discussion

3.1 General Remarks. As mentioned in the Introduction, the primary objectives of the present investigations were to measure both surface and within flow pressure fluctuations in the region of separating and reattaching flows. For the bodies selected and within the Reynolds number range of present experiments, boundary layer at separation was always laminar. This was followed by transition in the free shear layer and subsequent turbulent reattachment. Extensive investigative runs were made to assess the background noise levels of the facility, frequency contents of the unsteady pressure and velocity fields and the two-dimensionality of the flow field in the central region of the splitter plate. For brevity the results of these studies are not included here; however, they may be found in · Govinda Ram [12].

In addition to the measurements to be presented, the reattachment distance for the various models was quantitatively estimated using several techniques, Govinda Ram [12]. The nondimensional reattachment distances indicated in Table 1 are those obtained from surface flow visualization studies. A summary of experimental uncertainty in the present experimental studies is presented in Table 2.

3.2 Mean Pressure. The mean pressure distribution along the splitter plate for the various triangular nose models is shown in Fig. 3. As indicated in Table 1, the extent of blockage experienced by different bodies varies; however, in general, it is small. The distance x along the plate here is nondimensionalized with respect to the mean reattachment length, X_R. In all the cases, the curves show that the mean pressure coefficient remains nearly constant up to about $x/X_R = 0.4$ and the pressure recovery is subsequently achieved. The base pressure coefficient values at $x/X_R = 0$ and denoted by C_{pb} vary significantly depending on the 2θ value of the triangular nose. The C_{pb} value is nearly -0.48 for $2\theta = 30$ deg; whereas its value for $2\theta = 180$ deg is -0.66. Roshko and Lau [13] have suggested that, to obtain a more universal collapse of the pressure distributions of the type presented in Fig. 3, a modified pressure coefficient C_p^* defined as follows,

$$C_p^* = (C_p - C_{pb})/(1 - C_{pb})$$

should be used. A plot of C_p^* versus x/X_R for the triangular nosed bodies shown in Fig. 4 shows a reasonably good collapse. It is interesting to note that C_p^* is negative quantity up to x/X_R value of about 0.5 for all the cases but has a relatively small magnitude.

3.3 Surface Pressure Fluctuation. The distribution of normalized rms pressure fluctuation values for a right angle corner blunt edge plate is shown in Fig. 5. The present results are compared with the earlier similar measurements by Kiya and

Table 3 Summary of maximum surface rms pressure fluctuation levels on two-dimensional bodies

Model	$C_p{}'_{max}$	$-C_{pb}$	$\dfrac{C_p{}'_{max}}{-C_{pb}}$
Triangular (2θ = 180 deg)	0.152	0.660	0.230
Triangular (2θ = 140 deg)	0.146	0.620	0.235
Triangular (2θ = 127 deg)	0.135	0.590	0.229
Triangular (2θ = 90 deg)	0.130	0.545	0.239
Triangular (2θ = 60 deg)	0.118	0.525	0.225
Triangular (2θ = 30 deg)	0.110	0.465	0.237
Right angle corner blunt edge plate	0.150	0.650	0.231
Semicircular nose	0.120	0.540	0.222
Elliptical nose	0.120	0.300	0.400

Fig. 9 Normalized rms values of pressure fluctuation in the separated bubble region for different freestream velocities (2θ = 180 deg model)
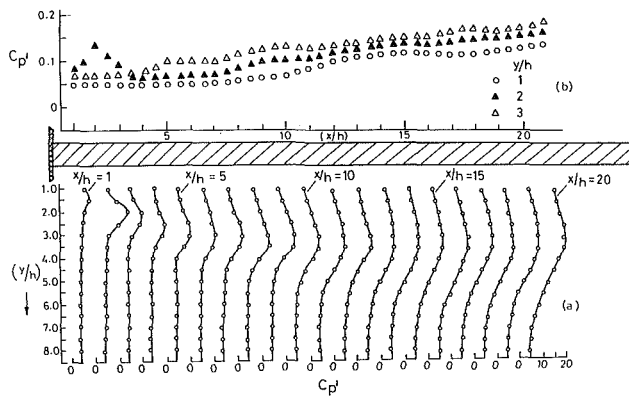
Fig. 8 (a) Normalized rms values of pressure fluctuation in the separated bubble region for different y/h values (2θ = 180 deg model, U_∞ = 12.9 m/s). (b) Normalized rms values of pressure fluctuation in the separated bubble region at fixed values of y/h (X_R/D = 8.8).

Fig. 10 Normalized rms values of pressure fluctuations in the separated and reattaching flow region for 85 mm diameter blunt nose circular cylinder (U_∞ = 12.9 m/s)

Sasaki [14], Hillier and Cherry [15], and Cherry et al. [11]. The size of the body and Reynolds number vary but the overall agreement for the various measurements shown in Fig. 5 is quite satisfactory. In particular, the present measurements agree very well with those of Kiya and Sasaki [14]. The reason for the systematic difference with other measurements is not known; except perhaps to suspect that background noise levels may have some bearing on this. Detailed distribution of measured normalized rms pressure fluctuation levels downstream of separation for an elliptical nose model is shown in Fig. 6. The fine spatial resolution was possible by the movement of the splitter plate inside the groove of the model nose. The levels start to increase from x/h of 2.0, which correspond to x/X_R of about 0.33, and then reach a maximum of about 12 percent of the dynamic head at x/h of about 6.0 corresponding to x/X_R of almost 1. As shown in Fig. 7, the distribution of surface pressure fluctuation levels for other two-dimensional bodies is also similar. The maximum normalized levels depend strongly on 2θ value for the triangular nose models. It is interesting to note that for these models, the levels are low up to x/X_R value of about 0.4, and this region from Fig. 4 also corresponds to the region where C_p^* is approximately zero, but has a small negative value. Therefore, there is a definite correspondence between the recovery of mean pressure and the increased levels of surface pressure fluctuations. Even though the semicircular and elliptical nose models have significantly differing geometries as compared to the triangular nose models,

the fluctuating pressure levels seem to fall between those corresponding to 2θ = 30 and 2θ = 180 deg.

A summary of the maximum normalized rms pressure fluctuation levels on the surface of the various two-dimensional bodies tested presently is given in Table 3. It is clear from Table 3, that the maximum value of the rms surface pressure fluctuation levels are obtained for the blunt shape that is the triangular nose model with 2θ = 180 deg and right angle corner blunt edge plate. As indicated in Govinda Ram [12], the maximum height of the shear layer based on zero mean velocity was observed for the 2θ = 180 deg triangular nose model among the similar shaped bodies. Further analysis of the results seems to indicate a correlation between the maximum of normalized rms pressure fluctuation levels with the $-C_{pb}$ value. With the exception of the elliptic nose, for which boundary layer at separation is expected to be the thickest, the ratio of the two, as indicated in Table 3, varies from 0.222 to 0.238. Taking into account the uncertainties in the measurements, the ratio ($C_p{}'_{max}/-C_{pb}$) seems to be relatively constant value of about 0.23. This would be a very useful finding, if it can be verified under other conditions, since measurement of $-C_{pb}$ is a much simpler task. It is significant to note here that Roshko and Lau [13] did not observe a good collapse of mean pressure data in the form C_p^* versus x/X_R for a body where the boundary layer thickness at separation was comparatively thicker.

3.4 Shear Layer Pressure Fluctuation. The probe microphone was traversed across the shear layer at fixed axial location for obtaining pressure fluctuation level distribution within the shear layer. Results of this exercise for a triangular nose model with 2θ = 180 deg are shown in Fig. 8 at a free-

Table 4 Comparison between pressure fluctuation and velocity fluctuation measurements

x/D	$\left[\dfrac{u'_{rms}}{U_\infty}\right]_{max}$	$\left[\dfrac{y}{D}\right]_{max \; u'_{rms}}$	$C_{p'max}$	$\left[\dfrac{y}{D}\right]_{max \; p'_{rms}}$	$\dfrac{C_{p'max}}{[u'_{rms}/U_\infty]max}$	k
0.1	0.213	0.157	0.077	0.121	0.361	1.69
0.5	0.242	0.265	0.108	0.247	0.446	1.84
0.9	0.247	0.281	0.148	0.239	0.599	2.42
1.1	0.258	0.265	0.159	0.242	0.616	2.38
1.3	0.239	0.270	0.159	0.242	0.665	2.78

Note: $X_R/D = 1.7$
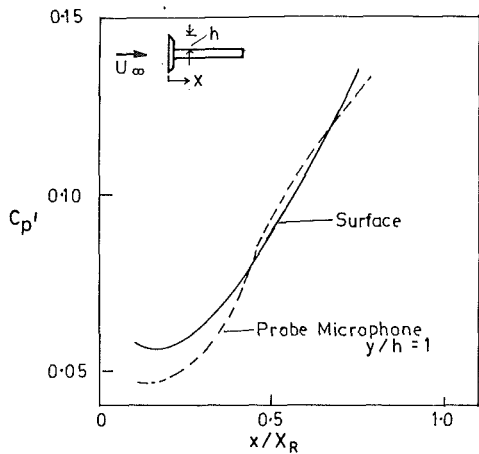
Fig. 11 Comparison of the pressure fluctuation levels within the flow measured close to the surface and at the surface for $2\theta = 180$ deg nose model

Fig. 12 Comparison of the pressure fluctuation levels within the flow measured close to the surface presently and at the surface (average results of Katz, for $R_{\theta d} = 2.89 \times 10^5$) for cylindrical blunt nose model

Fig. 13 Comparison of maximum rms values of pressure fluctuation in the separation bubble region and on the surface for various bodies

stream velocity U_∞ of 12.9 m/s. Also shown at the top of the figure are normalized rms pressure fluctuation levels at fixed values of y/h. The traverse gives a good qualitative and quantitative picture of the development of the shear layer subsequent to separation. There appears to be a local maxima in the fluctuation levels at x/h of 2.0; however, since the flow would be at a substantial angle to the probe, it may not be possible to resolve the exact maximum value in this region of the flow. Besides this local maxima, the subsequent maximum value seems to be reached upstream of reattachment at an axial location of x equal to about 0.75 X_R. This may be concluded from the results shown in Fig. 9. It is also to be observed from this figure that the normalized values show a good collapse at various freestream velocities except for the lowest velocity of 8.8 m/s. For other triangular nose models, the results were very similar; in particular, the maximum levels (except for the local maxima immediately downstream of separation) were observed at about, $x/X_R = 0.75$. This is in contrast to the observed location of maximum surface pressure fluctuation levels at x/X_R of about 0.9 for the same models.

Extensive measurements concerning flow development past blunt nose circular cylinders are available in the literature. These include mean surface pressure distribution measurements, mean velocity survey, turbulent velocity measurements, all by Ota [16], and more recently surface pressure fluctuation measurements by Katz [5]. To complement these results, the probe microphone was used to survey the pressure fluctuation distribution in the shear layer and these results are shown in Fig. 10. It should be mentioned that Ota's measurements were repeated presently by Govinda Ram [12] and generally very good agreement was obtained. In Table 4, some comparison between the present measurements of pressure fluctuation with those of Ota's velocity fluctuation measurements is made.

From the comparison shown in Table 4, it can be observed that the maximum fluctuation levels for both the velocity and pressure reach about the same axial location. However, there is a small difference in the vertical location, but the pressure
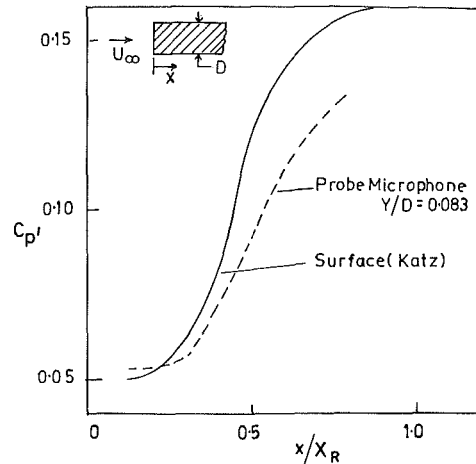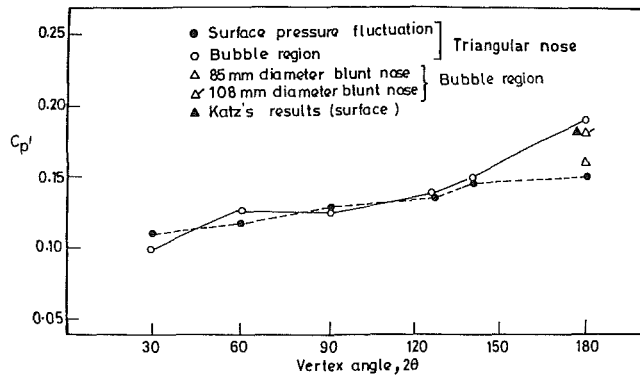
fluctuation profiles were relatively flat in the maximum region, whereas the velocity profiles show a much sharper peak. This would be associated with the pressure probe being much larger than the hot wire probe. The ratio of the two normalized values keeps on increasing in the downstream direction from separation with the variation being considerably reduced for $x/D > 0.9$. Again this may be a reflection on the limited spatial resolution of the probe microphone as compared to the hot wire probe. What is of interest is that the maximum value of the ratio of 0.665 is close to the value of 0.73 predicted by Arndt and Nilsen [10] for a round jet on the basis of a theory due to Kraichman [17]. Direct application of the theory to the present problem was not possible, since information concerning integral length scale of the turbulence is required and this was not readily available. If one looks for a correlation of the type,

$$C_{p'} = k\left[\frac{u'_{rms}}{U_\infty}\right]^2$$

the values of k obtained presently are also shown in Table 4.

In the developed region of the shear layer ($x/D > 0.9$), its magnitude varies from 2.38 to 2.78. Arndt and Nilsen [10] have suggested that k is approximately equal to 1.4 for isotropic turbulent flow; whereas its value should exceed 1.4 for shear flows and present observations are again consistent with this observation.

3.5 Comparison of Various Pressure Fluctuation Levels. On two models, namely the two-dimensional triangular nose model with $2\theta = 180$ deg and the cylindrical blunt nose model, the pressure fluctuation level measurements both within the flow and at the surface are available. A comparison of the measured surfaces levels with those measured by the probe microphone as close to the surface as possible would be of interest. This comparison is presented in Figs. 11 and 12 for the two models indicated. In Fig. 11, the results for the triangular nose model which were obtained presently show a good agreement except in the region immediately downstream of separation. However, the comparison in the case of cylindrical blunt nose shown in Fig. 12 is not as favorable. It should be noted that Katz [5] measurements were carried out in a water tunnel with an entirely different set of instrumentation. Both present and Katz measurements do not show a strong dependence on Reynolds number and hence the fact that the Reynolds number corresponding to the Katz measurements being about twice cannot explain the differences. In the present experiments, the surface pressure fluctuation measurements on the cylindrical blunt nose could not be carried out due to the unavailability of a suitable microphone adaptor for this purpose. Therefore, the explanation for the discrepancy in the two results must await further experimentation in the present facility. It is significant, though, that the overall agreement between the measurements carried out with the probe microphone close to the wall with the surface pressure fluctuation measurements is quite satisfactory at least in the case where both measurements were carried out in the same facility.

In Fig. 13, the maximum rms pressure fluctuation levels measured on the surface and by the probe microphone for various two-dimensional triangular nose models with different 2θ angle values are compared. Except for the blunt 180 degree model, for others, the maximum levels at the surface are very close to the maximum levels measured within the flow region. This has come as somewhat of a surprise. However, it should be noted that a local maximum immediately downstream of separation is not included in this comparison. Only for the 180 deg model there is a substantial difference between the two maximum levels. Also shown are results for the blunt circular models in the same figure for comparison. It is clear from Fig. 13, that with few exceptions, the maximum rms levels fall between 10 to 15 percent of the dynamic head. Present results seem to suggest this as a rather general conclusion, indicating that the maximum rms pressure fluctuation levels, whether at the surface or within the flow, do not exceed 15 percent of the dynamic head. Arndt and Nilsen [10] for a round jet have reported a maximum value of about 12 percent of the dynamic head and their finding supports the above statement.

4 Conclusions

The primary conclusions from the present experimental study are:

1. The maximum normalized rms surface pressure fluctua-

tion levels showed a dependence on the 2θ value of the triangular shaped fore-bodies and these varied from about 10 percent of the dynamic head for $2\theta = 30$ deg model to 15 percent for $2\theta = 180$ deg model. For other 2θ angle geometries the maximum levels were between the two extremes noted.

2. There appears to be a correlation between the maximum normalized value of the rms surface pressure fluctuation levels and the base pressure coefficient. For the two-dimensional fore-bodies used presently, the ratio $C_p'_{max}/(-C_{pb})$ has a value of about 0.23.

3. Except for the $2\theta = 180$ deg model, for all the other triangular nose model, the maximum rms pressure fluctuation levels in the shear layer are almost equal to the maximum surface rms pressure fluctuation levels. This finding has come as somewhat of a surprise. For the blunt $2\theta = 180$ deg model, the maximum pressure fluctuation level in the shear layer is larger by about 4 percent of the dynamic head.

4. In the overall context, the probe microphone response has been found to be quite satisfactory and could be developed into a reliable instrument for measurement of pressure fluctuation levels within the flow.

References

1 Blake, W. K., *Mechanics of Flow-Induced Sound and Vibration*, Academic Press, New York, 1986.

2 Arndt, R. E. A., and Ippen, A. T., "Rough Surface Effects on Cavitation Inception," ASME *Journal of Basic Engineering*, Vol. 90, 1968, pp. 249–261.

3 Arakeri, V. H., "A Note on the Transition Observations on an Axisymmetric Body and Some Related Fluctuating Wall Pressure Measurements," ASME Journal of Fluids Engineering, Vol. 97, No. 1, 1975, pp. 82–87.

4 Huang, T. T., and Hannan, D. E., "Pressure Fluctuations in the Region of Flow Transition," Rept. No. 4723, Dec. 1975, Naval ship R and D centre, Washington D.C.

5 Katz, J., "Cavitation Inception in Separated Flows," Ph.D. dissertation, California Institute of Technology, 1981.

6 Kermeen, R. W., and Parkin, B. R., "Incipient Cavitation and Wake Flow Behind Sharp Edge Disks," Rept. No. 85-4, Aug. 1957, Hydrodynamic Laboratory Report, California Institute of Technology.

7 Willmarth, W. W., "Pressure Fluctuations Beneath a Turbulent Boundary Layer," *Annual Review of Fluid Mechanics*, Vol. 7, 1975, pp. 13–38.

8 George, W. K., Benther, P. D., and Arndt, R. E. A., "Pressure Spectra in Turbulent Free Shear Flows," *Journal of Fluid Mechanics*, Vol. 148, 1984, pp. 155–191.

9 Blake, W. K., "Turbulent Boundary-Layer Wall-Pressure Fluctuation on Smooth and Rough Walls," *Journal of Fluid Mechanics*, Vol. 44, 1970, pp. 637–660.

10 Arndt, R. E. A., and Nilsen, A. W., "On the Measurement of Fluctuating Pressure in the Mixing Zone of a Round Jet," ASME Fluid Engineering Division, Paper No. 71-FE-31, 1971.

11 Cherry, N. J., Hillier, R., and Latour, M. E. M. P., "Unsteady Measurements in a Separated and Reattaching Flow," *Journal of Fluid Mechanics*, Vol. 144, 1984, pp. 13–46.

12 Govinda Ram, H. S., "Studies on Two-Dimensional Bubbles and Associated Unsteady Pressure Fields," Ph.D. thesis, Indian Institute of Science, 1988.

13 Roshko, A., and Lau, J. C., "Some Observations on Transition and Reattachment of a Free Shear Layer in Incompressible Flow," *Proc. Heat Transfer*, Fluid Mechanics Institute, Vol. 18, 1965, pp. 157–167.

14 Kiya, M., and Sasaki, K., "Free Stream Turbulence Effects on a Separation Bubble," *Journal of Wind Engg. and Ind. Aerodynamics*, Vol. 14, 1983, pp. 375–386.

15 Hillier, R., and Cherry, N. J., "The Effects of Stream Turbulence on Separation Bubbles," *Journal of Wind Engg. and Ind. Aerodynamics*, Vol. 8, 1981, pp. 49–58.

16 Ota, T., "An Axisymmetric Separated and Reattached Flow on a Longitudinal Blunt Circular Cylinder," ASME *Journal of Applied Mechanics*, Vol. 14, June 1975, pp. 311–315.

17 Kraichnan, R., "Pressure Field Within Homogeneous Anisotropic Turbulence," *Journal of Acoust. Soc. of America*, Vol. 28, No. 1, Jan. 1956, pp. 64–72.

Turbulent Boundary-Layer Development Around a Square-Sectioned U-Bend: Measurements and Computation

H. Iacovides

B. E. Launder

P. A. Loizou[1]

H. H. Zhao[2]

Mechanical Engineering Department,
UMIST, Manchester M60 1QD, U.K.

A computational and experimental study is reported of turbulent flow around a square-sectioned U-bend with a mean bend radius equal to 3.375 times the hydraulic diameter (D_H): the duct Reynolds number is 58,000. The bend geometry is the same as that for which Chang et al. (1983) have reported extensive LDA data except that in the latter experiment the bend was preceded by some thirty hydraulic diameters of straight ducting (thus the boundary layers filled the duct). In the present case, with the inlet section shortened to only 6 D_H, the boundary layer thickness at inlet to the bend was only about 0.15 D_H. Despite the thinner boundary layers a strong secondary flow is generated which, by 135° around the bend, appears to have broken down into a chaotic pattern. Computations of the flow using a three-dimensional finite-volume solver employing an algebraic second-moment (ASM) turbulence model are in generally close agreement with the experimental data and suggest that the secondary flow, in fact, breaks down into a system of five eddies on either side of the mid-plane, in place of the classical single vortex structure.

1 Introduction

Turbulent flow in curved ducts of uniform square cross-section has generic similarities to those arising in turbomachinery blading. Moreover, it offers a fundamental three-dimensional flow with unambiguous boundary conditions that is analyzable in a simple coordinate frame: it thus provides an important case for testing the capabilities of turbulence models in complex strain fields. An extensive review of the literature up to 1983 is provided by Chang et al., (1983), who also contributed what has come to be recognized as a searching set of experimental data of the flow around a U-bend with a mean bend radius (R_c) equal to 3.375 times the hydraulic diameter (D_H). While the flow in this case remains unseparated, the strong secondary flow produces a very complex streamwise flow distribution half-way around the bend with a pronounced trough in velocity near the inside of the bend. Initial attempts at computing the flow entirely failed to predict the presence of these troughs. A major weakness of these early studies was the use of wall functions to straddle the viscous and buffer layers—a technique which, though economical, is inappropriate for flows where the velocity vector parallel to the surface undergoes substantial skewing within the near-wall sublayer. Recently Iacovides et al. (1989) have reported computations

with a hybrid turbulence model in which Van Driest's form of the mixing-length hypothesis is adopted over the near-wall sublayer (covering the region where direct viscous effects are important) while, over the remainder of the cross-section, either the standard $k - \epsilon$ model or an algebraic second-moment (ASM) closure is employed. Significant improvements were achieved over earlier computations, especially when the ASM scheme was adopted. Nevertheless, agreement with experiment was far from complete, even with the most elaborate model adopted. There was little doubt that the main source of the discrepancy was the turbulence model as a limited amount of rechecking on an identically proportioned U-bend constructed at UMIST (Johnson and Launder, 1985) confirmed very closely the flow field measured by Chang et al., (1983).

While the experimental data discussed above evidently provided a searching test case for three-dimensional flow solvers, it could be argued that it was not an especially appropriate one for gaining an impression of the capabilities of such schemes in turbomachinery blading passages or intake ducting. In those applications the boundary layers were thin and the secondary flow (which is driven by the velocity deficit associated with the boundary layer of the streamwise flow) would be expected to differ significantly from that found in the Chang experiment, where the flow at bend entry was nearly fully developed.

Professor Whitelaw's team at Imperial College has reported extensive measurements of flow through curved square ducts with thin inlet boundary layers, including S-bends and 90 deg bends with thin inlet boundary layers (see, for example, Taylor
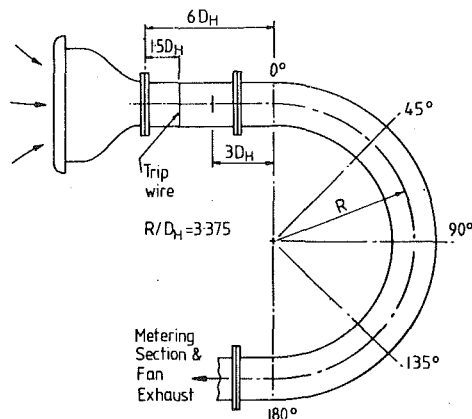
Fig. 1   Schematic diagram of test section

Fig. 2   Mean velocity profile at $3D_H$ ahead of bend entry

et al., 1982a,b) which provide good tests of the turbulence model in the immediate near-wall region. The longer period of straining associated with a U-bend, however, makes the predicted flow pattern more critically dependent on the outer layer turbulence model. Moreover, with a 90 deg bend there has been no breakdown reported of the secondary flow into multiple streamwise vortices. It is thus of considerable interest to ascertain whether, in the case of the U-bend, vortex breakdown still occurs when the inlet boundary layers are thin.

The present contribution reports experiments and computations of a U-bend flow of identical proportions to that considered by Chang et al., (1983), thus facilitating comparisons of similarities and differences in the two sets of results. The flow-prediction software employed, including the turbulence model adopted, is that presented in Choi et al., (1989). Section 2 describes the experimental program, while Section 3 gives an outline of the numerical scheme. The experimental and computational results are presented in Section 4.

2   Experimental Program

The apparatus used for the present study, Fig. 1, was that developed by Johnson and Launder (1985) save that the inlet tangent was here shortened to $6 D_H$. This is preceded by an entry contraction section containing a fine mesh screen and filter and providing a 5:1 area reduction by its downstream end. The square-sectioned duct had a side length D_H of 90 mm and a nominal mean radius of 0.61 m. It was fabricated from 10 mm perspex sheeting which provided smooth, rigid, transparent walls. The curved side walls were cemented permanently to the bottom wall, while the removable top wall was sealed to the side walls by soft rubber tubing inserted in grooves machined into the top of the side walls. The top is clamped down onto the side walls with threaded metal rods.

The boundary layers developing on the walls were tripped by means of fine wires affixed to the four sides at a distance approximately $1 D_H$ from the straight duct inlet. This led to normal turbulent boundary layers about 10 mm thick at entry to the U-bend section. The nominal Reynolds number based on bulk velocity and hydraulic diameter was 58,000. The bulk flow rate was in fact monitored by means of an orifice plate accommodated in a long length of straight circular piping just before inlet to the centrifugal fan, see Fig. 1. Further details on the apparatus and tolerances are provided by Johnson and Launder (1985).

All velocity measurements were obtained with DISA and TSI constant-temperature, hot-wire anemometers using standard DANTEC single and cross-wire probes. The wires were individually calibrated before and after each velocity traverse using the Sidall and Davies (1972) hot-wire response equation. The cross-wire probes were separately calibrated for yaw sen-

sitivity following Bradshaw (1971). The inlet velocity field was mapped at $3 D_H$ ahead of the bend entry and at the entry plane itself; then at 45 deg intervals around the bend. At each station, traverses across the duct were made along, typically, 15 vertical lines (the bend's symmetry plane being horizontal). All measurements were made with the axis of the hot-wire probe horizontal pointing directly upstream with the wires themselves lying in a horizontal plane. The probes connected to a holder with a vertical stem that passed through a slot in the top wall and were traversed vertically across the channel by means of a stepper motor.
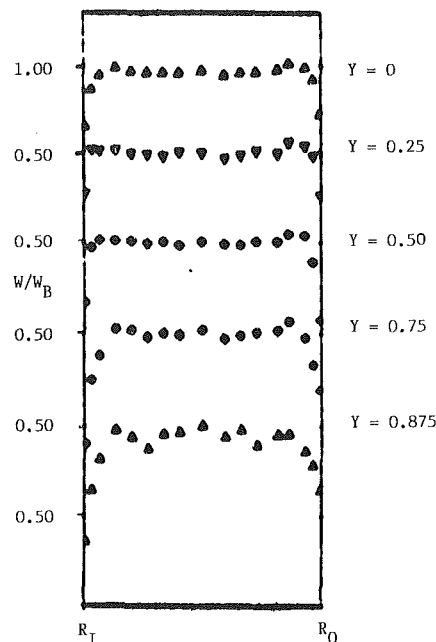
The hot-wire signals were sampled digitally at 900 samples per second. Mean and fluctuating (rms) values were based on 5120 records per point. A detailed assessment of accuracy for the present system applied to three-dimensional duct flows indicates a combined uncertainty in the mean streamwise velocity of approximately ± 3 percent. The corresponding uncertainty in the fluctuating velocity is ± 6 percent. It is difficult to ascribe an accurate uncertainty to the measurement of the mean radial velocity V. This component is considerably smaller than the streamwise velocity W (at least, in the region accessible to the hot-wire probe) and is thus especially susceptible to probe alignment or blockage errors. On the basis of data repeatability and the general smoothness of the profiles (while the data were acquired by making *vertical* traverses across the duct, the results are presented as *horizontal* velocity distributions to facilitate comparison with the earlier measurements of Chang), our view is that the uncertainty in V is within $\pm 0.05 W_B$, W_B denoting the bulk axial flow. Comparisons with computations in Section 4 suggest that there may be a systematic error in V of about $-0.04 W_B$.

Figure 2 shows the detailed mean velocity distribution at three hydraulic diameters upstream of the bend entry. The flow at this position is closely symmetric with no sign of the acceleration of the "inside" fluid that occurs closer to the bend. The mean velocity profiles at this position were used as the basis for ascribing initial conditions for the computations as described in the next section. The experimental results within the bend are presented in Section 4, in parallel with the corresponding computations.
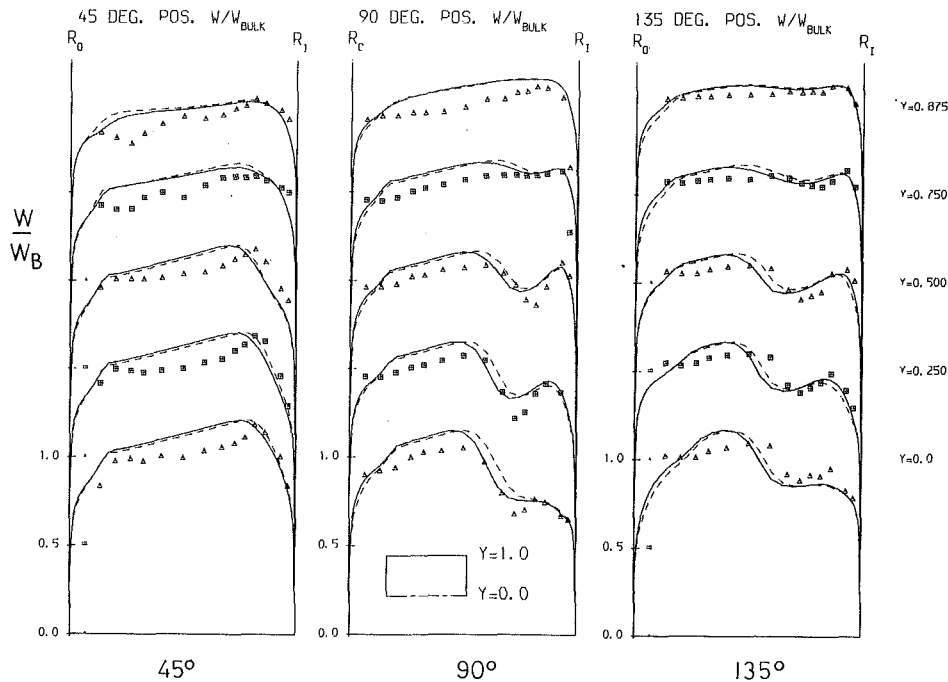
Fig. 3 Mean streamwise velocity profiles (a) 45 deg, (b) 90 deg, (c) 135 deg
Symbols: experiments
————: Fine-grid computations;
------: Coarse-grid computations
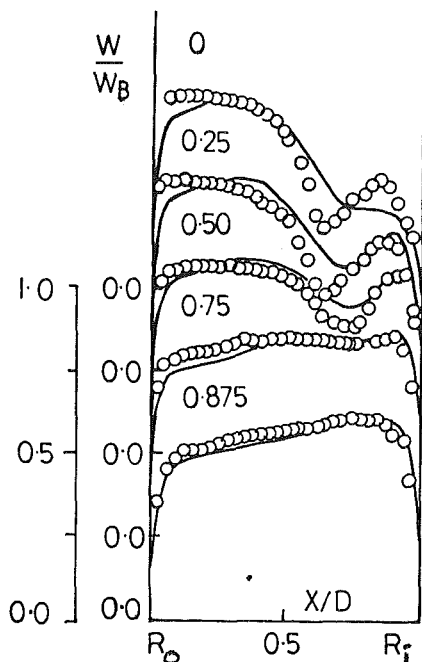
Fig. 3(d) Measurement and computation of U-bend flow with developed velocity profile at entry. Symbols Chang et al., 1983 experiment; Lines Choi et al., 1989 computation.

3 Computational Program

The three-dimensional semi-elliptic solver adopted for these computations has been extensively described in earlier publications (see Iacovides, 1986; Iacovides and Launder, 1985); a summary has also been recently provided in this journal (Choi et al., 1989). Here, therefore, it may suffice to note simply that it adopts a conventional staggered grid for pressure and velocity components, SIMPLE pressure-correction strategies and the QUICK treatment of cross-stream momentum transport. In the study by Choi et al., (1989) both $k - \epsilon$ eddy viscosity and algebraic-second-moment (ASM) closures were used to compute the U-bend flow of Chang et al., (1982). However, since the ASM results were clearly superior, that version alone has been considered in the present case. The detailed equations defining the model in cylindrical coordinates is given in the appendix of Choi et al., (1989). Across the near-wall sublayer Van Driest's form of the mixing-length hypothesis has been adopted. The value of the normalized wall distance coordinate at the changeover point from one model to another was typically 60 wall units, though inevitably this varied due to the streamwise and perimetral variations in the local friction velocity.

In Choi et al., the half cross-section on one side of the flow symmetry plane was mapped by a 25×47 grid with eight nodes across the sublayer/buffer region with the mixing-length schemes was adopted. Computations with the same number of nodes over the cross-section (and 100 streamwise planes) were also made here, though with a slightly shifted nodal concentration towards the walls in recognition of the thin inlet boundary layers. A further set of computations was made with twice the number of nodes (16) across the near-wall region. This region is crucial to resolve accurately because the secondary flow reaches its greatest value very close to the top (and bottom) walls. The number of streamwise planes was also increased by 50 percent; the grid adopted was thus $33 \times 63 \times 150$. It is these finer grid results on which attention is focused here; there are, however, only minor differences from those obtained with the coarser mesh.

The inlet flow was three-dimensional and it was therefore impractical to attempt to assign initial conditions working purely from the inevitably incomplete measured data field at $3 \, D_H$ upstream of the bend. Instead a separate calculation was made (with an identical grid in the cross-sectional plane) of developing flow in a straight duct starting from a *very* thin
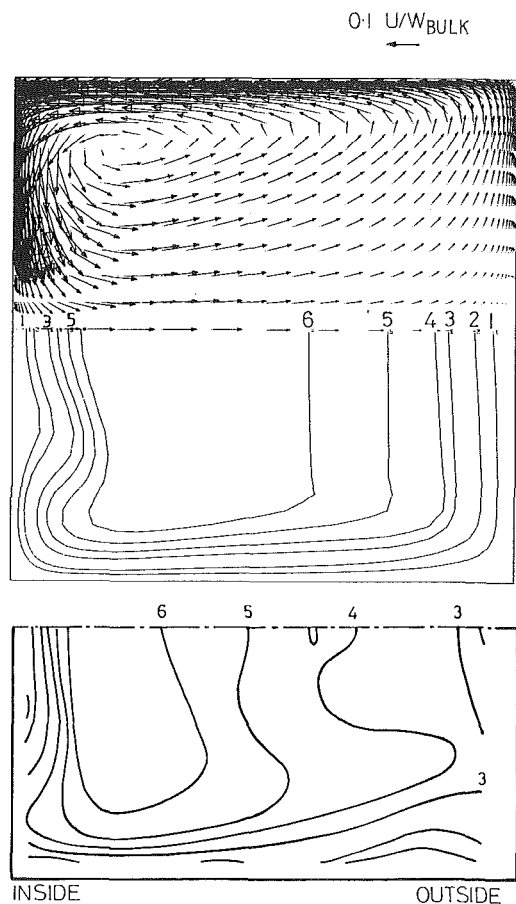
Fig. 4 Axial velocity contours and secondary velocity vectors at 45 deg. (a) Computed velocity vectors; (b) computed axial velocity contours; (c) measured axial velocity contours.

Fig. 5 Axial velocity contours and secondary velocity vectors at 90 deg. Key as Fig. 4

turbulent boundary that was assumed to be uniform around the duct perimeter. The mixing-length hypothesis was used to assign initial values of k and length scale (subject to a minimum k of 10^{-4} W$_B{}^2$ corresponding to the measured freestream turbulence intensity level). From this assumed initial state, the downstream development of the flow was computed until this computed boundary layer matched, as closely as possible, the measured mean velocity distributions. The computed fields of *all* the computed variables at this point were then used as the inlet conditions for the U-bend calculations. While the entry conditions determined in this way would not have been perfect, sensitivity tests convinced us that uncertainties in inlet profiles were not contributing significantly to differences between computed and measured behavior. For example, reducing the inlet velocity boundary layer thickness (at -3 D$_H$) to only 7 percent of that for the reported computations produced velocity profiles at 90 deg which differed from those to be shown below by amounts considerably less than between the coarse and fine-grid results at that position.[3]

As the scheme adopted was a semi-elliptic solver, only the pressure required the application of a downstream boundary condition. A pressure *gradient* that was uniform over the cross-section was applied together with a mean pressure level that was automatically adjusted to give the correct mass flow

---

[3]Another indicator of the relative insensitivity of the flow to the entry conditions is provided by a second series of experiments we carried out in the same apparatus where, at inlet, triangular gauze strips were fixed in the duct corners so as to produce there patches of low-momentum, high turbulence–intensity fluid. By the 90 deg station, however, the measured profiles were scarcely distinguishable from the data reported here. For that reason, the "gauze-strip" test will not be separately reported in the literature.
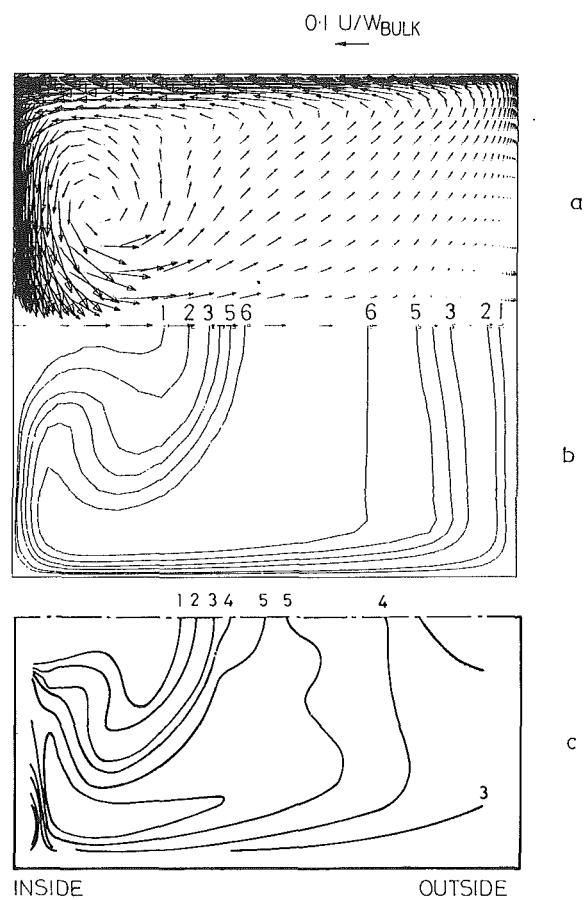
through the duct. The outlet was located 5 hydraulic diameters downstream of the duct exit.

4 Presentation and Discussion of Results

Figure 3 presents the measured and computed profiles of the streamwise mean velocity measured along five reference lines parallel to the symmetry plane at 45, 90 and 135 deg around the U-bend. The experimental features will first be noted. At the 45 deg station the irrotational vortex formed in the central region of the duct is still clearly evident, the peak velocity being displaced well toward the inside of the bend. This is the usual pattern reported in numerous earlier bend studies. By 90 deg the streamwise velocity displays a quite different appearance, however. Due to convective transfer of low momentum fluid by the near-wall secondary flow from the outside to the inside of the bend, a marked trough develops in the streamwise velocity at a normal distance of about 0.25 D$_H$ from the inner wall. The behavior is in fact not dissimilar from the 90 deg flow measured in an identically proportioned U-bend by Chang et al., (1983) reproduced in Fig. 3(d) (though with a slightly stretched vertical scale and with the curves sequenced in the reverse order). It is recalled that, for that case, the flow at bend entry was nearly fully-developed. Any thought that the much thinner boundary layers in the present study might have led to a simpler flow pattern is thus evidently unsubstantiated (indeed, evidence will be presented later that suggests a more chaotic flow may be created with the thinner entry boundary layers). Finally, the flow at 135 deg is broadly similar to that at 90 deg save that the velocity troughs have here become slightly less steep.

Turning to the computed results, we note first that at 45
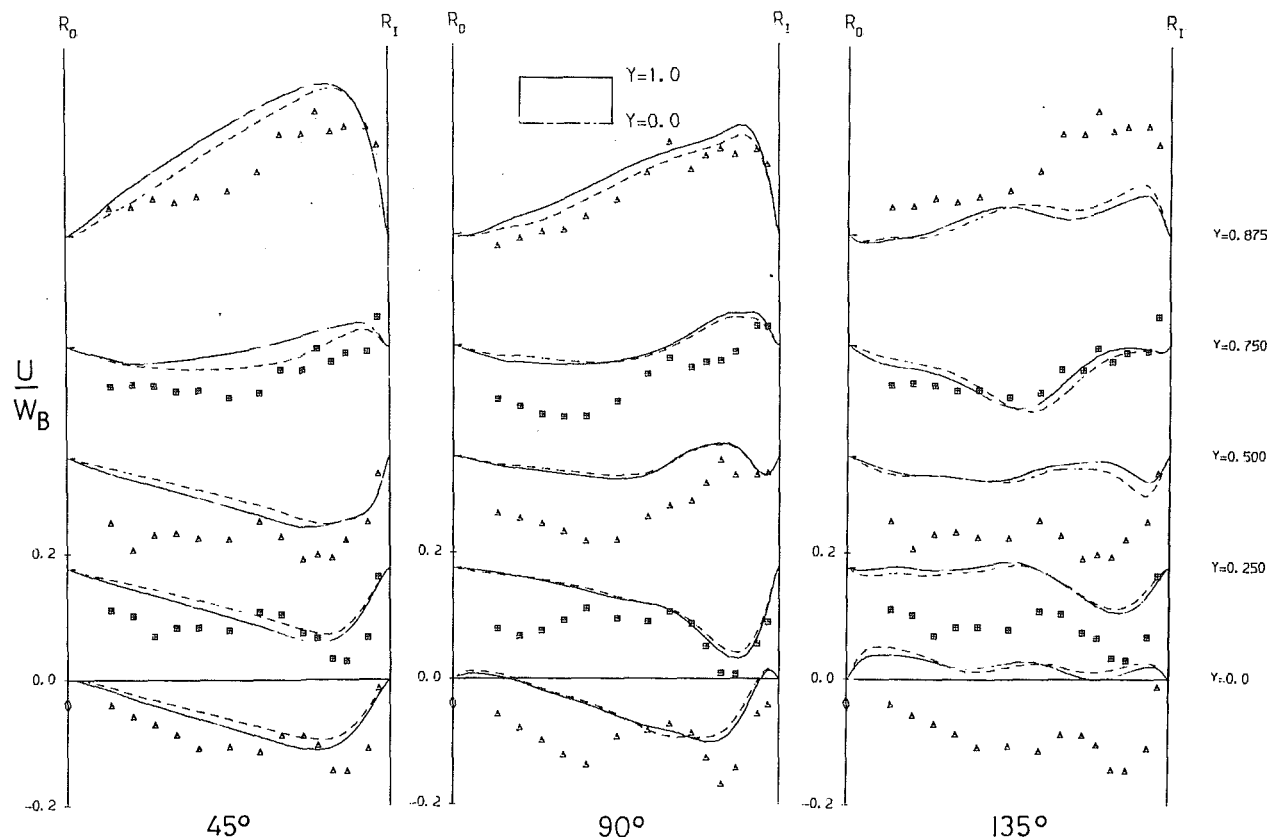
Fig. 6   Radial velocity profiles. Key as Fig. 3

and 90 deg there appears to be some inconsistency since the computed normalized velocity profile is nearly everywhere higher than the measured. (The integral of a graph of W/W_B over the duct should, of course, be precisely the same for computation and experiment.) This aberration probably arises from the fact that in the experiment W and W_B are measured independently. The other main feature is that, at 90 deg, the computations reproduce with reasonable fidelity the depression in streamwise velocity toward the inside of the bend—indeed, rather better than in the case of (nearly) fullly developed flow (Fig. 3(d)). The differences between the computed W profiles for the coarse and fine grids show the effect of doubling the nodal density across the sublayer. The main effect is seen to be to displace the profiles near the center plane ($Y=0$ and 0.25) slightly toward the outside of the bend. This in turn arises from the bend-induced secondary flow being slightly stronger in the case of the finer sublayer mesh *over the preceding portion* of the bend (see Fig. 6(a)). At 135 deg (Fig. 3(c)) agreement between computation and experiment (for the fine grid) has deteriorated somewhat: the computed profiles indicate that, relative to the 90 deg pattern, the troughs have been displaced to the left (i.e., toward the outer wall), whereas no such shift is seen in the experiments. This clearly suggests that the discrepancy has arisen from errors in computing the secondary flow pattern.

An alternative view of the axial velocity field is provided in Figs. 4 and 5 where the measured and computed velocity field data have been interpolated to provide a contour map of the streamwise velocity at 45 and 90 deg together with the corresponding computed secondary flow vectors. This presentation helps bring out the role of the secondary motion in modifying the streamwise flow. There is a strong secondary motion driven along a thin region adjacent to the top and bottom walls (due to the excess of the radial pressure gradient over that required for circular motion). This flow is deflected
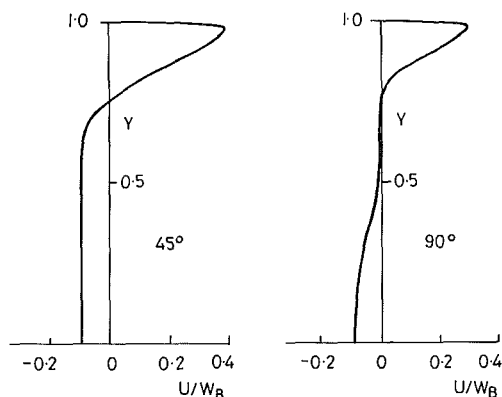
Fig. 7   Secondary velocity profiles along duct bisector normal to plane of symmetry. (a) 45 deg; (b) 90 deg

down the inside wall toward the duct mid-plane and a return flow occurs from the inside to the outside over the core region of the duct. This is the classical single-cell vortex flow that pertains at the 45-degree station. By 90 deg, the readjustments to the streamwise velocity field lead, through its coupling with the pressure field, to the eye of the secondary vortex being pushed far to the inside of the bend. This is what causes the development of "mushroom" shaped velocity contours near the inner wall as the return fluid is deflected away from the center plane; indeed, it is this displacement of low-momentum fluid near the center plane that is directly responsible for the "troughs" that have been noted in Fig. 3(b).

In Fig. 6 the measured and computed radial components of velocity are compared; a positive value denotes motion from the outer wall toward the inner. At 45 deg the flow along the near-wall line, $Y=0.875$, is positive, while for $Y=0.5$ and below it is uniformly negative. While the computed and meas-
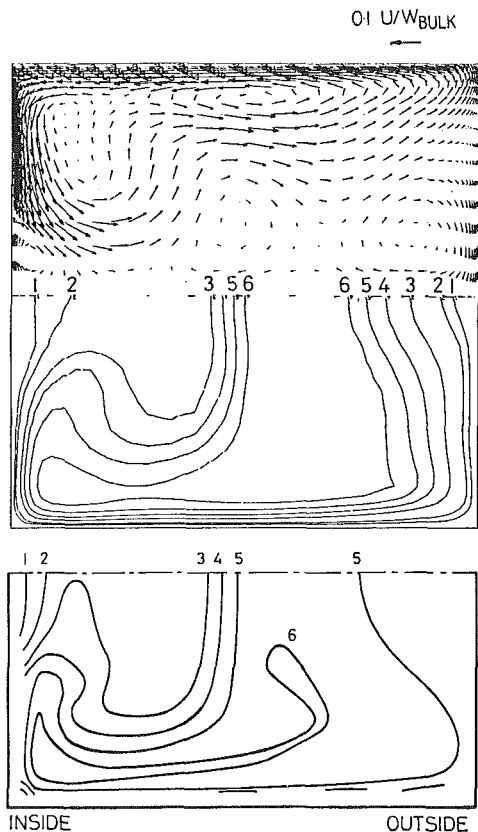
Fig. 8   Axial velocity contours and secondary velocity vectors at 135 deg. Key as Fig. 4

a) Streamwise intensity

b) Radial intensity

Fig. 9   Rms radial and axial turbulence intensities. Symbols: experiment; line: computations

ured shapes of the velocity profiles are broadly similar, near the wall the computed outside-to-inside flow is larger than calculated, whereas along the other lines the measured inner-to-outer return flow is generally larger than computed. This suggests that there may—for whatever reason—be a small bias in the measured values of V; certainly, if the data along all the constant Y lines are displaced by about $+0.04$ W_B (which is within the estimated uncertainty of V), agreement with experiment is greatly improved. It is not just the question of agreement with computation that suggests such an adjustment may be appropriate. If streamwise rates of change are negligible, the volumetric flow rate to the right across any radius should equal that to the left. The computational results at 45 and 90 deg shown in Fig. 7 do indicate that along the mid-duct radius a balance does very nearly exist—indicating that the contribution of streamwise changes is small. However, unless the indicated shift is applied to the radial velocity measurements in Fig. 6, it is hard to imagine the indicated balance being achieved. At 90 deg there seems to be a similar bias to the data, though possibly of slightly smaller magnitude. Now, moreover, one notices aspects of the general shape of the profiles that differ from experiment to computation, most notably the very irregular measured profiles of V along the lines $Y=0$ and 0.25. It is impossible to form a complete view of the secondary flow pattern in the experiment in the absence of data of the mean velocity normal to the center plane. The noted irregularities in the V distribution, however, convey an impression that at 90 deg the measured secondary flow may have reached a more chaotic state than in the computations. This suggestion is given support by the fact that at 135 deg the measured irregularities have become more pronounced. Moreover, at this station the computed profiles also exhibit a waviness that suggests a far more complex secondary flow pattern than at 90 deg. That this is so is vividly brought out
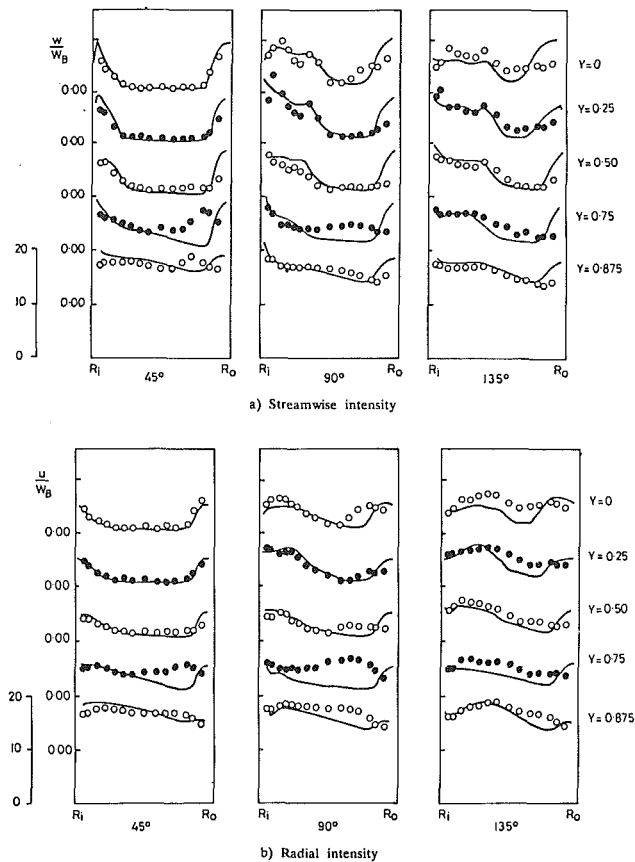
by the secondary velocity vector plot in Fig. 8. Whereas at 90 deg the computed flow is dominated by a single vortex centered toward the inside of the bend (though with a very small secondary vortex just visible near the junction of the center plane and inner wall), at 135 deg a system of no less than five secondary vortices is present. Indeed, the computed secondary flow field at this station is more chaotic than the predicted pattern at the same station for the case of fully developed entry flow, Choi et al., (1989).

The above extensive consideration of the secondary flow field leads to a plausible explanation for the deterioration in agreement in the predicted streamwise velocity between 90 and 135 deg. The detailed mean-flow picture up to the 90 deg station is largely dominated by a conventional single-cell secondary-flow vortex. Shortly before 90 deg, however, the *actual* secondary motion starts to break down into a system of multiple secondary eddies. While the computations also display such a breakdown, it begins somewhat later than in the experiment. Because errors in predicting the secondary flow at one position affect the primary velocity at *later* positions in the bend, it is not until the 135 deg station that the differences in the measured and computed secondary velocities propagate into the W velocity profiles.

Finally, Fig. 9 shows the measured and predicted profiles of the streamwise and radial rms velocities at the 45, 90, and 135 deg stations. There is generally rather close agreement between the experiment and computation. An exception, though, are the profiles along the line $Y=0.75$, where the experimental levels are strikingly higher than the computed. The fact that the differences seem to be confined to the outside (concave) half of the bend at 45 deg but that by 90 deg they have spread across most of the duct—despite the secondary flow along this line being from the inside to the outside—suggests that this may be associated with the formation of

Görtler vortices on the concave wall in the experiment that are not reproduced in the computations.

Conclusions

The following principal conclusions may be drawn from the present study:

1 The marked troughs in streamwise velocity that were the most notable feature of the experiment of Chang et al. on flow around a U-bend with nearly fully-developed inlet flow are still just as prominent in the present experiment in an identically proportioned U-bend where the inlet section was shortened to only six hydraulic diameters.

2 Computational results indicate that the troughs arise from the return secondary flow near the duct mid-plane being rapidly reduced by changes in the pressure field, thereby causing a deflection of this return flow with low streamwise velocity away from the symmetry plane. This in turn leads to an engulfment of high-velocity fluid closer to the inner wall.

3 The changes in the secondary flow pattern giving rise to the troughs in W velocity seem to be the first stage in a breakdown in the secondary motion into numerous smaller-scale vortices: the computed secondary field exhibits five such vortices at 135 deg.

4 The computed flow field, based on the ASM/mixing-length hybrid turbulence model that was the most successful version used by Choi et al., (1989) in predicting the data of Chang et al., (1982), did reasonably well in predicting the present flow also—indeed, somewhat better than it did for Chang's case. There is some evidence, however, that the breakdown of the secondary flow into multiple vortices occurs later in our predictions than in the experiment and this is probably why the streamwise velocity is predicted less well at 135 than at 90 deg.

References

Bradshaw, P., 1971, "An Introduction to Turbulence and Its Measurement," Pergamon Press.

Chang, S. M., Humphrey, J. A. C., and Modavi, A., 1983, "Turbulent Flow in a Strongly Curved U-Bend and Downstream Tangent of Square Cross-Sections," *Physico-Chemical Hydrodynamics*, Vol. 4, p. 243.

Choi, Y. D., Iacovides, H., and Launder, B. E., 1989, "Numerical Computation of Turbulent Flow in a Square-Sectioned 180° Bend," ASME JOURNAL OF FLUIDS ENGINEERING, Vol. 111, p. 59.

Iacovides, H., 1986, "Momentum and Heat Transport in Flow Through 180° Bends of Circular Cross-Section,"Ph.D. thesis, Faculty of Technology, University of Manchester.

Iacovides, H., and Launder, B. E., 1985, "ASM Predictions of Turbulent Flow and Heat Transfer in Coils and U-bends," *Proc. 4th Int. Conf. on Numerical Methods in Laminar and Turbulent Flow*, Pineridge Press, Vol. 2, p. 1023.

Johnson, R. W., and Launder, B. E., 1985, "Local Nusselt Number and Temperature Field in Turbulent Flow Through a Heated Square Sectioned U-bend," *Int. J. Heat and Fluid Flow*, Vol. 6, p. 177.

Sidall, R. G., and Davies, T. W., 1972, "An Improved Response Equation for Hot-Wire Anemometry," *Int. J. Heat Mass Transfer*, Vol. 15, p. 367.

Taylor, A. K. M. F., Whitelaw, J. H., and Yianneskis, M., 1982a, "Curved Ducts with Strong Secondary Motion: Velocity Measurements of Developing Laminar and Turbulent Flow," ASME JOURNAL OF FLUIDS ENGINEERING, Vol. 104, p. 350.

Taylor, A. K. M. F., Whitelaw, J. H., and Yianneskis, M., 1982b, "Developing Flow in S-shaped Ducts—Part I: Square Cross-Section Duct," Rep. FS/82/7, Imperial College Fluids Section (also NASA CR3550).

Application of Momentum Integral Methods and Linearized Potential Theory for Predicting Separation Bubble Characteristics

D. M. Stropky
Graduate Research Assistant,
Department of Mechanical Engineering,
University of British Columbia,
Vancouver, B.C., Canada

N. Djilali
Bombardier, Inc., Canadair Aerospace Group,
Montreal, Quebec, Canada

I. S. Gartshore
Professor.

M. Salcudean
Professor, Department Head.
Mem. ASME

Department of Mechanical Engineering,
University of British Columbia,
Vancouver, B. C., Canada V6T 1W5

A new viscous-inviscid interaction procedure of the semi-inverse type has been developed to predict two-dimensional separated flows. The method is applied to incompressible flow over an external backward-facing step, using linearized potential theory for the inviscid region and a simple modification of Pohlhausens' momentum-integral method in the viscous region. The modified Pohlhausen method, which approximates the reverse flow region with a region of "dead-air," is first tested without the viscous-inviscid procedure to predict fully developed laminar and turbulent flow in a plane symmetric sudden expansion. Comparisons are made with experimental data, other calculation methods, and finite difference predictions using a modified version of an elliptic code (TEACH-II). Reasonable predictions of the sudden expansion and backward-facing step flows are obtained, provided that the step-height to boundary-layer thickness ratio is large enough for the Pohlhausen type velocity profiles to be effective. The relative simplicity of the zonal equations coupled with the viscous-inviscid interaction procedure makes the present calculation method computationally attractive. The method should also prove useful in more complex separated flow situations, such as bluff-body aerodynamics.

Introduction

In recent years, prediction methods for separated flows have increasingly relied on numerical solutions of the full Navier-Stokes equations for laminar flow, or on Reynolds' equations for turbulent flows. This approach, exemplified by the widely used TEACH family of programs (Benodekar et al., 1983), has been used in a variety of geometries (see, e.g., Nallasamy (1987) for a review of turbulent flow calculations). The use of such global methods is, however, not always practical for design purposes because they require considerable computing facilities, and offer little analytical insight into a problem. A more effective approach to obtain solutions of engineering accuracy using reasonable computing resources is seen by some researchers (Kline, 1981; Eaton and Johnston, 1981) to lie in the use of zonal modeling. This approach recognizes that the flowfield can consist of different regions, each having dominant features. Different models coupled with optimum solution methods are used to compute each region. Recent studies (see, e.g., Briley and McDonald, 1984; Kwon and Pletcher, 1986) have shown that flows with finite separation regions can be adequately modeled using "Viscous-Inviscid Interaction" (VII) methods.

Most VII methods use boundary-layer approximations to model the viscous region. Formally, these approximations assume the growth rate of the boundary layer to be small ($d\delta/dx \ll 1$) and that velocities normal to the wall (v) are

much smaller in general than those parallel to the wall (u). This is not strictly valid for reattaching flows (Bradshaw and Wong, 1972), where large local values of $d\delta/dx$ may occur, and where u and v may be comparable. The boundary-layer equations have, nevertheless, been used in several recirculating flow calculation methods, and evidence has been accumulating that, for flows with small, confined separation regions, they provide a useful approximation. For instance, the separated flow calculations of Briley and McDonald (1975) and Ghia et al. (1975) compared well with numerical solutions of the full Navier-Stokes equations.

The main advantage of the boundary-layer equations is the simplicity with which they can be solved numerically using a computationally inexpensive, single-pass, forward marching procedure. Flow separation, however, prohibits forward-marching because of the flow reversal. An expedient way of avoiding this problem is to neglect the streamwise convective derivative in the backflow region. The implications of this approximation (known as the "FLARE" approximation, proposed by Reyhner and Flügge-Lotz (1968)) were examined in some detail by Briley and McDonald (1984).

The boundary-layer equations can be further simplified by the use of approximate integral techniques (Schlichting, 1979). These methods are simple and their limitations for attached flow are well understood. Several authors (Lees and Reeves, 1964; Crimi and Reeves, 1976; Moses et al., 1978; Woolley and Kline, 1979) have applied integral techniques to separated flows using VII methods. All of these methods are iterative, and many use auxiliary schemes to remove convergence

problems. In addition, most of these VII procedures cannot be generalized to other classes of flows or to different methods of solving the governing equations. Finally, because of the difficulty in dealing with discontinuous geometries when using classical integral methods, only separation from smooth surfaces has been considered.

In this paper, a simple, efficient, and general procedure for predicting separated, interacting viscous-inviscid flows is presented. The method is applied to predict flow over an external backward-facing step. Linearized potential theory is used in the inviscid region and a modified Pohlhausen momentum-integral model is used in the viscous zone. The reasons for selecting the step case are threefold: (i) the separation point is fixed, (ii) techniques used to deal with the discontinuous geometry apply directly to flow around bluff bodies, (iii) the external step has not been solved by any VII method. To separately assess the modified momentum-integral model (MIM), it is first tested on fully developed (i.e., the VII procedure is not required) internal flow past a plane symmetric expansion.

The Momentum-Integral Model

Laminar Flow. Figure 1 illustrates the model of flow in a sudden expansion. All lengths are nondimensionalized by the step-height and velocities by the average velocity upstream of the expansion. The separated viscous flow is divided into two regions for analysis. Integral boundary-layer equations are used in both regions, but with different assumptions. In region ①, corresponding to $u > 0$, velocity profiles are approximated by the single parameter family given by Pohlhausen (see, e.g. Schlichting, 1979). In region ② (the backflow region), all fluid momentum and the wall shear stress are neglected. This assumption extends the FLARE approximation by neglecting *all* convection in the reverse flow region. A brief outline of the formulation is given below.

Nondimensionalized, the steady two-dimensional laminar boundary-layer equations are,
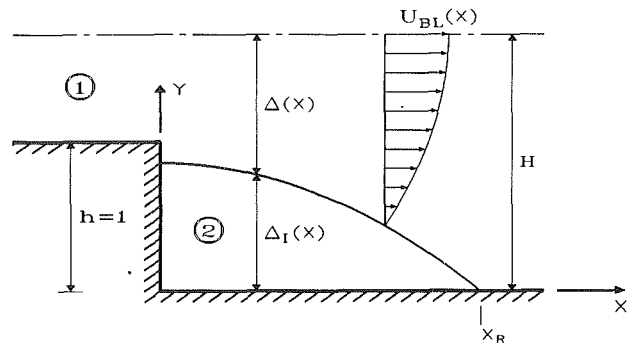
Fig. 1 Modeling of two-dimensional sudden expansion flow

$$x\text{-momentum} \quad \hat{u}\frac{\partial \hat{u}}{\partial x} + \hat{v}\frac{\partial \hat{u}}{\partial y} = -\frac{1}{2}\frac{dC_p}{dx}$$
$$+ \frac{1}{R_h}\frac{\partial^2 \hat{u}}{\partial y^2} \qquad (1)$$

$$continuity \quad \frac{\partial \hat{u}}{\partial x} + \frac{\partial \hat{v}}{\partial y} = 0 \qquad (2)$$

In region ① velocity profiles are assumed to be of the form

$$\frac{\hat{u}}{U_{BL}} = f(\eta) + \Lambda g(\eta) \quad (0 \le \hat{u} \le U_{BL}) \qquad (3)$$

where $f(\eta)$ and $g(\eta)$ are functions of the dimensionless coordinate $\eta = [y - \Delta_I]/\Delta$, and Λ is the usual Pohlhausen pressure gradient parameter, given in nondimensional terms as,

$$\Lambda = -\frac{1}{2}\frac{\Delta^2 R_h}{U_{BL}}\frac{dC_p}{dx} \qquad (4)$$

Substituting equations (2) and (3) into equation (1) and integrating from $y = \Delta_I$ to $y = H$,

Nomenclature

C_f = shear stress coefficient ($= \tau/q$)
C_p = pressure coefficient ($= (p - p_\infty)/q$ or $(p - p_s)/q$)
$C_1, \ldots, C_7$ = velocity profile constants
ER = expansion ratio ($= H/(H-1)$)
$f(\eta), g(\eta)$ = velocity profile functions
$f_1, \ldots, f_N$ = spliced cubic polynomials
h = step height
H = ratio of downstream channel width to step-height
H_{12} = shape factor ($= \Delta^*/\Theta$)
L_R = reattachment length
p = pressure
q = dynamic pressure ($= 1/2 \rho U_\infty^2$ for external flow) ($= 1/2 \rho \hat{u}_s^2$ for internal flow)
R_h = Reynolds number ($= h U_\infty/\nu$ or $h\hat{u}_s/\nu$)
$\hat{u}, \hat{v}$ = velocities in streamwise and transverse directions ($\hat{u} = u/U_\infty$ or $u/\hat{u}_s$), similarly for $\hat{v}$
U_{BL}, U_{POT} = bounding velocities for viscous and inviscid regions
U_∞ = undisturbed freestream velocity
x, y = nondimensional cartesian coordinates
x_R = reattachment location
x_o, x_N = interaction region endpoint locations
x' = redeveloping boundary layer virtual origin

Δ = boundary layer thickness (in step-heights)
Δ_I = recirculation bubble height (in step-heights)
Δ_1 = displacement line (in step-heights)
Δ^* = displacement thickness
$$\left(= \int_0^\infty \left[1 - \frac{\hat{u}}{U_{BL}}\right]dy\right)$$
η = velocity profile similarity variable
Θ = momentum thickness
$$\left(= \int_0^\infty \frac{\hat{u}}{U_{BL}}\left[1 - \frac{\hat{u}}{U_{BL}}\right]dy\right)$$
Λ = pressure gradient parameter
ν = kinematic molecular viscosity
ν_t = eddy viscosity
ρ = fluid density
τ = shear stress

Subscripts

n = cubic function index
N = number of cubics
p = perturbation location index
s = value at step location

Prescripts

Δ = perturbation

$$\begin{rcases} [1-(C_1+C_3)-(C_2+C_4)\Lambda - C_5\Lambda^2]\,\frac{d}{dx}\,(U_{BL}^2\Delta) \\[2mm] -(C_2+C_4+2C_5\Lambda)\,U_{BL}^2\Delta\,\frac{d\Lambda}{dx} \\[2mm] =[-C_6+(1-C_7)\Lambda]\,\frac{U_{BL}}{R_h\Delta} \end{rcases} \quad (5)$$

where $C_1 \ldots C_7$ are constants determined from the profile functions $f(\eta)$ and $g(\eta)$. The constants and corresponding functions are listed in Appendix A.

Specifying $\hat{v}_H = -\displaystyle\int_{\Delta_I}^{H} \frac{\partial \hat{u}}{\partial x}\,dy = 0$ (centerline symmetry condition) yields,

$$(1-C_1-C_2\Lambda)\,\frac{d}{dx}\,(U_{BL}\Delta)-C_2 U_{BL}\Delta\,\frac{d\Lambda}{dx}=0 \quad (6)$$

Finally, neglecting all fluid momentum and the wall shear stress, integration of equation (1) through region ② gives,

$$\Lambda\left(\frac{ER}{\Delta(ER-1)}+C_7-1\right)=-C_6 \quad (7)$$

where ER is the channel expansion ratio. Note that the above approximation does not allow calculation of reversing flows. In effect, the reverse flow is replaced by a region of dead air.

The set of equations (5)–(7) are solved numerically, for U_{BL}, Δ, and Λ using a Runge-Kutta routine. Integration begins just downstream of the expansion, with the imposed condition of fully developed flow upstream of the expansion. For a given expansion ratio, equation (7), together with continuity of mass and centerline velocity across the expansion, determine the initial conditions for the separated region. This results in discontinuities in Λ and Δ across the step, so the initial velocity profile extends some distance below the top of the step (see Fig. 1). The physical condition of zero flow at the step face is not met, but Acrivos and Schrader (1982) show that this condition is not necessary for boundary-layer calculations.

The discontinuities also result in limitations to the method, i.e., $ER \geq 1.20$ for a fourth-order profile. In the limit of a very small step, the effects on the boundary-layer are localized near the wall, so it is not surprising that the Pohlhausen profiles fail at low ER.

Turbulent Flow. The formulation of the turbulent flow problem proceeds in essentially the same fashion as the laminar case, but uses, instead of equation (1), the time averaged boundary-layer equation,

$$\hat{u}\,\frac{\partial \hat{u}}{\partial x}+\hat{v}\,\frac{\partial \hat{u}}{\partial y}=-\frac{1}{2}\,\frac{dC_p}{dx}+\frac{1+\lambda}{R_h}\,\frac{\partial^2 \hat{u}}{\partial y^2} \quad (8)$$

where $\lambda = \nu_t/\nu$, and ν_t is the eddy viscosity. Additional assumptions are required to determine the eddy viscosity.

Several experimental studies (Eaton and Johnston, 1981; Ruderich and Fernholz, 1986; Djilali, 1987) suggest that, over (about) the first half of the separation bubble, the separated shear layer has an overall growth rate similar to that of a plane mixing layer. Prandtl's free shear layer model (Schlichting, 1979) was therefore used to determine ν_t over the first half of the bubble (ν_t is assumed constant across the shear layer). Modeling a mixing layer with zero velocity on one side,

$$\lambda = \alpha b_{0.1} R_h U_{BL} \quad (9)$$

The characteristic width, $b_{0.1}$, is the distance between $(\hat{u}/U_{BL})^2 = 0.1$ and $(\hat{u}/U_{BL})^2 = 0.9$, and $\alpha = 0.014$. The rate of growth of the shear layer is given by,

$$\frac{db_{0.1}}{dx}=0.098 \quad (10)$$

After integration and substitution into equation (9), the eddy viscosity is given by,
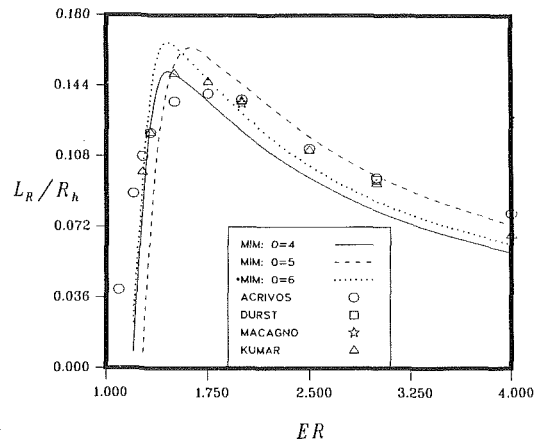
Fig. 2 Effect of expansion ratio on reattachment length for laminar flow
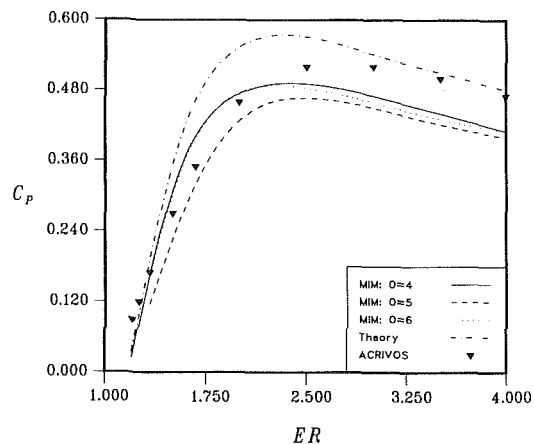
Fig. 3 Effect of expansion ratio on reattachment pressure coefficient for laminar flow

$$\lambda \approx 0.00137\,R_h\,U_{BL}\,(x+x_t) \quad (11)$$

where the virtual origin, x_t, is determined using the width of the shear layer at the separation, i.e.,

$$x_t = \frac{b_{0.1}(0)}{0.098} \quad (12)$$

A simple way of accounting for the experimentally observed change of growth rate at $x/x_R \approx 0.5$ is to apply equation (11) for $0 < x/x_R \leq 0.5$, and then to "freeze" the value of λ for $x/x_R > 0.5$.

The laminar velocity profiles of the previous section are inadequate for describing turbulent flow. New turbulent profiles in the form of equation (3) were developed to provide better estimates of the turbulent shear strain and shape factors. These profiles describe the range $(1.3 < H_{12} < 2.6)$ of shape factors found in attached flow with adverse pressure gradient, analogous to the laminar profiles of the previous sections. Appendix A lists these profiles and associated constants.

Results. Acrivos and Schrader (1982) noted, for laminar flow, that the use of the Reynolds number to nondimensionalize the boundary-layer equations leads to a reattachment length which is proportional to the Reynolds number. Figure 2 shows L_R/R_h plotted against ER for Pohlhausen profiles from fourth to sixth order, along with the results of other more detailed calculations. The results are good, considering the crude assumptions made in the separated region. The failure of the model at low ER is apparent, as is a slight dependence of the results on the order of the profile.

The calculated pressure rise to reattachment as a function of expansion ratio is shown in Fig. 3. The curve denoted
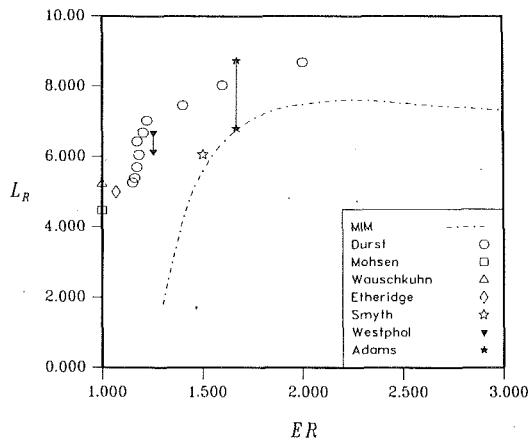
Fig. 4 Effect of expansion ratio on reattachment length for turbulent flow

"Theory" is derived from simple momentum balance, assuming a parabolic velocity profile at the step, a Karman-Pohlhausen separation profile at reattachment, and no friction at the walls, and constant pressure across the channel. All calculations lie below this bound as expected, except at low ER, for reasons explained previously. Agreement with the finite-difference calculations of Acrivos is again satisfactory.

Figure 4 illustrates turbulent flow calculations carried out over a range of expansion ratios. The resulting (Reynolds number independent) reattachment lengths are plotted along with available experimental data. Some of the experimental data are for single-sided sudden expansions; however Abbott and Kline (1962) show that for $ER \leq 1.5$, the results are synonymous with the symmetric case. Comparisons to the MIM are poor in this range (where the single parameter profiles are inadequate); however for $ER \geq 1.5$ agreement is reasonable.

Methods and assumptions used in the MIM allow for very efficient calculations of the flowfield. The solution times for all cases tested were less than 0.5 seconds on an IBM 3081 mainframe computer. This is at least one order of magnitude faster than finite-difference solutions to the boundary-layer equations. In the next section a new viscous-inviscid interaction procedure is presented. This procedure is applied, using linearized potential theory and the MIM, to predict the flow over an external backward-facing step.

A New Viscous-Inviscid Interaction Procedure

Zonal models require that the viscous and inviscid regions interact, and that their solutions match at the interface boundary (i.e., a boundary-value problem). Several iterative algorithms have been developed to compute the interaction, and most can be placed into one of three classes: direct, inverse, or semi-inverse.

In the direct scheme, an estimate of the displacement thickness, $\delta^*(x)$, is applied to the inviscid equations yielding the boundary-layer edge velocity distribution, $U_{IN}(x)$. This distribution is applied to the viscous equations to yield a new $\delta^*(x)$ distribution, and the process repeats to convergence. A singularity in the boundary-layer equations at separation makes this method unsuitable for separated flow (Briley and McDonald, 1984).

The inverse method applies $\delta^*(x)$ to the viscous equations which yield $U_{VIS}(x)$. This velocity distribution is applied to the inviscid equations yielding a new estimate of $\delta^*(x)$ and the process repeats. This method does not encounter a singularity at separation, but is inefficient (Williams, 1986) for solving problems in external flow.

The semi-inverse method applies an estimate of $\delta^*(x)$ to both sets of equations yielding $U_{VIS}(x)$ and $U_{IN}(x)$. These

velocity distributions are combined to generate a correction formula used to update $\delta^*(x)$ and the process repeats until the velocities match. Williams (1986) indicated that the semi-inverse method would be most useful for a mixture of attached and separated flow in external aerodynamics.

The present authors' first attempts at solving the external step with zonal methods and integral techniques involved using semi-inverse correction procedures proposed by other authors (Crimi and Reeves, 1976; Kwon and Pletcher, 1986). These methods were not easily adapted to the problem and convergence was difficult to obtain. A new correction procedure was therefore developed. The new semi-inverse VII procedure is readily adapted because the correction formulae are derived through perturbation of the governing equations. The method is suited to integral methods because the perturbations can be applied to $\delta^*(x)$, which arises naturally with these methods.

The concept is illustrated using the governing equation for the inviscid region, the linearized Hilbert integral (Briley and McDonald, 1984), often used in inviscid "slender-body" theory. The integral can be written (in non-dimensional form),

$$U_{POT}(x) = 1 + \frac{1}{\pi} \int_{-\infty}^{+\infty} \frac{\frac{d}{d\xi}\{\Delta^*(\xi)\}}{x - \xi}\, d\xi \qquad (13)$$

where $U_{POT} = U_{IN}/U_\infty$. A small perturbation to $\Delta^*(x)$ yields the perturbation to the external velocity, as follows.

$$U_{POT}(x) + \triangle U_{POT}(x) = 1$$

$$+ \frac{1}{\pi} \int_{-\infty}^{+\infty} \frac{\frac{d}{d\xi}\{\Delta^*(\xi) + \triangle \Delta^*(\xi)\}}{x - \xi}\, d\xi$$

subtracting equation (13),

$$\triangle U_{POT}(x) = \frac{1}{\pi} \int_{-\infty}^{+\infty} \frac{\frac{d}{d\xi}\{\triangle \Delta^*(\xi)\}}{x - \xi}\, d\xi \qquad (14)$$

Similarly, the boundary-layer equations are perturbed and then linearized to yield $\triangle U_{BL}(x)$. Both $\triangle U_{POT}(x)$ and $\triangle U_{BL}(x)$ are functions of the original independent variables and, additionally, are functions of $\triangle \Delta^*(x)$. The objective is to find the function $\triangle \Delta^*(x)$ which satisfies the following equation,

$$U_{POT}(x) + \triangle U_{POT}(x) = U_{BL}(x) + \triangle U_{BL}(x) \qquad (15)$$

The linearizations involved require successive applications of equation (15) until $\triangle \Delta^*(x) \approx 0$. Solving equation (15) analytically is not feasible. Instead, the velocities are matched at N control points $(x_1, x_2, \ldots, x_N)$, and equation (15) is written as,

$$U_{POT}(x_n) + \triangle U_{POT}(x_n) = U_{BL}(x_n) + \triangle U_{BL}(x_n)$$

$$[n = 1, 2, \ldots, N] \qquad (16)$$

The solution of equations (16) requires that $\triangle \Delta^*(x)$ have N degrees of freedom. This is done by constructing $\Delta^*(x)$ from N spliced cubic polynomials whose endpoints coincide with the N control points. The shapes of these cubic polynomials are governed by their endpoint values $(\Delta^*(x_n), n = 1, 2, \ldots, N)$, and by enforcing continuity of slope between polynomial pieces. The perturbation of $\Delta^*(x)$ due to a displacement $\triangle h_p$ at the endpoint x_p is termed the pth influence function of $\Delta^*(x)$ and is written $\triangle \Delta_p^*(x)$. The *complete* perturbation function, $\triangle \Delta^*(x)$, is the sum of all N influence functions, i.e.,
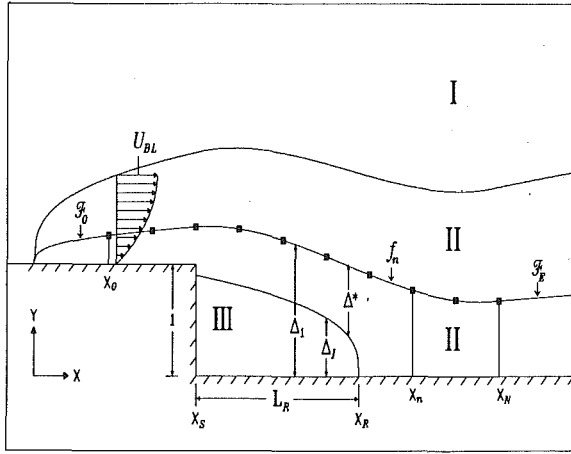
Fig. 5 Model of a backward-facing step in external flow

Fig. 6 Effect of Reynolds number and momentum thickness at the step on reattachment length for laminar flow. Data for O'Leary et al. and Leal et al. compiled by Denham and Patrick (1974)

$$\Delta \Delta^*(x) = \sum_{p=1}^{N} \Delta \Delta_p^*(x) = \sum_{p=1}^{N} K_p(x) \times \Delta h_p \qquad (17)$$

The N free parameters (Δh_p) in equation (17) give $\Delta \Delta^*(x)$ the required degrees of freedom. The pth influence function is a linear function of Δh_p, and this reduces equations (16) to a system of N independent, linear, algebraic equations. A detailed description of this new procedure is found in the thesis by Stropky (1988).

Application to an External Backward-Facing Step

Laminar Flow. The methods of the previous sections are now combined to solve the external step. Figure 5 gives the essential geometry, along with variables used in the problem. All lengths have been nondimensionalized by the step height, and all velocities are scaled on the undisturbed free stream velocity. Region I contains the inviscid flow; equation (13) is used to calculate the interface velocity for this region. Regions II and III comprise the viscous layer, with the interface velocity predicted using the MIM.

Nondimensionalized, the governing equations are,

$$\text{Region I} \quad U_{POT}(x) = 1 + \frac{1}{\pi} \int_{-\infty}^{+\infty} \frac{\dfrac{d}{d\xi}\{\Delta_1(\xi)\}}{x - \xi} \, d\xi \qquad (18)$$

Here Δ_1 replaces $\Delta^*(=\delta^*/h)$ because of the flow separation (see Fig. 5).

$$\text{Region II} \quad \frac{d}{dx}(\Theta U_{BL}^2) + \Delta^* U_{BL} \frac{dU_{BL}}{dx} = \frac{1}{2} C_{fI} \qquad (19)$$

$$\text{Region III} \quad U_{BL} \frac{dU_{BL}}{dx} \Delta_I = -\frac{1}{2} C_{fI} \qquad (20)$$

where C_{fI} is the shear stress coefficient at $y = \Delta_I$.

The same velocity profiles used for the sudden expansion are used here. Timmans' (Rosenhead, 1953) external flow profiles are also used as they are more accurate in regions of adverse pressure gradient (for attached flow at least). These profiles and associated constants are given in Appendix A.

The initial conditions for the viscous equations (at $x = x_o$) correspond to those of a boundary layer in zero pressure gradient (i.e., $\Lambda = 0$), and assume that x_o is far enough from the step so as not to be influenced by it. The elliptic nature of the inviscid equation requires that $\Delta_1(x)$ be defined for all x. Figure 5 shows $\Delta_1(x)$ comprised of spliced cubics ($f_n(x)$ $n = 1, 2, \ldots, N$) in the region $x_o \le x \le x_N$, termed the *interaction region*. This is the region in which the interface velocites are matched. Fitted smoothly into the first and last cubics are the curves $\mathfrak{F}_o(x)$ and $\mathfrak{F}_E(x)$. These curves are of
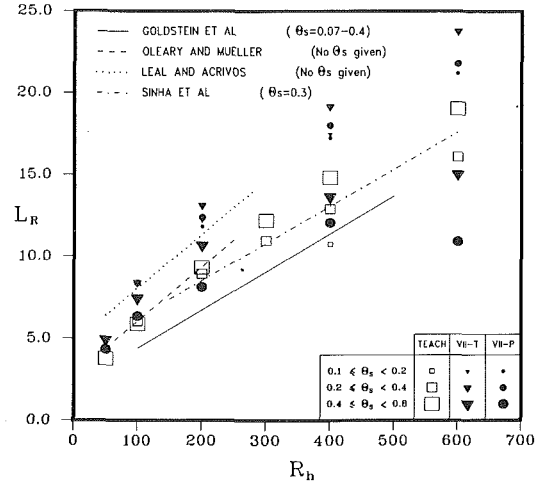
the form $\Delta_1 = 1 + A x^{1/2}$ and $\Delta_1 = A(x - x')^{1/2}$ respectively, where A, B, and x' are constants (x', the virtual origin of the redeveloping boundary layer, is found as part of the solution). This form of Δ_1 arises from analysis of the boundary-layer equations in zero pressure gradient, and ensures that the solution far from the step is that of an undisturbed boundary layer. This particular form of Δ_1 was critical for a robust solution to this problem, and the key integral involved is given in Appendix B for reference.

Results. Finite-difference results for an internal BFS (i.e., no-slip or free-slip condition on the wall opposite the step) are abundant, but no results were found which simulated the conditions of external flow. For computational comparison, the TEACH-II (Benodekar and Gosman, 1983) code was modified to simulate a BFS in external flow. This was done by applying a zero pressure gradient condition (Abdullah, 1988) along the length of the computational domain at the wall opposite (and twenty step heights away from) the step. Comparison with a no-slip wall showed significant changes in pressure distribution and profile shape factors, however changes in reattachment length were ≤ 5 percent. Experimental results are also extensive, however only those which most nearly simulated external flow conditions were chosen for comparison.

Figure 6 shows a plot of reattachment length (L_R) versus R_h for the TEACH-II and VII codes (VII-T is with Timmans' profiles, and VII-P is with fifth order Pohlhausen profiles), along with some experimental results. The momentum thickness at the step (Θ_s) is shown to be an important parameter, although it is often ignored. For $R_h \ge 100$ larger values of Θ_s produce longer reattachment lengths, except in the VII model for the largest values of Θ_s (where the MIM becomes inadequate). This trend, also observed by Goldstein et al. (1970), can be explained with the inviscid velocity equation (18). As the boundary layer gets thicker (i.e., larger Θ_s), any changes that the step induces in Δ_1 become relatively smaller, resulting in a reduction to the slope of Δ_1. From equation (18), this causes U_{POT} to shift towards 1, and since $C_p = 1 - U_{POT}^2$, the pressure is lower. The lower pressure allows the slow moving fluid near the bottom of the detached shear layer to penetrate further downstream before it is forced to reattach.

Overall comparison between TEACH-II and experiment is good, but the VII model consistently overpredicts values of L_R. Modeling the reverse flow region with dead air results in values of $\|\Lambda\|$ which are somewhat lower than the true separated profile values. Examination of the momentum equations show that as a result dC_p/dx is underpredicted,
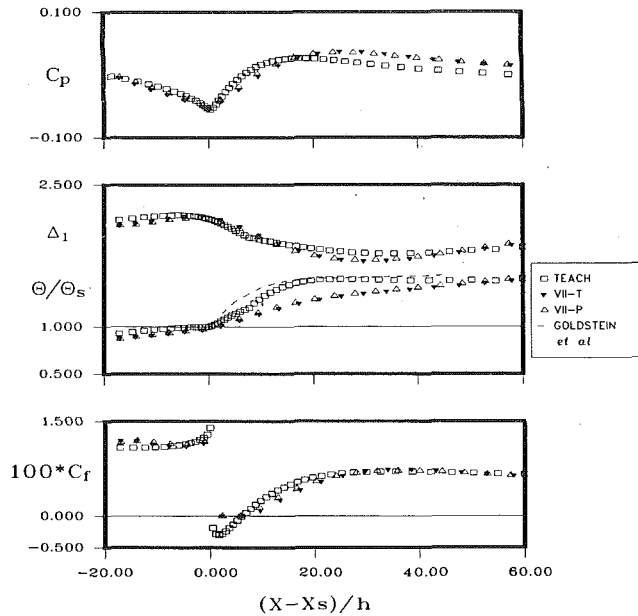
Fig. 7 Comparison of laminar flow integral parameters from VII, TEACH, and experiment for the case $\Theta_s \approx 0.48$, $R_h = 100$

Fig. 8 Effect of momentum thickness at the step on reattachment length for turbulent flow. Data for Narayanan, Tani, and Baker compiled by Eaton and Johnston (1981).

Fig. 9 Comparison of turbulent flow integral parameters from VII, TEACH, and experiment for the case $\Theta_s \approx 0.07$, $R_h = 60,000$

resulting in overpredictions of L_R. The TEACH-II model uses a bounded-skew hybrid differencing scheme which reduces the numerical error known as "false-diffusion," experienced by lower order schemes. Hackman (1982) showed, for a BFS, that numerical underpredictions in L_R of up to 20 percent can occur when low order schemes are used.

Figure 7 shows a comparison of integral parameters from TEACH-II and VII for the case $R_h = 100$ and $\Theta_s \approx 0.48$. Examination of the equations again reveal that, due to low values of $\|\Lambda\|$ used in the recirculation region, the gradient of Θ is reduced, resulting in the slight underpredictions shown. Experimental data from Goldstein et al. (1970) agree well with the TEACH-II predictions. The assumption of zero shear stress in the recirculation region is obviously wrong, but the effects outside that region appear to be minimal. Note that in all cases the choice of velocity profile used in the VII predictions has little effect on results, in fact, less than for the sudden expansion.

To enable comparison between the efficiency of the two codes, solutions were considered converged when less than a 0.5 percent change in L_R occurred between successive iterations. Grid independence was established to within a 1 percent change in L_R. The range of execution parameters for TEACH-II was 110-160 global iterations in 500-1000 seconds on an IBM 3081 mainframe computer, while for the VII method the range was 5-9 iterations in 0.7-2.5 seconds.

Turbulent Flow. The same turbulence model used in the separated viscous region of the sudden expansion calculations is applied to the BFS model. Outside this region, viscous calculations are performed using a momentum equation developed from power law velocity profiles (Duncan et al.) together with an entrainment equation and skin friction correlation (Strawn et al., 1984). In nondimensional form these equations are,

$$\frac{d}{dx}(\Theta^{\frac{m+3}{m+1}}) = a R_h^{-\frac{2}{m+1}} - \frac{b}{U_{BL}}\frac{dU_{BL}}{dx}\Theta^{\frac{m+3}{m+1}} \quad (21)$$

$$\frac{1}{U_{BL}}\frac{d}{dx}[U_{BL}\Theta H^*] = E \quad (22)$$

$$C_f = 0.0651(1-2\Omega)^{1.77}\left(\frac{\Omega}{\Theta R_h H_{12}}\right)^{0.23} \quad (23)$$
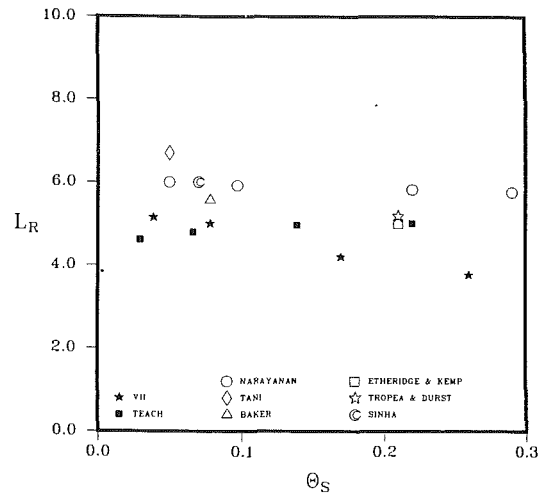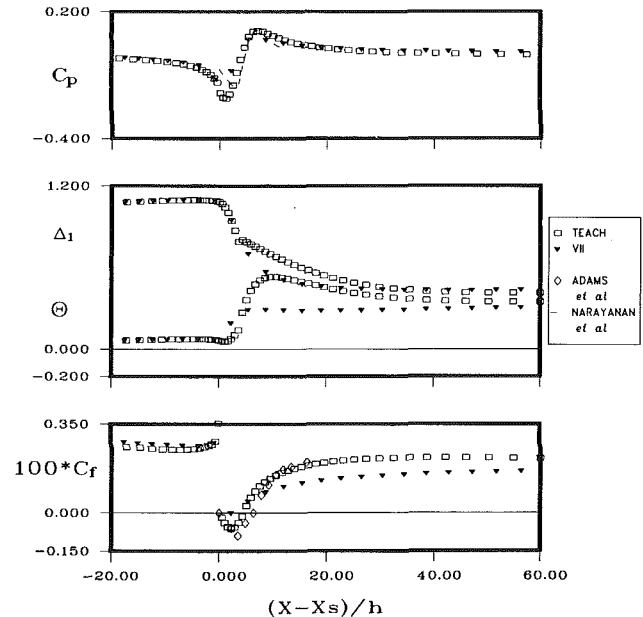
The constants a, b, and m depend on the R_x. The functions $H^* = (\Delta - \Delta^*)/\Theta$, E, and $\Omega = \Delta^*/\Delta$ depend on H_{12} and are listed in Appendix C.

The form of the curves $\mathcal{F}_o(x)$ and $\mathcal{F}_E(x)$ (see Fig. 5) are $\Delta_1 = 1 + Ax^{4/5}$ and $\Delta_1 = A(x-x')^{4/5}$, respectively, so the integral given in Appendix B can again be used to solve the inviscid equation. The virtual origin, x', as in the laminar case, is determined as part of the solution.

Results. The present VII turbulence model was formulated using constant values for a, b, and m throughout the entire domain. These values ($a = 0.0163$, $b = 4.00$, and $m = 7$) correspond to 1/7 power velocity profiles. The Reynolds number based on x_o (see Fig. 5) was kept constant at 6×10^6, which allowed both x_o and R_h to vary, (because $R_{xo} = x_o U_\infty / \nu = x_o R_h$) and this allowed the boundary-layer thickness at the step to vary.

Figure 8 shows results for L_R versus Θ_s from the TEACH-II and VII models, along with several experimental results. The results are scattered, but show a slight trend towards decreas-

Journal of Fluids Engineering

ing reattachment length with increasing momentum thickness, opposite to the laminar case. The TEACH-II programs used the standard $k-\epsilon$ turbulence model (Benodekar et al., 1983), modified to account for the preferential influence of normal stresses (over shear stresses) in promoting the transfer of turbulent energy from large to small eddies (Leschziner and Rodi, 1981). The scatter in the experimental results may be due to imposed pressure gradient (Kuehn, 1980). Results are encouraging, considering the assumptions in the VII model. The VII results were found to be Reynolds number independent in the range tested ($10^4 \le R_h \le 10^7$).

Figure 9 shows a comparison of integral parameters from the TEACH-II and VII codes for the case $R_h = 60,000$ and $\Theta_s \simeq 0.7$. Adams and Johnston (1988) claim that C_f may be independent of ER so their results are included for comparison. The results of Badri Narayanan et al. (1974) are also included, as their experiments simulated external flow conditions. Comparisons are fair, but again the momentum growth is underpredicted, probably for the same reason as the laminar case. TEACH-II predicts a redeveloped $H_{12} = 1.18$ which is somewhat low, while VII gives a more reasonable $H_{12} = 1.38$, however shear stress comparisons favor TEACH-II.

Computed cases for the turbulent VII code required 6-12 iterations and 1.7-4.4 seconds on the IBM 3081. The corresponding TEACH results were 110-230 iterations and 700-1600 seconds.

Conclusions

A general semi-inverse viscous-inviscid interaction (VII) method has been developed for predicting the flow field arising from a combination of inviscid flow and separated viscous flow. This method, combined with a simple momentum-integral model (MIM) and linearized potential theory (the "Hilbert" integral), was used to predict the essential features of flow over an external backward-facing step for both laminar and turbulent flow. Neither the linearized potential theory nor the MIM is essential to the method, but are used to devise as simple a model as possible while still retaining the essential physics of the problem.

The MIM was tested independently by predicting the essential flow features downstream of a fully developed sudden expansion. Modeling the reverse flow region with a region of dead air allowed for an efficient method of solving the boundary-layer equations. The turbulent case used a very simple "eddy-viscosity" model to compute the mean shear stress. Resulting reattachment lengths are in fair agreement with other more sophisticated methods and experimental data.

Largely as a basis for comparison with the VII method, finite-difference predictions using an elliptic computer code (TEACH-II) were made for the backward-facing step. Predictions by the VII model compare reasonably well to TEACH-II and experimental results, except for underpredictions in the growth of the momentum thickness in the recirculation region. Overall, it appears that the VII model captures much of the essential physics in this challenging flow domain. The relative simplicity of the governing equations coupled with the speed of the VII method makes the technique computationally attractive. Solution times are typically 1 to 2 orders of magnitude lower than for fully elliptic finite-difference codes. The VII method can be applied to more complex geometries, such as flow around bluff bodies, and could become an important engineering design tool for situations in which zonal modeling is possible.

Acknowledgments

References

Abbott, D. E., and Kline, S. J., 1962, "Experimental Investigation of Subsonic Turbulent Flow Over Single and Double Backward-Facing Steps," ASME *Journal Basic Engineering*, Sept. pp. 317-325.

Abdullah, Z., 1988, a personal communication.

Acrivos, A., and Schrader, M. L., 1982, "Steady Flow in a Sudden Expansion at High Reynolds Numbers," *Phys. Fluids*, Vol. 25, No. 6.

Adams, E. W., Johnston, J. P., and Eaton, J. K., 1984, "Experiments on the Structure of Turbulent Reattaching Flow," Thermoscience Div., Dept. Mech. Eng., Stanford Univ., Report MD-43.

Adams, E. W., and Johnston, J. P., 1988, "Flow Structure in the Near-Wall Region of a Turbulent Separated Flow," *AIAA J.*, Vol. 26, No. 8, pp. 932-939.

Badri Narayanam, M. A., Khadgi, Y. N., and Viswanath, P. R., 1974, "Similarities in Pressure Distribution in Separated Flow behind Backward-Facing Steps," *Aero. Quart.*, Nov., pp. 305-312.

Benodekar, R. W., Gosman, A. D., and Issa, R. I., 1983, "The TEACH-II Code for the Detailed Analysis of Two-Dimensional Turbulent Recirculating Flow," Dept. Mech Eng., Imperial College, Rept. FS/83/3.

Bradshaw, P. B., and Wong, F. Y. F., 1972, "The Reattachment and Relaxation of a Turbulent Shear Flow," *J. Fluid Mech.*, Vol. 52, pp. 113-135.

Briley, W. R., and McDonald, H., 1975, "Numerical Prediction of Incompressible Separation Bubbles," *J. Fluid Mech.*, Vol. 69, pp. 631-656.

Briley, W. R., and McDonald, H., 1984, "A Survey of Recent Work on Interacted Boundary Layer Theory for Flow with Separation," *Num. Phys. Aspects of Aero. Flows II*, Springer-Verlag, pp. 141-162.

Crimi, P., and Reeves, B. L., 1976, "Analysis of Leading Edge Separation Bubbles on Airfoils," *AIAA Journ.*, Vol. 13, No. 11.

Denham, M. K., and Patrick, M. A., 1974, "Laminar Flow over a Downstream-Facing Step in a Two-Dimensional Flow Channel," *Trans. Inst. Chem. Engrs.*, Vol. 52, pp. 361-367.

Djilali, N., 1987, "An Investigation of Two-Dimensional Flow Separation with Reattachment," Ph.D. thesis, U.B.C., pp. 86-87.

Duncan, W. J., Thom, A. S., and Young, A. D., *Mechanics of Fluids*, Second Edition, Edward Arnold Publishers Ltd.

Durst, F., Melling, A., and Whitelaw, J. H., 1974, "Low Reynolds Number Flow over a Plane Symmetric Sudden Expansion," *J. Fluid Mech.*, Vol. 64, pp. 111-128.

Durst, F., and Tropea, C., 1981, "Turbulent Backward-Facing Step Flows in Two-Dimensional Ducts and Channels," *Proc. 3rd Symp. on Turbulent Shear Flows*, Univ. California, Davis, 18.1-18.6.

Eaton, J. K., and Johnston, J. P., 1981, "A Review of Research on Subsonic Turbulent Flow Reattachment," *AIAA J.*, Vol. 19, pp. 1093-1100.

Etheridge, D. W., and Kemp, P. H., 1978, "Measurements of Turbulent Flow Downstream of a Rearward-Facing Step," *J. Fluid Mech.*, Vol. 86, pp. 545-566.

Ghia, K. N., Ghia, N., and Tesch, W. A., 1975, "Evaluation of Several Approximate Methods for Laminar Incompressible Separation by Comparison with Complete Navier-Stokes Solutions," *Flow Separation*, AGARD CP168, p. 6.1.

Goldstein, R. J., Eriksen, V. L., Olson, R. M., and Eckert, E. R. G., 1970, "Laminar Separation, Reattachment and Transition of the Flow over a Downstream-Facing Step," ASME *Journal of Basic Engineering*, Dec., pp. 732-741.

Hackman, L. P., 1982, "A Numerical Study of the Turbulent Flow over a Backward Facing Step using a Two-Equation Turbulence Model," Ph.D. thesis, University of Waterloo.

Kline, S. J., 1981, "Universal or Zonal Modelling—the Road Ahead," Proc. 1980-1981 AFOSR-HTTM Stanford Conference on Complex Turbulent Flows, eds. S. J. Kline, B. J. Cantwell, and G. M. Lilley, Thermosciences Div., Dept. of Mech. Eng., Stanford University, Calif.

Kuehn, D. M., 1980, "Effects of Adverse Pressure Gradient on the Incompressible Reattaching Flow over a Rearward-Facing Step," *AIAA J.*, Vol. 18, No. 1, pp. 343-344.

Kumar, A., and Yajnik, K. S., 1980, "Internal Separated flows at Large Reynolds Number," *J. Fluid Mech.*, Vol. 97, pp. 27-51.

Kwon, O. K., and Pletcher, R. H., 1986, "A Viscous-Inviscid Interaction Procedure—Part 1: Method for Computing Two-Dimensional Incompressible Separated Channel Flows," ASME JOURNAL OF FLUIDS ENGINEERING, Vol. 108, pp. 64-70.

Lees, L., and Reeves, B. L., 1964, "Supersonic Separated and Reattaching Laminar Flows: I. General Theory and Application to Adiabatic Boundary-Layer/Shock-Wave Interactions," *AIAA J.*, Vol. 2, No. 11, pp. 1907-1920.

Leschziner, M. A., and Rodi, W., 1981, "Calculation of Annular and Twin Parallel Jets using Various Discretization Schemes and Turbulence-Model Variations," ASME JOURNAL OF FLUIDS ENGINEERING, Vol. 103, pp. 352-360.

Macango, E. O., and Hung, T. K., 1966, "Laminar Eddies in a Two-Dimensional Conduit Expansion," *La Houille Blanche*, No. 4, pp. 391-401.

Mohsen, A. M., 1967, "Experimental Investigation of the Wall Pressure Fluctuations in Subsonic Separated Flows," Boeing Co. Report, No. D6-17094.

Moses, H. L., Jones, R. R., and O'Brian, W. F., 1978, "Simultaneous Solution of the Boundary Layer and Freestream with Separated Flow," *AIAA J.*, Vol. 16, No. 1, pp. 61-66.

Nallasamy, M., 1987, "Turbulence Models and their Applications to the Prediction of Internal Flows: a Review," *Computers & Fluids*, Vol. 15, pp. 151-194.

Reyhner, T. A., and Flügge-Lotz, I., 1968, "The Interaction of a Shock

Wave with a Laminar Boundary Layer," *Int. J. of Nonlinear Mech.*, Vol. 3, No. 2, pp. 173–199.

Rosenhead, L., 1963, *Fluid Motion Memoirs–Laminar Boundary Layers*, Oxford University Press, pp. 292–332.

Ruderich, R., and Fernholz, H. H., 1986, "An Investigation of a Turbulent Shear Flow with Separation, Reverse Flow, and Reattachment," *J. Fluid Mech.*, Vol. 163, pp. 283–322.

Schlichting, H., 1979, *Boundary Layer Theory*, Seventh Edition, McGraw-Hill.

Sinha, S. N., Gupta, A. K., and Oberai, M. M., 1981, "Laminar Separating Flow over Backsteps and Cavities Part 1: Backsteps," *AIAA J.*, Vol. 19, No. 12, pp. 1527–1530.

Smyth, R., 1979, "Turbulent Flow over a Plane Symmetric Sudden Expansion," *J. Fluid Mech.*, Vol. 101, pp. 348–353.

Strawn, R. C., Ferziger, J. H., and Kline, S. J., 1984, "A New Technique for Computing Viscous-Inviscid Interactions in Internal Flows," ASME JOURNAL OF FLUIDS ENGINEERING, Vol. 106, pp. 79–84.

Stropky, D. M., 1988, "A Viscous-Inviscid Interaction Procedure," M.A.Sc. thesis, chapter 3, U.B.C.

Wauschkuhn, H., and Vasante, R. O. M., 1975, "Die Turbulente Grenzschicht Hinter Einem Ablsüngsgebiet," *Zeitschrift f. Flugwissenschaften*, Heft 1.

Westphal, R. V., Johnston, J. P., and Eaton, J. K., 1984, "Experimental Study of Flow Reattachment in a Single Sided Sudden Expansion," NASA Contractor Report 3765.

Williams, B. R., 1986, "The Prediction of Separated Flow Using a Viscous-Inviscid Interaction Method," *Aero. Journ.*, pp. 185–197.

Woolley, R. L., and Kline, S. J., 1979, "A Procedure for Computation of Fully Stalled Flows in Two-Dimensional Passages," *J. Fluid Mech.*, Vol. 101, pp. 348–353.

A P P E N D I X A

Pohlhausen Polynomial Profiles (Θ *is the degree of polynomial*)

	$\Theta = 4$	$\Theta = 5$	$\Theta = 6$
$f(\eta)$	$2\left(\eta - \eta^3 + \dfrac{1}{2}\eta^4\right)$	$\dfrac{5}{3}\left(\eta - \eta^4 + \dfrac{3}{5}\eta^5\right)$	$2\eta - 5\eta^4 + 6\eta^5 - 2\eta^6$
$g(\eta)$	$\dfrac{1}{6}\,(\eta - 3\eta^2 + 3\eta^3 - \eta^4)$	$\dfrac{1}{4}\,(\eta - 2\eta^2 + \eta^4 - \eta^5)$	$\dfrac{1}{10}\,(2\eta - 5\eta^2 + 10\eta^4 - 10\eta^5 + 3\eta^6)$

Timman Profiles

	$\Lambda \geq 0$	$\Lambda \leq 0$
$f(\eta)$	$1 - \dfrac{4}{3\sqrt{\pi}}\displaystyle\int_{\eta}^{\infty} e^{-\eta^2}\,d\eta$	$1 - \dfrac{4}{3\sqrt{\pi}}\displaystyle\int_{\eta}^{\infty} e^{-\eta^2}\,d\eta$
$g(\eta)$	$\dfrac{1}{2}\,e^{-\eta^2} - \dfrac{2}{3\sqrt{\pi}}\displaystyle\int_{\eta}^{\infty} e^{-\eta^2}\,d\eta$	$\dfrac{1}{2}\,e^{-\eta^2}(2+\eta^2) - \dfrac{4}{3\sqrt{\pi}}\displaystyle\int_{\eta}^{\infty} e^{-\eta^2}\,d\eta$

Turbulent Profiles ($\Lambda \leq 0$)

	$\eta \leq 0.2538$	$\eta \geq 0.2538$
$f(\eta)$	$10.41\eta - 290.8\eta^3 + 707.1\eta^4$	$\eta^{1/7}$
$g(\eta)$	$0.5144\eta - 0.5\eta^2 - 20.01\eta^3 + 55.14\eta^4$	0

Velocity Profile Constant Values

Profile Constant	Pohlhausen $\Theta = 4$	Pohlhausen $\Theta = 5$	Pohlhausen $\Theta = 6$	Timman $\Lambda \geq 0$	Timman $\Lambda \leq 0$	Turbulent $\Lambda \leq 0$
$C_1 = \displaystyle\int_0^{\infty} (1 - f)$	$\dfrac{3}{10}$	$\dfrac{1}{3}$	$\dfrac{2}{7}$	.7523	.7523	.125
$C_2 = -\displaystyle\int_0^{\infty} g$	$\dfrac{-1}{120}$	$\dfrac{-1}{60}$	$\dfrac{-1}{105}$	$-.06699$	$-.3555$	$-.004699$
$C_3 = \displaystyle\int_0^{\infty} f(1 - f)$	$\dfrac{37}{315}$	$\dfrac{775}{6237}$	$\dfrac{985}{9009}$	.2894	.2894	.8224
$C_4 = \displaystyle\int_0^{\infty} g(1 - 2f)$	$\dfrac{-1}{945}$	$\dfrac{-25}{16632}$	$\dfrac{-19}{18018}$	.007335	$-.07936$	$-.002478$
$C_5 = -\displaystyle\int_0^{\infty} g^2$	$\dfrac{-1}{9072}$	$\dfrac{-47}{110880}$	$\dfrac{-1}{6435}$	$-.003797$	$-.07370$	$-.0001165$
$C_6 = f'(0)$	2	$\dfrac{5}{3}$	2	.7523	.7523	10.41
$C_7 = g'(0)$	$\dfrac{1}{6}$	$\dfrac{1}{4}$	$\dfrac{1}{5}$	.3761	.7523	.5144

Calculation of $I(x, x') = \int_{x_1}^{x_2} \dfrac{\dfrac{d}{d\xi}[(\xi - x')^B]}{x - \xi} d\xi$

Here it will be assumed that B has the form $(m+1)/(m+3)$, as this follows from power law velocity profiles. Using the following substitutions,

$$\chi = x - x', \quad z = \left(\frac{\xi - x'}{\chi}\right)^{\frac{1}{m+3}}, \quad z_1 = \left(\frac{x_1 - x'}{\chi}\right)^{\frac{1}{m+3}},$$

$$z = \left(\frac{x_2 - x'}{\chi}\right)^{\frac{1}{m+3}}$$

the integral is transformed to,

$$I = \frac{m+3}{2 \chi^{\frac{2}{m+3}}} \int_{z_2}^{z_1} \frac{z^m}{z^{m+3} - 1} dz \qquad (1)$$

Using partial fractions, the integrand is rewritten in the following manner,

$$\frac{z^m}{z^{m+3} - 1} = \sum_{i=0}^{m+2} \frac{\lambda_i}{z - \omega_i} \qquad (2)$$

where $\omega_0, \omega_1, \ldots, \omega_{m+2}$ are the $m+3$ complex roots of the equation $z^{m+3} = 1$. After some algebra, the coefficients λ_i can be written as,

$$\lambda_i = \frac{\omega_i^{m+1}}{m+3}$$

Substituting into equation (2) and then equation (1),

$$I = \chi^{-\frac{2}{m+3}} \sum_{i=0}^{m+2} \omega_i^{m+1} \ln(z - \omega_i) \Big|_{z_2}^{z_1} \qquad (3)$$

For $m = 1, 3, 5, \ldots$

There are real roots at $z = \pm 1$ so that the two terms for $\omega_i^{m+1} \ln(z - \omega_i)$, become $\ln(z - 1)$ and $\ln(z + 1)$. For the rest of the terms, pair into complex conjugates as follows,

$$\omega_k^{m+1} \ln(z - \omega_k) + \omega_{(m+3)-k}^{m+1} \ln(z - \omega_{(m+3)-k})$$

$$= [\Phi_k + i\Psi_k] \ln[z - (\alpha_k + i\beta_k)] + [\Phi_k - i\Psi_k] \ln[z - (\alpha_k - i\beta_k)] \qquad (4)$$

where,

$$\alpha_k = \cos \frac{2\pi k}{m+3} \quad \beta_k = \sin \frac{2\pi k}{m+3} \quad \Psi_k = \cos 2\pi \frac{m+1}{m+3} k$$

$$\Phi_k = \sin 2\pi \frac{m+1}{m+3} k$$

Extracting the real part of equation (4),

$$\Gamma_k = \Phi_k \ln[(z - \alpha_k)^2 + \beta_k^2] + 2\Psi_k \arctan\left[\frac{\beta_k}{z - \alpha_k}\right]$$

Substituting into equation (3),

$$I = \chi^{-\frac{2}{m+3}} \left\{ ln\,|z^2 - 1| + \sum_{k=1}^{\frac{m+1}{2}} \Gamma_k \right\} \Big|_{z_2}^{z_1} \Leftarrow m = 1, 3, 5, \ldots$$

For $m = 2, 4, 6, \ldots$

There is a real root at $+1$ leading to the term $\ln(z - 1)$. Following the previous analysis,

$$I = \chi^{-\frac{2}{m+3}} \left\{ ln\,|z - 1| + \sum_{k=1}^{\frac{m+2}{2}} \Gamma_k \right\} \Big|_{z_2}^{z_1} \Leftarrow m = 2, 4, 6, \ldots$$

APPENDIX C

Entrainment and Skin Friction Correlations

Correlations taken from the paper by Strawn et al. are written in terms of the shape factor, H_{12}, as follows.

	$H_{12} \leq 1.6$	$H_{12} > 1.6$
H^*	$3.15 + \dfrac{1.72}{H_{12} - 1}$	$4.5455 + 295 \exp(-3.325 H_{12})$
E	$.0306[.8234(H_{12} - 1.1)^{-1.287} + .3]^{-.6169}$	$.0306[1.5501(H_{12} - .6778)^{-3.064} + .3]^{-.6169}$
Ω	$\dfrac{H_{12}}{H_{12} + 3.15 + \dfrac{1.72}{H_{12} - 1}}$	$\dfrac{H_{12}}{H_{12} + 4.5455 + 295 \exp(-3.325 H_{12})}$

Scaling Turbulent Wall Layers

Ronald L. Panton

Mechanical Engineering Department,
University of Texas,
Austin, TX 78712

The two-layer concept is a framework for interpreting events and constructing mathematical models of turbulent wall layers. In this paper an asymptotic theory is constructed employing the idea that the interaction between the layers is the most important aspect. It is shown that the matching process for the layers can be used to define a characteristic scale, u^*, and to produce an equation that relates u^* to the known parameters; U_∞, ν, h, e, and dp/dx. At infinite Reynolds number the scale u^* is equal to u_τ, the friction velocity, but they are distinct at moderate Reynolds numbers. The theory produces very simple results. For instance, the overlap velocity laws are logarithmic with an invariant von Kármán constant; at low Reynolds numbers the additive constant changes while the slope remains the same. The effect of low Reynolds numbers on the Reynolds stress in the overlap layer is also analyzed. A composite expansion explains the strong Reynolds number effect on the stress profiles. This occurs because the mixing of outer and inner layer phenomena take place at different locations as the size of the overlap region changes. The location of the maximum Reynolds stress is given by $y^+{}_{max} = (Re/k)^{1/2}$. The overlap region was not found to be a region of constant stress, as put forth in many heuristic arguments.

Introduction

A fundamental precept of the theory of turbulent wall regions is the two-layer structure. As is well known, most of the flow consists of the outer layer with a velocity profile determined by inviscid Reynolds stresses. Viscous stresses compete with Reynolds stresses in a much thinner inner layer, and become dominant at the wall itself. The theory originally consisted of the "law of the wall" and the "defect law." The functional form for the "law of the wall" was proposed by Prandtl as a nondimensional extension of the log profile. Credit for the most general form for the "velocity defect law" is given to von Kármán. By somewhat different methods, Prandtl (see Durand (1935)) and von Kármán (1930) derived the log laws employing mixing length arguments. Izakson (1937) and Millikan (1938), using what we would now call an asymptotic matching procedure, took an important step by putting the theory in a simpler form that was independent of mixing length assumptions. Later, Gill (1968) defined the mathematical restrictions required for the log laws.

From a mathematical standpoint, the modern theory is a singular perturbation that can be represented by two matched asymptotic expansions. Several second-order analyses have been previously published. The major ones are Tennekes (1968), Yajnik (1970), Afzal and Yajnik (1973), Bush and Fendell (1972), (1973), and Afzal (1976). The last paper describes the distinguishing features of each work. A related analysis for flow over an acoustic surface is Liu and Libby (1986). Asymptotic expansions of a function are nonunique. Many gauge functions are asymptotically equal. Thus, while the first term in an expansion is reasonably well defined, subsequent terms can differ depending on the sequence of gauge functions chosen and on the scaling parameters employed in the nondimensional variables.

In this paper a second-order asymptotic theory of wall layers is constructed that has a different nondimensional basis. A major aspect of the present approach is that a distinction between the turbulence scale u^* and the wall shear u_τ is carefully maintained. This was prompted by several issues. The first comes from low Reynolds number experiments. Flow visualization and structure studies are necessarily done at low Reynolds numbers. Several investigators, for example Kline et al. (1967) and Blackwelder and Haritonidis (1983), find that u^*, the scale determined from the log region of the velocity profile, is 10 to 15 percent different from u_τ, the friction velocity determined from the wall shear stress.

A completely equivalent observation to $u^* \neq u_\tau$ is that the slope of the log region velocity profiles, normalized with u_τ, shows an increase above the nominal value $1/\kappa = 1/0.41$. Direct Navier-Stokes calculations, which can only be done at low Reynolds numbers, show this tendency for boundary layers, Spalart (1988), and also for channel flows, Kim, et al. Moin, and Moser (1987).

Another motive for this research concerns the behavior of turbulence quantities. Many of these quantities do not have curves, as a function of y^+, that are independent of Reynolds number. The Reynolds stress is an important example that has been documented experimentally by Wei and Willmarth (1989) and by Tiederman and Harder (1989). Spalart's work for boundary layers shows similar effects. For example, the location of the maximum Reynolds stress is not at a constant value of y^+. An empirical equation by Long and Chen (1981) is $y^+{}_{max} = 1.89Re^{*1/2}$. Sreenivasan (1987) also discovered this trend and arrived at the same equation with a coefficient of 2 instead of 1.89.

This "nonsimilar" behavior of the maximum Reynolds

---

stress prompted Long and Chen (1981) to propose a three-layer structure for turbulent wall-layers. Afzal (1982a), Afzal (1982b), Afzal and Bush (1985) have continued the three-layer theme in several variations. A somewhat related issue is the fact that Alfredsson and Johansson (1984) have found that certain turbulence quantities have curves that collapse better when scaled in mixed variables, that is the geometric mean $\sqrt{(u^*U_\infty)}$. The proper interpretation for this has been uncertain.

The paper begins in section 1 with a review of the mathematical parameters and functional relations for wall layers. The inner layer is considered in section 2 and the outer layer in section 3. The matching process is applied in section 4 where u^* is defined and the velocity laws derived. Relations for the Reynolds stress are produced in section 5. A coherent discussion of the results and comparison with experiments and computer simulations is presented in section 6, while a summary and acknowledgment paragraph conclude the article.

1 Problem Description

The situations under consideration are turbulent wall layers, where development in the flow direction is so slow that local parameters are sufficient to describe the flow. Channel flows and pipe flows meet these requirements exactly, however, some approximations are necessary for boundary layers; Townsend (1976), Hinze (1956), Tennekes and Lumley (1972). The parameters that specify a flow are the density ρ, kinematic viscosity ν, free-stream or centerline velocity U_∞, pipe radius or boundary layer thickness h, wall roughness e, and pressure gradient dp/dx. In boundary layers dp/dx can be independently assigned, but in pipe flow it cannot. The independent variable is the distance from the wall, y, and the dependent variables are the velocity, $U(y)$, and Reynolds stress, $<uv>(y)$. Note that the wall shear stress is not taken as a known parameter. It is a dependent quantity in the complete problem. If all of the above parameters (less dp/dx in pipes and channels) are specified, then the wall shear is determined by the flow. Prandtl took the stress as a known quantity because he extracted a local example of a fully turbulent region of constant Reynolds stress.

The focus is on the theory directly related to determining $U(y)$ and $<uv>(y)$. There are other quantities of interest in turbulence such as scalar transport, viscous dissipation, intermittency, and so on, however, they do not fall in the scope of the current discussion.

In general, the functional form of a turbulent velocity profile is

$$U=U\left(y;\ U_\infty,\ h,\ \nu,\ e,\ \rho,\ \frac{dp}{dx}\right) \qquad (1.1)$$

In this relationship only ρ and dp/dx have the dimension of mass. Hence, they must appear together

$$U=U\left(y;\ U_\infty,\ h,\ \nu,\ e,\ \frac{1}{\rho}\ \frac{dp}{dx}\right) \qquad (1.2)$$

Boundary conditions are $U=0$ at $y=0$ and $U=U_\infty$ at $y=h$. A similar set of functional relations exist for the Reynolds stress with boundary conditions of zero at both locations.

The two most important ideas in the analysis are the two-layer assumption and the empirical fact that for smooth walls the shear stress coefficient slowly approaches zero as the Reynolds number approaches infinity.

2 Inner Layer

Assume the now classical division of the turbulent region into two layers. The *outer layer*, which covers most of the region, has a velocity profile determined by inviscid turbulent stresses. This situation cannot exist near the wall because of the no-slip condition. The no-slip condition requires that the turbulent fluctuations, the Reynolds stress, and the first two derivatives of Reynolds stress are all zero at the wall. Thus, there must exist an *inner layer* which, at the wall itself, is completely viscous. The theory is constructed for the limit where the inner layer is thin compared to the outer layer.

The first consideration is the length scale in the inner region, which by assumption cannot be h. Since the theory must be valid for $e=0$ and $dp/dx=0$, these parameters also cannot be candidates for scales. It would be reasonable to guess that the two remaining parameters would form inner length and velocity scales as ν/U_∞ and U_∞, however, as will be shown, this is incorrect. Let us introduce u^* as an unspecified velocity scale for the inner region and take the inner length scale as ν/u^*. The scale u^* is related to the other parameters in some as yet unknown way;

$$u^*=u^*\left(U_\infty,\ h,\ \nu,\ e,\ \frac{1}{\rho}\ \frac{dp}{dx}\right) \qquad (2.1)$$

Turbulent wall-layers are a very unusual singular perturbation problem in that the inner scaling is not simply related to the known parameters in the problem. Equation (2.1) must be determined as part of the analysis. Using ν and u^* to scale the variables gives

$$u^+=\frac{U}{u^*},\ y^+=\frac{y\ u^*}{\nu},\ e^+=\frac{e\ u}{\nu},$$

$$\Pi=\frac{\nu}{\rho\ u_*^3}\ \frac{dp}{dx},\ \mathrm{Re}^*=\frac{h\ u^*}{\nu} \qquad (2.2)$$

The size of the inner region compared to the outer is the preferred Reynolds number Re* and is the perturbation parameter.

In the inner region, the nondimensional velocity profile has the mathematical form

$$u^+=\frac{U}{u_*}=f(y^+,\ e^+,\ \Pi,\ \mathrm{Re}^*) \qquad (2.3)$$

An asymptotic expansion for Re* $\Rightarrow \infty$ is

$$u^+\sim f_0(y^+;\ e^+)+f_1(y^+;\ e^+,\ \Pi)\epsilon_1(\mathrm{Re}_*)+\ .\ .\ . \qquad (2.4)$$

This isolates the Reynolds number dependence into gauge functions $\epsilon_1(\mathrm{Re}^*)$, $\epsilon_2(\mathrm{Re}^*)$, . . . , and makes the functions f_0, f_1, . . . independent of Reynolds number. A proper scale for $U(y)$ will make f_0 a finite nontrivial function. The gauge functions are left unspecified until it is seen what forms are acceptable. The first term, f_0, is commmonly called "the law of the wall." Note that it is an experimental fact, but not a requirement, that f_0 does not depend upon Π. The Reynolds stress has a similar expansion (with possibly different gauge functions)

$$\frac{-<uv>}{u_*^2}\sim g_0(y^+;\ e^+,\ \Pi)+g_1(y^+;\ e^+,\ \Pi)\epsilon_1(\mathrm{Re}_*)+\ .\ .\ .$$

$$\qquad (2.5)$$

The wall shear stress coefficient is based on U_∞. It is

$$C_f\equiv\frac{\tau_w}{1/2\rho U_\infty^2}\ =\ \frac{2\ \nu}{U_\infty^2}\ \frac{dU}{dy}\bigg|_0$$

$$=2\left(\frac{u_*}{U_\infty}\right)^2\ [f_0'(0;\ e^+)+f_1'(0;\ e^+,\ \Pi)\epsilon_1(\mathrm{Re}_*)+\ .\ .\ .] \qquad (2.6)$$

As $\text{Re}_* \Rightarrow \infty$, $\epsilon_1(\text{Re}_*) \Rightarrow 0$, so in this limit, the shear stress is equal to the first term in the bracket. We can now see why the scale u^* cannot be U_∞. If u^* were taken proportional to U_∞, the shear stress would become constant, $C_f \sim f'(0)$. This would contradict the second major assumption; namely that $C_f \Rightarrow 0$ as $\text{Re}^* \Rightarrow \infty$. Hence, u^* cannot equal U_∞ and the relation (2.1) is a necessary assumption.

Next consider the momentum equation for pipe or channel flow. This case is somewhat simpler than boundary layers as no approximations are needed. There are no essential differences between boundary layers and pipes in the first-order theory. The dimensional momentum equation is integrated once to give

$$- <uv> + \nu \frac{dU}{dy} = \frac{\tau_w}{\rho}\left[1 - \left(\frac{y}{h}\right)\right] \qquad (2.7)$$

The term $(\tau_w/\rho)/(y/h))$ represents the pressure gradient driving the flow. A similar term occurs in boundary layers that represents convection. Boundary conditions are $<uv> = 0$ at both $y = 0$ and $y = h$. As the viscous term is negligible in the outer layer $- <uv>$, must decrease directly with y/h. Hence, we can expect $- <uv>$ to rise from 0 at the wall, reach a maximum in the inner layer, and then decline to zero at the centerline. Writing the momentum equation in inner variables gives

$$- \frac{<uv>}{u_*^2} + \frac{du^+}{dy^+} = \left(\frac{u_\tau}{u}\right)^2\left[1 - \frac{y^+}{\text{Re}^*}\right] \qquad (2.8)$$

The presumed physics of the inner layer requires both Reynolds and viscous stress to be present. This justifies the assumption made in (2.5) that u^{*2} is the proper scale for the Reynolds stresses and additionally shows that the sequence of gauge functions for $<uv>$ is the same as that for u^+. Furthermore, $\epsilon_1 = 1/\text{Re}^*$ will fit with the last term on the right. Inserting the expansions (2.4) and (2.5) into (2.8), and collecting terms of distinct order yields

$$g_0 + f_0' = f_0'(0) \qquad (2.9)$$
$$g_1 + f_1' = f_1'(0) - y^+ \qquad (2.10)$$

The problem is not completely determined without a closure hypothesis on the Reynolds stress. It is not necessary to close the system for our pruposes. Since f_0 does not depend upon Π, we can surmise that g_0 does not depend upon Π either. One should also note that since $- <uv>$ reaches a maximum in the inner region and then falls to zero in the outer region, that u^* is also the proper scale for turbulent motions in the outer region. With these facts about the Reynolds stress we can turn attention to the outer layer.

3 Outer Layer

The outer layer is inviscid so ν is of secondary importance as a parameter. The length scale is h and we try U_∞ as reasonable scale for changes in the velocity. The velocity must climb from some small value in the inner layer to the centerline value of U_∞. Asymptotic expansions for the velocity profile and Reynolds stresses in the outer region are functions of $\eta = y/h$. They are

$$\frac{U(y)}{U_\infty} = F(\eta; e^+, \Pi, \text{Re}^*)$$

$$\frac{U(y)}{U_\infty} \sim F_0(\eta; e^+, \Pi) + F_1(\eta; e^+, \Pi)\hat{\epsilon}_1(\text{Re}_*) + \ldots \qquad (3.1)$$

and

$$\frac{- <uv>(y)}{u_*^2} \sim G_0(\eta; e^+, \Pi) + G_1(\eta; e^+, \Pi)\hat{\epsilon}_1(\text{Re}_*) + \ldots \qquad (3.2)$$

The gauge functions are not necessarily the same as those in the inner expansion.

The momentum equation in outer variables does not reveal any new information, however, the equation for turbulent kinetic energy does. In outer variables the equation is

$$\frac{- <uv>}{u_*^2} \frac{dF_0}{d\eta} = \frac{u_*}{U_\infty}\left[\Phi_* + \frac{d}{d\eta}\left(\frac{<vp>}{\rho u_*^3}\right.\right.$$
$$\left.\left. + \frac{1/2<\nu q^2>}{u_*^3}\right)\right] \qquad (3.3)$$

Here the assumption that all turbulent fluctuations scale with u^* has been employed.. The symbol Φ is used for the dissipation, p for pressure fluctuations, and $q^2/2$ for the kinetic energy. In the limit of large Reynolds number the fact that $C_f \Rightarrow 0$ implies through (2.6) that $u^*/U_\infty \Rightarrow 0$, hence the right side of (3.3) is zero and

$$\frac{dF_0}{d\eta} = 0$$

Integrating and applying the boundary condition at $\eta = 1$ gives

$$F_0 = \text{constant} = 1$$

When the Reynolds number becomes large, the outer layer is a block of weakening turbulence ($u^*/U_\infty \Rightarrow 0$) with a uniform velocity U_∞. Furthermore, in order for (3.3) to produce a nontrivial equation for the next approximation, F_1, the gauge function $\hat{\epsilon}_1$ must be set equal to u^*/U_∞. Equation (3.1) then becomes the classic defect law

$$\frac{u(y) - U_\infty}{U_\infty \hat{\epsilon}_1} = \frac{u(y) - U_\infty}{u^*} \sim F_1(\eta, \Pi) + \ldots \qquad (3.4)$$

The velocity scale u^* measures the departure of the outer profile from the block flow U_∞, an effect of the Reynolds stresses that scale on u^*. Experiments show that F_1 does not depend on e^+.

We have now seen how u^*, introduced as the inner layer scale, has become the proper scale for both the turbulence and velocity defect in the outer layer. The velocity u^* is the scale for both the inner and outer regions, while U_∞ has been relegated to the role of a reference.

4 Overlap Region

When a problem is split into two regions we lose boundary conditions on each problem. The inner expansion can no longer be required to meet the condition on the centerline and the outer expansion can no longer be expected to obey the no-slip condition. Matching the two expansions replaces the lost boundary conditions. Here we will match in an intermediate limit $\text{Re}^* \Rightarrow \infty$ with Y fixed, where the intermediate variable is defined as

$$Y = \frac{y^+}{\text{Re}_*^\alpha} = \frac{y^+}{\text{Re}_*^{1/2}}$$
$$Y = \eta \text{Re}_*^{1-\alpha} = \eta \text{Re}_*^{1/2}$$

For the present problem $0 < \alpha < 1$. The logic is unchanged for any α in this range, however, $\alpha = 1/2$ is chosen to make it easier to follow. Note that $\alpha = 0$ produces the inner variable whereas $\alpha = 1$ yields the outer variable.

Matching requires that the difference between the inner (2.4) and outer (3.1) expansions vanish in the intermediate limit. This means that the coefficient of each distinct order in Re^* will be zero. Thus, matching requires

$$\lim_{\substack{\mathrm{Re}_* \Rightarrow \infty \\ Y \text{ fixed}}} \left\{ F\left(\frac{Y}{\sqrt{\mathrm{Re}_*}}\right) - \frac{u^*}{U_\infty} f(Y\sqrt{\mathrm{Re}_*}) \right\} = 0$$

$$\lim_{\substack{\mathrm{Re}_* \Rightarrow \infty \\ Y \text{ fixed}}} \left\{ 1 + \frac{u^*}{U_\infty} F_1\left(\frac{Y}{\sqrt{\mathrm{Re}_*}}\right) + \hat{\epsilon}_2 F_2\left(\frac{Y}{\sqrt{\mathrm{Re}_*}}\right) + \ldots \right.$$

$$\left. - \frac{u^*}{U_\infty} f_0(Y\sqrt{\mathrm{Re}_*}) - \frac{u^*}{U_\infty} \epsilon_1 f_1(Y\sqrt{\mathrm{Re}_*}) - \ldots \right\} = 0 \qquad (4.2)$$

Grouping terms according to order is complicated because $F_1(\eta \Rightarrow 0) \Rightarrow \infty$, $f_0(y^+ \Rightarrow \infty) \Rightarrow \infty$, while $u^*/U_\infty \Rightarrow 0$; therefore their products are indeterminate forms. It turns out that both are finite and so the first-order match requires

$$\frac{U_\infty}{u^*} = f_0(y^+ \Rightarrow \infty) - F_1(\eta \Rightarrow 0) \qquad (4.3)$$

Next, consider matching the mean vorticity of the inner and outer layers. This procedure turns out to be completely equivalent to the Isakson-Millikan method. In intermediate variables the matching is

$$\lim_{\substack{\mathrm{Re}_* \Rightarrow \infty \\ Y \text{ fixed}}} \left\{ \frac{u^*}{U_\infty} F_1'\left(\frac{Y}{\sqrt{\mathrm{Re}_*}}\right) \frac{d\eta}{dY} \right.$$

$$+ \frac{u^*}{U_\infty} \hat{\epsilon}_1 F_2'\left(\frac{Y}{\sqrt{\mathrm{Re}_*}}\right) \frac{d\eta}{dY} + \ldots$$

$$- \frac{u^*}{U_\infty} f_0'(Y\sqrt{\mathrm{Re}_*}) \frac{dy^+}{dY}$$

$$\left. - \frac{u^*}{U_\infty} \hat{\epsilon}_1 f_1'(Y\sqrt{\mathrm{Re}_*}) \frac{dy^+}{dY} - \ldots \right\} = 0 \qquad (4.4)$$

Again indeterminate forms occur since $F_1'(\eta \Rightarrow 0) \Rightarrow \infty$ and $f_0'(y^+ \Rightarrow \infty) \Rightarrow 0$. An extra Y has been inserted below to help show the proper grouping. The first-order matching condition is

$$\frac{u^*}{U_\infty} \frac{1}{Y} \left[F_1'\left(\frac{Y}{\sqrt{\mathrm{Re}_*}}\right) \frac{Y}{\sqrt{\mathrm{Re}_*}} \right.$$

$$\left. - f_0'(Y\sqrt{\mathrm{Re}_*}) \, Y\sqrt{\mathrm{Re}_*} \right] = 0 \qquad (4.5)$$

That is

$$\eta F_1'(\eta) = y^+ f_0'(y^+) = \frac{1}{\kappa} \qquad (4.6)$$

As this holds over a range of values, each expression must be constant.

It is important to digress for a moment to discuss the constant in (4.6). In dimensional terms the equation in the overlap region is

$$\frac{dU_0}{d(\ln y)} = \frac{u^*}{\kappa}$$

Any scale has an arbitrary size; that is, if u^* is the proper scale then $C u^*$ is also proper for any constant C. It would be most straightforward, from the present point of view, to set $\kappa = 1$ in (4.6) and let the inner-outer interaction determine the magnitude of u^*. Obviously, in order to blend the theory into previous custom, one must take κ as the von Kármán constant for a high Reynolds number flow. This means that the size of u^* should be fixed so that for $\mathrm{Re}_* \Rightarrow \infty$ it equals the friction velocity. The friction velocity is defined by

$$u_\tau \equiv \sqrt{\frac{\tau_w}{\rho}} \qquad (4.7)$$

Substituting (4.7) into (2.6) relates the u^* scale to the friction velocity.

$$u_\tau^2 = u_*^2 [1 + f_1'(0; \, e^+, \, \Pi)\epsilon_1(\mathrm{Re}_*) + \ldots] \qquad (4.8)$$

In (4.8) the additional requirement $f_0'(0) = 1$ sets the size of u^*. This means that close to the wall $f_0 = y^+$ (to first order $u^+ = y^+$ and $u^* = u_\tau$).

Previous workers have taken u_τ as the scaling parameter and hence have slightly different functions for the dependent variables. This makes no difference in first-order results, but does thereafter. In (4.8) if we had arbitrarily made $u^* \equiv u_\tau$ that would require $f_i'(0) = 0$ for $i \geq 1$. This introduces additional boundary conditions on f_i for $i \geq 1$ ($f_i(0) = 0$, $f_i'(0) = 0$) that somehow are compensated for in the matching process. This is not incorrect but it produces a mathematically more complicated theory.

Returning to the analysis and solving (4.6) yields the famous logarithmic velocity laws

$$f_0 = \frac{1}{\kappa} \ln y^+ + C_1(e^+) \qquad (4.9)$$

$$F_1 = \frac{1}{\kappa} \ln \eta + C_2(\Pi) \qquad (4.10)$$

Substituting (4.9) and (4.10) into (4.3) allows us to find the scale relation proposed in (2.1)

$$\frac{U_\infty}{u^*} = \frac{1}{\kappa} \ln \mathrm{Re}_* + C_1(e^+) - C_2(\Pi) \qquad (4.11)$$

This is commonly called the logarithmic skin friction law since u^* is roughly the same as u_τ. In the present context this equation defines u^* in terms of the known parameters of the flow. It is not considered a bonus of the analysis, but plays the role of the restraining equation to determine the "unspecified" velocity scale u^*. The constants C_1 and C_2 are independent of Reynolds number; they are universal in the same sense that κ is universal.

We can demand that u^* satisfy (4.11) exactly only if u^* is otherwise undefined. If u^* had been identified as the wall shear stress, that is $u^* \equiv u_\tau$ for all Reynolds numbers, then in the matching process (4.11) is satisfied only asymptotically and a higher order term is left over. Subsequently, the higher order term is involved in the next order match in (4.2). Ultimately logarithms appear in the second order and the equivalent von Kármán constant becomes dependent on Reynolds number. Distinguishing between u^* and u_τ allows (4.11) to be satisfied exactly and results in the simplest structure for the theory.

Next the second order analysis is described. To match at second order we need to set

$$\hat{\epsilon}_2 = \frac{u^*}{U_\infty} \epsilon_1$$

Then (4.2) shows that the missing second-order boundary condition is replaced by

$$f_1(y^+ \Rightarrow \infty) = F_2(\eta \Rightarrow 0) \qquad (4.12)$$

Matching the mean vorticity (4.4) gives

$$\frac{u^*}{U_\infty} \frac{\hat{\epsilon}_1}{Y} \left[F_2'\left(\frac{Y}{\sqrt{\mathrm{Re}_*}}\right) \frac{Y}{\sqrt{\mathrm{Re}_*}} \right.$$

$$\left. - f_1'(Y\sqrt{\mathrm{Re}_*}) \, Y\sqrt{\mathrm{Re}_*} \right] = 0 \qquad (4.13)$$

Solving (4.13) yields the following overlap expressions for $F_2(\eta)$ and $f_1(y^+)$

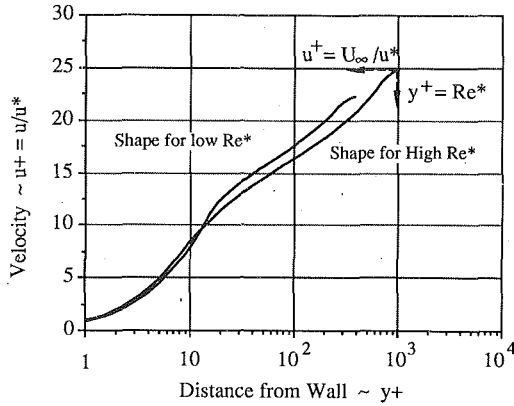$$f_1 = \frac{1}{\kappa_2} \ln y^+ + C_3 \qquad (4.14)$$

Fig. 1   Effect of Re* on velocity profiles

Fig. 2   First-order composite expansion for Reynolds stress

Fig. 3   First-order composite expansion in outer variables

$$F_2 = \frac{1}{\kappa_2} \ln \eta + C_4 \qquad (4.15)$$

The second-order velocity does not really follow a logarithmic law as we shall find that κ_2 is infinite. Substitute (4.14) and (4.15) into (4.12) to obtain the second-order restraining equation

$$0 = \frac{1}{\kappa_2} \ln \mathrm{Re}_* + C_3 - C_4$$

Since C_3 and C_4 are independent of Re_* it must be that $1/\kappa_2 = 0$ and the constants are equal.

$$\frac{1}{\kappa_2} = 0, \quad C_3 = C_4 \qquad (4.16)$$

The second-order inner and outer velocities approach the same constant in the overlap region. All of the logarithmic dependence is contained in the first-order profiles (4.9) and (4.10) which have a constant slope. Figure 1 shows the trends expected for typical profiles.

5   Reynolds Stress

A key element in turbulence is the behavior of the Reynolds stresses. Recall that the "nonsimilar" behavior of the Reynolds stresses has lead others to propose a three-layer structure and to introduce mixed scaling. The limiting forms, that is the forms that are valid in the matching region, for the inner and outer representations, $g_0(y^+ \Rightarrow \infty)$ and $G_0(\eta \Rightarrow 0)$ can be found from the velocity overlap laws and the integrated momentum equation written in the appropriate variables (2.7). The result for the inner layer is physically a statement that the Reynolds stress g_0 at any location y^+ is the wall shear minus the viscous stress at y^+; the pressure force being negligible because the area upon which it acts is so small.

$$\frac{-<uv>}{u^*} = g_0 = 1 - \frac{1}{\kappa y^+} \qquad (5.1)$$

In the outer layer the Reynolds stress G_0 is the wall shear minus the pressure force, pressure times the area from 0 to η. In nondimensional form this is

$$\frac{-<uv>}{u^*} = G_0 = 1 - \eta \qquad (5.2)$$

The same equation is valid for boundary layers with zero pressure gradients, except for a coefficient multiplying η that depends upon the thickness definition. In boundary layers, the convection of momentum replaces the pressure force as the physical process causing the stress to decrease.

Normally, individual inner or outer expansions are *not* very good representations of the true answer in the matching region at finite Reynolds numbers. As Re_* varies, the overlap region
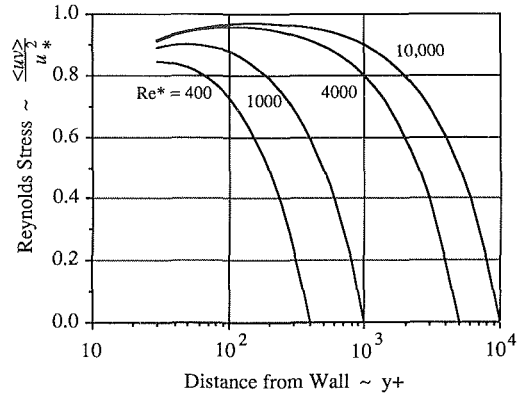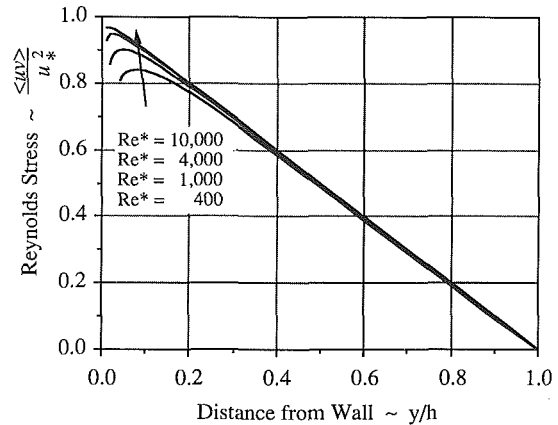
changes size and contains different portions of inner and outer physics, so to speak. An exact mathematical example in Panton (1984) illustrates this phenomenon. A uniformly valid expansion displaying Reynolds number effects can be extracted from the two expansions by forming a "composite expansion" by the method described by Van Dyke (1965); Nayfeh (1973) gives further historical references. Let the symbol $G_0^n]_i^m$ stand for the n-term outer expansion, expressed in inner variables, expanded for $\mathrm{Re} \Rightarrow \infty$, and truncated at m-terms. This is the behavior of g, and of G, in the overlap region. A first-order additive composite expansion is defined as

$$\frac{-<uv>}{u_*^2} = g_{\text{composite}} = g_0 + G_0 - G_0^1]_i^1$$

If y^+ is small then g_0 is the correct answer and G_0 takes on values of the overlap region which are cancelled out by the last term. If y^+ is large G_0 is the correct answer and g_0 is cancelled by the last term. At intermediate values the expression mixes the two relations at positions dictated by the size of the Reynolds number.

$$\frac{-<uv>}{u_*^2} = g_{\text{composite}} = 1 - \frac{1}{\kappa y^+} + 1 - \eta - 1$$

$$\frac{-<uv>}{u_*^2} = g_{\text{composite}} = 1 - \frac{1}{\kappa y^+} - \frac{y^+}{\mathrm{Re}_*} \qquad (5.3)$$

Although simple in concept and form, this lowest-order equation shows a strong Reynolds number dependence. The behavior is shown in Fig. 2 in inner variables and Fig. 3 in outer variables.

The process can be continued to second order since the second-order velocity has been found to be the constant C_3 in the overlap region. The second-order inner momentum equation (2.13) shows that the Reynolds stress reflects two physical

effects; the decrease in wall shear, $f_1'(0)$, and the fact that the wall layer is thick enough to have significant pressure forces, the y^+ term. In the overlap region the second-order Reynolds stress is

$$g_1 = f_1'(0) - y^+ \qquad (5.4)$$

Here $f_1'(0)$ is the second-order slope of the velocity at the wall; an unknown constant from the inner solution. For the second-order outer momentum equation, the analysis produces the effect of viscous stresses and the "reduced" wall shear (that is, the difference between u^* and u_τ);

$$G_1 = -F_1' + f_1'(0)[1 - \eta]$$

$$G_1 = -\frac{1}{\kappa \eta} + f_1'(0)[1 - \eta] \qquad (5.5)$$

The second-order composite expansion has the same trends as the first order but includes the wall shear effect $f_1'(0)$;

$$\frac{-<uv>}{u_*^2} = g_{\text{composite}}^2 = g_0 + \epsilon_1 g_1 + G_0 + \hat{\epsilon}_1 G_1 - G_0^2]_i^2$$

$$\frac{-<uv>}{u_*^2} = \left[1 + \frac{f_1'(0)}{\mathrm{Re}_*}\right]\left[1 - \frac{y^+}{\mathrm{Re}_*}\right] - \frac{1}{\kappa y^+}$$

$$\frac{-<uv>}{u_*^2} = \left[1 + \frac{f_1'(0)}{\mathrm{Re}_*}\right][1 - \eta] - \frac{1}{\kappa \eta \mathrm{Re}_*} \qquad (5.6)$$

The first group of terms in these equations is really $(u_\tau/u^*)^2$ by induction using (4.8). The term $[1 - \eta]$ naturally scales on u_τ while the last term, which arises from the overlap velocity profile, naturally scales on u^*. This distinction arises in the second order but not in the first order; that is (5.3).

For most of the Reynolds number range, the location and value of the maximum Reynolds stress are adequately given by the first-order results

$$y_{\text{max}}^+ = \sqrt{\frac{\mathrm{Re}_*}{\kappa}} \quad \text{or} \quad \eta_{\text{max}} = \frac{1}{\sqrt{\kappa \, \mathrm{Re}_*}} \qquad (5.7)$$

$$\frac{<uv>_{\text{max}}}{u_*^2} = 1 - \frac{2}{\sqrt{\kappa \, \mathrm{Re}_*}} \qquad (5.8)$$

Note that the position of the maximum Reynolds stress moves to higher values of y^+ with increasing Reynolds number, but is actually closer to the wall in terms of η. Because the overlap velocity expressions were used, the equations above are only strictly valid in the overlap region. The empirical equations proposed by Sreenivasan and by Long for $y^+{}_{\text{max}}$ are exactly this form, except the coefficient $1/\sqrt{\kappa} = 1.56$ compares to their values of 2.0 and 1.89 respectively. The maximum point remains in the log region as the Reynolds number becomes large.

It is interesting to note that defining a "Reynolds stress defect" yields a function of the intermediate variable only

$$\frac{1 - g_{\text{comp}}}{1/\sqrt{\mathrm{Re}_*}} = Y + \frac{1}{\kappa \, Y}$$

This is merely a rearrangement of (5.3). In general one cannot expect composite expansions to be functions of the intermediate variable alone without any Reynolds number dependence.

6 Discussion and Summary

The concept that turbulent wall-layers consist of two layers leads to many strikingly simple results. The theory, as presented here, employs u^* as the turbulence and velocity scale. The matching process produces an equation to define u^* from the other parameters of the flow, namely,

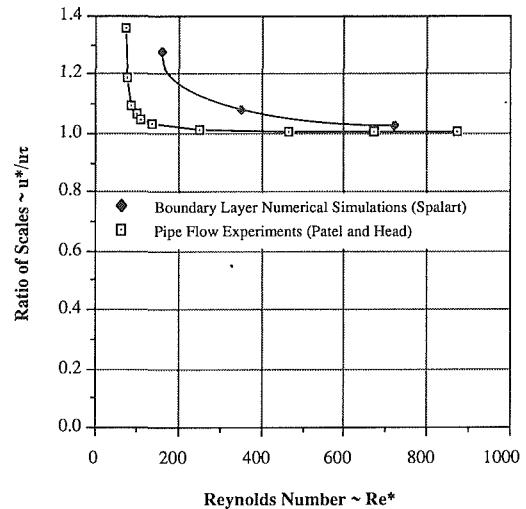$$\frac{U_\infty}{u^*} = \frac{1}{\kappa} \ln \frac{u^* h}{\nu} + C_1 - C_2 \qquad (6.1)$$

Fig. 4 Comparison of velocity scale to friction velocity

The other historical roles for u^*, a measure of the maximum Reynolds stress and a measure of the wall friction, become approximations that are exact only at high Reynolds numbers. For example, the wall shear relation is

$$u_\tau = u_*[1 + f_1'(0; e^+, \Pi)\epsilon_1(\mathrm{Re}_*) + \ldots]^{1/2} \qquad (6.2)$$

Figure 4 shows the ratio u^*/u_τ determined from the experiments of Patel and Head (1976) on pipe flow and from direct Navier-Stokes simulations of Spalart (1988) for a boundary layer. In pipe flow these quantities are found independently; the pressure drop indicates u_τ and (6.1) together with the measured U_∞ will yield u^*. Second-order effects, $f_1'(0)$, for pipes, channels, and boundary layers are not necessarily identical. In pipes and channels (2.10) shows that the pressure gradient term $(-y^+)$ is active in the second-order momentum balance in the inner region. Figure 4 indicates that second-order velocity effects begin below $\mathrm{Re}^* < 300$ in pipe flow but at somewhat higher value for constant pressure boundary layers.

The overlap velocity profiles, when scaled by u^*, have a slope $1/\kappa$ that is independent of Reynolds number. This slope is an alternate way to determine u^* (with the constant κ as found at $\mathrm{Re}^* \Rightarrow \infty$). The overlap laws are

$$\frac{u}{u^*} \sim \frac{1}{\kappa} \ln y^+ + C_1 + \frac{1}{\mathrm{Re}_*} C_3 \qquad (6.3)$$

$$\frac{u - U_\infty}{u^*} \sim \frac{1}{\kappa} \ln \eta + C_2 + \frac{1}{\mathrm{Re}_*} C_3 \qquad (6.4)$$

Moreover, when u^* is used in forming y^+, the overlap behavior is exactly $\ln y^+$; higher order terms do not contain y^+. Except for u^*, all of the constants in the above relations; κ, C_1, C_2, C_3, and $f_1'(0)$ are independent of Reynolds number. The additive constant in (6.3) and (6.4) increases as $1/\mathrm{Re}_*$ due to second-order effects. Presumably, noting the trends established by the matching relations (4.2) and (4.4), the next terms are proportional to $1/\mathrm{Re}^{*2}$. Figure 1 illustrates the effect of Reynolds number on the shape of velocity profiles. If one insists on using u_τ as the scale, substitution of (6.2) into (6.3) shows that both the slope and level of the log region will change with Reynolds number.

There is some concern that at very low Reynolds numbers the overlap region may not exist. Spalart found that at his lowest Reynolds number the log region was essentially a point, or possibly nonexistent. In the present theory the overlap existence can be tested by comparing u^* as determined from (6.1) to the value determined from (6.3). The practical dif-
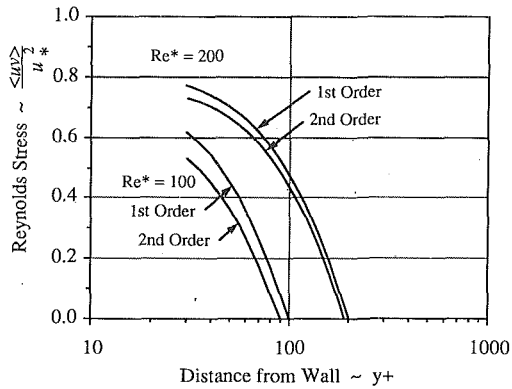
430 / Vol. 112, DECEMBER 1990

Transactions of the ASME

Downloaded 02 Jun 2010 to 171.66.16.101. Redistribution subject to ASME license or copyright; see http://www.asme.org/terms/Terms_Use.cfm

Fig. 5 Second-order Reynolds stress

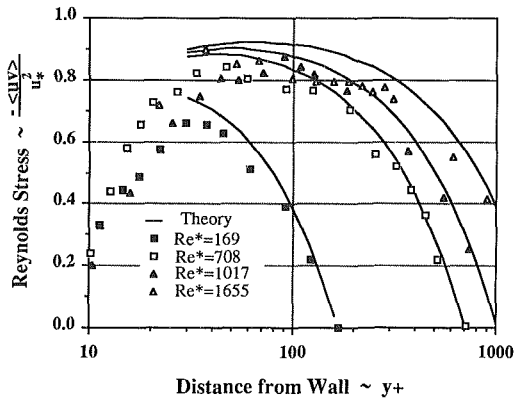**Fig. 6 Reynolds stress on channel flow (Wei and Willmarth) compared to theory**

Fig. 7 Reynolds stress in channel flow (Triederman and Harder) compared to theory

ficulties are that C_1 and C_2 are not known accurately and that (6.1) is a steep curve at low Re.

There are actually only three constants involved in the first order overlap laws; κ could be absorbed into the other constants, (u^*/κ), (κC_1), (κC_2). This would be equivalent to adjusting the definition of u^* so that the constant in (4.6) would be one. It is instructive to redefine the constants, let $C_1 = \exp(\kappa C_1)$ and $C_2 = \exp(\kappa C_2)$, and rewrite the velocity laws in the "canonical" form

$$\frac{U}{u^*/\kappa} = \ln \frac{y}{\nu/(u^*C_1)} \qquad (6.5)$$

$$\frac{U - U_\infty}{u^*/\kappa} = \ln \frac{y}{h/C_2} \qquad (6.6)$$

In this form it appears that u^*/κ is the velocity scale, $\nu/(u^*C_1)$ is the inner region length scale, and h/C_2 is the outer region length scale. Equation (6.1) is a relation between the two length scales, the velocity scale, and U_∞

$$\frac{U_\infty}{u^*/\kappa} = \ln \frac{\nu/(u^*C_1)}{h/C_2} \qquad (6.7)$$

The relations (6.5), (6.6), and (6.7) suggest that it might be useful to include C_1 or C_2 in the inner or outer length scales for situations where these constants vary with another parameter.

One further comment on scales. In pipe and channel flows h and u^* are well-defined and accordingly the constants in (6.1) uniquely determined. In boundary layers u^* is again uniquely determined as the slope of $u = (u^*/\kappa) \ln y + \text{constant}$. However, $h = \delta$ is implicitly defined by the choice of C_2 in (6.1). For example, Townsend (1976) suggested that $C_2 = 0$ would be acceptable. On the other hand, if δ is defined in some way then, a specific value of C_2 is associated with that defini-
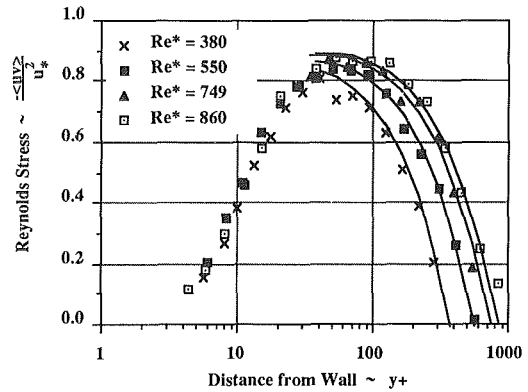
tion. Consistency cannot be expected unless C_2 and δ are consistently chosen.

Turbulence properties in the overlap region in principle require composite asymptotic expansions. This situation is brought about because the overlap layer changes size directly with the Reynolds number. There, inner-layer physics transitions to outer-layer physics. Any different algebraic behavior, such as the Reynolds stress, will be mixed in different amounts and occur at different locations as the Reynolds number varies. The velocity profiles are a deceptive situation because the inner, outer, and composite expansions are all logarithmic. Thus, Reynolds number effects on the velocity profiles are minimal.

The Reynolds stress is clearly an example of a turbulence property with a strong Reynolds number dependence even in the first-order theory (to be precise the composite expansion formed from first-order results). Practically, since the viscous stress is negligible in the outer region, the velocity profile does not matter and the stress equation remains valid. It is

$$\frac{-<uv>}{u_*^2} = \frac{u_\tau^2}{u_*^2}\left[1 - \frac{y^+}{\text{Re}_*}\right] - \frac{1}{\kappa y^+} \qquad (6.8)$$

It is also something of an accident that (6.8) satisfies the complete unapproximated momentum equation (2.8). Another interesting result is that (6.8) shows that the total stress, which is the first two terms on the right-hand side, contains a Reynolds number dependence. Only as $\text{Re} \Rightarrow \infty$ is the total stress constant.

The effect of extremely low Reynolds numbers is shown in Fig. 5 where the second-order theory (for pipes) is plotted. In order to construct this curve experimental data on u^*/u_t from Fig. 4 was used. Experimental data of Wei and Willmarth (1989) from a 5:1 aspect ratio channel flow is shown in Fig. 6. The theoretical curves are the first-order theory; in other words $u^*/u_t = 1$ in (6.8). Only in the lowest Reynolds number curve, $\text{Re}^* = 169$, should there be any effect caused by $u^* \neq u_t$. These are extremely difficult measurements to make and the agreement must be considered as very good. Another set of channel flow experiments by Tiederman and Harder (1989) is given in Fig. 7. Here all of the curves are at Reynolds numbers where first-order theory is probably adequate. In fact, the authors report that the log region has the usual von Kármán constant. The curves of Fig. 7 also show a nice collapse for $y^+ < 30$.

A clear physical picture of Reynolds number effects can be gained by noting that (2.8) represents a force balance on an element of fluid extending from the wall to the position y^+. The first term on the right-hand side is the wall shear stress, from which the second term subtracts the net pressure force acting on the area from 0 to y^+, and the last term subtracts the viscous stress. If the Reynolds number is low, the inner viscous region is effectively thicker and subjected to a larger effect

from the pressure forces. When Re* = 4000 the maximum Reynolds stress is within 5 percent of ρu^{*2} and the viscous and pressure force are almost completely separated in their regions of influence. The main effect of lower Reynolds numbers is to increase the size of the viscous layer (compared to h) so that pressure forces (convective effects in the case of boundary layers) become important in progressively lower portions of the overlap region. Truly second-order effects occur at very low Reynolds numbers when the pressure acts on the region $y^* < 30$ and causes $u^* \neq u_t$. Figure 4 shows that it takes quite low Re* values for this to happen.

With regard to flow visualization experiments and direct numerical simulations, both of which can only be done at low Reynolds number, the general nature of the present results are very encouraging. The second-order effects on U and $- <uv>$ are minor. Physical events found in flow visualization experiments and direct numerical simulations are indeed representative of high Reynolds number events. The primary Reynolds number effect will be the scale building processes that occur in the log region and expand with Re* so that turbulent scales can grow from ν/u^* to size h.

The scale determined by the inner-outer interaction has been made conceptually distinct from the scale determined by the wall shear stress. This brings forth some new possibilities. One may attempt to correlate turbulent wall-layers containing phenomena that displace u^* from u_t. Special events may exist (in either the inner or outer layers) that affect the overlap interaction (u^*) and the very near wall flow in the inner layer (u_τ) differently. For examples consider outer layers with three-dimensional effects or high free-stream turbulence or inner layers with roughness, riblets or polymers. A conceptual difference between u^* and u_τ may offer an advantageous basis for organizing these flows.

Acknowledgment

References

Afzal, N., 1976, "Millikan's Argument at Moderately Large Reynolds Number," *Phys. Fluids*, Vol. 1, pp. 600–602.

Afzal, N., 1982a, "A Sub-Boundary Layer within the Two Dimensional Turbulent Boundary Layer," *J. Mech. Theor. & Appl.*, Vol. 1, p. 963.

Afzal, N., 1982b, "Fully Developed Turbulent Flow in a Pipe: An Intermediate Layer," *Ingen.-Archiv.*, Vol. 52, pp. 355–377.

Afzal, N., and Bush, W. B., 1985, "A Three-Layer Asymptotic Analysis of Turbulent Channel Flow," *Proc. Indian Acad. Sci. (Math. Sci.)*, Vol. 94, pp. 135–148.

Afzal, N., and Yajnik, K., 1973, "Analysis of Turbulent Pipe and Channel Flows at Moderately large Reynolds Number," *J. Fluid Mech.*, Vol. 61, pp. 23–31.

Alfredsson, P. H., and Johansson, A. V., 1984, *Phys. Fluids*, Vol. 27.

Blackwelder, R. F., and Haritonidis, J. H., 1983, "Scaling the Bursting Frequency in Turbulent Boundary Layers," *J. Fluid Mech.*, Vol. 132, pp. 87–103.

Bush, W. B., and Fendell, F. E., 1972, "Asymptotic Analysis of Turbulent Channel and Boundary Layer Flow," *J. Fluid Mech.*, Vol. 56, pp. 657–681.

Bush, W. B., and Fendell, F. E., 1973, "Asymptotic Analysis of Turbulent Channel Flow for Mea Turbulent Closure," *Phys Fluids*, Vol. 16, pp. 1189–1197.

Coles, D. E., and Hirst, E. A., 1968, *Proceedings Computation of Turbulent Boundary Layers 1968 AFOSR-IFP*, Stanford Conference, p. 13.

Durand, W. F., 1935, *Aerodynamic Theory*, Vol. 3, p. 119.

Gill, A. E., 1968, *J. Math. Phys.*, Vol. 47, p. 437.

Hinze, J. O., 1956, *Turbulence*, McGraw-Hill, New York.

Izakson, A., 1937, "On the Formula for the Velocity Distribution Near Walls," *Tech. Phy.* USSI IV, Vol. 2, p. 155.

Kim, J., Moin, P., and Moser, M., 1987, "Turbulence Statistics in Fully Developed Channel Flow Low Reynolds Number," *J. Fluid Mech.*, Vol. 177, pp. 133–165.

Kline, S. J., Reynolds, W. C., Schraub, J. A., and Rustadler, P. W., 1967, "The Structure of Turbulent Boundary Layers," *J. Fluid Mech.*, Vol. 30, pp. 741–773.

Liu, T. M., and Libby, P. A., 1986, "Theoretical Study of Turbulent Flow over an Acoustic Surface," AIAA-86-0391, pp. 1–10.

Long, R. R., and Chen T-C, 1981, "Experimental Evidence for the Existence of the 'Mesolayer' Turbulent Systems," *J. Fluid Mech.*, Vol. 105, pp. 19–59.

Millikan, C. B., 1938, "A Critical Discussion of Turbulent Flows in Channels and Circular Tubes," *Proc. 5th Int. Cong. Appl. Mech.*, Cambridge, pp. 386–392.

Nayfeh, A. H., 1973, *Perturbation Methods*, Wiley-Interscience, New York.

Panton, R. L., 1984, *Incompressible Flow*, Wiley-Interscience, New York.

Patel, V. C., and Head, M. R., 1969, "Some Observations on Skin Friction and Velocity Profiles in Fully Developed Pipe and Channel Flows," *J. Fluid Mech.*, Vol. 38, pp. 181–201.

Prandtl, L., 1932, "Zur Turbulenten Stromung in Rohren und Langs Platten," *Ergeb. Aerod. Versuch.*, Goettingen, IV Lieferung, p. 18.

Spalart, P. R., 1988, "Direct Simulation of a Turbulent Boundary Layer up to $R_\theta = 1410$," *J. Fluid Mech.*, Vol. 187, p. 61.

Sreenivasan, K. R., 1987, "A Unified View of the Origin and Morphology of the Turbulent Boundary Layer Structure," *Proc. IUTAM Symp. Turbulence Management & Relaminarization*, Leipmann, H. W. and R. Narasimha, eds., p. 37.

Tennekes, H., and Lumley, J. L., 1972, *A First Course in Turbulence*, MIT Press.

Tiederman, W. G., and Harder, K. J., 1989, Private communication.

Townsend, A. A., 1956, *The Structure of Turbulent Shear Flow*, Cambridge Univ. Press.

v. Kármán, TH., 1930, Mechanische Aehnlichkeit und Turbulenz," *Proc. Third Int. Cong. App. Mech.*, Stockholm, p. 83.

Van Dyke, M., 1965, *Perturbation Methods*, Parabolic Press, Stanford.

Wei, T., and Willmarth, W. W., 1990, "Reynolds Number Effects on the Structure of a Turbulent Channel Flow," *J. Fluid Mech.*

Yajnik, K. S., 1970, "Asymptotic Theory of Turbulent Shear Flows," *J. Fluid Mech.*, Vol. 42, pp. 411–427.

L. C. Thomas

H. M. Kadry

King Fahd University of
Petroleum and Minerals,
Dhahran, Saudi Arabia

A One-Parameter Integral Method for Turbulent Transpired Boundary Layer Flow

This paper presents the development of a practical one-parameter integral method for transpired turbulent boundary layer flow. The method involves the use of one-parameter polynomial approximations for total stress and the solution of the familiar integral momentum equation. The method is compared with experimental data and numerical solutions for a range of near equilibrium boundary layers.

Introduction

As pointed out by Cousteix (1981), integral methods and numerical field methods of analyzing turbulent boundary layer flows are complementary. In addition to being efficient and easy to use, well-developed integral methods for turbulent flow are generally just as accurate as the numerical field methods. Since the 1968 Stanford Conference, integral methods have been generalized to account for the effects of history, compressibility, three-dimensionality, extra rates of strain, wall curvature, and free-stream turbulence. However, the integral solution approaches featured at the recent 1981 Stanford Conference are not applicable to transpired turbulent boundary layer flows.

On the other hand, several integral methods have been devised for transpired laminar boundary layers. For example, the standard one-parameter Pohlhausen method has been adapted to laminar boundary layer flow with suction by Torda (1952) and Prandtl (1935). Other integral methods have been developed for laminar flow with transpiration by Schlichting (1979), Thwaites (1949), Truckenbrodt (1956), Mangler (1948), Head (1957), and Liu (1962). However, except for the rather involved multiple-parameter method of integrals (MIR) formulation by Liu (after Dorodnitsyn, 1960), none of these early methods have provided a basis for generalization to turbulent flow.

In this connection, a practical one-parameter integral approach has recently been developed for laminar transpired boundary layer flow (Thomas and Amminger, 1988) which can be generalized to turbulent flow. The objective of this paper is to extend this one-parameter integral method in such a way as to provide a practical and efficient computational tool for analyzing turbulent transpired boundary layer flows.

Analysis

To develop a one-parameter integral method for turbulent boundary layer flow, the velocity distribution will be expressed in terms of the boundary layer thickness δ and mixing length ℓ, with closure accomplished by use of the integral momentum equation,

$$\frac{f_x}{2} = \frac{1}{r_0} \frac{d}{dx} (r_0 \, \delta_2) + \frac{\delta_2}{U_\infty} \frac{dU_\infty}{dx} (2+H) - \frac{\bar{v}_0}{U_\infty} \qquad (1)$$

where the displacement and momentum thicknesses are defined by

$$\delta_1 = \int_0^\infty \left(1 - \frac{\bar{u}}{U_\infty}\right) dy \qquad (2)$$

$$\delta_2 = \int_0^\infty \frac{\bar{u}}{U_\infty}\left(1 - \frac{\bar{u}}{U_\infty}\right) dy \qquad (3)$$

and $H = \delta_1/\delta_2$.

Following the approach developed by Thomas and Amminger (1988) and Thomas and Hasani (1989), supplementary boundary layer approximations for total stress $\bar{\tau}$ are used to establish realistic representations for the velocity distribution associated with turbulent boundary layers. The applicable distribution in $\bar{\tau}$ for plane and thin axisymmetric boundary layer flows with mild to moderate pressure gradients and transpiration is represented by the Nth order polynomial

$$\frac{\bar{\tau}}{\bar{\tau}_0} = \sum_{n=0}^{N} a_n \xi^n + B_M \frac{\bar{u}}{U_\infty} \qquad (4)$$

where $\xi = y/\delta$, $B_M = \rho \bar{v}_0 U_\infty / \bar{\tau}_0 = v_0^+ U_\infty^+$, $v_0^+ = \bar{v}_0/U^*$, $U_\infty^+ = U_\infty/U^* = \sqrt{2/f_x}$, and $U^* = \sqrt{\bar{\tau}_0/\rho}$. The coefficients a_n are specified in accordance with the Couette law,

$$\frac{\bar{\tau}}{\bar{\tau}_0} = 1 + \beta_\delta \xi + B_M \frac{\bar{u}}{U_\infty} = 1 + P^+ y^+ + v_0^+ u^+ \qquad (5a)$$

near the wall, the constraints

$$\frac{\partial \bar{\tau}}{\partial y} = 0 \text{ and } \bar{\tau} = 0 \qquad (5b,c)$$

$$\frac{\partial \bar{u}}{\partial y} = 0 \text{ and } \bar{u} = U_\infty \qquad (5d,e)$$

at the outer edge of the boundary layer, and higher order conditions. Using the primary constraints given by equations (5a)–(5e) and setting $N=3$, equation (4) gives rise to a one-parameter 3rd order approximation of the form

$$\frac{\bar{\tau}}{\bar{\tau}_0} = 1 + \beta_\delta \xi + B_M \frac{\bar{u}}{U_\infty} - (3 + 2\beta_\delta + 3B_M)\xi^2 + (2 + \beta_\delta + 2B_M)\xi^3 \qquad (6a)$$

or, in terms of wall variables,

$$\frac{\bar{\tau}}{\bar{\tau}_0} = 1 + P^+ y^+ + v_0^+ u^+ - (3 + 2P^+ \delta^+ + 3v_0^+ U_\infty^+)\xi^2 + (2 + P^+ \delta^+ + 2v_0^+ U_\infty^+)\xi^3 \qquad (6b)$$

Although more accurate higher order one- and two-parameter approximations can be developed for $\bar{\tau}$, equation (6) proves to be quite adequate for mild to moderate pressure gradients and rates of transpiration.

To incorporate this supplementary boundary layer approximation for $\bar{\tau}$ into the formulation of an integral method for turbulent boundary layer flows, the mean velocity $\bar{u}$ is expressed in terms of $\bar{\tau}$, mixing length ℓ, and wall variables by

$$\frac{\bar{\tau}}{\bar{\tau}_0} = \frac{\partial u^+}{\partial y^+} + \left(\ell^+ \frac{\partial u^+}{\partial y^+}\right)^2 \qquad (7)$$

or

$$u^+ = 2 \int_0^{y^+} \frac{\bar{\tau}/\bar{\tau}_0 \, dy^+}{1 + (1 + 4\ell^{+2} \bar{\tau}/\bar{\tau}_0)^{1/2}} \qquad (8)$$

With $\bar{\tau}$ and ℓ appropriately specified, equation (8) can be numerically integrated to compute the distributions in u^+ across the boundary layer. For near equilibrium turbulent boundary layers with moderate pressure gradients and transpiration rates, the mixing length can be approximated by

$$\ell^+ = \kappa y^+ [1 - \exp(-\frac{y^+}{a^+})] \qquad \text{inner region} \qquad (9a)$$

$$\ell^+ = \alpha_0 \delta^+ \qquad \text{outer region} \qquad (9b)$$

where the damping parameter a^+ is given by

$$a^+ = \frac{25}{d[v_0^+ + b \, P^+ /(1 + c \, v_0^+)] + 1} \qquad (10)$$

with $b = 4.25$ and $c = 10$ for $P^+ \leq 0$, $b = 2.9$ and $c = 0$ for $P^+ > 0$, $d = 7.1$ for $v_0^+ \geq 0$, and $d = 9$ for $v_0^+ < 0$, and

$$\alpha_0 = A_0 \left(\frac{6000}{\mathrm{Re}_{\delta_2}}\right)^{118} \left(1 - A_1 \frac{\bar{v}_0}{U_\infty}\right) \quad \text{for } \mathrm{Re}_{\delta_2} \leq 6000$$

$$\alpha_0 = A_0 \left(1 - A_1 \frac{\bar{v}_0}{U_\infty}\right) \quad \text{for } \mathrm{Re}_{\delta_2} \geq 6000 \qquad (11)$$

with $A_0 = 0.07$ and $A_1 = 67.5$ after Andersen et al. (1972). Referring to Thomas and Hasani (1989), calculations for $\bar{\tau}$ and u^+ based on equations (6)–(11) compare favorably with experimental data for a wide range of conditions.

These relations can be used to express the displacement and momentum thicknesses in terms of v_0^+ and P^+. The displacement thickness δ_1 is written in terms of wall variables by

$$\delta_1 = \int_0^\infty \left(1 - \frac{\bar{u}}{U_\infty}\right) dy = \frac{\nu}{U^*} \int_0^\infty \left(1 - \frac{u^+}{U_\infty^+}\right) dy^+ \qquad (12)$$

or

$$\frac{\delta_1 U_\infty}{\nu} = \mathrm{Re}_{\delta_1} = I_1 \qquad (13)$$

where

$$I_1 = \int_0^\infty (U_\infty^+ - u^+) dy^+ \qquad (14)$$

Similarly, the momentum thickness δ_2 is written as

$$\delta_2 = \int_0^\infty \frac{\bar{u}}{U_\infty}\left(1 - \frac{\bar{u}}{U_\infty}\right) dy = \frac{\nu}{U^*} \int_0^\infty \frac{u^+}{U_\infty^+}\left(1 - \frac{u^+}{U_\infty^+}\right) dy^+ \qquad (15)$$

or

$$\frac{\delta_2 U_\infty}{\nu} = \mathrm{Re}_{\delta_2} = \frac{I_2}{U_\infty^+} \qquad (16)$$

where

$$I_2 = \int_0^\infty u^+ (U_\infty^+ - u^+) dy^+ \qquad (17)$$

With v_0^+, P^+, and δ^+ specified, the wall variable integral parameters I_1 and I_2 can be computed by numerical integration.

--------- Nomenclature ---------

a_n = coefficients associated with equation (4)
a^+ = dimensionless damping parameter
A_0, A_1 = constant in equation (11)
b, c, d = constants in equation (10)
B_M = blowing parameter $(= \rho \bar{v}_0 U_\infty / \bar{\tau}_0)$
F = dimensionless transpiration rate $(= \bar{v}_0 / U_\infty)$
f_x = Fanning friction factor
H = shape factor $(= \delta_1 / \delta_2)$
I_1 = defined by equation (14)
I_2 = defined by equation (17)
K = acceleration parameter $(= \nu dU_\infty / dx / U_\infty^2)$
ℓ = mixing length
ℓ^+ = dimensonless mixing length $(= \ell U^* / \nu)$
N = total number of coefficients
P^+ = dimensionless pressure gradient parameter $[= \nu d\bar{P}/dx/(\rho U^{*3})]$

r_0 = radius of curvature
Re_{δ_1} = displacement thickness Reynolds number $(= \delta_1 U_\infty / \nu)$
Re_{δ_2} = momentum thickness Reynolds number $(= \delta_2 U_\infty / \nu)$
$]u$ = mean velocity in x direction
u^+ = dimensionless mean velocity $(= \bar{u}/U^*)$
U^* = friction velocity $(= \sqrt{\bar{\tau}_0/\rho})$
U_∞ = free-stream velocity
U_∞^+ = dimensionless free-stream velocity $(= U_\infty / U^* = \sqrt{2/f_x})$
$\bar{v}$ = mean velocity in y-direction
$\bar{v}_0$ = mean transpiration velocity
v_0^+ = dimensionless transpiration velocity $(= \bar{v}_0 / U^*)$
x = streamwise direction

y = direction normal to surface
y^+ = dimensionless distance $(= yU^*/\nu)$
$\mathbf{Z}_2$ = defined by equation (21)
α_0 = mixing length parameter for outer region
β_δ = dimensionless pressure gradient parameter $(= \delta \, d\bar{P}/dx/\bar{\tau}_0)$
δ = boundary layer thickness
δ^+ = dimensionless boundary layer thickness $(= \delta U^*/\nu)$
δ_1 = displacement thickness, equation (12)
δ_2 = momentum thickness, equation (15)
ξ = dimensionless distance $(= y/\delta)$
κ = constant equal to 0.41
$\bar{\tau}$ = mean total stress
$\bar{\tau}_0$ = mean wall shear stress
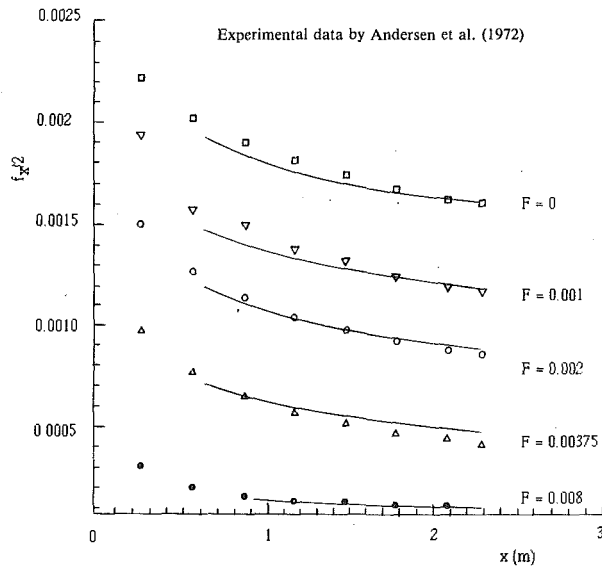ρ = density
ν = kinematic viscosity

Fig. 1(a) Friction factors for transpired turbulent boundary layer flow: $m = 0$
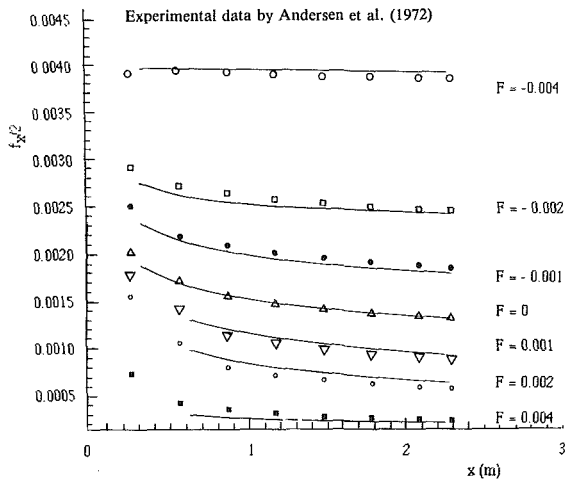

Fig. 1(b) Friction factors for transpired turbulent boundary layer flow: $m = -0.15$

To incorporate the paramters I_1 and I_2 into the integral momentum equation, equation (1) is put into the form

$$\frac{1}{r_0} \frac{d}{dx} (r_0 \mathrm{Re}_{\delta_2}) = \frac{U_\infty}{\nu} \left[\frac{f_x}{2} + \frac{\bar{v}_0}{U_\infty} - K(1+H) \mathrm{Re}_{\delta_2} \right] \quad (18)$$

Substituting equation (16) into equation (18) and using the dimensionless wall variable format, the integral momentum equation becomes

$$\frac{1}{r_0} \frac{d}{dx} \left(r_0 \frac{I_2}{U_\infty^+} \right) = \frac{U_\infty}{\nu} \left[\frac{1}{U_\infty^{+2}} (1 + v_0^+ U_\infty^+) \right.$$
$$\left. - K(1+H) \frac{I_2}{U_\infty^+} \right] \quad (19)$$

where

$$H = \frac{\delta_1}{\delta_2} = \frac{I_1}{I_2} U_\infty^+ \quad (20)$$

A noniterative numerical solution is developed by putting equation (19) into the form

$$\frac{d}{dx} \left(\frac{I_2}{U_\infty^+} \right) = \frac{U_\infty}{\nu} \left[\frac{1}{U_\infty^{+2}} (1 + v_0^+ U_\infty^+) \right.$$

$$\left. - K(1+H) \frac{I_2}{U_\infty^+} \right] - \frac{I_2}{U_\infty^+} \frac{1}{r_0} \frac{dr_0}{dx} = Z_2 \quad (21)$$

or

$$\frac{dI_2}{dx} = U_\infty^+ \left(Z_2 + \frac{I_2}{U_\infty^{+2}} \frac{dU_\infty^+}{dx} \right) \quad (22)$$

These equations have been incorporated into a single three-point finite-difference code which computes $(I_2/U_\infty^+)_{i+1}$, $(I_2)_{i+1}$, and $(f_x)_{i+1}$ on the basis of calculations for $(Z_2)_i$, $(U_\infty^+)_i$, and $(U_\infty^+)_{i-1}$; the friction factor f_x is expressed in terms of I_2/U_∞^+ and I_2 by

$$\frac{f_x}{2} = \frac{I_2/U_\infty^{+2}}{I_2} \quad (23)$$

After f_x has been evaluated at station $i+1$, v_0^+, P^+, and a^+ are evaluated, ξ is approximated by $\xi = y/\delta_i$, u^+, I_1, and I_2 are computed by a single numerical integration loop, and δ^+ is evaluated. These results are then used to move to the next station.

Results

Calculations for Fanning friction factor f_x obtained by means of the proposed one-parameter integral method are compared in Figs. 1(a) and 1(b) with experimental data obtained by Andersen et al. (1972) by use of the modern Reynolds stress method for transpired near equilibrium boundary layers. The integral solution results for f_x are generally within 5 percent of the experimental data for dimensionless transpiration rates $F = \bar{v}_0/U_\infty$ ranging from -0.008 to 0.004. The corresponding calculations for the distributions in dimensionless velocity u^+ are compared with representative data in Figs. 2(a) and 2(b). These figures indicate that the quality of the present integral solution calculations is quite good for velocity u^+ as well as friction factor f_x.

Andersen's data for $m = 0$ and $F = 0.00375$, and $m = -0.15$ and $F = -0.004$ were used at the 1981 Stanford Conference on Complex Turbulent Flows as a basis for testing various computational methods. The five methods tested for both of these flows included the numerical codes of Orlandi, Rodi, Donaldson, Pletcher and Wilcox (see Kline et al. 1981). (None of the integral methods presented at the conference were tested for the transpired flows.) The numerical calculation results obtained by these methods are compared with the present integral solution calculations in Figs. 3(a) and 3(b). The integral solution results are observed to compare very favorably with the results obtained by these numerical approaches.

The present calculations were made on an IBM 3033 (MVS/TSO), with the CPU time required for each run generally less than 1 s.

Conclusion

Supplementary boundary layer approximations for total stress of the form recently employed in the analysis of laminar flow have been combined with standard inputs for mixing length to develop a practical integral method for turbulent transpired boundary layer flows. The method has been found to provide calculations for friction factor and velocity that are in good agreement with data associated with a wide range of blowing and suction rates and that compare favorably with numerical solution results presented at the 1981 Stanford Conference. The method is simple, very efficient, and provides a basis for generalization to heat transfer.
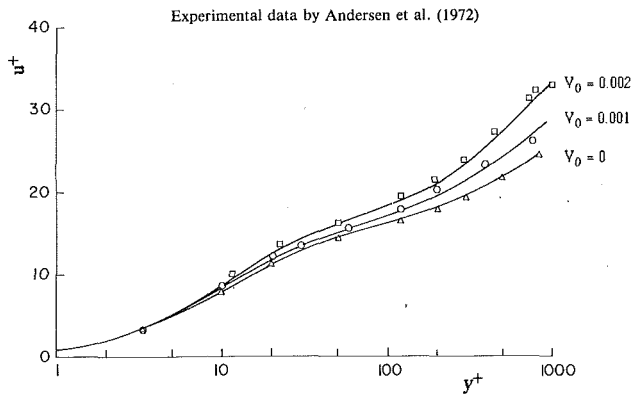
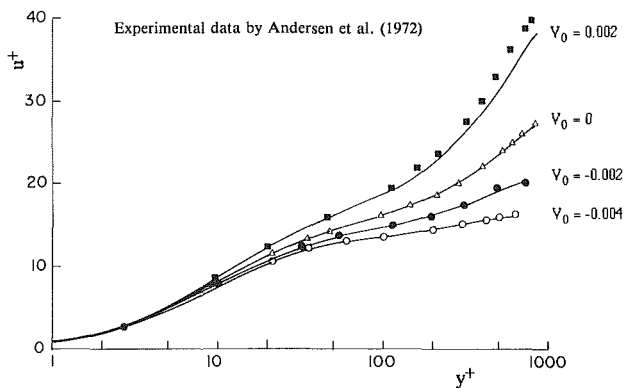Fig. 2(a) Velocity distributions for transpired turbulent boundary layer flow: $m = 0$, $x = 70$ in.

Fig. 2(b) Velocity distributions for transpired turbulent boundary layer flow: $m = -0.15$, $x = 70$ in.

Fig. 3(a) Comparison of integral and numerical solutions for transpired turbulent boundary layer flow: $m = 0$, $F = 0.00375$
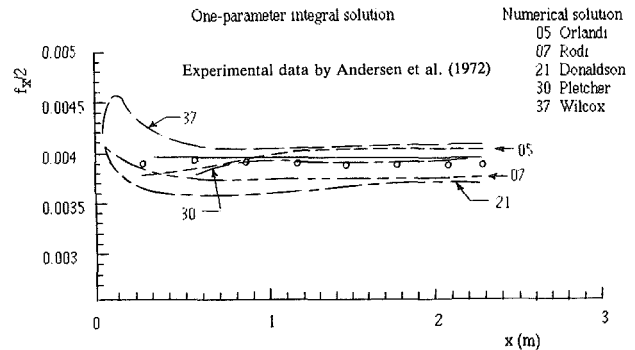
Fig. 3(b) Comparison of integral and numerical solutions for transpired turbulent boundary layer flow: $m = -0.15$, $F = -0.004$

References

Andersen, P. S., Kays, W. M., and Moffat, R. J., 1972, "The Turbulent Boundary Layer on a Porous Plate: An Experimental Study of the Fluid Mechanics for Adverse Free-Stream Pressure Gradients," Dept. of Mech. Eng., Stanford University, Stanford, CA.

Cousteix, J., "Integral Methods," 1980-81 AFOSR-HTTM-Stanford Conference on Complex Turbulent Flows, Stanford University, Stanford, CA.

Dorodnitsyn, A. A., 1960, *Advances in Aeronautical Sciences*, Vol. 3, Pergamon Press, New York.

Head, M. R., 1957, Aeronaut. Res. Council London, RM-3123.

Kline, S. J., Cantwell, B. J., and Lilley, G. M., 1981, 1980-81 AFOSR-HTTM-Stanford Conference on Complex Turbulent Flows, Stanford University, Stanford, CA.

Lui, S. T., 1962, *Zh. Vych. Mat. Mat. Fiz.*, Vol. 2, pp. 666-683.

Mangler, W., 1948, "Speical Exact Solutions," Monographs Aerodynamische Versuchsanstalt Zu Gottingen, Section 1.2.

Prandtl, L., 1935, "The Mechanics of Viscous Fluids," *Aerodynamic Theory*, Vol. III, Springer, Berlin, pp. 34-208.

Schlichting, H., 1979, *Boundary Layer Theory*, 7th ed., McGraw-Hill, New York.

Thwaites, B., 1949, "The Development of Laminar Boundary Layers Under Conditions of Continuous Suction," Part II, Rept. Aeronaut. Research Council London, No. 12699.

Thomas, L. C., and Amminger, W. L., 1988, "A Practical One-Parameter Integral Method for Laminar Incompressible Boundary Layer Flow with Transpiration, ASME *Journal of Applied Mechanics*, Vol. 110, p. 474.

Thomas, L. C., and Hasani, S. M. F., 1989, "Supplementary Boundary-Layer Approximations for Turbulent Flow," ASME JOURNAL OF FLUIDS ENGINEERING, Vol. 111, p. 420.

Torda, T. P., 1952, "Boundary Layer Control by Continuous Surface Suction or Injection," *J. Math. Phys.*, Vol. 31, pp. 206-213.

Truckenbrodt, E., 1956, "Ein Einfaches Naeherungsverfahren, zum Berechnen der Laminaren Reibungsschicht mit Absaugung," *Forschung Ingenieur Wesen*, Vol. 22, pp. 147-157.

Acknowledgment

The authors wish to acknowledge the support provided for this study by King Fahd University of Petroleum and Minerals.

S. S. Chu*

S. K. Miller
Undergraduate Student.

W. L. Chow[1]
Professor of Mechanical Engineering.
Fellow ASME

Department of Mechanical and
Industrial Engineering,
University of Illinois at
Urbana-Champaign,
Urbana, IL 61801

Quasi-Steady Discharge of Fluid From a Vessel Through a Poppet Valve

Previously established characteristics of steady-state discharge through a valve are employed for the study of quasi-steady discharge from a vessel. Experimental examination of the problem has also been carried out. The data obtained in the laboratory fully supported the validity of the quasi-steady approach to this type of unsteady flow problems.

Introduction

Recent studies on the steady discharge of a fluid from a vessel through an axisymmetric control valve have been carried out by the method of hodograph transformation. It was believed that an inviscid analysis on these problems would be adequate to describe the flow and to estimate the rate of discharge, since the viscous effects should be very small. The effect of gravity is also neglected so that an axisymmetric geometry can be maintained. Hodograph transformation employs the speed and the streamline angle of the fluid as independent variables, while all other quantitites such as the potential function and the stream function, including also the physical coordinates x, r are treated as dependent variables. The initial analysis of the problem was performed for the incompressible flow case (Chow et al., 1987). Figure 1(a) shows a schematic diagram of the axisymmetric geometry of the valve and the vessel. It was noted that due to the tremendous drop in pressure along the wall near the opening, a simple momentum balance will show that the asymptotic state of the flow must assume the horizontal uniform flow G shown in this figure. The corresponding hodograph is shown in Fig. 1(b), where the velocity has been normalized by v_∞ and the streamline angle θ has been normalized by α ($\alpha = -90$ deg). An interesting feature for this problem is that the hodograph exhibits an overlapping boundary which corresponds to the diversion of the free stream surface by the valve in the physical flow field. An average value of the stream function was employed for the overlapping boundary in order to produce the realistic geometry of the free stream-surfaces. The study was later extended to cover the compressible flow regime where both subcritical and supercritical flow conditions were examined (Weng et al., 1987a, 1987b). Although there is not much difference between cases of subcritical flow and incompressible flow, the supercritical flow condition is much more complicated, since the sonic line and the adjacent free jet

boundaries must be established together with the internal elliptic flow field.

The hodograph for the supercritical case is shown in Fig. 2, where V is normalized by V^*, the velocity of the fluid at the sonic flow condition. The curves on top of the graph are the well-known two-dimensional simple wave characteristics. To facilitate numerical computations, an additional transformation was introduced (Weng et al., 1987b). Figure 3 presents one set of results obtained for the supercritical flow case where lines of constant velocity, including the sonic line spanning across the opening, and the adjacent free jet boundaries are
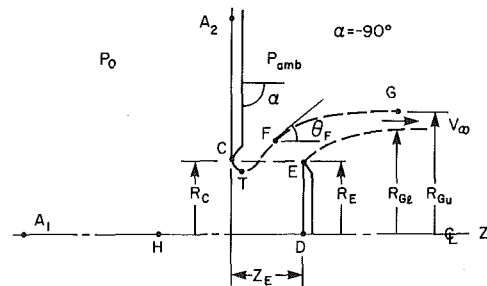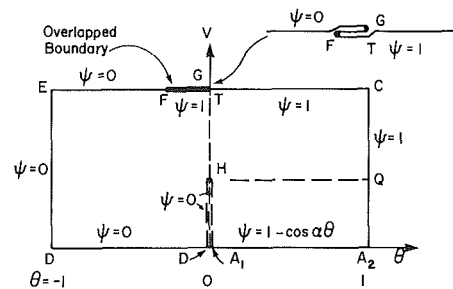

Fig. 1(a)   The physical flow field

Fig. 1(b)   The corresponding hodograph

Fig. 1   Incompressible flow discharge from a vessel through an axisymmetric valve

---

Fig. 2 The hodograph of supercritical flow conditions

Fig. 4 Discharge characteristics for subcritical flow conditions
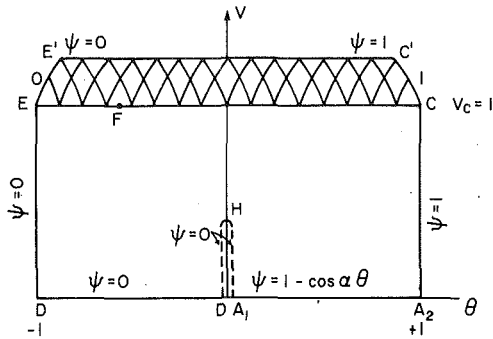

Fig. 3 Results showing a supercritical flow condition including surfaces of free-jet
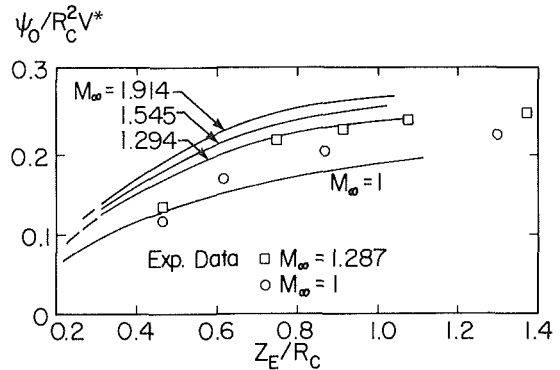
Fig. 5 Discharge characteristics for supercritical flow discharge (adapted from Weng et al., 1987b)

shown. Point F separates the sonic line into two parts which is the only point on the sonic line where waves from the two opposing corners, C and E, may intercept. Figure 4 presents the discharge characteristics for the subcritical flow where $\psi_0/R_c^2 V_\infty$ is plotted against the opening position Z_E/R_C of the valve, and the actual flow rate of discharge from the vessel is $2\pi\rho_\infty\psi_0$; ρ_∞ being the density of the fluid at the asymptotic state G where the uniform velocity is V_∞. Figure 5 presents the discharge $\psi_0/R_c^2 V^*$ under the supercritical flow condition, and the actual rate of flow from the vessel is $2\pi\rho_0\psi_0$; ρ_0 being the density of the fluid at the stagnation state. A simple sequence of tests has been carried out in the laboratory and the experimental data are also presented in Fig. 5, which agreed fairly well with the results of computations.

The present effort is directed to the application of the results of steady flow to the unsteady aspect of the problem. As long as the events in the initial transient period can be ignored, the discharge from an isolated vessel of a fixed finite volume through a valve reaches a state of quasi-steady, and the results for steady flow are readily applicable.

Experimental investigation of the unsteady flow problem has also been carried out and the data obtained in the laboratory are compared with the results of computation. Detailed consideration and discussion of this study are given in the following sections.

Analytical Considerations

For a reservoir of fixed finite volume v filled with a gas of initial pressure $P_{0,0}$ and initial temperature, $T_{0,0}$ one may differentiate the equation of state

$$P_0(t)v = m(t) RT_0(t) \tag{1}$$

to obtain

_____ Nomenclature _____

A, C, D, E, F, G, H, T = points in the flow field and the hodograph

C_0 = velocity of sound corresonding to the reservoir condition

m = mass within the reservoir

M = Mach number

P_a, P_{amb}, P_0 = ambient pressure and the pressure within the reservoir

R, Z = radial and axial coordinates

t = time

T_0 = temperature within the reservoir

V = velocity

v = volume

x = $P_0/P_{0,0}$

γ = ratio of the specific heats

τ = dimensionless time

ψ = stream function

ρ = density

θ = streamline angle

Superscript

$*$ = condition for sonic flow

Subscript

$C, E, F, G_e, G_u, 1, 2$ = refer to points in the flow field

∞ = refers to the condition along the free jet boundary

0 = refers to the condition inside the reservoir

$0, 0$ = the initial condition inside the reservoir

ref = the reference value

Fig. 6 Quasi-steady discharge characteristics through a valve

$$\frac{1}{X}\frac{dX}{dt} = \frac{1}{m}\frac{dm}{dt} + \frac{T_{0,0}}{T_0}\frac{d\frac{T_0}{T_{0,0}}}{dt} \qquad (2)$$

where

$$X = p_0/p_{0,0}$$

If isentropic expansion is stipulated for the gas remaining in the reservoir, so that

$$\frac{T_0}{T_{0,0}} = X^{\frac{\gamma-1}{\gamma}} \qquad (3)$$

Equation (2) can be reduced into

$$\frac{1}{\gamma X}\frac{dX}{dt} = \frac{1}{m}\frac{dm}{dt} \qquad (4)$$

One may now assume that at the initial time $t=0$, the valve suddenly opens to a position Z_E/R_C. At any subsequent time, the time rate of mass variation in the reservoir is given by

$$\frac{dm}{dt} = -2\pi\rho_{ref}\frac{\psi_0}{R_C^2 V_{ref}}R_C^2 V_{ref} \qquad (5)$$

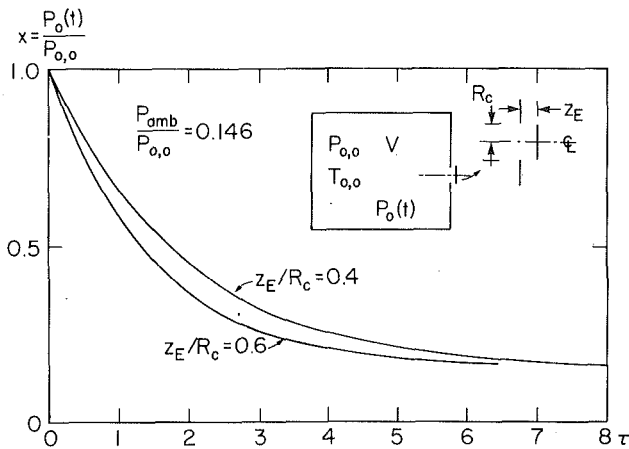according to the discharge characteristics through a valve for supercritical flow (Fig. 5, $\rho_{ref} = \rho_0$ and $V_{ref} = V^*$) or for subcritical flow (Fig. 4, $\rho_{ref} = \rho_\infty$, and $V_{ref} = V_\infty$). The factor defined by

$$f\left(\frac{P_a}{P_0}\right) = \frac{\psi_0}{R_C^2 V_{ref}} \qquad (6)$$

can be readily obtained from either Fig. 5 or Fig. 4 according to the prevailing ambient to reservoir pressure ratio $P_a/P_0(t)$. The reservoir pressure history $P_0/P_{0,0}(t)$ can then be found by integrating equation (4). The detailed working formula can be derived as follows:

For an initial high reservoir pressure $P_{0,0}$ ($P_a/P_{0,0} < (2/\gamma+1)^{\gamma/\gamma-1} = 0.528$ for $\gamma = 1.4$) so that supercritical flow discharge prevails in the initial period of the flow, equation (4) yields

$$\frac{X^{\frac{1-3\gamma}{2\gamma}}}{f}dX = -2\gamma\sqrt{\frac{2}{\gamma+1}}\frac{\pi R_C^2}{v}\sqrt{\gamma R T_{0,0}}\ dt \qquad (7)$$

Upon defining

$$\tau = \frac{\pi R_C^2}{v}\sqrt{\gamma R T_{0,0}}t = \frac{\pi R_C^2}{v}C_{0,0}\ t \qquad (8)$$
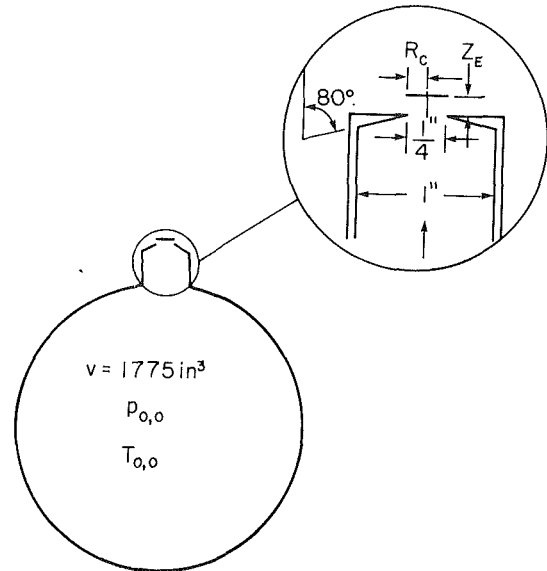
Fig. 7 Test model for quasi-steady experiments

$C_{0,0}$ being the velocity of sound corresponding to $T_{0,0}$, equation (7) can be integrated to yield

$$\int_{X=1}^{X}\frac{X^{\frac{1-3\gamma}{2\gamma}}}{f}dX = -2\gamma\left(\frac{2}{\gamma+1}\right)^{1/2\gamma} \qquad (9)$$

Equation (9) applies until X reaches the value X^* corresponding to $P_a/P_0(t) = (2/\gamma+1)^{\gamma/\gamma-1}$. Afterwards, the discharge becomes subcritical and the pressure history curve should be given by

$$\int_{X^*}^{X}\frac{X^{\frac{3(1-\gamma)}{2\gamma}}dX}{f\left[1 - \frac{P_a/P_{0,0}}{X}^{\frac{\gamma-1}{\gamma}}\right]^{1/2}} = -2\gamma\sqrt{\frac{2}{\gamma-1}}\left(\frac{P_a}{P_{0,0}}\right)^{1/\gamma}(\tau-\tau^*) \qquad (10)$$

where $f = \psi_0/R_C^2 V_\infty$ can be directly read off from Fig. 4 with linear interpolation for intermediate values if it is necessary. It is obvious from equation (10) that $\tau \to \infty$ as $X \to P_a/P_{0,0}$ as it should. A typical set of results of calculation for the case of $P_a/P_{0,0} = 0.146$ is presented in Fig. 6.

Experimental Program

In order to check the validity of the quasi-steady analysis, a series of unsteady flow experiments has been carried out in the laboratory. A spherical volume of 1775 cubic inches is mounted underneath a platform with a conical orifice of 1/4 in. diameter built-in as its outlet of discharge. The conical angle is 80 degrees (Fig. 7). A 1/4 in. diameter disk simulating the valve is externally mounted with a fixed distance from the orifice. The valve and its support are in turn covered with a hood which can be suddenly removed. A pressure pick-up is installed to track the pressure variation within the spherical volume, and its signal is fed directly into the Fluke 2280A Data Logger which prints out the pressure at constant time intervals. The temperature of the fluid is also recorded and printed.

Fig. 8 Quasi-steady discharge characteristics, $Z_E/R_C = 0.5$ (uncertainty estimate for $X = \pm 0.5$ percent)
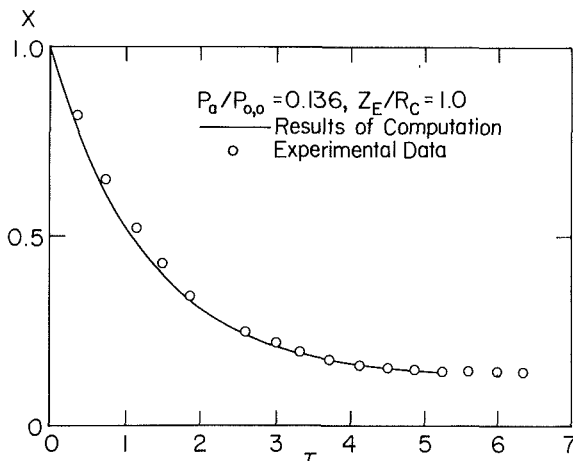
Fig. 9 Quasi-steady discharge characteristics, $Z_E/R_C = 1.0$ (uncertainty estimate for $X = \pm 0.5$ percent)

Comparisons of the Experimental Data With the Results of Computations

With the spherical volume and the system charged with air to a specific initial value $P_{0,0}$, the hood is suddenly opened and the printed records from the Data Logger present the histories of the pressure and temperature of the air within the volume. 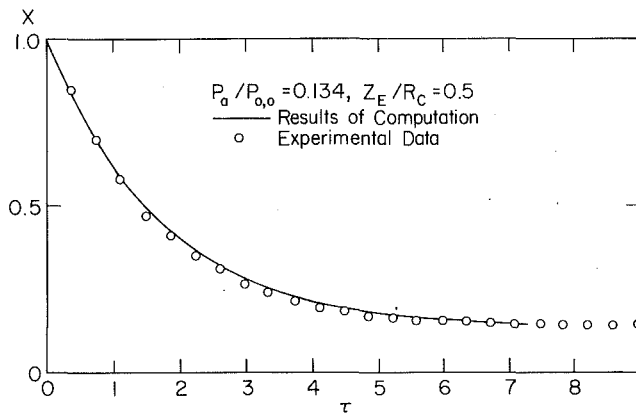Comparisons of the experimental data with the results of computations compatible with the testing conditions are presented in Figs. 8 and 9. They all show fairly good agreements. Similarly good agreements have been observed in many other cases not reported here. It should be mentioned that even though the conical flow angle approaching to the orifice is 80 deg in the test, the steady flow results for 90 deg conical approaching flow (Figs. 4 and 5) are employed for the quasi-steady analysis, since it has been found that differences between them is fairly small (see also Fig. 9 in Chow et al., 1987). Obviously, the results are not very sensitive to this slight difference in geometry. Nor is it sensitive to the finite velocity of the upstream approaching flow. Apparently an area ratio of 1/16 (see Fig. 7) is small enough that it can be essentially treated as if the velocity of the upstream approaching flow were vanishingly small. Accurate computations with all these factors taken into account are possible.

It is also strongly believed that this quasi-steady analysis may also be employed for cases of any other opening characteristics of the valve.

Conclusion

Based on this investigation, it is obvious that a quasi-steady analysis is quite adequate to describe the unsteady empty process from a reservoir. It in turn, reflects the usefulness of the technique of hodograph transformation in the establishment of the steady flow characteristics.

Acknowledgment

References

Chow, W. L., Ting, A. L., and Psai, P. H., 1987, "Discharge from a Vessel Through and Axisymmetric Control Valve," *Journal of Applied Mechanics*, Vol. 54, pp. 447–452.

Weng, Z. M., Alice, A. L., and Chow, W. L., 1987a, "Effect of Compressibility on Discharge Through a Control Valve," *Proc., of Inter-national Conference of Fluid Mechanics*, Peking University Press, Beijing, China, pp. 1095–1100.

Weng, Z. M., Ting, A. L., and Chow, W. L., 1987b, "Discharge of a Compressible Fluid Through a Control Valve," ASME *Journal of Applied Mechanics*, Vol. 54, pp. 995–960.

Interference Drag of a Turbulent Junction Vortex

F. J. Pierce

Mechanical Engineering Department,
Virginia Polytechnic Institute and State
University,
Blacksburg, VA 24061-0238,
Fellow ASME

S. K. Nath

Research Engineer
E. I. duPont,
Richmond, VA 23261

The interference drag identified with the junction of a streamlined cylindrical body and a flat plate was investigated. The junction drag was calculated from a set of detailed, self consistent, high quality data using a control volume approach. The drag for the isolated flat plate and streamlined cylinder making up the junction was calculated using boundary-layer solvers together with surface pressure measurements. For the particular and relatively thick body under consideration, the results show a significant increase in drag due to the junction. These and other available results indicate that the interference drag has a systematic dependence on the thickness to chord ratio. The junction vortex wake increases the downstream flat plate drag significantly. Because of this effect, a unique value for the drag force, drag coefficient, or induced drag coefficient for a junction vortex flow would require that the geometry be specified in detail. The induced drag and the total pressure losses identified with the junction are also reported.

Introduction

Flow in the junction or corner formed by a streamlined cylindrical body and a flat plate is of considerable interest. This type of flow is found in wing-fuselage junctions, around bridge piers in rivers, strutwall intersections, and between turbomachine blades and endwalls. The dominant feature of such a flow is a vortex system which wraps around the body, with the flow described as a junction or horseshoe vortex. The flow in such a junction is three-dimensional, complex, and separated. The mean flow measurements of Pierce and Harsh [1] show a well defined vortex structure all around the body with strong secondary flows. In the context of this paper, secondary flow is taken to mean flows in the y and z directions. Real time smoke flow visualizations show a strongly time variant flow with large changes in the scale and position of the principal vortex structure.

The drag due to such a junction has been of concern for many years because of mutual interference effects of the body and the adjacent flat plate boundary layers. Drag in a junction can be expected to differ because the flow is markedly different from the conventional boundary layer flow on each surface considered separately. Typically the interference drag in such a junction is defined as the difference between the actual drag in the junction flow, and the sum of the drags due to the flat plate and the body, considered separately. An induced drag for the junction, similar to that in wing theory, is also sometimes calculated from the kinetic energy of the secondary flow, where it is assumed that the kinetic energy of the secondary flow is solely responsible for the drag due to the junction.

Over the years, a number of investigators [2-5] have concerned themselves with the interference drag of a turbulent junction flow. Reported results vary widely, both in magnitude and even in sign. Hawthorne [2] used an inviscid small perturbation technique to analyze the flow over a body projecting from a wall. The boundary layer on the wall was modeled by assuming a nonuniform upstream velocity profile, and the drag on the body was computed from the kinetic energy of the secondary flow. Hawthorne also reported results from experiments conducted by Ling [6] on a NACA 16-006 strut (Re = 2.01×10^6/m to 2.58×10^6/m). The drag on the strut was obtained by Ling from direct force measurements for both uniform and nonuniform upstream flows. The interference drag was then estimated from the difference in drag values for the uniform and nonuniform upstream velocity profiles. The experimental results indicated a small increase in drag (about 3-4 percent) for the nonuniform upstream velocity profile. In one case, the induced drag was also computed from the kinetic energy of the secondary flow using the experimental velocity profiles, and was found to be only about 38 percent of the interference drag value obtained from the direct force measurement.

Hoerner [3] presents experimental data compiled from various sources for the interference drag for the junction of a wing with a plane wall. His results suggest that the interference drag can be negative below thickness ratios (thickness/chord) of about 8 percent. The interference drag is small for thickness ratios of about 3 percent, and is seen to increase with increasing thickness ratio.

Barber [4] presented experimental results for the flow around a strut placed on a flat plate boundary layer. Number 65 series symmetric struts were used in his experiments with Re = 5.45×10^6/m. He found that the interference drag was small if the boundary layer on the plate at the strut leading edge was thick in comparison to the chord length. For a thin boundary layer, his results indicate a significant increase in drag for the junction. He concluded that the drag depended on
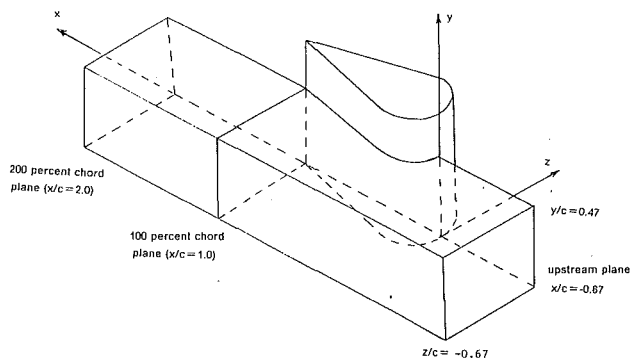
Fig. 1 The streamlined body, the coordinate system, and the measurement planes for the two control volumes

the boundary-layer thickness, with larger interference drag for a thinner boundary layer.

Kubendran et al. [5] used a 1.5:1 elliptical leading edge attached to an afterbody of constant thickness. Their experiment at $Re = 9.84 \times 10^5/m$ showed that the interference drag was small (3 percent) and negative. They also calculated the induced drag due to the secondary flow and showed that it was a small fraction (0.15 percent) of the total drag due to the junction.

It was found that considerable differences exist in the reported results for the interference drag of a turbulent junction vortex. This paper presents the losses and the interference drag for a turbulent junction vortex calculated from an extensive set of high quality data, together with boundary-layer computations for the isolated plate and cylinder. In contrast to the other experiments where wake survey techniques were used, the extensive data available in this work permitted a control volume approach to be used here to calculate the drag. The control volume approach eliminates the need for any assumptions about the upstream and surrounding flow.

Experiment

The experiments were carried out in the open-circuit, subsonic wind tunnel described in Menna and Pierce [7]. Air is drawn in the wind tunnel through a rectangular inlet 3.66 m wide and 2.44 m high. A nozzle with a 16:1 area ratio contraction designed to produce a nonaccelerating uniform flow at the exit throat follows the inlet. Following the throat, there is a straight, constant cross section channel 0.91 m wide and 0.61 m high. The body was placed at the test section located 5.0 m downstream of the inlet throat of the wind tunnel. The wind tunnel discharges into a large, temperature controlled laboratory. To insure self-consistent data, dynamic similarity for the experiments was achieved by maintaining a constant unit Reynolds number, V_*/ν, of $1.34 \times 10^6/m$ at the wind tunnel throat.

The streamlined cylindrical body, along with the coordinate system, is shown in Fig. 1. The flat sides of the cylinder terminate in a sharp trailing edge and are tangent to the circular leading edge of the body. The cylinder has a leading edge diameter of 127 mm, a chord length of 298 mm, and a height of 229 mm. The Reynolds number of the flow was 183,000 based on the body thickness, and 430,000 based on the body chord.

The two separate control volumes shown in Fig. 1. were used for the results presented here. Control volume I, CVI, extends only up to the 100 percent chord plane ($x/c = 1.0$) and control volume II, CVII, extends to the 200 percent chord plane ($x/c = 2.0$). Both the side (x,y) plane at $z/c = 0.67$ and the top (x,z) plane at $y/c = 0.47$ showed only small effects due to the body, but with nonzero momentum flux quantities. The upstream (y,z) plane at $x/c = -0.67$ showed small but clear effects of the body, with yaw and pitch angles in the approach flow of up to 3.5 and 1.5 degrees, respectively. The approach boundary layer was approximately 90 mm thick with a momentum thickness Reynolds number of 12,500. The upstream symmetry plane ($x/c < 0$, $z/c = 0$) showed negligible yaw in several initial profiles at different locations and a zero yaw was subsequently assumed for this plane. Flow across the downstream symmetry ($x/c > 1$, $z/c = 0$) was measured, with occasional yaw angles up to 5 degrees in the near wake of the body.

Distributions of the three components of velocity, total pressure, and static pressure were measured on all the surfaces bounding the control volumes, except the solid surfaces, using a five-hole biconic Prandtl type pressure probe. A computer controlled data acquisition system was used to acquire and store the data. Surface pressure distributions were measured on the body and the floor. Surface flow visualizations were made on the floor and the body. A more thorough discussion of the procedures, techniques, details of the data acquisition process, and the calibration of the five-hole probe can be found in Pierce and Harsh [1] or Pierce et al. [8]. Complete results, together with statistically meaningful uncertainties for each of the extensive tabulated data values, can be found in Pierce et al. [8], and Pierce et al. [9].

The various calculations for CVI were based on about 3200 sets of averaged measurements of velocity, static pressure, or total pressure from 84 profiles with 36 sets of averaged measurements per profile, plus 164 sets of averaged measurements for the top of the region. Profiles used nonuniform spacing with more data taken where large gradients occurred. CVII used about 5400 sets of averaged measurements from 140 profiles with 36 sets of averaged measurements per profile, plus about 314 sets of averaged measurements for the top of this larger region. Profiles of data were taken at variable intervals of 6.4 mm to 25.4 mm along the x and z axes, with smaller spacings used closer to the body and where larger gradients were encountered. Representative results are shown in graphical form in Figs. 2 through 5.

Figure 2 shows the x or u component of the velocity at the 200 percent chord transverse plane. All velocities have been nondimensionalized by the tunnel nozzle throat velocity. With

---

Nomenclature

|							
A	=	Area	D_J	=	drag due to junction	Re	= Reynolds number
c	=	chord length	D_I	=	interference drag	t	= body thickness
C_{DI}	=	interference drag coefficient	I	=	induced drag	V_*	= freestream velocity at the throat
			F	=	force		
C_{pT}	=	total pressure coefficient	P_T, P_S	=	total and static pressures	u,v,w	= components of velocity
D_B	=	drag due to the body alone	P_T^*	=	total pressure at the throat	V_n	= normal velocity
CVI	=	control volume I	Q	=	dynamic pressure in the	δ	= boundary layer thickness
CVII	=	control volume II			free stream	δ^*	= displacement thickness
D_{FP}	=	drag due to the flat plate alone	Q_*	=	dynamic pressure at the throat	ΔP	= loss in power
						ρ	= density of air
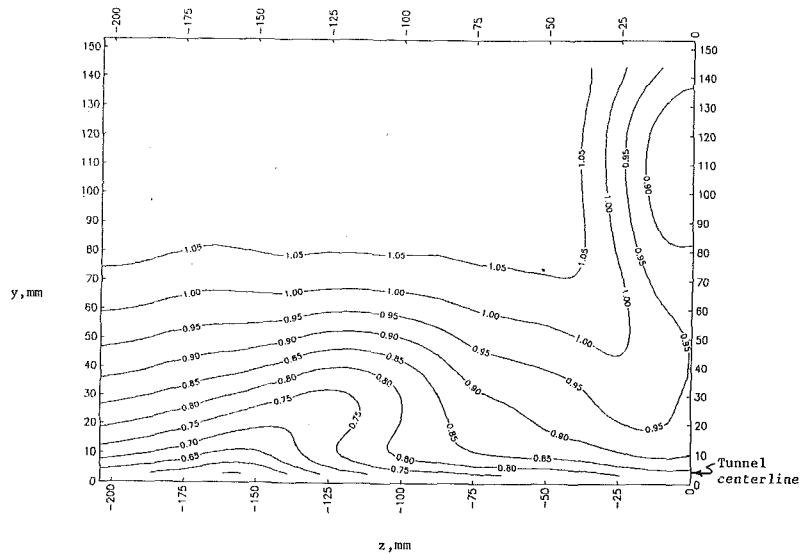
Fig. 2 The u component velocity distribution in the 200 percent chord transverse plane. Maximum uncertainty in u/V^* is ± 0.007.

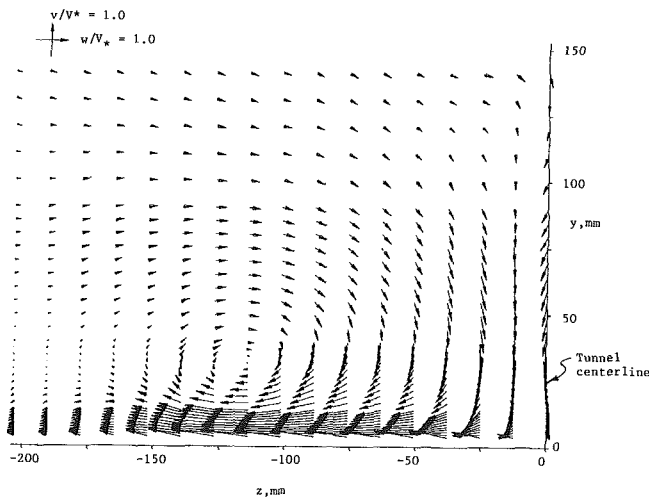Fig. 3 The secondary velocity distribution in the 200 percent chord transverse plane. Maximum uncertainty in v/V^* or w/V^* is ± 0.007.

some small acceleration in the tunnel due to side wall boundary layer growth, nondimensionalized freestream velocities near the test section are slightly larger than one. A boundary layer like velocity profile is seen on the floor, away from the body and the principal junction vortex. The entrainment of freestream flow into the vortex structure is clearly seen. The boundary layer off the side of the body is seen in the wake structure along the right edge of the figure. Figure 3 shows the secondary velocity field at this same plane. This figure also shows the distribution of measurement points for this plane. One vortex structure is seen clearly, and this is referred to as the principal vortex. Vorticity calculations show the strength of the principal vortex decreases significantly as the flow develops around the body. Evidence of the yaw present on the downstream symmetry plane of the tunnel is seen in the wake flow off the body trailing edge. Figure 4 shows the static pressure distribution, as a static pressure coefficient, on this same plane. The static pressure is seen to be essentially constant across the plane. Figure 5 shows the total pressure distribution, again as a total pressure coefficient, on this plane. This figure is very similar to the distribution of the u component of the velocity. This is to be expected since the streamwise or x component of the velocity dominates the flow, and since the static pressure is essentially constant in this

plane, the total pressure variations are dictated by the velocity field. The boundary layer like flow on the floor away from the vortex and body, the entrainment of the freestream flow into the vortex structure, and the wake from the boundary layer off the side of the body are all clearly seen. The two transverse (yz) planes at the 100 and 200 percent chord positions show similar behavior, with a single, large, well-defined vortex and strong secondary flows. Results for the 100 percent transverse plane are shown in Pierce and Harsh [1]. The upstream transverse plane is more boundary layer-like, with small amounts of secondary flow characterized by maximum yaw and pitch angles of 3.5 and 1.5 degrees, respectively. The flow in the side and the top surfaces bounding the control volumes is well behaved, with only small mass flows found across these planes.

A rigorous statistical analysis of the uncertainties in the experimental data was made, with details in Pierce and Harsh [1] or Pierce, et al. [8]. Typical uncertainties in the nondimensionalized velocity components ranged from ± 0.001 to ± 0.0007. The total pressure and the static pressure coefficients had typical uncertainties of ± 0.01 and ± 0.02, respectively. One measure of the quality of the data is given by the mass balance for the control volumes. For CVI the mass balance was within one percent, and was of the order of five percent for the CVII. These values include the effects of the approximations in the numerical integration process. For quantities computed by a control volume analysis, the estimated uncertainties for CVI and CVII were estimated at 3 and 8 percent, respectively. For quantities computed over any single transverse plane of measurements, the uncertainties were estimated to be less than 3 percent.

Analysis and Results

Induced Drag. The induced drag is identified with the mean secondary flow kinetic energy, and was calculated from the measured velocity data as

$$I = Q_* \int \frac{v^2 + w^2}{V_*^2} dA$$

Values of this induced drag were calculated for the three transverse planes and results are given in Table 1. There is very little secondary flow in the uptsream plane, hence the small value of the induced drag there. The induced drag increased substantially in the 100 percent chord plane, and decreased between the 100 percent and the 200 percent chord planes, in-

Journal of Fluids Engineering
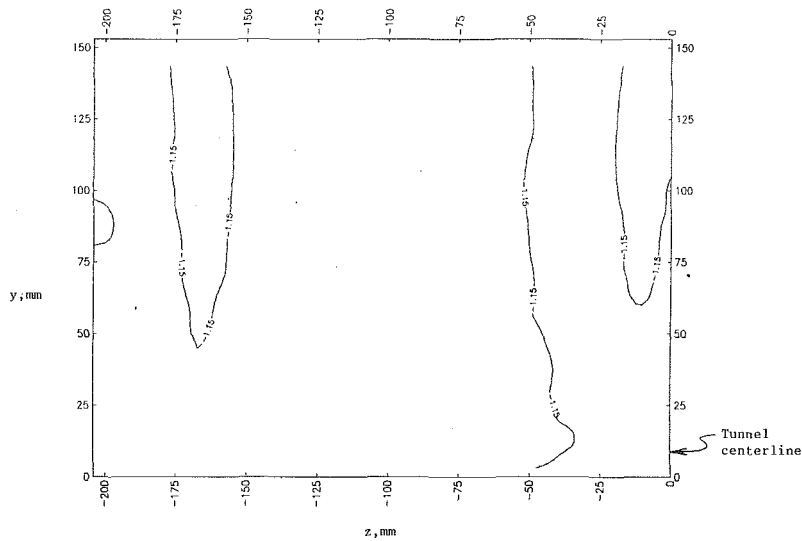
Fig. 4 The static pressure distribution in the 200 percent chord transverse plane. Typical uncertainty in the pressure coefficient is ± 0.02.
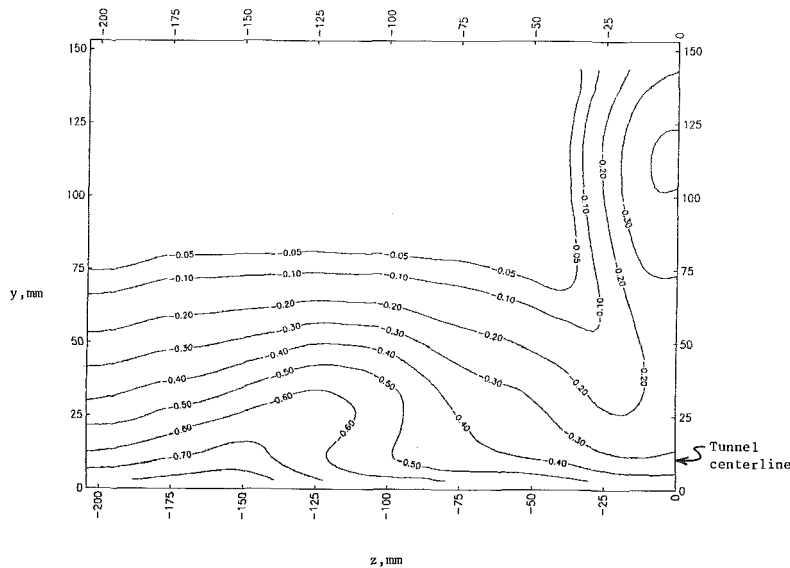
Fig. 5 The total pressure distribution in the 200 percent chord transverse plane. Typical uncertainty in the pressure coefficient is ± 0.01.

Table 1 Properties at transverse planes

	Upstream plane	100 percent Chord	200 percent Chord
Induced drag, I (N)	0.006	0.067	0.015
Mass averaged total pressure coefficient, $\bar{C}_{pT}$	0.121	0.156	0.181
Pressure force (N)	2.655	2.656	2.654

dicating that much of the secondary flow energy is dissipated in this near wake region. The utility of induced drag values for a junction vortex flow is questioned by these results, which show a decrease in induced drag from the 100 to 200 percent transverse planes, while the junction drag, reported below, increases as the control volume is extended downstream. For both control volumes, the calculated induced drag was significantly less than the junction drag. Similar underpredictions were also reported by Hawthorne [2] and Kubendran et al. [5].

Total Pressure Loss. The total pressure data from the five-hole probe measurements was expressed as a total pressure coefficient, which can be interpreted as a total pressure loss coefficient

$$C_{pT} = \frac{p_T - p_T^*}{Q_*}$$

where the conditions at the throat of the wind tunnel were used as reference quantities. Since the transverse planes surveyed were relatively large and included the dominant effects of the vortex system, mass averaged total pressure coefficients were evaluated to gain some indication of the distribution of the total pressure losses for the junction flow. The

Table 2 Results of the control volume analysis

	Control volume I	Control volume II
Power loss, ΔP (watts)	6.06	9.63
Junction drag, D_J (N)	0.666	0.806
Flat plate drag, D_{FP} (N)	0.077	0.129
Body drag, D_B (N)	0.043	0.043
Interference drag, I (N)	0.546	0.634

mass averaged total pressure coefficient was computed from

$$\bar{C}_{pT}^{\cdot} = \frac{\int C_{pT}\rho V_n dA}{\int \rho V_n dA}$$

and results for the three transverse planes are given in Table 1. The mass averaged total pressure coefficient increases continuously from the upstream plane to the 200 percent chord plane. Note that an increase in total pressure coefficient indicates a loss in the fluid total pressure. The increase in this coefficient from the 100 percent to the 200 percent chord plane indicates that in addition to the losses in the corner flow along the streamlined body, an additional loss also takes place in the near wake region.

For the incompressible flow case, the time rate of loss of mechanical energy, or the mechanical power loss, was also computed for the control volume with

$$\Delta P = \int V_n C_{pT} Q_* dA = \int \rho V_n [p_s/\rho + 1/2(u^2 + v^2 + w^2) - p_T^*/\rho]dA$$

where the integration was carried out over all the surfaces bounding the control volumes. Table 2 gives the losses in mechanical power for the control volumes. These values also show the additional loss in the near wake region, relative to the loss in the corner region itself, and are consistent with the behavior in the mass average total pressure coefficient.

Junction Drag. The drag due to the junction was calculated from the velocity and pressure data using a momentum balance for the control volumes shown in Fig. 1. Writing the momentum equation in the x direction for a control volume, one has

$$\Sigma F_X = \int_A \rho u_X \bar{u} \cdot d\bar{A}$$

For the control volumes shown in Fig. 1, one has

$$D_J + F_I - F_e = \int \rho u_X \bar{u} \cdot d\bar{A}$$

where D_J is the drag due to the junction, F_I is the pressure force on the inlet plane, and F_e is the pressure force on the exit plane. Note that there may be a flux of momentum over all the planes of the control volumes, except for the solid surfaces, and momentum fluxes were found for the top and the side surfaces.

The pressure forces computed from the measured data over the appropriate planes are shown in Table 1. Since the pressure forces were essentially equal for the transverse planes, the net pressure forces on both control volumes were taken to be zero.

The drag due to the junction for the two control volumes is given in Table 2. Note that the total drag of the junction is twice the drag value for the control volume, since the control volume included only one half of the body-floor junction.

Drag Due to the Isolated Flat Plane and Body. The drag for the boundary layer on the flat plate, representing the bottom of the control volumes and considered alone, was computed by a strip integral method due to Moses [10]. The initial conditions necessary for the program were taken from earlier experiments on the undisturbed two-dimensional boundary layer in the same wind tunnel.

The drag on the body alone was considered in two parts, pressure drag from pressure forces integrated over the surface, and viscous drag due to shear forces integrated over the surface.

The pressure drag for the body was computed from the measured surface pressure distribution on the vertical side of the body. The pressure distribution was measured with 0.51 mm diameter pressure taps distributed over the body surface, using a Datametrics model 5900 digital micromanometer. The measured pressure distribution over the finite cylindrical surface was in very good agreement with a two-dimensional potential flow solution for the body as reported in Pierce and Harsh [1]. Relatively small departures from the potential distribution were found, even near the body-floor corner. Integration of the experimental pressure distribution gave a near zero pressure drag value, as would be the case for a potential flow pressure distribution.

The viscous drag due to the boundary layer on the body was also computed numerically. A two-dimensional boundary layer analysis was performed for the idealized boundary-layer flow over the sides of the body. The Pohlhausen laminar, one parameter integral method and Moses turbulent two-parameter integral method [8] were used. The freestream edge condition for these calculations was the surface pressure distribution resulting from a two-dimensional potential flow solution for the body. Based on cylinder surface flow visualizations, transition was assumed to occur at 85 degrees from the stagnation line. The calculation was continued from this point using the turbulent integral method. The initial conditions required by the turbulent integral calculation were obtained by equating the laminar momentum thickness to the turbulent momentum thickness at the point of transition, and arbitrarily increasing the skin friction coefficient by a factor of two. This later assumption had little effect on the turbulent boundary-layer calculations after a few millimeters downstream of the transition point, as revealed by a systematic variation of the initial value of the skin friction coefficient. The viscous drag for the body was computed from the skin friction coefficients resulting from the boundary layer solution.

Interference Drag. The interference drag was defined as the difference between the drag due to the junction, and the sum of the drags of the flat plate and the body, taken in isolation. The interference drag was computed from

$$D_I = D_J - (D_{FP} + D_B)$$

The computed values of the interference drag for the two control volumes are given in Table 2. The interference drag (and interference drag coefficient) increased by 16 percent for CVII relative to CVI. The ratio of the interference drag to the drag of the isolated plate floor and body is 4.55 for CVI and 3.67 for CVII.

It is noted that the increase in the junction drag for CVII compared to CVI is almost three times larger than the drag identified with the added length of isolated flat plate. This is attributed to the effects of the junction propagated downstream into the wake region on the endwall. This result makes the specification of an interference drag coefficient (or drag coefficient) dependent on a complete specification of the end wall or flat plate geometry.

Contrast the case of a body set on an endwall which terminates at the body trailing edge, with the same body set on an endwall which extends for some distance downstream of the trailing edge of the body. As seen from the results for CVI and CVII, the effects of the wake of the junction propagating into the downstream endwall boundary layer are significant. The specification of any interference drag coefficient (or the corner drag coefficient) would require a complete specification of the physical junction, particularly the details on the endwall following the junction.

All earlier studies reviewed included details of the upstream endwall, usually to provide information about the approach boundary layer, but little detail is typically reported about the

Table 3 Summary of interference drag coefficients

	t/c	δ/c	C_{DI}
Present case			
Control volume I	42.6%	27.4%	0.21
Control volume II	42.6%	27.4%	0.25
Hawthorne [2]	20%	39.7%[a]	0.054
Hoerner [3]	40%	10%	0.3
Barber [4]	20%	12%	0.11
Kubendran [5]	4.75%	3.1%	−0.016

[a]The value of δ/c was calculated by assuming $\delta/\delta^* = 8$ for a typical boundary layer.

endwall behind the body. Hoerner [3], Barber [4], and Kubendran et al. [5] all show an unspecified length of endwall which appears to extend beyond the body of their junctions. As a result, the comparison made in Table 3 must be viewed with some caution. Nonetheless, based on the differences found between CVI and CVII, the differences seen in the table are generally larger than would likely be attributable only to wake effects on the trailing endwall sections.

Table 3 summarizes and compares the present values of the interference drag and other values reported in the literature for this type of junction flow. The interference drag C_D was calculated based on the thickness area and was defined as

$$C_{D_I} = D_I/Qt^2$$

In the case of Hawthorne, only one representative value from his table was chosen.

From the limited number of interference drag coefficient values available for this type of junction flow, it appears that a proper value of the interference drag is still an open question. The reported results varied widely, although a few observations can be made. The boundary-layer thickness to chord ratio does not seem to have a conclusive effect. This is seen from the widely varying interference drag values for δ/c of the same order, as in the cases of the present result vs Hawthorne and Hoerner vs Barber. The effect of the thickness to chord ratio tends to be more pronounced and systematic. For very small values of t/c, the interference drag given by Kubendran was found to be negative. This supports Hoerner's conjecture that for $t/c < 0.08$, the interference drag can be negative. It also appears that for t/c ratios of less than 0.2, the interference drag is small. For higher t/c ratios, around 0.4, the interference drag appears to be substantially larger.

Conclusions

The interference drag due to the junction of a streamlined cylindrical body and a flat plate obtained from a detailed set of experimental data was reported using a control volume approach for the junction drag calculations. For the body under consideration, a significant increase in drag due to the junction flow was found. From a review of these and earlier published results, it appears that the interference drag is dependent on the body thickness to chord ratio. For thickness to chord ratios up to 0.2, the interference drag appeared to be small, whereas it can be substantially larger for higher body thickness to chord ratios.

The effect of the junction flow on the endwall boundary layer in the wake of the body was clearly seen. As a result, the specification of a junction drag coefficient or an interference drag coefficient requires a complete specification of the geometry, including details of any endwall section following the intersection.

The secondary kinetic energy of the mean flow was found to be a maximum in the trailing edge transverse plane, and dissipated to a large extent at one chord length downstream from the trailing edge. Total pressure losses were seen to increase throughout. Significant losses were found downstream of the trailing edge.

References

1 Pierce, F. J., and Harsh, M. D., "The Mean Flow Structure Around and Within a Turbulent Junction Vortex—Part II. The Separated and Junction Vortex Flow," ASME JOURNAL OF FLUIDS ENGINEERING, Vol. 110, Dec. 1988, pp. 415–423.

2 Hawthorne, W. R., "The Secondary Flow About Struts and Airfoils," Journal of Aeronautical Sciences, Vol. 21, No. 9, Sept. 1954, pp. 588–708.

3 Hoerner, S. F., Fluid Dynamic Drag, Hoerner Fluid Dynamics, Bricktown, NJ, 1965.

4 Barber, T. J., "An Investigation of Strut Wall Intersection Losses," AIAA Journal, Vol. 15, No. 10, Oct. 1978, pp. 676–681.

5 Kubendran, L. R., McMahon, H., and Hubbert, J., "Interference Drag in a Simulated Wing-Fuselage Juncture," NASA Cr-3811, 1984.

6 Ling, A. T., "Study of Secondary Flow Effects on Single Symmetrical Airfoils," M.S. thesis, Massachusetts Institute of Technology, 1952.

7 Menna, J. D., and Pierce, F. J., "The Mean Flow Structure Around and Within a Turbulent Junction Vortex—Part I. The Upstream and Surrounding Three-Dimensional Boundary Layer," ASME JOURNAL OF FLUIDS ENGINEERING, Vol. 110, Dec. 1988, pp. 406–414.

8 Pierce, F. J., Kim, C. M., and Harsh, M. D., "The Mean Flow Structure of a Turbulent Junction Vortex," Rept. VPI-E-87-6, Mechanical Engineering, Virginia Polytechnic Institute and State University, Blacksburg, VA, Apr. 1987 (available from NTIS).

9 Pierce, F. J., Kim, C. M., Nath, S., and Shin, J., "The Mean Flow Structure in the Near Wake of a Turbulent Junction Vortex," Rept. VPI-E-87-26, Mechanical Engineering, Virginia Polytechnic Institute and State University, Blacksburg, VA, Dec. 1987 (available from NTIS).

10 Moses, H. L., "A Strip Integral Method for Predicting the Behavior of Turbulent Boundary Layers," Computation of Turbulent Boundary Layers–1986, AFOSR–Stanford Conference, Vol. 1, Thermosciences Division, Dept. of Mechanical Engineering, Stanford University, 1986, pp. 76–82.

Prediction of Airflow With Swirl in Perforated Polyethylene Tubes

E. Brundrett
Department of Mechanical Engineering,
University of Waterloo,
Waterloo, Ontario, Canada N2L 3G1

The influence upon flow of fan induced inlet swirl is examined for two commonly used sizes of uniformly perforated polyethylene ventilation tubes (polytubes). Swirl is present at the inlet of most polytubes that are directly connected to a supply fan whether or not an antiswirl device is used. Four experimentally obtained inlet swirl angles are examined using swirl modified pressure recovery coefficients, pipe friction factors, and orifice discharge equations. A computational procedure divides the polytube into five equal length segments to obtain a rapid yet acceptably accurate procedure. An iterative microcomputer spreadsheet solves the resulting set of simultaneous equations, providing pressure and flow discharge profiles along the tube that are in very good agreement with the experimental data and with the data of others. An extension of the analysis for uniformly spaced orifices indicates that supply swirl angles greater than 25 deg and large length to diameter ratios should be avoided.

Introduction

Thin walled polytubes have been employed for greenhouse and industrial building ventilation for several decades, and recently have been used to distribute solar heated air in several automotive factories. They may be characterized as thin walled perforated pipes that have total wall orifice areas that are usually one to two times the cross-sectional area of the tube. Typically, the ratio of polytube length to diameter is 30 to 100, with tube diameters of 450 mm to 610 mm being common in North America. The tube orifices are punched out of the polytube wall in matching pairs at 0.5 m to 1 m spacings and are typically 50 mm to 70 mm in diameter. The wall thickness of the tube is deliberately kept as thin as possible (0.05 mm to 0.15 mm) to reduce loss of light transmission in overhead greenhouse applications, and to minimize the cost of fabrication. Hence, Bailey (1975a) has recommended a minimum internal static pressure of 20 Pa to ensure wrinkle free inflation, smooth pipe friction losses, and greater uniformity of orifice discharge along the polytube.

Early investigations of flow from orifices in perforated pipes were based on limited assumptions regarding friction loss, pressure regain, and orifice discharge coefficients. Keller (1949) examined uniformly perforated pipes of relatively short length. He calculated the outflow from orifices and longitudinal slots of short pipes with reasonable results by assuming that both the static regain coefficient and friction factor were constant. Dow (1950) extended his investigation to include Reynolds dependent friction losses for both laminar and turbulent flow. He reported good experimental agreement with his predictions, but only investigated short lengths of pipe. Howland (1953) included a flow dependent orifice discharge coefficient in his

analysis but assumed a static regain coefficient of unity and calculated pressure loss from the friction factor obtained from the inlet Reynolds number. He obtained good agreement between analysis and experiment, probably because the ratio of stagnation to static pressure was small along the duct. Haerter (1963) recognized that the static regain coefficient could vary along the length of the pipe, but retained a constant value for his short duct studies.

The most complete study was conducted by Bailey (1975b) who examined in detail the properties of flow from a single orifice installed in a thin walled pipe. He obtained correlations for the orifice discharge coefficient based on the static pressure of the pipe that exhibited a strong dependency upon the ratio of pipe static pressure to pipe dynamic pressure. A similar dependency was observed for the angle of discharge of flow from the orifice. Finally, he obtained the static regain coefficient as a function of the ratio of the upstream duct velocity to the duct velocity reduction due to orifice discharge, further modified by the ratio of orifice to duct diameters. The correlation required the calculation of static regain at each orifice for polytube pressure profile predictions. Bailey included Reynolds number dependency in his calculation of friction loss, and obtained good agreement between the predicted and experimental polytube pressure and orifice flow profiles for one polytube. The standard deviation of the analytical to experimental pressure profile would appear to be ±2.6 percent (as obtained from the graphical data of his paper). The standard deviation of the analytical to experimental orifice flow profiles would appear to be ±3.2 percent (again, as obtained from the graphical data of his paper). The prediction technique although lengthy, did provide good results via a computer based iterative solution procedure. His work did not include the effect of inlet flow swirl.

A later paper by Saunders and Albright (1984) analytically

and experimentally examined discharge from twelve polytubes. The analyses included a friction factor based on a galvanized steel pipe with 40 slip joints per 100 ft (30.5 m) even though Bailey (1975a,b) had shown that polytubes exhibited smooth pipe behavior. The orifice discharge coefficient was based on the polytube static pressure and was increased from an initial value of 0.64 to a range of 0.720–0.786 to obtain better agreement with the experimental data. No correlation was provided to explain the adjustment of the discharge coefficient. Also, the pressure profiles along the duct required adjustment by means of a statistically derived parameter based on the total upstream pressure of the flow and the ratio of orifice to tube diameters. The investigation did not include any reported inlet swirl studies, nor did it specify in detail the analytical solution procedure. The standard deviation of the predicted pressure profiles was reported as ±12.4 percent and the standard deviation of the orifice discharge profiles was reported as ±5.3 percent with a reported average error of prediction of −5.1 percent.

An apparently less complicated correlation of flow from wall orifices was obtained by Dittrich and Graves (1956) in a much earlier study of gas turbine combustor liners by using the ratio of the static pressure drop across the orifice to the total upstream pressure of the gas. A more recent study by Rogers and Hersh (1976) also utilized the total upstream pressure of the flow to calculate discharge from thick walled orifices.

Their procedure computed the upstream angle of approach and cross-sectional area of the orifice discharge streamtube. They compared their method to the calculation of an imaginary flow scoop or "LID" placed in the flow above the orifice with the scoop angle defined by the approach angle of the streamtube, that is, by the upstream ratio of wall normal to tangential velocities of the streamtube. The procedure was iterative but appeared to require fewer empirical correlations than the conventional method using static pressure drop across the orifice and flow dependent empirical discharge coefficients. Unfortunately, their results are not directly applicable to polytube analysis since thick wall orifices were investigated for very low orifice to upstream velocity ratios.

Finally, swirl flow in polytubes was recently examined and reported by Brundrett and Vermes (1987) for two typical sizes of tube and four inlet swirl conditions. They were able to correlate the increased friction loss of the swirling flows by

calculating the increased path length of the flow and by using a Reynolds dependent friction correlation that was 6 percent lower than the smooth pipe correlation of Haaland (1983). Also, they observed that the inlet swirl of the flow reduced nearly linearly from polytube inlet to end for uniformly spaced orifices. However, no flow prediction procedure was provided.

Analysis of Swirl Flow in Polytubes

Airflow with swirl in a perforated polytube is subdivided into five equal length segments in this analysis. The choice of five segments evolved from a desire to reduce the computational labor of the orifice by orifice procedures of earlier studies. Computations based on three segments were examined and rejected because the downstream predictions were inaccurate. By a process of trial and error, five segments were found to provide good agreement with the experimental data of Brundrett and Vermes (1987). Additional segments provided only a marginal improvement in accuracy and considerably increased the time required for a solution.

The flow entering the first polytube segment is the supply flow, but in general the inflow of a segment is designated as Q_{in}. The discharge of all the orifices of the segment (Q_{or}) is assumed to occur at the mid point of the segment (Fig. 1), and from continuity the outflow of the segment (Q_{out}) is,

$$Q_{out} = Q_{in} - Q_{or} \qquad (1)$$

The average velocity of the segment is obtained from equation (1) and the polytube cross sectional area as,

$$V_{ave} = \frac{Q_{in} + Q_{out}}{2A_{tube}} = \frac{V_{in} + V_{out}}{2} \qquad (2)$$

However, note that the average velocity squared of the segment $(V)^2_{ave}$ is defined by,

$$(V)^2_{ave} = \frac{V^2_{in} + V^2_{out}}{2} \qquad (3)$$

The pressure change from the inlet value (P_{in}) to the outlet value (P_{out}) is due in part to static pressure regain as fluid is discharged and the flow in the polytube decreases, permitting recovery of some of the kinetic energy of the flow, and is expressed as,

——————— Nomenclature ———————

A_{or} = total orifice area of a segment, equation (17), m^2
A_{st} = discharge streamtube area, equation (17), m^2
C_r = static regain coefficient, equation (23)
C_α = streamtube area coefficient, equations (17), (24)
d = individual orifice diameter, mm
D = polytube diameter, mm
f = friction coefficient, equation (5)
L = total length of polytube, m
L_{swirl} = path length of flow in a segment, m
P = static pressure, Pa
P_{total} = total pressure, equation (15), Pa
ΔP_f = friction pressure loss, equation (6), Pa

ΔP_r = static pressure regain, equation (4), Pa
Q = flow, m^3/s
ΔQ_{error} = percent closure error of computed flow, equation (12), m^3/s
R_D = Reynolds number based on V_{ave} and D
V = average velocity obtained at any cross section, m/s
V_{ave} = average velocity of a segment, equation (2), m/s
$(V)^2_{ave}$ = segment averaged velocity squared, equation (3)
V_{perp} = perpendicular component of discharge velocity, equation (19)
V_{tave} = total velocity at mid point of segment, Fig. 1, equation (14)
X_{mid} = distance from tube inlet to

segment mid position, m, Fig. 1
α = discharge streamtube angle to orifice, Fig. 1
ρ = fluid density, kg/m^3
ϕ = swirl angle of the flow, Fig. 1
Φ = static regain coefficient of Bailey (1975b), equation (21)

Subscripts

ave = averaged property
in = property at segment inlet
or = property at orifice
out = property at segment outlet
seg = property at segment mid point
supply = property of the supplied fluid
swirl = property related to the swirl of the flow

$$\Delta P_r = C_r \rho \left(\frac{V_{\text{in}}^2 - V_{\text{out}}^2}{2} \right) \tag{4}$$

where, C_r the empirically obtained coefficient of static regain is examined in detail below.

The friction factor (f) in swirling polytube flow recommended by Brundrett and Vermes (1987) is used in this analysis,

$$(f)^{-0.5} = 1.86 \log \left(\frac{R_D}{6.9} \right) \tag{5}$$

The Reynolds number of the tube segment (R_D) is defined using the average velocity of the segment (V_{ave}) and hence, the friction loss of the segment is,

$$\Delta P_f = f \left(\frac{L_{\text{swirl}}}{D} \right) \left(\frac{\rho (V)_{\text{ave}}^2}{2} \right) \tag{6}$$

Now,

$$L_{\text{swirl}} = \frac{L_{\text{seg}}}{\cos(\phi_{\text{seg}})} \tag{7}$$

is the actual path length of the fluid at the wall in the tube segment (L_{seg}) defined by the average swirl angle for the segment (Fig. 1). A linear reduction of the supply swirl angle (ϕ_{supply}) from tube inlet to end as recommended by Brundrett and Vermes (1987) is adopted. Then, ϕ_{seg} is defined by,

$$\phi_{\text{seg}} = \left(1 - \frac{X_{\text{mid}}}{L} \right) \phi_{\text{supply}} \tag{8}$$

Combining the static pressure regain and friction loss effects, the static pressure at the end of the segment is,

$$P_{\text{out}} = P_{\text{in}} + \Delta P_r - \Delta P_f \tag{9}$$

and, the average pressure for the segment is,

$$P_{\text{ave}} = \frac{P_{\text{in}} + P_{\text{out}}}{2} \tag{10}$$

As mentioned, the inlet values of pressure, flow and swirl angle for the first segment are the supply values provided by the attached fan or plenum. The computed outlet values Q_{out} and P_{out} are the inlet values for the next segment of the polytube. The process is repeated until the outlet values of the fifth segment (the tube end) are computed. No outflow can occur from the end of a sealed polytube. Hence, the computed outflow of the fifth segment must be zero or else the supply pressure or supply flow must be adjusted until the computed outflow is zero, i.e.,

$$Q5_{\text{out}} = Q_{\text{supply}} - Q1_{\text{or}} - Q2_{\text{or}} - Q3_{\text{or}} - Q4_{\text{or}} - Q5_{\text{or}} = 0 \tag{11}$$

Since $Q5_{\text{out}}$ will be zero for the correct combination of supply pressure and flow, the percentage error of closure of the chosen inlet pressure and flow can be expressed as,

$$\Delta Q_{\text{error}} = \left(\frac{Q5_{\text{out}}}{Q_{\text{supply}}} \right) \times 100 \tag{12}$$

Next, the vectorial total velocity (V_{tave}) in the polytube at the mid point of the segment will consist of the longitudinal or x direction component as defined by the continuity equation and a cross flow component due to the swirl of the flow. The resulting velocity vector has no radial velocity component (Fig. 1) and is defined by the segment averaged swirl angle as,
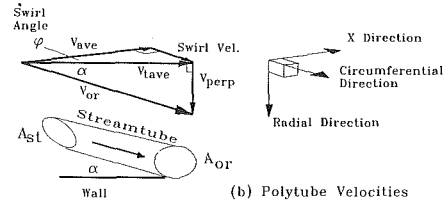
$$V_{\text{tave}} = \frac{V_{\text{ave}}}{\cos(\phi_{\text{seg}})} \tag{13}$$

and,

$$(V)_{\text{tave}}^2 = \frac{(V)_{\text{ave}}^2}{\cos^2(\phi_{\text{seg}})} \tag{14}$$
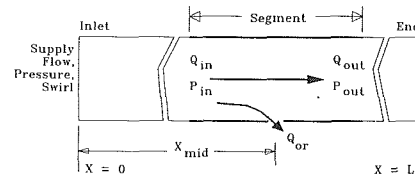
Fig. 1 Geometrical parameters for the analysis of swirling flow in polytubes, (a) polytube dimensions and parameters, (b) polytube velocities V_{ave}, V_{tave}, and V_{or}

Now, the total pressure of the swirling polytube flow at the mid point (P_{total}) will be identical to that of fluid being discharged through the orifice except for the small orifice pressure loss, i.e.,

$$P_{\text{total}} = P_{\text{ave}} + \frac{\rho (V)_{\text{tave}}^2}{2} \approx P_{\text{or}} + \frac{\rho V_{\text{or}}^2}{2} \tag{15}$$

For thin walled orifices the orifice gauge pressure should be very close to the room value, and hence nearly zero. This assumption was not valid for the study of Rogers and Hersh (1976), who discovered that the orifice wall pressure varied around the orifice lip by as much as ±50 percent of the dynamic pressure of the duct velocity. However, the wall thickness of their orifices was greater than the orifice diameter, whereas the orifice diameter of polytubes is at least 400 times the wall thickness.

Hence, assuming that $P_{\text{or}} = 0$,

$$V_{\text{or}} \approx \left(\frac{2P_{\text{ave}}}{\rho} + (V)_{\text{tave}}^2 \right)^{0.5} \tag{16}$$

Now, $V_{\text{or}} > V_{\text{tave}}$ due to the conversion of the static pressure of the polytube segment to velocity pressure. Also, V_{or} has a radial velocity component to permit outflow through the wall orifices. The radial velocity component V_{perp} must be obtained by computation such that it satisfies the continuity equation for orifice flow when combined with the true or wall perpendicular orifice area (A_{or}). The radial velocity component will create an angle of approach α of the streamtube to the wall when added vectorially to V_{tave} to obtain V_{or} (Fig. 1).

Now, the discharge streamtube area (A_{st}) for V_{or} is related to the wall perpendicular orifice area by the approach angle α as,

$$A_{\text{st}} \approx \sin(\alpha) A_{\text{or}} = C_\alpha \sin(\alpha) A_{\text{or}} \tag{17}$$

Where A_{or} is the total area of the orifices of the segment located for this analysis at the mid point of the segment (Fig. 1); and C_α is an empirically determined streamtube area coefficient that will be examined below.

Now, the orifice discharge (Q_{or}) of the segment can be expressed as,

$$Q_{\text{or}} = A_{\text{st}} V_{\text{or}} \tag{18}$$

and the component of orifice velocity that is perpendicular to the polytube wall is (Fig. 1),

$$V_{\text{perp}} = \frac{Q_{\text{or}}}{A_{\text{or}}} \tag{19}$$

We now complete the cycle by defining α in terms of V_{perp} and V_{tave} (Fig. 1) as described above, as,

$$\alpha = \arctan\left(\frac{V_{\text{perp}}}{V_{\text{tave}}}\right) \qquad (20)$$

The set of equations (1) to (10) and (13) to (20) must be solved simultaneously for Q_{or}, Q_{out}, and P_{out} to provide the starting values of flow and pressure for the next segment, repeated segment by segment. Then, equations (11) and (12) are calculated to see if the chosen values of supply pressure and flow provide a value of $Q5_{\text{out}}$ that is acceptably close to zero. If not, new supply values must be selected and the computations are repeated. Usually, the selection of supply pressure and flow are interrelated by the hydraulic characteristics of the supply fan. The iterative microcomputer spreadsheet used to solve the flow equations 1 to 20 is described next.

Computation of Swirl Flow in Polytubes

Initial programming was done using SuperCalc 3.2, but no modification of the equations or spreadsheet layout was required when the work was transferred to SuperCalc 4 and later to SuperCalc 5. The spreadsheet was instructed to repeat the iterative calculations of equations 1 to 20 for the five polytube segments until a suitable level of accuracy had been achieved. Usually, 30 to 50 automatically performed iterations and approximately 10 seconds were required to solve the equations to the fourth place of accuracy for all flows and pressures.

The spreadsheet was initialized by installing arbitrary values of pressure and orifice flow in the appropriate spreadsheet cells, and then by linking the cells, within a column and column by column, via equations 1 to 20. Once this process has been completed, the spreadsheet was set to iterative computation mode. Downstream propagation of the solution for continuity is achieved by equations (1), (11), and (12), and for pressure by equations (4), (6), and (9). Upstream adjustments of velocity and hence of flow are achieved by equations (2), and (3), while upstream adjustments of pressure are achieved by equation (10).

Evaluation of the Airflow Predictions

Static Regain Coefficient. Bailey (1975b) examined flow from one pipe wall mounted orifice and based upon the upstream (v_1) and downstream (v_2) velocities recommended the following correlation,

$$C_r = 0.78 + \Phi \log\left[\frac{v_1}{v_1 - v_2}\right] \qquad (21)$$

where,

$$\Phi = 0.284 + 0.098 \log\left[\frac{d}{D}\right] \qquad (22)$$

Care should be exercised in the application of equation (21) since his results indicate that $0.14 \le \Phi \le 0.28$. Also, for large numbers of orifices mounted along a polytube (say 50 pairs) $v_1/(v_1 - v_2) \approx 50$ near the polytube inlet, and thus equation (21) yields a value of $C_r \approx 1.2 \gg 1.0$.

An alternative method of evaluation of the static regain coefficient is permitted by dividing the polytube into five segments as described above. If it is assumed that approximately 20 percent of the flow is discharged in each section, then the exit velocity of segment one is approximately 80 percent of the inlet value. If static regain occurs in a manner similar to that of a conical diffuser, then an exit velocity that is 80 percent of the inlet value can be related to an equivalent diffuser exit area that is 1.25 times the inlet area. Also, the length to inlet diameter ratio is 10 for each segment of a polytube with a 610 mm diameter and an overall length of 30.5 m. The second

Table 1 Comparison of the predicted values of pressure and orifice flow to the experimental data of Brundrett and Vermes (1987), (which exhibit experimental errors on pressure of ± 2 Pa and on flow of ± 0.5 m^3/s or ± 5 percent).

Polytube	Test 1	Test 2	Test 3	Test 4
		Dimensions		
Diameter	610 mm	457 mm	610 mm	457 mm
Length	30.5 m	30.5 m	30.5 m	30.5 m
Orifice dia.	62.4 mm	62.4 mm	62.4 mm	62.4 mm
Orif. spacing	549 mm	603 mm	549 mm	603 mm
Orif. pairs	56	51	56	51
Swirl control	Yes	Yes	No	No
		Experiment		
ϕ_{supply}	13.5°	23°	31°	38°
Q_{supply} (m^3/s)	2.89	2.61	2.88	2.13
ΣQ_{or} (m^3/s)	2.89	2.67	2.84	2.23
		Calculated		
ΣQ_{or} (m^3/s)	2.89	2.61	2.88	2.13
ΔQ_{error} (Eqn. 12)	+0.23%	-0.57%	+1.19%	+1.17%
		Standard Deviation is $\pm 0.89\%$		
	Pressure profile compared to experiment (Figs. 4 and 5)			
Standard dev.	± 0.59 Pa	± 1.07 Pa	± 0.72 Pa	± 0.64 Pa
Maximum dev.	+0.8 Pa	-1.8 Pa	-1.1 Pa	-1.2 Pa
C_r coef. (Fig. 2)	0.556	0.496	0.408	0.276
	Orifice profile compared to experiment (Figs. 6 and 7)			
Standard dev.	$\pm 0.71\%$	$\pm 1.52\%$	$\pm 0.72\%$	$\pm 1.44\%$
Maximum dev.	-1.0%	+3.1%	+1.1%	+2.1%

segment has velocities that are 80 percent and 60 percent of the inlet value to segment one, and by continuity the equivalent area ratio is 1.33. Continuing the evaluation for the remaining segments, the average area ratio of the polytube is found to be 2.0; when the last 5 percent of the polytube is neglected to retain a finite velocity ratio for the fifth segment.

For typical diffuser boundary layers White (1986 (Fig. 6.27)) recommends a static regain coefficient of 0.558 for an area ratio of 2 and a length to diameter of 10. The flow in a diffuser of this geometry has very little wall friction, since the boundary layer velocity gradient approaches zero at the diverging walls. Hence although not directly applicable to polytube static regain, this diffuser coefficient does provide at least a reasonable first estimate. For a length to diameter ratio of 10, the chart (with some extrapolation) indicates that $0.52 \le C_r \le 0.59$ over the area ratio range of 1.25 to 2.5. This would suggest that a nearly constant value of C_r could be adopted along a polytube divided into five computational segments. Hence, initially the static regain coefficient C_r was set to 0.558 for each segment of the polytubes for the analysis of the four supply swirl angle tests of Brundrett and Vermes (1987) obtained from 610 mm and 457 mm polytubes (Table 1). A single polytube supply fan was used for both tubes, by directly connecting it to the 610 mm polytube, and by using a 610 mm to 457 mm contraction for the smaller polytube.

Test were performed with and without a swirl control device mounted at the fan exit. The six blades of the device were set to remove all swirl when the fan discharged directly to the room. However, due to the higher pressure demand supply swirl still occurred when the fan was connected to either polytube with the swirl control device (Table 1). However, significantly higher values of ϕ_{supply} occurred without the swirl control device, particularly when the fan swirl was amplified by the contraction piece (38 deg for the 457 mm tests). Flow swirl angles were obtained by means of a thread telltale mounted on the tip of a 2 mm probe positioned normal to the wall with the tip 50 mm inward from the tube wall. The thread seen externally through the nearly transparent polyethylene wall was compared to an externally mounted protractor (Brundrett and Vermes 1987).

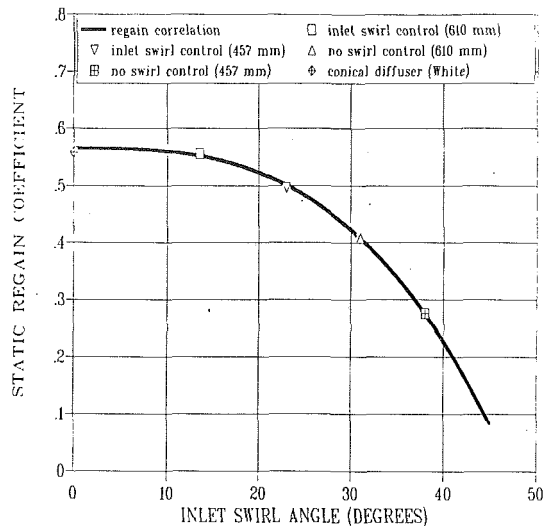Considerable care was taken to ensure that the static pressure

Fig. 2 Comparison of the computationally determined static regain coefficients (C_r) of the four polytube experiments to the zero swirl diffuser value of White (1986), and to the recommended correlation (equation (23))
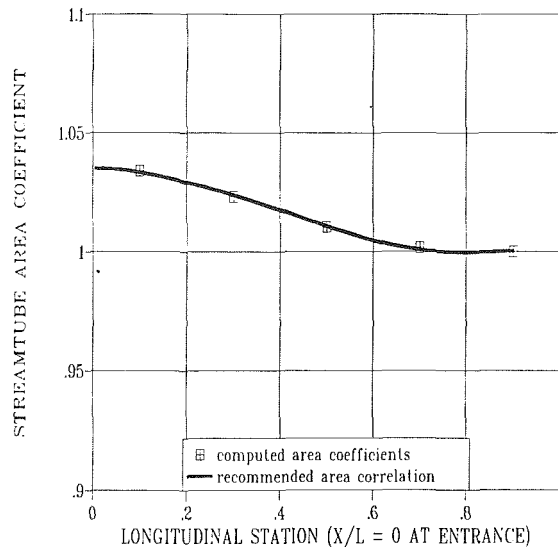

Fig. 3 Comparison of the computationally determined streamtube area coefficient (C_α) to the recommended correlation (equation (24))

Fig. 4 Comparison of experimental and predicted pressures profiles for flow in the 610 mm polytube with and without an antiswirl device installed at the fan exit

profiles were obtained from Pitot-static probes that were correctly aligned to the swirling flow. Also, measurements of orifice discharge were obtained with probes aligned to the exit angle of the flow of each orifice. Total flow into the fan was obtained by using the recommended flow averaging procedures of the ASME Power Test Codes and compared favorably with the total of the orifice flows (Table 1). Brundrett and Vermes (1987) observed that flow and pressure measurements taken at five to six locations along a polytube were sufficient to characterize the flow and to obtain continuity balances of orifice to fan flow to within ±5 percent and usually to within ±2.5 percent (Table 1).

The analysis of pressure along the 610 mm polytube with swirl control device ($\phi_{\text{supply}} = 13.5$ deg) gave static pressure profiles that were in best agreement with the experimental data when the diffuser static regain coefficient ($C_r = 0.558$) was reduced slightly to 0.556 (Table 1). The remainder of the tests required more significant reductions of the static regain coefficient to obtain the best fit to the experimental data (Table 1, Fig. 2) becoming as low as $C_r = 0.276$ for the 457 mm test without the swirl control device ($\phi_{\text{supply}} = 38$ deg). The supply swirl angle correlation of the static regain coefficient obtained by stepwise multiple regression analysis is,

$$C_r = 0.565 - 5.28 \times 10^{-6} \phi_{\text{supply}}^3 \qquad (23)$$

The correlation has a coefficient of determination of 0.9991, a fit of the analytically obtained values of C_r to within ±1 percent and to within +1.2 percent of the static regain value extracted from the zero swirl diffuser data of White (1986). It was found that negligible improvement in pressure profile agreement was achieved by altering the static regain coefficient in segments 2 to 4 from the value for segment 1. However, an average of the segment 1 and 0.558 values of C_r gave the best agreement in every case for segment 5.

Streamtube Coefficient. Computed orifice discharge was compared with data of Brundrett and Vermes (1987). An initial value of $C_\alpha = 1.0$ gave too low a total discharge, particularly for the first three segments of each polytube. Good agreement with the experimental data was obtained by a very small adjustment of the coefficient in the range $1.0 \le C_\alpha \le 1.035$ (Fig. 3) defined by a stepwise multiple regression analysis as,

$$C_\alpha = 1.035 - 0.163 \left(\frac{X_{\text{mid}}}{L}\right)^2 + 0.134 \left(\frac{X_{\text{mid}}}{L}\right)^3 \qquad (24)$$

The coefficient of determination is 0.997, and the correlation of the analytically derived coefficients is to within ±0.1 percent. This correlation was used segment by segment to obtain the required values of C_α for equation (17) for both the 610 mm and 457 mm experimental data, with the single exception of segment one of the 457 mm test without a swirl control device, for which $C_\alpha = 1.01$ rather than 1.035 gave better results. However, the experimental data of this test is somewhat in question regarding orifice flow (Table 1), since the polytube and hence the orifices were vibrating extensively due to the very large supply swirl angle and related unstable flow conditions.

Pressure Profile Predictions. The two 610 mm pressure profile analyses for flow with and without a swirl control or antiswirl device are shown in Fig. 4. Good agreement is obtained from the prediction procedure when the static regain coefficients of Table 1 are employed (tests 1 and 3, respectively). Of greater interest is the successful prediction of the 457 mm test data with and without an antiswirl device shown in Fig. 5 (tests 2 and 4, respectively). There is a dramatic droop
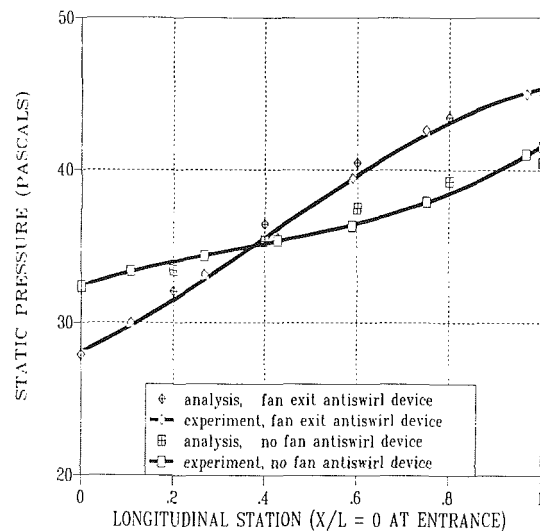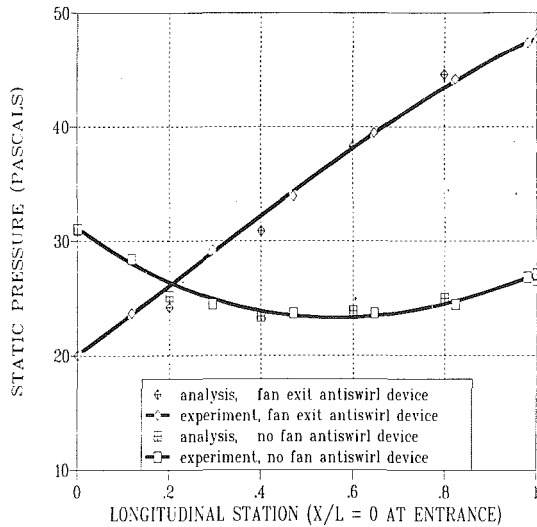
Fig. 5 Comparison of experimental and predicted pressures profiles for flow in the 457 mm polytube with and without an antiswirl device installed at the fan exit
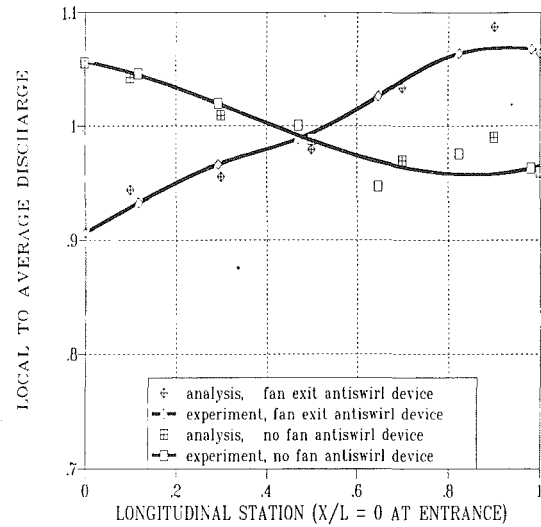

Fig. 7 Comparison of experimental and predicted orifice flow profiles for flow in the 457 mm polytube with and without an antiswirl device installed at the fan exit
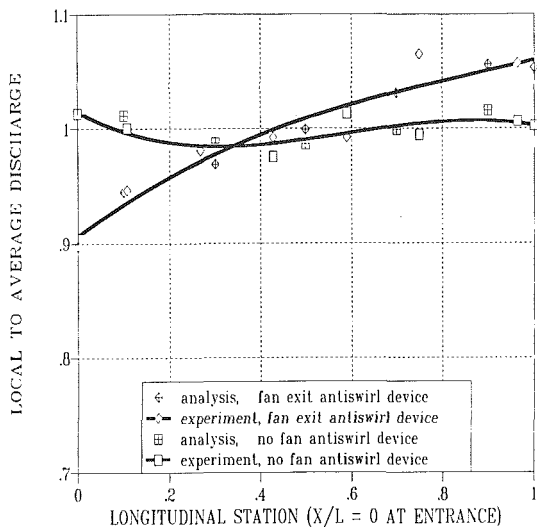

Fig. 6 Comparison of experimental and predicted orifice flow profiles for the 610 mm polytube with and without an antiswirl device installed at the fan exit

in the experimental static pressure data of test 4 that is faithfully tracked by the computed values. The pressure droop is associated with the very low static regain coefficient and the much longer flow path due to the large swirl angle of the supply flow without a swirl control device.

The maximum deviation of a calculated pressure from the experimental data is -1.8 Pa (Table 1, test 2), and the maximum standard deviation of the calculated pressure profile from the comparable experimental pressure profile is ± 1.07 Pa, while the average standard deviation of all of the predicted to experimental data is ± 0.76 Pa. The good agreement of the five segment computational procedure precluded the need to examine calculations employing more segments, and is the recommended procedure.

Orifice Flow Predictions. The predicted and experimental orifice flow profiles for the two 610 mm tests are shown in Fig. 6 (Table 1, tests 1 and 3), and for the two 457 mm tests in Fig. 7 (Table 1, tests 2 and 4). Again, the computed values of orifice flow along the polytubes are at least as reliable as the experimental data of both polytube sizes. There is a maximum deviation of $+3.1$ percent (Table 1), a maximum standard

ard deviation of ± 1.5 percent, and an average standard deviation for the four tests of ± 1.2 percent (Table 1). Also, it can be seen that there is a significant and undesirable shift of the discharge to segments 1 and 2 when there is a large supply swirl angle (Figs. 6 and 7).

Discussion of Results

The pressure and orifice flow predictions are in very good agreement with the experimental data (Table 1, Figs. 4–7) for all four tests. In particular, the predicted pressure profile for the 457 mm polytube without a swirl control device is most gratifying (Fig. 5), due to the very large swirl angle of the supply flow and the unusual pressure droop along the polytube. The combination of equations 4 and 23 for static regain and equations 5 to 8 for friction loss faithfully tracked the experimental pressure data.

The prediction of the discharge from the five segments is also very good, and in general appears to be at least as accurate as the experimentally determined data (Figs. 6 and 7). It should be noted that the discharge profile varies significantly along each of the polytubes even though the orifices are evenly spaced. For both polytubes the discharge in the fifth segment is significantly greater than that of the first segment when an antiswirl device is installed at the fan exit; a condition favored for many ventilation applications.

During the development of the solution procedure it was found that the correct average values were required for the solution of the mid segment continuity balance and the overall pressure change of the segment. Hence, $(V)^2_{ave}$ (equation (3)) must be used to obtain the pressure loss, while V_{ave} (equation (2)) is used to obtain the mid segment Reynolds number. Also, $(V)^2_{tave}$ the total velocity of the flow at the mid point of a segment (equation (14)) must be used to define the total kinetic and pressure energy of the flow (equation (15)); whereas, $\dot{V}_{tave}$ must be used to correctly define the approach angle (α) of the discharge streamtube to the polytube wall and orifice (Fig. 1, equation (20)). Then, the grouping of all of the orifices of a segment at the mid point permits the solution of one cycle of discharge related equations for each of the five equal length segments. A slight computational improvement in prediction of the first segment end point pressure was obtained when the inlet segment length was made 80 percent of the length of the remaining sections. However, the adjustment did not result in a significant improvement in flow prediction, and was not examined further. Modification of the spreadsheet to other
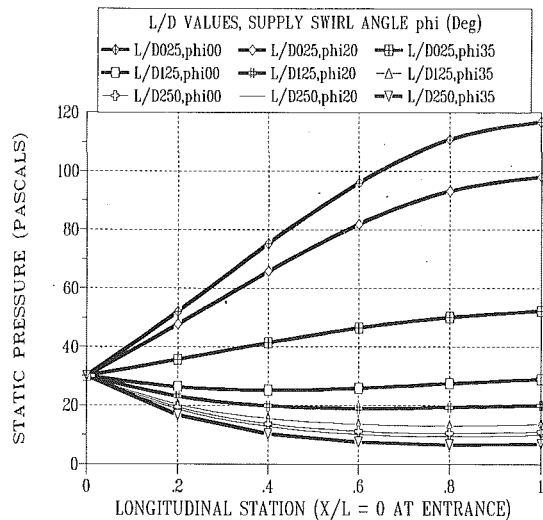
Fig. 8 Influence of L/D = 25, 125, 250, and ϕ_{supply} = 0, 20, 35 deg on the polytube pressure profile for AR = 1.5 (L/D25, phi35 indicates L/D = 25, ϕ_{supply} = 35 deg etc.)
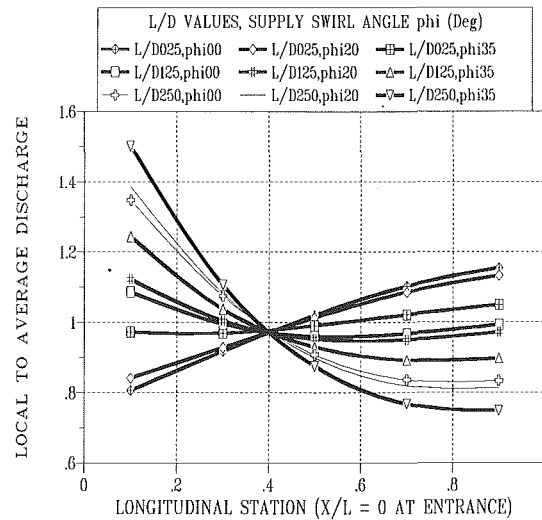

Fig. 9 Influence of L/D = 25, 125, 250, and ϕ_{supply} = 0, 20, 35 deg on the polytube discharge profile for AR = 1.5 (L/D25, phi35 indicates L/D = 25, ϕ_{supply} = 35 deg etc.)

polytube dimensions was best achieved by a number of progressive steps, such as the adjustment of polytube diameter from 610 mm to 457 mm. The continuity check after each adjustment of diameter indicated the required direction for supply flow and pressure adjustment, which in every case was readily satisfied to within ±1.5 percent. When developed, the new polytube geometry and supply conditions were saved as solution templates for future predictions.

It was observed that the predicted flow and pressure profiles were not influenced by adjustments in polytube diameter by ±5 mm, nor by length adjustments of ±1 m. However, adjustments of the 62.4 mm orifice diameter by ±1 mm produced a ±4 percent adjustment in total orifice flow. In fact, the early analysis of the experimental data exhibited a consistent +2 percent error in the continuity balance for the given experimental supply conditions. A detailed examination of the two polytubes when inflated revealed that the orifice diameters where on average 62.4 mm (Table 1) and not 62.9 mm as reported by Brundrett and Vermes (1987).

Extended Predictions

Prediction of Previous Work. There are surprisingly few sets of published data for flow in polytubes that provide sufficient information for a full analysis of the flow. In particular, only Brundrett and Vermes (1987) report the supply swirl angle. However, the polytubes investigated by Bailey (1975a) and by Saunders and Albright (1984) are believed to have negligible supply swirl angles, due to the experimental setup. Bailey investigated one polytube that was connected to a large plenum and tabulated his results. Saunders and Albright connected their polytubes to a well designed wind tunnel, but only presented their results graphically. Hence, a possible error of interpretation of their data of ±4 percent may exist due to the small size of the published graphs. Nevertheless, assuming a supply swirl angle for these cases of 0 deg is a reasonable assumption for the probable range of 0 deg $\leq \phi_{supply} \leq$ 10 deg. The resulting predictions of supply flow are in very good agreement with their experimental data for the reported values of supply pressure (Table 2), and provide an independent check of the prediction method. Also, the data provide a significant extension of the polytube and supply parameters to include most practical applications, since the ranges, 17.5 $\leq L/D \leq$ 142.9, 25 mm $\leq d \leq$ 130 mm, 305 mm $\leq D \leq$ 762 mm, 0.788 m³/s $\leq Q_{supply} \leq$ 4.75 m³/s, and 42 $\leq$ orifice number $\leq$ 272 are successfully predicted.

Table 2 Comparison of experimental and predicted supply flow for three investigations of other researchers; Case A, Bailey (1975a); Cases B and C, Saunders and Albright (1984) (tubes 6 and 11, respectively).

Experimental parameters	Case A	Case B	Case C
Polytube length (L)	55.6 m	13.5 m	13.4 m
Polytube diameter (D)	389 mm	305 mm	762 mm
L/D	142.9	44.3	17.5
Orifice diameter	25 mm	48 mm	130 mm
Number of orifices	272	64	42
Area Ratio (AR)	1.13	1.56	1.22
ϕ_{supply} (Estimated)	0°	0°	0°
P_{supply}	25 Pa	30 Pa	20 Pa
Q_{supply} (m³/s)	0.788	1.077	4.725
$Q_{predicted}$ (m³/s)	0.785	1.076	4.879
ΔQ (m³/s)	−0.003	−0.001	+0.154
$\Delta Q\%$ Error	−0.38%	−0.09%	+3.26%

Extended Examination of the Supply Swirl Angle and L/D. The influence of supply swirl has been examined for AR = 1.5 for L/D = 25, 125, 250, and for ϕ_{supply} = 0, 20, 35 deg. The predicted pressure profiles (Fig. 8) clearly demonstrate the reduction of static pressure regain associated with large supply swirl angles, while the larger values of L/D demonstrate the increasing influence of friction loss, particularly when combined with a large supply swirl angle. The predicted discharge profiles (Fig. 9) show that a large supply swirl angle significantly distorts the profile by creating an adversely greater discharge in the first half of the polytube. Consequently, it is recommended that the supply flow be controlled by an antiswirl device if required so that ϕ_{supply} < 25 deg. Also, it is recommended that AR < 1.75 be selected (Saunders and Albright (1984)), and that if possible L/D < 150 be selected.

Conclusions

This investigation has endeavored to describe the mechanisms controlling swirling flow in polytubes, for geometries commonly found in North American applications, and to provide a solution procedure for their prediction.

The controlling parameters for pressure along a polytube are a proposed swirl correlation for static pressure regain, and a previously reported correlation for friction loss that is dependent upon local swirl angle and local Reynolds number. The computational procedure divides the polytube into five equal segments and computes average properties at the mid

point of each segment before computing the end of segment pressure change from the inlet value due to static regain and friction loss. Very good agreement with experimental data is achieved by the prediction method. The standard deviations of the predicted to experimental pressure profiles are well within the error bounds of the experimental data (± 2 Pa) and are ± 1.1 Pa for the four polytubes.

Orifice flow is predicted by combining all of the orifice area of a segment at the mid-point. The total pressure of the polytube flow upstream of the midpoint and the ratio of orifice perpendicular velocity to upstream total velocity are used to iteratively solve for the orifice discharge. A streamtube area coefficient is developed that permits very good agreement with experimental data. The coefficient changes from 1.035 at the polytube inlet to a value of unity at the polytube end for all but one experimental point. It is well described by a simple correlation that appears to be independent of polytube and orifice diameters, at least for commercial tube geometries. The standard deviations of the predicted to experimental orifice discharges are well within the experimental error bounds and are ± 1.5 percent. Also, total discharge is predicted to within ± 1.2 percent for each polytube; and the predicted supply flow is in good agreement with that data of two other sources.

The computation of swirling polytube flow requires iterative solution for given values of supply pressure, flow, and swirl angle. An electronic spreadsheet is used to solve the flow and pressure equations by setting it to iterative mode and by specifying four place accuracy. The spreadsheet is readily modified for new geometries. Combinations of supply conditions must be modified until the total flow from the polytube equals the supply flow to within an acceptable level of accuracy. Then valid supply combinations for given polytube geometries can be used for design purposes and the spreadsheets can be saved as future solution templates. An extension of the analysis for uniformly spaced orifices indicates that the supply swirl angle should be limited to 25 deg and that large ratios of length to diameter should be avoided, due to significant reductions in static pressure regain and due to an undesirable increase of discharge from the first half of the polytube.

References

Bailey, B. J., 1975a, private communication based on the internal report, "Temperature Uniformity in Glasshouses Heated with Ducted Air," Nat. Inst. Agr. Eng. (UK) Dept Note DN/G/562/2101.

Bailey, B. J., 1975b, "Fluid Flow in Perforated Pipes," *J. Mech. Eng. Sc.*, Vol. 17, pp. 338–347.

Brundrett, E., and Vermes, P. T., 1987, "Evaluation of Tube Diameter and Fan Induced Swirl in Polyethylene Ventilation Tubes," *Trans. ASAE*, Vol. 30, pp. 1131–1136.

Dittrich, R. T., and Graves, C. C., 1956, "Discharge Coefficients for Combustor-liner Air-entry Holes," NACA TN 3663.

Dow, W. M., 1950, "The Uniform Distribution of a Fluid Flowing Through a Perforated Pipe," ASME *Journal of Applied Mechanics*, Vol. 17, pp. 431–438.

Haaland, S. E., 1983, "Simple and Explicit Formulas for The Friction Factor in Turbulent Pipe Flow," ASME *Journal of Fluids Engineering*, Vol. 105, p. 89.

Haerter, A. A., 1963, "Flow Distribution and Pressure Changes Along Slotted or Branched Ducts," *ASHREA Jl.*, Vol. 5, pp. 47–59.

Howland, W. E., 1953, "Design of Perforated Pipe for Uniformity of Discharge," *Proc. 3rd Midwestern Conf. on Fluid Mechanics*, pp. 687–701.

Keller, J. D., 1949, "The Manifold Problem," ASME *Journal of Applied Mechanics*, Vol. 16, pp. 77–85.

Rogers, T., and Hersh, A. S., 1976, "Effect of Grazing Flow on Steady-State Resistance of Isolated Square-edged Orifices," NASA CR-2681.

Saunders, D. D., and Albright, L. D., 1984, "Airflow from Perforated Polyethylene Tubes," *Trans. ASAE*, Vol. 27, pp. 1144–1149.

White, F. M., 1986, *Fluid Mechanics*, Second Edition, McGraw-Hill, New York, NY.

W. Bober

Associate Professor.
Mem. ASME

W. L. Chow

Professor.
Fellow ASME

Department of Mechanical Engineering,
Florida Atlantic University,
Boca Raton, FL 33431

Nonideal Isentropic Gas Flow Through Converging-Diverging Nozzles

A method for treating nonideal gas flows through converging-diverging nozzles is described. The method incorporates the Redlich-Kwong equation of state. The Runge-Kutta method is used to obtain a solution. Numerical results were obtained for methane gas. Typical plots of pressure, temperature, and area ratios as functions of Mach number are given. From the plots, it can be seen that there exists a range of reservoir conditions that require the gas to be treated as nonideal if an accurate solution is to be obtained.

Introduction

In recent years there has been a significant increase in the operating pressures of power plants, oil and gas fields, and transmission lines [1]. Since orifices and valves are an integral part of such systems, there is an interest in studying the flow through such devices under high pressure conditions. Under such conditions, nonideal gas behavior may be an important characteristic of the flow. A historical review of real-fluid isentropic flow models has been given by Sullivan [2]. More recently, Fagerlund and Winkler [1] utilized the Redlich-Kwong equation of state, along with other thermodynamic relations, to determine a correction factor for valve sizing. However, in their study, they only considered the thermodynamics involved in the process and assumed the isentropic exponent to be a constant. Their work did not include the study of a gas flow through a valve, which is our ultimate goal.

The flow of an ideal, compressible gas through control valves and orifices has been recently studied by Chow et al. [3, 4]. Although our interest is in extending this work to include nonideal gas behavior, it seemed appropriate to first tackle a less difficult problem, such as the flow of a compressible gas through a converging-diverging nozzle, taking into account the nonideal behavior of the gas. Successful analysis of the nozzle problem would provide the necessary background in dealing with the more difficult problems of flows through valves and orifices.

One-dimensional compressible flow through nozzles, diffusers, and ducts is well-developed and is covered in any standard fluids textbook containing a chapter on compressible flow [5, 6]. However, in nearly all instances, the treatment assumes ideal gas behavior. For gas flows at high pressure, one must treat the gas as nonideal in order to obtain an accurate description of the flow. A nonideal gas flow analysis was carried out by Tsien [7]. He used van der Waal's equation of state and small perturbation theory to analyze gas flows through

nozzles under conditions where deviations from the ideal gas relations are not negligible. He further assumed that the specific heat at constant volume varied only with temperature according to a quadratic law. In this paper, a further study of nonideal gas flows through nozzles is carried out. The Redlich-Kwong equation of state is used and the specific heats at constant pressure and constant volume are considered to vary with both density and temperature. A computer program was developed to solve the flow equations by the Runge-Kutta method utilizing density as the independent variable. The program may then be used with any gas as the working fluid by merely changing the input data. Numerical results were obtained for methane gas. Plots of pressure, temperature and area ratios (i.e., p/p_0, T/T_0, and A/A^*, respectively) versus the Mach number, M, are given for two different reservoir conditions; one leads to a flow that is far from ideal and the other close to ideal.

Technical Discussion

The equations of conservation of mass, momentum and energy for frictionless, adiabatic flow are:

$$\rho A V = \text{constant} = \dot{m}_0 \tag{1}$$

$$\frac{dp}{\rho} + V dV = 0 \tag{2}$$

$$h + \frac{V^2}{2} = h_0 \quad \text{or} \quad dh + V dV = 0 \tag{3}$$

Since,

$$T ds = dh - \frac{dp}{\rho} = dh - \tilde{v} dp \tag{4}$$

it becomes obvious from equations (2) and (3) that the flow must be isentropic and

$$dh = \tilde{v} dp \tag{5}$$

A differential equation for T with $\tilde{v}$ (or ρ) as the independent variable can be developed as follows:

$$ds = \frac{c_{\tilde{v}}}{T} dT + \left[\frac{\partial p}{\partial T}\right]_{\tilde{v}} d\tilde{v} \qquad (6)$$

For a constant entropy process,

$$\left[\frac{dT}{d\tilde{v}}\right]_s = -\frac{T}{c_{\tilde{v}}}\left[\frac{\partial p}{\partial T}\right]_{\tilde{v}} \qquad (7)$$

The Redlich-Kwong equation of state [8] is used; i.e.,

$$p = \frac{RT}{\tilde{v}-b} - \frac{a}{T^{0.5}\,\tilde{v}(\tilde{v}+b)} = \frac{\rho RT}{1-b\rho} - \frac{a\rho^2}{T^{0.5}(1+b\rho)} \qquad (8)$$

where

$$a = 0.4278\,\frac{R^2 T_c^{2.5}}{p_c} \text{ and } b = 0.0867\,\frac{RT_c}{p_c} \qquad (9)$$

For any particular gas a and b are constants. Values for p_c and T_c for various gases can be found in reference [8].
From equation (8), $(\partial p/\partial T)_{\tilde{v}}$ can be determined; i.e.,

$$\left[\frac{\partial p}{\partial T}\right]_{\tilde{v}} = \frac{R}{\tilde{v}-b} + \frac{a}{2T^{3/2}\,\tilde{v}(\tilde{v}+b)} \qquad (10)$$

Substituting equation (10) into equation (7) gives

$$\left[\frac{dT}{d\tilde{v}}\right]_s = -\frac{T}{c_{\tilde{v}}}\left[\frac{R}{\tilde{v}-b} + \frac{a}{2T^{3/2}\,\tilde{v}(\tilde{v}+b)}\right] \qquad (11)$$

In terms of the density, ρ, the above equation becomes

$$\left[\frac{dT}{d\rho}\right]_s = \frac{T}{\rho^2 c_{\tilde{v}}}\left[\frac{R\rho}{1-b\rho} + \frac{a\rho^2}{2T^{3/2}(1+b\rho)}\right] = f(T, \rho;\, c_{\tilde{v}}(T, \rho)) \qquad (12)$$

An expression for $c_{\tilde{v}}$ which takes into account real gas behavior [8] can be determined as follows:

$$ds = c_{\tilde{v}}\frac{dT}{T} + \left[\frac{\partial p}{\partial T}\right]_{\tilde{v}} d\tilde{v} = \left[\frac{\partial s}{\partial T}\right]_{\tilde{v}} dT + \left[\frac{\partial s}{\partial \tilde{v}}\right]_T d\tilde{v}$$

Therefore:

$$\left[\frac{\partial s}{\partial T}\right]_{\tilde{v}} = \frac{c_{\tilde{v}}}{T} \text{ and } \left[\frac{\partial s}{\partial \tilde{v}}\right]_T = \left[\frac{\partial p}{\partial T}\right]_{\tilde{v}}$$

Noting that the mix derivatives must be the same regardless of the order of differentiation, one obtains,

$$\left[\frac{\partial}{\partial \tilde{v}}\left[\frac{c_{\tilde{v}}}{T}\right]\right]_T = \left[\frac{\partial}{\partial T}\left[\frac{\partial p}{\partial T}\right]_{\tilde{v}}\right]_{\tilde{v}}$$

or

$$\frac{1}{T}\left[\frac{\partial c\tilde{v}}{\partial \tilde{v}}\right]_T = \left[\frac{\partial^2 p}{\partial T^2}\right]_{\tilde{v}}$$

Integrating at a fixed temperature, from zero pressure specific volume to an arbitrary specific volume gives

$$c_{\tilde{v}}(T, \rho) - c_{\tilde{v}}^+(T) = T\int_\infty^{\tilde{v}} \left[\frac{\partial^2 p}{\partial T^2}\right]_{\tilde{v}} d\tilde{v} \qquad (13)$$

where $c_{\tilde{v}}^+$ is the zero pressure specific heat at constant volume (zero pressure corresponds to infinite specific volume). From equation (10),

$$\left[\frac{\partial^2 p}{\partial T^2}\right]_{\tilde{v}} = -\frac{3a}{4\,T^{5/2}\tilde{v}(\tilde{v}+b)} \qquad (14)$$

Substituting equation (14) into equation (13), integrating and replacing $\tilde{v}$ with $1/\rho$ gives:

$$c_{\tilde{v}}(T,\rho) = c_{\tilde{v}}^+(T) + \frac{3a}{4\,bT^{3/2}}\ln(1+b\rho) \qquad (15)$$

The ideal gas (or zero pressure) specific heats are related by the equation

$$c_{\tilde{v}}^+ = c_p^+ - R \qquad (16)$$

The specific heat, c_p^+, can be determined by a fourth degree polynomial [8]; i.e.,

$$\frac{c_p^+}{R} = A_0 + A_1 T + A_2 T^2 + A_3 T^3 + A_4 T^4 \qquad (17)$$

The values for the coefficients A_0 through A_4 and R for various gases can be found in reference [8]. An equation for u can be obtained from [8]:

$$du = c_{\tilde{v}}dT + \left[T\left[\frac{\partial p}{\partial T}\right]_{\tilde{v}} - p\right] d\tilde{v} \qquad (18)$$

Substituting equations (8) and (10) into equation (18) and integrating at constant temperature gives:

$$u(T, \tilde{v}) - u^+(T) = \frac{3}{2}\int_\infty^{v} \frac{a}{T^{1/2}\,v'(v'+b)} dv'$$

or

$$u(T, \rho) = u^+(T) - \frac{3a}{2bT^{1/2}}\ln(1+b\rho) \qquad (19)$$

where $u^+(T)$ is the zero pressure internal energy and is given by:

$$U^+(T) = \int_0^T c_v^+(T')dT' \qquad (20)$$

Substituting equations (16) and (17) into equation (20) gives:

$$u^+(T) = R\left[(A_0-1)T + \frac{A_1}{2}T^2 + \frac{A_2}{3}T^3 + \frac{A_3}{4}T^4 + \frac{A_4}{5}T^5\right] \qquad (21)$$

The enthalpy, h, can then be determined by

$$h = u + \frac{p}{\rho} \qquad (22)$$

Knowing h, the velocity, V, can be determined by integrating equation (3), i.e.,

---

Nomenclature

a, b = constants in Redlich-Kwong equation of state
A = cross-sectional area of nozzle
c = speed of sound
c_p = specific heat at constant pressure
$c_{\tilde{v}}$ = specific heat at constant volume
h = enthalpy/unit mass
k = $c_p/c_{\tilde{v}}$ = ratio of specific heats

M = Mach number
n = $\rho c^2/p$ = polytropic exponent
p = pressure
R = gas constant
s = entropy/unit mass
T = temperature
$\tilde{v}$ = specific volume
V = average fluid velocity
Z = compressibility factor
ρ = mass density

Subscripts

0 = stagnation or reservoir properties
p = constant pressure
s = constant entropy
$\tilde{v}$ = constant volume

Superscripts

$*$ = property values at M = 1
$+$ = property values at zero pressure

$$V = \sqrt{2(h_0 - h)} \qquad (23)$$

All the terms necessary for solving equation (12) by the Runge-Kutta method have now been defined. Having ρ and T, p can be determined by equation (8). To introduce the Mach number, M, into the solution, one needs to obtain an expression for the speed of sound, c. It is given by:

$$c^2 = \left[\frac{\partial p}{\partial \rho}\right]_s = -\tilde{v}^2 \left[\frac{\partial p}{\partial \tilde{v}}\right]_s \qquad (24)$$

From equation (8), it can be determined that

$$\left[\frac{\partial p}{\partial \tilde{v}}\right]_s = -\frac{RT}{(\tilde{v}-b)^2} + \frac{R}{(\tilde{v}-b)}\left[\frac{\partial T}{\partial \tilde{v}}\right]_s + \frac{a(2\tilde{v}+b)}{T^{1/2}\,\tilde{v}^2(\tilde{v}+b)^2}$$
$$+ \frac{a}{2\,T^{3/2}\,\tilde{v}(\tilde{v}+b)}\left[\frac{\partial T}{\partial \tilde{v}}\right]_s \qquad (25)$$

Substituting equations (11) and (25) into equation (24) and replacing $\tilde{v}$ with $1/\rho$ gives:

$$c^2 = \frac{RT}{(1-b\rho)^2}\left[1 + \frac{R}{c_{\tilde{v}}}\right] + \frac{aR\rho}{c_{\tilde{v}}\,T^{1/2}\,(1-b^2\rho^2)}$$
$$+ \frac{a^2\rho^2}{4\,c_{\tilde{v}}\,T^2\,(1+b\rho)^2} - \frac{a(2+b\rho)\rho}{T^{1/2}\,(1+b\rho)^2} \qquad (26)$$

The Mach number, M, is defined by

$$M = \frac{V}{c} \qquad (27)$$

Then equations (23), (26), and (27) give M.

The area, A, can then be found from equation (1). Since the reservoir area is assumed to be infinitely large, one must assign a value to the area at any section downstream of the reservoir, thus establishing $\dot{m}_0$. This initial area value is strictly arbitrary and does not affect the terms of interest, i.e., p/p_0, T/T_0, A/A^* as functions of the Mach number. The area A^*, which is the area where the Mach number is 1.0, is determined as part of the solution, i.e., by interpolating between the points immediately surrounding M = 1.0.

In carrying out the program, a (p,T) combination may be reached that lies outside the validity range of equation (8). In that case, the program should be halted. For a valid solution one should require that:

$$T_r > 1.0, \text{ for } P_r > 1.0 \text{ and } T > T_{sat}, \text{ for } P_r < 1.0$$

where (T_r, P_r) are the reduced temperature and pressure respectively and T_{sat} is the saturated vapor temperature. T_{sat} may be determined by a Clapeyron type equation [8] i.e.,

$$\ln (p_{sat}) = B_0 + \frac{B_1}{T_{sat}} + B_2 \ln (T_{sat})$$
$$+ B_3 (T_{sat}) + B_4 (T_{sat})^2 + B_5 (T_{sat})^3 \qquad (28)$$

Constants B_0 through B_5 can be determined by fitting experimental (p_{sat}, T_{sat}) data for the gas of interest to equation (28). Experimental saturation data for various gases can be found in reference [9].

To examine the effect of nonideal gas behavior on gas flows through nozzles and diffusers, a comparison can be made between the ratios p/p_0, T/T_0 and A/A^* computed as described above and those same ratios computed by assuming an ideal gas with the ratio of specific heats, k, equal to a constant (the reservoir value). The ideal gas formulas [5] are:

$$\frac{T}{T_0} = \left[1 + \frac{k-1}{2}M^2\right]^{-1} \qquad (29)$$

$$\frac{p}{p_0} = \left[1 + \frac{k-1}{2}M^2\right]^{-\frac{k}{k-1}} \qquad (30)$$

$$\frac{A}{A^*} = \frac{1}{M}\left[\frac{1 + \frac{k-1}{2}M^2}{\frac{k+1}{2}}\right]^{\frac{k+1}{2(k-1)}} \qquad (31)$$

A similar comparison can be made for the mass flow rates per unit area. The ideal gas formula [6] in nondimensional form is:

$$\frac{\dot{m}\sqrt{RT_0}}{Ap_0} = \sqrt{k}\,M\left[1 + \frac{k-1}{2}M^2\right]^{-\frac{k+1}{2(k-1)}} \qquad (32)$$

To determine the reservoir value for k, the specific heat, c_p, must be determined. This can be accomplished by noting that [8]:

$$c_p = c_{\tilde{v}} + T\left[\frac{\partial p}{\partial T}\right]_{\tilde{v}}\left[\frac{\partial \tilde{v}}{\partial T}\right]_p = c_p^+ - R$$
$$+ \frac{3a\,\ln(1+b\rho)}{4b\,T^{3/2}} + T\left[\frac{\partial p}{\partial T}\right]_{\tilde{v}}\left[\frac{\partial \tilde{v}}{\partial T}\right]_p \qquad (33)$$

The term $(\partial p/\partial T)_{\tilde{v}}$ is given by equation (10) and $(\partial \tilde{v}/\partial T)_p$ can be obtained from equation (8). In terms of ρ, $(\partial \tilde{v}/\partial T)_p$ becomes:

$$\left[\frac{\partial \tilde{v}}{\partial T}\right]_p = \frac{\dfrac{R\rho}{(1-b\rho)} + \dfrac{a\rho^2}{2T^{3/2}(1+b\rho)}}{\dfrac{a(2+b\rho)\rho^3}{\sqrt{T}\,(1+b\rho)^2} - \dfrac{RT\rho^2}{(1-b\rho)^2}} \qquad (34)$$

Finally, to start the program, the reservoir value for ρ needs to be determined. Since pressure and temperature are the variables that are usually measured, one is faced with determining ρ from equation (8). At this point, it is convenient to introduce the compressibility factor Z, where

$$Z = \frac{p\tilde{v}}{RT} \qquad (35)$$

Equation (35) can be used to eliminate $\tilde{v}$ from equation (8) giving a cubic equation for Z; i.e.,

$$Z^3 - Z^2 + \left[\frac{ap}{R^2T^{2.5}} - \frac{b^2p^2}{R^2T^2} - \frac{bp}{RT}\right]Z - \frac{abp^2}{R^3T^{3.5}} = 0 \qquad (36)$$

For a given p and T, the above cubic equation can be solved by the algebraic method. The root of interest is readily ascertained. This is discussed in greater detail in the section entitled, Results.

Results

First, the overall technique of utilizing the Runge-Kutta method was tested by applying the technique to an ideal gas with k equal to 1.4. The computer program accurately reproduced the isentropic tables found in any standard textbook containing a chapter on compressible flow.

Next, the sub-program needed to evaluate the compressibility factor, Z, was developed and tested with methane as the working fluid. This sub-program is used at the very beginning of the calculations to evaluate Z_0, which is used to determine ρ_0. This sub-program solves equation (36), a cubic equation, by the algebraic method. To ascertain the root of interest, equation (36) was rewritten in terms of T_r and p_r, and different sets of (p_r, T_r) combinations were substituted into the modified equation. For $T_r \gtrless 1$, one real root and two imaginary roots were always obtained. For $T_r < 1$ and $p_r < 1$, three real roots were sometimes obtained. However, the formula that gave the real root for the case $T_r > 1$ always produced a Z value that was in good agreement with the compressibility chart in ref-
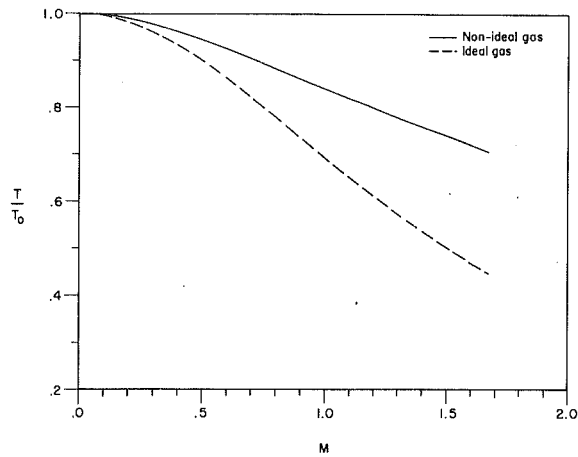
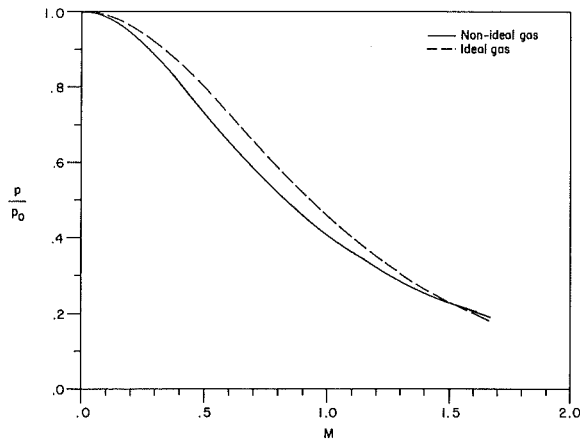Fig. 1 Temperature ratio versus Mach number (reservoir conditions: $(p_r)_0 = 5$, $(T_r)_0 = 1.4$, $k_0 = 1.884$)

Fig. 3 Area ratio versus Mach number (reservoir conditions: $(p_r)_0 = 5.0$, $(T_r)_0 = 1.4$, $k_0 = 1.884$)

Fig. 2 Pressure ratio versus Mach number (reservoir conditions: $(p_r)_0 = 5.0$, $(T_r)_0 = 1.4$, $k_0 = 1.884$)

Fig. 4 Temperature ratio versus Mach number (reservoir conditions: $(p_r)_0 = 0.8$, $(T_r)_0 = 3.0$, $k_0 = 1.209$)

Fig. 5 Pressure ratio versus Mach number (reservoir conditions: $(p_r)_0 = 0.8$, $(T_r)_0 = 3.0$, $k_0 = 1.209$)

erence [8], as long as the (p_r, T_r) combination was on the vapor side of the saturation line.

Once satisfied that the computer program was operating properly, several runs were made for methane gas at different reservoir conditions, i.e., at different $(p_r)_0$, $(T_r)_0$ values. The program produced tables similar to the isentropic tables found in standard textbooks containing a chapter on compressible flow. However, the tables produced by the program are valid only at the $(p_r)_0$, $(T_r)_0$ used in the program.

For illustrative purposes, two typical cases were selected for presentation in this paper. In the first case, the reservoir reduced pressure and temperature values were 5.0 and 1.4, respectively, which for methane gas corresponds to a pressure of 232 bars and a temperature of 267.0 K. Reduced pressure and temperature values for the second case were 0.8 and 3.0, respectively. For methane gas, these correspond to a pressure of 37.12 bars and a temperature of 572.1 K. The first case represents a gas which is far from ideal, while the second is a gas that is close to ideal. Plots of p/p_0, T/T_0 and A/A^* for these two cases are shown in Figs. 1–6. Figures 1 and 4 give the temperature ratio versus Mach number. Figures 2 and 5 give the pressure ratio versus Mach number and Figs. 3 and 6 give the area ratio versus Mach number. From these figures it can be seen that the pressure and area ratios are less sensitive to non-ideal gas effects than is the temperature ratio. It can be seen from Figs. 1–3, that at reservoir conditions cited in those figures, a gas, such as methane, would have to be treated as non-ideal for an accurate description of the flow. For this case a saturated state was reached at M = 1.67. Any further increase in the Mach number would result in a two-phase flow
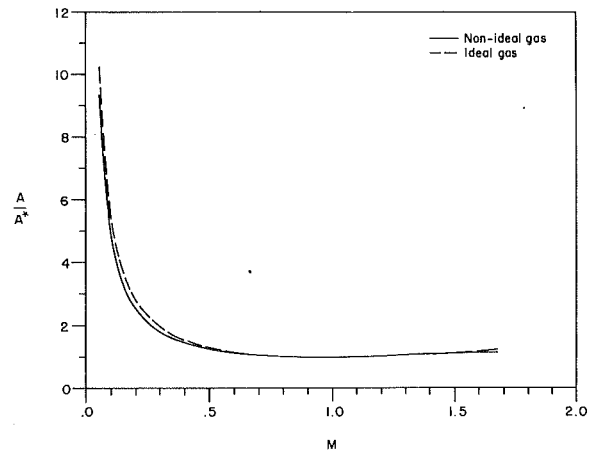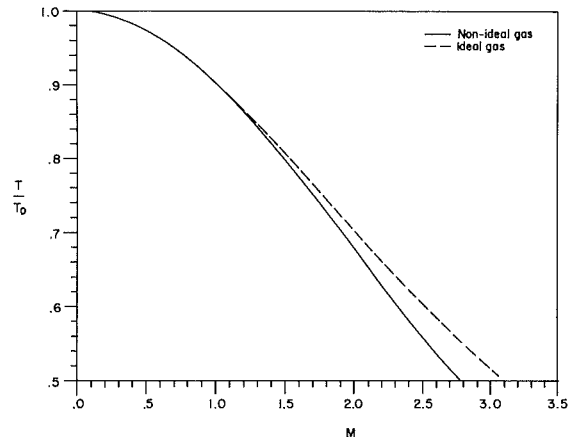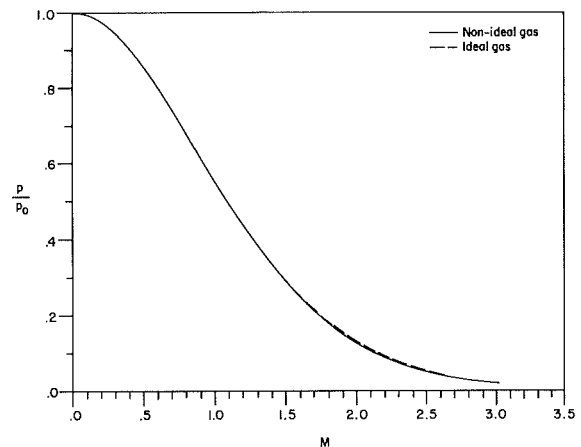
situation, which is beyond the scope of the present formulation.

In all cases tested the difference between the ideal gas temperature ratio and the non-ideal gas temperature ratio increased with Mach number. To ascertain that this result was not caused by the numerical technique, the program was modified by setting the numerical coefficients, a and b, in equation (8) and A_1, A_2, A_3, and A_4, in equation (17), equal to zero. This reduced the equation of state (equation (8)) to that of an ideal gas, c_v equal to a constant and $u = c_v T$. No other changes in the program were made. In this modified program, the difference between the temperature ratio obtained by the Runge-Kutta
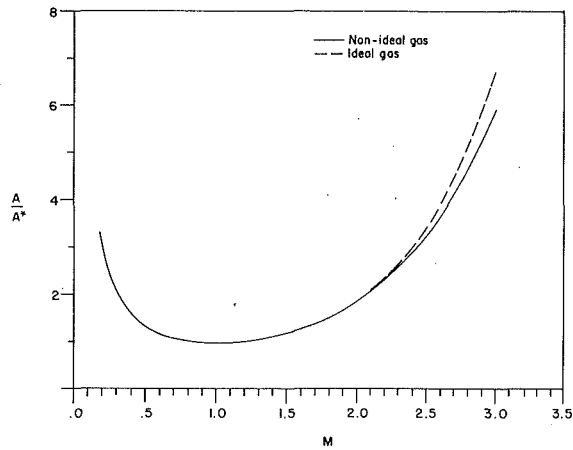
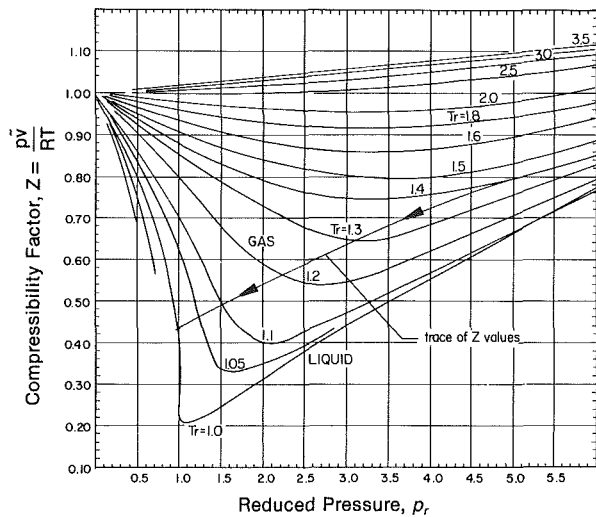Fig. 6 Area ratio versus Mach number (reservoir conditions: $(p_r)_0 = 0.8$, $(T_r)_0 = 3.0$, $k_0 = 1.209$)

Fig. 7 Trace of Z values (reservoir conditions: $(p_r)_0 = 1.4$, $Z_0 = 0.8002$; chart reproduced from B. F. Dodge, *Chemical Engineering Thermodynamics*, McGraw-Hill

Fig. 8 Specific heat at constant pressure versus Mach number (reservoir conditions: $(p_r)_0 = 5.0$, $(T_r)_0 = 1.4$)

Fig. 9 Specific heat at constant pressure versus Mach number (reservoir conditions: $(p_r)_0 = 0.8$, $(T_r)_0 = 3.0$)

Fig. 10 Zero pressure c_p contributive to overall value versus Mach number (reservoir conditions: $(p_r)_0 = 5.0$, $(T_r)_0 = 1.4$)

method and the temperature ratio obtained by equation (29) completely disappeared over the entire Mach number range ($0 < M \leq 3.0$) computed by the program.

Note that for the reservoir conditions given in Fig. 5, there is hardly any difference between the ideal gas and the nonideal gas pressure ratios over the entire Mach number range covered by the program. However, this is not the case with the temperature ratios. As can be seen in Fig. 4, a distinct difference in the temperature ratios begins at M $\sim$ 1.2.

In Fig. 7, a trace of the Z values for the high pressure case ($(p_r)_0 = 5.0$ and $(T_r)_0 = 1.4$) is superimposed on a compressibility chart. The direction of the arrow indicates the direction of increasing Mach number. As can be seen from this figure, the trace for this case, approaches the saturation line fairly close to the critical point. This leads to a relatively large value for c_p in that region. This is discussed in greater detail in the next paragraph. For the lower pressure case, the Z values remain close to 1.0 over the entire range covered by the program.

Although c_p was not directly used in the overall problem formulation, it is a term of interest in many gas flow situations. Equations (33), (10) and (34) give c_p. Figures 8 and 9 are plots of c_p versus M. For the high pressure case, c_p varied from 3,759 J/kg-K at M = 0.0 to 28,000 J/kg-K at M = 1.67. The sharp increase in c_p occurs for (p, T) values in the vicinity of the critical point. At the critical point, c_p is very large (see Fig. 5 in reference [10]). For the low pressure case, c_p varied from
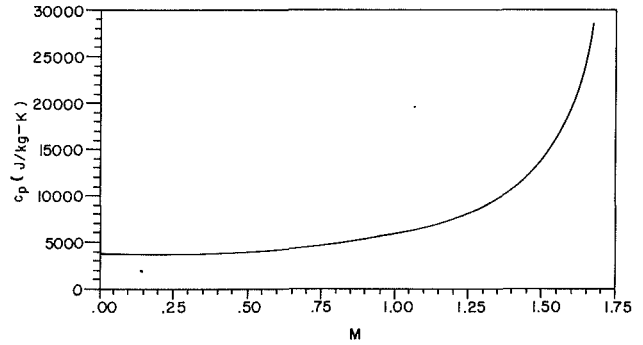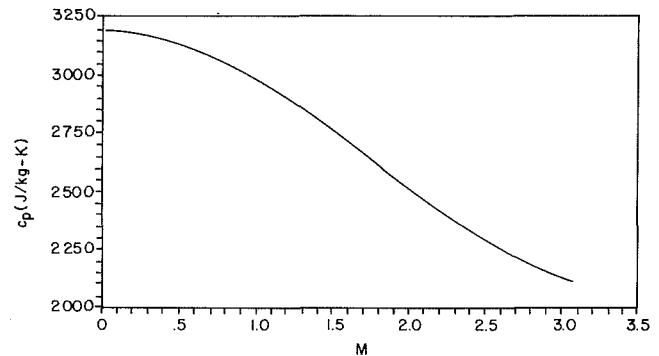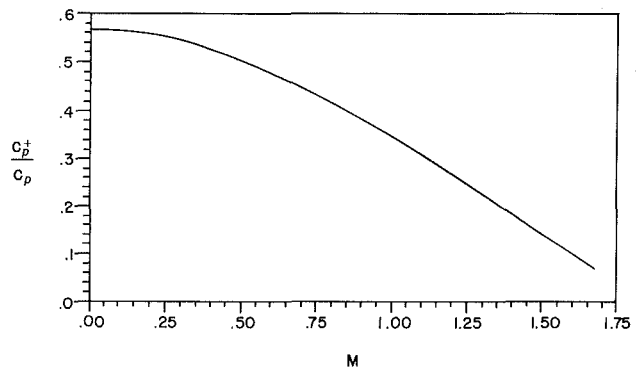
3,191 J/kg-K at M = 0.0 to 2,125 J/kg-K at M = 3.0.

Plots of c_p^+/c_p versus M are given in Figs. 10 and 11. This ratio is a measure of the contribution of the zero pressure specific heat to the overall value of c_p (see equation (33)). A low ratio value implies a small contribution from the zero pressure term to the overall value. Pressure (or density) effects on c_p are introduced from the third and fourth terms on the right hand side of equation (33). For the high pressure case, these terms contribute approximately 43 percent to its overall value at M = 0.0, where c_p = 3,759 J/kg-K and 93 percent at M = 1.67, where c_p = 28,000 J/kg-K.

The most common and simplest engineering model for an arbitrary isentropic real or perfect gas flow is the polytrope model [2] represented by $p\tilde{v}^n$ = constant, where the exponent, $n = \rho c^2/p$. Figures 12 and 13 are plots of n versus M. From these figures, it can be seen that for the high pressure case n varied from 2.89 at M = 0.0 to 1.94 at M = 1.67. For the low pressure case, n varied from 1.21 at M = 0.0 to 1.32 at M = 3.0. For the high pressure case, the large variation in n would render the polytrope model a poor representation of the thermodynamic process that takes place.
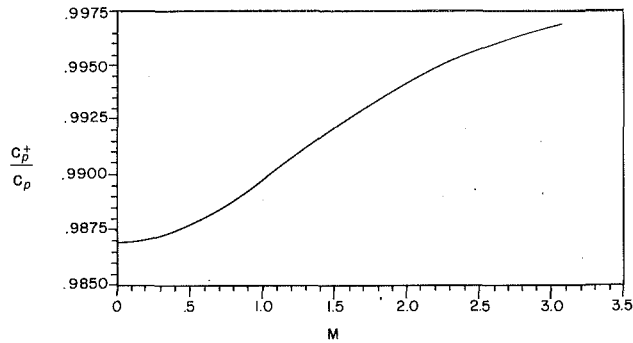
Fig. 11 Zero pressure c_p contribution to overall value versus Mach number (reservoir conditions: $(p_r)_0 = 0.8$, $(T_r)_0 = 3.0$)
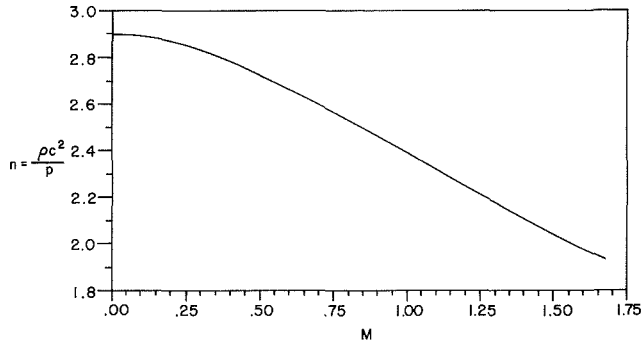

Fig. 13 Polytropic exponent versus Mach number (reservoir conditions: $(p_r)_0 = 0.8$, $(T_r)_0 = 3.0$)

Fig. 12 Polytropic exponent versus Mach number (reservoir conditions: $(p_r)_0 = 5.0$, $(T_r)_0 = 1.4$)

Fig. 14 Nondimensional mass flow rate per unit exit area (reservoir conditions: $(p_r)_0 = 5.0$, $(T_r)_0 = 1.4$, $k_0 = 1.884$)

Finally, the tables developed by the program would provide the means for determining such items as: (a) the maximum back pressure that will choke the nozzle, assuming that the ratio of the exit area to the throat area is known; and (b) the mass flow rate per unit throat area, if the back pressure is known. A plot of the nondimensionalized mass flow rate per unit exit area versus the ratio of the exit pressure to the reservoir pressure is given for a converging nozzle in Fig. 14. Curves for both the nonideal gas and the ideal gas are given. For the reservoir conditions indicated in that figure, the nozzle becomes choked at an exit pressure ratio of 0.4060 for the nonideal gas. For the ideal gas ($k_0 = 1.884$), the nozzle becomes choked at an exit pressure ratio of 0.4584, a difference of 12.9 percent. From the figure it can be seen that the maximum difference in the mass flow rates per unit exit area computed by the two different methods occurs at the critical pressure ratio (the choked condition). The percent difference in the choked mass flow rates per unit exit area is 18.8 percent. However, for the lower reservoir pressure case covered in this study, the percent difference in the choked mass flow rates per unit exit area is of the order of 0.14 percent.

Conclusions

A method for treating nonideal gas flows through converging-diverging nozzles was formulated. According to the numerical results, there exists a range of flow conditions that require a gas to be treated as nonideal if an accurate solution is to be obtained. The experience obtained by the authors in dealing with the nonideal gas aspects of this problem will be invaluable to their ultimate goal of developing a method for treating nonideal gas flows through orifices and control valves.

References

1 Fagerlund, A. C., and Winkler, R. J., "The Effect of Non-ideal Gases on Valve Sizing," *Adv. Instrum.*, Vol. 37, No. 3, 1982, pp. 1323-1333.

2 Sullivan, D. A., "Historical Review of Real-Fluid Isentropic Flow Models," JOURNAL OF FLUIDS ENGINEERING, Vol. 103, 1981, pp. 258-266.
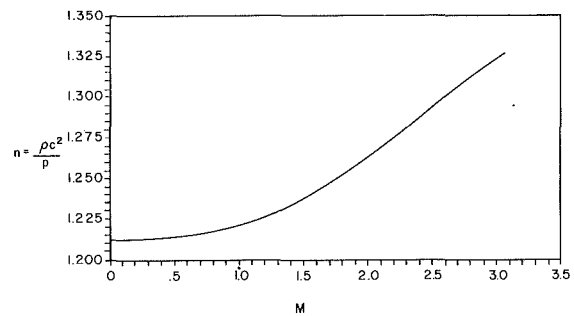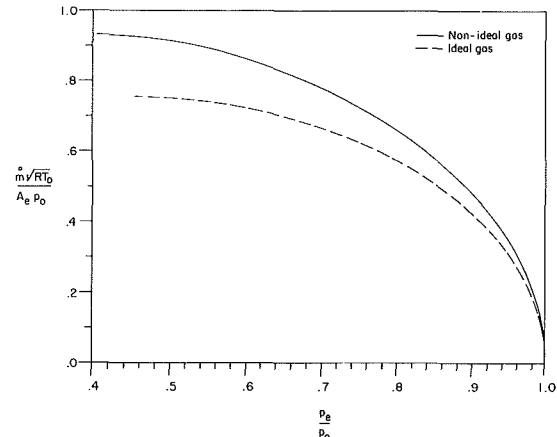
3 Chow, W. L., Ting, A. L., and Psai, P. H., "Discharge from a Vessel Through an Axisymmetric Control Valve," ASME *Journal of Applied Mechanics*, Vol. 54, 1987, pp. 447-452.

4 Weng, Z. M., Ting, A. L., and Chow, W. L., "Discharge of a Compressible Fluid Through a Control Valve," ASME *Journal of Applied Mechanics*, Vol. 54, 1987, pp. 955-960.

5 Bober, W., and Kenyon, R. A., *Fluid Mechanics*, Wiley, New York, 1980.

6 Shapiro, A. H., *The Dynamics and Thermodynamics of Compressible Fluid Flow*, Ronald Press, New York, 1953.

7 Tsien, H. S., "One-Dimensional Flows of a Gas Characterized by Van Der Waal's Equation of State," *J. Math. Phys.*, Vol. 25, 1947, p. 301-317.

8 Wark, K., Jr., *Thermodynamics*, McGraw-Hill, New York, 1988.

9 Starling, K. E., *Fluid Thermodynamic Properties for Light Petroleum Systems*, Gulf Publishing Co., Houston, TX, 1973.

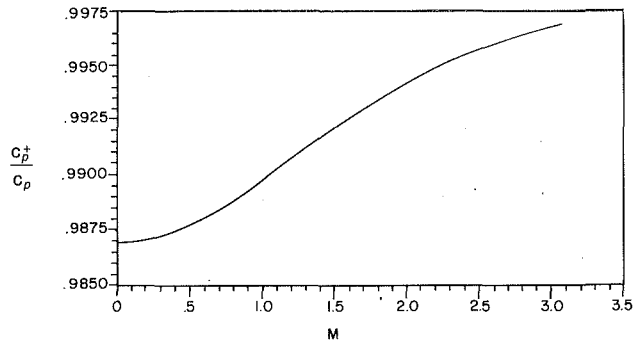10 Keenan, J. H., Keyes, F. G., Hill, P. G. and Moore, J. G., *Steam Tables*, Wiley, New York, 1978.

Fig. 11 Zero pressure c_p contribution to overall value versus Mach number (reservoir conditions: $(p_r)_0 = 0.8$, $(T_r)_0 = 3.0$)
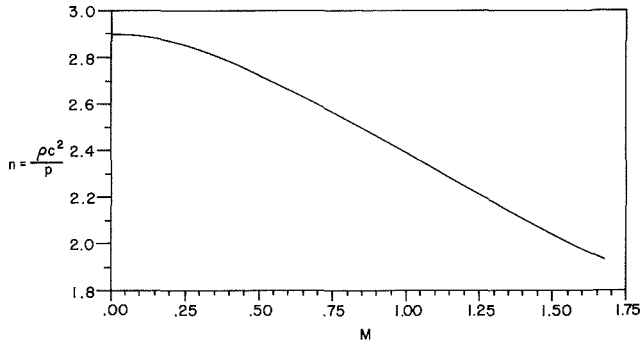

Fig. 13 Polytropic exponent versus Mach number (reservoir conditions: $(p_r)_0 = 0.8$, $(T_r)_0 = 3.0$)

Fig. 12 Polytropic exponent versus Mach number (reservoir conditions: $(p_r)_0 = 5.0$, $(T_r)_0 = 1.4$)

Fig. 14 Nondimensional mass flow rate per unit exit area (reservoir conditions: $(p_r)_0 = 5.0$, $(T_r)_0 = 1.4$, $k_0 = 1.884$)

Finally, the tables developed by the program would provide the means for determining such items as: (a) the maximum back pressure that will choke the nozzle, assuming that the ratio of the exit area to the throat area is known; and (b) the mass flow rate per unit throat area, if the back pressure is known. A plot of the nondimensionalized mass flow rate per unit exit area versus the ratio of the exit pressure to the reservoir pressure is given for a converging nozzle in Fig. 14. Curves for both the nonideal gas and the ideal gas are given. For the reservoir conditions indicated in that figure, the nozzle becomes choked at an exit pressure ratio of 0.4060 for the nonideal gas. For the ideal gas ($k_0 = 1.884$), the nozzle becomes choked at an exit pressure ratio of 0.4584, a difference of 12.9 percent. From the figure it can be seen that the maximum difference in the mass flow rates per unit exit area computed by the two different methods occurs at the critical pressure ratio (the choked condition). The percent difference in the choked mass flow rates per unit exit area is 18.8 percent. However, for the lower reservoir pressure case covered in this study, the percent difference in the choked mass flow rates per unit exit area is of the order of 0.14 percent.

Conclusions

A method for treating nonideal gas flows through converging-diverging nozzles was formulated. According to the numerical results, there exists a range of flow conditions that require a gas to be treated as nonideal if an accurate solution is to be obtained. The experience obtained by the authors in dealing with the nonideal gas aspects of this problem will be invaluable to their ultimate goal of developing a method for treating nonideal gas flows through orifices and control valves.

References

1 Fagerlund, A. C., and Winkler, R. J., "The Effect of Non-ideal Gases on Valve Sizing," Adv. Instrum., Vol. 37, No. 3, 1982, pp. 1323–1333.
2 Sullivan, D. A., "Historical Review of Real-Fluid Isentropic Flow Models," JOURNAL OF FLUIDS ENGINEERING, Vol. 103, 1981, pp. 258–266.
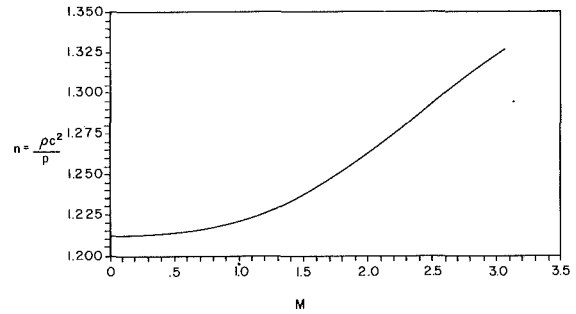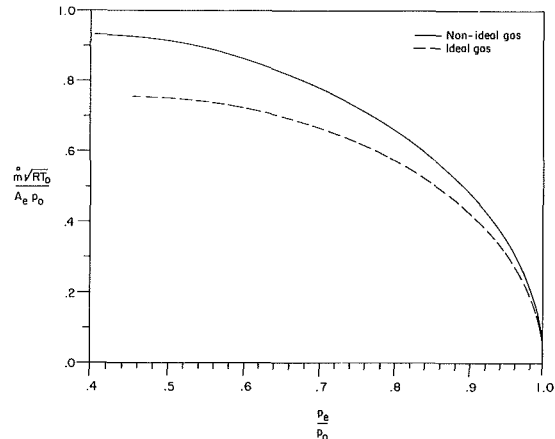
3 Chow, W. L., Ting, A. L., and Psai, P. H., "Discharge from a Vessel Through an Axisymmetric Control Valve," ASME Journal of Applied Mechanics, Vol. 54, 1987, pp. 447–452.
4 Weng, Z. M., Ting, A. L., and Chow, W. L., "Discharge of a Compressible Fluid Through a Control Valve," ASME Journal of Applied Mechanics, Vol. 54, 1987, pp. 955–960.
5 Bober, W., and Kenyon, R. A., Fluid Mechanics, Wiley, New York, 1980.
6 Shapiro, A. H., The Dynamics and Thermodynamics of Compressible Fluid Flow, Ronald Press, New York, 1953.
7 Tsien, H. S., "One-Dimensional Flows of a Gas Characterized by Van Der Waal's Equation of State," J. Math. Phys., Vol. 25, 1947, p. 301–317.
8 Wark, K., Jr., Thermodynamics, McGraw-Hill, New York, 1988.
9 Starling, K. E., Fluid Thermodynamic Properties for Light Petroleum Systems, Gulf Publishing Co., Houston, TX, 1973.
10 Keenan, J. H., Keyes, F. G., Hill, P. G. and Moore, J. G., Steam Tables, Wiley, New York, 1978.

———————————— D I S C U S S I O N ————————————

Marcel Vinokur[1]

The method for treating nonideal isentropic gas flows described by Bober and Chow can be simplified and also generalized to a larger class of equations of state. Let the thermal equation of state be given by

$$p = \sum_n f_n(T)g_n(\bar{v}), \qquad (37)$$

where the $f_n(T)$ are twice differentiable analytic functions of

[1]Sterling Software, Palo Alto, CA 94303.

T and the $g_n(\tilde{v})$ are differentiable and also integrable in closed form, subject to the restriction that

$$p \to RT/\tilde{v} \text{ as } \tilde{v} \to \infty. \tag{38}$$

All known analytic empirical thermal equations of state satisfy these conditions. From equation (37) one obtains

$$\left(\frac{\partial s}{\partial \tilde{v}}\right)_T = \left(\frac{\partial p}{\partial T}\right)_{\tilde{v}} = \sum_n f_n'(T)g_n(\tilde{v}), \tag{39}$$

and

$$\left(\frac{\partial p}{\partial \tilde{v}}\right)_T = \sum_n f_n(T)g_n'(\tilde{v}). \tag{40}$$

The caloric equation of state is obtained in terms of the zero pressure specific heat at constant volume $c_{\tilde{v}}^+(T)$, where $c_{\tilde{v}}^+(T)$ and $c_{\tilde{v}}^+(T)/T$ are both integrable in closed form. The caloric equation of state can then be written as

$$u = u^+(T) + \sum_n [Tf_n'(T) - f_n(T)] \int_\infty^v g_n(\tilde{v})d\tilde{v}, \tag{41}$$

where the zero pressure internal energy $u^+(T)$ is given by

$$u^+(T) = \int_0^T c_{\tilde{v}}^+(T)dT. \tag{42}$$

The corresponding expression for $c_{\tilde{v}}$ is

$$c_{\tilde{v}} = c_{\tilde{v}}^+(T) + T\sum_n f_n''(T) \int_\infty^v g_n(\tilde{v})d\tilde{v}. \tag{43}$$

The speed of sound c can then be determined from

$$c^2 = -\tilde{v}^2 \left[\left(\frac{\partial p}{\partial \tilde{v}}\right)_T - \frac{T}{c_{\tilde{v}}}\left(\frac{\partial p}{\partial T}\right)_{\tilde{v}}^2 \right]. \tag{44}$$

The specific heat at constant pressure c_p is most simply calculated from

$$c_p = -\frac{c_{\tilde{v}}c^2}{\tilde{v}^2\left(\dfrac{\partial p}{\partial \tilde{v}}\right)_T}. \tag{45}$$

The entropy can be obtained by integrating equation (38). It can be expressed as

$$s = s(T_0, \tilde{v}_0) + s^+(T) - s^+(T_0)$$
$$+ \sum_n \left[f_n'(T) \int_\infty^v g_n(\tilde{v})d\tilde{v} - f_n'(T_0) \int_\infty^{v_0} g_n(\tilde{v})d\tilde{v} \right], \tag{46}$$

where $s^+(T)$ is given by the indefinite integral

$$s^+(T) = \int \frac{c_{\tilde{v}}^+(T)}{T} dT, \tag{47}$$

and T_0, $\tilde{v}_0$ is some arbitrary reference state.

For isentropic flow from a reservoir with T_0 and p_0 given, the corresponding value of $\tilde{v}_0$ would in general be obtained from equations (37) and (40) using Newton's iteration. Instead of integrating

$$\left(\frac{\partial T}{\partial \tilde{v}}\right)_s = -\frac{T}{c_{\tilde{v}}}\left(\frac{\partial p}{\partial T}\right)_{\tilde{v}} \tag{48}$$

to obtain $T(\tilde{v})$, as is done in the discussed paper, it is much simpler to solve for $T(\tilde{v})$ (or $\tilde{v}(T)$) using Newton's iteration from equation (46) by setting

$$s - s(T_0, \tilde{v}_0) = 0. \tag{49}$$

The choice of $\tilde{v}$ or T as independent variable depends on the nature of equation (37) and the function $c_{\tilde{v}}^+(T)$. For the particular equations of Bober and Chow, the equation relating T and $\tilde{v}$ can be written as

$$s^+(T) - s^+(T_0) + R\ln\left(\frac{\tilde{v} - b}{\tilde{v}_0 - b}\right)$$
$$+ \frac{a}{2b}\left[T_0^{-3/2}\ln\left(1 + \frac{b}{\tilde{v}_0}\right) - T^{-3/2}\ln\left(1 + \frac{b}{\tilde{v}}\right) \right] = 0, \tag{50}$$

where

$$s^+(T) =$$
$$R\left[(A_0 - 1)\ln T + A_1 T + \frac{1}{2} A_2 T^2 + \frac{1}{3} A_3 T^3 + \frac{1}{4} A_4 T^4 \right]. \tag{51}$$

For this case it would appear to be more efficient to choose T as the independent variable.

Acknowledgment

Authors' Closure

The authors would like to thank Dr. Vinokur for his eloquent generalization of the thermodynamics involved in the problem of a "Nonideal Isentropic Gas Flow Through Converging-Diverging Nozzles." In fact, as a result of his review, we were able to simplify our original version of the paper. In a more recent paper, one entitled, "Nonideal Gas Effects for the Venturi Meter," our approach follows more closely the method that is outlined in his Comment.

T and the $g_n(\tilde{v})$ are differentiable and also integrable in closed form, subject to the restriction that

$$p \rightarrow RT/\tilde{v} \quad \text{as} \quad \tilde{v} \rightarrow \infty. \tag{38}$$

All known analytic empirical thermal equations of state satisfy these conditions. From equation (37) one obtains

$$\left(\frac{\partial s}{\partial \tilde{v}}\right)_T = \left(\frac{\partial p}{\partial T}\right)_{\tilde{v}} = \sum_n f'_n(T) g_n(\tilde{v}), \tag{39}$$

and

$$\left(\frac{\partial p}{\partial \tilde{v}}\right)_T = \sum_n f_n(T) g'_n(\tilde{v}). \tag{40}$$

The caloric equation of state is obtained in terms of the zero pressure specific heat at constant volume $c_{\tilde{v}}^+(T)$, where $c_{\tilde{v}}^+(T)$ and $c_{\tilde{v}}^+(T)/T$ are both integrable in closed form. The caloric equation of state can then be written as

$$u = u^+(T) + \sum_n [Tf'_n(T) - f_n(T)] \int_\infty^v g_n(\tilde{v}) d\tilde{v}, \tag{41}$$

where the zero pressure internal energy $u^+(T)$ is given by

$$u^+(T) = \int_0^T c_{\tilde{v}}^+(T) dT. \tag{42}$$

The corresponding expression for $c_{\tilde{v}}$ is

$$c_{\tilde{v}} = c_{\tilde{v}}^+(T) + T \sum_n f''_n(T) \int_\infty^v g_n(\tilde{v}) d\tilde{v}. \tag{43}$$

The speed of sound c can then be determined from

$$c^2 = -\tilde{v}^2 \left[\left(\frac{\partial p}{\partial \tilde{v}}\right)_T - \frac{T}{c_{\tilde{v}}} \left(\frac{\partial p}{\partial T}\right)_{\tilde{v}}^2 \right]. \tag{44}$$

The specific heat at constant pressure c_p is most simply calculated from

$$c_p = -\frac{c_{\tilde{v}} c^2}{\tilde{v}^2 \left(\dfrac{\partial p}{\partial \tilde{v}}\right)_T}. \tag{45}$$

The entropy can be obtained by integrating equation (38). It can be expressed as

$$s = s(T_0, \tilde{v}_0) + s^+(T) - s^+(T_0)$$
$$+ \sum_n \left[f'_n(T) \int_\infty^v g_n(\tilde{v}) d\tilde{v} - f'_n(T_0) \int_\infty^{v_0} g_n(\tilde{v}) d\tilde{v} \right], \tag{46}$$

where $s^+(T)$ is given by the indefinite integral

$$s^+(T) = \int \frac{c_{\tilde{v}}^+(T)}{T} dT, \tag{47}$$

and T_0, $\tilde{v}_0$ is some arbitrary reference state.

For isentropic flow from a reservoir with T_0 and p_0 given, the corresponding value of $\tilde{v}_0$ would in general be obtained from equations (37) and (40) using Newton's iteration. Instead of integrating

$$\left(\frac{\partial T}{\partial \tilde{v}}\right)_s = -\frac{T}{c_{\tilde{v}}} \left(\frac{\partial p}{\partial T}\right)_{\tilde{v}} \tag{48}$$

to obtain $T(\tilde{v})$, as is done in the discussed paper, it is much simpler to solve for $T(\tilde{v})$ (or $\tilde{v}(T)$) using Newton's iteration from equation (46) by setting

$$s - s(T_0, \tilde{v}_0) = 0. \tag{49}$$

The choice of $\tilde{v}$ or T as independent variable depends on the nature of equation (37) and the function $c_{\tilde{v}}^+(T)$. For the particular equations of Bober and Chow, the equation relating T and $\tilde{v}$ can be written as

$$s^+(T) - s^+(T_0) + R \ln\left(\frac{\tilde{v} - b}{\tilde{v}_0 - b}\right)$$
$$+ \frac{a}{2b} \left[T_0^{-3/2} \ln\left(1 + \frac{b}{\tilde{v}_0}\right) - T^{-3/2} \ln\left(1 + \frac{b}{\tilde{v}}\right) \right] = 0, \tag{50}$$

where

$$s^+(T) =$$
$$R\left[(A_0 - 1)\ln T + A_1 T + \frac{1}{2} A_2 T^2 + \frac{1}{3} A_3 T^3 + \frac{1}{4} A_4 T^4 \right]. \tag{51}$$

For this case it would appear to be more efficient to choose T as the independent variable.

Acknowledgment

Authors' Closure

The authors would like to thank Dr. Vinokur for his eloquent generalization of the thermodynamics involved in the problem of a "Nonideal Isentropic Gas Flow Through Converging-Diverging Nozzles." In fact, as a result of his review, we were able to simplify our original version of the paper. In a more recent paper, one entitled, "Nonideal Gas Effects for the Venturi Meter," our approach follows more closely the method that is outlined in his Comment.

Hisashi Matsuda

Research & Development Center,
Toshiba Corporation,
Kawasaki 210, Japan

Sei-ichi Iida

Professor.

Michio Hayakawa

Research Instructor.

Department of Mechanical Engineering II,
Hokkaido University,
N13 W8, Sapporo 060, Japan

Coherent Structures in a Three-Dimensional Wall Jet

The formation mechanism of streamwise vortices in the near field of the three-dimensional wall jet discharging from a circular nozzle along a flat plate is studied experimentally using a conditional sampling technique. Ensemble-averages of the lateral velocity component indicate the presence of large-scale horseshoe-like structures, whose legs are inclined and stretched to form the streamwise vortices in the mixing region of the jet. Based on the present result, a coherent structure model for the near field of the wall jet is proposed.

1 Introduction

The three-dimensional turbulent jet discharging over a solid wall (hereinafter termed as "the 3D wall jet") has attracted much attention from numerous researchers because of its relevance to many practical applications. However, there have been few investigations which are concerned with coherent structures of this flow, in comparison to other (unbounded) jet flows.

As to the near field, Sforza and Herbst (1970) inferred the existence of horseshoe vortices, from irregularities in the lateral direction of the mean streamwise velocity. Morton et al. (1978) demonstrated the presence of organized structures by means of the concentration spectrum analysis and the two-point space-time correlation technique, but did not address either the spatial geometry or the streamwise evolution of those structures. For the far field, Davis and Winarto (1980) found large-scale motion in the plane perpendicular to the main flow, through velocity correlation measurements. They suggested that this motion contributed to the significantly large spreading rate of the flow in the lateral direction, which is one of the prominent features of the 3-D wall jet.

Recently, we made a comparative study of 3-D jets discharging from a circular nozzle over a flat wall and a convex wall, and obtained clear evidence for the presence of secondary flows (Iida and Matsuda, 1988). Equicontours of the mean streamwise vorticity $\Omega_X (= \partial W/\partial Y - \partial V/\partial Z)$ for the flatwall case are reproduced in Fig. 1. Here, the coordinates are designated as X, Y, and Z in the streamwise, vertical (perpendicular to the wall) and lateral direction, respectively, and the corresponding mean velocity components are U, V, and W. Broken and solid lines indicate positive (clockwise, when viewed from the upstream side) and negative (counterclockwise) Ω_X, respectively, and dotted lines indicate the vertical position Y_m of the local maximum mean velocity U_m at each Z section. Contour levels of vorticity are nondimensionalized by U_m (at $Z=0$) and the nozzle diameter D. Since the flow is symmetrical with respect to $Z=0$, it is apparent that two pairs of streamwise
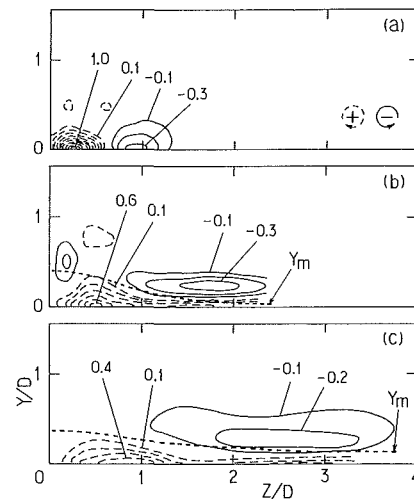

Fig. 1 Equicontours of mean streamwise vorticity; values are nondimensionalized by U_m and D. (a) $X/D = 5$, (b) $X/D = 10$, (c) $X/D = 15$.

vortices exist in the present flowfield. One pair is located in the wall region ($Y < Y_m$) of the central portion of the jet and the other pair is in the mixing region ($Y > Y_m$).

This result and the observation of Davis and Winarto suggest that streamwise vortices should play important roles in the development of the 3-D wall jet. In this respect, Launder and Rodi (1983) reviewed earlier works and made elaborate discussion on the generation mechanism of streamwise vorticity in the 3-D wall jet. However, their qualitative argument has remained speculative due to limited experimental information.

The purpose of the present study was to reveal quantitatively the formation mechanism of the streamwise vortices observed by our previous work (Fig. 1). Our basic idea was that nominally azimuthal structures occurring in the mixing layer, as in the unconfined jet (e.g., Crow and Champagne, 1971), would be distorted as they advect downstream and form the streamwise vortices. Thus, adopting a conditional sampling technique to the near field of the 3-D wall jet, we have obtained the ensemble-averaged velocity field in the plane perpendicular to
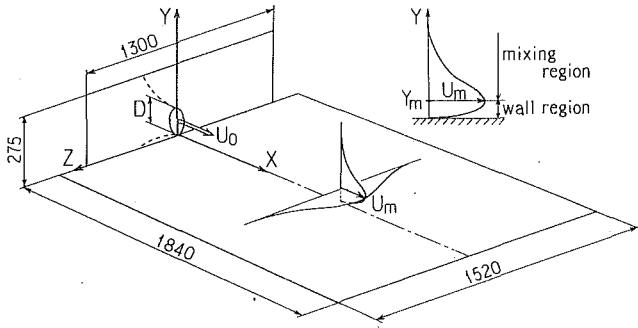
Fig. 2 Experimental arrangement and main notation

the main flow and examined relationships between the azimuthal structures and the streamwise vortices.

2 Experimental Apparatus

The experiment was carried out in a low-speed air jet facility. The nozzle diameter was 50 mm, and the area contraction ratio of the nozzle was 17.6. A 5 mm-thick flat plate of 1840 mm length and 1520 mm width was aligned tangentially (with no offset) to the inner surface of the nozzle. There was no gap between the nozzle exit and the upstream end of the plate. A large flange (1300 mm $\times$ 275 mm) was attached at the exit plane so that the development of the jet was free from ambiguous effects of the nozzle thickness and disturbances from the upstream side of the exit plane. The experimental arrangement is schematically shown in Fig. 2, which also includes the main notation to be used.

All measurements were performed at a Reynolds number (based on exit velocity and nozzle diameter) of 1.6×10^5. This corresponds to the exit velocity U_0 of about 48 m/s. At this speed, the exit turbulence level measured on the nozzle axis was 0.6 percent. The initial boundary layer was laminar, and its thickness was approximately 1 mm.

Velocity measurements were made with a home-made hot-wire anemometer set. To perform conditional sampling measurements, two hot-wire probes were used: one was a single-wire for a reference probe and the other a cross-wire for a sampling probe. Each wire element was 1 mm in length and 5 μm in diameter. The two probes were movable independently of each other via three-dimensional traversing mechanisms. In order to minimize probe interference, the reference probe and the sampling probe were inserted in the direction parallel to the Z-axis and the Y-axis, respectively.

Velocity signals were recorded by an analog data recorder (TEAC R-210A), and then processed digitally by a mini-computer (MELCOM 70/25). The sampling rate of the A/D conversion for each channel of the records was 4.5 KHz. Hot-

wire calibration was made at the exit section of the jet, using a standard Pitot tube connected to an alcohol-filled manometer of the minimum reading of 0.05 mm. The calibration was done approximately every one hour, and the second-order polynomial fitting was used for the voltage-to-velocity conversion. The error of the velocity calculation was estimated to be within 2 percent for the velocity range larger than approximately 0.02 U_0.

Since the symmetry of the mean velocity field with respect to the jet centerplane had been confirmed in the same facility, all data presented below were taken only in the half domain ($Z \geq 0$) of the jet. Throughout this paper, "the wall region" denotes the region between the wall ($Y = 0$) and the vertical position Y_m, and "the mixing region" denotes the region outside of Y_m (Fig. 2).

3 Technique and Procedures

To perform conditional sampling measurements in natural flows, some suitable condition for trigger must be determined. For the free jet, it has been well-known that periodic structures occur in the potential core region, signatures of which are identified by the streamwise velocity fluctuations at the high-speed edge of the mixing layer (Yule, 1978; Brunn, 1979; Zaman and Hussain, 1984). It can be expected that a similar feature should exist in the present jet, at least in the region away from the wall.

In order to check this feature, we measured first the frequency spectrum of streamwise velocity fluctuations u'. Figure 3 shows the streamwise variation of the velocity spectrum on the jet centerplane ($Z = 0$). The vertical position is $\eta = (Y - D)/X = -0.15$, which corresponds to the optimal position for capturing the signatures of structures in the free jet case (e.g., Bruun, 1977). It is readily seen that after the transitional behavior with sharp peaks near the jet exit, the spectrum shows a clear hump in $X/D = 1.5 \sim 4$. The Strouhal number ($f_p D/U_0$) of the center frequency f_p of the hump at $X/D = 3$ is about 0.4, the value being consistent with the preferred mode of the free jet (Ho and Hurre, 1984). A quite similar result was also obtained at both lateral sides of the jet, i.e., at $Y/D = 0.5$ and $(r - D/2)/X = -0.15$. Here, r is the radial distance from the nozzle axis.

These results imply that the evolution of quasi-periodic structures in the upper region of the jet ($Y/D \gtrsim 0.5$) is not substantially affected by the presence of the wall within the streamwise range covered by the present experiment. Figure 4 shows the vertical variation of the spectrum at $X/D = 1.75$, where the remnant of the transitional behavior of the spectrum has disappeared (Fig. 3). The clear spectrum hump is observed in $\eta = -0.15 \sim -0.4$ ($Y/D = 0.74 \sim 0.30$). Based on these spectrum analyses, we determined to adopt as the detection signal, the streamwise velocity fluctuations u' at $X/D = 1.75$,

---

Nomenclature

D	=	nozzle diameter	W	=	time-mean value of velocity component in Z direction
Re	=	Reynolds number	X	=	streamwise distance from nozzle exit
T	=	time with respect to trigger instant	ΔX	=	$U_{ph} \Delta T$
ΔT	=	zero-cross time of $<w_c>$	Y	=	vertical distance from wall
U	=	time-mean value of velocity component in X direction	Y_m	=	Y at $U = U_m$
U_m	=	local maximum value of U	Z	=	lateral distance from jet centerplane
U_0	=	jet exit velocity	f	=	frequency of velocity fluctuations
U_{ph}	=	phase velocity of large-scale structure	f_p	=	center frequency of spectral hump
V	=	time-mean value of velocity component in Y direction	r	=	radial distance from nozzle axis

u	=	instantaneous streamwise velocity component
w	=	instantaneous lateral velocity component
$<w_c>$	=	$<w> - W$
Ω_X	=	time-mean streamwise vorticity
η	=	$(Y - D)/X$
θ	=	azimuthal angle
σ	=	rms value of detection signal
τ	=	time shift of ΔT in streamwise direction
$< >$	=	ensemble average

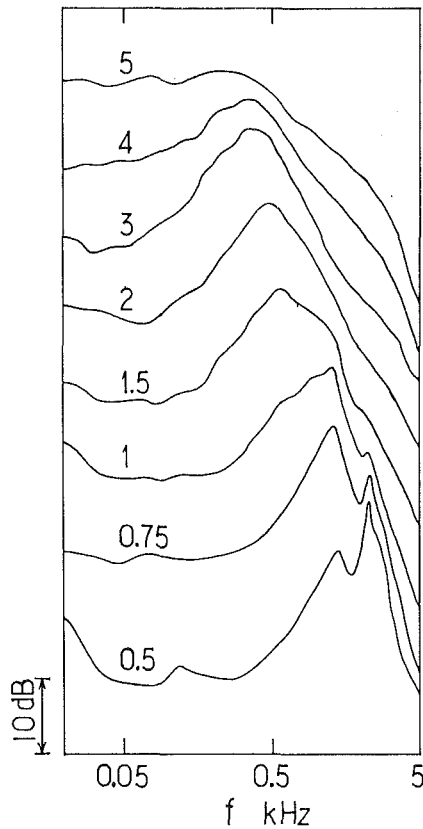Fig. 3 Spectra of u-fluctuations for different X stations ($\eta = -0.15$, $Z = 0$); numbers denote X/D

Fig. 4 Spectra of u-fluctuations for different Y positions ($X/D = 1.75$); numbers denote η

$Y/D = 0.5$, and $Z/D = 0$ (except for the data shown in Fig. 7). Following earlier studies of the free jet (Brunn, 1977; Zaman and Hussain, 1984), the detection criterion was assigned such that u' was greater than 2σ, σ being the rms value of u'.

The lateral velocity component w was used as the eduction signal because our primary interest was to find a possible relationship between the nominally azimuthal structures in the mixing layer and the streamwise vortices. The ensemble averages of w, associated with the passage of structures in the mixing layer, were obtained at various positions in the flowfield. The number of events for averaging was 1000.

An example of the ensemble averages of the detection signal u and the eduction signal w is shown in Fig. 5. Here, $<u_c>= <u> - U$ and $<w_c> = <w> - W$; $<\ >$ means the ensemble average. Time increases from left to right, and the trigger instant is denoted as $T = 0$. The number of structures which satisfied the detection criterion was approximately 20 percent of the total number of passing structures, that has been estimated from the center frequency (450 Hz) of the spectral hump at the detection location.

4 Results and Discussion

Figures 6(a) and 6(b) present the ensemble averages of w obtained at $X/D = 1.75$ for $Y/D > 0.5$ and $Y/D \leq 0.5$, respectively. Each velocity trace includes $<w_c>$ for a duration of about 3.5 ms, and vertical lines denote the trigger instant ($T = 0$). For reference, the sectional contour of the nozzle (i.e., $r/D = 0.5$) is depicted by a dotted line. Over a wide extent in the Y–Z plane, $<w_c>$ shows a characteristic temporal variation which changes from a large positive value to a large negative value near the trigger instant. (Such a characteristic velocity pattern will be hereinafter termed as "the large $<w_c>$-variation" for simplicity.)

In the upper half region of the jet (Fig. 6(a)), the large $<w_c>$-variation at each meridian plane (including $\theta = 90$ deg
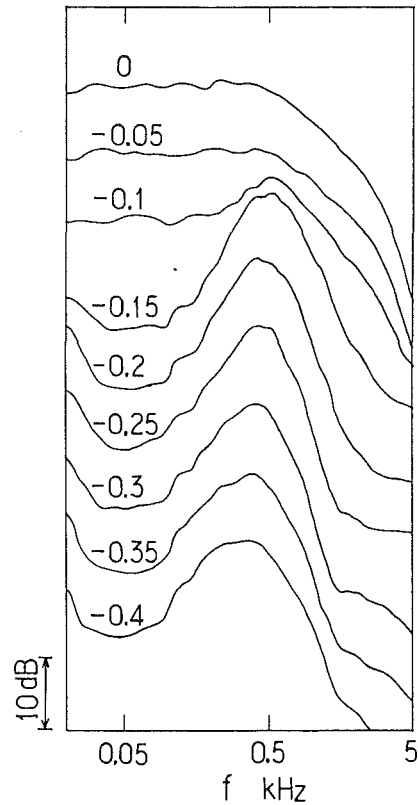
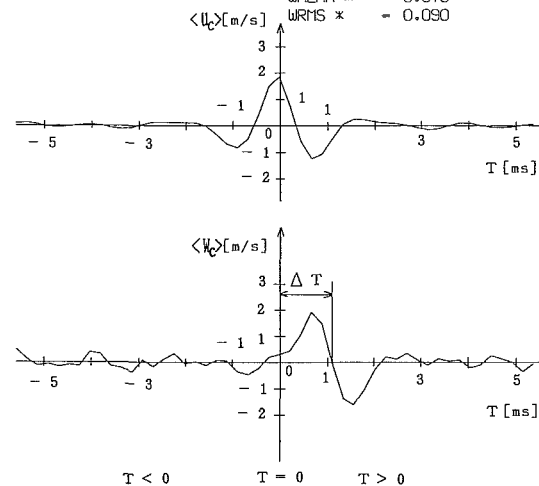

Fig. 5 An example of ensemble averages of detection signal and sampling signal. Measurement locations are ($X/D = 1.75$, $Y/D = 0.5$, $Z/D = 0$) for u and ($X/D = 2.4$, $Y/D = 0.04$, $Z/D = 0.24$) for w. (Uncertainty in $<u_c> = \pm 2$ percent, in $<w_c> = \pm 4$ percent, in $T = \pm 0.017$ ms.)

in Fig. 6(b)) has a maximum amplitude at $r/D = 0.4 \sim 0.6$, suggesting the presence of a vortex-ring-like structure in this region. Note that the amplitude is smaller at $\theta = 0$ deg and 22.5 deg. This is expected because the transverse velocity component of a ring-like structure should decrease in w and instead, increase in v with decreasing θ.

In the lower part of the jet (Fig. 6(b)), maxima of the $<w_c>$-variations are observed in the area surrounded by ($Y/D = 0.5$, $Z/D = 0.34 \sim 0.58$) and ($Y/D = 0.02$, $Z/D = 0.24 \sim 0.36$).

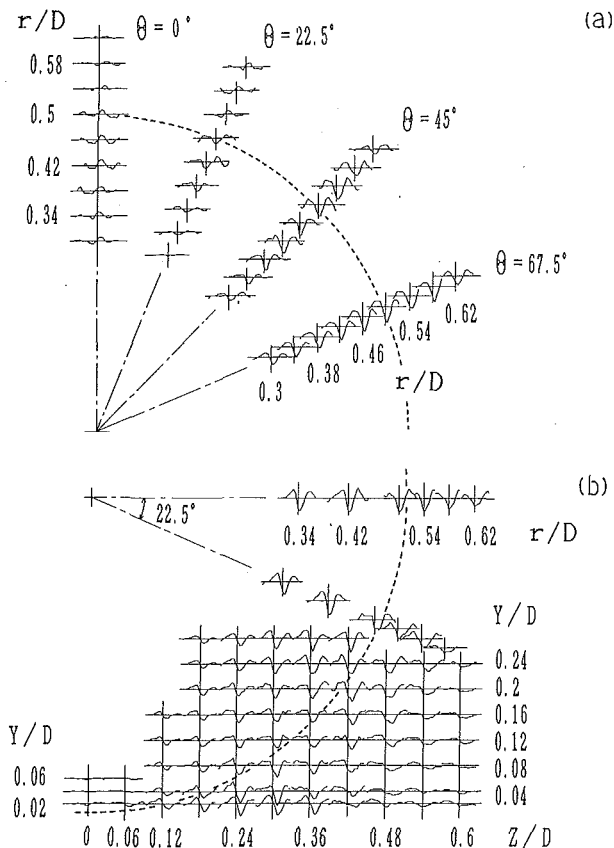Fig. 6 Ensemble averages $<w_c>$ in Y-Z plane at X/D = 1.75. (a) Y/D > 0.5, (b) $Y/D \leq$ 0.5.

Fig. 7 Vertical variation of zero-cross time of $<w_c>$. (a) X/D = 1.75, (b) X/D = 2.4, (c) X/D = 3.0. (Uncertainty in Y/D = ± 0.001, in ΔT = ± 0.1 ms.)

That is, the maxima occur not along a constant r line but in a limited z range in which the z-location of the maximum gradually moves toward the jet centerline as the distance from the wall decreases. This suggests that the shape of the structure in Y/D < 0.5 (including both sides of Z = 0) is not like a vortex ring but more like two vertical rollers; the distance between the rollers decreases with decreasing Y. Moreover, the zero-cross time at which $<w_c>$ changes from positive to negative, tends to delay near the wall.

Putting together the results of Fig. 6(a) and 6(b), the large-scale structure, on the average, seems to be similar to the horseshoe vortex, which is somewhat inclined in the streamwise direction near the wall.

Similar measurements were also made at X/D = 2.4 and 3.0; the reference probe was placed at the respective X positions on the nozzle axis. The results were essentially the same as Fig. 6. In Fig. 7, the zero-cross time ΔT of $<w_c>$ is plotted for the three X positions; for the definition of ΔT, see Fig. 5. Here, the large $<w_c>$-variations with a maximum amplitude at each Y location were selected to determine ΔT. The vertical variation of ΔT increases with increasing X/D.

In order to evaluate the spatial inclination of the structure, further measurements were performed at X/D = 2.1, 2.4 and 3.0 for the lower part of the jet, by fixing the reference probe at X/D = 1.75. The results are shown in Fig. 8(a–c). As the trigger instant being the same for all $<w_c>$ traces of Fig. 8 and 6(b), the duration τ during which the structure travels over the distance between successive X positions, is estimated from comparing the zero-cross time of $<w_c>$. This procedure yields approximately the local phase velocity of the structure, U_{ph}. Note that the large $<w_c>$-variations in Figs. 8 and 6(b) can be regarded as the events caused by a common structure because τ is always smaller than the mean passage interval of large-scale structures. For example, the zero-cross time ΔT at
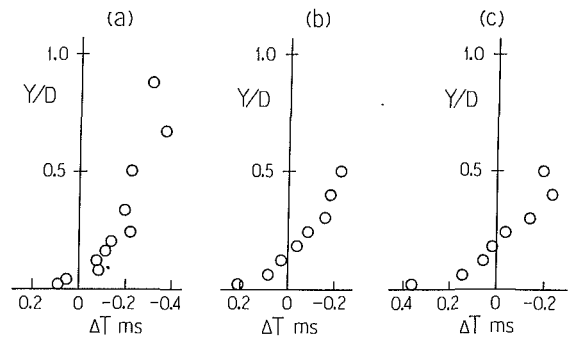
Y/D = 0.02 and Z/D = 0.3 is 0.09 ms at X/D = 1.75 and 2.1 ms at X/D = 3.0; hence the difference is less than 2.22 ms (= 1/450 Hz).

By using the local phase velocity thus obtained, the zero-cross time ΔT of Fig. 7 was transformed into the streamwise distance ΔX (= $U_{ph} \Delta T$), adopting Taylor's hypothesis. The result is shown in Fig. 9. The figure clearly shows that the structure inclination with respect to the Y-axis progressively increases with increasing X, especially in $Y/D \leq 0.1$.

The results of Figs. 6 and 9 imply that as they advect downstream, the horseshoe-like structures are inclined and stretched near the wall; thus, their legs should be observed as counter-rotating streamwise vortices when viewed in the Y–Z plane. Taking into account the direction of circulation of the structure, the inclined legs should correspond to the streamwise vortices in the mixing region, i.e., the secondary flow shown by solid lines in Fig. 1.

In order to confirm this correspondence, the vertical distributions of the mean velocity W were compared with those $<w_c>$. A typical example is shown in Fig. 10 for X/D = 1.75. The lateral position is Z/D = 0.3 where the secondary flow away from the centerplane toward the outer edge of the jet was observed most clearly at this X position. The intense W component is indeed closely related to the large $<w_c>$-variations which are associated with the horseshoe-like structures. Since the structures occur quasi-periodically, the strength of the secondary flow may not be constant in time but intensified in accordance with the passage of the structures.

Based on the present results, a coherent structure model for the nearfield 3-D wall jet (discharged from a round nozzle) is schematically shown in Fig. 11. As discussed above, solid lines indicate the horseshoe-like structure whose legs manifest themselves as the streamwise vortices in the mixing region, which appear to contribute to the considerably large, lateral spreading rate of the 3-D wall jet.

Signatures of the streamwise vortices in the wall region, corresponding to broken lines in Fig. 1, have not been identified by the present experiment. However, the mean velocity field in the wall region has always intense lateral vorticity (≃ $\partial U/\partial Y$) as well as moderately large vertical vorticity (≃ $\partial U/\partial Z$) with symmetry about the jet centerplane. Therefore, once the concentration of the lateral vorticity occurs, this would be easily bent and be subjected to rapid stretching in the streamwise direction. We conjecture that this would be the formation mechanism of the streamwise vortices in the wall region, as is schematically depicted by dotted lines in Fig. 11. However, it remains unclear whether these two pairs of vortices are basically independent of each other, or are parts of a single vortex loop.

5 Concluding Remarks

Motivated by our previous experimental evidence for the presence of a pair of streamwise vortices in an initially axi-
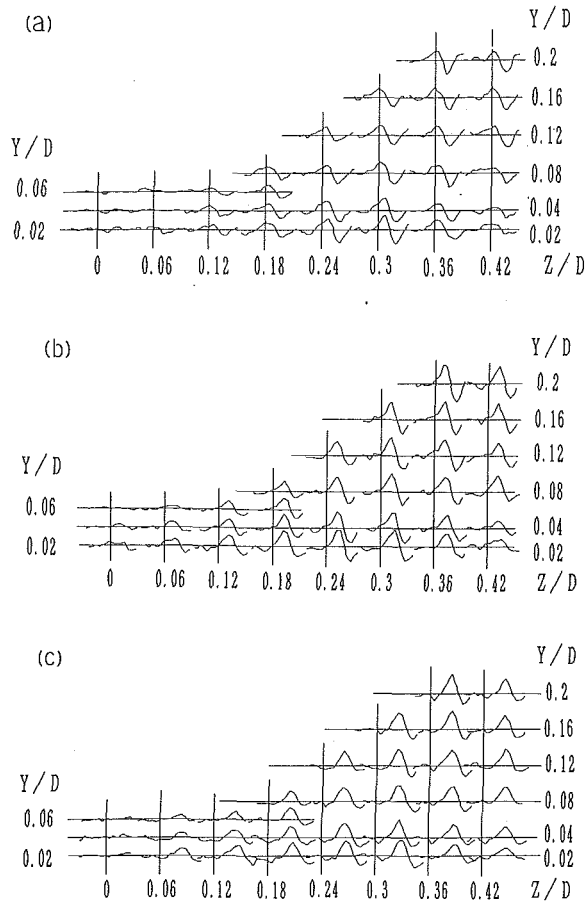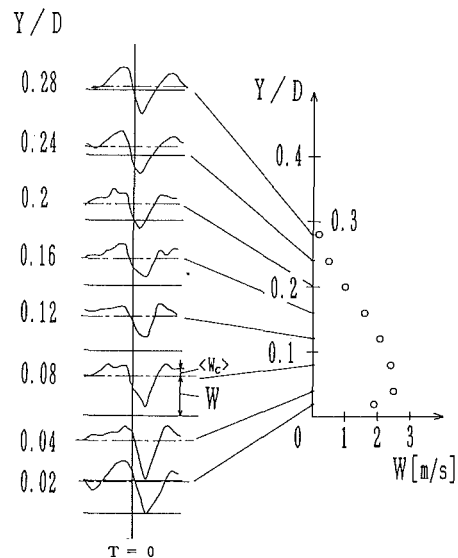
Fig. 8 Ensemble averages $<w_c>$ at three X stations; reference probe is fixed at (X/D = 1.75, Y/D = 0.5, Z/D = 0). (a) X/D = 2.1, (b) X/D = 2.4, (c) X/D = 3.0.
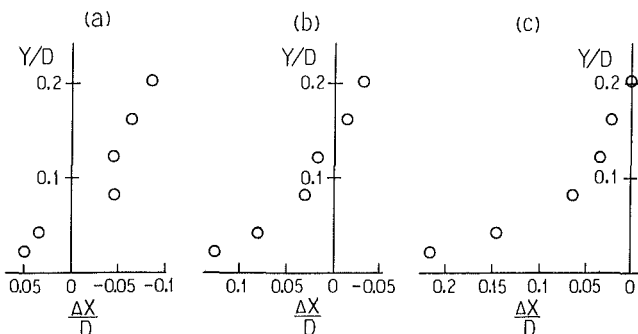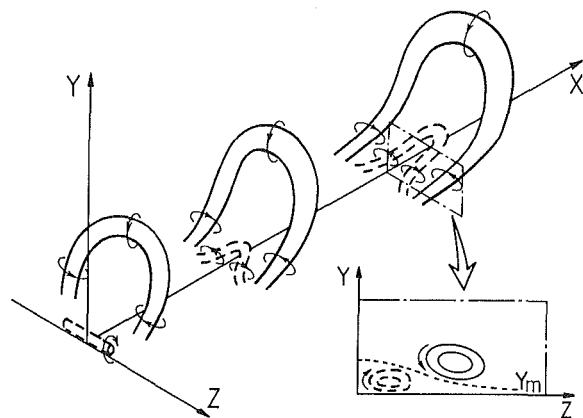

Fig. 9 Inclination of large-scale structure in X-Y plane. (a) X/D = 2.1, (b) X/D = 2.4, (c) X/D = 3.0. (Uncertainty in Y/D = ± 0.001, in $\Delta X/D$ = ± 0.04)

Fig. 10 Correspondence between $\langle w_c \rangle$ and time-mean value W(X/D = 1.75). (Uncertainty in Y/D = ± 0.001, in $\langle w_c \rangle$ and W = ± 4%)

Fig. 11 A conceptual model of coherent structures in the near region of a three-dimensional wall jet

symmetric wall jet, the formation mechanism of the vortices in the near field has been studied, by using a conditional sampling technique. Organized motion associated with the nominally azimuthal structures in the mixing layer has been educed as the characteristic temporal variation of the ensemble-averaged lateral velocity component over a wide extent in the flow. Detailed spatio-temporal information of this velocity variation enabled us to infer the configuration of the dominant large-scale structure.

The results suggest that the structure, on the average, has a shape similar to the horseshoe vortex which is inclined to the streamwise direction. Specifically, the structure was found to be progressively inclined near the wall as it advects downstream. This observation strongly suggests that the inclined legs of the horseshoe-like structure result in the streamwise vortices in the mixing region, and are responsible for the larger spreading rate of the jet in the lateral direction. A possible mechanism of forming the streamwise vortices in the wall region has been also discussed qualitatively.

Based on these results and considerations, a coherent structure model for the present flow has been proposed. It seems to us that the present model, yet being somewhat speculative, would be a basic flow module of the three-dimensional turbulent wall jet over a flat wall, even in the far field.

Acknowledgment

References

Bruun, H. H., 1977, "A Time-Domain Analysis of the Large-Scale Flow Structure in Circular Jet," *Journal of Fluid Mechanics*, Vol. 83, pp. 641–671.

Bruun, H. H., 1979, "A Time-Domain Evaluation of the Large-Scale Flow Structure in a Turbulent Jet," *Proceedings of Royal Society*, Series A, London, Vol. 367, pp. 193–218.

Crow, S. C., and Champagne, F. H., 1971, "Orderly Structure in Jet Turbulence," *Journal of Fluid Mechanics*, Vol. 48, pp. 547–591.

Davis, M. R., and Winarto, H., 1980, "Jet Diffusion from a Circular Nozzle above a Solid Plane," *Journal of Fluid Mechanics*, Vol. 101, pp. 201-221.

Ho, Chih-Ming, and Hurre, P., 1984, "Perturbed Free Shear Layers," *Annual Review of Fluid Mechanics*, Vol. 16, pp. 365-424.

Iida, S., and Matsuda, H., 1988, "An Experimental Study of Circular Turbulent Wall-Jet along a Convex Wall," *Transaction of Jpn. Soc. Mech. Engr.*, Series B, Vol. 54, No. 498, pp. 354-360 (in Japanese).

Launder, B. E., and Rodi, W., 1983, "The Turbulent Wall Jet—Measurements and Modeling," *Annual Review of Fluid Mechanics*, Vol. 15, pp. 429-459.

Morton, J. B., Catalano, G. D., and Humphris, R. R., 1978, "Some Two-Point Statistical Properties of a Three-Dimensional Wall Jet," *AIAA Journal*, Vol. 16, No. 7, pp. 693-698.

Sforza, P. M., and Herbst, G., 1970, "A Study of Three-Dimensional, Incompressible, Turbulent Wall Jets," *AIAA Journal*, Vol. 8, No. 2, pp. 276-283.

Yule, A. J., 1978, "Large Scale Structure in the Mixing Layer of a Round Jet," *Journal of Fluid Mechanics*, Vol. 89, pp. 413-432.

Zaman, K. B. M. Q., and Hussain, A. K. M. F., 1984, "Natural Large-Scale Structures in the Axisymmetric Mixing Layer," *Journal of Fluid Mechanics*, Vol. 138, pp. 325-351.

Flow in a Channel With a Time-Dependent Indentation in One Wall

M. E. Ralph
PA Consulting Group,
London, SW1W 9SR, England

T. J. Pedley
Department of Applied Mathematical Studies,
University of Leeds,
Leeds LS2 9JT, England

Computations and flow visualization experiments have been carried out on 2-D flow in a channel, with an indentation in one wall that can move in and out. There is plane Poiseuille flow upstream and attention is focussed on the flow downstream of the indentation. Four time-courses of indentation motion are examined: I oscillation between a flush and an indented postion; II advance from flush to indented, after which it remains stationary; III retraction to flush from a steady indentation; IV small amplitude oscillation about a substantially indented position. Various values of Reynolds number, Re, and Strouhal number, St, are employed ($250 \leq Re \leq 911$; $0.01 \leq St \leq 0.1$). The results show that (a) vorticity waves and eddies are generated in cases I and II (as in reference [11]); (b) in case II at higher experimental Re the flow does not become steady because the steady flow is unstable to a Rayleigh wave, on the shear layer bounding the main separation region, whose wavelength is significantly less than that of the vorticity wave; (c) in case III the waves that are generated at each parameter set seem to be Rayleigh waves not vorticity waves; (d) in case IV short waves give way to longer waves whose amplitude is comparable with the mean indentation height not the oscillation amplitude. Although resembling vorticity waves these do not propagate like the forced waves of case I and presumably represent a nonlinear interaction between Rayleigh waves, vorticity waves, and the very long, weak waves present even in steady flow. Further downstream, in many cases, the 2-D waves break down into turbulence via 3-D disturbances.

Introduction and Methods

A detailed understanding of unsteady separated flow in nonuniform and time-dependent conduits is of importance both in conventional mechanical engineering and in bioengineering. In particular, such understanding is a necessary prerequisite for explaining the self-excited oscillations that develop when fluid flows through an externally compressed collapsible tube, such as an artery or vein [2, 4]. This paper describes the results of Navier–Stokes computations and flow visualization experiments on the flow of an incompressible viscous fluid in a two-dimensional channel in which part of one wall is moved in and out in a prescribed way (Fig. 1). In the experiments, the undisturbed width of the channel, a, is 10 mm while its depth in the perpendicular direction is 100 mm; the indentation has a plane center portion 100 mm long, with smooth, deformable (but stiff) slopes at each end. The height of this center portion above the plane of the undisturbed wall is taken to be $a\epsilon h(\hat{t}/T)$ where $0 < \epsilon < 1$, h is a positive function with maximum value 1 (or close to it), $\hat{t}$ is the time variable and T is the time-scale for the motion of the indentation. Sufficiently far upstream there is steady Poiseuille flow with mean velocity U_0. The flow downstream of the indentation depends on three dimensionless parameters as well as the dimensionless function $h(t)$: Reynolds number, Re ($= aU_0/\nu$, where ν is the kinematic viscosity of the fluid), Strouhal number, St ($= a/U_0 T$) and amplitude parameter ϵ.

Previous papers [17, 11, 13, 14] have concentrated exclusively on sinusoidal oscillations between an indented and a flush position:

$$h(t) = \frac{1}{2}(1 - \cos 2\pi t). \qquad (1)$$

The experiments in [17, 11] were for Re and St in the ranges $475 < Re < 1265$ and $0.005 < St < 0.077$, respectively, and most results had $\epsilon = 0.38$ (some limited data were obtained for $\epsilon = 0.28$ and $\epsilon = 0.57$). The previous numerical work [13, 14] was concerned with simulating and explaining experimental observations. In the present work four different time-courses of indentation motion are investigated, as shown in Fig. 2.

I: $h(t)$ given by (1), but parameter space is more systematically covered in both the computations, with Re = 250, 500, 750 and St = 0.01, 0.02, 0.05, 0.1, and in the experiments, where the upper limits of Re and St were 911 and 0.05, respectively; ϵ is taken to be 0.4 in the computations, and a little below in the experiments. In each of cases I, II, III six

Table 1 Parameter values in experimental runs

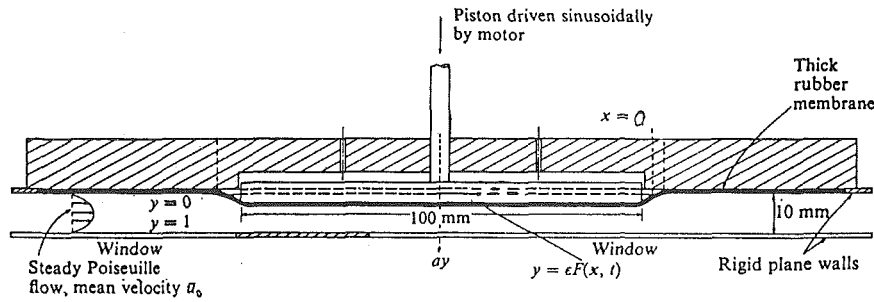| Runs	$\epsilon(\pm 0.01)$	$Re(\pm 10)$	$St(\pm 0.002)$
1	0.32	260	0.050
2	0.35	500	0.023
3	0.32	530	0.047
4	0.39	720	0.011
5	0.35	840	0.019
6	0.34	910	0.039

Fig. 1 Sketch of the experimental channel mid-plane with dimen-sionless variables marked, from [11]
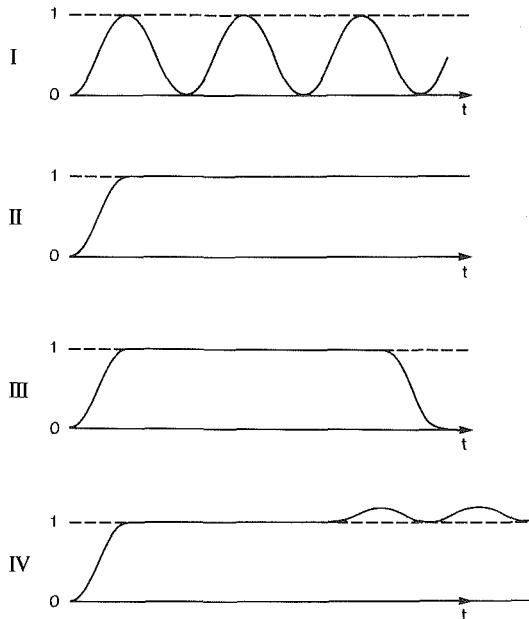
Fig. 2 Time-course of the function $h(t)$ in each of the four cases examined

Fig. 3(a)

Fig. 3(b)

Fig. 3 Computed positions of wave crests and troughs in Case I. $\epsilon = 0.4$, Re = 750 (solid curves), 500 (dashed curves), 250 (dash-dot curves). (a) St = 0.02, (b) St = 0.05. Uncertainty in x is estimated to be ± 0.05.

experimental runs were performed, with parameter values as given in Table 1.

II: The indentation starts flush (and steady), moves to an indented position, and stays there; i.e., $h(t)$ is given by (1) for $0 \le t \le 0.5$, and $h(t) = 1$ for $t > 0.5$. The same parameter values were used as in case **I**, excluding St = 0.1 in the computations.

III: As in **II** to start with, and then when the flow has become essentially steady, the indentation is retracted back to the flush position: $h(t)$ is given by (1) for $0 \le t \le 0.5$, $h(t) = 1$ for $0.5 < t \le T_0$, $h(t) = 1/2 [1 + \cos 2\pi(t - T_0)]$ for $T_0 < t \le T_0 + 0.5$, $h(t) = 0$ for $t > T_0 + 0.5$.

IV: A relatively small amplitude oscillation about an already indented position: $h(t) = 1/2(1 - \cos 2\pi t)$ for $t \le 0.5$, $h(t) = 1$ for $0.5 < t \le T_0$, $h(t) = 1 + (\epsilon' / \epsilon)(1/2) [1 - \cos 2\pi(t - T_0)]$ for $t > T_0$ where $\epsilon = 0.4$, $\epsilon' = 0.05$ and 0.1. (It did not prove possible to perform the experiments in Case IV, so only computed results are available.)

The experimental method, as in [17, 11], consisted of seeding the flow with light-reflecting pearl-essence flakes (Mearlmaid AA), illuminating the centerplane of the channel with a collimated beam of light, and photographing the flow there at a sequence of measured times after the start of the wall motion. Observations in [11] showed the flow in the centerplane to be essentially two-dimensional. The positions of important flow structures were measured from the photographs. The numerical method, using finite differences in a rectangular domain derived from the physical one by a coordinate transformation, was described fully in [13].

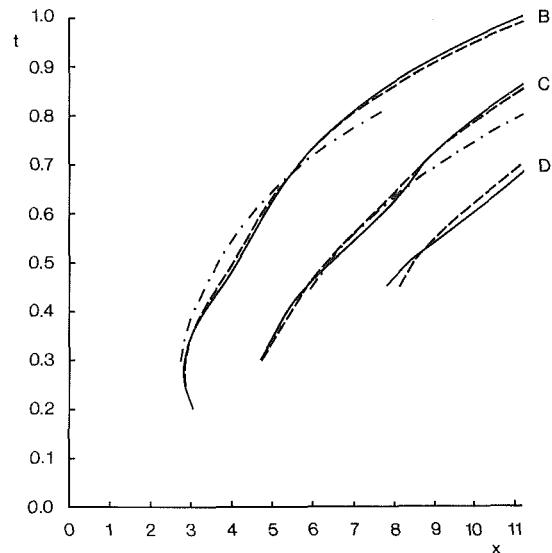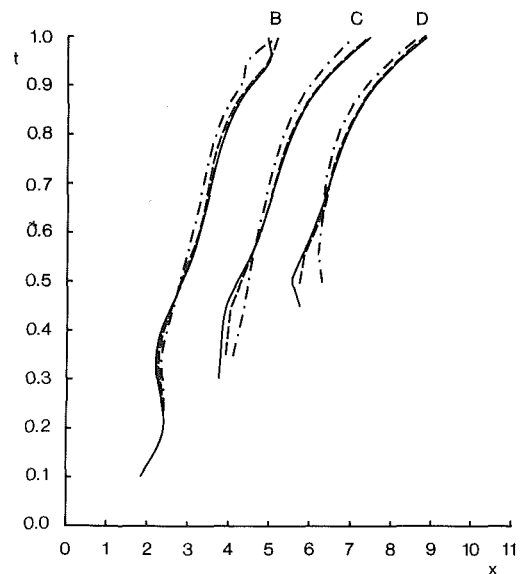The earlier studies, in case **I**, showed that a train of *vorticity waves* is generated downstream of the indentation every cycle. The wave front propagates at about the mean fluid speed, approximately three times the crest propagation speed. The

Table 2 Variation of the maximum value of $(\psi_{CL}-\psi_{\parallel})$ with Re and St in case I. Figures in parenthesis denote times at which maxima occur. Uncertainty is estimated to be ±0.01.

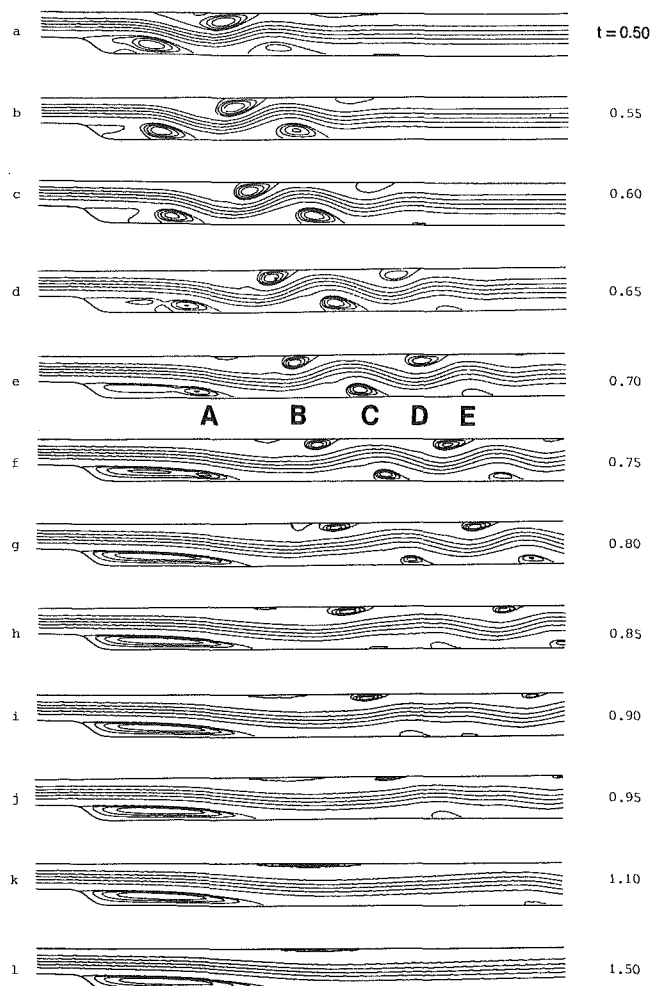|	Re = 250	500	750
St = 0.01	0.050 (0.50)	0.189 (0.55)	0.271 (0.55)
0.02	0.099 (0.55)	0.266 (0.55)	0.324 (0.55)
0.05	0.273 (0.60)	0.413 (0.55)	0.457 (0.55)
0.10	0.492 (0.60)	0.633 (0.60)	-

Table 3 Variation of the maximum value of $(\psi_{max}-1)$ with Re and St in case I. Figures in parenthesis denote times at which maxima occur. Uncertainty is estimated to be ±0.01.

	Re = 250	500	750
St = 0.01	0 (0.50)	0.005 (0.50)	0.019 (0.50)
0.02	10^{-4} (0.50)	0.032 (0.55)	0.066 (0.55)
0.05	0.108 (0.65)	0.218 (0.65)	0.266 (0.65)
0.10	0.560 (0.75)	0.715 (0.75)	-
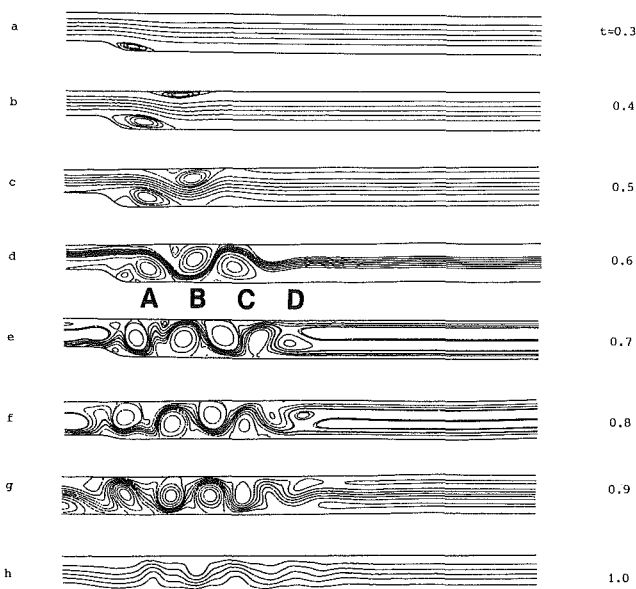
Fig. 4 Computed instantaneous streamline plots: Case I. Re = 500, St = 0.1, $\epsilon = 0.4$

Fig. 5 Computed instantaneous streamline plots: Case II. Re = 500, St = 0.05, $\epsilon = 0.4$

waves are manifest as displacement waves on the core flow streamlines with amplitude of $O(\epsilon a)$; under the crests and above the troughs of these waves (henceforth both crests and troughs will be referred to as crests) regions of recirculation (eddies) are observed. The motion in the eddies becomes concentrated at the downstream end of the eddies; sometimes the eddies are seen to double up into two, corotating eddies. Late in the cycle the motion may become three-dimensional and turbulent, but by the end of the cycle all disturbances are swept away downstream and the motion is once more undisturbed. These observations were reproduced and explained by the numerical work of [13]. In [17, 11] a weakly nonlinear, *inviscid* theory was developed which explained the generation and propagation of the waves and (at larger values of St) gave

good predictions of wave crest positions; discrepancies at smaller St were investigated in [14] by comparing the Navier–Stokes solutions with full solutions of the inviscid Euler equations, at various amplitudes. It was shown in particular that the Euler solution and the small-amplitude inviscid theory agreed almost perfectly for $\epsilon\leq0.2$ as long as account was taken of the acceleration and deceleration of the downstream mean flow caused by the motion of the indentation.

Results and Discussion

Here we treat each case separately, presenting the computational results first and experimental observations second. Uncertainties in the numerical results have been estimated by comparing computations using different mesh sizes (see [13, 14]). In all cases the wave crests, and the eddies that form beneath them, are referred to by letter as in [11, 13, 14]: eddy A is the separated eddy attached to the lee slope of the indentation, eddy B is the first to appear on the opposite, plane wall, eddy C is the next on the same side as eddy A, etc. (see Figs. 4 and 5).

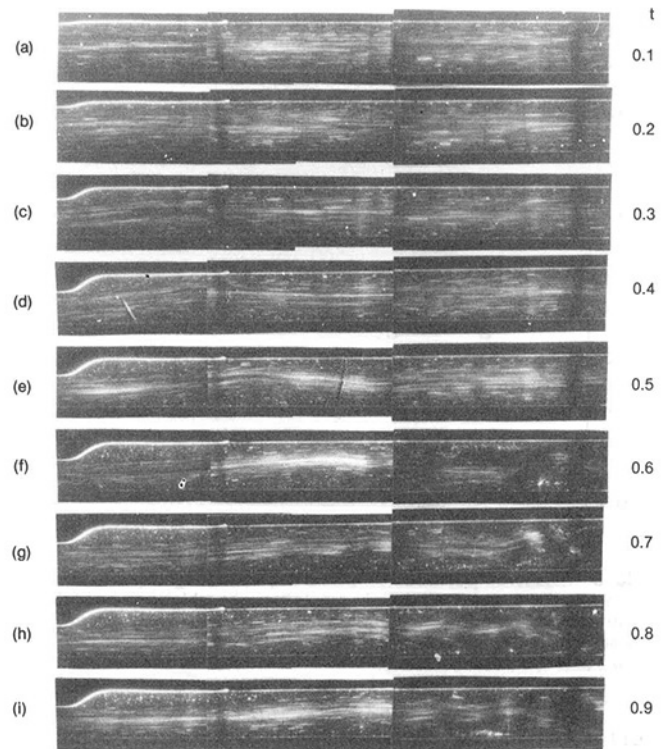**Case I.** For $St\leq0.05$ the results are qualitatively unchanged. Vorticity waves are generated and propagate downstream; computed positions of the wave crests (defined as turning points of the core-flow streamlines) are plotted for the three values of Re and for $St=0.02$, 0.05 in Fig. 3. As observed experimentally in [11], there is little dependence on Re, but both the wavelength and the crest propagation speed
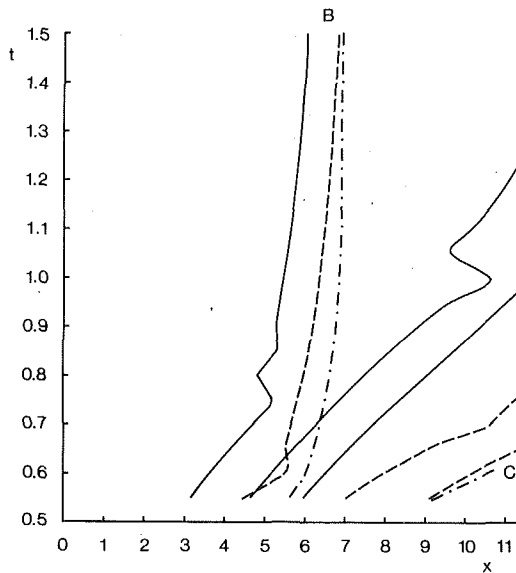
Fig. 6 Computed positions of wave crests and troughs in Case II. $\epsilon = 0.4$, Re $= 500$, St $= 0.05$ (solid curves), 0.02 (dashed curves), 0.01 (dash-dot curves). Uncertainty in x is estimated to be ± 0.05.

Fig. 7 Flow visualization photographs for Case II, run 5 ($\epsilon = 0.35 \pm 0.01$, Re $= 840 \pm 10$, St $= 0.019 \pm 0.002$)

decrease as St is increased; this is also consistent with the inviscid theory [11]. The main effect of Reynolds number is to influence the amplitude of the wave and, correspondingly, the strength of the eddies; for example, crest D was undetectable for Re $= 250$ at St $= 0.02$, (Fig. 3(a)), and was undetectable for Re $= 500$ at St $= 0.01$. A measure of wave amplitude is the maximum value, in space and time, of $\psi_{CL} - \psi_{\parallel}$ where ψ_{CL} is the value of the streamfunction at the centerline and $\psi_{\parallel}$ is the value in unsteady, parallel flow at the same instantaneous flow rate. Changes in this quantity can be thought of as reflecting changes in the core flow; its computed values are given in Table 2. A measure of eddy strength is the temporal maximum of $\psi_{max} - 1$, where ψ_{max} is the instantaneous spatial maximum in stream function over the flow field, while 1 is the constant value of ψ on the unindented wall; ψ_{max} usually occurs within eddy B. The values of $\psi_{max} - 1$ are given in Table 3; in both tables the figures in brackets are the (dimensionless) times at which the maximum is achieved. Both tabulated quantities increase with Re and St; the former always occurs at $t = 0.55 \pm 0.05$, while the latter occurs at a larger value of t as St is increased, virtually independent of Re over the small range considered.

The flow becomes more complicated and interesting for St $= 0.1$, because in that case the amplitude of the oscillatory component of the flow downstream of the indentation is greater than the steady component, so the mean flow reverses its direction. Streamline plots (Fig. 4) show the generation of waves and eddies as before, with a shorter wavelength as predicted theoretically [11], but there are numerous differences, all attributable to the mean flow reversal. First, the waves no longer continue to propagate downstream during the second half of the cycle; indeed, between $t = 0.6$ and $t = 0.8$ there is a small upstream propagation. Second, there is a relatively large region of reversed parallel flow near the walls, downstream of eddy C (Fig. 4(d)). Third, the secondary recirculation embedded within eddy B is stronger than at lower values of St. Fourth, and most dramatic, each eddy B, C, D becomes detached from the wall on which it first forms (Fig. 4(e)) while the reversed, continuous "core" flow streams through the gap so formed; the eddy becomes temporarily attached to the opposite wall before reverting to its original wall when the flow moves forward again (Fig. 4(g)). This phenomenon is also seen in wavy-walled channel flows [15]. In the case of eddy B, the main stream separates the principal ed-

dy center from the secondary, counter-rotating part; in the case of wave E, the eddy is formed in the center of the channel (compare flow type VII of [12]).

As can be seen from Table 1, it was unfortunately not possible to achieve a value of St as high as 0.1 in the experiments, and for St < 0.05 the observed flow patterns were very similar to those described in [11]. The only departure from the patterns computed in [13] or above consisted in the development of three-dimensional disturbances for $t > 0.7$.

Case II. The simple inviscid theory of [11] predicts the generation of a train of vorticity waves in this case just as in the oscillatory case, and the prediction is borne out by the present computations, for all the tested values of Re (up to 750) and St (up to 0.05). The main features of the flow are most easily seen at larger values of St, and computed streamline plots are given in Fig. 5 for Re $= 500$, St $= 0.05$; only the second half of the cycle is shown, because the flow is identical to that of case I for $t \leq 0.5$.

We note first that not only the wave crests but also the wave front continues to propagate downstream for some time after the piston has stopped moving, and new eddies E, F, etc. develop as in the oscillatory Case I (compare Fig. 4 of [13]). On the other hand, the maximum wave amplitude or eddy strength, as measured by $(\psi_{max} - 1)$ or $\max(\psi_{CL} - \psi_{\parallel})$, decreases monotonically with time for $t > 0.5$, in contrast to case I. The difference is presumably due to the amplifying effect, in case I, of the deceleration of the flow downstream of the moving indentation (as discussed more fully in [14]). The effect on the waves of varying Re and St is predictable: decreasing either Re or St decreases the strength of the wave; decreasing St again increases the wavelength, etc.

Figure 5 reveals that eddy doubling occurs in this case as in case I, where usually (but not always: see [11]) it occurs for $t > 0.5$, while the piston is retracting. There are, however, considerable differences, especially as regards the doubling of eddy B, as can be seen by comparing Fig. 5 with Fig. 4 of [13]. In this case the appearance of a new, corotating eddy upstream
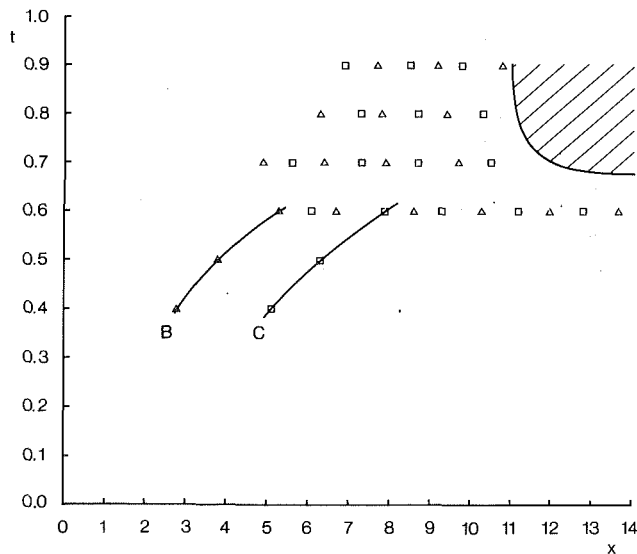
Fig. 8 Measured positions of crests (△) and troughs (□) in the case shown in Fig. 7. Solid curves join crests/troughs which can be identified with eddies B and C. Shaded region represents approximate extent of three-dimensional flow. Uncertainties in x and t are estimated to be ± 0.2 and ± 0.02 respectively.

Fig. 9 Computed instantaneous streamline plots: Case III. Re = 500, St = 0.05, $\epsilon = 0.4$

of the first is not apparently preceded by a counter rotating eddy on the wall (though there is a kink in the core-flow streamlines—see Fig. 5(e)). Moreover, the secondary eddy B does not propagate off downstream with the primary one, but remains behind, becoming very much longer as time goes on. In the case of eddy C, the secondary eddy does continue to propagate. The wave crests associated with eddies B and C (i.e., the sites of greatest displacement of the core-flow streamlines) become associated with the secondary eddy. Thus computed plots of wave-crest positions show an enormous difference between eddies B and C (and D) (Fig. 6): waves C and D continue to propagate, while wave B almost comes to rest. Note that the kink in the plot for wave C at St = 0.05 comes from the transfer of the greatest streamline displacement from the primary to the secondary eddy (cf [13], Fig. 5).

In fact, what Figs. 5 and 6 reveal is that a finite train of vorticity waves is generated as the indentation moves into the channel. It continues to propagate downstream, dispersing and changing amplitude according to the laws governing vorticity waves in a parallel-sided channel (leading to the linearized Korteweg-de Vries equation, with group velocity three times bigger than phase velocity, if the amplitude is small and viscosity is negligible [17, 11]). After that wave train has gone, the flow settles down to a viscous-dominated steady state, and it is the interaction between the back of the wave train and the eventual steady flow that causes the unfamiliar behavior of eddy B.

It is of interest to enquire whether the flow at $t = 1.5$, depicted in Fig. 5l, has become steady or not. It appears that eddy B is still shrinking, and one might suppose that there would be no separated eddy on the wall opposite the indentation in steady flow. However, Armaly et al. [1] have shown experimentally and computationally in a similar geometry (a right-angled, backward-facing step) that there is a range of steady Reynolds numbers for which such an eddy does exist: $400 < \text{Re} < 6600$ (the flow is laminar at the bottom end of this range but becomes fully turbulent at the top end). Indeed, a weak eddy C exists for $1200 < \text{Re} < 2300$. Thus the presence of an eddy B is not an indication that the flow is not yet steady.

For the low Strouhal number case (St = 0.01) we have checked numerically for convergence to a steady state; this is important in the computations for case III below because we use the flow at $t = 1.5$, St = 0.01 as the supposedly steady initial
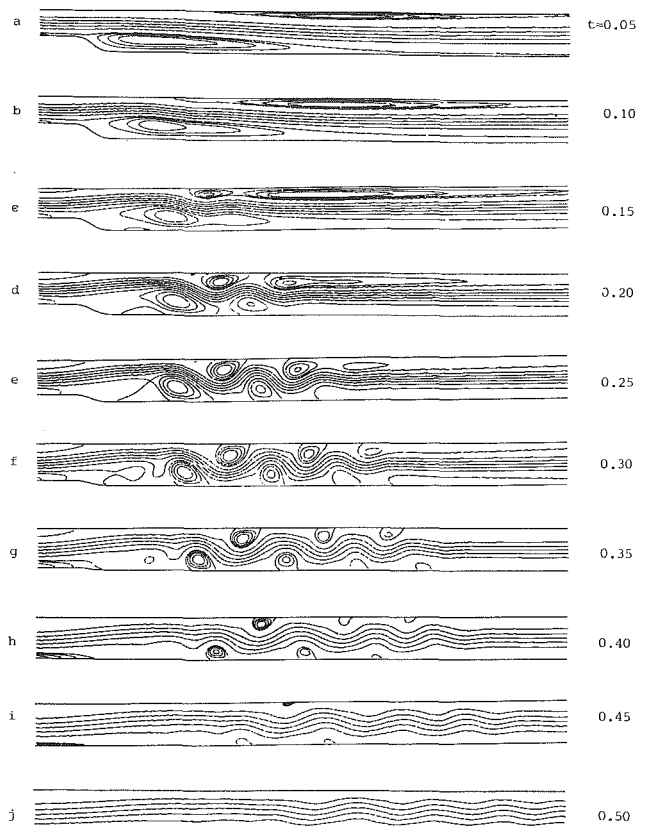
condition before the piston is retracted. A sensitive variable is the location of the reattachment point of the eddy, A, that forms on the downstream slope of the indentation. For Re = 250 and 500 (and St = 0.01) this had converged to at least two decimal places by $t = 1.5$; for Re = 750 it had converged to only one decimal place, but the flow was still used as the initial condition because experiments showed that a steady state could then not be achieved in practice anyway.

The experimental observations do not add anything to the above computations at low and intermediate Reynolds numbers (runs 1–3 of Table 1). Quantitative measurements of crest positions could be made for only a short time after the indentation motion was halted, because of the decay in wave amplitude, so are not plotted here; where comparison with computations was possible it was favorable.

In the higher Reynolds number flows, however (runs 4–6), the experimental results were significantly different from the computed ones. This is illustrated by photographs of run 5, with Re = 840, St = 0.019 (Fig. 7). We see that a vorticity wave indeed develops as predicted at early times, and crest B is clearly visible by $t = 0.5$ and crest C by $t = 0.6$ (Fig. 7(e, f)). However, as this long wavelength feature decays, a shorter length-scale disturbance grows (Figs. 7(g, h, i)) and persists as long as the piston is held in the indented position: the "steady state" is in fact unstable. The disturbances appear to originate near the reattachment point of eddy A, are amplified as they propagate and become three-dimensional further downstream (not shown).

When the positions of the wave crests were plotted at different times it was possible, as in [11], to follow the propagation of waves B and C for t up to 0.6 (as in [11] the maximum uncertainty in measured wave-crest position was estimated to be ± 0.15). Thereafter, however, the smaller wavelength disturbances arose and were impossible to track (see Fig. 8).

The reason is that the phase of these disturbances, relative to the motion of the indentation, was not the same each time the experiment was repeated, so a complete picture of their motion could not be built up from timed, still photographs taken from a number of repetitions of the experiment. This reinforces the conclusion that the short waves arise from a genuine instability and therefore cannot be entirely deterministic like the basic vorticity waves. Sufficiently far downstream the disturbances themselves experience a transition to three-dimensionality, and then break up.

The quantitative reason for asserting that the disturbances are not vorticity waves arises from measuring the wavelength of the two-dimensional disturbance. This can, from Fig. 7 or 8, be estimated as between 1.5 and 2.0 channel widths, compared with 5.2 channel widths for the forced vorticity wave (from Fig. 8). Similarly, we can rule out Tollmien–Schlichting waves associated with the undisturbed Poiseuille flow as the basic instability mode because the least stable of such waves, at such moderate values of Re, has a wavelength of approximately π times the channel width [6], still about double that observed. Hall and Parker [7] showed that abrupt deceleration dramatically reduces the critical value of Re below that of plane Poiseuille flow (to about 150), but does not greatly affect the least stable wavelength.

The only candidate left for the instability mechanism, therefore, is a Rayleigh (or Kelvin–Helmholtz) instability of the steady flow in which a shear layer bounds the primary separated eddy A. The inflection point in the shear layer will in that case be the source of the destabilization. Such an interpretation is consistent with the observations of Cherdron et al. [5], who noted that disturbances in flow through a sudden expansion originated in that shear layer, and with the theory of Tutty and Cowley [18], who showed that Rayleigh instabilities can arise in interactive as well as classical boundary layer computations of unsteady, separated flow. More quantitatively, it also agrees with estimates of the most unstable wavelength of a free shear layer. Michalke [9, 10] examined the inviscid instability of an unbounded parallel shear layer whose undisturbed velocity profile was given by

$$u = \frac{1}{2}U_0 [1 + \tanh(y/\delta)], \qquad (2)$$

and found the most unstable wavelength (for spatially growing waves) to be $2\pi\delta/\alpha$, where $\alpha \approx 0.40$. Similar results were obtained for viscous flow by Betchov and Szewczyk [3]. Now the width of a shear layer formed by a stream of fluid of speed U_0, flowing over a stagnant region starting at $x = 0$, is given by

$$2\delta = k\sqrt{U_0/\nu x},$$

where the constant k can be estimated to be about 5.0, by comparing the numerical results of Lock [8] with the profile (2). Thus when Re = 840 (Fig. 7) the most unstable wavelength λ, is given approximately by

$$\frac{\lambda}{a} = 1.4\sqrt{x/a}. \qquad (3)$$

Assuming that the growing disturbances originate at a distance of between a and $2a$ from the edge of the indentation, this gives $\lambda/a = 1.4 - 2.0$, in fair agreement with observation. Michalke's theory also showed that the phase speed of the disturbances is approximately $0.5U_0$, faster than that of the vorticity wave ($\approx 0.3U_0$).

It may be asked why the instability observed experimentally did not also appear in the Navier–Stokes computations, since small errors inevitably arise and can act as the initial perturbation. In our view, the answer is that such perturbations are extremely small, so the critical Reynolds number for visible growth will probably be larger than in the experiments (the lowest experimental value of Re for which these disturbances were observed was 720; the highest value of Re in the com-
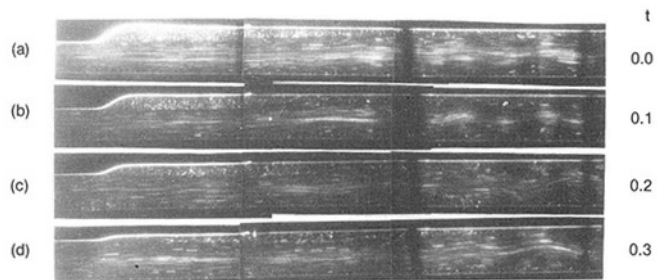

Fig. 10 Flow visualization photographs in Case III, run 5 ($\epsilon = 0.35 \pm 0.01$, Re = 840 ± 10, St = 0.019 ± 0.002)

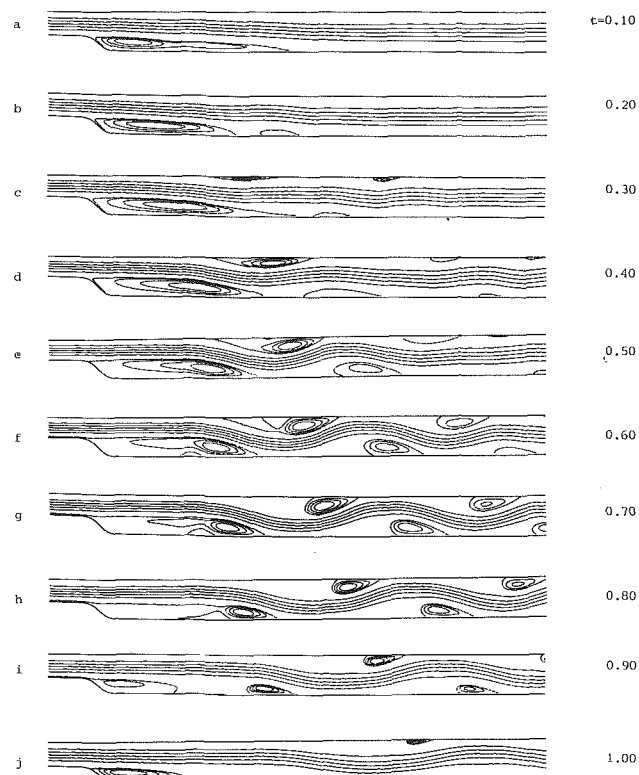

Fig. 11 Computed instantaneous streamline plots: Case IV: Re = 500, St = 0.05, $\epsilon = 0.4$, $\epsilon' = 0.1$

putations was 750). That our computations are capable of incorporating such instabilities is shown in the next section.

Case III. All the times t referred to in this section are measured from T_0, the time at which the retraction begins. The time T used for calculating the Strouhal number is still taken to be the period of the sinusoidal oscillation of which the retraction occupies half. Computed instantaneous streamline plots for a flow with Re = 500 and St = 0.05 (cf Fig. 4) are given in Fig. 9. Notable features are as follows. Initially (Fig. 9(a)) a large separation region is formed on the unindented wall, because of the deceleration of the flow. Next, kinks appear in the dividing streamlines of each of the two separated flow regions (Fig. 9(b)), and then each of these regions breaks up into a number of eddies (Figs. 9(c, d, e)). The peak eddy strength, as measured by ($\psi_{max} - 1$), is reached at $t = 0.25$, although new waves continue to appear at the downstream end of the wave packet until about $t = 0.40$ (Fig. 9(h)). By $t = 0.50$ all the eddies have decayed and there is no reversed wall shear anywhere.

Plotting wave crest positions shows (a) that the phase speed of these waves is about $0.6U_0$ for various values of Re and St, and (b) that their wavelengths are about 40 percent smaller
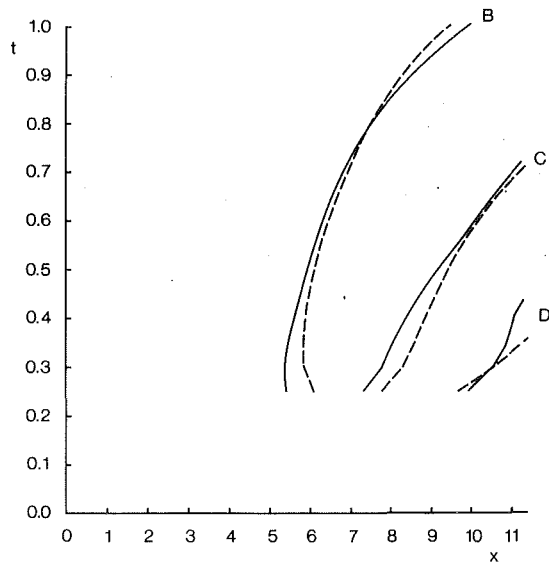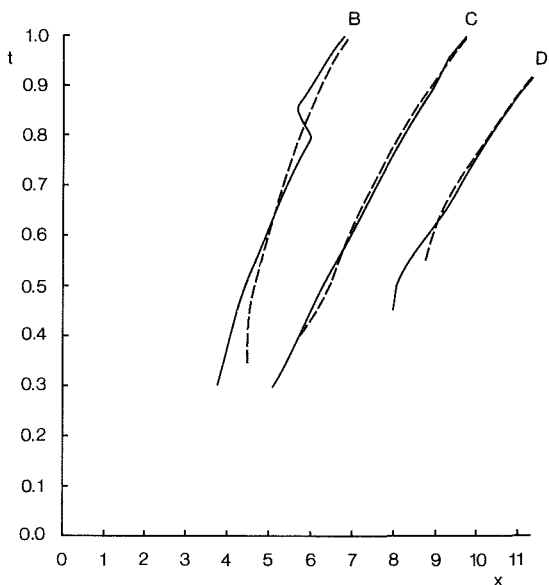
Fig. 12(a)

Fig. 12(b)

Fig. 12 Computed positions of wave crests and troughs in Case IV. $\epsilon = 0.5$, Re = 500, $\epsilon' = 0.1$ (solid curves), 0.05 (dashed curves). (a) St = 0.02, (b) St = 0.05. Uncertainty in x is estimated to be ± 0.05.

Table 4 Variation of the maximum value of $(\psi_{max} - 1)$ with St and ϵ' in case IV (Re = 500 $\epsilon = 0.5$). Figures in parenthesis denote times at which maxima occur. Uncertainty is estimated to be ± 0.01.

	$\epsilon' = 0.05$	0.1
St = 0.01	0.003 (0.45)	0.019 (0.50)
0.02	0.008 (0.50)	0.036 (0.50)
0.05	0.048 (0.65)	0.133 (0.60)

Rayleigh instability) and the mechanism by which they grow to a large amplitude (deceleration of the flow). In the present case we suggest that deceleration both makes the flow unstable, through the occurrence of inflection points in the velocity profile, and causes the disturbances to be amplified. As demonstrated clearly in [14], however, vorticity waves are formed without a local flow deceleration (with flow rate fixed downstream of the oscillating indentation instead of upstream), but when there is a deceleration their amplitude grows larger and more quickly. In the present case, or Sobey's, apparently the only way of telling which generation mechanism is operative is by measuring the disturbance wavelength and comparing it with theory or with the previous results using an oscillating indentation.

As in case II, the experimental observations agreed qualitatively with the numerical predictions in the lower Reynolds number runs (1–3). In the higher Reynolds number runs (4–6), however, the experiments could not be expected to match the computations, because the steady flow was already unstable at the beginning of the manoeuvre (see case II). This meant that the initial condition was neither approximately steady nor well-defined, because the retraction of the piston could not be synchronised with the phase of the instability wave. It is nevertheless of some interest to see the effect of the retraction on the wave, and an example is given (run 5) in Fig. 10. We observe clearly the amplification of the short-scaled disturbance as the flow is decelerated, followed by a reduction in amplitude as the indentation approaches the flush position. The wavelength remains approximately constant, at 1.5–2.0 channel widths.

Case IV. Here small amplitude ($\epsilon' = 0.1$) oscillations with St = 0.01, 0.02, and 0.05 were superimposed on the steady indentation with $\epsilon = 0.4$ and Re = 250 or 500; experiments were not feasible in this case. The initial condition for the computation was the (effectively) steady flow achieved after the $\epsilon = 0.4$ indentation was moved in and held fixed until $t = 1.5$ (case II above).

Instantaneous streamline plots for the flow with St = 0.05 and Re = 500 are shown in Fig. 11. Initially ($t = 0.1$) there is destabilization of the shear layer bounding eddy A (Fig. 11(a)), despite the fact that the flow is accelerating at that time. Then a part of eddy A breaks off (Fig. 11(b)), and a small amplitude, short-scaled wave, presumably a Rayleigh wave again, propagates downstream (Fig. 11(c)). Subsequently, the most upstream of the eddies on the unindented wall expands across the channel, as does the propagating part of eddy A (Fig. 11(d)); from this time on it is natural to identify these recirculation zones as eddies B and C, because of their resemblance to the corresponding eddies in Case I. A large amplitude, relatively long wave then develops, its front propagating rapidly along the channel (Figs. 11(e, f)), while individual crests move more slowly downstream. It is striking that the amplitude of the wave is comparable with the mean indentation height rather than with the amplitude of the piston motion. Indeed, the plots of Fig. 11 are qualitatively indistinguishable from those for case I at similar parameter

than those formed in case I at similar values of Re and St, suggesting that different dynamics are involved. The wavelengths, in fact, are close to those observed experimentally at the higher Reynolds numbers in case II, and the phase speed is close to that predicted for Rayleigh waves by Michalke [9, 10]. In the present case, too, the waves that propagate downstream appear to originate from the initial disturbances (Fig. 6(b, c)). We suggest, therefore, that this wave is also a consequence of Rayleigh instability of the decelerating shear flow, beginning to grow when the inflection points in the velocity profile become strong enough, and is not a forced vorticity wave like those computed in cases I and II. It is interesting to note that there is a strong resemblance to the experimental observations of Sobey [16, Fig. 8] made during the deceleration phase of oscillatory flow past a fixed indentation (at a lower value of Re = 160), indicating a similar mechanism there too.

It is important to recognize the distinction between the initial cause of the wavy disturbances (vorticity wave or

values (compare Fig. 4 of [13], for Re = 507, St = 0.037), and it is tempting to identify these longer waves with the vorticity waves described in earlier publications. However quantitative comparisons indicate significant differences. First, and probably unimportant, the eddy strengths are somewhat lower than in case I (compare Table 4 with Table 3). Second, wavelengths and crest velocities are different: the crest positions for St = 0.02 and 0.05 (Re = 500) are plotted in Fig. 12(a) and (b), which should be compared with Fig. 3(a) and (b). The wavelengths in case IV are uniformly greater than in case I, and the phase velocities also differ, being greater in case IV at St = 0.05 and lower at St = 0.02.

A detailed explanation of these results is not available. The early short-scale wave is again presumably an instability wave associated with the shear layer bounding eddy A in the initial state. The later, long-wavelength wave, which develops for $t \geq 0.3$ (Fig. 11), may perhaps be generated by amplification, as a result of deceleration, of the very weak wave present in steady flow (see Armaly et al. [1] and Fig. 5l). Its propagation and persistence could then be explained by the vorticity wave mechansim, but the observed wavelength and propagation speed would result from a nonlinear interaction between the long weak wave in steady flow, the initial burst of short-scale (Rayleigh) waves and the vorticity waves themselves. Understanding this interaction is an important task for the future.

Acknowledgments

References

1 Armaly, B. F., Durst, F., Pereira, J. C. F., and Schönung, B., "Experimental and Theoretical Investigation of Backward-Facing Step Flow," *J. Fluid Mech.*, Vol. 127, 1983, pp. 473–496.

2 Bertram, C. D., Raymond, C. J., and Pedley, T. J., "Mapping of Instabilities During Flow Through Collapsed Tubes of Differing Length," *J. Fluids Structures*, Vol. 4, 1990, pp. 125–154.

3 Betchov, R., and Szewczyk, A. B., "Stability of a Shear Layer Between Parallel Streams." *Phys. Fluids*, Vol. 6, 1963, pp. 1391–1396.

4 Cancelli, C., and Pedley, T. J., "A Separated-Flow Model for Collapsible Tube Oscillations," *J. Fluid Mech.*, Vol. 157, 1985, pp. 375–404.

5 Cherdron, W., Durst, F., and Whitelaw, J. H., "Asymmetric Flows and Instabilities in Symmetric Ducts With Sudden Expansions," *J. Fluid Mech.*, Vol. 84, 1978, pp. 13–31.

6 Ghaddar, N. K., Korczak, K. Z., Mikic, B. B., and Patera, A. T., "Numerical Investigation of Incompressible Flow in Grooved Channels. Part 1. Stability and Self-Sustained Oscillations," *J. Fluid Mech.*, Vol. 163, 1986, pp. 99–127.

7 Hall, P., and Parker, K. H., "The Stability of the Decaying Flow in a Suddenly Blocked Channel," *J. Fluid Mech.*, Vol. 75, 1976, pp. 305–314.

8 Lock, R. C., "The Velocity Distribution in the Laminar Boundary Layer Between Parallel Streams," *Quart. J. Mech. Appl. Math.*, Vol. 4, 1951, pp. 42–63.

9 Michalke, A., "On the Inviscid Stability of the Hyperbolic Tangent Velocity Profile," *J. Fluid Mech.*, Vol. 19, 1964, pp. 543–556.

10 Michalke, A., "On Spatially Growing Disturbances in an Inviscid Shear Layer," *J. Fluid Mech.*, Vol. 23, 1965, pp. 521–544.

11 Pedley, T. J., and Stephanoff, K. D., "Flow Along a Channel with a Time-Dependent Indentation in One Wall: the Generation of Vorticity Waves," *J. Fluid Mech.*, Vol. 160, 1985, pp. 337–367.

12 Ralph, M. E., "Oscillatory Flows in Wavy-Walled Tubes," *J. Fluid Mech.*, Vol. 168, 1986, pp. 515–540.

13 Ralph, M. E., and Pedley, T. J., "Flow in a Channel With a Moving Indentation," *J. Fluid Mech.*, Vol. 190, 1988, pp. 87–112.

14 Ralph, M. E., and Pedley, T. J., "Viscous and Inviscid Flows in a Channel With a Moving Indentation," *J. Fluid Mech.*, Vol. 209, 1989, pp. 543–566.

15 Sobey, I. J., "On Flow Through Furrowed Channels. Part 1. Calculated Flow Patterns," *J. Fluid Mech.*, Vol. 96, 1980, pp. 1–26.

16 Sobey, I. J., "Observation of Waves During Oscillatory Channel Flow," *J. Fluid Mech.*, Vol. 151, 1985, pp. 395–426.

17 Stephanoff, K. D., Pedley, T. J., Lawrence, C. J., and Secomb, T. W., "Fluid Flow Along a Channel With an Asymmetric Oscillating Constriction," *Nature*, Vol. 305, 1983, pp. 692–695.

18 Tutty, O. R., and Cowley, S. J., "On the Stability and the Numerical Solution of the Unsteady Interactive Boundary-Layer Equation," *J. Fluid Mech.*, Vol. 168, 1986, pp. 431–456.

M. S. Christodoulou
Department of Engineering.

J. T. Turner
Department of Engineering.

S. D. R. Wilson
Department of Mathematics.

University of Manchester,
Manchester, M13 9PL, England

A Model for the Low to Moderate Speed Performance of the Rotating Disk Skimmer

In an extensive experimental investigation (Christodoulou, 1985) the performance of a. disk skimmer rotating in the vertical plane and partially immersed in a liquid has been studied. The aim of the study was to examine the physical and hydrodynamic parameters governing the oil collection rate of the disk when used as one element of a rotating disk skimmer, a device commonly employed to recover oil and similar immiscible liquids from a water surface. This paper presents a theoretical solution for the flow field set up by the disk which has led to an improved understanding of the hydrodynamics of the disk drag-out problem at low to moderate speeds. Experimental data are presented and compared with the theoretical solutions: discrepancies are then explained in terms of departures from the original assumptions.

1 Introduction

Although oil spills have happened repeatedly in the past, significant public concern does not appear to have been aroused until the Torrey Canyon tanker disaster occurred in March 1967 (see, for example, Taylor, 1968 and Smith, 1968). During this major incident, considerable environmental damage was caused to the southern coastline of Britain and criticism was aroused regarding the effectiveness of the response by the authorities and the impact of the toxic chemical dispersants used to deal with the spillage.

In addition to transportation by tankers, vast quantities of oil produced offshore are conveyed to the land by means of ocean floor pipelines. Spillage, such as that which arose from the Ekofisk Bravo rig in the Norwegian sector of the North Sea in 1977 and, more recently, in the Bay of Mexico (1983) and the Arabian Gulf (1987), always remains a possibility.

The inevitability of such spills, and the need to minimize the environmental damage so caused, made it worthwhile to develop effective and easy to apply oil slick collection methods. These methods enable the oil to be separated from the sea without the use of chemicals and offer the possibility that some at least of the lost oil can be regained. Examination of the literature (see, for example, Cormack, 1983), shows that a variety of such mechanical devices have been proposed although the most popular method still appears to be the rotating disk skimmer, principally because of its ability to cope with wide variations in film thickness and oil viscosity up to perhaps 35m²/s.

1.1 Disk Skimmer Devices. In its simplest configuration, a rotating disk skimmer consists of a flat circular disk rotating about a horizontal axis with the disk partially immersed

through the oil film floating on the water. During rotation, the oil sticks preferentially to the surface of the disk and can then be scraped off and transferred to a collecting duct. Many commercial systems employing this principle already exist: disk diameters typically lie in the range from 300 mm to 800 mm, dependent upon the application (Cormack, 1983; Marcinowski, 1976; and Thomas, 1977).

A description of some experimental tests performed on one early commercial device—the Komara Miniskimmer produced by Vikoma Ltd.—has been given by Thomas and Davia (1980). Serious limitations in the performance were found when the rotating disk skimmer was operated in thin oil films or with high levels of viscosity. Moreover, these authors acknowledge that little was then known about the fluid mechanics of the oil film and the coupled water mass even though they recognized that these factors must determine the performance (or collection rate) of the disk.

Perhaps the most useful discussion of the hydrodynamics involved when an oil film is removed from the surface of another (immiscible) liquid has been given by Leibovich (1977)). Although the rotating disk was not analyzed in any detail, the discussion does offer some physical insight into a number of the features which limit the performance.

1.2 The Present Paper. This paper arises from an investigation (Christodoulou, 1985; Christodoulou and Turner, 1987) into the performance of disk skimming systems which has focused on the physics of the oil recovery process for a single disk. During the experimental part of the study, a single rotating disk was operated in "oil only" and "thin oil film" conditions.

Although a theoretical insight was clearly desirable, consideration of the fluid mechanics of the recovery operation indicated that a full three-dimensional analysis would be impossibly complicated. Subsequently, a simplified model was
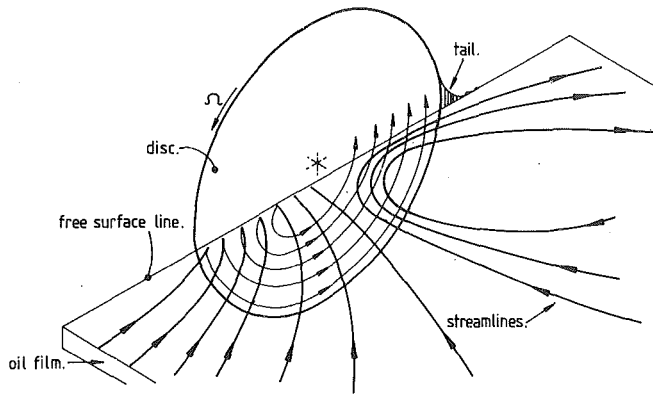
Fig. 1 Streamlines of the observed flow pattern near the disk

Fig. 2 Variation of oil recovery rate with rotational speed for different depths of immersion. (Uncertainty in rotational speed = ± 1/2 percent, in recovery rate = ± 2.5 percent, at 20:1 odds.)

developed by the third author. This is based on the known solution to a strictly two-dimensional (and therefore much simpler) problem, the plane drag-out problem. The nature of this solution, and the way it can be applied to the present case, is explained in section 3. The theory provides a reasonable explanation of the experimental results; and we may conclude that the underlying physics of the recovery process is adequately understood, at rotation speeds corresponding to capillary numbers up to about 10.

The rotating disk forms the basis of a commercially successful and widely applied skimming device; it is used in marine and inland waterways and for industrial effluent control.

2 Experimental Investigation

2.1 Apparatus. During a comprehensive postgraduate study (Christodoulou, 1985), specially designed apparatus was constructed so that laboratory experiments on rotating disks could be performed under carefully controlled conditions. The objective was to ensure that all the many parameters of the real system (except wave properties) could be varied systematically.

In the flow apparatus, oil is poured over a weir onto stagnant water contained in a large tank so as to form an even oil film thickness across the tank area and thus around the skimmer. The oil flowing beyond the rotating skimmer is allowed to escape over another weir into a collection vessel, from where it is pumped back into the main tank (see Christodoulou, 1985 for details).

When under test, the disk skimmer is mounted on a purpose-built drive device capable of accepting different types of disk. The rotational speed of the system is accurately regulated by a variable speed electric motor and both the motor and skimmer are mounted on a traversing arrangement
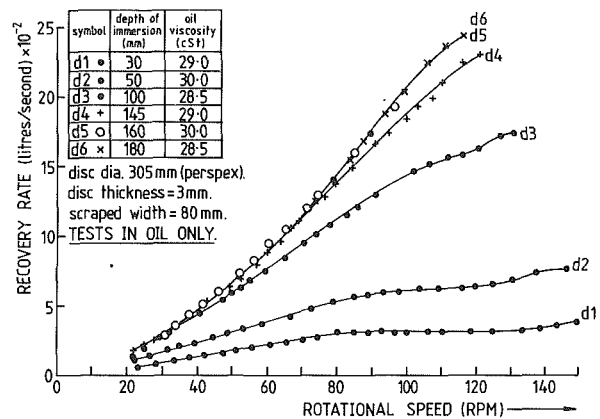
suspended from a sliding bridge: the depth of immersion of the disk into the tank and its position in the horizontal plane can be altered by transversing vertically and horizontally.

2.2 The Flow Field Set Up By A Rotating Disk. Details of the flow field set up by the action of a single rotating disk skimmer are reported in Christodoulou and Turner (1987). For the present paper, a brief summary of these findings will suffice.

Using the information derived from detailed velocity measurements with a laser anemometer, in combination with visualization of the oil film movement, a three-dimensional view of the flow induced by the disk has been gained. An impression of this flow pattern is shown as Fig. 1.

The flow patterns in the oil film and the water mass reveal a number of interesting features.

(i)   The movement of the oil film along the surface and its subsequent collection occurs symmetrically on either side of the plane of the disc.

(ii) It is clear that the oil film is drawn below the free surface at the start of the collection process where the disk rim first enters the liquid.

(iii) At the rear of the disk, no additional oil is collected by the reemerging disk surface as it moves up above the free surface. Instead, the surface oil in this region is directed away from the edge of the disk with a relatively high velocity.

(iv) There is a distinct "tail" of oil which forms above the free surface on the downstream edge of the disk. This consists of oil which has been flung off the disk, both above and below the free surface, by centrifugal action.

Nomenclature

c = experimentally determined constant ≈ 0.8.

d = $(\mu U/\rho g)^{1/2}$ (m)

g = acceleration due to gravity (m/s^2)

h = film thickness in plane dragout flow (m)

ℓ = L/R

x = horizontal coordinate in pick-up zone (Fig. 5) (m)

D = length scale of meniscus = $(\sigma/\rho g)^{1/2}$ (m)

H = thickness of oil film far from the disk (m)

L = height of centre of disc above free surface (m)

R = radius of disc (m) (Fig. 5)

Q = total flow rate on to the disk (m^3/s)

U = vertical velocity in plane drag-out flow (m/s)

Ca = capillary number = $\mu U/\sigma$

$\left.\begin{array}{c} K \\ \lambda \end{array}\right\}$ = numerical constants in equation (1)

μ = dynamic viscosity of oil (Ns/m^2)

ρ = density of oil (kg/m^3)

ν = kinematic viscosity of oil (m^2/s)

σ = surface tension of oil against air (kg/s^2)

Ω = angular velocity of disk (s^{-1})

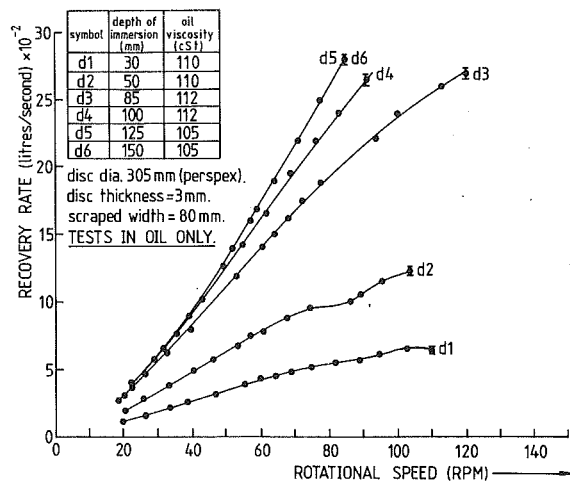**Subscript**

0 = evaluation at edge of disk (equation (5)).

Fig. 3 Variation of oil recovery rate with rotational speed for different depths of immersion. (Uncertainty in rotational speed = ± 1/2 percent, in recovery rate = ± 2.5 percent, at 20:1 odds.)

Overall, the experiments have established that the disk draws the oil film beneath the free surface in the vicinity of the downwards moving edge and that the disk is able to recover oil instead of water simply because the oil is the first of the two liquids to be encountered by the clean disc. The collection process does not depend upon the two liquids having different viscosity levels, contrary to the suggestion of previous workers (e.g., Leibovich (1977)), nor need the disk exert a preferential attraction for the oil as would be the case for an oleophilic material.

2.3 Performance Experiments. Initial experience showed the flow field set up by a disk rotating through an oil film floating on water to be extremely complex. Simplified experiments were therefore undertaken in which the recovery rate was measured with the disk operating solely in oil. A summary of the results from these experiments will be presented in this paper. The rest of the data, relating to the performance of the single disk skimmer when partly immersed in a thin oil floating on water, appears in Christodoulou and Turner (1987).

For the oil-only situation, detailed measurements have been made to study how the depth of immersion, viscosity of the oil, and the rotational speed, influence the oil recovery rate of the disk. The results of these experiments are summarized in Figs. 2 and 3.

2.3.1 Experimental Trends. In Fig. 2, each curve (1 to 6) represents the performance of the disk for a fixed depth of immersion. From an examination of these results, it is evident that varying the depth of immersion leads to significant changes in the recovery rate. More particularly, increasing the immersion improves the performance of the system at a fixed speed until the depth of immersion of the disk equals or exceeds the radius of the disc (curves 5 and 6). Thereafter, the performance becomes independent of the depth of immersion.

An important observation (curves 1, 2, and 3 in Fig. 2) is that the oil recovery rate increases in direct proportion to the rotational speed until a limiting value is reached. Above this speed, the rate of oil recovery remains sensibly constant.

When the performance of the disk was measured for an oil of different viscosity, the data showed similar trends to those in Fig. 2. Inspection of these results (presented in Fig. 3) reveals that a higher recovery rate is associated with the oil of higher viscosity and that the data scale roughly as the square root of the kinematic viscosity.

The scatter of the measured data has been discussed in detail in Christodoulou (1985). The errors are estimated to be about
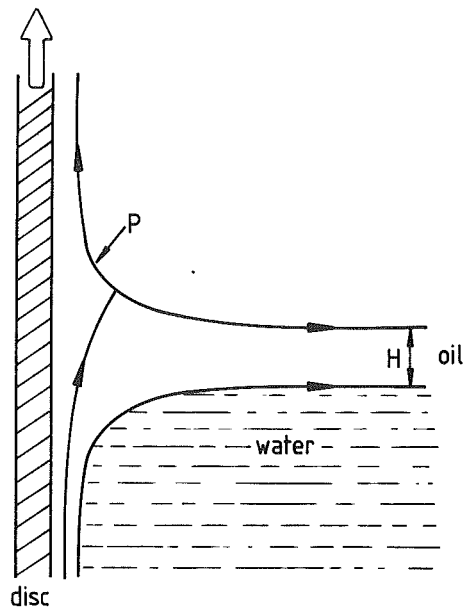

Fig. 4 Sketch of the streamlines of the flow field in a vertical cross-section normal to the plane of the disk

0.5 percent for the speed of rotation of the disk and about 2.5 percent for the pickup rate. The viscosity of the oil was obtained by reference to charts supplied by the manufacturer; the only significant error is that incurred in reading the charts, namely about 2 percent. The surface tension of the oil against air was measured with accuracy about 5 percent. (Of course this property value is well-known to be sensitive to factors such as surface contamination which are notoriously difficult to control in experimental practice.) All the above figures are at 95 percent confidence level.

Some of these measurements, together with others which are subject to negligible errors such as the disk radius and the oil density, are also used to evaluate the prediction of the theory to be presented later. The theoretical predictions are thus subject to errors of about 3 percent.

3 Theory

The fluid motion around the emerging side of the disk is sketched in Fig. 4 for a typical vertical section normal to the plane of the disk. The difficulty is to decide how much oil is drawn onto the disk in the neighborhood of P, the "pickup" region. Once this is done, the analytical description of the dynamics of the oil film as it moves on the disk under the influence of gravity and centrifugal force is relatively straightforward. This description would be necessary to estimate, for example, the edge losses, which will be a function of the rotational speed and the fluid properties. In practice, however, the aim is to reduce the edge losses as far as possible by modifying the cross-sectional shape of the disk and by running it half-immered. This analysis will therefore be omitted here in order to simplify the presentation.

For the purpose of this paper, a solution of the plane drag-out problem given by Wilson (1982) has been adapted to the special geometry of the rotating disk. In the plane drag-out problem, it is supposed that an infinite vertical plane is drawn vertically with speed U out of an infinite bath containing a single liquid of viscosity μ and surface tension σ. The key approximation is that the Capillary number $Ca = \mu U/\sigma$ is small: it can then be shown that the thickness of the entrained film is controlled by the fluid dynamics in or above the hydrostatic meniscus, the motion in the bulk liquid having no influence to
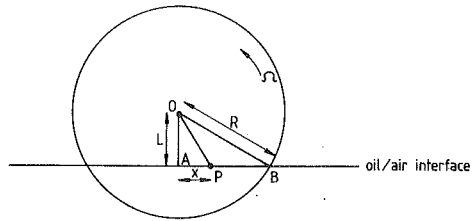
Fig. 5 Coordinates in the plane of the disk

the order of approximation considered. The result obtained by Wilson (1982) for the vertical plate is

$$h/d = 0.94581(\text{Ca})^{1/6} - 0.10685(\text{Ca})^{1/2} + \ldots \quad (1)$$

where h is the film thickness and $d = (\mu U/\rho g)^{1/2}$.

Agreement between predictions using equation (1) and experimental data for the rectilinear system is remarkably good, even for $\text{Ca} \simeq 1$. Furthermore, there is no apparent scatter of the data on account of the (neglected) inertial effects, as is shown, for example, by comparison with the experiments of Spiers et al. (1974). Although this agreement is surprising, and so far unexplained, similar behavior of the analytical solution can be expected in the present situation.

When the Capillary number Ca is between 1 and 10 the analytical theory just described is not applicable and no alternative theory, other than a numerical solution of the full equations, appears possible. However, the experimental data suggest that (1) should be replaced by

$$h/d = \text{constant} = c, \text{ say} \quad (2)$$

where $c \simeq 0.8$. This simplication will be used to give a semi-empirical formula for the pickup rates at speeds of rotation higher than those to which (1) applies. (The two formulas agree at $\text{Ca} \simeq 0.7$.)

The basis of the present calculation can now be understood by reference to Fig. 5. The point P is on the oil/air interface on the pickup side of the disk. The film thickness just above P is then assumed to be given locally by an expression of the form (1) or (2), in which U is replaced by the vertical component of the local velocity of the disk, and the physical constants are those for the particular oil considered. On this basis, the total pickup rate can be obtained by integrating along the segment AB.

This integration requires a number of rather important assumptions which need to be discussed.

(i) Firstly, the presence of the water has been completely ignored so that there is an obvious need to compare with data obtained for very thick film or oil only situations. However, it should be noted that the flow has a stagnation line on the free surface as indicated in Fig. 4 and that the same is true in the drag-out of a single liquid. This feature is not described in the analysis by Wilson (1982) because it involves terms of higher order than those retained. The existence of the stagnation line follows from the easily-made observation that the fluid on the horizontal free surface moves away from the rising plate (or disk). Thus, the fluid eventually dragged out originates from close to the plate, at some depth below the free surface.

(ii) The bulk motion of the liquid is negligible, under the assumptions which led to equation (1), and so we can expect the water to have no important effect provided that the oil meniscus near P (see Fig. 4) is dominated by hydrostatic effects. This requires that the submerged portion of the disk carries a stable oil film no thinner than that eventually dragged out so the stagnation stream surface can originate inside the oil film. Additionally, the thickness H of the oil layer ahead of the disc should not be less than the length

scale of the static meniscus. This length scale, $(\sigma/\rho g)^{1/2} = D$ say, has a value of approximately 2 mm for the oil used here. Both these conditions were met in the present experiments.

The velocity of the disk at P is not of course vertical nor independent of P. It is proposed to ignore the horizontal component of velocity of the disc on the ground that it will make no contribution to the volume of liquid withdrawn; and in fact it can be shown that a uniform horizontal motion can be superimposed on the solution of the plane drag-out problem (Wilson (1982)) without changing the result. The neglect of the variation in the vertical component of velocity with x will be valid if this variation is on a length scale which is large compared with the scale of the meniscus, that is if $R \gg D$. This certainly holds in the present case.

The centrifugal effects in the rotating disk system lead to genuine and obvious changes from the rectilinear case which cannot be accounted for in any simple manner. In order to apply the results of the rectilinear case as described above it is necessary to assume that centrifugal effects are negligible. The vertical component of the centrifugal acceleration is small compared with gravity if $L\Omega^2/g \ll 1$. This parameter did not exceed about 0.5 in the experiments and was typically much smaller. So we expect the approximation to be adequate at low to moderate speeds and for large depths of immersion, corresponding to small values of L.

In the case of rectilinear withdrawal, the volumetric pickup rate per unit width, Q, is given by

$$Q = Uh - \frac{1}{3}g\frac{h^3}{\nu} \quad (3)$$

where U is the vertical speed and h, the thickness of the film, is given by equation (1) or (2). To adapt this to the present case we use (3) with U replaced by its local value at P, which is the vertical component Ωx. Note that U appears not only explicitly in (3) but implicitly by way of the quantities d and Ca.

Consider first the formula (1), for low to moderate speeds. Substituting into (3) and integrating with respect to x from zero to $(R^2 - L^2)^{1/2}$ gives the total pickup rate on one face of disk. This can be written in the dimensionless form

$$\frac{Q}{\Omega R^2 d_0} = \frac{3}{8}\lambda(1 - \ell^2)^{4/3} \, \text{Ca}_0^{1/6} +$$

$$+ \left(\frac{1}{3}K - \frac{1}{9}\lambda^3\right)(1 - \ell^2)^{3/2} \, \text{Ca}_0^{1/2} \quad (4)$$

Here λ and K denote the numerical coefficients in (1), $\ell = L/R$, and d_0 and Ca_0 denote the values of d and Ca corresponding to the extreme edge of the disk, so that

$$d_0 = \left(\frac{\mu\Omega R}{\rho g}\right)^{1/2}, \quad \text{Ca}_0 = \frac{\mu R \Omega}{\sigma}. \quad (5)$$

Note also that after (1) is substituted into (3), the result is found by expanding in powers of Ca with only the first two terms being retained; the higher powers are neglected because terms of the same order were neglected in (1).

At higher speeds, equation (1) does not apply; but the pickup rate is still given by (3) and we can use the empirical relation (2) to evaluate it. In this way we obtain

$$\frac{Q}{\Omega R^2 d_0} = \frac{2}{5}(1 - \ell^2)^{5/4}(c - \frac{1}{3}c^3) \quad (6)$$

and $c \simeq 0.8$.

Since the vertical speed of the disk increases toward the outer edge of the disk there will be a range of rotational speeds in which, strictly speaking, the inner, slower moving portions of the disk require the application of equation (1) while the outer portions require equation (2). The resulting integral for the pickup rate can be written down but is extremely complicated. Since the result then lies between that given by equa-
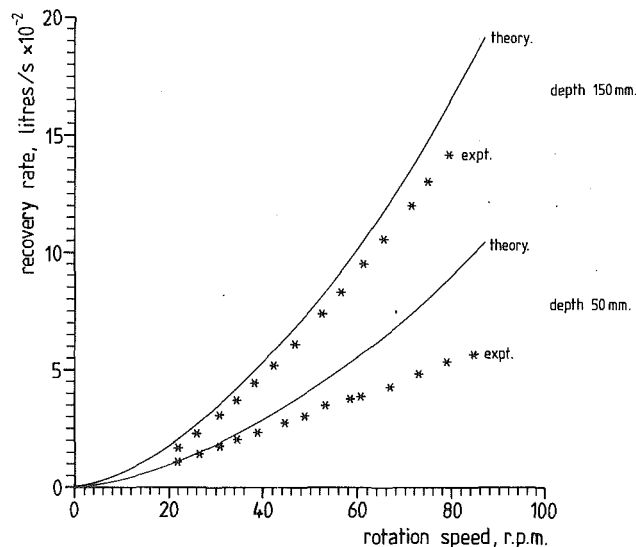
Fig. 6 Comparison of theory and experiment at two depths of immersion for oil of viscosity 30cS ($0.3m^2/s$).
_____ theory; * experiment.
(Uncertainty in experimental data as in Fig. 2, in theoretical curve ∓3 percent.)

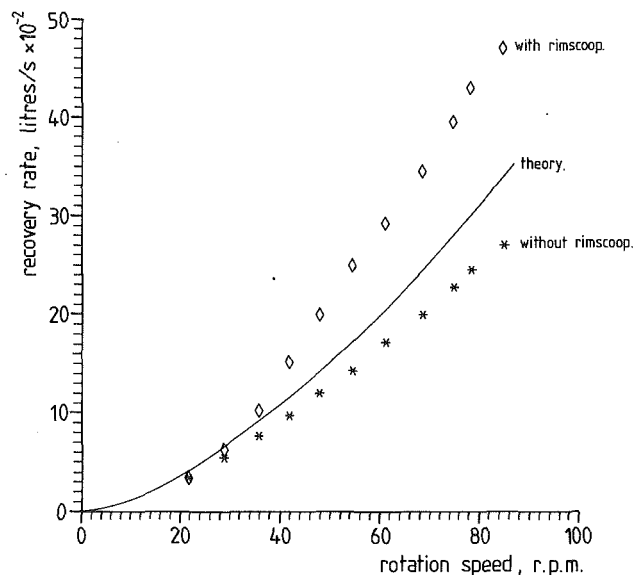Fig. 7 Use of rim scoop to estimate tail losses; depth of immersion 125 mm, oil viscosity 105cS ($1.05m^2/s$).
_____ theory, ◊ with rim scoop, * without rim scoop.
(Uncertainty as in Fig. 6.)

tions (4) and (6), it was thought preferable to deal with this case by smoothly interpolating between (4) and (6) (rather than between (1) and (2)).

The resulting predictions have been made for selected cases and are compared with experimental data in the next section.

4 Comparison With Experiment

An important source of uncertainty is the estimation of the amount of oil thrown off the edge of the disk by centrifugal action and therefore not collected by the scraper. Not all the oil which reached the edge of the disk was lost; much of it was retained in a kind of thickened "bead" of liquid held on to the rim of the disk by surface tension. Near the free surface, however, some escaped in the tail indicated in Fig. 1; this was more significant at low depths of immersion, when gravity would also tend to pull liquid off the disk.

In some experiments the tail losses were simply ignored; then we should expect the theory to overestimate the pickup rate. In other experiments the oil in the tail was collected by introducing a scoop at the level of the free surface. However it was clear from a visual inspection of the flow that this arrangement would also collect some oil thrown up from the submerged portion of the disk, that is, oil which was never properly "picked up" on to the disk in the manner considered in the theory. We should therefore expect the theory to underestimate the pickup rate in these cases.

In Fig. 6, theory and experiment are compared for a disk of radius 150 mm rotating in oil of viscosity 30cS ($0.3m^2/S$). Other data are given in the caption. No rim scoop was used so the pickup rate is measured net of tail losses. It is clear that the agreement is much better for the larger depth of immersion, because the tail losses were smaller and the neglect of centifugal effects more secure, as explained above.

In Fig. 7 we see the results of a further series of experiments, this time in oil of viscosity 105 cS, in which a rim scoop was employed to pick up the oil thrown off in the tail. This oil was collected and measured separately. For the reason explained above the theory falls between the two series of measurements.

On the basis of these comparisons it may be concluded that the theory gives a satisfactory estimate for disks which are approximately half-immersed. At smaller depths, edge losses and centrifugal effects cause serious discrepancies. However the half-immersed configuration is probably of most practical relevance.

References

Christodoulou, M. S., 1985, "Hydrodynamic Performance of Rotating Disc Skimmers," Ph.D. thesis, University of Manchester.

Christodoulou, M. S., and Turner, J. T., 1987, "Experimental Study And Improvement Of The Rotating Disc Skimmer," Proceedings of 1987 Oil Spill Conference, Baltimore, MD.

Cormack, D., 1983, Response To Oil And Chemical Marine Pollution, Applied Science Publishers.

Leibovich, S., 1977, "Hydrodynamic Problems In Oil-Spill Control and Removal," Journal of Petroleum Technology, Mar.

Marcinowski, H. J., 1976, "The Separation Of Oil From Water Surface," In IOPPEC, Part III, Hamburg.

Smith, J. E., 1968, "Torrey Canyon—Pollution And Marine Life," Marine Biology Association, Plymouth Laboratory Report XIV, Cambridge Univ. Press.

Spiers, Subbaraman, and Wilkinson, 1974, "Free Coating Of A Newtonian Liquid Onto A Vertical Surface," Chem. Eng. Sci., Vol. 29, p. 389.

Taylor, W., 1968, "Torrey Canyon Exercise Mop Up," Report No. 52, Mar., Admiralty Oil Laboratory, Fairmile, Surrey.

Thomas, D. H., and Davia, N. C., 1980, "Komara Miniskimmer: An Assessment Of Performance," Report No. LR 340 (OP), Warren Spring Laboratory, Stevenage, UK.

Thomas, G. W., 1977, "Oil Recovery Devices," Technical Memorandum No. 132 083, B. P. Research Centre, Sunbury-On-Thames.

Wilson, S. D. R., 1982, "The Drag-out Problem In Oil Film Coating Theory," Journal of Engineering Mathematics, Vol. 16, p. 209.

T. Yoshida

Associate Professor of
Aerospace Engineering,
Department of Mechanical and
Precision System,
School of Science and Engineering,
Teikyo University,
Toyosatodai, Utsunomiya, 320, Japan

K. Takayama

Professor of Gasdynamics,
Institute of Fluid Science,
Tohoku University,
Sendai, 980, Japan

Interaction of Liquid Droplets With Planar Shock Waves

Interactions and breakup processes of 1.50-mm-diameter ethyl alcohol droplets and 5.14-mm-diameter water bubbles with planar shock waves were observed using double-exposure holographic interferometry. Experiments were conducted in a 60 mm × 150 mm cross-sectional shock tube for shock Mach number 1.56 in air. The Weber numbers of droplets and liquid bubbles were 5.6×10^3 and 2.9×10^3, respectively, while the corresonding Reynolds numbers were 4.2×10 and 1.5×10^5. It is shown that the resulting holographic interferogram can eliminate the effect of the mists produced by the breakup of the droplets and clearly show the structure of a disintegrating droplet and its wake. This observation was impossible by conventional optical flow visualization. It is demonstrated that the time variation of the diameter of a breaking droplet measured by conventional optical techniques has been overestimated by up to 35 percent.

1 Introduction

As well as being an interesting research problem in gasdynamics, the phenomenon of droplet breakup by a high-speed gas stream has many important applications, such as chemical processes in two-phase flows, spray drying, rain damage, space technology (ablation and rocket nozzle flow), liquid fuel injection, aerosol formation, and steam turbine blade erosion. Hence, the interaction of liquid droplets with shock waves has been studied over the past three decades [1–8]. Recently, a comprehensive review on the shattering of liquid drops was presented [9]. Using flash photography, Lane [1] observed the breakup process of droplets with diameters from 0.5 mm to 4.0 mm in steady and transient gas flows and determined the critical condition at which the breakup occurs. Engel [2] observed the interaction process of water droplets of diameters 1.4 mm and 2.7 mm with shock Mach numbers 1.3, 1.5, and 1.7 by means of flash photography. Hanson et al. [3] observed the breakup of drops by air blasts using flash photography. Ranger and Nicholls [4] conducted a study to find the rate of drop shattering, the breakup time, the drop displacement, and the drop deformation for a range of conditions generated by two-phase detonations using the individual photographs with an image converter camera and the streak pictures. Körner [5] analyzed the boundary layer flow around a droplet and showed its effect on the droplet breakup at high-speed flows. Sophisticated use of the flash X-ray method was demonstrated by Reinecke and Waldman [6]. They used water droplets containing lead compound to enhance the X-ray image and determined, although not by a very clear-cut image, the three-dimensional breakup structure of droplets exposed to strong shock waves.

Studies of the interaction of droplets with shock waves were

mainly conducted in shock tubes [7, 8]. It is widely recognized that the shock tube is a useful tool for shock-droplet interaction study. In previous studies, schlieren and shadowgraph methods were used. However, it is impossible by these methods to visualize the fine structure of the shattering droplets. Therefore, it is a major goal of the present study to re-examine this classical problem by holographic interferometry, which is capable of visualizing the detailed structure of the shattering droplets. The experiment was conducted in a 60 mm × 150 mm cross-sectional shock tube. The breakup processes of 1.50 mm diameter ethyl alcohol droplets and 5.14-mm-diameter water bubbles were observed by double-exposure holographic interferometry using a Q-switched ruby laser as a light source.

The Weber numbers, based on the droplets and liquid bubbles, were 5.6×10^3 and 2.9×10^3, respectively, while the corresponding Reynolds numbers were 4.2×10^4 and 1.5×10^5. The shock Mach number was 1.56 in air, which corresponds to the local flow Mach number of 0.65 and the stream velocity of 264 m/s behind the shock wave.

As will be shown subsequently, the resulting interferograms can eliminate the effect of the mists produced by the breakup of the droplet. It is clearly shown that the shattering droplet has a fine structure which by conventional flow visualization looks like a fireball. By comparing the diameter of the breaking droplet which was measured from the holographic interferogram with that measured from the image hologram which is equivalent to a shadowgram, it is concluded that the time variation of the diameter of a breaking droplet in previous works was overestimated by up to 35 percent.

2 Experiment

Shock Tube. The experimental setup is shown schematically in Fig. 1. The low pressure channel of the shock tube was 60 mm × 150 mm in cross section and 5 m long; the high pressure chamber was 230 mm in diameter and 1.5 m
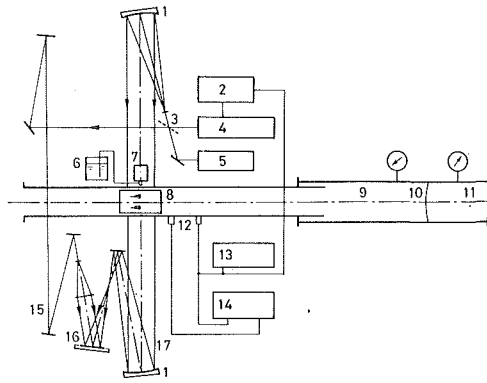
Fig. 1 Experimental setup and optical arrangment. 1-300 mm diameter paraboloidal schlieren mirrors, 2-laser controller, 3-beam splitter, 4-ruby laser (22Hd, Apollo Lasers Inc.), 5-He-Ne laser, 6-test liquid, 7-vibrator, 8-150 mm × 250 mm observation window, 9-low pressure channel (60 mm × 150 mm, 5 m), 10-diaphragm (polyester film), 11-high pressure chamber (230 mm diameter × 3 m), 12-pressure transducers, 13-transient recorder, 14-universal counter, 15-reference beam, 16-holographic film, 17-object beam

long. The circular cross section and the rectangular cross section were connected by a cookie-cutter.

The diaphragm was a polyester film 0.188 mm thick. The test gas was air at room temperature and atmospheric pressure. The driver gas was helium.

The shock velocity was measured using pressure transducers (Kistler model 603A) located 250 mm apart just in front of the test section. The shock wave Mach number was Ms = 1.56. By changing the delay time, experiments were conducted with identical initial conditions. A very good repeatability was obtained.

The observation was carried out using double-exposure holographic interferometry [10–15]. It is demonstrated that holographic interferometric flow visualization is particularly useful for shock-droplet interaction studies [11].

Holographic Interferometry. A schematic diagram of the present optical arrangement is also shown in Fig. 1. The present optical system consisted of a set of two paraboloidal schlieren mirrors of 300-mm-diameter and 3-m focal length, a beam splitter which can transmit 60 percent of the laser beam intensity to the object beam, auxiliary planar mirrors and lenses. The object lenses were combined to give a sharply focused image of the phenomenon. A Q-switched ruby laser (Apollo Lasers Inc., 22HD, 2 J/pulse and 30 ns pulse width) was used as the light source.

The angle between the reference beam and the object beam was about 20 degrees, and the difference in their path lengths was less than 10 mm. The magnification of the image in the test section was about 0.6. The film used was an Agfa 10E75 100 mm × 125 mm sheet film.

The hologram was processed by a Kodak D-19 developer at 293 K for 4.5 minutes in a double exposure. Super Fuji Fix was used as a fixer. Reconstruction of holograms was carried out using an argonion laser (wavelength 514.5 nm). The distortion of the image, which is attributed to the difference of the wavelength in taking the holograms and in reconstructing the holograms, was found not to be significant. This is easily modified by computer-aided image processing.

Although the image holographic technique was used here, the information on three-dimensional phenomena such as the mist distribution over a shattering drop could be stored even on the hologram. Therefore, the reconstructed holographic interferogram can distinguish the mist distribution much better than conventional optical flow visualization techniques.

Weber Number. In this experiment, the shattering droplet diameters obtained by shadowgraphs and holographies are compared. In order to obtain a stripping-type breakup, as the previous researchers conducted, the Weber number of the order of 10^3 was selected in this experiment. The shock number 1.56 can be stably performed with this experimental setup. Then, the diameters of a droplet and liquid bubble were determined to be 1.50 mm and 5.14 mm, respectively. Their Reynolds numbers were resultant; however, they were useful to assume the airflow densities, pressure distributions around a droplet, and so on.

Production of Ethyl Alcohol Droplets and Water Bubbles. As shown in Fig. 1, uniformly sized ethyl alcohol droplets 1.50 mm in diameter were produced by the longitudinal vibration of a nozzle. Using a double cylindrical nozzle, water bubbles were produced which contained air within them. These bubbles had an outer diameter of 5.14 mm and a liquid film thickness of 0.29 mm.

3 Results and Discussion

Ethyl Alcohol Droplets. In Figs. 2(*a*) and 2(*b*), interferograms are shown which were taken at time $t = 26.7$ and 82.1 μs after the shock wave passed the leading edge of the droplets. The shock Mach number, M_s, is 1.56 and the local flow Mach number given behind the shock wave is $M_2 = 0.65$. This corresponds to a local flow velocity of 264 m/s.

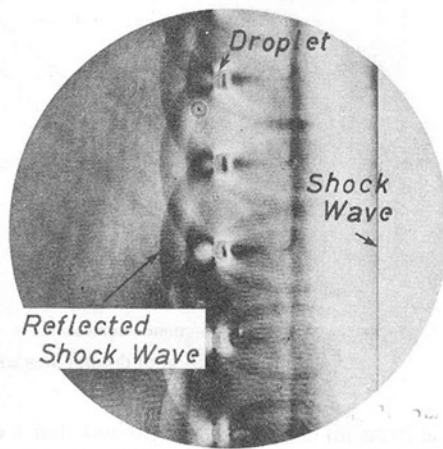The reflected shock wave can be seen in front of the droplet

─────── Nomenclature ───────

a = longitudinal diameter of a liquid droplet or a liquid bubble measured from the holographic interferogram

a' = longitudinal diameter of a liquid droplet or a liquid bubble measured from the shadowgraph

a_0 = sound velocity of gas in front of a shock wave

a_2 = local sound velocity of gas behind a shock wave

b = transverse diameter of a liquid droplet or a liquid bubble measured from the holographic interferogram

b' = transverse diameter of a liquid

uid droplet or a liquid bubble measured from the shadowgraph

D = diameter of a liquid droplet

D_b = outer diameter of a liquid bubble

D_i = inner diameter of a liquid bubble

M_2 = local Mach number of a uniform flow behind a shock wave ($= u_2/a_2$)

M_s = shock Mach number ($= U_s/a_0$)

Re = Reynolds number of a liquid droplet ($= u_2 D/\nu_a$)

Re_b = Reynolds number of a liquid bubble ($= u_2 D_b/\nu_a$)

t^* = dimensionless time ($= tu_2\sqrt{\rho_2/\rho_l}/D$ or $tu_2\sqrt{\rho_2/\rho_l}/D_b$)

u_2 = particle velocity of a uniform flow behind a shock wave

U_s = velocity of a shock wave

We = Weber number of a liquid droplet ($= \rho_2 u_2^2 D/2\sigma$)

We_b = Weber number of a liquid bubble ($= \rho_2 u_2^2 D_b D_i/2(D_b + D_i)\sigma$)

ν_a = kinematic viscosity of a uniform flow behind a shock wave

ρ_2 = density of a uniform flow behind a shock wave

ρ_1 = liquid density

σ = surface tension
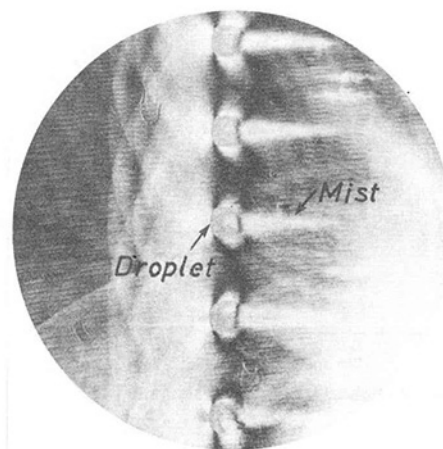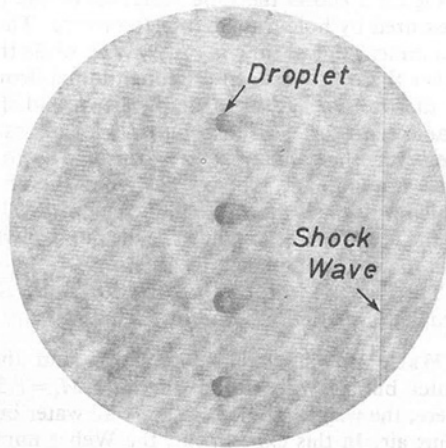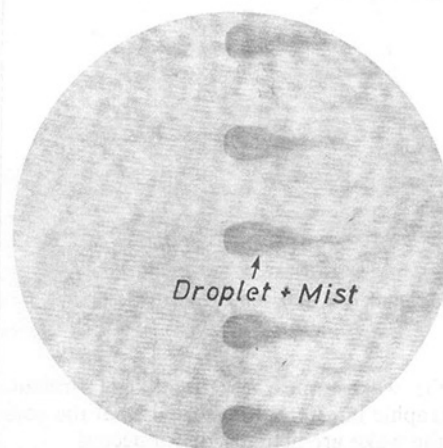
Fig. 2 Interaction of ethyl alcohol droplets with shock waves. (a) and (c) correspond to reconstructed and nonreconstructed holograms of the same experiment, respectively. The same applies to (b) and (d).

and quickly decays to a sonic wave around the droplet. Therefore, these wave interactions will not influence the deformation and shattering of the droplets. The boundary layer separation can be seen over the droplets in Fig. 2(a). In Fig. 2(b), although the core of the shattering droplet may be decreasing, the shattered parts or mists are leaving from the core surface and the resulting shape of the shattering droplet looks like a fireball whose apparent diameter is larger than the original size. Therefore, no detailed wave interaction could be observed. It is reported that the above-mentioned processes are strongly dependent on the Weber number. Figure 2 is for $W_e = 5.6 \times 10^3$, where the Weber number is defined as equation (1),

$$We = \frac{\rho_2 \, u_2^2 D}{2 \, \sigma} , \qquad (1)$$

where ρ_2, u_2, D and σ are the density, the uniform flow velocity behind the shock wave, the droplet diameter and its surface tension, respectively.

Figures 2(c) and 2(d) show shadowgraphs which correspond to Figs. 2(a) and 2(b). These shadowgraphs are enlarged direct prints of the image holograms from which the holographic interferograms of Figs. 2(a) and 2(b) are reconstructed. The image holograms are equivalent to the direct shadowgraphs.

Photographs of the Shadowgraphs. In Fig. 2, the planar

shock waves propagate from left to right. The induced flow behind the shock wave moves toward the right.

Since the schlieren or the shadowgraph method has been used in the previous flow visualization studies, the fireballs shown in Figs. 2(c) and 2(d) are familiar interaction patterns. It is clearly found that in the interferogram, the major part of the breaking droplet can be distinguished from the mist and the wake, whereas in the shadowgraph, this fine structure is no longer observable. In Figs. 2(a), 2(b), 2(c), and 2(d), the magnification of the image is identical. It is immediately found that the shadowgram record overestimates the diameter of the breakup liquid droplet since the mists which were formed during the breaking-up process cause the volume of the droplet to buldge.

The present scheme is image holography, however. This process is partially similar to real-time diffuse holography, since the liquid droplets in the mist and the wake scatter the collimated object beam and act as a diffuser. Not only the wave interaction but also the mist distribution over shattering droplets and their wakes can be seen in the interferograms, whereas they cannot be observed in the shadowgraph. Therefore, three-dimensional information of the mist and the wake can be visualized after reconstructing the present holograms. It is observable in Fig. 2 that the boundary layer is separated behind the droplet and a wake region exists. The corresponding shadowgraph shows that the images of the core
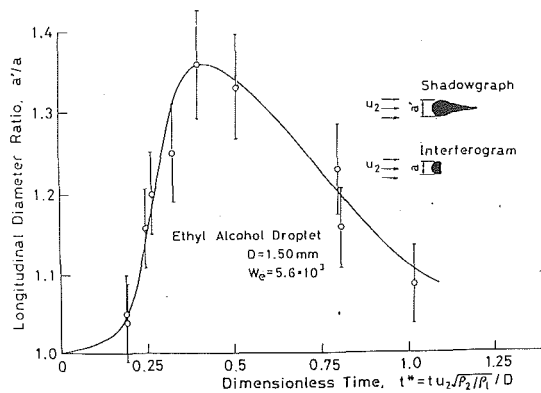
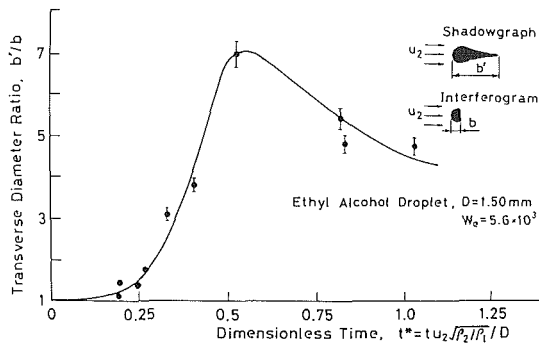**Fig. 3 Time variation of longitudinal diameter ratio**

Fig. 4 Time variation of transverse diameter ratio

Fig. 5 Deformation of droplet size with time

of a droplet and the wake appear to fuse like a fireball. However, the holographic interferogram reveals that the core of the droplet and the wake are actually disconnected.

Figure 3 shows the time variation of the longitudinal diameter ratio a'/a, where a' is the longitudinal droplet diameter measured from the shadowgraphs, for example in Figs. 2(c) and 2(d), and a is the longitudinal diameter measured from the interferograms as in Figs. 2(a) and 2(b). The horizontal axis is the dimensionless time $tu_2\sqrt{\rho_2/\rho_1}/D$. The droplet diameter given by the shadowgraph is always larger than that obtained from the interferogram. The ratio of these diameters corresponds to the time variation of the mist distribution at the droplet surface. This ratio reaches a maximum of 35 percent. This discrepancy is sometimes important when there is a need to estimate the drag force acting on the shattering drops.

In Fig. 4, the time variation of the ratio b'/b for transverse diameter is shown in a similar manner to Fig. 3, where b' is the droplet transverse diameter given by the shadowgraph and b is that obtained by the interferogram. It is found that the ratio of the transverse diameter of the droplet is surprisingly different due to the difference of the recording systems. In the shadowgraph, the tail and the head of the fireball cannot be distinguished. Therefore, b' is apparently longer.

In the shock-drop interaction which eventually causes the droplet breakup, the important effect of unsteady drag force [16], [17] should be considered. It is known that when a shock wave propagates over a cylinder, an enormous unsteady drag force is generated at in the initial stage [18]. A similar trend must occur when the shock wave hits the drops. For very strong shock waves, it is also necessary to take into account the wave interaction inside the droplet, since the pressure wave is induced in the liquid phase as well. This internal wave interaction is caused by the shock wave propagating over the droplet surface and the reflection at the leeward surface of the droplet, and it accelerates the shattering process. Reinecke and
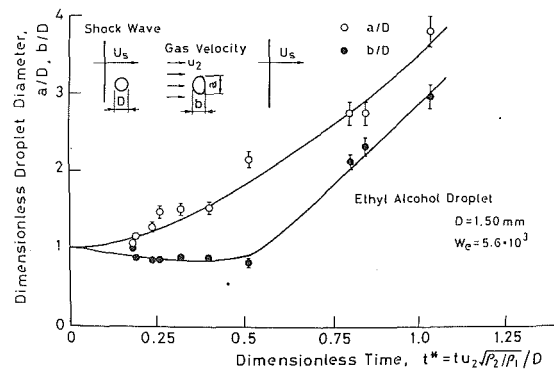
Waldman [6] experimentally showed that a droplet was shattered explosively immediately after a strong shock wave hit the droplet.

Figure 5 shows the time variation of the droplet diameter measured by holographic interferometry. The horizontal axis is a dimensionless time $tu_2\sqrt{\rho_2/\rho_1}/D$; while the vertical axis is either the ratio between the longitudinal droplet diameter, a, or the transverse droplet diameter, b, and the initial droplet diameter, D. The value of a/D increases monotonously. However, the value of b/D is constant up to a dimensionless time $t^* = 0.5$, i.e., about 15D from the shock front, after which it begins to increase monotonously. This starting point of the variation is thought to be the point at which the breakup and the shattering begin to accelerate.

The increase in the value of a/D and b/D means that the droplet is shattering in a bowl shape.

Water Bubbles. The interaction and the breakup of a water bubble with shock waves of $M_s = 1.56$ are observed. Here, the water bubble is a thin-wall water bubble which contains air. In this experiment, the Weber number is 2.9×10^3. Here, the Weber number for water bubbles is defined as equation (2),

$$\mathrm{We}_b = \frac{\rho_2 u_2^2 D_b D_i}{2(D_b + D_i)\sigma}, \qquad (2)$$

where D_b and D_i are the outer and inner diameters of the water bubble. D_b is 5.14 mm and the wall thickness of 0.29 mm. The contributions from both inner and outer surfaces are taken into account.

Two sequential holographic interferograms are shown in Figs. 6(a) and 6(b). The interaction and the eventual breakup of the water bubbles are compared. The corresponding shadowgraphs are shown in Figs. 6(c) and 6(d). In Figs. 6(a) and 6(b), the wave interaction can be seen much more clearly than in the cases of the liquid drops, since the bubble diameter is much larger. At the earlier stage, the fringe distribution at the shoulder of the bubble indicates the boundary layer separation. It is interesting to note that at the earlier stage, the water bubble resists the shock just like a solid body. However, as time passes it deforms quickly and because it is hollow the wake and mist generation cannot be seen.

The water bubble contains air, and hence the process of its deformation and breakup is significantly different from that of a pure liquid droplet. The distribution of the mist at the bubble surface is restricted to a narrow limit at the rear of the water bubble; therefore, no distinct wake can be observed. Also, the difference between the bubble diameter as evaluated from the holographic interferograms and the corresponding shadowgraphs is found to be negligible.

Figure 7 shows the time variation for the water bubble diameter obtained from the interferograms. The time variation of the ratios of the longitudinal diameter a/D_b and the transverse diameter b/D_b is different from that obtained for
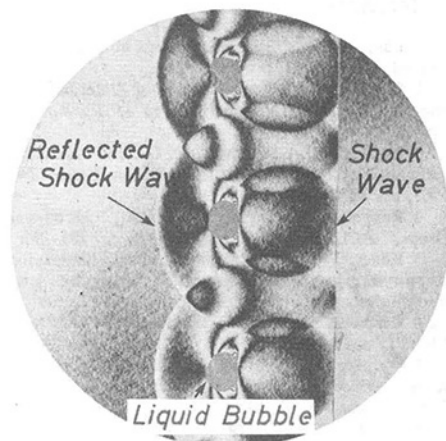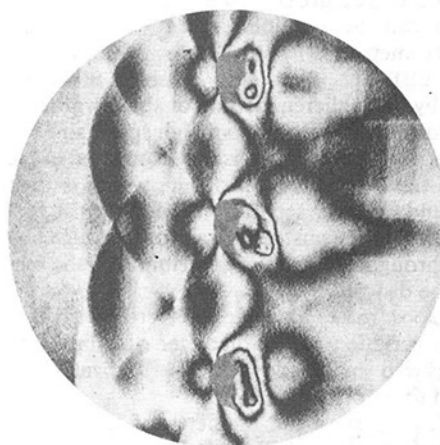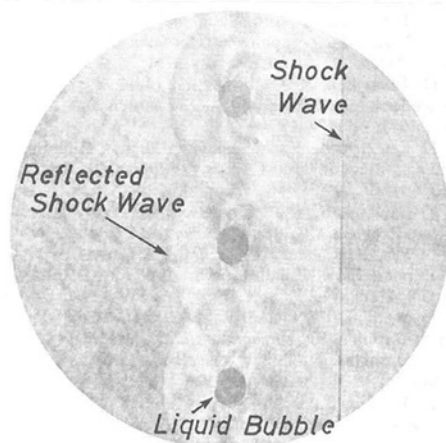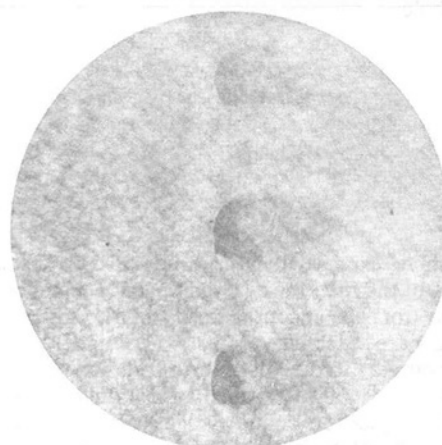
Fig. 6(a)

Fig. 6(b)

Fig. 6(c)

Fig. 6(d)

Fig. 6 Interaction of water bubbles with shock waves. (a) and (c) correspond to reconstructed and nonreconstructed holograms of the same experiment, respectively. The same applies to (b) and (d).

ethyl alcohol droplets where, due to the existence of the wake, the transverse diameter was elongated significantly.

Breakup Time. Holographic interferometry is also useful to determine the breakup time and the breakup distance of a stripping-type droplet breakup. In previous experiments, shadowgraph and schlieren methods were used to determine the breakup time of droplets. However, due to the light scattering by the micromist, it was very difficult to distinguish the unstripped part of the droplet in the later stage of the breakup process. On the other hand, using holographic interferometry, it is possible to visualize the remaining unstripped part of the disintegrating droplet. The breakup time is defined as a time period between initiation of the interaction of the incident shock wave with the droplet and the moment when the unstripped part of the droplet loses its opaqueness on a film. From the holograms, it is clearly seen that while the remaining part of the droplet looks opaque, the microspray in the wake has a diffuse appearance. In previous shadowgraphs, the structure of shattering droplets could not be distinguished. However, use of the present holographic interferometry makes the unstripped part of the droplet clearly visible.

4 Conclusion

The interaction and the breakup of ethyl alcohol droplets and water bubbles with shock waves have been observed by us-

Fig. 7 Deformation of water bubble diameter with time
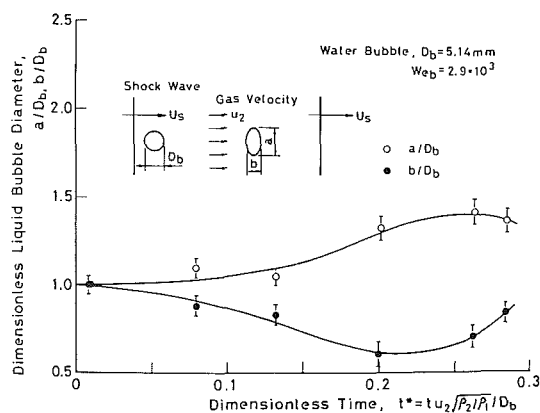
ing holographic interferometry. It should be emphasized that holographic interferometry provides a new understanding of the shattering liquid droplets. This has been the first experimental effort to observe the precise mechanism of the interaction and the breakup of liquid droplets or liquid bubbles with planar shock waves.

As a result, the following conclusions were obtained.

1. It is shown that the structure of shattering liquid droplets and liquid bubbles can be obtained more exactly using holographic interferometry. The structure obtained by holography looks different from the fireball structure observed in the past by the schlieren method or shadowgraphs.

2. When a liquid droplet is exposed to a high speed air flow behind a shock wave, the liquid droplet is first elongated in the direction normal to the flow direction of air, which is then followed by the boundary layer separation induced mist formation. It is supposed that the unsteady drag force induced by shock propagation throught the droplet contributes to the early deformation of the droplet.

3. With double-exposure holographic interferometry, it is shown that the time variation of the diameter of a breaking liquid droplet measured by shadowgraph visualization is overestimated by up to 35 percent.

4. There is no difference in the diameter of a breaking liquid bubble as found by a shadowgraph or a double-exposure holographic interferogram. Because it is hollow the spreading mist is not so much to obscure the diameter of a breaking liquid bubble.

Acknowledgment

References

1 Lane, W. R., "Shatter of Drops in Streams of Air," *Ind. Eng. Chem.*, Vol. 43, No. 6, 1951, pp. 1312–1317.

2 Engel, O. G., "Fragmentation of Waterdrops in the Zone behind an Air Shock," *J. Res. of National Bureau of Standard*, Vol. 60, Mar. 1958, pp. 245–280.

3 Hanson, R. A., Domich, E. G., and Adams, H. S., "Shock Tube Investigation of the Breakup of Drops by Air Blasts," *Phys. Fluids*, Vol. 6, No. 8, 1963, pp. 1070–1080.

4 Ranger, A. A., and Nicholls, J. A., "Aerodynamic Shattering of Liquid Drops," *AIAA J.*, Vol. 7, No. 2, 1969, pp. 285–290.

5 Köner, W., "Die Zerstörung eines Flüssigkeitstrofpfens Aufgrund von Aerodynamicschen Kräften," Deutsche Luft- und Raumfahrt, Forschungsbericht, 70-05, 1970, pp. 1–99.

6 Reinecke, W. G., and Waldman, G. D., "Shock Layer Shattering of Cloud Drops in Reentry Flight," AIAA Paper, 75-152, 1975, pp. 1–22.

7 Harper, E. Y., Grube, G. W., and Chang, I-D, "A Unified Theory of Raindrop Breakup," *Shock Tube Research*, Proc. 8th International Shock Tube Symp., Paper No. 63, 1971.

8 Simpkins, P. G., "Droplet Response to Accelerations Induced by Weak Shock Waves," ibid. Paper No. 64, 1971.

9 Wierzba, A., and Takayama, K., "Experimental Investigation on Liquid Droplet Breakup in a Gas Stream," Rep. Inst. High Speed Mech., Tohoku Univ., Vol. 53, 1987, pp. 1–99.

10 Takayama, K., and Watanabe, W., "Shock Wave Transition over Concave Walls—Holographic Interferometric Observation," Mem. Inst. High Speed Mech., Tohoku University, Vol. 45, 1980, pp. 1–33.

11 Takayama, K., "Application of Holographic Interferometry to Shock Wave Research," *Proc. SPIE—The Intern. Soc. for Optical Engineering*, Vol. 398, 1983, pp. 174–180.

12 Lauterborn, W., and Ebeling, K. J., "High-Speed Holography of Laser Induced Breakdown in Liquids," *Applied Physics Letters*, Vol. 31, 1977, pp. 663–664.

13 Lauterborn, W., "Cavitation Bubble Dynamics—New Tools for an Intricate Problem," *J. Applied Scientific Research*, Vol. 38, 1982, pp. 165–178.

14 Lee, Y. J., and Kim, J. H., "A Review of Holography Application in Multiphase Flow Visualization Study," ASME JOURNAL OF FLUIDS ENGINEERING, Vol. 108, No. 3, Sept. 1986, pp. 279–288.

15 Watt, D. W., and Vest, C. M., "Digital Interferometry for Flow Visualization," *Experiments in Fluids*, Vol. 5, 1987, pp. 401–406.

16 Simpkins, P. G., and Bales, E. L., "Water-drop Response to Sudden Accelerations," *J. Fluid Mech.*, Vol. 55, No. 4, 1972, pp. 629–639.

17 Temkin, S., and Mehta, H. K., "Droplet Drag in an Accelerating and Decelerating Flow," *J. Fluid Mech.*, Vol. 116, 1982, pp. 297–313.

18 Takayama, K., and Itoh, K., "Unsteady Drag of Circular Cylinders and Aerofoils in Transonic Shock Tube Flows," Rep. Inst. High Speed Mech., Tohoku Univ., Vol. 51, 1986, pp. 1–43.

Jing-Fa Tsai
Associate Professor.

Yih-Nan Chen
Professor.

Institute of Naval Architecture,
National Taiwan University,
Taipei Taiwan

A Generalized Approach on Equilibrium Theory of Cavitation Nuclei in Liquid-Gas Solutions

The availability of a single bubble-droplet system is derived from energy conservation and the principle of entropy. The equilibrium and critical conditions are determined by minimizing the availability without any assumption on the volume of the bubble-droplet system. It is found that the compressibility effect of the liquid-gas solution can be neglected in such a small bubble-droplet system and dilute solution condition. The results of the present analyses confirm previous conclusions reached by Cha that a bubble can remain in a state of stable equilibrium provided that the ratio of the total number of moles of gas to the total number of moles of the liquid is not extremely small and the external pressure falls between a dissolution limit and a cavitation limit.

1 Introduction

It is well known that the theoretical tensile strength of pure liquids is much larger than that ever observed. This disagreement between theory and observation leads one to postulate the existence of weak spots in liquids. The nuclei with undissolved gas and uncondensed vapor in liquids are the most likely weak spots. Cavitation is then considered as the unstable growth of nuclei when pressure is reduced. The problem of the stability of nuclei thus becomes an important topic for predicting the cavitation inception.

The problem of stability of gas bubble in an infinite liquid-gas solution was first analyzed by Epstein and Plesset [1] in 1950. It was concluded that a gas bubble would grow in a supersaturated solution, collapse in an undersaturated solution, and even in a saturated solution, the bubble would be forced into solution due to surface tension effect. In 1977, Mori et al. [2] reanalyzed the same problem by considering a bubble in a finite liquid-gas solution. They studied the problem both analytical and experimentally. It was shown that stable equilibrium was possible and that a dissolution limit of bubble existed. A similar thermodynamic instability analysis was done by Cha [3] in 1981. Cha concluded that a bubble could remain in a state of stable equilibrium provided that the ratio of the total number of moles of the solute to the total number of moles of solvent in the system is not extremely small and that the system pressure falls between an upper bound (dissolution limit) and a lower bound (cavitation limit).

After Cha's report in 1981, there were many discussions and arguments on whether the bubble is stable or not [4–6]. The main arguments were: (*a*) Epstein and Plesset analyzed the problem with an infinite liquid-gas solution. Cha and Mori et al. analyzed the problem with a finite liquid-gas solution. A bubble in an infinite liquid-gas solution implies that the dif-

fuse gas across the bubble boundary does not change the gas concentration in the liquid-gas solution. That is not the case. The diffuse gas does change the gas concentration in the liquid-gas solution. The finite liquid-gas solution approach is more reasonable than the infinite liquid-gas solution approach. (*b*) Cha used the Helmholtz free energy to derive the equilibrium and critical conditions. This approach leads one to assume that the bubble-droplet system has a total constant volume to match the mechanical equilibrium condition, but this assumption implies that the molar volume of liquid-gas solution is equal to the molar volume of gas. Mori et al. used the Gibbs free energy to reach the same conditions, and they assumed that the volume of droplet was constant to match the
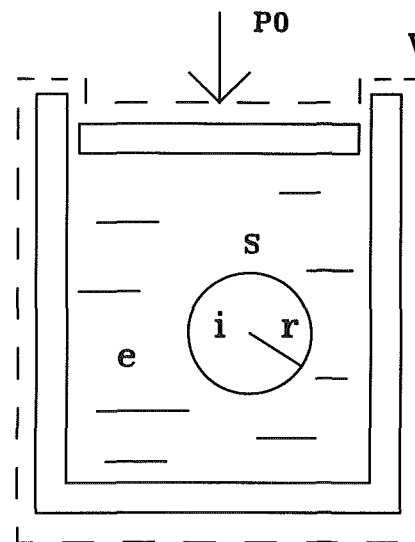

Fig. 1 Bubble-droplet system

mechanical equilibrium condition. This assumption implies that there is no phase change between gas and liquid droplet. Both assumptions contradict themselves with the thermodynamic theory, which is applied to analyze the bubble-droplet system for phase change.

In this paper, the thermodynamic theory was applied to analyze a finite two-component two-phase bubble-droplet system. The availability of the bubble-droplet was drived first. The equilibrium and critical conditions were then derived without any assumption on the volume of the system. Finally, the compressibility effect of the liquid-gas solution is estimated.

2 Formulation of the Problem

Figure 1 shows a bubble which contains the free gas and vapor suspended in a dilute liquid-gas solution. The boundary of the droplet of the liquid-gas solution is allowed to expand or contract to keep the external pressure on surface constant, and it is also impermeable for both the liquid and the gas.

The equations of the conservation of energy and the entropy principle for the material volume can be written as

$$\frac{d}{dt}(E^i + E^e + E^s) + \int_{\partial V}(q_i - \tau_{ij}u_j)n_i dS - \int_V (\rho g_i u_i)dV = 0$$

$$(1)$$

$$\frac{d}{dt}(\eta^i + \eta^e + \eta^s) + \int_{\partial V}(q_i/T)n_i dS \geq 0 \qquad (2)$$

In equation (1), the kinetic energy term is neglected under the assumption of slow thermodynamic process or quasi-static process. By neglecting the effect of the gravitational force, the stress τ_{ij} is $-P_0\delta_{ij}$, which holds on the boundary ∂V. The temperature is assumed to be constant throughout V. The heat flux term in equations (1) and (2) can be eliminated to obtain the following equation

$$\frac{d}{dt}[(E^i - T\eta^i) + (E^e - T\eta^e) + (E^s - T\eta^s) + P_0(V^i + V^e)] \leq 0 (3)$$

Equation (3) implies that the availability is minimum when the system is in a stable equilibrium state. Let $A = (E^i - T\eta^i) + (E^e - T\eta^e) + (E^s - T\eta^s) + P_0(V^i + V^e)$ denote availability [7] and F denotes the Helmholtz free energy, the availability A can be rewritten as

$$A = F^i(T,V^i,N_g^i,N_l^i) + F^e(T,V^e,N_g^e,N_l^e) + \sigma 4\pi r^2 + P_0(V^i + V^e)$$

$$(4)$$

3 Conditions of Equilibrium

From the conservation of mass

$$N_g^i + N_g^e = N_g = \text{const. and } N_l^i + N_l^e = N_l = \text{const.} \qquad (5)$$

The availability A is a function of N_g^i, N_l^i, V^i and V^e for constant temperature T and pressure P_0. The variation of the Helmholtz free energy, F^i and F^e, can be expressed as

$$dF^i = -P^i dV^i + \mu_g^i(T,V^i,X_g^i)dN_g^i + \mu_l^i(T,V^i,X_l^i)dN_l^i \qquad (6)$$

$$dF^e = -P^e dV^e + \mu_g^e(T,V^e,X_g^e)dN_g^e + \mu_l^e(T,V^e,X_l^e)dN_l^e \qquad (7)$$

By applying equations (5), (6), and (7), the variation of availability becomes

$$dA = \left(P_0 + \frac{2\sigma}{r} - P^i\right)dV^i + (P_0 - P^e)dV^e$$
$$+ [\mu_g^i(T,V^i,X_g^i) - \mu_g^e(T,V^e,X_g^e)]dN_g^i$$
$$+ [\mu_l^i(T,V^i,X_l^i) - \mu_l^e(T,V^e,X_l^e)]dN_l^i \qquad (8)$$

Since the parameters V^i, N_g^i, N_l^i and V^e are independent, the equilibrium conditions are

$$P_0 + 2\sigma/r - P^i = 0 \qquad (9)$$

$$P_0 - P^e = 0 \qquad (10)$$

$$\mu_g^i(T,V^i,X_g^i) = \mu_g^e(T,V^e,X_g^e) \qquad (11)$$

$$\mu_l^i(T,V^i,X_l^i) = \mu_l^e(T,V^e,X_l^e) \qquad (12)$$

4 Stability Criteria

For the determination of the stability criteria, the second variation of A needs to be calculated, and also the explicit expression of the chemical potentials is required. By the assumption of ideal mixtures and solutions, the chemical potentials can be written as

$$\mu_g^i(T,V^i,X_g^i) = \mu_{g0}^i(T) - RT\ln(V^i/(N_g^i RT)) \qquad (13)$$

$$\mu_l^i(T,V^i,X_l^i) = \mu_{l0}^i(T) - RT\ln(V^i/(N_l^i RT)) \qquad (14)$$

$$\mu_g^e(T,V^e,X_g^e) = \mu_{gH}^e(T,V^e) + RT\ln X_g^e \qquad (15)$$

$$\mu_l^e(T,V^e,X_l^e) = \mu_{lR}^e(T,V^e) + RT\ln X_l^e \qquad (16)$$

where Henry's convection is

$$\mu_{gH}^e(T,V^e) = \lim_{X_g^e \to 0} \mu_g^e(T,V^e,X_g^e) \qquad (17)$$

and Raoult's convention is

$$\mu_{lR}^e(T,V^e) = \lim_{X_l^e \to 1} \mu_l^e(T,V^e,X_l^e) \qquad (18)$$

Nomenclature

A = availability
A_{ij} = the partial derivatives of A with respect to V^i, N_l^i, N_g^i, and V^e
E = internal energy
F = Helmholtz free energy
g = gravitational force
J = Joule
K = Henry's constant
$N_{\text{sub}}^{\text{super}}$ = mole number of each component at each phase
N_g = total mole number of gas
N_l = total mole number of liquid
n_i = outer normal vector of droplet surface
$O(NN)$ = order of the negative term of the numerator

$O(PN)$ = order of the positive term of the nummerator
$O(ND)$ = order of the negative term of the denominator
$O(PD)$ = order of the positive term of the denominator
$P_{\text{sub}}^{\text{super}}$ = partial pressure
$P_a \ldots P_d$ = critical pressure
P_v = vapor pressure
P_0 = external applied pressure
q = heat flux
R = universal gas constant
r = radius of bubble
S = surface area of droplet
T = temperature

u_i = velocity vector
V = volume
X = mole fraction
ρ = density
σ = surface tension
μ = chemical potential
ν = partial mole volume
η = entropy

Subscripts

g = gas component
l = liquid component

Superscripts

i = internal of bubble, gas phase
e = external of bubble, condensed liquid phase
s = interface of bubble and droplet

The second order variation of A can be written as

$$d^2A = \sum_i \sum_j A_{ij} d(a_i) d(a_j) \tag{19}$$

where $a_i = V^i$, N_g^i, N_l^i, V^e for $i = 1, 2, 3, 4$, and $A_{ij} = \partial^2 A / (\partial a_i \partial a_j)$
The second-order partial derivatives of A are

$$A_{11} = -2\sigma/(3rV^i) + P^i/V^i \tag{20}$$

$$A_{21} = A_{12} = A_{31} = A_{13} = -RT/V^i \tag{21}$$

$$A_{41} = A_{14} = 0 \tag{22}$$

$$A_{22} = RT/N_g^i + RTX_l^e/N_g^e \tag{23}$$

$$A_{33} = RT/N_l^i + RTX_g^e/N_l^e \tag{24}$$

$$A_{32} = A_{23} = -RT/(N_g^e + N_l^e) \tag{25}$$

$$A_{42} = -\partial \mu_g^e/\partial V^e = A_{24} = \partial P^e/\partial N_g^e \tag{26}$$

$$A_{43} = -\partial \mu_l^e/\partial V^e = A_{34} = \partial P^e/\partial N_l^e \tag{27}$$

$$A_{44} = -\partial P^e/\partial V^e \tag{28}$$

Equation (19) is of the quadratic form in dV^i, dN_l^i, dN_g^i and dV^e. In order to get $d^2A > 0$, the quadratic form must be positive-definite. The conditions for the positive-definite quadratic form are

$$\left| A_{ij} \right|_n > 0 \quad \begin{array}{l} i \leq n \\ j \leq n \end{array} \quad n = 1,2,3,4 \tag{29}$$

For $n = 1$

$$P_0 > -4\sigma/(3r) \tag{30}$$

For $n = 2$

$$P_0 > -4\sigma/(3r) + P_l^i/(X_l^e + X_g^e N_l/(N_l - P_l^i V^i/(RT))) \tag{31}$$

For $n = 3$

$$P_0 > -4\sigma/(3r) + (N_l X_g^e P_g^i + N_g X_l^e P_l^i)/[N_g (X_l^e)^2 + N_l (X_g^e)^2] \tag{32}$$

Let the right-hand side of equations (30), (31), and (32) be denoted as P_a, P_b, and P_c respectively, it is found that $P_c > P_b > P_a$. The results are the same as that reported by Cha [3].

In order to calculate the fourth criteria, the following exact relations are required

$$\begin{aligned} \nu_g^e &= (\partial V^e/\partial N_g^e)_{P^e, N_l^e} \\ &= -[(\partial P^e/\partial N_g^e)_{V^e, N_l^e}]/[(\partial P^e/\partial V^e)_{N_g^e, N_l^e}] \end{aligned} \tag{33}$$

and

$$\begin{aligned} \nu_l^e &= (\partial V^e/\partial N_l^e)_{P^e, N_g^e} \\ &= -[(\partial P^e/\partial N_l^e)_{V^e, N_g^e}]/[(\partial P^e/\partial V^e)_{N_g^e, N_l^e}] \end{aligned} \tag{34}$$

Therefore, for $n = 4$

$$[P^i - 2\sigma/(3r)][u(\partial P^e/\partial V^e) + vRT] > [w(\partial P^e/\partial V^e) + xRT]RT/V^i \tag{35}$$

where
$$u = (\nu_g^e)^2/N_l^i + (\nu_l^e)^2/N_g^i + (1/N_g^e + 1/N_l^e)(\nu_{gl}^e)^2$$
$$v = 1/(N_g^i N_l^i) + X_l^e/(N_l^i N_g^e) + X_g^e/(N_g^i N_l^e)$$
$$w = (\nu_l^e - \nu_g^e)^2$$
$$x = 1/N_l^i + 1/N_g^i + 1/N_l^e + 1/N_g^e$$

In equation (35), the compressibility of the liquid-gas solution is the only negative term, and it will determine the critical condition. All possible cases are discussed as follows:

Case 1: When $[u(\partial P^e/\partial V^e) + vRT] > 0$, then

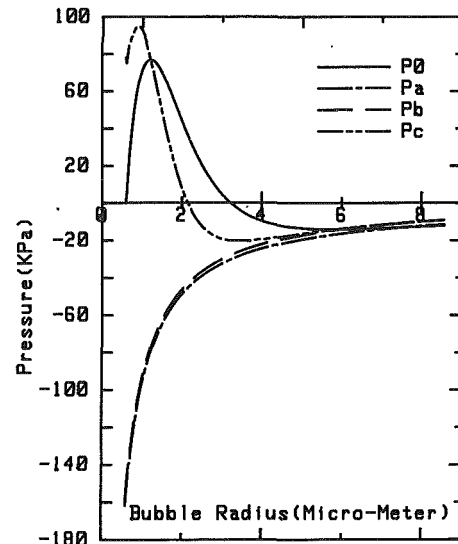$$P_0 > -4\sigma/(3r) + RT[w(\partial P^e/\partial V^e) + xRT]/\{[u(\partial P^e/\partial V^e) + vRT]V^i\} \tag{36}$$

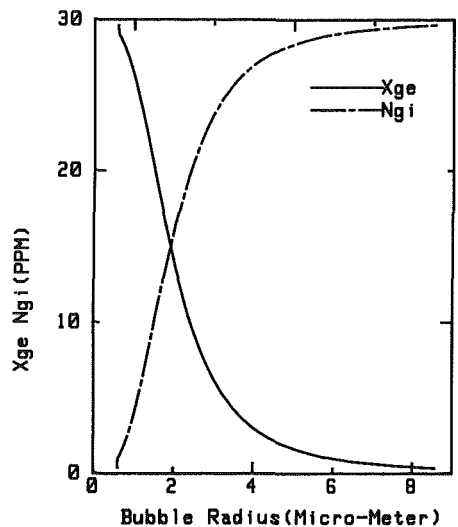Fig. 2 Typitical equilibrium and critical pressure

Ng/N1=30PPM

Fig. 3 Typitical free gas and fraction of dissolved gas

Let the right-hand side of equation (36) be denoted as P_d, when

Case 1(a): $P_d > P_c$

It shows that the system is stable when the pressure P_0 is greater than P_d.

Case 1(b): $P_d < P_c$

It shows that the system is stable when the pressure P_0 is greater than P_c.

The above two cases show that the system is stable when the equilibrium pressure P_0 is greater than the critical pressure P_c or P_d.

Case 2: When $[u(\partial P^e/\partial V^e) + vRT] < 0$, then $P_0 < P_d$

Case 2(a): $P_d > P_c$

In this case, the system is stable when P_0 is greater than P_c and less than P_d. The unstable condition occurs at either $P_0 \leq P_c$ or $P_0 \geq P_d$.

Equilibrium Curve

Ng/Nl = 45PPM
Ng/Nl = 35PPM
Ng/Nl = 25PPM
Ng/Nl = 20PPM
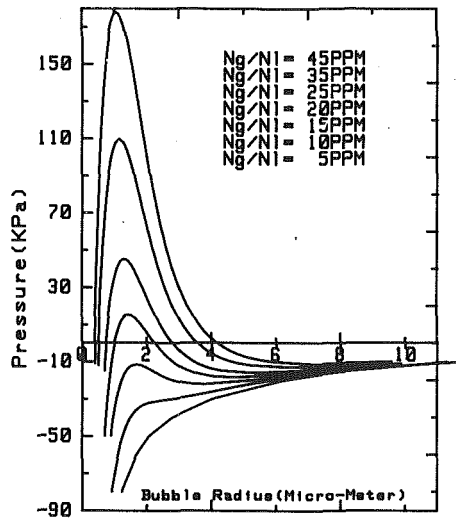Ng/Nl = 15PPM
Ng/Nl = 10PPM
Ng/Nl = 5PPM

Fig. 4 Family of equilibrium

Case 2(b): $P_d < P_c$

In this case, the system is always unstable.

5 Numerical Results

In order to calculate the stability criteria, the quantity of each parameter needs to be known. For given P_0, P^e is determined from equation (10). P^i is determined when the bubble radius is determined. The remaining unknowns are N_l^i, N_g^i, V^i and V^e. Two chemical equilibrium conditions already exist. The other two conditions needed are the constitution equation of gas phase and liquid-gas solution. On the assumption of ideal gas, the constitution equation of gas phase exists. Unfortunately, there is no constitution equation for liquid-gas solution. Therefore N_l^i, N_g^i and V^i can only be solved with the above mentioned equations.

Under the ideal solution assumption, the chemical equilibrium condition of gas component can be rewritten as

$$P_g^i = KX_g^e \qquad (37)$$

It is assumed that the vapor pressure of the solution is equal to the vapor pressure of the pure solvent. This gives

$$P_l^i = P_v \qquad (38)$$

On the assumption of ideal gas law

$$P_g^i = N_g^i RT/V^i \qquad (39)$$

$$P_l^i = N_l^i RT/V^i \qquad (40)$$

The mole fraction can be expressed as

$$X_g^e = (N_g - N_g^i)/(N_g + N_l - N_g^i - N_l^i) \qquad (41)$$

Then the system of equations become

$$N_g^i RT/V^i + P_v = P_0 + 2\sigma/r \qquad (42)$$

$$K(N_g - N_g^i)/(N_g + N_l - N_g^i - N_l^i) = N_g^i RT/V^i \qquad (43)$$

$$P_v = N_l^i RT/V^i \qquad (44)$$

In a bubble-droplet system, for a given temperature T, the parameter K, P_v and R are determined. In this system, the total gas content N_g, the total liquid content N_l, and the external applied pressure P_0 are given, then the above three equations can be used to solve the three parameter N_g^i, N_l^i, and r (or V^i). Figure 2 shows the typical results for $N_g = 3.0*10^{-15}$ mole (Nitrogen gas), $N_l = 1.0*10^{-10}$ mole, $T = 293$ K, $R = 8.313$ J-K-mol^{-1}, and $\sigma = 7.32 \times 10^{-2}$ N/m. It was found that the

Table 1 Order estimation of P_d

Parameters	$w(\partial P/\partial V)$	xRT	$u(\partial P/\partial V)$	vRT
$N_g/N_l = 30$ppm, $N_l = 10^{-10}$ $r_0 = 3.1 \times 10^{-6}$	-10^{14}	10^{19}	-10^{30}	10^{34}
$N_g/N_l = 30$ppm, $N_l = 10^{-9}$ $r_0 = 10.6 \times 10^{-6}$	-10^{13}	10^{18}	-10^{28}	10^{32}
$N_g/N_l = 30$ppm, $N_l = 10^{-7}$ $r_0 = 108.8 \times 10^{-6}$	-10^{11}	10^{17}	-10^{25}	10^{28}
$N_g/N_l = 30$ppm, $N_l = 10^{-5}$ $r_0 = 1091.3 \times 10^{-6}$	-10^{10}	10^{16}	-10^{23}	10^{26}

cavitation limit is due to $P_0 < P_c$ and the dissolution limit was also due to $P_0 < P_c$. When pressure approaches the dissolution limit, the bubble disappears suddenly. The phenomenon is due to the complete dissolving of the free gas within the bubble and was verified by the experiment of Mori et al. [2]. Figure 3 shows free gas content and mole fraction of dissolved gas for $N_g/N_l = 30$ ppm by mole. Figure 4 shows the equilibrium curves for different gas contents.

6 Estimation of P_d

Since there is no constitution equation for liquid-gas solution, the fourth critical condition can not be calculated. However, under the following assumptions, P_d can be estimated.

(1) It is assumed that the liquid-gas solution is a sufficient dilute solution. The partial molar volume of liquid-gas solution is approximately the molar volume of pure liquid.

$$\nu_{gl}^e \cong \nu_l^e \qquad (45)$$

The bulk modulus of liquid-gas solution is also approximately the bulk modulus of pure liquid.

$$V^e \frac{\partial P^e}{\partial V^e} \cong V_l^e \frac{\partial P^e}{\partial V_l^e} \cong 3.22 \times 10^5 \text{psi} \cong 2.2 \times 10^9 \text{Pa} \qquad (46)$$

(2) It is assumed that the partial molar volume of condensed gas (or dissolved gas) is approximately the order of pure liquid, then it gives

$$O(\nu_g^e) \cong O(\nu_f^e) \cong O(\nu_{gl}^e) \qquad (47)$$

On the basis of these assumptions, equation (36) can be estimated as shown in Table 1 for $P_0 = P_v$. Table 1 shows that in equation (36) the negative term of the numerator is much smaller than the positive term of the numerator, and the negative term of the denominator is also much smaller than the positive term of the denominator. This implies that the critical condition of P_d is approximately the condition of P_c at low pressure.

For high pressure (dissolution limit), N_g^i and N_l^i approach zero. In equation (36), $\partial P^e/\partial V^e$ is approximately constant, u is of the order of $(1/N_l^i + 1/N_g^i)$, v is of the order of $1/(N_l^i N_g^i)$. So the denominator approaches vRT as N_g^i and N_l^i approach zero. The numerator also approaches xRT by the same reason. This gives

$$P_0 > -4\sigma/(3r) + (x/v)RT/V^i \qquad (48)$$

Since equation (48) is exactly the same as equation (35), P_d approaches P_c at high pressure region. Therefore, the critical condition P_c determines the dissolution limit and cavitation limit. The incompressible assumption in literatures [2, 3] that $\partial P/\partial V$ is zero is not correct. The fact is that, for such a small bubble-droplet system and sufficient dilute solution condition, the negative compressibility term is much smaller than the positive term in equation (36). The negative compressibility term can be neglected when the critical conditions are determined. Case 2 which was discussed in section 4 will never appear in this system.

7 Conclusions

A generalized and rigorous approach on the equilibrium of cavitation nuclei in liquid-gas solution is introduced in this paper. It is found that the equilibrium conditions and the critical conditions are the same as that reported by Cha [3]. The following conclusions are drawn:

(1) The form of energy which is used to determine the equilibrium and stability conditions is the availability. Without using the availability, some assumptions should be made on the bubble-droplet system to match the required mechanical equilibrium conditions, as shown in literature [2, 3].

(2) For such a small finite bubble-droplet system and sufficient dilute solution, the compressibility effect of the liquid-gas solution can be neglected when the critical condition is determined.

(3) The bubble-droplet system can remain in a stable equilibrium state and possess the dissolution limit and the cavitation limit.

References

1 Epstein, P. S., and Plesset, M. S., "On the Stability of Gas Bubbles in Liquid-Gas Solutions," *The Journal of Chemical Physics*, Vol. 18, No. 11, 1950, p. 1502.
2 Mori, Y., Hijikata, K., and Nagatani, T., "Fundamental Study of Bubble Dissolution in Liquid," *Int. J. Heat Mass Transfer*, Vol. 20, 1977, pp. 41–50.
3 Cha, Y. S., "On the Equilibrium of Cavitation Nuclei in Liquid-Gas Solutions," ASME JOURNAL OF FLUIDS ENGINEERING, Vol. 103, Sept. 1981, pp. 425–431.
4 Plesset, M. S., and Sadhal, S. S., "On the Stability of Gas Bubbles in Liquid-Gas Solutions," *Proc. IUTAM Symposium*, Pasadena, 1981.
5 Cha, Y. S., "On Bubble Cavitation and Dissolution," *Int. J. Heat Mass Transfer*, Vol. 26, No. 8, 1983, pp. 1173–1180.
6 Franklin, R. E., McMillan, J., and J. Rozewicz, "The Stability and Concentration of Gas Micro-Bubbles in Liquids," *ASME Int. Symposium on Cavitation Inception*, New Orleans, 1984.
7 Muller, I., *Thermodynamics*, Pittman Publishing, 1985, pp. 246–251.

A. S. Ramamurthy

Professor,
Faculty of Engineering,
Concordia University,
Montreal, Canada, H3G 1M8.
Mem. ASME

R. Balachandar

Research Associate,
Faculty of Engineering,
Concordia University,
Montreal, Canada, H3G 1M8.
Assoc. Mem. ASME

The Near Wake Characteristics of Cavitating Bluff Sources

The influence of cavitation on vortex shedding behind constrained sharp-edged bluff prisms is studied experimentally. At a given blockage, the length of the vortex formation region is found to increase as the cavitation number of the flow is reduced. The vortex appears to be stabilized from breaking up in the partially cavitating regime of flow. Test results indicate that the separation velocity is the proper velocity scale to reduce or eliminate blockage effects.

Introduction

In studies related to flow past bluff bodies conducted in wind and water tunnels, the rigid boundaries of the test section prevent the lateral displacement of the streamlines, thereby causing the test conditions to deviate from prototype performance. Information regarding the influence of wall interference or blockage on flow characteristics is therefore required to provide suitable corrections. The effects of blockage on test results have been the subject of many previous investigations (Allen and Vincenti; 1944; Maskell, 1963; Ramamurthy, 1973, 1989; and Roshko 1954). Some of the earlier studies have indicated that the separating streamline velocity is the proper velocity scale to normalize the drag and Strouhal number to eliminate blockage effects. Basic studies related to the effects of cavitation on bluff body wakes have also been dealt with by several investigators (Ramamurthy, 1977; Syamala Rao, 1975; Varga, 1966; and Young and Holl, 1966). Young and Holl (1966) measured the vortex shedding frequency behind two-dimensional symmetric wedges and found that cavitation produces negligible effects on the vortex shedding frequency with decreasing cavitation number σ down to as low as half the incipient value. As σ is further reduced and choking conditions are approached, vortex shedding becomes random and highly intermittent. The results of Ramamurthy (1977) agree qualitatively with the observations of Young and Holl (1966). However, the results of Syamala Rao (1975) indicate that the vortex shedding frequency increases to very large values as choking conditions are approached. The results of Syamala Rao (1975) are expected to be highly dependent on the Reynolds numbers of the flow, since circular bluff bodies were used as the cavitating source. Extensive theoretical and experimental studies have been conducted to measure the geometric characteristics of flow past supercavitating hydrofoils at very low cavitation numbers (Knapp et al., 1970). Appel (1961) observed the development of cavitation along a two-dimensional surface of separation. His work led to the speculation that the vortices become stabilized against further break up, as cavitation occurs within the core of the vortices generated. Vigander (1965) sup-

ports this hypothesis related to vortex stabilization due to the presence of a vapor core.

In the present study, the effects of blockage and cavitation on the vortices shed in the near wake of sharp-edged bluff bodies were observed. The size and shape of the bodies chosen (Fig. 1(a)) were such that the observed incipient cavitation index σ_i values would be reasonably high. Consequently, the effect of gas content and nuclei characteristics of the water used would not significantly influence the results related to σ_i (Arakeri, 1981). Further, the fixed separating edges ensured the reduction or elimination of Reynolds number effects (Balachandar et al., 1988) in interpreting the test results. The blockage ranged from 9.7 to 32.5 percent. The aspect ratio of the test models were low and ranged from 1.54 to 2.12. Using periodic strobe illumination, the length of the vortex formation region (Fig. 1(a)) was measured. The location of the region of vortex formation precedes the region of erosion due to cavitation. As such, locating the zone of vortex formation assists in interpreting cavitation erosion results. The stability of the vortex against break up in the presence of cavitation was visually observed.

Experimental Setup and Procedure

The water tunnel used in the study had a 10:1 contraction preceding the test section and yielded a nearly uniform velocity at the test section. The test section was 101.6 mm high, 50.8 mm wide, and 508 mm long (Fig. 1(b)). This equipment is designated as "Tunnel A." The test section had plexiglas windows to facilitate visual observations. Experiments were carried out to check the quality of flow in the unobstructed test section. Spanwise uniformity check of the axial velocity distributions were made at a section 50 mm downstream from the inlet in a horizontal plane perpendicular to the flow. Figure 1(c) shows typical velocity distributions obtained for a range of flow rates using a 15mW dual beam He-Ne laser doppler velocimeter (TSI Inc.) in the forward scatter mode. In Fig. 1(c), the velocities are normalized by the centerline velocity U_c. The velocities appear to be uniform to within 3 percent over the mid 80 percent of the span. Furthermore, the ratio of the average velocity to the centerline velocity was of the

b/B = 0.097, 0.243, 0.325
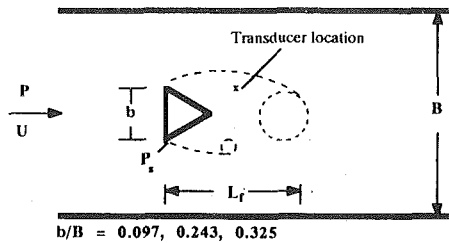
Fig. 1(a) Flow past a constrained bluff body

(Top view)

(Front View)

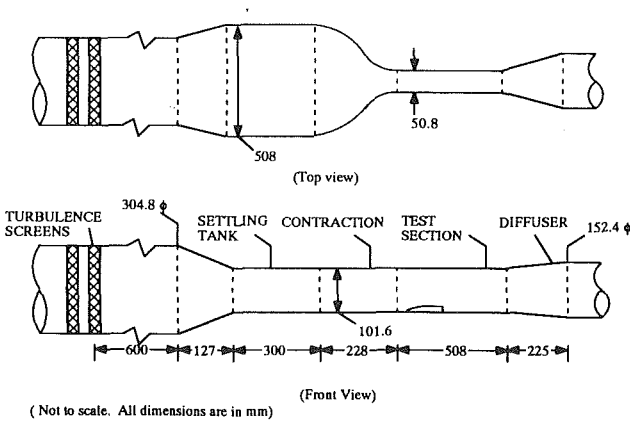(Not to scale. All dimensions are in mm)
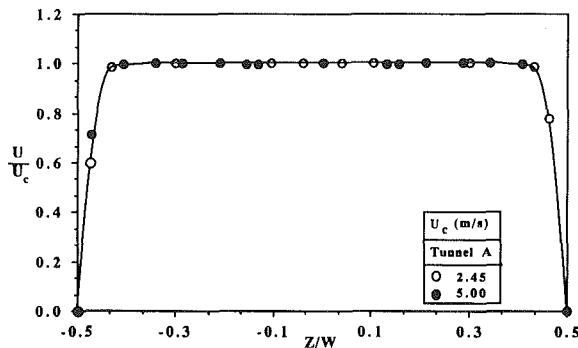
Fig. 1(b) Experimental setup

Fig. 1(c) Span-wise velocity distribution (Tunnel A)

order of 0.94. This is a good indication of the two-dimensionality of the flow in the test section and compares qualitatively with standard two-dimensional flow investigations (Vigander, 1965; Kim, 1986). Following Adams et al. (1988), a mass balance check was made over the entire test section assuming two-dimensional flow. The mass balance checks to within 3 percent. The turbulence levels in the test section varied from 1 to 3.5 percent. The higher values of turbulence intensity occurred when the pressure in the test section was very low and were generally associated with a small number of tests conducted at extremely low values of cavitation numbers. At these low cavitation numbers, the flow was either choking or

very close to choking conditions. Experiments were also conducted in an auxiliary tunnel (Tunnel B) which yielded lower aspect ratios for a given blockage. For example a blockage of 24.3 percent yielded aspect ratios ($AR =$ Test body width/body height) of 2.12 and 0.13 for the two tunnels respectively.

Polished equilateral prisms made of brass formed the basic test bodies. The different blockages tested are indicated in Fig. 1(a). In Fig. 1(a), the height of the test section, the height of the body, and the blockage are denoted by B, b, and b/B, respectively. The accuracy in the linear measurements of b and B was $\pm$ 0.02 mm. A pressure tap 0.5 mm in diameter was located at the center of the front face of the cavitating body to measure the stagnation pressure. The two separating pressures (P_s) were measured by means of pressure taps located in the rear of the body at a distance of 2 mm from the separating edges. Using calibrated pressure gages, the positive pressures were measured to the nearest 1.72 kPa (0.25 psi), while the negative pressures were measured to the nearest 6.35 mm (0.25 in.) of mercury. The prismatic bodies were always mounted such that the front face was normal to the flow. During each test run, the water temperature was noted to the nearest 0.25°C. During the test series, the temperature ranged from 22 to 24°C and the air content ranged from 17 to 24 ppm. However, during any specific run, the change in air content was negligibly small. The freestream pressure P was computed from the stagnation pressure and was also confirmed by direct measurement. The flow was measured with the help of a standard 60 deg V-notch. The depth of flow over the notch was measured to the nearest 0.10 mm. The accuracy of discharge measurement is estimated to be 3 percent.

The frequency of pressure pulsations in the wake was obtained with the help of pressure transducers located on the tunnel wall close to the edge of the free shear layer (Fig. 1(a)). The output signal from the transducer demodulator was fed to a Fast Fourier Transform Analyser (Wavetek, 5830-A) to carry out the spectral analysis. The associated instrumentation is shown in Fig. 2. A stroboscope (Bruel and Kjaer, Type 4912) and a battery of powerful lights aided visual observation. During any given test run, the internal generator of the strobe was manually set at the vortex shedding frequency "f" determined from the spectral measurements. The length of vortex formation region L_f (Fig. 1(a)) was obtained visually under periodic illumination of the strobe. The presence of cavitation in the core of the vortices aided the flow visualization process. The plexiglas window was provided with a measuring grid to facilitate the measurement of the length of the vortex formation region L_f. Several measurements were made during a given run and the values presented are the average values of L_f. The accuracy of measurement of L_f was 1.6 mm.

It should be noted that the separating pressure P_s is obtained by direct measurement while U_s is obtained assuming inviscid, irrotational flow and applying the energy principle along the separating streamline, i.e., $U_s = U(1 - C_{ps})^{0.5}$ (Birkhoff, 1957). Here, C_{ps} is the separating pressure coefficient. In the forthcoming results, the discrepancy in the reported values of the σ, S, and C_{ps} are estimated to be of the order of ± 0.03, ± 0.005 and ± 0.03, respectively.

Nomenclature

AR = width of bluff body/b
b = height of bluff body
B = height of test section
b/B = blockage
C_{ps} = separation pressure coefficient
C_{px} = wake pressure coefficient at any location x along wake axis (Inset, Fig. 5)
f = frequency of vortex shedding

L_f = length of vortex formation region
P = freestream pressure
P_s = separating pressure
S = $f\,b/U$, Strouhal number
U = freestream velocity
U_c = test section center line velocity
U_s = separating velocity
ρ = density of fluid

σ = cavitation number
$\sigma = \dfrac{P - P_v}{\frac{1}{2}\rho U^2}$, cavitation number
σ_i = incipient cavitation number
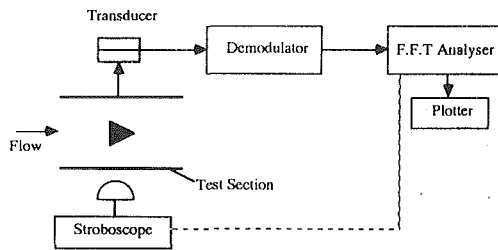$\sigma_s = \dfrac{P - P_v}{\frac{1}{2}\rho U_s^2}$

Fig. 2 Instrumentation

Fig. 3 Variation of Strouhal number with σ

Analysis of Results

The distinct alternate vortex shedding mechanism and the formation of the Karman vortex street of bluff body wakes are well known. For most of the range of cavitation number, σ studied in the present investigation, the flow behind the body behaved in a manner characteristic of bluff body wakes. In the present series of tests, at any blockage and at very large values of σ, the values of the Strouhal number, S obtained (Fig. 3) are comparable with those reported in literature for non-cavitating flow past constrained sharp-edged normal flat plates (Abernathy, 1962; Ramamurthy and Ng, 1973). This served to calibrate the equipment and procedures used in the present series of tests. Figure 3 shows the variation of the Strouhal number S with cavitation number σ for $b/B = 0.097$ and 0.243. Similar to previous observations (Ramamurthy, 1977 and Young, 1966), the value of S remains constant at the noncavitating value over a range of σ. When one reduces σ further, the value of S increases, followed by a reduction in S as choking conditions are approached. Also indicated in Fig. 3 are the values of the inception cavitation numbers σ_i of the bodies used in the present series of tests.

With the strobe generator being set at the frequency of vortex shedding, the wake appeared to be frozen. This enabled the measurement of the length of formation L_f (Fig. 1(a)). Figure 4 shows the variation of L_f with σ for three typical blockages of 0.097, 0.243, and 0.325. At any given blockage, as the value of σ is reduced, L_f increases. Following Sarpakaya's (1979) model regarding the formation of vortex behind bluff bodies, one notes that the shear layer joining the separation point to one of the vortices begins to develop instabilities and is drawn across the wake in response to the reduction in the base pressure due to the vortex growth across the wake. This nearly corresponds to a time when the sheet drawn in has the least circulation or is most permeable. The stretching, diffusion and dissipation of vorticity tends to break up the deforming shear layer. This causes the shedding of the first vortex. The shedding of the other vortex across the wake does not commence until circulation in its feeding sheet reduces to a minimum making the sheet most susceptible to diffusion. Observations also indicate that a decrease in cavitation number tends to make the wake more quiescent. Moreover, the region immediately behind the body is far less turbulent when compared with conditions related to non-cavitating or incipiently cavitating flows. The reduced wake turbulence causes the diffusion of the separating sheet to be delayed, providing more time for the vortex to travel further downstream in its natural course and this consequently increases L_f.

Some remarks regarding the measurement of L_f are also in order. As mentioned earlier, several measurements were made during a given run and the values presented are the average values of L_f. A typical average value of L_f was 32.0 mm at $\sigma = 2.89$ for $b/B = 0.097$. At very large values of σ (noncavitating conditions), visual observations were not possible and hence the value of L_f could not be determined. At values of σ slightly below incipient conditions, the cavitation bubbles formed in the core of the vortices, thus assisting flow visualization. 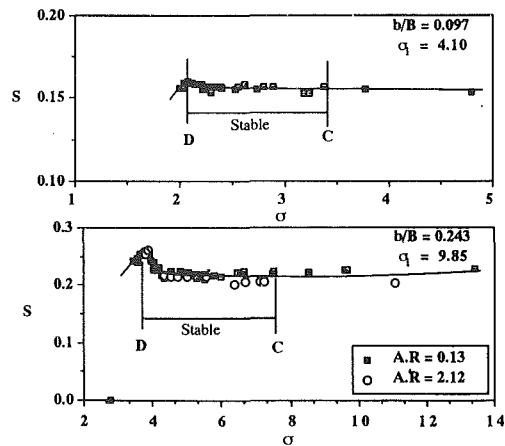At these values of σ, all the cavitation bubbles were observed only in the vortex cores and not in the region immediately behind the body. The cavitation bubbles collapsed immediately on reaching the high pressure regions. The vortices were visible only for a few body widths downstream. As the value of σ was reduced to reach partially cavitating conditions (range CD-Fig. 3), the presence of a vapor core in the vortices facilitated excellent visual observations. Since the ambient wake pressures for these conditions were lower, the collapse of the cavitation bubbles did not occur immediately and the Karman vortex street was distinctly visible several body widths downstream of the cavitating source. The oscillations of the cavity tip were predominantly in the lateral direction. The vortices appeared to be very stable and confirmed the observations of Appel (1961) that cavitation stabilizes the vortex and prevents its further break up. In the range CD (Fig. 3), as σ is reduced, both the lateral and longitudinal vortex spacing were reduced. A similar observation was made earlier by Young and Holl (1966). However, as the value of σ was reduced beyond the point D (Fig. 3), large axial oscillations of the cavity tip were observed. Under these circumstances, the errors associated with the measurements of L_f are expected to be large. With the approach of choking conditions, the longitudinal spacing between the two rows of vortices was reduced considerably. Under these conditions, the vortices did not appear to be stable. Further, the rolling up of the shear layers appeared to be less distinct. At the same time, vortex shedding also became more or less intermittent and random. The cavity as a whole appeared to be filled with vapor with the onset of choking conditions.

In studies related to noncavitating flows, it has been reported by Davies (1976) and several others that the vortices distort and are generally noncircular. As they move downstream, vorticity diffuses and further dissipation is enhanced by turbulence. Vortices are also subjected to strain fields imposed by neighboring vortices (Sarpakaya, 1979). These factors generally contribute to the break up of the vortex. As indicated earlier, in the partially cavitating regime of flow (region CD in Fig. 3), the wake tends to become more and more quiescent and attains a reduced level of turbulence compared to the noncavitating flow conditions. Further, the presence of vapor in the vortex core tends to reduce diffusion and keep the vortex circular. Consequently, cavitation tends to keep the vortex from fragmenting and this aids stabilization. Incidentally, as one reduces the value of σ, the maximum radius of the visible portion of the vortex appeared to shrink with increasing L_f. The effect of blockage on L_f is clearly discernible from Fig. 4. However, at a given blockage, one notes from Fig. 4 that aspect ratio does not seem to have significant effect on the values of L_f. In this context, it may be added that even for flow past a circular cylinder where the separation points are strongly affected by the flow Reynolds number, West and Apelt
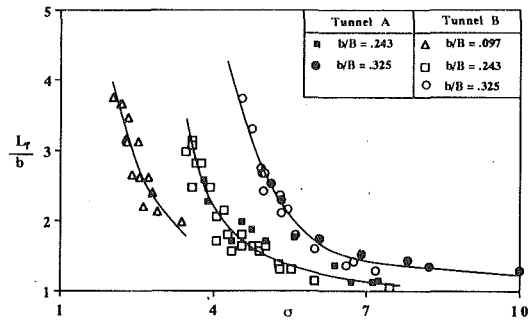
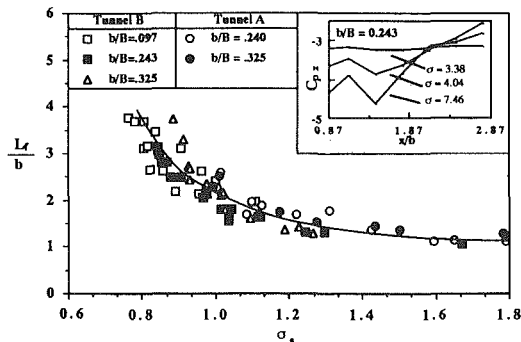**Fig. 4 Variation L_f/b with σ**

Fig. 5 Variation L_f/b with σ, inset: centerline wake pressure distribution at various σ

(1982) have found that S is strongly influenced by blockage but seems to be unaffected by the aspect ratio.

A reduction in the value of σ beyond inception conditions, increases the cavity width and decreases the cavity pressure. Consequently, the separating streamline velocity increases. An attempt was made to absorb blockage effects by using a modified cavitation number σ_s obtained through the use of the separating velocity U_s as the scaling parameter. Figure 5 shows the variation of L_f with σ_s. The data seem to be fairly well clustered around a single curve for the range of blockage tested. This indicates that U_s is the proper velocity scale to reduce or eliminate blockage effects. At very large values of σ, since the vortex is formed very close to the rear tip of the prism, it is expected that L_f would be influenced by the afterbody of the prism. As seen from the Inset of Fig. 5, at these values of σ, the afterbody of the prism severely influences the wake pressure coefficients C_{px}. In the inset of Fig. 5, x is reckoned from the stagnation point and $x/b = 0.87$ indicates the rear tip of the prism. However, in the present tests, it should be noted that at comparable blockages, the values of S obtained in noncavitating flows match fairly well with those obtained in previous wind tunnels studies behind normal flat plates with no significant afterbodies (Abernathy, 1962; Ramamurthy, 1973). Furthermore, as seen from the inset of Fig. 5, when σ is reduced to very low values, the wake pressures become more or less constant. Visual observations indicate that the general wake region is now filled with vapor. Consequently, the values of L_f are not expected to be influenced by the afterbody of the prism at lower values of σ, as the vortices are now being formed further downstream. The higher uncertainties in the estimation of L_f at very low σ values contributed to the increased scatter of the plotted points at lower cavitation numbers (Fig. 5).

Conclusions

The length of formation region of the vortex behind the cavitating source increases with decreasing cavitation number. The aspect ratio of the test models were low $(1.54 < AR < 2.12)$ and the blockage ranged from 9.7 percent to 32.5 percent. The vortex appears to be stable in the partially cavitating regime of flow where only lateral oscillations of the cavity tip caused by the alternate vortex shedding is discernible in the wake. At very low values of σ, large axial oscillations of the cavity are also observed. Further, the lateral and longitudinal spacing of the vortex street tend to decrease with decreasing σ. Visual observations indicate that the vortices tend to be less stable as choking conditions are reached. In tests related to the determination of L_f/b under cavitating conditions, the separation velocity is the proper velocity scale to reduce or eliminate blockage effects.

References

Abernathy, F. H., 1962, "Flow Over an Inclined Flat Plate," ASME *Journal of Basic Engineering*, Vol. 84, Sept., pp. 380–388.

Adams, E. W., and Eaton, J. K., 1988, "An LDA Study of Backward Facing Step Flow, Including the Effects of Velocity Bias," ASME JOURNAL OF FLUIDS ENGINEERING, Vol. 110, Sept.

Allen, H. J., and Vincenti, W. G., 1944, "Wall Interference in a Two-Dimensional Flow Wind Tunnel, With Consideration for the Effect of Compressibility," Technical Report No. 782, NACA, Washington, D.C.

Appel, D. W., 1961, "Cavitation Along Surfaces of Separation," ASME Paper No. 60-WA-265.

Arakeri, V. H., 1981, "Inception of Cavitation from a Backward Facing Step," JOURNAL OF FLUIDS ENGINEERING, Vol. 103, June, pp. 288–293.

Balachandar, R., Ranganthan, Y., and Ramamurthy, A. S., 1988, "Evaluation of Cavitation Damage Characteristics Using a Profilometer," *Proc. Inst. Mech. Enggs.*, Vol. 202, No. C5.

Birkhoff, G., and Zarantonello, E. H., "Jets, Wakes and Cavities," Academic Press, New York.

Davies, M. E., 1976, "A Comparison of the Wake Structure of a Stationary and Oscillating Bluff Body Using a Conditional Averaging Technique," *J. Fluid Mechanics*, Vol. 75, pp. 209–231.

Kim Nae Hyun, 1986, "Experimental Investigation of Oscillating Flow Downstream of a Two-Dimensional Cavity," M.S. thesis, Dept. of Mechanical Engineering, The Penn. State University.

Knapp, R. T., Daily, J. W., and Hammitt, F. G., 1970, *Cavitation*, McGraw-Hill, New York.

Maskell, E. C., 1957, "A Theory of Blockage Effects on Bluff Bodies and Stalled Wings in a Closed Wind Tunnel," Reports and Memorandum, 3400, Aeronautics Research Council.

Ramamurthy, A. S., and Lee, P. M., 1973, "Wall Effects on Flow Past Bluff Bodies," *J. Sound Vib.*, Vol. 31, No. 4, Academic Press Inc., London, 1973, pp. 443–451.

Ramamurthy, A. S., and Ng, C. P., 1973, "Effect of Blockage on Steady Force Coefficient," *J. Engg. Mechanics, Trans. ASCE*, Vol. 99, pp. 755–772.

Ramamurthy, A. S., and Bhaskaran, P., 1977, "Constrained Flow Past Cavitating Bluff Bodies," ASME JOURNAL OF FLUIDS ENGINEERING, Vol. 99, No. 4, pp. 717–726.

Ramamurthy, A. S., Balachandar, R., and Diep, Vo, 1989, "Blockage Correction for Sharp-edged Bluff Bodies," *J. Engrg. Mechanics, Trans. ASCE*, Vol. 115, No. 7, July, pp. 1569–1576.

Sarpkaya, T., 1979, "Vortex Induced Oscillations—A Selective Review," ASME *Journal of Applied Mechanics*, Vol. 46, June, pp. 241–257.

Syamala Rao, B. C., and Chandrashekara, D. V., 1975, "Some Characteristics of Cavity Flow Past Cylindrical Inducers in a Venturi," ASME Paper No. 75-WA/FE-7.

Varga, J., and Sebestyen, G. Y., 1966, "Determination of the Frequencies of Wakes Shedding from Circular Cylinders," *Acta Technicia Academiae Scient. Hungaricae*, Vol. 53, pp. 91–108.

Vigander, S., 1965, "An Experimental Study of Wall Pressure Fluctuations in a Cavitating Turbulent Shear Flow," Report No. 21, Studies in Engineering Mechanics, University of Kansas.

West, G. S., and Apelt, C. J., 1982, "The Effect of Tunnel Blockage and Aspect Ratio on the Mean Flow Past a Circular Cylinder with Reynolds Number Between 10^4 and 10^5," *J. Fluid Mech.*, Vol. 114, pp. 361–377.

Young, J. O., and Holl, J. W., 1966, "Effects of Cavitation on Periodic Wakes Behind Symmetric Wedges," ASME *Journal of Basic Engineering*, Mar., pp. 163–176.

Lisheng Suo
Research Fellow.

E. B. Wylie
Professor.
Fellow ASME

Department of Civil Engineering,
The University of Michigan,
Ann Arbor, MI 48109

Complex Wavespeed and Hydraulic Transients in Viscoelastic Pipes

The classic formula for waterhammer wavespeed is extended to calculate the complex-valued, frequency-dependent wavespeed in a viscoelastic pipe, which takes into account the effect of viscoelasticity of pipe wall material on wave propagation. With the complex wavespeed, the standard impedance or transfer matrix is directly used to analyze resonating conditions in systems including viscoelastic pipes, and the impulse response method presented previously by the authors is applied to compute nonperiodic transients. Numerical results are compared with experimental data and good agreement is observed.

Introduction

A number of researchers have addressed the issue of hydraulic transients in viscoelastic pipes. Their methods may generally be divided into two categories: the method of characteristics (MOC) and frequency-response-based methods.

In the MOC, a term representing the retarded wall deformation is included and evaluated from the creep compliance of the wall material that was simulated by means of Kelvin-Voigt elements. Rieutord and Blanchard (1979) adapted the standard MOC and presented a theoretical study of the effect of viscoelastic properties of pipe wall material on transients. Gally et al. (1979) compared the calculated waterhammer in polyethylene pipes with laboratory test data, showing a good agreement between numerical and experimental results. Abo-Ismail, et al. (1983) provided a similar study but included the frequency-dependent friction for laminar flow. Güney (1983) proposed later a modified MOC model that took into account the effects of time-varying diameter and thickness, cavitation, and frequency-dependent friction. Ghilardi and Paoletti (1986) investigated the application of viscoelastic pipes added to pipeline systems as suppressors of pressure surges.

In the methods of the second category, the effect of viscoelastic properties is modeled through a frequency-dependent wavespeed, a_e, and a separate, frequency-dependent damping factor, α. By incorporating the complex creep compliance into the unsteady momentum and continuity equations, Meissner (1976) derived the wavespeed and damping factor for an oscillating pressure wave propagating in a thin-walled viscoelastic pipe.

$$a_e = \left\{ \frac{\rho}{2} \left[\left(\frac{D}{e} J'(\omega) + \frac{1}{K} \right) + \sqrt{ \left(\frac{D}{e} J'(\omega) + \frac{1}{K} \right)^2 + \left(\frac{D}{e} J''(\omega) \right)^2 } \right] \right\}^{-\frac{1}{2}} \tag{1}$$

$$\alpha = \frac{1}{2} \rho \omega \frac{D}{e} a_e J''(\omega)$$

where ω is circular frequency, K and ρ the liquid bulk modulus and density, D and e the inside diameter and wall thickness of the pipe, and $J'(\omega)$ and $J''(\omega)$ the storage and loss compliances of the wall material. Using wavespeed a_e and damping factor α, Hirschmann (1979) studied the resonating conditions in viscoelastic pipes with a modified impedance method. Franke and Seyler (1983) utilized an impulse response method to calculate waterhammer, although the treatment of such factors as fluid inertia, boundary conditions, and friction loss in the method was not entirely satisfactory.

This paper presents an alternative approach to deal with hydraulic transients in viscoelastic pipes. A complex-valued and frequency-dependent wavespeed is first formulated, including the effect of the viscoelasticity of pipe-wall material on wave propagation. Using simply the complex wavespeed, the standard impedance or transfer matrix method is able to analyze oscillatory flow, and the impulse response method proposed previously by the authors (Suo and Wylie, 1989) is applied to compute nonperiodic transients. Examples are provided to compare numerical results with experimental data.

Complex-Valued Frequency-Dependent Wavespeed

The continuity and momentum equations describing one-dimensional unsteady pipe fluid flow are (Wylie and Streeter, 1983):

$$\frac{\dot{\rho}}{\rho} + \frac{\dot{A}}{A} + \frac{\partial v}{\partial x} = 0 \tag{2}$$

$$\frac{\partial p}{\partial x} + \rho\,\frac{\partial v}{\partial t} = 0 \qquad (3)$$

where v and p are the average velocity and pressure at a section, respectively; A is the cross-sectional area of the pipe; x is the distance along the pipe; t is time; and, a dot over a variable indicates the material derivative. In equation (3), friction (which is not important as far as wavespeed is concerned) has been neglected and horizontal flow is assumed.

For liquid flow, equation (2) may be rewritten as

$$\dot{p} + \rho \left[\frac{K/\rho}{1 + (K/A)(\dot{A}/\dot{p})} \right] \frac{\partial v}{\partial x} = 0 \qquad (4)$$

Assume a prismatic pipe, that is,

$$A = A(p(x,t)) \quad \text{or} \quad \frac{\dot{A}}{\dot{p}} = \frac{\Delta A}{\Delta p} \qquad (5)$$

and denote

$$a = \sqrt{\frac{K/\rho}{1 + (K/A)(\Delta A/\Delta p)}} \qquad (6)$$

Substituting equations (5) and (6) into equation (4), and neglecting the convection term, $v(\partial p/\partial x)$, leads to

$$\frac{\partial p}{\partial t} + \rho a^2 \frac{\partial v}{\partial x} = 0 \qquad (7)$$

Eliminating p from equations (3) and (7) yields

$$\frac{\partial^2 v}{\partial t^2} = a^2 \frac{\partial^2 v}{\partial x^2} \qquad (8)$$

This is a standard one-dimensional wave equation, which indicates that a defined by equation (6) is the corresponding wavespeed. Since no assumption has been made regarding the manner of pressure variation, equation (6) holds in the case when Δp varies with time, say sinusoidally, provided that ΔA which is due only to Δp can be properly evaluated.

Equation (6) may be applied to viscoelastic pipes. The strain of a viscoelastic material subject to a unit sinusoidal stress is fully described (Ferry, 1980) by its complex creep compliance $J^*(\omega) = J'(\omega) - iJ''(\omega)$. For a thin-walled pipe of diameter D and wall thickness e, term $\Delta A/A\Delta p$ may be easily evaluated from the principles of structural mechanics, and equation (6) is then expressed as

$$a = \sqrt{\frac{K/\rho}{1 + (KDJ^*/e)c}} = \sqrt{\frac{K/\rho}{1 + (KD/E^*e)c}} \qquad (9)$$

where $E^*(\omega) = E'(\omega) + iE''(\omega) = 1/J^*(\omega)$, the complex Young's modulus. Coefficient c is introduced to take into account the effect of pipe support conditions, as well as that of the wall thickness (Wylie and Streeter, 1983). Inasmuch as $J^*(\omega)$, or
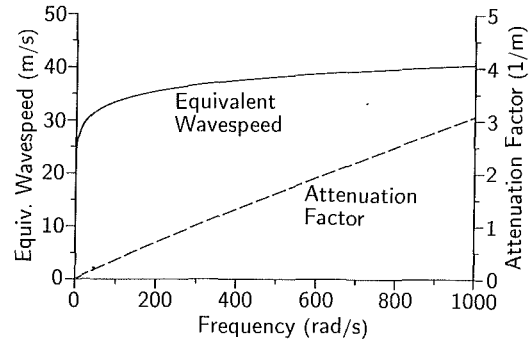

Fig. 1 Equivalent wavespeed and attenuation factor in a viscoelastic pipe. Data from Meissner (1976).

$E^*(\omega)$, is a complex-valued function of frequency, equation (9) yields a complex-valued, frequency-dependent wavespeed. Since equation (9) is identical in form to the classical wavespeed formula, it may be viewed as a wavespeed extension in the complex domain.

The physical meaning of the complex wavespeed is explained as follows. By denoting $a = a_r + ia_i$, where a_r and a_i are the real and imaginary parts, respectively, and defining

$$a_e \equiv \frac{|a|^2}{a_r} \quad \text{and} \quad \alpha \equiv \frac{\omega a_i}{|a|^2} \qquad (10)$$

a sine wave in the pipe may be expressed as

$$\Delta p = Pe^{i\omega(t - x/a)} = Pe^{-\alpha x}e^{i\omega(t - x/a_e)}$$

which means that a_e is an *equivalent wavespeed*, and α is an exponential *attenuation factor*. This also implies that the complex wavespeed is able to include the influence of the viscoelasticity of the wall material on wave propagation.

An analytical derivation presented in the Appendix reveals that equations (10), with a from equation (9) and $c = 1$, are identical to equation (1). This is easily understood as these equations originate from the same source. In fact equation (1) might be considered as a particular form of equation (9).

As an example of the application of equation (9), the computed a_e and α based on Meissner's (1976) data are illustrated in Fig. 1. In the example, $J'(\omega)$ and $J''(\omega)$ are evaluated from the calibrated creep compliance

$$J(t_1) = 1.366(10)^{-7}[\ln(t_1/3 + 1)]^{0.1632}\,\text{Pa}^{-1};\ t_1 = 2\pi/\omega \qquad (11)$$

and relations (Schwarzl, 1970)

$$J'(\omega) = J(t) - 0.855[J(2t) - J(t)],$$
$$t = 1/\omega. \qquad (12)$$
$$J''(\omega) = 2.12[J(t) - J(t/2)];$$

Other parameters are: inside diameter of the pipe $D = 38$ mm,
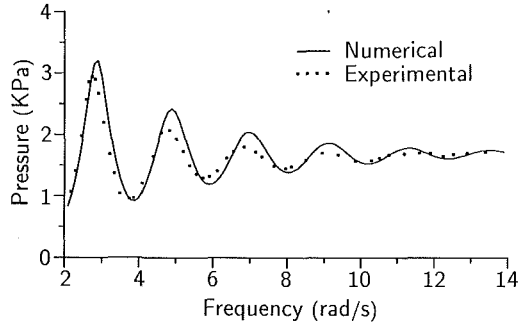
--- **Nomenclature** ---

A	=	cross-sectional area of pipe	e	=	thickness of pipe wall	P, p	= pressure
a	=	waterhammer wavespeed	i	=	$\sqrt{-1}$	s	= $\sigma + i\omega$, complex frequency
a_e	=	equivalent wavespeed	$J(t)$	=	creep compliance of viscoelastic material	t, t_1	= time
a_i, a_r	=	imaginary and real part of complex wavespeed	$J^*(\omega)$	=	$J'(\omega) - iJ''(\omega)$, complex creep compliance	v	= velocity
			$J'(\omega), J''(\omega)$	=	storage compliance and loss compliance	x	= distance along pipe
c	=	coefficient in equation (9)	J_0, J_l	=	parameters in Kelvin-Voigt model, equation (14), with $l = 1, \ldots, n$	α	= exponential attenuation factor
D	=	diameter of pipe				ρ	= density of liquid
$E^*(\omega)$	=	$E'(\omega) + iE''(\omega)$, complex Young's modulus				σ	= decaying factor
			K	=	bulk modulus of liquid	τ_l	= parameters in Kelvin-Voigt model, equation (14), with $l = 1, \ldots, n$
$E'(\omega), E''(\omega)$	=	storage modulus and loss modulus	l	=	length of pipe	ω	= frequency, rad/s

Table 1 Complex frequencies of the PVC pipe system

Order of harmonics	Measured natural frequency (rad/s)	Computed natural frequency (rad/s)	Computed decaying factor (1/s)
Fundamental	–	0.92	– 0.344
3	2.74	2.85	– 0.493
5	4.76	4.86	– 0.672
7	6.85	6.93	– 0.874
9	9.10	9.04	– 1.089
11	11.54	11.19	– 1.318
13	–	13.37	– 1.559

Fig. 2 Amplitude of pressure oscillation at upstream end of a PVC pipe. Data from Hirschmann (1979).

Fig. 3 Pulse propagation in a viscoelastic pipe. Data from Meissner (1976).

Fig. 4 Waterhammer in a polyethylene pipe system. Data from Güney (1977) and Gally et al. (1979).

wall thickness $e = 2.8$ mm, and Poisson's ratio of the wall material $= 0.5$, assumed constant.

Although the concepts of a_e and α are very useful in physical explanations of computational results, only the *single* complex wavespeed from equation (9) is needed in numerical analyses. This makes analysis procedures for both oscillatory flows and nonperiodic transients simpler, as demonstrated later in this paper. In addition, equation (9) permits the direct utilization of the parameter $E^*(\omega)$ of a viscoelastic material, which is generally the data most readily available from material tests.

Oscillatory Flow Analysis

The use of the complex wavespeed does not cause any trouble for an oscillatory flow analysis that proceeds in the complex domain. The frequency response analysis may be carried out by simply applying the standard impedance or transfer matrix method. In the free vibration analysis, only a little extra computational effort is involved in solving for the complex frequencies from the system equation which includes the relation of complex wavespeed vs. frequency. Practically, Fanelli et al. (1983) reported an experimental confirmation of the validity of the transfer matrix method in case of a complex wavespeed, which was calibrated from the test data on a Perspex pipe. Two more examples are shown here.

A frequency response analysis is performed using Hirschmann's (1979) data. A PVC pipe of length 44.85 m and diameter 39 mm is connected to a downstream reservoir and subject to a sinusoidal exciter at the upstream end. The complex wavespeed in the pipe is calculated from equation (9), based on the calibrated creep compliance:

$$J(t) = 1.034(10)^{-7} [\ln(25.13t + 1.06)]^{0.19} \quad Pa^{-1}; t = 1/\omega. \quad (13)$$

The computed amplitude of head oscillation at the exciter is graphed in Fig. 2, and compared with experimental measurements. A good agreement is observed.

The calculated complex wavespeed is then utilized to conduct the free vibration analysis of the PVC pipe system. The computed complex frequencies of the system, $s = \sigma + i\omega$ with σ the decaying factor and ω the natural frequency, are listed in Table 1 and compared with the measured resonance frequencies. Notice that the higher-order frequencies are not the odd
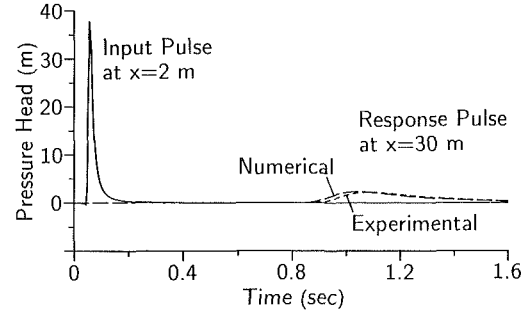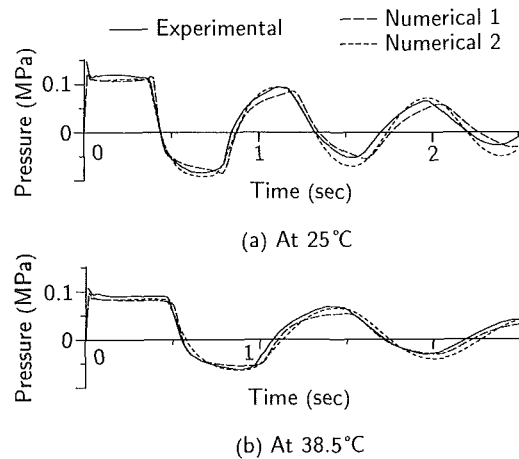
multiples of the fundamental, in contrast with the classic theory. The fact that $|\sigma|$ depends on and increases with ω reveals that vibrational components at higher frequencies decay faster.

Nonperiodic Transients

A variation in the impulse response method (Suo and Wylie, 1989), capable of dealing with various frequency-dependent factors, is used herein to compute nonperiodic transients. The method was developed from the frequency response analysis and incorporated the fast Fourier transform technique. The equations and numerical schemes, which are omitted here, may be found in the cited reference.

An example is given in Fig. 3, which shows the effect of the wall-material behavior on pulse propagation in a viscoelastic pipe. The measured pulse at $x = 2$ m in Meissner's (1976) test is utilized as the input pulse in the computation. The pulse passing through the section at $x = 30$ m is then computed, using the complex wavespeed, and compared with the recorded one. The severe dispersion and rapid attenuation of the pulse are easily visualized by examining the dependence of the equivalent wavespeed and attenuation factor upon frequency, as displayed in Fig. 1.

Figures 4 illustrates waterhammer pressures at the end of a polyethylene pipe due to a sudden closure of the downstream valve. The pipe is 43.1 m in length and 41.6 mm in diameter. The initial velocity in the pipe is 0.55 m/s. The numerical results from the impulse response method and the experimental data from Gally et al. (1979) at 25°C and 38.5°C, respectively, are included to show the strong influence of temperature on the transient behavior. The two numerical results in the figure are associated with two different ways of using the data that describe the properties of the same wall material (polyethylene). In both cases, the material test data, namely the storage modulus, $E'(\omega)$, and loss tangent, E''/E', obtained on a Rheovibron apparatus (Güney, 1977), form the basis of the analysis. According to Güney (1977), the data measured from the Rheovibron apparatus at different temperatures were consistent: the loss tangent, E''/E', was judged to be accurate and the modulus, E^*, was valid in relative values. However, the absolute value of the complex Young's modulus, $|E^*|$, was 30–40 percent smaller than the real physical value, as verified by tests made with the same polyethylene on other measuring devices, and by tests with copper (for which the value of E^* is well-known) on the Rheovibron. Therefore, measured values of E^* multiplied by a factor of 1.4 were used in the original MOC calculations (Güney, 1977, and Gally et al., 1979) and in the numerical analyses herein.

In particular, in the first case (dash lines), the complex wavespeed in the pipe is evaluated from equation (9), using directly the test data E^* (Güney, 1977). In the second case (dotted lines), the complex wavespeed is calculated from equation (9), based on the creep compliance corresponding to a generalized Kelvin-Voigt model

$$J(t) = J_0 + \sum_{l=1}^{n} J_l(1 - e^{-t/\tau_l}) \qquad (14)$$

The values of parameters J_0, J_l, and τ_l were calibrated from the test data obtained on the Rheovibron apparatus (Gally et al., 1979). The impulse response results in the second case and the MOC solution of Gally et al. agree closely with each other, and, for clearness, the latter is not shown in the figure.

The comparison in Fig. 4 indicates that, in general, numerical results agree with experimental data at both temperatures whether E^* or $J(t)$ was used. The discrepancy between the numerical results and test records is likely caused by the error in E^* or $J(t)$. However, the appreciable alteration of the pressure traces from the first case to the second manifests that an error must have been artificially introduced in the process of transferring the measured data, E^*, to the parameters of the Kelvin-Voigt elements, $J(t)$. Therefore, the use of a complex wavespeed calculated simply by inserting E^* into equation (9) appears superior in this respect to MOC.

As mentioned before, using a single complex wavespeed simplifies the numerical procedure, hence reduces the computational effort. The computation of any one of the examples presented in the paper, for instance, can be done within one half minute on an IBM-PC/AT with a math coprocessor.

Conclusion

The complex-valued and frequency-dependent wavespeed in a viscoelastic pipe may be calculated simply from the extended classic wavespeed formula, equation (9), which includes the dynamic effect of the viscoelasticity of pipe wall material. With the complex wavespeed, the standard impedance or transfer matrix method can be directly utilized to analyze oscillatory flow, and the impulse response method is effectively applied to calculate waterhammer. Examples show that numerical results agree with experimental data.

References

Abo-Ismail, A., Wassef, F. M., and Ahmed, S. M., 1983, "Fluid Transients in Pipes with Viscoelastic Walls," ASME Paper No. 83-FE-30.

Fanelli, M., Angelico, G., and Escobar, P., 1983, "Comprehensive Experimental Confirmation of Transfer Matrix Theory for Uniform Pipelines under Steady Pulsating Conditions," Proc. 4th Int. Conf. on Pressure Surges, BHRA Fluid Eng., Bath, England, pp. 379-391.

Ferry, J. D., 1980, Viscoelastic Properties of Polymers, Wiley, New York, 3rd Edition.

Franke, P. G., and Seyler, F., 1983, "Computation of Unsteady Pipe Flow with Respect to Visco-elastic Material Properties," J. of Hydraulic Research, IAHR, Vol. 21, No. 5, pp. 345-353.

Gally, M., Güney, M. Ş., and Rieutord, E., 1979, "An Investigation of Pressure Transients in Viscoelastic Pipes," ASME JOURNAL OF FLUIDS ENGINEERING, Vol. 101, Dec. pp. 495-499.

Ghilardi, P., and Paoletti, A., 1986, "Additional Viscoelastic Pipes as Pressure Surges Suppressors," Proc. 5th Int. Conf. on Pressure Surges, BHRA Fluid Eng., Hanover, F. R. Germany, pp. 113-121.

Güney, M. Ş., 1977, "Contribution à l'étude du phénomène de coup de bélier en conduite viscoélastique," Thèse de Docteur-Ingénieur, No. 274, Lyon, France.

Güney, M. Ş., 1983, "Waterhammer in Viscoelastic Pipes Where Cross-Section Parameters Are Time Dependent," Proc. 4th Int. Conf. on Pressure Surges, BHRA Fluid Eng., Bath, England, pp. 189-204.

Hirschmann, P., 1979, "Resonanz in visko-elastischen Druckleitungen," Mitt. Inst. f. Hydraulik und Gewässerkunde, Technische Universität München, No. 29, München.

Meissner, E., 1976, "Berechnung instationärer Strömungsvorgänge in Kunststoffleitungen," Mitt. Inst. f. Hydraulik und Gewässerkunde, Technische Universität München, No. 19, München.

Rieutord, E., and Blanchard, A., 1979, "Ecoulement non permanent en conduite viscoélastique—coup de bélier (Pulsating Viscoelastic Pipe Flow—Water-Hammer)," J. of Hydraulic Research, IAHR, Vol. 17, No. 3, pp. 217-229.

Schwarzl, F. R., 1970, "On the Interconversion between Viscoelastic Material Functions," Pure and Applied Chemistry, Vol. 23, No. 2/3, pp. 219-234.

Suo, L., and Wylie, E. B., 1989, "Impulse Response Method for Frequency-Dependent Pipeline Transients," ASME JOURNAL OF FLUIDS ENGINEERING, Vol. 111, No. 4, pp. 478-483.

Wylie, E. B., and Streeter, V. L., 1983, Fluid Transients, McGraw-Hill, New York, NY., 1978, Republished FEB Press, Ann Arbor, MI.

APPENDIX

Equation (9), with $c = 1$, can be written as

$$a = (\xi + i\eta)^{-\frac{1}{2}} \qquad (A.1)$$

where

$$\xi = \rho \left(\frac{1}{K} + \frac{D}{e} J' \right), \quad \text{and} \quad \eta = -\rho \frac{D}{e} J''. \qquad (A.2)$$

With $r = \sqrt{\xi^2 + \eta^2}$, $\cos \theta = \xi/r$, and $\sin \theta = \eta/r$, equation (A.2) becomes

$$a = [r(\cos \theta + i \sin \theta)]^{-\frac{1}{2}} = [re^{i\theta}]^{-\frac{1}{2}}$$

$$= \sqrt{\frac{1}{r}} \cos \frac{\theta}{2} - i\sqrt{\frac{1}{r}} \sin \frac{\theta}{2} \qquad (A.3)$$

Therefore,

$$a_r = \sqrt{\frac{1}{r}} \cos \frac{\theta}{2}, \quad a_i = -\sqrt{\frac{1}{r}} \sin \frac{\theta}{2},$$

$$\text{and} \quad |a|^2 = a_r^2 + a_i^2 = \frac{1}{r}.$$

According to equations (10),

$$a_e = \frac{|a|^2}{a_r} = \frac{1}{\sqrt{r} \cos \dfrac{\theta}{2}} = \left[\frac{1}{2} r (1 + \cos \theta) \right]^{-\frac{1}{2}}$$

$$= \left[\frac{1}{2} (\xi + r) \right]^{-\frac{1}{2}} \tag{A.4}$$

Substituting equation (A.2) into equation (A.4) yields the first expression in equation (1). Again, from equations (10)

$$\alpha = \frac{\omega a_i}{|a|^2} = -\omega \sqrt{r} \sin \frac{\theta}{2} = -\frac{1}{2} \omega \frac{1}{\sqrt{r} \cos \dfrac{\theta}{2}} r \sin \theta$$

$$= -\frac{1}{2} \omega a_e \eta = \frac{1}{2} \rho \omega a_e \frac{D}{e} J'' \tag{A.5}$$

which is the second expression in equations (1).

N.-S. Liu[1]

F. Davoudzadeh

W. R. Briley

S. J. Shamroth

Scientific Research Associates, Inc.
Glastonbury, CT 06033

Navier-Stokes Simulation of Transonic Blade-Vortex Interactions

Transonic strong blade-vortex interaction is numerically analyzed by solving the unsteady 2-D Navier-Stokes equations using an iterative implicit second order scheme. The dominant processes during the interaction are the development of large transverse pressure gradients in the upper leading edge region and the development of disturbances at the root of the lower surface shock wave. As a result of this interaction, high pressure pulses are emitted from the leading edge, and acoustic waves are radiated from the lower surface in a region originally occupied by a supersonic pocket. In addition, severe load variations occur when the vortex is within one chord length of the blade.

I Introduction

The interaction of concentrated vortices with blades often induces unsteady aerodynamic loading responsible for blade vibrations, aeroelastic instabilities, and impulsive noise. These effects of blade-vortex interaction (BVI) are especially significant in the transonic flow regime, in which the strength and position of the shock waves are sensitive to small changes in the flow parameters. Due to its common occurrence in many aerodynamic applications, BVI has been a subject of many experimental (Caradonna et al., 1984; Booth and Yu, 1986; Caradonna et al., 1988), analytic (Panaras, 1987); Lee and Smith, 1987; Poling et al., 1989) and computational (Sankar and Tang, 1985; Srinivasan and McCroskey, 1987; Rai, 1987; and Damodaran and Caughey, 1988) investigations. In addition, BVI acoustics based upon the near field aerodynamic computations have been examined by Baeder (1987), George and Lyrintzis (1988), and Hardin and Lamkin (1984).

The generic BVI problem can be viewed as an unsteady, three-dimensional close encounter of curved vortex filaments, at arbitrary intersection angles, with a blade that is in combined translational and rotational motion. Under certain operating conditions, a blade can encounter a vortex that is almost parallel to itself. Such an encounter is essentially two-dimensional but unsteady, and has been the focus of many BVI investigations.

At the present time, a key problem in computing flows containing concentrated vortices is the ability to preserve and convect these vortices in a finite-difference or finite-volume grid without false numerical diffusion due to truncation error, artificial dissipation and turbulence modeling. This problem is so serious that, even for high-order accurate algorithms, quite fine grid spacing is usually needed (Rai, 1987). In some cases this problem of false numerical diffusion of a concentrated vortex can be alleviated by prescribing the structure of the convecting vortex flow field rather than calculating it as a part of the solution. In fact, this prescribed-vortex approach has been used in a large number of BVI calculations based upon potential, Euler, or thin layer Navier-Stokes equations (Srinivasan, and McCroskey 1987; Damodaran and Caughey, 1988; and George and Lyrintzis, 1988). This approach requires a priori knowledge of the shape, size and position of the vortex in order to be effective. Sankar and Tang (1985) suggested another technique for minimizing false diffusion of the vortex, namely, the vortex flow field is calculated as a part of the solution that is obtained by modifying the numerical dissipative operator to act on the difference between the instantaneous total field values and some presumed vortex field values, thereby removing a large part of the spurious dissipation of the vortex structure. More recently, strong BVI problems (Rai, 1987) were solved by using a fifth-order accurate upwind-biased scheme without employing any vortex preservation techniques.

In the present work, the ensemble-averaged, time-dependent Navier-Stokes equations are solved on a body fitted grid around a NACA0012 airfoil in two dimensions to study strong interaction of a Lamb-type vortex with a stationary blade. The Navier-Stokes equations are solved by using an iterative implicit finite-difference scheme with second-order spatial and temporal accuracies. Furthermore, simple vortex preservation techniques are used to minimize the amount of spurious numerical dissipation and eddy viscosity caused by the presence of the vortex during its convective motion towards the leading edge of the blade. This technique is different from those just outlined. Details of the present technique will be given in Sections II and IV.A. The effects of

this strong BVI on the aerodynamic performance of the blade and the concurrent emission of pressure waves are presented.

II Governing Equations and Solution Algorithm

The equations used are the ensemble-averaged, time-dependent Navier–Stokes equations which can be written in vector form as

Continuity

$$\frac{\partial \rho}{\partial t} + \nabla \cdot \rho U = 0 \tag{1}$$

Momentum

$$\frac{\partial \rho U}{\partial t} + \nabla \cdot (\rho U U) = -\nabla P + \nabla \cdot (\pi + \pi^T) \tag{2}$$

Energy

$$\frac{\partial \rho h}{\partial t} + \nabla \cdot (\rho U h) = -\nabla \cdot (Q + Q^T) + \frac{DP}{Dt}$$
$$+ \Phi + \rho \epsilon \tag{3}$$

where ρ is density, U is velocity, P is pressure, π is the molecular stress tensor, π^T is the turbulent stress tensor, h is enthalpy, Q is the mean heat flux vector, Q^T is the turbulent heat flux vextor, Φ is the mean flow dissipation rate, and ϵ is the turbulence energy dissipation rate.

In regard to the numerical method, the basic scheme used is a Linearized Block Implicit ADI procedure of Briley and McDonald (1980). The splitting error and the linearization error associated with this basic scheme are removed by introducing an inner ADI iterative procedure at each time step. The temporal accuracy is increased to second-order by using three-point backward time differencing. On convergence of the inner iteration the scheme becomes a fully implicit nonlinear backward time difference scheme. A more detailed discussion of these improvements is given by Rai (1987); and Briley and McDonald (1986), and such an iterative implicit three-time-level ADI scheme is used in the present study. In addition, three point central differences are used to approximate the spatial derivatives. The spatial accuracy is second-order except for the use of numerical dissipation discussed subsequently.

In addition to the numerical scheme for solving the equations, the following issues also need to be considered: artificial dissipation and turbulence modeling. When calculating high Reynolds number flows using centered spatial differencing, some artificial dissipation is needed to maintain numerical stability and to suppress spurious oscillations in the numerical results. The approach used in the present effort is based upon the use of a second-order anisotropic artificial dissipation term. Introduction of the second-order terms for artificial dissipation formally reduces the scheme to first-order. However, the added second-order artificial dissipation term is preceded by an adjustable parameter which can be reduced so as to progressively reduce the effect of this term. The parameter, termed AVISC in the figures which will be presented, is essentially equivalent to an inverse cell Reynolds number so that a specification of AVISC of 0.05 limits the maximum cell Reynolds number to 20. Details of this approach are given by Weinberg et al. As for the turbulence modeling, the present effort uses a simple mixing length model where the turbulent viscosity is related to local mean velocity gradients via a local mixing length. For the region upstream of the trailing edge of the blade, the mixing length is specified in the usual boundary layer manner (Weinberg et al., 1986).

Obviously, both artificial dissipation and turbulence viscosity are sources of false diffusion and distortion of a vortex convected in a finite-difference grid. In the present

work, the effects of artificial dissipation on the vortex structure are optimized by specifying a proper value of the adjustable parameter which controls the amount of added dissipation, and this value is determined from a separate set of calculations in which the effects of this parameter's magnitude on the preservation of a free vortex convected over a long distance are examined. To minimize the spurious diffusion of vortex structure due to the turbulence model, the turbulent viscosity is set to be zero in a region ranging between the inflow section to a section which is approximately one chord length upstream of the leading edge of the blade. The turbulent viscosity then gradually blends into the values provided by the employed mixing length model. The numerical results obtained show these simple techniques to be effective in preserving the vortex during its convection toward the blade.

III Vortex Model and Preservation Tests

A Lamb-type vortex is chosen for simulating the BVI problem. This vortex has a finite core. Furthermore, the vortex used in the experimental investigation of Caradonna et al. (1984) has a structure that resembles a Lamb-type vortex. The principal parameters that characterize the vortex are its strength Γ and the radius of its core r_c. The cylindrical velocity distribution at a point at a distance r from the vortex core center is given by

$$v_\theta = \frac{\Gamma}{2\pi r} \frac{r^2}{r^2 + r_c^2} \tag{4}$$

The pressure and density fields induced by this vortex in a uniform freestream can be determined from the radial momentum equation and the constant total enthalpy flow relation, namely:

$$p_v = p_\infty \exp(f(r)) \tag{5}$$

$$\rho_v = \left(\frac{\gamma}{\gamma - 1} \frac{1}{h_\infty - 1/2 v_\theta^2} \right) p_v \tag{6}$$

where γ is the ratio of the specific heats, "∞" denotes the freestream condition and

$$h_\infty = \frac{\gamma}{\gamma - 1} \frac{p_\infty}{\rho_\infty} \tag{7}$$

$$f(r) = \frac{2D}{E^{1/2}} \left[\tan^{-1} \left(\frac{2r^2 + B}{E^{1/2}} \right) - \frac{\pi}{2} \right] \tag{8}$$

with

$$D = 1/2 \left(\frac{\Gamma}{2\pi} \right)^2 \frac{\rho_\infty}{p_\infty}$$
$$B = 2r_c^2 - D(\gamma - 1)/\gamma$$
$$E = 4r_c^4 - B^2 > 0$$

It is noted here that equations (4), (5), and (6) satisfy the governing equations for steady, inviscid, and adiabatic two-dimensional flows.

The vortex disturbance field is then given by

$$\Delta u_v = -v_\theta \sin\theta$$
$$\Delta v_v = v_\theta \cos\theta$$
$$\Delta \rho_v = \rho_v - \rho_\infty$$
$$\Delta p_v = p_v - p_\infty$$

where u_v and v_v are the velocity components in a cartesian coordinate system with its origin fixed at the center of the vortex and θ is the azimuthal angle in this vortex-fixed coordinate system. The initial conditions simulating the presence
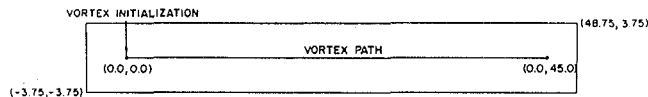
Fig. 1 Computational domain and the vortex path for the vortex preservation tests
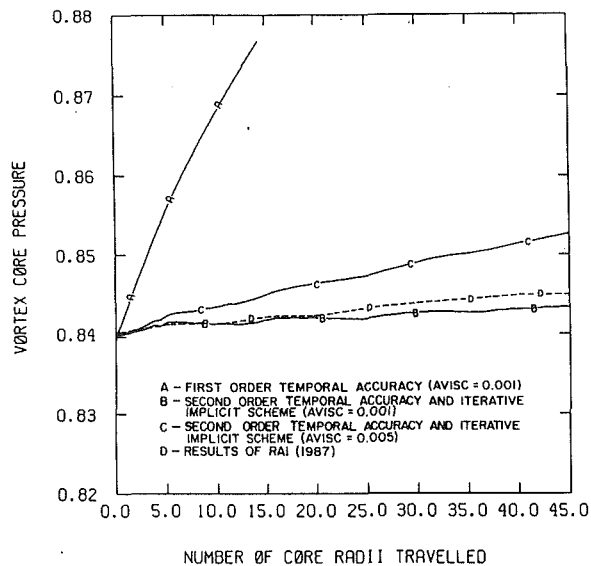

NUMBER ØF CØRE RADII TRAVELLED

Fig. 2 Vortex decay rates for different schemes

A – FIRST ORDER TEMPORAL ACCURACY (AVISC = 0.001)
B – SECOND ORDER TEMPORAL ACCURACY AND ITERATIVE IMPLICIT SCHEME (AVISC = 0.001)
C – SECOND ORDER TEMPORAL ACCURACY AND ITERATIVE IMPLICIT SCHEME (AVISC = 0.005)
D – RESULTS OF RAI (1987)

of a vortex in a steady and uniform flow region of some background flow field can be constructed as follows:

$$u = u_b + \Delta u_v$$
$$v = v_b + \Delta v_v$$
$$\rho = \rho_b + \Delta \rho_v$$
$$p = p_b + \Delta p_v$$

where "b" denotes some background flow. It is noted here that the vortex must be placed in a region in which u_b, v_b, ρ_b, and p_b are steady and uniform.

Calculations are started from this initial condition, integrating equations (1)–(3) on a fixed grid to follow the convection of this vortex through the computational grid. As previously mentioned, the numerical dissipation tends to weaken and sometimes distort the gradients in the vortex and diffuse it, thereby reducing its strength. A good measure of the vortex preserving capability of a given numerical scheme is the vortex core pressure, which is a minimum and must be maintained at its original value as the vortex convects with a uniform freestream. A series of vortex preservation test calculations have been carried out to investigate the effects of the numerical scheme, resolution, and artificial dissipation on the vortex preservation. In these calculations, the reference length is the vortex core radius, the reference flow conditions are the free stream conditions with the Mach number $M_\infty = 0.536$. The computational domain is shown in Fig. 1. The results presented in Fig. 2 are obtained with uniform grid spacing $\Delta x = \Delta y = 1/8$ and constant time step $\Delta t = 0.02$. In addition, the exact solution corresponding to the vortex moving in a freestream is imposed on all the boundaries. Curve A was obtained with the standard Linearized Block Implicit ADI scheme, first-order accuracy in time and a value of AVISC = .001. This should be regarded as the base case. It is very dissipative for the vortex preservation problem. Curve B was obtained with the iterative implicit ADI scheme which has second-order time accuracy. The third curve, curve C, was obtained with the iterative implicit scheme and AVISC = .005. A considerable improvement is noticed with the iterative implicit
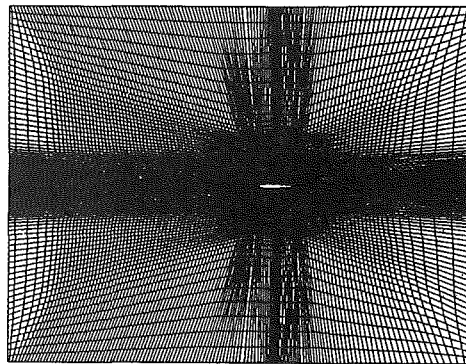

Fig. 3 Grid distribution for BVI simulation

scheme, even with AVISC = .005, and this is the scheme used in the present work. Both curve B and C are obtained with KITER = 3 and DTAU = 3.0, where KITER is the number of sub-iterations used per time step and DTAU is the iteration step size. Based on our experience, these values represent an optimal use of computer resources for the present iterative implicit scheme. For the purpose of comparison, the vortex preservation capability of an iterative implicit fifth-order upwind-biased scheme (Rai, 1987) is also included (curve D). It is noted here that this curve was obtained with $\Delta x = \Delta y = 1/4$.

IV Blade Vortex Interactions

A. Grid, Boundary Conditions and Artificial Dissipation. Figure 3 illustrates the grid distribution used for the BVI simulation. The total number of grid points is 144×118. The inflow boundary is located at 7 chords from the blade leading edge while the outflow boundary is located at 5 chords from the blade trailing edge. The distance between the top boundary and the chord line of the NACA0012 airfoil is 5 chord lengths. The geometric configuration is symmetric about the chord line. Along the inflow boundary, the total pressure, the total temperature, and the inflow angle are specified. The pressure is obtained by extrapolation. Along the outflow, top and bottom boundaries, the static pressure is specified, the velocity and the total temperature are obtained by extrapolation. On the blade surface, nonslip conditions are imposed. The density is obtained by solving the continuity equation and the surface temperature is specified as the constant, freestream total temperature.

The specification of boundary values depends on the problem under consideration. In order to treat the BVI problem, the background flow first must be determined. In the present work, the background flow is the asymptotic steady-state transonic flow past a NACA0012 airfoil section; therefore, the specified boundary values correspond to that of a steady uniform freestream with zero angle of attack. When the vortex is introduced into the transonic flow field at a point upstream of the blade, the boundary values must take into account the existence of this vortex, e.g., the inflow angle will not be zero and generally is not uniform along the inflow boundary. In addition, as the vortex is convecting toward the blade, these boundary values are changing with time. For the present simulation, they are taken from the composite "vortex in a freestream" solution.

A spatially varying artificial dissipation was used in the BVI calculation presented here. Upstream of the blade AVISC was set to 0.005. Based upon the vortex preservation studies this should keep the vortex decay within allowable levels prior to the interaction. However, it should be recognized that the vortex preservation studies were done on a uniform grid whereas the present calculation is done on a nonuniform grid. Downstream of the airfoil leading edge station the value of
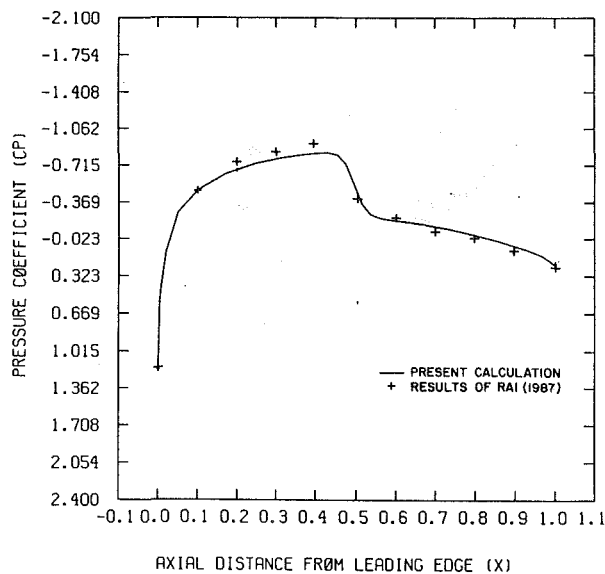
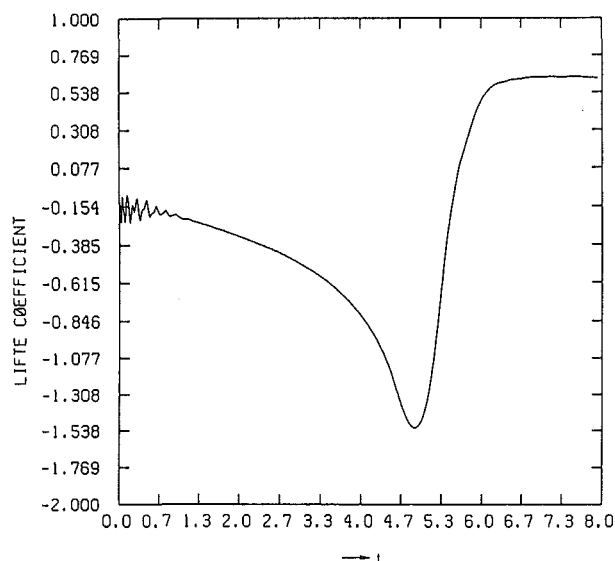Fig. 4 Blade surface pressure distribution (background flow)

AXIAL DISTANCE FROM LEADING EDGE (X)
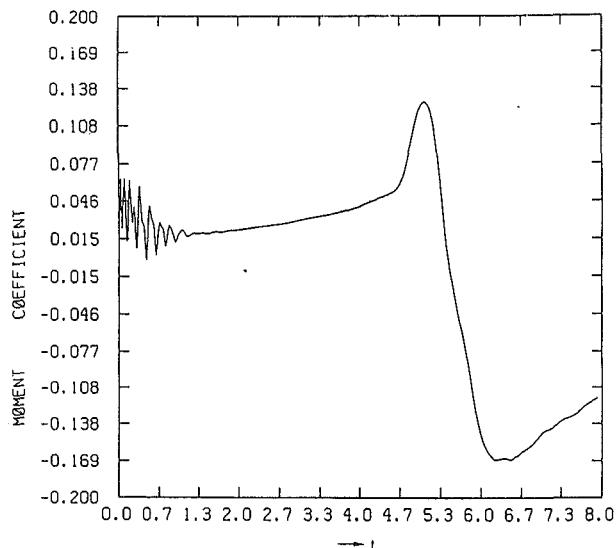
PRESENT CALCULATION
+ RESULTS OF RAI (1987)

Fig. 6 Time history of the quarter-chord pitching moment coefficient, C_M

Fig. 5 Time history of the lift coefficient, C_L
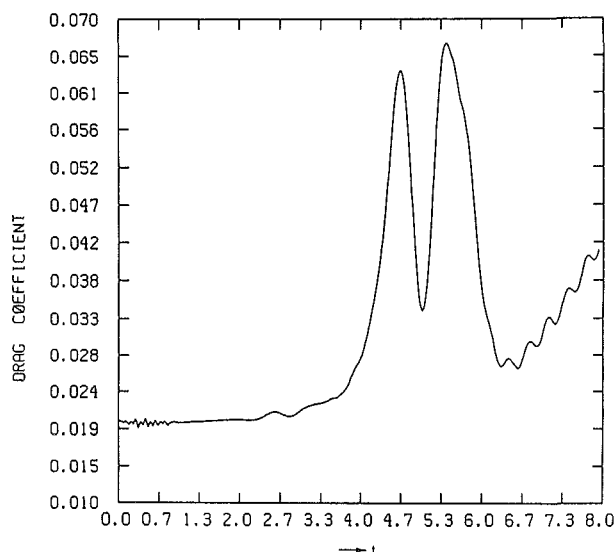
Fig. 7 Time history of the drag coefficient, C_D

AVISC was set at 0.05 except in the immediate vicinity of the leading and trailing edge locations where it was set to 0.5. The relatively high value of 0.5 was required due to the combination of the highly stretched, highly skewed grids and the marginal resolution of the flow in these large gradient regions. Based upon our past experiences, the effects of this relatively high artificial viscosity being applied in this small region are very localized and do not degrade the solution accuracy. The regions of different AVISC values were blended at boundaries to avoid discontinuous changes in the artificial dissipation.

B. Flow Parameters. The reference length is the chord length of the blade and the reference flow conditions are the free stream condition with $M_\infty = 0.8$ and $Re = 1.0 \times 10^6$. The background flow is a steady transonic flow with shock waves standing in the middle of the blade. Furthermore, the flow is symmetric about the chord line; hence, the lift coefficient (C_L) is zero. The surface pressure distribution of this background flow is shown in Fig. 4. Also included is the distribution obtained with a fifth-order upwind-biased scheme (Rai, 1987). The two sets of results are in good agreement.

The dimensionless strength and core radius of the vortex are -1.6 and 0.2, respectively, where the minus sign indicates that the vortex has a clockwise sense. The initial location of the vortex center is at a point 5 chords upstream of the airfoil leading edge ($x_v = -5.0$) and 0.26 chords belows ($y_v = -0.26$). The calculation is carried out from $t = 0$ to $t = 8$ with constant time step $\Delta t = 0.005$, constant sub-iteration step, DTAU = 3.0, and fixed number of sub-iterations per time step, KITER = 3. It is further noted here that the time t is made dimensionless by freestream velocity and the blade chord length.

C. Results and Discussion. The time histories of the aerodynamic coefficients during the blade-vortex-shock interactions are described in Figs. 5, 6, and 7. It should be noted that the small amplitude variations occurring for t up to 1.0 are due to the impulsive introduction of the vortex into the background flow, and these small amplitude oscillations have been damped out long before the onset of significant blade vortex interactions. Furthermore, these coefficients are evaluated in terms of static pressure; they do not include the contribution of viscous stresses. The lift coefficient (C_L) and the quarter-chord pitching moment coefficient (C_M) are
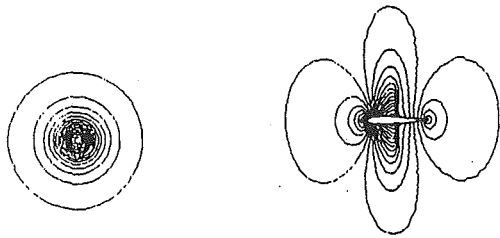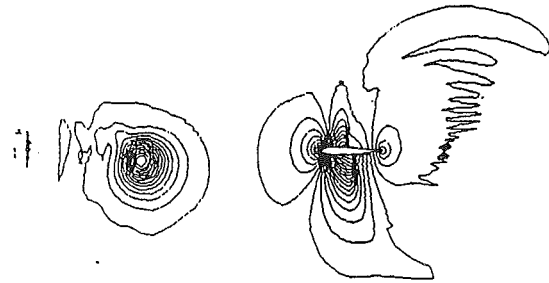
Fig. 8(a) Static pressure contours (t = 0)
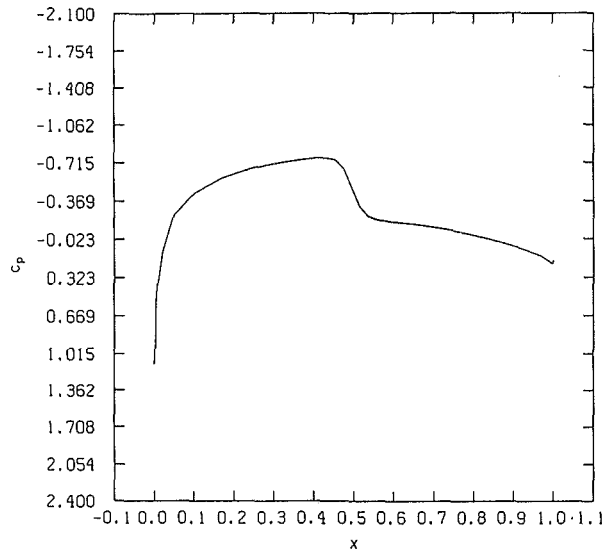

Fig. 9(a) Static pressure contours (t = 2.0)
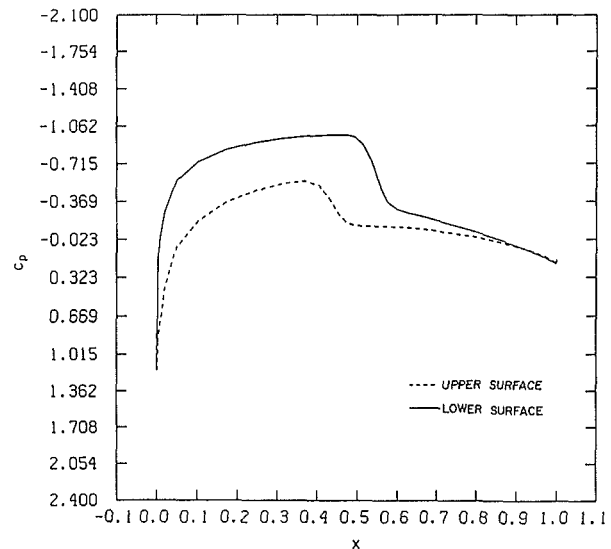

Fig. 8(b) Surface C_p (t = 0)

Fig. 9(b) Surface C_p (t = 2.0)

shown in Figs. 5 and 6, respectively. It should be noted that the background flow is a nonlifting case and that any lift generated during the interaction is induced by the vortex. Since the vortex flow is revolving in the clockwise direction, when the vortex is approaching the blade, it induces nonuniform and unsteady velocities that result in negative angles of attack at the blade. This influence changes to increasing angles of attack after the vortex has reached the blade. Severe load variations occur during the time period from $t = 4.0$ to $t = 6.0$; i.e., when the vortex is within one chord length of the blade leading edge. During this period of time, C_L and C_M change their signs, while C_D undergoes rapid variation exhibiting two distinct temporal maxima (Fig. 7). The behavior of these coefficients is qualitatively the same as that obtained by other investigators.

The interaction between the vortex and the blade with a shock is further elucidated in terms of the instantaneous static pressure distribution at several selected time stations. Figure 8 (a) gives the pressure contours over the entire computational domain at $t = 0$, while Fig. 8(b) gives the distribution of static pressure coefficient on the blade surface at $t = 0$. This is the starting flow field. As the vortex convects towards the blade, the upper surface shock moves in the upstream direction; its strength is decreasing and the extent of the associated supersonic pocket also is reducing. On the other hand, the lower surface shock moves in the downstream direction with increased strength. In addition to the motion of the shock waves, pressure difference between the upper and lower surfaces starts to build up. These generic features are illustrated in Figs. 9(a) and (b), which are obtained at $t = 2.0$. The outer pressure contours on the aft region of the blade shows some "wiggles;" however, this is in a region of nearly uniform

pressure and, therefore, the presence of these wiggles is not significant, but represents small changes in a nearly uniform field.

The flow field at $t = 4.0$, i.e., when the vortex core is about one chord length upstream of the blade, is shown in Figs. 10(a) and (b). The upper surface supersonic pocket practically has disappeared. The lower surface shock wave becomes stronger and is located in a further downstream position; at the shock's root the flow shows signs of separation. In addition, a significant transverse pressure gradient exits in the leading edge region. At $t = 4.5$, this leading edge transverse pressure gradient becomes the dominant feature of the interaction. In addition, the lower surface shock stops moving toward the trailing edge, in spite of the fact that its strength is still increasing. These features are depicted in Figs. 11(a) and (b).

When $t = 5.0$, the vortex core "hits" the blade, the averaged Mach number inside the lower surface supersonic pocket increases to approximately 2. Most of the disturbances on this surface will propagate downstream until reaching the shock. Part of the disturbance is able to leave the supersonic pocket near the outer region of the shock. However, the remainder seems to build up at the root of the shock, as indicated by Fig. 12(b). At the same time, a high pressure disturbance starts to be released from the upper surface of the leading edge, as indicated by Fig. 12(a). The state of the flow at this moment is very volatile. Within a short period of time, this process of disturbance build-up has collapsed, as illustrated by Fig. 13 at $t = 5.5$. The shock is no longer an approximately normal shock but has an oblique leg which intersects the blade wall upstream of the intersection location at $t = 5.0$ (Fig. 12(a)). The emission of a high pressure pulse from the upper surface of the leading

Journal of Fluids Engineering

edge is evident from Fig. 13(*a*); this high pressure pulse then propagates upstream in a domain including the frontal region of the entire leading edge (see Fig. 14(*a*)). Between this frontal high pressure region and the lower surface shock wave, a low pressure pulse is propagating towards the lower outer boundary. Figures 12(*b*), 13(*b*), and 14(*b*) illustrate the collapse of the disturbance building up process and the subsequent relaxation of the strength and the location of the shock wave on the lower surface.

The general features of the flow at $t = 6.0$ are: the existence of a supersonic pocket on the lower surface, significant flow separation originating at the root of the shock, the appearance of vortex remnants near the blade trailing edge, and the development of supersonic flow on the upper surface. Subsequently, the lower surface supersonic pocket continually reduces its extent and eventually disappears by $t = 8.0$. The
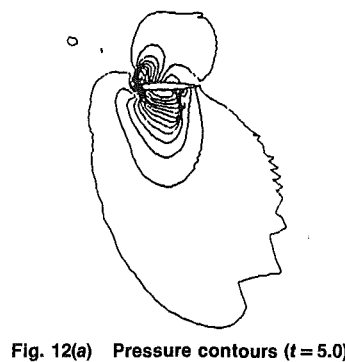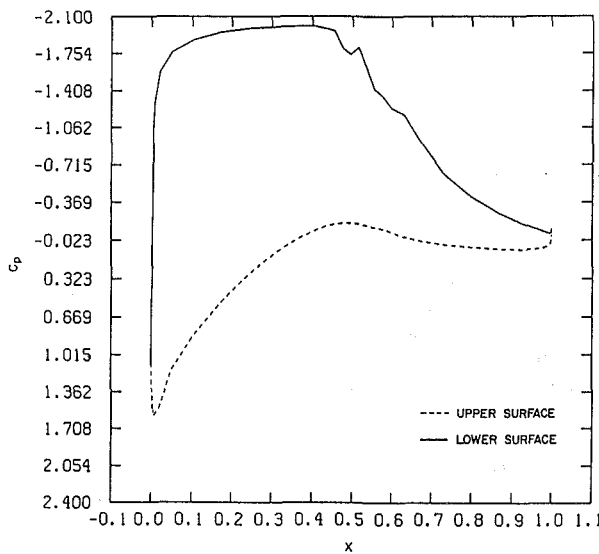

Fig. 10(*a*)   Pressure contours (*t* = 4.0)
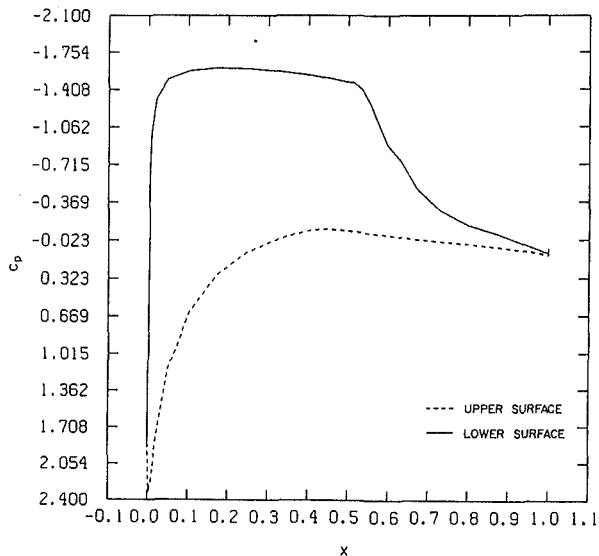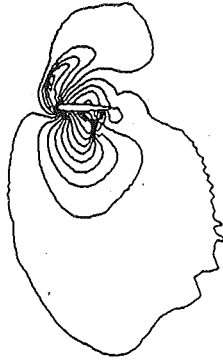

Fig. 11(*b*)   Surface C_p (*t* = 4.5)
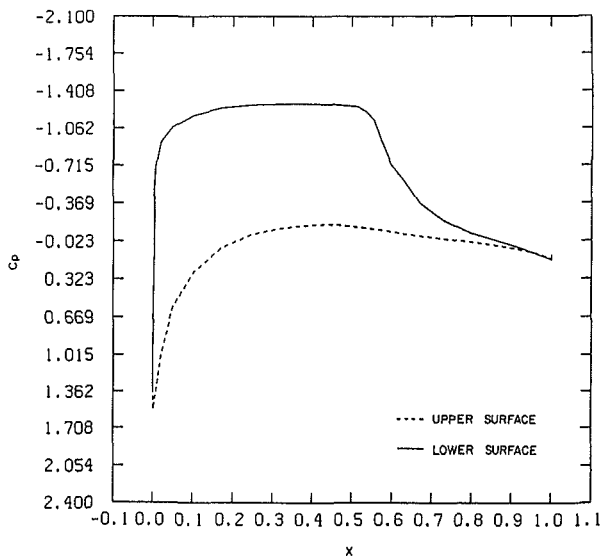
Fig. 10(*b*)   Surface C_p (*t* = 4.0)

Fig. 12(*a*)   Pressure contours (*t* = 5.0)

Fig. 11(*a*)   Pressure contours (*t* = 4.5)

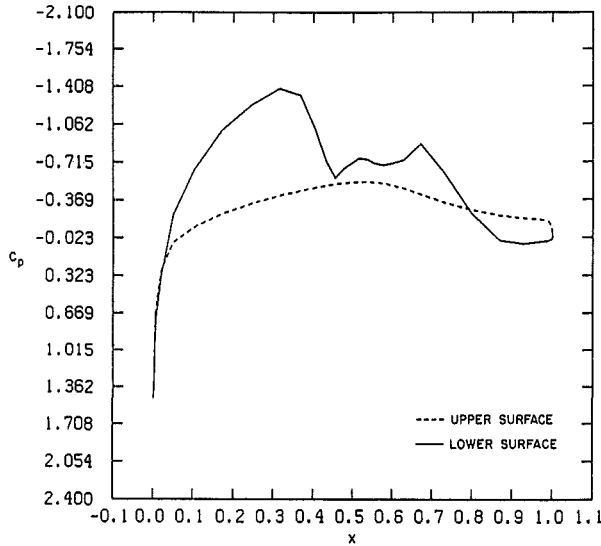Fig. 12(*b*)   Surface C_p (*t* = 5.0)

Fig. 13(a)   Pressure contours ($t = 5.5$)

Fig. 13(b)   Surface C_p ($t = 5.5$)

Fig. 14(b)   Surface C_p ($t = 6.0$)

Fig. 15   Surface C_p ($t = 8.0$)

Fig. 14(a)   Pressure contours ($t = 6.0$)
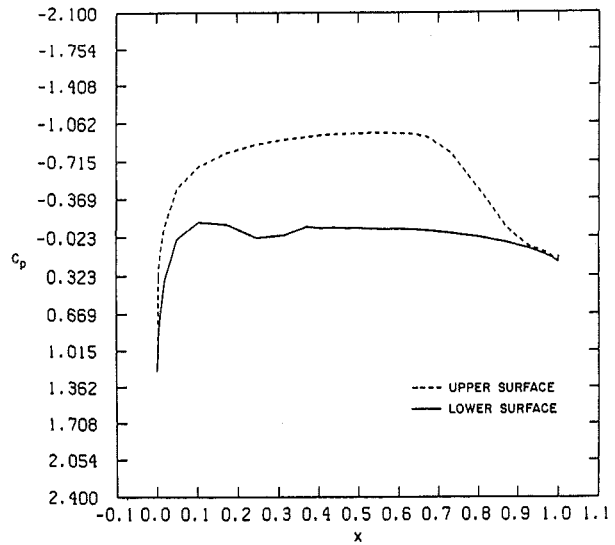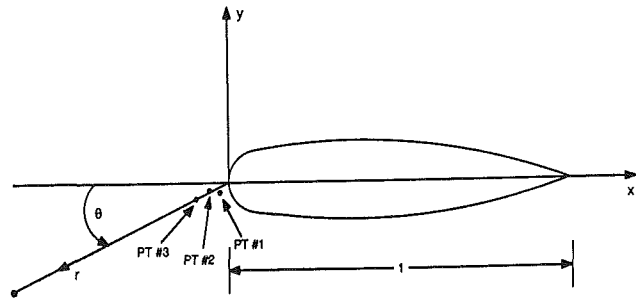
POINT #	r	θ
1	2.31×10^{-2}	28.76°
2	5.40×10^{-2}	25.71°
3	10.73×10^{-2}	26.01°

Fig. 16   Points where scaled pressure disturbance are calculated

lower surface shock moves toward the leading edge with continually diminished strength and then vanishes. At $t = 8.0$, the vortex remnants have been further convected downstream. The flow on the lower surface does not exhibit any appreciable separation and is entirely transonic. Furthermore, about 70 percent of the upper surface is covered by a supersonic pocket,

with compression waves appearing near the trailing edge of the blade (Fig. 15).

The radiation of pressure pulses from the leading edge region as a result of the blade-vortex interaction is further in-
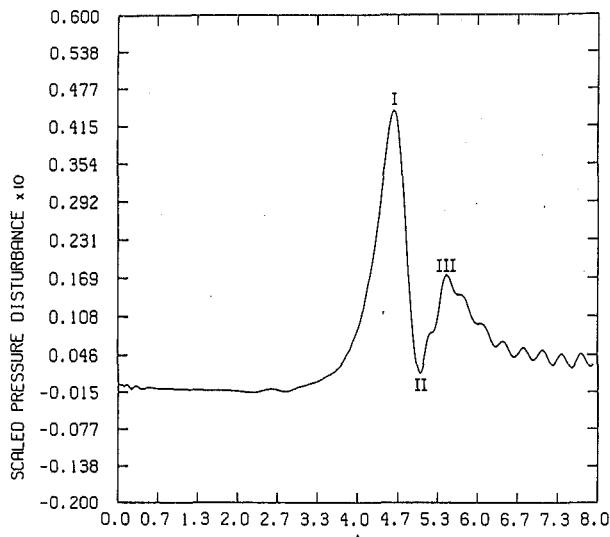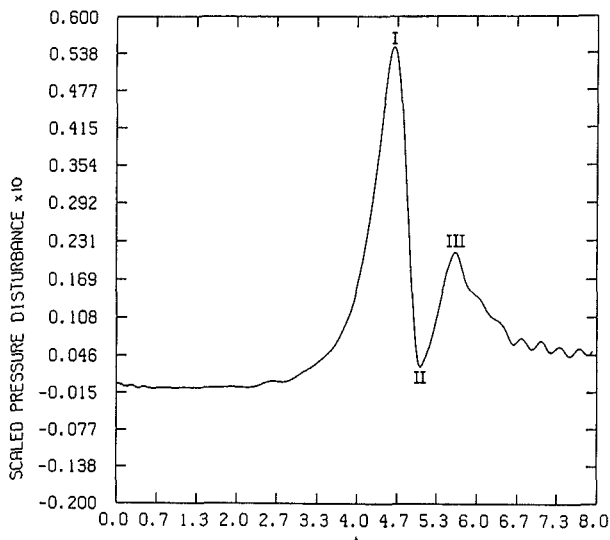
Fig. 17(a)   Scaled p′ at point 1

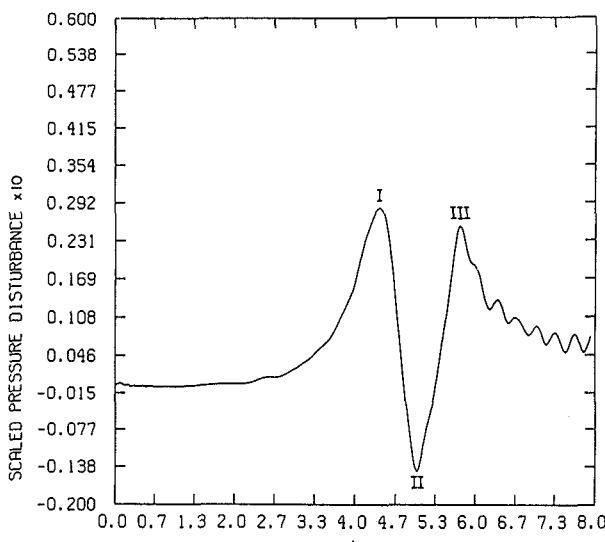**Fig. 17(b)   Scaled p′ at point 2**

Fig. 17(c)   Scaled p′ at point 3

vestigated in terms of the scaled pressure disturbance. In the two-dimensional linear far field, the amplitude of propagating waves is proportional to $1/r^{1/2}$, where r is the distance to the origin of the disturbance. The scaled pressure disturbance is obtained by subtracting the steady-state background value from the instantaneous BVI solution, and the result is multiplied by $r^{1/2}$, where r is the distance to the leading edge. Figure 16 defines the points at which the time histories of the scaled disturbances are recorded and presented in Figs. 17(a), (b), and (c). The first peak, I, is due to the interaction between the incoming vortex and the leading edge, when the vortex center is within one chord length of the blade. The valley II, is associated with the passage of the vortex core through these points, and the peak, III, originates from the upper surface of the leading edge, after the vortex core hits the blade, as described before.

The present simulation has focused on the near field BVI effects. A meaningful simulation of the propagation of resulted pressure disturbances to the far field would require a much larger computational domain, much finer meshes in mid and far fields, and perhaps, more sophisticated far field boundary conditions. In other words, substantially more computer resources are required. George and Lyrintzin (1988) introduced a Kirchhoff method of extending the computed 2-D mid field results to the 3-D far field to alleviate the problem.

Although experimental and other numerical results are not available for direct comparison with the present BVI results, the time histories of C_L and C_M (Figs. 5 and 6) are in qualitative agreement with those obtained in other simulations (e.g., Srinivasan and McCroskey, 1987). Furthermore, the present free vortex convection results (Fig. 2) and the isolated blade results (Fig. 4) compare well with those obtained by different methods (e.g., Rai, 1987). It is also noted here that, throughout the entire duration of the simulation and with $\Delta t = 0.005$ as used here, the maximum relative change of the dependent variables has not exceeded 6 percent over any given time step, indicating that an adequate temporal resolution has been obtained. The computation has been carried out on a CRAY-XMP system and required a CPU time of 0.48×10^{-3} s per grid node per time step (with 3 sub-iterations per time step).

V   Concluding Remarks

Due to its significant effects on the performance of aerodynamic components and its role in the noise generation, Blade-Vortex Interaction has been a subject of many investigations. A key problem in computing BVI is the dissipation and distortion of vortices caused by false numerical diffusion. Various algorithms have been used to alleviate this problem, with varying degrees of success and computational costs. In the present work, the two-dimensional, unsteady Navier–Stokes equations are solved by using an iterative implicit finite-difference scheme with second-order temporal accuracies and using three-point central spatial differences with very small amounts of added artificial dissipation. The improved accuracy of this differencing procedure has been demonstrated by vortex preservation test calculations. This improved algorithm is then applied to simulate a strong interaction between a Lamb-type vortex and a NACA0012 airfoil under the transonic condition.

It is observed that severe load variations occur when the vortex is within one chord length of the blade leading edge. The dominant processes of the interaction are the development of a large transverse pressure gradient in the upper leading edge region and the building up of disturbances at the root of the lower surface shock wave. These processes lead to a volatile state which eventually collapses. The relaxation of the flow is accompanied with the emission of a high pressure

pulse from the leading edge region and the radiation of acoustic waves from the collapsing supersonic pocket on the lower surface. The propagation of these pressure waves to the far field has not been tracked in the present simulation. The calculation is terminated at a time station indicating the emergence of supersonic flow over a large part of the upper surface, while the flow on the lower surface of the blade is transonic throughout.

Acknowledgments

References

Baeder, J. D., 1987, "Computation of Non-linear Acoustics in Two-Dimensional Blade-Vortex Interactions," The 13th European Rotorcraft Forum, Arles, France, Sept.

Booth, E. R., and Yu, J. C., 1986, "Two-dimensional Blade-Vortex Flow Visualization Investigation," *AIAA Journal*, Vol. 24, No. 9, pp. 1468–1473.

Briley, W. R., and McDonald, H., 1980, "On the Structure and Use of Linearized Block Implicit Schemes," *Journal of Comp. Physics*, Vol. 34, No. 1, pp. 54–72.

Briley, W. R., and McDonald, H., 1986, "Accuracy and Iterative Convergence Rate of ADI Schemes for Scalar Convection," SRA Report R86-900050-F, June.

Caradonna, F. X., Laub, G. H., and Tung, C., 1984, "An Experimental Investigation of the Parallel Blade Vortex Interaction," The 10th European Rotorcraft Forum, The Hague, Holland, Aug.

Caradonna, F. X., Lautenschlager, J. L., and Silva, M. J., 1988, "An Experimental Study of Rotor-Vortex Interactions," AIAA paper 88-0045, Reno, Nevada, Jan.

Damodaran, M., and Caughey, D. A., 1988, "Finite Volume Calculation of Inviscid Transonic Airfoil-Vortex Interaction," *AIAA Journal*, Vol. 26, No. 11, pp. 1346–1353.

George, A. R., and Lyrintzis, A. S., 1988, "Acoustics of Transonic Blade-Vortex Interactions," *AIAA Journal*, Vol. 26, No. 7, pp. 769–776.

Hardin, J. C., and Lamkin, S. L., 1984, "Aeroacoustic Interaction of a Distributed Vortex with a Lifting Joukowski Airfoil," AIAA paper 84-2287, Oct.

Lee, D. J., and Smith, C. A., 1987, "Distortion of the Vortex Core During Blade/Vortex Interaction," AIAA paper 87-1243, Honolulu, Hawaii, June.

Panaras, A. G., 1987, "Numerical Modeling of the Vortex/Airfoil Interaction," *AIAA Journal*, Vol. 25, No. 1, pp. 5–11.

Poling, D. R., Dadone, L., and Telionis, D. P., 1989, "Blade-Vortex Interaction," *AIAA Jounral*, Vol. 27, No. 6, pp. 694–699.

Rai, M. M., 1987, "Navier–Stokes Simulations of Blade-Vortex Interaction Using High-Order Accurate Upwind Schemes," AIAA paper 87-0543, Reno, Nevada, Jan.

Sankar, L. N., and Tang, W., 1985, "Numerical Solution of Unsteady Viscous Flow Past Rotor Sections," AIAA paper 85-0129, Reno, Nevada, Jan.

Srinivasan, G. R., and McCroskey, W. J., 1987, "Numerical Simulations of Unsteady Airfoil-Vortex Interactions," *Vertica*, Vol. 11, No. 112, pp. 3–28.

Weinberg, B. C., Yang, R.-J., McDonald, H., and Shamroth, S. J., 1986, "Calculation of Two- and Three-Dimensional Transonic Cascade Flow Fields Using the Navier–Stokes Equations," ASME *Journal of Engineering for Gas Turbines and Power*, Vol. 108, pp. 93–102.

Application of an Implicit Relaxation Method Solving the Euler Equations for Time-Accurate Unsteady Problems

A. Brenneis

A. Eberle

Messerschmitt-Bölkow-Blohm GmbH,
D-8000 München 80,
Federal Republic of Germany

A numerical procedure is presented for computing time-accurate solutions of flows about two and three-dimensional configurations using the Euler equations in conservative form. A nonlinear Newton method is applied to solve the unfactored implicit equations. Relaxation is performed with a point Gauss-Seidel algorithm ensuring a high degree of vectorization by employing the so-called checkerboard scheme. The fundamental feature of the Euler solver is a characteristic variable splitting scheme (Godunov-type averaging procedure, linear locally one-dimensional Riemann solver) based on an eigenvalue analysis for the calculation of the fluxes. The true Jacobians of the fluxes on the right-hand side are used on the left-hand side of the first order in time-discretized Euler equations. A simple matrix conditioning needing only few operations is employed to evade singular behavior of the coefficient matrix. Numerical results are presented for transonic flows about harmonically pitching airfoils and wings. Comparisons with experiments show good agreement except in regions where viscous effects are evident.

Introduction

The computation of unsteady flows around flight configurations of the next generation (e.g., highly swept wings, supercritical airfoils, large three-dimensional effects) requires numerical methods placed higher in the hierarchic order than those based on the potential equation. The assumptions and simplifications made in the potential equation restrict the codes based on them to flows with weak and moderately strong shocks (nonlinear potential equation) and to thin airfoils with small oscillation amplitudes (TSP method). As the solution of the Navier-Stokes equations is connected with extremely large CPU times, the problem of turbulence modeling, and the laminar-turbulent transition, the development of numerical methods for unsteady problems has been focused on the Euler equations in the past decade. Existing codes are based on explicit schemes [1–6], implicit approximate-factorization (AF) schemes [7–9] or on hybrid schemes [10]. The explicit time-stepping schemes suffer from the limitation of the global time step which is necessary to treat time-accurate unsteady problems and which leads to an enormous number of time steps and consequently to large CPU times. The great disadvantage of the approximate-factorization scheme is that optimal convergence in two dimensions is obtained at a value of the time step that is not known a priori. It can be found by trial and

error only and varies from problem to problem, although it usually corresponds to a CFL number of the order of 10 only. Additionally, in three dimensions the stability restrictions are stronger and reduce the maximum CFL number considerably. Therefore the saving of computational time in the AF scheme versus the explicit scheme is reduced further through extension from two to three dimensions.

The Euler code developed in [11] and described in this paper solves the unfactored implicit Euler equations by means of a relaxation method. The advantages of this iterative scheme, applicable to steady and truly unsteady flows, is that it is unconditionally stable in a linear stability analysis both in two and three dimensions, the CFL number can be arbitrarily high and the maximum damping occurs at large time steps. Hence it is less sensitive to the choice of time step than the AF method. Furthermore, the algorithm used with its high degree of vectorization is optimally suited to supercomputers.

The unsteady solver INFLEX is based on the well proven steady Euler code EUFLEX [12] using characteristic flux extrapolation. The unfactored implicit equation are solved by a nonlinear Newton method following [13] in order to obtain time-accurate solutions. Relaxation is performed with a point Gauss-Seidel technique with the so-called checkerboard scheme. The two and three-dimensional versions, INFLEX2 and INFLEX3, were tested on the conventional NACA 64A010 [14], the supercritical NLR 7301 airfoil [15], and on several high and low-aspect ratio wings [15,16].

Governing Equations

The conservation law vector form of the three-dimensional, dimensionless unsteady Euler equations in curvilinear coordinates

$$\xi = \xi(x,y,z,t)$$
$$\eta = \eta(x,y,z,t)$$
$$\zeta = \zeta(x,y,z,t)$$
$$\tau = t \tag{1}$$

with the Cartesian velocity components u, v, w can be written as

$$\frac{\partial \phi}{\partial \tau} + \frac{\partial E}{\partial \xi} + \frac{\partial F}{\partial \eta} + \frac{\partial G}{\partial \zeta} = 0. \tag{2}$$

$\phi = J(\rho,\rho u,\rho v,\rho w,e)^T$ is the solution vector and

$$E = J(\tilde{E}\xi_x + \tilde{F}\xi_y + \tilde{G}\xi_z), \tag{3a}$$

$$F = J(\tilde{E}\eta_x + \tilde{F}\eta_y + \tilde{G}\eta_z), \tag{3b}$$

$$G = J(\tilde{E}\zeta_x + \tilde{F}\zeta_y + \tilde{G}\zeta_z), \tag{3c}$$

are the fluxes normal to the faces $\xi = \text{const.}$, $\eta = \text{const.}$ and $\zeta = \text{const.}$

$$J = x_\xi (y_\eta z_\zeta - y_\zeta z_\eta) + x_\eta (y_\zeta z_\xi - y_\xi z_\zeta) + x_\zeta (y_\xi z_\eta - y_\eta z_\xi) \tag{4}$$

is the Jacobian of the inverse mapping, representing the volume of the cell, and the quantities such as ξ_x, ξ_y etc. are the metrics of transformation related to the x, y, z-coordinate system through relationships, e.g.,

$$\xi_x = \frac{y_\eta z_\zeta - y_\zeta z_\eta}{J},$$

$$\xi_y = \frac{x_\zeta z_\eta - x_\eta z_\zeta}{J}. \tag{5}$$

$\dot{x},\dot{y},$ and $\dot{z}$ in the Cartesian fluxes

$$\tilde{E} = \begin{bmatrix} \rho(u-\dot{x}) \\ \rho u(u-\dot{x})+p \\ \rho v(u-\dot{x}) \\ \rho w(u-\dot{x}) \\ e(u-\dot{x})+pu \end{bmatrix}, \quad \tilde{F} = \begin{bmatrix} \rho(v-\dot{y}) \\ \rho u(v-\dot{y}) \\ \rho v(v-\dot{y})+p \\ \rho w(v-\dot{y}) \\ e(v-\dot{y})+pv \end{bmatrix},$$

$$\tilde{G} = \begin{bmatrix} \rho(w-\dot{z}) \\ \rho u(w-\dot{z}) \\ \rho v(w-\dot{z}) \\ \rho w(w-\dot{z})+p \\ e(w-\dot{z})+pw \end{bmatrix} \tag{6}$$

are the velocity components of the moving cell, ρ is the density, p the pressure, and the total energy per unit volume for a perfect gas is

$$e = \frac{p}{\gamma-1} + \frac{1}{2}\rho(u^2 + v^2 + w^2). \tag{7}$$

Numerical Algorithm

Global Time Step. Time consistency is required for the treatment of unsteady problems. This means that the unsteady evolution must be computed with a uniform time step over the whole computational domain. This global time step is defined as

$$\Delta t \leq \Delta t_{max} = \min_{i,j,k} \left(\frac{J \cdot CFL}{\lambda_{max}} \right)_{i,j,k}, \tag{8}$$

where λ_{max} is the maximum eigenvalue of the cell i, j, k. Due to the restriction of the CFL number for explicit methods this can lead to an enormous number of time steps

$$N = \frac{T}{\Delta t}, \tag{9}$$

Nomenclature

A,B,C = Jacobians of the fluxes E, F, and G
CFL = Courant-Friedrichs-Lewy number
c = airfoil chord
c_{AC} = mean aerodynamic chord
c_p = pressure coefficient
c_r = wing-root chord
CT = Computational Test Case
E,F,G = fluxes
e = total energy per volume
$\text{Im}(\ )$ = imaginary part of ( )
J = Jacobian of the inverse mapping
k = reduced frequency
M = Mach number
N = number of points
p = static pressure
$\text{Re}(\ )$ = real part of ( )
RES = residua
t,τ = nondimensional time
U_∞ = freestream velocity
u,v,w = velocity components in streamwise, normal and cross-stream directions, respectively
x,y,z = nondimensional Cartesian coordinates in streamwise, spanwise and vertical directions, respectively
$\dot{x},\dot{y},\dot{z}$ = velocity components of the moving cell
$\alpha(t)$ = instantaneous angle of attack
α_0 = mean value of the angle of attack

α_1 = pitch oscillation amplitude
$'\alpha_1$ = nondimensionalized by α_1, per radian
γ = ratio of specific heats
Δt = time step
$\Delta t/\text{cycle}$ = number of time steps per cycle
$\Delta\text{Mag}(c_p^1)$ = magnitude of lifting pressure coefficient
$\Delta\phi(c_p^1)$ = phase between lifting pressure and wing pitch angle, deg (positive for pressure leading motion)
ϵ_{rel} = upper bound for iteration process
λ = eigenvalue
ρ = density
ϕ = conservative solution vector
ξ,η,ζ = transformed nondimensional coordinates in x, y, and z directions, respectively
ω = under relaxation factor, angular frequency

Subscripts
m = mean value
max = maximum
i,j,k = cell index

Superscripts
n = time index
μ = nonlinear iteration state
ν = Gauss-Seidel subiteration count
1 = first component of the Fourier analysis

dependent on the smallest cell in the computational domain (T is a characteristic time interval, e.g., period of oscillation or relaxation time).

Implicit Scheme. In order to reduce the number of time steps per cycle and thus the overall computational time an implicit procedure, which allows time steps with CFL $>> 1$, is applied to solve equation (2). The first order in the time-discretized implicit form of (2) reads

$$\frac{\phi^{n+1}-\phi^n}{\Delta\tau} + E_\xi^{n+1} + F_\eta^{n+1} + G_\zeta^{n+1} = 0. \tag{10}$$

Because of its nonlinearity this equation is not directly solvable for the dependent variable ϕ^{n+1}. Therefore a sequence of approximations denoted by ϕ^μ such that

$$\lim_{\mu>1}\phi^\mu \rightarrow \phi^{n+1} \tag{11}$$

is constructed.

Linearizing the fluxes

$$E^{\mu+1} = E^\mu + \frac{\partial E^\mu}{\partial\phi}\Delta\phi^{\mu+1} + O(\Delta\tau^2) + ...,$$

$$F^{\mu+1} = F^\mu + \frac{\partial F^\mu}{\partial\phi}\Delta\phi^{\mu+1} + O(\Delta\tau^2) + ...,$$

$$G^{\mu+1} = G^\mu + \frac{\partial G^\mu}{\partial\phi}\Delta\phi^{\mu+1} + O(\Delta\tau^2) + ... \tag{12}$$

around the iteration state μ, a nonlinear Newton method [13] can easily be yielded:

$$\frac{\Delta\phi^{\mu+1}}{\Delta\tau} + (A^\mu\cdot\Delta\phi^{\mu+1})_\xi + (B^\mu\cdot\Delta\phi^{\mu+1})_\eta + (C^\mu\cdot\Delta\phi^{\mu+1})_\zeta =$$

$$-\left[\frac{\phi^\mu-\phi^n}{\Delta\tau} + E_\xi^\mu + F_\eta^\mu + G_\zeta^\mu\right] \equiv \text{RHS}. \tag{13}$$

The flux differences E_ξ, F_η, and G_ζ are approximated via a third-order characteristic flux extrapolation scheme, using sensor functions to detect shocks, where the scheme reduces to first-order accuracy [12]. The principal feature of the characteristic flux extrapolation scheme is a Godunov-type averaging procedure based on an eigenvalue analysis of the Euler equations by means of which the fluxes are evaluated at the finite-volume face (linear locally one-dimensional Riemann solver) which separates constant sets of flow variables on either side. All nonlinear terms at time level μ are collected together in the quantity RHS (right-hand side). On the left-hand side (LHS) upwind differencing of order one or two is used. The solution vector $\Delta\phi^{\mu+1}$ from equation (13) leads to the update

$$\phi^{\mu+1} = \phi^\mu + \Delta\phi^{\mu+1}. \tag{14}$$

Converging $\Delta\phi$ to zero on the LHS of equation (13), the implicit formulation of equation (10) with $\mu\rightarrow n+1$ remains on the RHS. A^μ, B^μ, and C^μ are the true Jacobians of the fluxes E^μ, F^μ, and G^μ at the nonlinear iteration state μ.

Relaxation Method. Because the numerical solution of the Newton method in two or more dimensions is too time-consuming and the application of an approximate-factorization scheme in three dimensions leads to tremendous time-step restrictions, a relaxation technique is used to solve the unfactored implicit Euler equations. The discretized form of equation (13) for a point Gauss-Seidel (GS) iteration reads

$$\left[\frac{I}{\Delta\tau} + \text{DIAG}_{i,j,k}^\mu\right]\cdot\Delta\phi_{i,j,k}^{\nu+1} = \omega\cdot\text{RHS}_{i,j,k}^\mu + \text{ODIAG}_{i,j,k}, \tag{15}$$

where

$$\text{DIAG}_{i,j,k}^\mu = (T\Lambda^+T^{-1})_{i+1/2,j,k}^\mu - (T\Lambda^-T^{-1})_{i-1/2,j,k}^\mu$$
$$+ (T\Lambda^+T^{-1})_{i,j+1/2,k}^\mu - (T\Lambda^-T^{-1})_{i,j-1/2,k}^\mu$$
$$+ (T\Lambda^+T^{-1})_{i,j,k+1/2}^\mu - (T\Lambda^-T^{-1})_{i,j,k-1/2}^\mu \tag{16}$$

is a $5*5$ matrix containing the sum of the eigenvalue splitted Jacobians connected with $\Delta\phi_{i,j,k}$. The definitions of the diagonal matrix $\Lambda^\pm$ and the nonsingular matrix T are given in [11,17]. $\text{ODIAG}_{i,j,k}$ consists of the complementary eigenvalue splitted Jacobians and the $\Delta\phi$'s of the neighboring points:

$$\text{ODIAG}_{i,j,k} = - (T\Lambda^-T^{-1})_{i+1/2,j,k}^\mu\Delta\phi_{i+1,j,k}$$
$$+ (T\Lambda^+T^{-1})_{i-1/2,j,k}^\mu\Delta\phi_{i-1,j,k}$$
$$- (T\Lambda^-T^{-1})_{i,j+1/2,k}^\mu\Delta\phi_{i,j+1,k}$$
$$+ (T\Lambda^+T^{-1})_{i,j-1/2,k}^\mu\Delta\phi_{i,j-1,k}$$
$$- (T\Lambda^-T^{-1})_{i,j,k+1/2}^\mu\Delta\phi_{i,j,k+1}$$
$$+ (T\Lambda^+T^{-1})_{i,j,k-1/2}^\mu\Delta\phi_{i,j,k-1}. \tag{17}$$

ν indicates the GS-subiteration count and I is the identity matrix. The under-relaxation factor ω compensates for errors of different spatial orders of accuracy on RHS and LHS, thus ensuring convergence. During the ν-iterations DIAG$^\mu$ and RHS$^\mu$ rest at the level μ, whereas ODIAG is evaluated using the latest available values of $\Delta\phi$. The expression in the brackets is called coefficient matrix $\overline{\text{LHS}}$, and $\omega\cdot$RHS$+$ODIAG the $\overline{\text{RHS}}$. By applying the so-called checkerboard scheme, in which points are divided into black and white ones, a high degree of vectorization is achieved.

Matrix Conditioning. Sudden breakdowns of computer runs without any indications of divergence of the solution were caused by dividing by zero during the Gauss-elimination process of the local system of equation (15). Detailed investigations in [11] brought to light that for certain geometry specification and Mach numbers the diagonal elements of the coefficient matrix $\overline{\text{LHS}}$ in equation (15) are zero.

In order to avoid the singular behavior of the coefficient matrix the equation system (15) is modified. Multiplying matrix $\overline{\text{LHS}}$ by the transformation matrix M from the right, which converts the conservative variables to the nonconservative ones, yields the matrix

$$\overline{\text{LHS}}^* = \overline{\text{LHS}}\cdot\text{M}, \tag{18}$$

the diagonal elements of which $\underline{\text{cannot}}$ be zero. After solving the system

$$\overline{\text{LHS}}^*\cdot\Delta\phi^* = \overline{\text{RHS}}, \tag{19}$$

with $\Delta\phi^* = M^{-1}\Delta\phi$, the solution vector must be substituted back to get

$$\Delta\phi = \text{M}\cdot\Delta\phi^*. \tag{20}$$

This matrix conditioning requires only a few operations because of the sparse nature of matrix M:

$$\text{M} = \begin{bmatrix} 1 & 0 & 0 & 0 & 0 \\ u & \rho & 0 & 0 & 0 \\ v & 0 & \rho & 0 & 0 \\ w & 0 & 0 & \rho & 0 \\ \dfrac{\Phi}{\gamma-1} & \rho u & \rho v & \rho w & \dfrac{1}{\gamma-1} \end{bmatrix}, \tag{21}$$

with $\Phi = \dfrac{\gamma-1}{2}(u^2+v^2+w^2)$.

Convergence Criteria. Applying a relaxation method for the treatment of unsteady problems requires that the nonlinear iterations between two time steps converge ($\Delta\phi\rightarrow 0$). Because in numerical method $\Delta\phi^{\mu+1}$ is never identically zero, another criterion must be introduced to stop the iteration process. Then

the latest calculated solution vector $\phi^{\mu+1}$ from equation (14) will be considered as the valid one. The assumption for this, however, is that $\Delta\phi^{\mu+1+m}(m>1)$, which would be generated by continuing the nonlinear iteration process, is small compared with $\phi^{\mu+1}$:

$$\Delta\phi^{\mu+1+m} << \phi^{\mu+1} \quad (m>1). \tag{22}$$

Two limiting criteria for the iteration process were tested. The first one is

$$\frac{RES^{\mu+1}}{RES^I} < \epsilon_{rel}, \quad (\mu+1\geq2, \ \mu=0,1,2,...) \tag{23}$$

with

$$RES = \max_{i,j,k}\left[\frac{|\Delta\rho|+|\Delta\rho u|+|\Delta\rho v|+|\Delta\rho w|+|\Delta e|}{|\rho|+|\rho u|+|\rho v|+|\rho w|+|e|}\right]. \tag{24}$$

The norm $|\ \ |$ defines the absolute value of the argument. The second stronger criterion is

$$\left|\frac{\Delta\phi^{\mu+1}}{\phi^{\mu+1}}\right| < \epsilon_{rel}. \tag{25}$$

It requires that for any cell and any component of the solution vector $\Delta\phi^{\mu+1}$ is less than $\phi^{\mu+1}$ multiplied by an upper bound ϵ_{rel}.

Boundary Conditions

Due to the artificial boundaries of the computational domain and the physical condition at the solid body surface, two different types of boundary conditions have to be implemented into the code.

At the farfield boundaries formally all flow quantities are prescribed. The sign of the eigenvalues at the cell faces forming the farfield boundary is used to automatically select the proper characteristic variables from the data offered. This guarantees correct wave absorbtion at the farfield boundaries.

The solid body boundary condition characterized by the vanishing normal velocity is incorporated the following way: All cell face flow quantities at a solid body boundary can be regrouped as a sum of two elements

$$\phi = R_1 + R_2, \tag{26}$$

where the subscripts indicate the alignment with the two extreme characteristics. Either R_1 or R_2 can be easily obtained from the kinematic flow condition. Assuming for the moment that ϕ is the normal momentum component then, because of $\phi=0$, the quantity R_1 is

$$R_1 = -R_2 \tag{27}$$

if the characteristic labeled 1 requires data outside the body which are not available there. Otherwise

$$R_2 = -R_1 \tag{28}$$

In any case one of the two quantities is always known and used for the remaining components of the variable vector.

Grid Generation

All calculations reported here were done on H-type (2D) and H-H type (3D) grids with fixed farfield boundaries. The meshes were generated using the higher-order elliptic grid-generation systems developed by Schwarz [18] which solve Poisson equations. Due to the inherent smoothness in solving elliptic systems and the fact that boundary slope discontinuities are not propagated into the field, solutions of elliptic systems are a convenient method for constructing boundary-fitted coordinate systems.

In order to completely specify the geometry of the first two grid cells adjacent to the boundary, a sixth-order system

$$\nabla^6 x^i = 0 \quad (i=1,2,3) \tag{29}$$
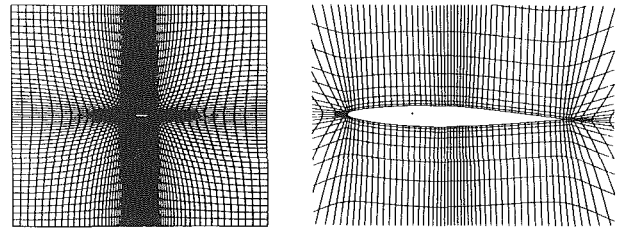
(a) overall view   (b) partial view

Fig. 1   Computational mesh for the NACA 64A010 airfoil (88 * 48 points)

is employed. This partial differential equation of the order six is implemented as three systems of second-order equations (Poisson and Laplace equations). These linear algebraic equations in the physical domain are discretized by central differences and solved with point Gauss-Seidel iterations. The resulting grid points $(x,y,z)_{i,j,k}$ and the source terms are stored. After each time step in the flowfield computation the wing surface is moved and the mesh is deformed, rearranged by one to two grid iterations. The checkerboard scheme is used to speed up the generation procedure as in the Euler solver.

Results and Discussion

The two and three-dimensional codes (INFLEX2 and INFLEX3) were applied to the NACA 64A010 [14], the NLR 7301 airfoil [15], a rectangular supercritical wing (RSW wing) [16], the LANN wing [16], and the F-5 fighter wing [15]. All configurations performed pitching oscillations with a harmonically varying angle of attack

$$\alpha(t) = \alpha_0 + Re(\alpha_1 \cdot e^{i\omega t}) = \alpha_0 + \alpha_1 \cdot \cos(\omega t) \tag{30}$$

about an axis normal to the root chord. α_0 is the mean value of the angle of attack and α_1 the oscillation amplitude. The reduced frequency, which is the important similarity parameter for flows with unsteady boundary conditions, is defined as

$$k = \frac{\omega \cdot c}{2U_\infty}. \tag{31}$$

U_∞ is the freestream velocity and c either the chord length of the airfoil, the wing root c_r, or the mean aerodynamic chord length c_{AC}, and may not be confused with the velocity of sound. The surface pressure coefficient $c_{p(x/c,t)}$ is decomposed by Fourier analysis into the mean value of the local surface pressure coefficient $c_{pm(x/c)}$ and the nth complex component (real (in-phase) and imaginary (out-of-phase) parts) of the locally unsteady pressure coefficient per radian.

All computations (SIEMENS VP200 vector computer) were started with parallel flow and were carried out for two or three cycles to ensure that the surface pressure is repeated periodically from cycle to cycle. As the wave propagation is inversely proportional to the frequency and as the reduced frequency was low in most of the test cases examined, two cycles normally were sufficient to establish the periodic regime in the vicinity of the airfoil or wing. All results reported here have been obtained with the LHS-discretization of equation (15), which is first order accurate in space.

Basic investigations into the relaxation scheme were performed on the conventional NACA 64A010 airfoil. It oscillated about the one-quarter point at a Mach number of 0.8. $\alpha_0=0$ deg, $\alpha_1=1$ deg, and the reduced frequency varied between 0.01 and 0.303. The airfoil geometry was taken from [19] and the numerical results were compared with the measurements [20]. The grid used with 88 points in x and 48 points in z direction is shown in Fig. 1.

The resulting pressure distribution ($k=0.202$) on the upper surface for the third cycle is plotted in Fig. 2. The shock-wave excursion and the increase and decrease of the shock strength
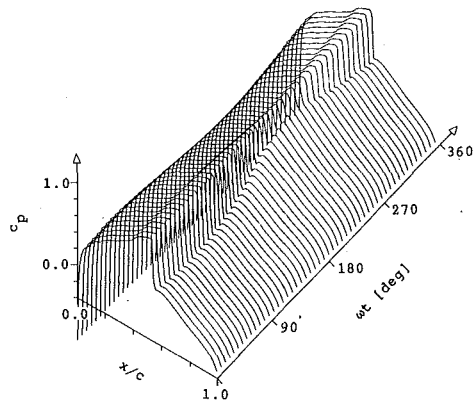
Fig. 2 Time history of the upper-surface pressure coefficients for the third cycle, NACA 64A010, CT6: $M = 0.8$, k = 0.202, $\alpha_0 = 0.0$ deg, $\alpha_1 = 1.0$ deg

can be seen very well. The shock wave reaches its maximum strength and its most downstream position with a phase shift to the angle of attack. This phase shift between angle of attack and pressure response becomes apparent in the appearance of the out-of-phase component of the harmonic analysis of the pressure, Fig. 3. The imaginary part increases as the real part decreases with increasing reduced frequency (especially upstream of the shock wave). For the limiting case $k \rightarrow 0$ (quasisteady), the out-of-phase component must disappear due to the vanishing dynamic effects. The reason for the minor change to the complex components aft of the shock wave is explained by the nature of the pressure response. In front of the shock the pressure response is sinusoidal, whereas it is nearly constant behind it. Agreement with the experimental data there is good [11]. The local pressure coefficient in the shock region, Fig. 4, is distorted. The peaks in the computational results on the grid S, F, and VF are caused by Zierep singularities due to the lack of viscous effects. The rise of numerical viscosity due to a decrease in the number of grid points (grid C) smoothes the pressure distribution. This result, however, should not be misinterpreted as replacing a Navier–Stokes solution, since inherent numerical viscosity can neither be correlated to a Reynolds number nor be used for simulating a boundary layer. The rapid pressure rise and the following pressure recovery due to the different velocity of wave propagation upstream and downstream is reproduced well.

As the CPU time depends primarily on the number of time steps per cycle, computations were done to show the influence of CFL variations on the result, Fig. 5. The c_p-distribution with 25 Δt/cycle (CFL = 3200) is shifted horizontally (to the left) with respect to the one with 200 Δt/cycle (CFL = 400). This leads to an increase in the real part and a decrease in the imaginary part of the harmonic analysis. The reason for simulating a lower frequency by a higher CFL number is the dispersion error, induced by the truncation errors of the odd derivative terms. The investigations in [11] showed that 50 to 100 time steps per cycle are adequate to obtain a good result. The best quality with respect to the explicit one is obtained with 200 Δt/cycle. In order to get a first estimation only 25 Δt/cycle are sufficient. The computational efforts for various Δt/cycle and of the explicit solution are listed in Table 1. It can be seen that considerable CPU-time saving is possible by reducing time steps per cycle without loss of accuracy.

Further examinations showed that there is no influence of grid refinement on the accuracy of the unsteady pressures. However, emphasis should be placed on fine discretization at the leading edge and in the shock-wave region for good reproduction of the curvature and the suction peak and not to smooth out the shock by numerical viscosity. The number of Gauss-Seidel iterations (IGS) depends on both the Δt/cycle and on the grid refinement. The finer the grid and the higher
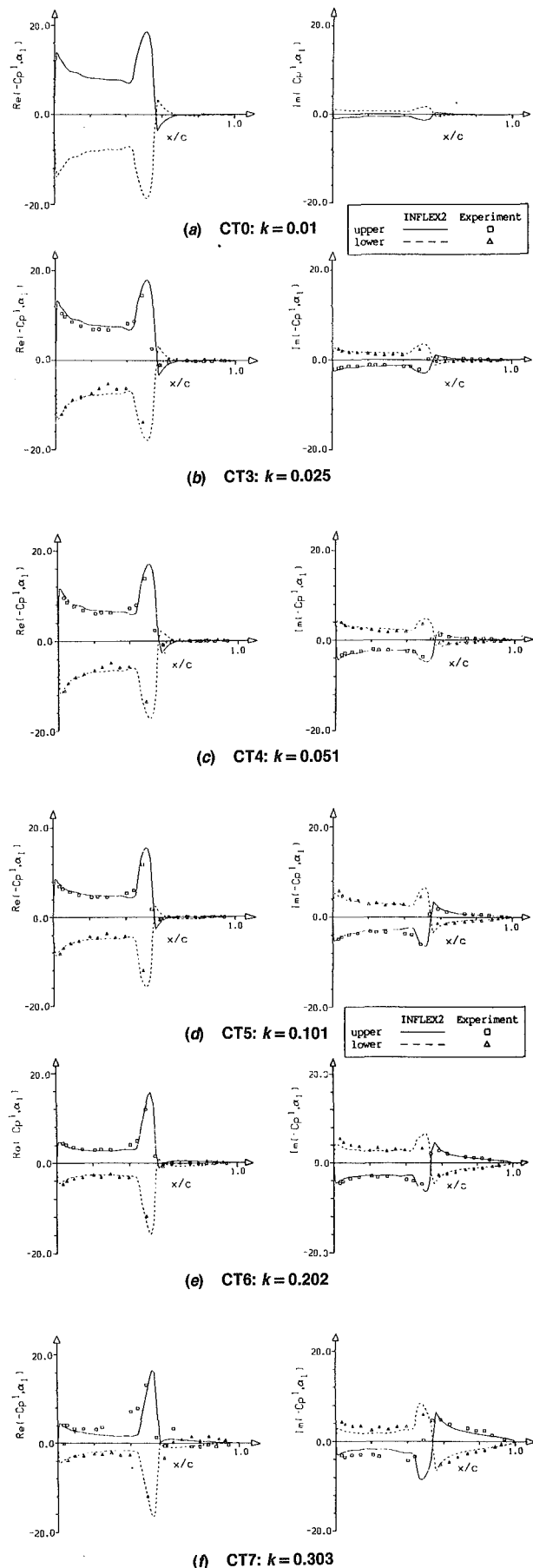

(a) CT0: k = 0.01

(b) CT3: k = 0.025

(c) CT4: k = 0.051

(d) CT5: k = 0.101

(e) CT6: k = 0.202

(f) CT7: k = 0.303

Fig. 3 Comparison of the unsteady pressure distribution for the NACA 64A010, CT6: $M = 0.8$, $\alpha_0 = 0.0$ deg, $\alpha_1 = 1.0$ deg

the CFL number, the higher must IGS be in order to avoid oscillations in the pressure distribution downstream of the shock. During every nonlinear iteration the relaxation scheme must have adequate time, e.g., Gauss-Seidel iterations, to
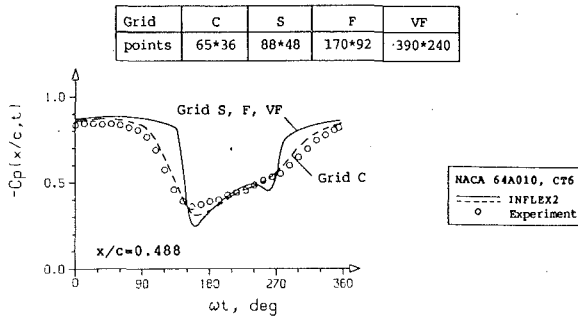

Grid	C	S	F	VF
points	65*36	88*48	170*92	·390*240

Fig. 4 Local surface pressure coefficients in the shock region, CT6
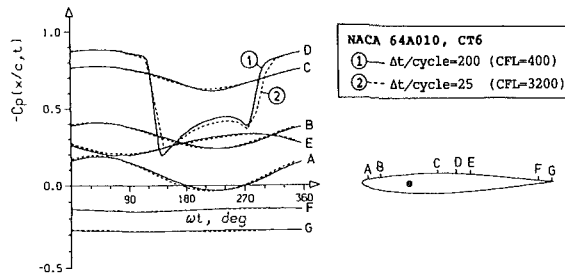
Fig. 5 Comparison of the local pressure coefficients on the upper surface at various CFL numbers, CT6

Table 1 Comparison of the CPU times of the explicit and implicit algorithm for the NACA 64A010, CT6

	explicit[a]	implicit			
CFL	0.4	400	800	1600	3200
Δt/cycle	17580	200	100	50	25
CPU [min/cycle] (SIEMENS VP200)	20.6	3.9	2.1	1.46	0.8

[a]The explicit algorithm was applied to a modified mesh with the wake cells being discarded. This causes an acceleration of the explicit code by a factor of ten.

transport the perturbations $\Delta\phi$ through the computational domain.

The Gauss distributions of the relative residua, test case CT6 with Δt/cycle = 200, IGS = 3 and a bound value $\epsilon_{rel} = 0.1$, are shown in Fig. 6 for the two different criteria 1 und 2, equation (23) and equation (25), which are satisfied after 7 and 11 nonlinear iterations (INL), respectively. The maxima of the curves with criterion 1 are shifted to the right by one half to one order of magnitude with respect to criterion 2. But it is more important that the maximum values of $\Delta\phi/\phi$ are of the same order of magnitude (with the exception of $\Delta\rho w/\rho w$) or that the maximum $\Delta\phi/\phi$ with criterion 2 is greater than with criterion 1 in a few cells only. But these cells are the reason for the rise of nonlinear iterations, which increases the CPU times by about 60 percent. The results obtained with criteria 1 and 2 do not show any difference, whether in the mean and unsteady pressure distribution, the local c_p-distribution, or in the transitional behavior towards a periodic state.

The distribution of $\Delta\rho/\rho$ with criteria 1 and 2 in the vicinity of the airfoil is illustrated in Fig. 7. The maximum residua appear in the shock-wave region. This can be explained by the indifferent position of the shock wave which is not located exactly at the cell face but moves in the cell. This is caused by a sign change of the eigenvalues at the cell face and by the connected flux-vector splitting. In contrast to ρ, ρu, and e the maximum residua of $\Delta\rho w/\rho w$ do not appear in the vicinity of the airfoil but randomly distributed over the whole computational domain, Fig. 8. The explanation for this could be as follows: The dimensionless variables ρ, ρu, and e are of the same order of magnitude and normally much greater than ρw. Relative variations of ρw, either caused by perturbations or numerical errors, can become greater than those of the other variables and distributed fortuitously. The application of criterion 1 is given preference over criterion 2 because of the reduced CPU times needed, producing equivalent results.

Up to now little has been said about the influence of viscous effects on the results. All the diagrams in Fig. 3 show a clear overprediction of the shock strength of the numerical result compared with the measured data and a shock position slightly aft of that observed in the experiment. This is due to the absence of viscosity in the Euler equations. These phenomena are stronger on supercritical airfoils, e.g., the NLR 7301 airfoil, Fig. 9. The calculated mean pressure and the first harmonic analysis for the design condition, $M = 0.721$, $k = 0.181$, $\alpha_0 = -0.19$ deg, $\alpha_1 = 0.5$ deg, are compared with measurement
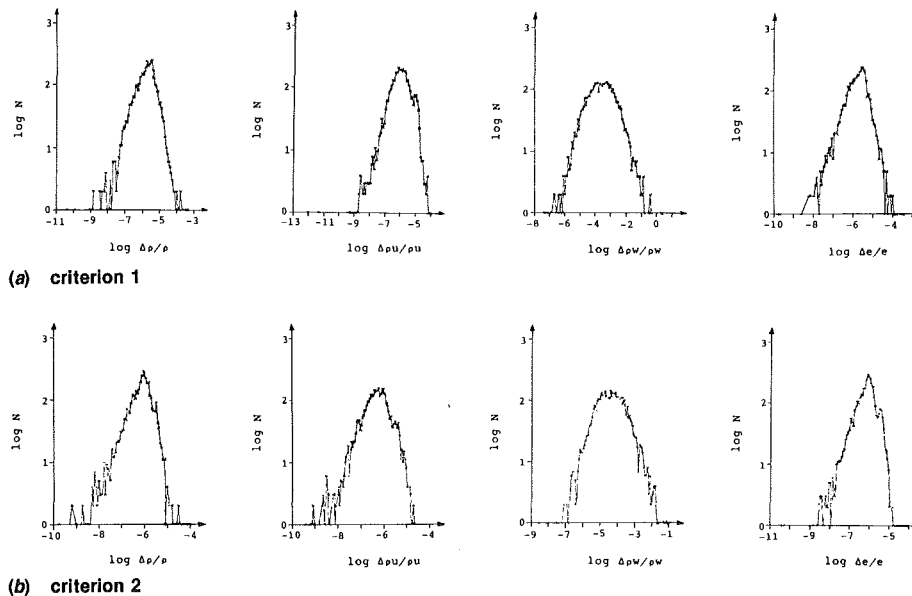

(a) criterion 1

(b) criterion 2

Fig. 6 Gauss distributions of the relative residua, NACA 64A010, CT6
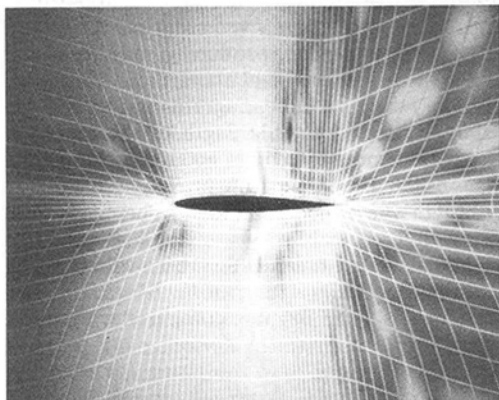
[20] in Fig. 10. The pitching axis is located at 40 percent of the chord. On the upper surface the computed c_{pm} shows two weak shocks at about $x/c = 0.25$ and $x/c = 0.6$ in contrast to the measurement plateau. The real and imaginary parts on the lower surface are predicted well, whereas on the upper surface agreement is poor. Only the qualitative behavior is reproduced.
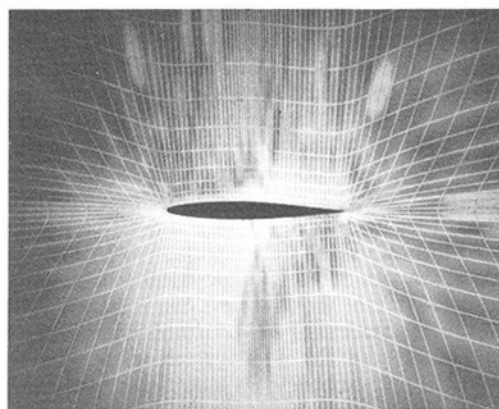
The sensitivity of the flow to changes in freestream Mach number, incidence and location of transition strip (dashed-dotted line in Fig. 10) is discussed in [21]. The influence of the boundary layer on the c_p-distribution is demonstrated in Fig. 11 for subsonic flow with $M = 0.5$, $\alpha_0 = 0.4$ deg, by coupling the Euler solution with a first-order boundary-layer solution [22]. The boundary layer causes an increase of pressure on the upper and a decrease on the lower surface. The calculated c_{pm} with the boundary layer correlates much better than without it. No differences were noticed in the real and imaginary parts at this low free-stream Mach number [11]. However, when shocks appear the situation changes dramatically: Due to the downshift position of the shock in c_{pm} and the overprediction of the shock strength, the peak in the unsteady components is overpredicted and shifted rearwards, too. Two different effects are responsible for the discrepancies between inviscid and viscous flow: First, the boundary layer limits the pressure rise and shifts the shock location upstream with respect to the inviscid flow. Second, the differing displacement thickness on upper and lower surface decambers the airfoil, changes the geometry (chord to thickness ratio, incidence), and displaces the shock.

Finally, some examples of three-dimensional applications are presented. Computational results from INFLEX3, XTRAN3S [23] (a nonlinear transonic small disturbance code)

and RHOIV [23,24] (a linear lifting surface kernel function) on a rectangular wing, Fig. 12, with a supercritical airfoil are compared with experimental data [25] in Fig. 13 and Fig. 14. The resulting pressure magnitude of the upper and lower surfaces, Fig. 13, computed by INFLEX3, agrees very well with the experiment over the whole wing. Note especially the good agreement at the most outboard section toward the trailing edge. At the leading edge, XTRAN3S shows an overpredicting oscillating behavior at the inboard station and an underpredicting behavior at the outboard stations. The RHOIV results, presented for 0.31, 0.59, and 0.811 fractional span stations, are underestimated in the forward half of the wing. The suction peak at the leading edge, of course, is not predicted by linear theory. With the exception of the XTRAN3S result at the most inboard station, phase agreement is good over the forward two-thirds of the chord for the three computational methods, Fig. 14. Toward the trailing edge the results due to XTRAN3S and RHOIV deviate considerably, whereas INFLEX3 represents the decreasing phase qualitatively well. The discrepancy
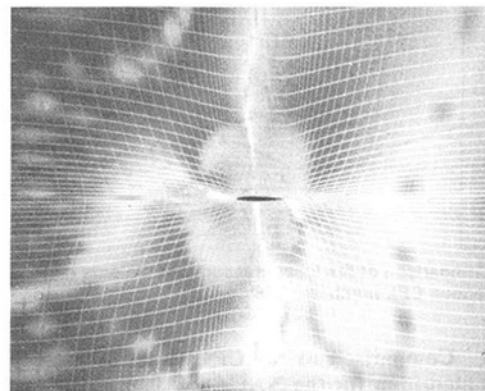

(a) overall computational domain

10⁻⁸   10⁻⁶   10⁻⁴   10⁻²   10⁰

(b) vicinity of airfoil

Fig. 8 Distribution of $\Delta\rho w/\rho w$

(a) criterion 1, INL = 7

10⁻¹¹   10⁻⁹   10⁻⁷   10⁻⁵   10⁻³

(b) criterion 2, INL = 11

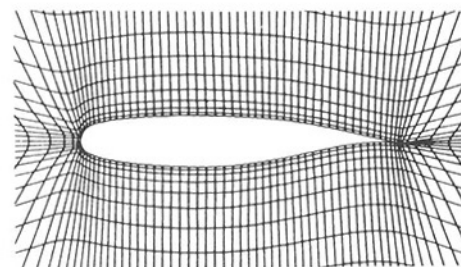Fig. 7 Distribution of $\Delta\rho/\rho$

Fig. 9 Partial view of the computational mesh for the NLR 7301 airfoil (108 * 74 points)

a)   b)

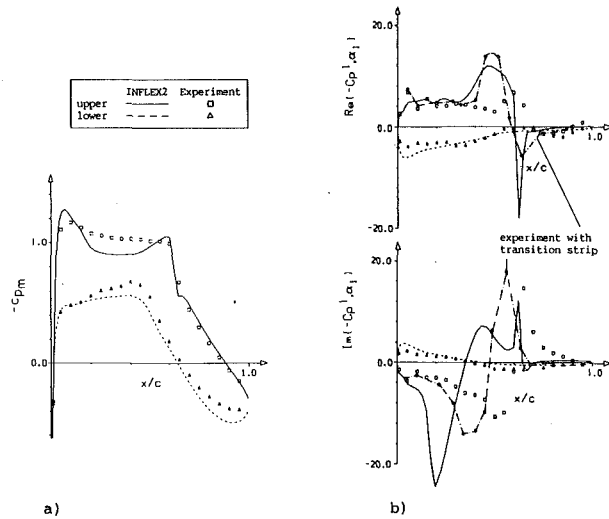**Fig. 10 Comparison of the measured and calculated mean (a) and unsteady pressure (b) distribution over the NLR 7301. M = 0.721, k = 0.181, $\alpha_0 = -0.19$ deg, $\alpha_1 = 0.5$ deg**
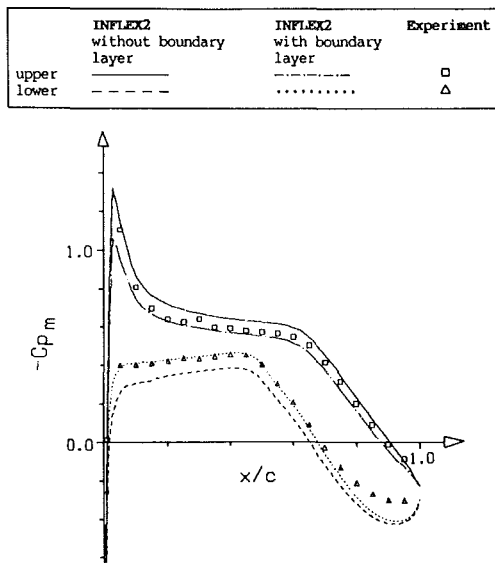

Fig. 11 Comparison of the mean pressure distribution with and without boundary layer over the NLR 7301. M = 0.5, $\alpha_0 = 0.5$ deg
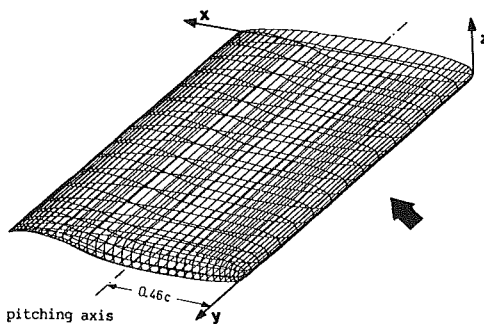

Fig. 12 Rectangular wing with supercritical airfoil (RSW wing)

Fig. 13 Comparison of the measured and calculated magnitude of the unsteady pressure distribution over the RSW wing. M = 0.7, k = 0.178, $\alpha_0 = 2.0$ deg, $\alpha_1 = 1.0$ deg
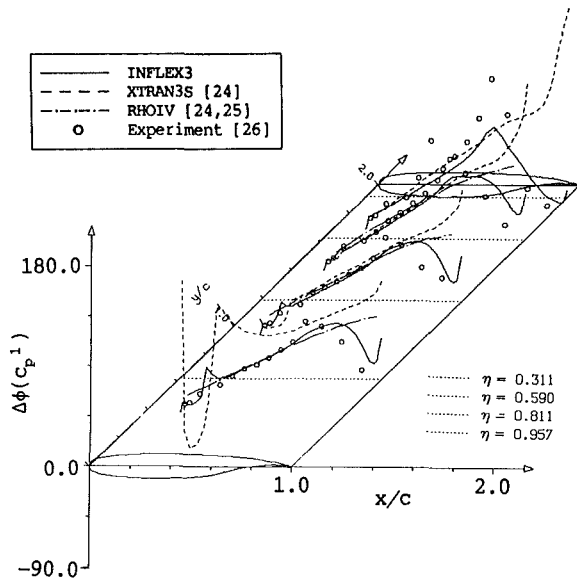
Fig. 14 Comparison of the measured and calculated phase of the unsteady pressure distribution over the RSW wing. M = 0.7, k = 0.178, $\alpha_0 = 2.0$ deg, $\alpha_1 = 1.0$ deg

Table 2 Comparison of the CPU times of the explicit and implicit algorithm for the rectangular wing with supercritical airfoil

	explicit	implicit
CFL	0.4	120
Δt/cycle	33540	110
CPU [min/cycle] (SIEMENS VP200)	926.6	77.15

shown may be attributed to viscous effects, which start to influence the flow near the trailing edge.

The CPU times of the explicit and implicit solution for the test case described above are listed in Table 2. The implicit algorithm is about twelve times faster than the explicit one even on this relatively rough grid (69 * 30 * 34 points). Grid refinement enhances the acceleration factor, as in the two-
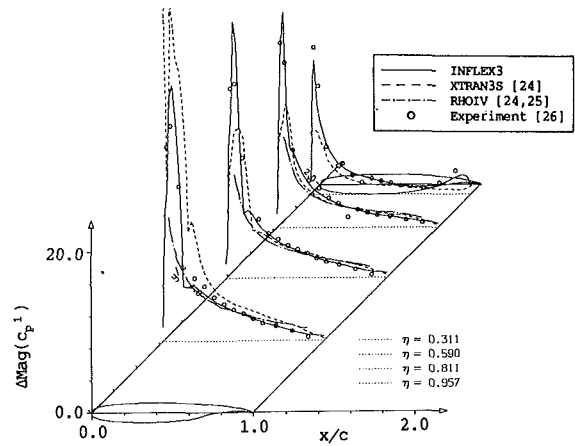
dimensional case. The gain of the CPU times implicit-explicit is not reduced through extension from two to three dimensions. This fact is one of the great advantages of the relaxation method employed.

The LANN wing, a typical transport-type wing with a high aspect ratio, leading- and trailing-edge sweep and supercritical airfoils, is shown in Fig. 15. The results presented here refer to the design cruise condition: M = 0.82, $k_{AC} = 0.076$, $\alpha_0 = 0.6$ deg, $\alpha_1 = 0.25$ deg. The pitching axis is located at 62.1 percent of the root chord from the wing apex. The computation was performed on a grid with 80 * 38 * 46 points and with 100 Δt/cycle.

The mean pressure distribution (Fig. 16), the real (Fig. 17), and the imaginary parts (Fig. 18) are in good agreement with
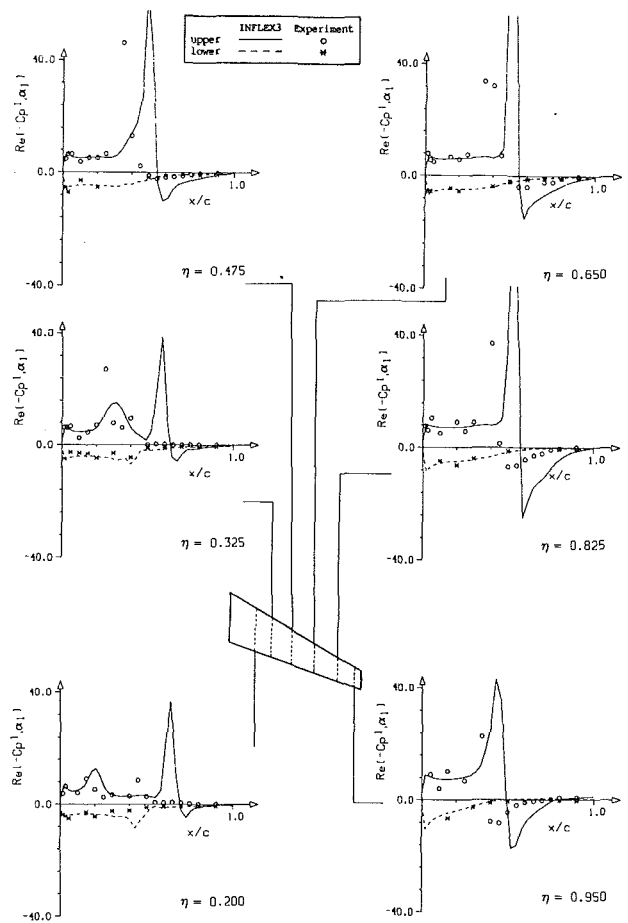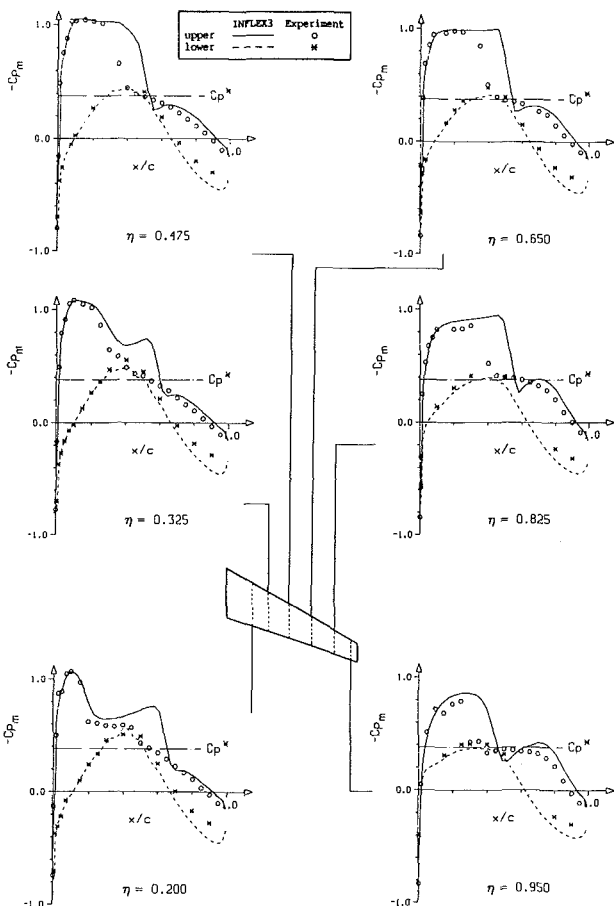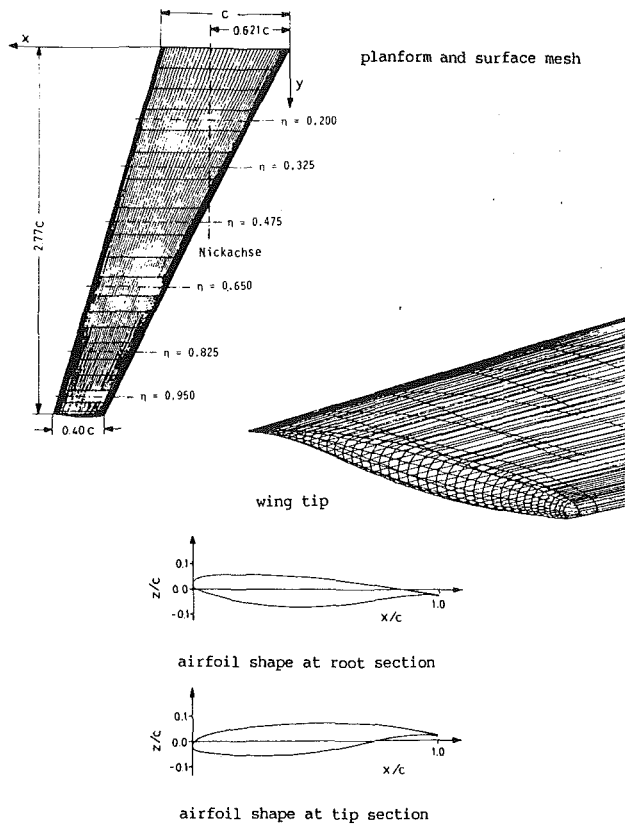
Fig. 15   LANN wing

planform and surface mesh

wing tip

airfoil shape at root section

airfoil shape at tip section

Fig. 16   Spanwise comparison of the measured and calculated mean pressure distribution over the LANN wing. $M = 0.82$, $k_{AC} = 0.076$, $\alpha_0 = 0.6$ deg, $\alpha_1 = 0.25$ deg

Fig. 17   Spanwise comparison of the measured and calculated in-phase component on the LANN wing. $M = 0.82$, $k_{AC} = 0.076$, $\alpha_0 = 0.6$ deg, $\alpha_1 = 0.25$ deg

experimental data [26] on the lower surface. On the upper surface the leading-edge suction peak of the mean pressure distribution is represented exactly at all fractional sections. Due to the shift of the shock location aft of the measured shock position and the overprediction of the shock strength, indicating that noticeable viscous effects are present in the real flow, the peaks in the in-phase and out-of-phase components are shifted downwards and over-predicted, too. With the exception of this, the unsteady pressures are reproduced well by INFLEX3.

The F-5 fighter wing shown in Fig. 19 is characterized by a small aspect ratio, a large leading-edge sweep, and a high taper ratio. The airfoil geometry, which is of a modified NACA 65-A-004.8 section, and the experimental data are taken from [27]. The assumption of rigid body motion was dropped and the measured aeroelastic mode shape was used to simulate the real body motion [27]. The calculation of the transonic test case ($M = 0.95$, $k_r = 0.132$, $\alpha_0 = 0.0$ deg, $\alpha_1 = 0.523$ deg) was performed on a grid with $106 * 54 * 58$ points and a CFL number equivalent to $100 \, \Delta t$/cycle.

The comparison between the computed mean surface pressure distribution and the experimental one is favorable at all span stations, Fig. 20. The suction peak at the leading edge on the lower surface due to the droop nose is reproduced exactly. The shock, both on the upper and on the lower surfaces, is overpredicted and located aft of the experimental one. Consequently, the peaks in the real and imaginary parts, Fig. 21 and Fig. 22, are overpredicted and too far downstream, too. Except for these small deviations the results from computation and measurement correlate very well.
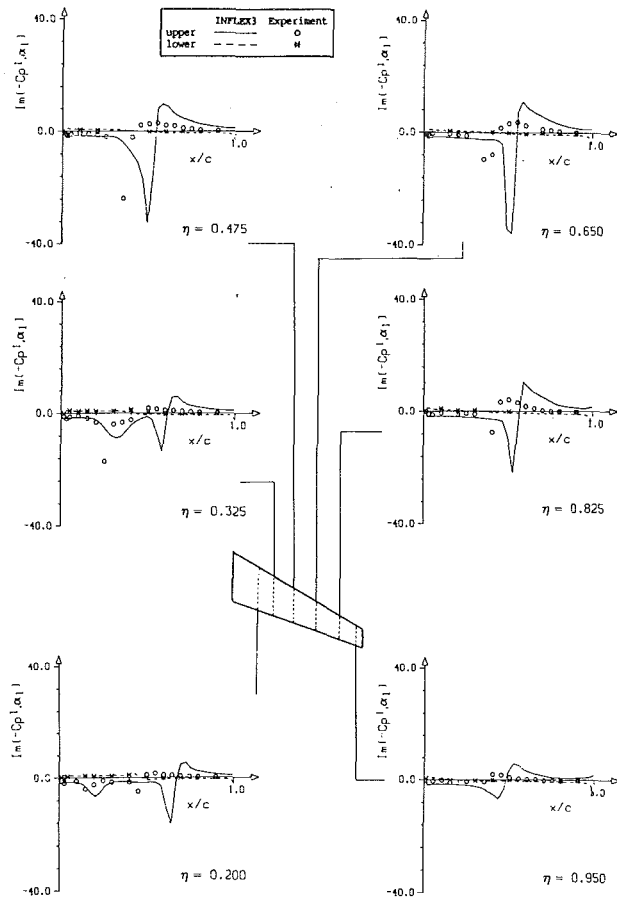
Fig. 18 Spanwise comparison of the measured and calculated out-of phase component on the LANN wing. $M = 0.82$, $k_{AC} = 0.076$, $\alpha_0 = 0.6$ deg, $\alpha_1 = 0.25$ deg
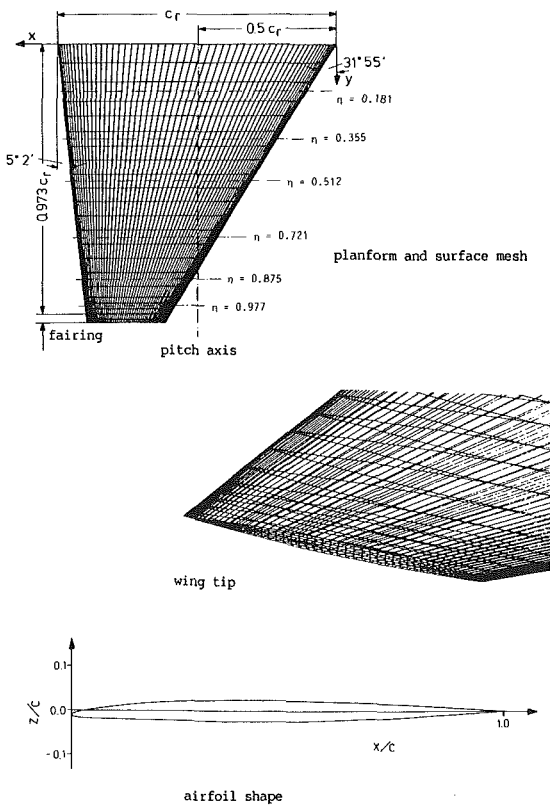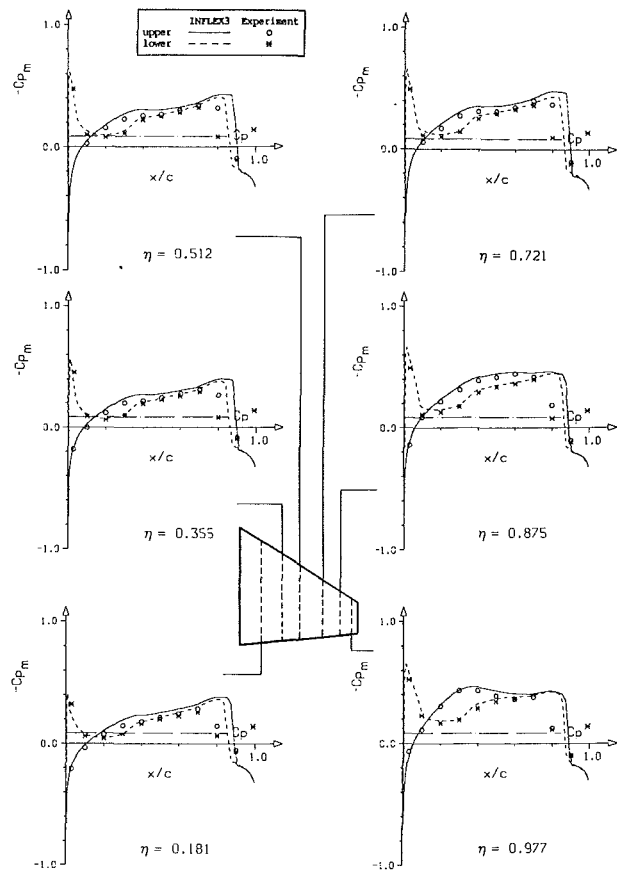

Fig. 19 F-5 fighter wing

Fig. 20 Spanwise comparison of the measured and calculated mean pressure distribution over the F-5 fighter wing. $M = 0.95$, $k_r = 0.132$, $\alpha_0 = 0.0$ deg, $\alpha_1 = 0.523$ deg

Conclusions

A relaxation method solving the unfactored implicit Euler equations was applied to compute time-accurate unsteady transonic flows about two and three-dimensional wings with conventional and supercritical airfoils. Investigations with respect to grid refinement, variation of CFL number, number of Gauss-Seidel iterations and the convergence criterion were carried out: No influence of grid refinement on the accuracy of the unsteady pressure was observed. 50 to 100 time steps per cycle are sufficient. Comparing calculated results with experimental data showed good agreement in cases where viscous effects are negligible (leading-edge region, conventional airfoils). However, the results on supercritical airfoils demonstrated that viscous effects should be taken into account for this type of airfoil. The overprediction of the shock strength and the location of the shock aft of the experimental shock position are due to the absence of viscosity in the numerical procedure. Three-dimensional effects were simulated very well.

The application of the implicit relaxation scheme considerably reduces the computational times with respect to explicit codes. Both the acceleration factor and the unconditional stability in a linear stability analysis are maintained by extension from two to three dimensions.

References

1 Magnus, R. J., and Yoshihara, H., "Unsteady Transonic Flows over an Airfoil," *AIAA Journal*, Vol. 13, No. 12, Dec. 1975, pp. 1622–1628.

2 Jameson, A., and Venkatakrishnan, V., "Transonic Flows about Oscillating Airfoils Using the Euler Equations," AIAA Paper 85-1514, 1985.

3 Smith, G. E., Whitlow, W. Jr., and Hassan, H. A., "Unsteady Transonic Flows Past Airfoils Using the Euler Equations," AIAA Paper 86-1764-CP, June 1986.

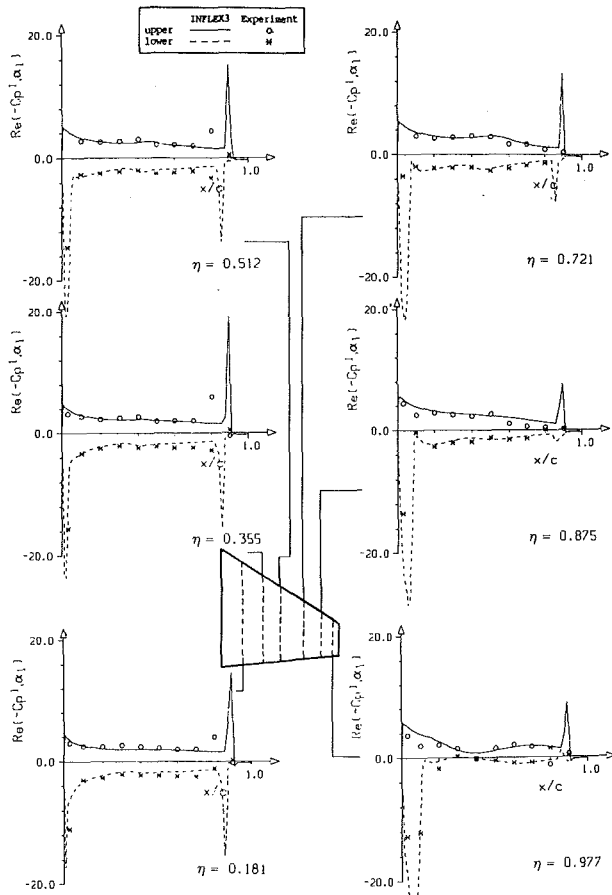4 Deslandes, R., "Eine Explizite Methode zur Lösung der Eulergleichungen

Fig. 21 Spanwise comparison of the measured and calculated in-phase component on the F-5 fighter wing. $M=0.95$, $k_r=0.132$, $\alpha_0=0.0$ deg, $\alpha_1=0.523$ deg
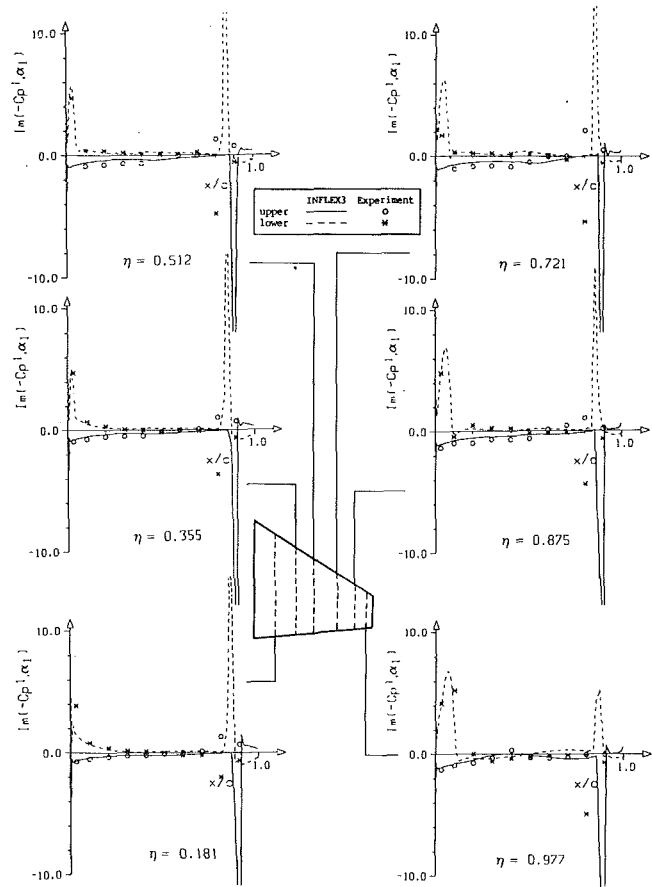
Fig. 22 Spanwise comparison of the measured and calculated out-of phase component on the F-5 fighter wing. $M=0.95$, $k_r=0.132$, $\alpha_0=0.0$ deg, $\alpha_1=0.523$ deg

Angewandt auf Instationäre Ebene Strömungen," MBB/LKE121/S/PUB/257, 1986.

5 Belk, D. M., Janus, J. M., and Whitfield, D. L., "Three-Dimensional Unsteady Euler Equations Solutions on Dynamic Grids," AIAA Paper 85-1704, July 1985.

6 Jameson, A., Schmidt, W., and Turkel, E., "Numerical Solutions of the Euler Equations by Finite Volume Methods Using Runge-Kutta Time-Stepping Schemes," AIAA Paper 81-1259, June 1981.

7 Steger, J. L., "Implicit Finite-Difference Simulation of Flow about Arbitrary Two-Dimensional Geometries," *AIAA Journal*, Vol. 16, No. 7, July 1978, pp. 679–686.

8 Chyu, W. J., Davis, S. S., and Chang, K. S., "Calculation of Unsteady Transonic Flow Over an Airfoil," *AIAA Journal*, Vol. 19, No. 6, June 1981, pp. 684–690.

9 Chyu, W. J., and Davis, S. S., "Numerical Studies of Unsteady Transonic Flow Over an Oscillating Airfoil," in AGARD CP-374: "Transonic Unsteady Aerodynamics and Its Aeroelastic Applications," Paper No. 3, Jan. 1985.

10 Sankar, N. L., Wake, B. E., and Lekoudis, S. G., "Solution of the Unsteady Euler Equations for Fixed and Rotor Wing Configurations," *Journal of Aircraft*, Vol. 23, No. 4, Apr. 1986, pp. 283–289.

11 Brenneis, A., "Berechnung Instationärer Zwei- und Dreidimensionaler Strömungen um Tragflügel Mittels eines Impliziten Relaxationsverfahrens zur Lösung der Eulergleichungen," Doctoral thesis, UniBw München, FORT-SCHRITT-BERICHT VDI 7/165, Düsseldorf, 1989.

12 Eberle, A., "3D Euler Calculations Using Characteristic Flux Extrapolation," AIAA Paper 85-0119, 1985.

13 Chakravarthy, S. R., "Relaxation Methods for Unfactored Implicit Upwind Schemes," AIAA Paper 84-0165, 1984.

14 Brenneis, A., and Eberle, A., "Unsteady Transonic Flows Past Airfoils Using a Fast Implicit Godunov-Type Euler Solver," *Proceedings of the 7th GAMM Conference on Num. Meth. in Fluid Mechanics* (ed.: Deville, M.), Notes on Numerical Fluid Mechanics, Vol. 20, Vieweg, Braunschweig-Wiesbaden, 1988, pp. 37–47.

15 Brenneis, A., and Eberle, A., "Unsteady Transonic Flows Past Airfoils and Wings Using a Fast Implicit Godunov-Type Euler Solver," 16th Congress

of the International Council of the Aeronautical Sciences. Aug. 28 to Sept. 2, 1988, Jerusalem/Israel.

16 Schmatz, M. A., Brenneis, A., and Eberle, A., "Verification of an Implicit Relaxation Method for Steady and Unsteady Viscous and Inviscid Flow Problems," in AGARD-CP-437: "Validation of Computational Fluid Dynamics," 2nd to 5th May, 1988, Lisbon/Portugal.

17 Warming, R. F., Beam, R. M., and Hyett, B. J., "Diagonalization and Simultaneous Symmetrization of the Gasdynamic Matrices," *Mathematics of Computation*, Vol. 29, No. 132, Oct. 1975, pp. 1037–1045.

18 Schwarz, W., "Elliptic Grid Generation System for Three-Dimensional Configurations Using Poisson Equations," *Numerical Grid Generation in Computational Fluid Dynamics*, 1st ed., Pineridge Press, 1986, pp. 341–352.

19 Abbott, I. H., and von Doenhoff, A. E., *Theory of Wing Sections*, Dover Publications, New York, 1958.

20 "Compendium of Unsteady Aerodynamic Measurements," AGARD-R-702, Aug. 1982.

21 Tijdeman, H., "Investigations of the Transonic Flow Around Oscillating Airfoils," NLR TR 77090 U, 1977.

22 Monnoyer, F., "SOB2D, a FORTRAN Program for the Calculation of Two-Dimensional Boundary Layers," MBB-LKE122-AERO-MT-780, 1987.

23 Seidel, D. A., Bennett, R. M., and Ricketts, R. H., "Some Recent Applications of XTRAN3S," AIAA Paper 83-1811, July 1983.

24 Redman, M. C., and Rowe, W. S., "Prediction of Unsteady Aerodynamic Loadings Caused by Leading Edge and Trailing Edge Control Surface Motions in Subsonic Compressible Flow—Computer Program Description," NASA CR 132634, 1975.

25 Ricketts, R. H., Sanford, M. C., Watson, J. J., and Seidel, D. A., "Subsonic and Transonic Unsteady and Steady Pressure Measurements on a Rectangular Supercritical Wing Oscillated in Pitch," NASA TM 85765, Part I and II, 1984.

26 Zwaan, R. J., "LANN Wing. Pitching Oscillation," Data Set 9, AGARD-R-702, Compendium of Unsteady Aerodynamic Measurements, Addendum No. 1, 1982.

27 Tijdeman, et al., "Transonic Wind Tunnel Tests on an Oscillating Wing With External Stores," AFFDL-TR-78-194, Dec. 1978.

Prediction of Anisotropy of the Near-Wall Turbulence With an Anisotropic Low-Reynolds-Number k − ε Turbulence Model

Hyon Kook Myong[1] and Nobuhide Kasagi[2]

1 Introduction

Among the various turbulence models in existence, the $k − \epsilon$ model is currently most popular and applicable to many practical complex flows with reasonable computational economy and accuracy. However, several fundamental problems still remain to be resolved. Among them, the failure to predict the limiting behavior of Reynolds stresses with increasing anisotropy toward the wall is common to the $k − \epsilon$ models previous developed (see, e.g., Patel et al., 1985; Myong and Kasagi, 1990). Recently, the authors proposed an improvement on the low-Reynolds-number $k − \epsilon$ model so as to correctly reproduce the wall-limiting behavior of turbulence quantities (Myong and Kasagi, 1990) and demonstrated that the accuracy in predicting the near-wall turbulence is of primary importance in the heat transfer analysis of high Prandtl number fluids (Myong and Kasagi, 1989a). The prediction of near-wall turbulence anisotropy with the $k − \epsilon$ model is yet to be challenged.

Since the $k − \epsilon$ models commonly assume an isotropic eddy diffusivity in modeling a Reynolds stress tensor, they yield highly inaccurate predictions for the normal Reynolds stresses, and fail to deal with certain important flow phenomena such as secondary flows in noncircular ducts and separated flows, where the anisotropic normal Reynolds stresses play an important role. In view of this shortcoming of the $k − \epsilon$ model, Reynolds stress models are often used instead, because they certainly have a much greater potential for predicting the anisotropy of Reynolds stresses. However, although the second moment transport equations can be derived in exact forms, the higher-order correlations included need to be modeled with some drastic assumptions of unknown validity; even the principles and basic techniques for their modeling have not been established yet, at least, in the near-wall region. Moreover, it is costly to solve simultaneously a set of highly nonlinear coupled differential equations for each individual component of the Reynolds stress tensor, and sometimes the numerical computation may become unstable. Therefore, it is desirable to develop an extended version of the $k − \epsilon$ model for dealing with the turbulence anisotropy without making it considerably more complex in its structure.

[1]Research Associate, Research Center for Advanced Science and Technology, The University of Tokyo, Tokyo 153 Japan.

[2]Professor, Department of Mechanical Engineering, The University of Tokyo, Tokyo 113 Japan.

Recently, a new proposal of anisotropic $k − \epsilon$ models based on anisotropic eddy diffusivity representation has been made by Nisizima and Yoshizawa (1987) (hereafter NY) and Speziale (1987) (SP). Their models reproduced reasonably well the anisotropic normal Reynolds stresses in turbulent channel flows, but did not work well in the near-wall region where the anisotropy is strongest. The authors (Myong, 1988; Myong and Kasagi, 1989b) have also proposed an anisotropic low-Re $k − \epsilon$ model with similar additional anisotropic terms in the eddy diffusivity representation, but with a different approach: the model is valid right up to the wall.

In this paper, the authors' anisotropic $k − \epsilon$ model is briefly introduced and compared with the previous ones. Then, the validity of the newly developed model is examined by its application to simple two-dimensional turbulent shear flows.

2 A New Anisotropic k − ε Model

The failure to predict the individual normal Reynolds stresses with the $k − \epsilon$ model is essentially attributed to the isotropic structure of the eddy diffusivity representation, in which a linear relationship between $-\overline{u_i u_j}$ and the mean strain tensor $S_{ij}(\equiv \partial U_i/\partial x_j + \partial U_j/\partial x_i)$ is assumed. Seeking the simplest possible way to resolve this problem, we try to introduce additionally nonlinear quadratic terms of the mean velocity gradients; this approach is similar to derivation of the constitutive equation for a viscous fluid of Stokes.

It is generally known that, for simple wall-bounded shear flows, the current isotropic $k − \epsilon$ model predicts the turbulence quantities better than other higher order models, but fails to predict each normal Reynolds stress correctly. This fact implies that the two transport equations used in the $k − \epsilon$ model are sufficiently accurate in these flows and that the anisotropy of Reynolds stresses should be reflected by anisotropy in modeling the constitutive equation. Especially, in the k-equation, each term except for the turbulent diffusion term is exact and thus does not need to be modeled. It is noticed that both the diffusion and production terms are just quadratic forms of the terms such as mean velocity gradients and turbulent kinetic energy gradients. In the local equilibrium region far from the wall, only the production and dissipation terms are of importance and they balance approximately each other with negligible diffusion effects, while the individual normal Reynolds stresses have the anisotropic characteristics even in this region.

Based on the above consideration, it is assumed that the nonlinear effects, i.e., the deviations of the Reynolds stresses from the isotropic eddy diffusivity model, could be deduced from the interrelationship among the fundamental processes in the turbulent kinetic energy budget. Consequently, from simple decomposition of each term in the k-equation the nonlinear constitutive equation is given as a function of nonlinear quadratic terms of the mean velocity gradient and the anisotropic diffusion term of k in our newly developed anisotropic $k − \epsilon$ model. The resulting form of the proposed anisotropic model is as follows:

$$\frac{Dk}{Dt} = \frac{\partial}{\partial x_j}\left[(\nu+\nu_t/\sigma_k)\frac{\partial k}{\partial x_j}\right] - \overline{u_iu_j}\frac{\partial U_i}{\partial x_j} - \epsilon \qquad (1)$$

$$\frac{D\epsilon}{Dt} = \frac{\partial}{\partial x_j}\left[(\nu+\nu_t/\sigma_\epsilon)\frac{\partial \epsilon}{\partial x_j}\right]$$
$$- C_{\epsilon_1}\frac{\epsilon}{k}\overline{u_iu_j}\frac{\partial U_i}{\partial x_j} - C_{\epsilon_2}f_2\frac{\epsilon^2}{k} \qquad (2)$$

$$\overline{u_iu_j} = \frac{2}{3}k\delta_{ij} - \nu_t\left(\frac{\partial U_i}{\partial x_j}+\frac{\partial U_j}{\partial x_i}\right) + \frac{k}{\epsilon}\nu_t\sum_{\beta=1}^{3}C_\beta\left(S_{\beta ij} - \frac{1}{3}S_{\beta\alpha\alpha}\delta_{ij}\right)$$
$$+ \frac{2}{3}\nu\frac{k}{\epsilon}W_{ij}(n,m)\left(\frac{\partial\sqrt{k}}{\partial x_n}\right)^2 \qquad (3a)$$

where:
$$S_{1ij} = \frac{\partial U_i}{\partial x_\gamma}\frac{\partial U_j}{\partial x_\gamma}, \quad S_{2ij} = \frac{1}{2}\left(\frac{\partial U_\gamma}{\partial x_i}\frac{\partial U_j}{\partial x_\gamma}+\frac{\partial U_\gamma}{\partial x_j}\frac{\partial U_i}{\partial x_\gamma}\right),$$

$$S_{3ij} = \frac{\partial U_\gamma}{\partial x_i}\frac{\partial U_\gamma}{\partial x_j} \qquad (3b,c,d)$$

$$\nu_t = C_\mu\sqrt{k}L = C_\mu f_\mu\frac{k^2}{\epsilon} \qquad (4)$$

$$f_\mu = (1+3.45/\sqrt{R_t})[1-\exp(-y^+/70)] \qquad (5)$$

$$f_2 = \{1-(2/9)\exp[-(R_t/6)^2]\}[1-\exp(-y^+/5)]^2 \qquad (6)$$

$$W_{ij}(n,m) = -\delta_{ij} - \delta_{in}\delta_{jn} + 4\delta_{im}\delta_{jm} \qquad (7)$$

$$\sigma_k = 1.4, \ \sigma_\epsilon = 1.3, \ C_{\epsilon_1} = 1.4, \ C_{\epsilon_2} = 1.8,$$

$$C_\mu = 0.09, \ R_t = \frac{k^2}{\nu\epsilon} \qquad (8)$$

Note that the indices n and m denote the coordinate normal to the wall and the streamwise coordinate, respectively; summation convention does not apply to n and m. The more details of the model are referred to Myong (1988).

Compared with its isotropic version (Myong and Kasagi, 1990), only the Reynolds stress tensor in equation (3) has additive third and fourth nonlinear quadratic terms on the right-hand side. The third term is derived from the interrelationship between production and dissipation terms in the k-equation, and plays a role to exhibit anisotropic characteristics of each Reynolds stress over the whole flow field except the immediate vicinity of the wall. The fourth one is derived from the balance between the diffusion and dissipation terms, and is crucial to have the model satisfy the wall-limiting condition of normal Reynolds stresses. It is noted here that the third term exhibits the general frame invariance necessary for the broadest range of application, but the fourth one does not, because the invariant condition is not generally satisfied in the immediate vicinity of a plane interface where turbulence is quasi-two-dimensional due to the blocking of a normal velocity component.

The eddy diffusivity of momentum ν_t in equation (3) is the same as that in the isotropic near-wall $k-\epsilon$ model (Myong and Kasagi, 1990). Thus, the present anisotropic $k-\epsilon$ model is supplemented with the original transport equations of k and

ϵ, but broadens the range of applicability while maintaining most of its popular features.

There are some similarities between the present and two other models, although both the theoretical approaches and the resulting forms are different from each other. The SP model can be considered as a special case of a more complex one of the NY model (Speziale, 1987). On the contrary, the present model seems likely to be a more general version; it can be applied right up to the wall and takes the same form as the NY model in the high turbulent Reynolds number region far from the wall, where the fourth term in equation (3a) can be neglected.

The distinct difference between the present anisotropic model and the NY and SP models lies in the explicit appearances of the eddy diffusivity in the third term and of the fourth term, both of which are crucial to predict the strong anisotropy of normal Reynolds stresses in the near-wall region. In the region except for the immediate vicinity of the wall, the fourth term is neglected and thus the present model has a form similar to those of the NY and SP models. In this case, however, the quantity $\nu_t k/\epsilon$ in the third term is replaced by k^3/ϵ^2 in the NY model and by L^2 in the SP model, respectively. It is evident that the above quantity is proportional to $\nu_t k/(\epsilon f_\mu)$ in the NY model and $f_\mu\nu_t k/\epsilon$ in the SP model. Since the modification function f_μ is much less than unity in this region, the previous models' predictions for the near-wall normal Reynolds stresses are much different from those of the present model as is shown later.

3 Results and Discussion

The anisotropic $k-\epsilon$ model is applied to simple two-dimensional shear flows; channel and flat plate flows, and sink flows. For these flows, the usual boundary layer approximation can be assumed. Consequently, the nonlinear quadratic terms in equation (3a) do not contribute to the Reynolds shear stress and the normal Reynolds stresses are algebraically obtained. Therefore, the predictions of the mean velocity, k and ϵ are not influenced by the anisotropy, and the transport equations to be solved are identical with those of the usual isotropic $k-\epsilon$ model. The details on the numerical method are found elsewhere (Myong, 1988). The model constants C_1, C_2, and C_3 are given respectively as 0.8, 0.45, and -0.15 by computer optimization, but one model constant C_2 does not appear in the present cases.

Before evaluating the performance of the proposed anisotropic $k-\epsilon$ model, some of the features of its isotropic version (MK model) should be mentioned, since the results of this base model influence greatly the prediction of the normal Reynolds stresses. The MK model is known to resolve two serious weaknesses common to previous $k-\epsilon$ models: i.e., it reproduces excellently all the major turbulence quantities such as $-\overline{uv}$, k, and ϵ near the wall with the correct wall-limiting behavior, and also the distribution of ν_t even in the region far from the wall. As a result, the MK model's predictions are found to be in close agreement with available experimental and theoretical results over a wide range of Reynolds number (Myong and Kasagi, 1990). Hence, in order to evaluate the anisotropic representation of the Reynolds stress tensor, the MK model is presently used. The numerical results obtained at comparatively low Reynolds number will only be shown below, because of the limited paper length and the abundant reliable data available at these Reynolds numbers, although the present conclusion has also been validated at higher Reynolds numbers.

Figure 1 shows the predicted mean velocities in fully developed channel and flat plate flows along with the experimental data of Karlsson and Johansson (1988) and the results of direct numerical simulation (DNS) of Kim et al. (1987); agreement is excellent.

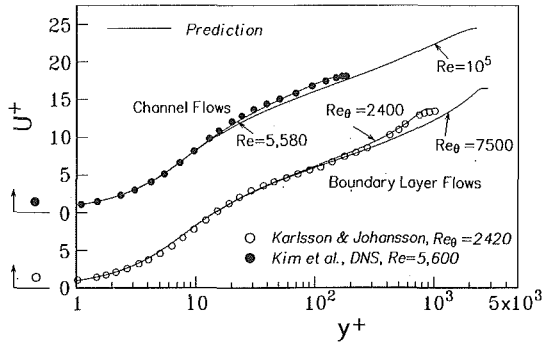The typical predicted wall-limiting behavior of each normal

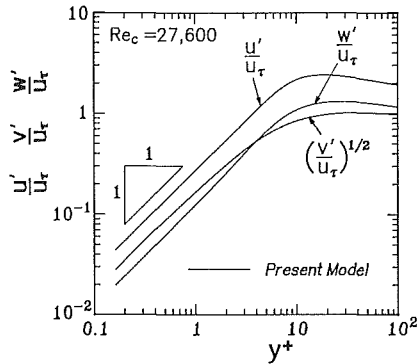**Fig. 1** Predicted mean velocity profiles for the channel and flat plate flows

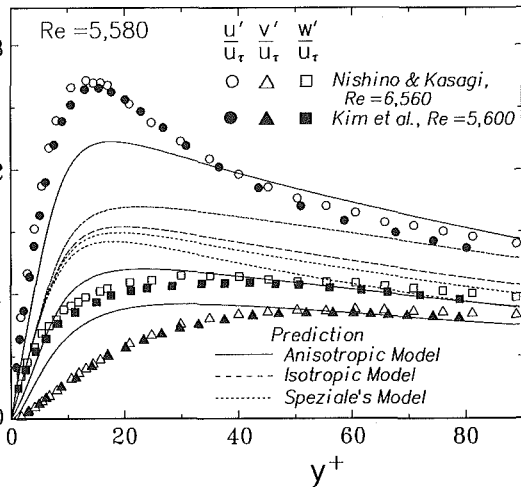**Fig. 2** Wall-limiting behavior of three normal Reynolds stresses

Fig. 3 Distributions of normal Reynolds stresses near the wall in a channel flow (Re = 5580)

Fig. 4 Distributions of normal Reynolds stresses near the wall in a flat plate flow ($Re_\theta = 2400$)
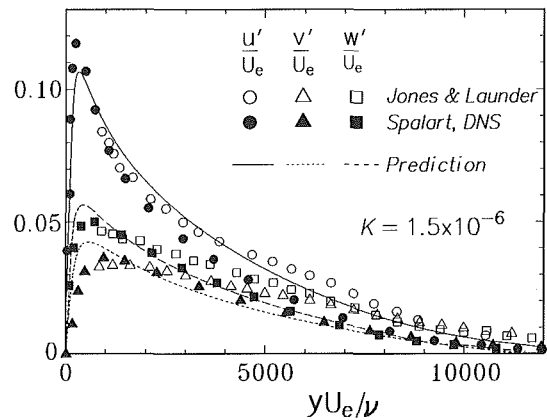
Fig. 5 Distributions of normal Reynolds stresses in a sink flow ($K = 1.5 \times 10^{-6}$)

Reynolds stress is shown in Fig. 2. Note that the superscript (′) indicates the rms value. It is seen that the present model reproduces correctly the dependence of each component upon the distance from the wall; i.e., $u \propto y$, $v \propto y^2$ and $w \propto y$. This prediction is possible only when the fourth term in the constitutive equation of $\overline{u_i u_j}$ is introduced in an adequate form. Note that the distributions of the three dimensionless normal stresses close to the wall are only a little dependent on both the flow field and the Reynolds number.

Figure 3 shows the near-wall normal Reynolds stresses in the channel flow along with the DNS results (Kim et al., 1987) and the experimental data (Nishino and Kasagi, 1989). Also included are the results of the isotropic eddy diffusivity model and those of the SP model. It is obvious that the isotropic
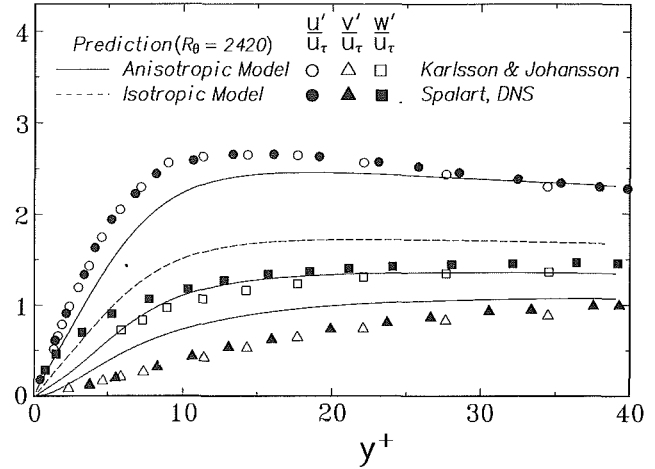
model fails to predict each normal Reynolds stress across the entire region. The SP model also fails to predict the anisotropy in the near-wall region, giving the results similar to the isotropic model, while the present anisotropic model predicts best the distributions of normal Reynolds stresses including the maximum values and their positions. This large discrepancy in the near-wall region comes from the different eddy diffusivity representations as pointed out previously. Note that, although not shown here, the present anisotropic model also predicts the relative correlation coefficients of $-\overline{uv}/u'v'$ in reasonable agreement with the available data for a wide range of Reynolds numbers (Myong, 1988).

The normal Reynolds stresses predicted for a flat plate flow are shown in Fig. 4, along with the experimental data (Karlsson and Johansson, 1988) and the DNS results (Spalart, 1988). It is found that the present anisotropic model again predicts reasonably well the overall distributions of the normal Reynolds stresses. Finally, Fig. 5 shows the results predicted for a sink flow along with some other experimental and numerical data (Jones and Launder, 1972; Spalart, 1986). Agreement is quite good over the whole shear layer thickness even in this case.

4 Concluding Remarks

This paper shows that the anisotropic $k - \epsilon$ model proposed by the present authors (Myong, 1988; Myong and Kasagi, 1989b) is able to reproduce the distributions of anisotropic normal Reynolds stresses right up to the wall with the correct wall-limiting behavior. Although the nonlinear terms in the

eddy diffusivity model have not influenced the mean flow dynamics in the present flow cases, this anisotropic model is confirmed to reproduce as well more complex flows influenced by the anisotropic Reynolds stresses, e.g., secondary flows in a square duct; such applications will be reported elsewhere.

References

Jones, W. P., and Launder, B. E., 1972, "Some Properties of Sink-Flow Turbulent Boundary Layers," *J. Fluid Mech.*, Vol. 56, pp. 337–351.

Karlsson, R. I. and Johansson, T. G., 1988, "LDV Measurements of Higher Order Moments of Velocity Fluctuations in a Turbulent Boundary Layer," *Laser Anemometry in Fluid Mechanics III*, ed. by R. J. Adrian et al., LADOAN Ins. Superior, Tecnico, Lisbon.

Kim, J., Moin, P., and Moser, R., 1987, "Turbulent Statistics in Fully Developed Channel Flow at Low Reynolds Number," *J. Fluid Mech.*, Vol. 117, pp. 133–166.

Myong, H. K., 1988, "Fundamental Studies on Two-Equation Turbulence Model for Numerical Predictions of Wall-Bounded Shear Flow and Heat Transfer," Dr. Eng. thesis, The University of Tokyo.

Myong, H. K., and Kasagi, N., 1989a, "Numerical Prediction of Turbulent Pipe Flow Heat Transfer for Various Prandtl Number Fluids With the Improved $k-\epsilon$ Turbulence Model," *JSME Int. J.*, Series II, Vol. 32, pp. 613–622.

Myong, H. K., and Kasagi, N., 1989b, "Toward an Anisotropic $k-\epsilon$ Turbulence Model Taking Into Account the Wall-Limiting Behavior of Turbulence," *Proc. Int. Symp. on Computational Fluid Dynamics NAGOYA*, Nagoya, Japan, pp. 269–274.

Myong, H. K., and Kasagi, N., 1990, "A New Approach to the Improvement of $k-\epsilon$ Turbulence Model for Wall-Bounded Shear Flow," *JSME Int. J.*, Series II, Vol. 33, pp. 63–72.

Nishino, K., and Kasagi, N., 1989, "Turbulence Statistics Measurement in a Two-Dimensional Channel Flow Using a Three-Dimensional Particle Tracking Velocimeter," *7th Symp. on Turbulent Shear Flows*, Stanford Univ., pp. 22.1.1–1.6.

Nisizima, S., and Yoshizawa, A., 1987, "Turbulent Channel and Couette Flows Using an Anisotropic $k-\epsilon$ Model," *AIAA J.*, Vol. 25, pp. 414–420.

Patel, V. C., Rodi, W., and Scheuerer, G., 1985, "Turbulence Models for Near-Wall and Low-Reynolds Number Flows: A Review," *AIAA J.*, Vol. 23, pp. 1308–1319.

Spalart, P. R., 1986, "Numerical Study of Sink-Flow Boundary Layers," *J. Fluid Mech.*, Vol. 172, pp. 307–328.

Spalart, P. R., 1988, "Direct Simulation of a Turbulent Boundary Layer up to $R_\theta = 1410$," *J. Fluid Mech.*, Vol. 187, pp. 61–98.

Speziale, C. G., 1987, "On Nonlinear $k-l$ and $k-\epsilon$ Models of Turbulence," *J. Fluid Mech.*, Vol. 178, pp. 459–475.

Flow Through an Orifice From a Transverse Stream

K. A. Andrews[1] and R. H. Sabersky[2]

Flow through orifices has been investigated thoroughly and a large amount of information on discharge coefficients and losses is available. Almost all of these results presuppose that the approaching flow is symmetrical in respect to the orifice. Very little information, however, is available for flows such as those through an orifice located in the wall of a pipe which itself carries a fluid. The present investigation consists of a set of exploratory experiments to obtain discharge coefficients for this kind of orifice flows and, in particular, to ascertain the effect of the velocity in the pipe on these coefficients.

Introduction

The flow through orifices has been studied and investigated most thoroughly. Practically every text book on fluid

[1] Major, U.S. Army, USMA, West Point, NY.

[2] Professor Emeritus, Mechanical Engineering, California Institute of Technology, Pasadena, CA.

mechanics offers a discussion on the subject and quotes rather precise values for velocity and discharge coefficients. Almost all of this work, however, envisions a flow which approaches the orifice symmetrically. Surprisingly, however, only a small amount of information is available for unsymmetrical flows. We were interested in particular in the discharge through an orifice in a wall over which a fluid is flowing in a direction normal to the centerline of the orifice. This is the kind of flow that would take place, for example, through an orifice drilled into the wall of a straight pipe. It is also of concern in the design of boundary layer control systems in which the growth and stability of the boundary layer is to be controlled by withdrawing fluid through orifices in the wall along which the boundary layer is forming.

We were interested, in particular, in flow for which the dynamic pressure of the flow along the wall is significant in relation to the dynamic pressure in the orifice. For those instances we wanted to obtain an indication of the extent to which the dynamic pressure of the main stream might be "recovered," thereby leading to an increased discharge through the orifice. The present experiments were designed only to show the general magnitude of this effect, and the absolute accuracy of the data was not considered to be of primary importance in this exploratory series of experiments.

A most thorough review of the flow in orifices in general is found in the *Handbook of Hydraulic Resistance*, by Idel'Chick (1986). That review is also one of the few references that contain some information on the type of orifice flow being considered, based on the data by Khanzhonkov (1959). Perhaps the paper most pertinent to the present work, however, is that by Thomas and Cornelius (1982), who considered the same type of flow that we have investigated.

Experimental Installation

The test section consisted of a 26.1 mm I.D. lucite pipe with a circumferential slot as the orifice. This orifice slot was formed as the space between two matched tubes which were held in position by a surrounding housing as shown schematically in Fig. 1. The slot was adjusted to widths between 0.13 mm and 0.5 mm. These rather small sizes were selected as they might correspond, at least roughly, to the sizes and associated Reynolds numbers of interest in boundary layer control work. The length of straight pipe upstream of the test orifice was 102 mm. For all the operating conditions, the external flow at the orifice consisted of a rather thin laminar boundary layer (less than 1.5 mm) and an undisturbed core. Provisions were made for measuring the flow rate through the pipe, the flow rate through the slot and the static pressure drop across the slot.

Results of Experiments

Several series of experiments were conducted. For each series the slot width was fixed and a definite pipe flow rate was selected and maintained constant. The flow rate through the
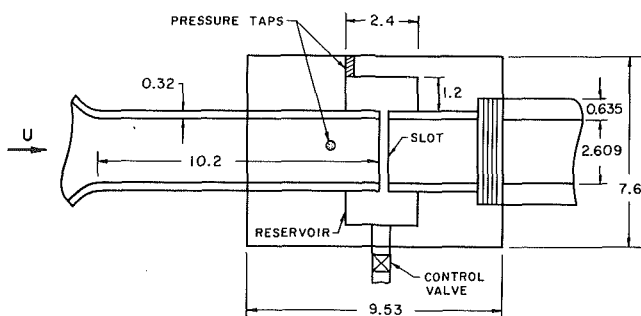

Fig. 1 Diagram of test section (dimensions in centimeters)

eddy diffusivity model have not influenced the mean flow dynamics in the present flow cases, this anisotropic model is confirmed to reproduce as well more complex flows influenced by the anisotropic Reynolds stresses, e.g., secondary flows in a square duct; such applications will be reported elsewhere.

References

Jones, W. P., and Launder, B. E., 1972, "Some Properties of Sink-Flow Turbulent Boundary Layers," *J. Fluid Mech.*, Vol. 56, pp. 337-351.

Karlsson, R. I. and Johansson, T. G., 1988, "LDV Measurements of Higher Order Moments of Velocity Fluctuations in a Turbulent Boundary Layer," *Laser Anemometry in Fluid Mechanics III*, ed. by R. J. Adrian et al., LADOAN Ins. Superior, Tecnico, Lisbon.

Kim, J., Moin, P., and Moser, R., 1987, "Turbulent Statistics in Fully Developed Channel Flow at Low Reynolds Number," *J. Fluid Mech.*, Vol. 117, pp. 133-166.

Myong, H. K., 1988, "Fundamental Studies on Two-Equation Turbulence Model for Numerical Predictions of Wall-Bounded Shear Flow and Heat Transfer," Dr. Eng. thesis, The University of Tokyo.

Myong, H. K., and Kasagi, N., 1989a, "Numerical Prediction of Turbulent Pipe Flow Heat Transfer for Various Prandtl Number Fluids With the Improved $k-\epsilon$ Turbulence Model," *JSME Int. J.*, Series II, Vol. 32, pp. 613-622.

Myong, H. K., and Kasagi, N., 1989b, "Toward an Anisotropic $k-\epsilon$ Turbulence Model Taking Into Account the Wall-Limiting Behavior of Turbulence," *Proc. Int. Symp. on Computational Fluid Dynamics NAGOYA*, Nagoya, Japan, pp. 269-274.

Myong, H. K., and Kasagi, N., 1990, "A New Approach to the Improvement of $k-\epsilon$ Turbulence Model for Wall-Bounded Shear Flow," *JSME Int. J.*, Series II, Vol. 33, pp. 63-72.

Nishino, K., and Kasagi, N., 1989, "Turbulence Statistics Measurement in a Two-Dimensional Channel Flow Using a Three-Dimensional Particle Tracking Velocimeter," *7th Symp. on Turbulent Shear Flows*, Stanford Univ., pp. 22.1.1-1.6.

Nisizima, S., and Yoshizawa, A., 1987, "Turbulent Channel and Couette Flows Using an Anisotropic $k-\epsilon$ Model," *AIAA J.*, Vol. 25, pp. 414-420.

Patel, V. C., Rodi, W., and Scheuerer, G., 1985, "Turbulence Models for Near-Wall and Low-Reynolds Number Flows: A Review," *AIAA J.*, Vol. 23, pp. 1308-1319.

Spalart, P. R., 1986, "Numerical Study of Sink-Flow Boundary Layers," *J. Fluid Mech.*, Vol. 172, pp. 307-328.

Spalart, P. R., 1988, "Direct Simulation of a Turbulent Boundary Layer up to $R_\theta = 1410$," *J. Fluid Mech.*, Vol. 187, pp. 61-98.

Speziale, C. G., 1987, "On Nonlinear $k-l$ and $k-\epsilon$ Models of Turbulence," *J. Fluid Mech.*, Vol. 178, pp. 459-475.

Flow Through an Orifice From a Transverse Stream

K. A. Andrews[1] and R. H. Sabersky[2]

Flow through orifices has been investigated thoroughly and a large amount of information on discharge coefficients and losses is available. Almost all of these results presuppose that the approaching flow is symmetrical in respect to the orifice. Very little information, however, is available for flows such as those through an orifice located in the wall of a pipe which itself carries a fluid. The present investigation consists of a set of exploratory experiments to obtain discharge coefficients for this kind of orifice flows and, in particular, to ascertain the effect of the velocity in the pipe on these coefficients.

Introduction

The flow through orifices has been studied and investigated most thoroughly. Practically every text book on fluid

[1] Major, U.S. Army, USMA, West Point, NY.
[2] Professor Emeritus, Mechanical Engineering, California Institute of Technology, Pasadena, CA.

mechanics offers a discussion on the subject and quotes rather precise values for velocity and discharge coefficients. Almost all of this work, however, envisions a flow which approaches the orifice symmetrically. Surprisingly, however, only a small amount of information is available for unsymmetrical flows. We were interested in particular in the discharge through an orifice in a wall over which a fluid is flowing in a direction normal to the centerline of the orifice. This is the kind of flow that would take place, for example, through an orifice drilled into the wall of a straight pipe. It is also of concern in the design of boundary layer control systems in which the growth and stability of the boundary layer is to be controlled by withdrawing fluid through orifices in the wall along which the boundary layer is forming.

We were interested, in particular, in flow for which the dynamic pressure of the flow along the wall is significant in relation to the dynamic pressure in the orifice. For those instances we wanted to obtain an indication of the extent to which the dynamic pressure of the main stream might be "recovered," thereby leading to an increased discharge through the orifice. The present experiments were designed only to show the general magnitude of this effect, and the absolute accuracy of the data was not considered to be of primary importance in this exploratory series of experiments.

A most thorough review of the flow in orifices in general is found in the *Handbook of Hydraulic Resistance*, by Idel'Chick (1986). That review is also one of the few references that contain some information on the type of orifice flow being considered, based on the data by Khanzhonkov (1959). Perhaps the paper most pertinent to the present work, however, is that by Thomas and Cornelius (1982), who considered the same type of flow that we have investigated.

Experimental Installation

The test section consisted of a 26.1 mm I.D. lucite pipe with a circumferential slot as the orifice. This orifice slot was formed as the space between two matched tubes which were held in position by a surrounding housing as shown schematically in Fig. 1. The slot was adjusted to widths between 0.13 mm and 0.5 mm. These rather small sizes were selected as they might correspond, at least roughly, to the sizes and associated Reynolds numbers of interest in boundary layer control work. The length of straight pipe upstream of the test orifice was 102 mm. For all the operating conditions, the external flow at the orifice consisted of a rather thin laminar boundary layer (less than 1.5 mm) and an undisturbed core. Provisions were made for measuring the flow rate through the pipe, the flow rate through the slot and the static pressure drop across the slot.

Results of Experiments

Several series of experiments were conducted. For each series the slot width was fixed and a definite pipe flow rate was selected and maintained constant. The flow rate through the
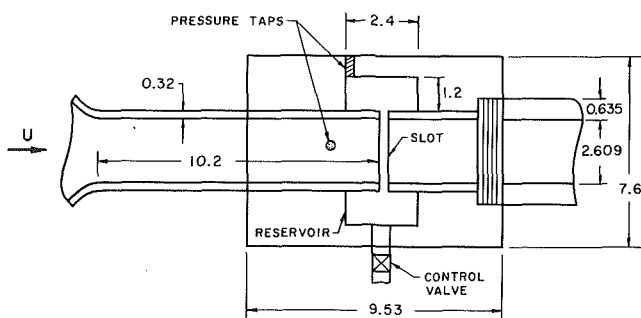

Fig. 1 Diagram of test section (dimensions in centimeters)

slot was then systematically varied by adjusting the control valve that regulates the discharge from the reservoir just downstream of the slot.

The results are given in terms of a discharge coefficient which is defined by the following equation.

$$Q_s = u_s A_s = c_d A_s \sqrt{2\Delta p/\rho}$$

where Q_s is the volume flow rate through the slot, A_s is the cross-sectional area of the slot, u_s is the average velocity in the slot, ρ is the fluid density, and Δp is the static pressure difference across the slot as discussed earlier. With this definition of c_d, any "pressure recovery" from the dynamic pressure in the main stream would show up as an increase in c_d. In making this statement, it is realized that the fluid entering the orifice is drawn from the boundary layer which has a velocity gradient. The dynamic pressure of this fluid is, therefore, much lower than that for the average velocity in the pipe, U.

Taking into account random errors it is estimated that c_d can be determined within 7 percent for high slot flow rates and within 17 percent for the low flow rates. Similar estimates apply to the parameter S_a. The ratio U/u_s is believed to be accurate to within about 10 percent. We have to add to these estimates the systematic error due to the inaccuracies of determining the slot widths. This error could be as high as 23 percent for the 0.13 mm slot and decreases to 6 percent for the 0.50 mm slot. Even though these errors are large by general standards, they are sufficiently small so that the major effects of interest will not be obscured and so that it will certainly be possible to detect trends such as those brought about by increases in the velocity of the main stream.

In the first graph, Fig. 2, the discharge coefficient is shown as a function of the Reynolds number in the orifice slot, which is defined as

$$\text{Re}_s = \frac{u_s w}{\nu}$$

where w is the slot width, ν is the kinematic viscosity and u_s is again the velocity in the slot. For zero pipe flow, the points for c_d are marked by crosses. The other points on the graph correspond to a series of runs at various main stream velocities, that is at various flow rates in the pipe. Of particular interest are the results for the highest velocity, 6 m/s in the present series, as they correspond to the highest available dynamic pressure. The experimental points are given by solid squares. In Fig. 2(a), for a slot width of 0.13 mm, it is seen that the effective discharge coefficient is above that for zero pipe flow, although the increase is only about 20 percent. Similar trends may be observed from Figs. 2(b) and 2(c) which have been prepared for the wider orifice slots of 0.24 mm and 0.5 mm, respectively. In Fig. 2(c) the increase in the discharge coefficients, over that for zero pipe flow, reaches as much as 40 percent at high orifice flows. At low orifice flows, however, there is actually a measurable decrease in the discharge coefficient, which might well be explained by the effect of the stream on the local flow pattern into the orifice.

There is a second way in which we should like to present the data in order to emphasize the role that the dynamic pressure recovery might play in increasing the flow through the orifice slot. For this purpose, we assume that the discharge coefficient is not affected by the pipe flow conditions and that it remains equal to c_{do}, the discharge coefficient that is measured at a given Re_s for zero pipe flow. Any increase in orifice flow is then attributed entirely to the partial recovery of the dynamic pressure of the main stream, and this assumed recovery is denoted by Δp_s^*. Consequently we can write

$$Q_s = u_s A_s = c_{do}\sqrt{\frac{2}{\rho} (p_w + \Delta p_s^* - p_R)}$$

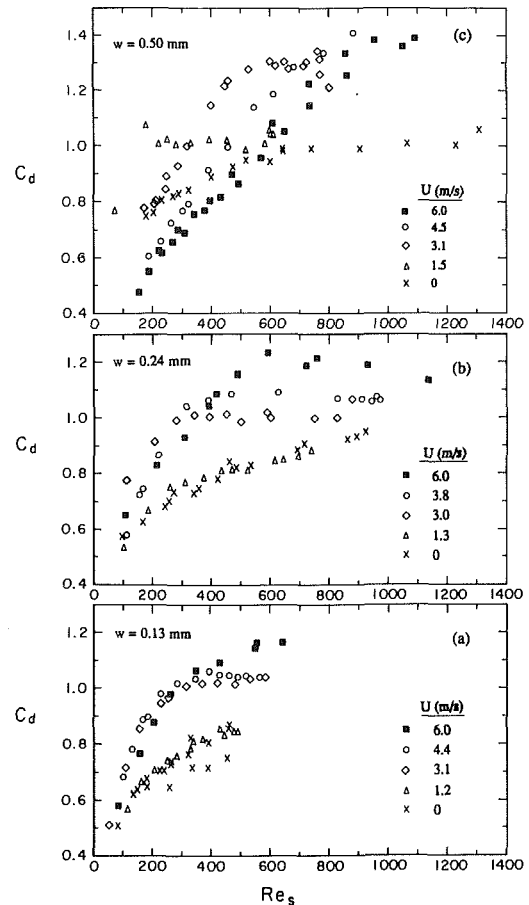where p_w and p_R are the static pressures immediately upstream

Fig. 2 Discharge coefficient c_d versus Reynolds number, Re_s, for different pipe velocities and slot widths

and downstream of the slot respectively. The coefficient c_d used so far was defined earlier by the relation

$$Q_s = u_s A_s = c_d \sqrt{\frac{2}{\rho} (p_w - p_R)}$$

The somewhat artificial quantity Δp_s^* may be obtained in terms of c_d from these two equations.

We may now form the ratio

$$\frac{\Delta p_s^*}{1/2\rho U^2} \equiv S_a$$

which gives the fraction of the available dynamic pressure, $(1/2\rho U^2)$, which is "recovered" and serves to increase the flow through the orifice slot. (Again it is understood that the available dynamic head in the boundary layer is actually lower than this reference value of $1/2\rho U^2$.)

The ratio S_a is represented in Fig. 3(a) to 3(c) as a function of U/u_s for the three slot widths respectively. As the data are meaningful only for relatively high dynamic pressures the data for the lowest main stream velocity have been omitted from these graphs. In Fig. 3(a) the results for the narrowest slot are shown, and it is seen that there is some pressure "recovery," Δp_s^*, for the entire range of experiments. When U/u_s is of the order unity, the recovery reaches 60 percent for a pipe velocity of 3 m/s, but this peak decreases to about 30 percent as the main stream velocity rises to 6 m/s. For the wider orifice slot, $w = 0.24$ mm, again some recovery is shown over the whole range (see Fig. 3(b)). The maximum, however, is now only 20 percent. For the widest slot, 0.5 mm, (Fig. 3(c)) the peak for a pipe velocity of 3.1 m/s is only 10 percent and for a main stream velocity of 6 m/s the maximum increase measured is only 4 or 5 percent.
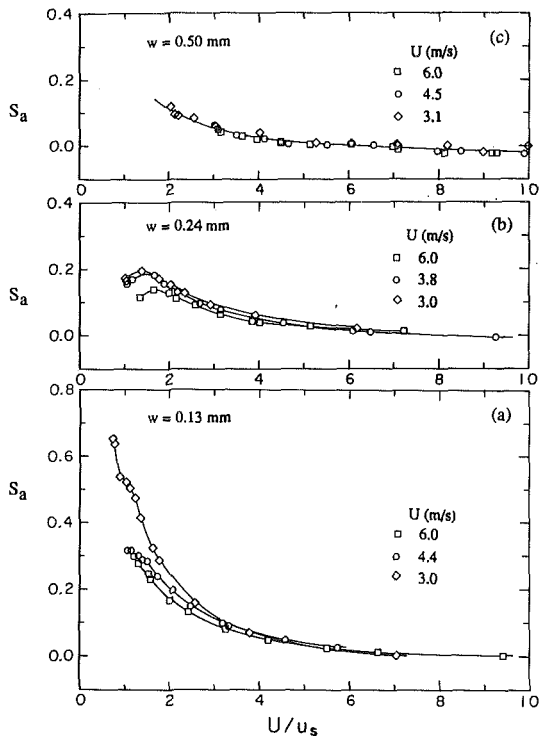
Fig. 3 Recovery factor S_a versus U/u_s at constant values of U for different slot widths

Discussion and Conclusions

The results clearly show that the discharge coefficient can differ significantly from the usually quoted coefficients which apply to symmetrical inflow originating from a large reservoir. In the present series of experiments increases in discharge coefficients of as much as 30–40 percent have been measured. In some instances, on the other hand, slight decreases, of the order of 10 percent were noted. Qualitatively the changes are rather easily explainable. The flow pattern into the orifice is quite different from that encountered in the more "traditional" orifice flow. It is unsymmetrical and greatly influenced by the velocity as well as the velocity profile of the main stream along the wall. In addition, and most importantly, the stream along the wall may have a dynamic pressure which can be very significant compared to the dynamic pressure that corresponds to the velocity in the orifice itself. This dynamic pressure certainly must be the principal factor giving rise to the increases in the discharge coefficient. The effectiveness of this dynamic pressure in promoting flow through the orifice is greatest when the velocity ratio U/u_s is of the order unity. When U/u_s is small compared to unity, the dynamic pressure tends to be negligible, and when U/u_s is large compared to unity, the dynamic pressure of main stream first has to be converted into static pressure, before producing increased flow in the orifice. This type of conversion is generally inefficient, and explains at least in part the decrease of c_d as U/u_s increases beyond the value corresponding to the peak. The decrease in Re_s that is associated with an increasing ratio of U/u_s is an additional factor producing a similar effect.

In closing we want to repeat that the present study was an exploratory one and was by no means meant to be a definitive work on the subject. Among the factors that were not systematically varied are the thickness of the boundary layer in relation to the width of the slot, the velocity gradient in the boundary layer, the effects of laminar or turbulent flow in the boundary layer, as well as the geometrical aspects of the orifice slots. Continued study of all of these aspects might well be worthwhile and we hope that our study raised enough unanswered questions to encourage further work.

References

Idel'Chik, I. E., 1986, *Handbook of Hydraulic Resistance*, Hemisphere Publishing Corporation, New York.

Khanzhonkov, V. I., 1959, "Resistance to the Discharge Through an Orifice in the Wall in the Presence of the Passing Stream," *Prom. Aerodin.*, Oborongiz, Moscow, Vol. 15, pp. 5–19.

Thomas, A. S. W., and Cornelius, K. C., 1982, "Investigation of a Laminar Boundary-Layer Suction Slot," *AIAA Journal*, Vol. 20, No. 6, pp. 790–796.

The Mean Flow Structure on the Symmetry Plane of a Turbulent Junction Vortex[1]

C. J. Baker.[2] In their recent paper the authors, after examination of their own experimental data and that of others, suggest that for a turbulent junction (or horseshoe) vortex, two vortex systems exist for $R_D < 10^6$ and four vortex systems exist for $R_D > 10^6$. The only data that is not in accord with this is that of the present writer [3], who observed a 4 vortex system for $R_D = 1.1 \times 10^5$. This note is thus written partly by way of self-justification, and also to set out another criterion for when two- or four- vortex systems exist.

First, consider the datasets that are used by the author, that are set out on Table 1. The work of the present writer [3] used surface oil flow visualization to determine vortex number. The observed oil flow patterns were, to the writer's mind, completely unambiguous and showed the two separation line/two attachment line pattern that is characteristic of a four vortex system. They can thus be regarded as reliable.

Second, consider the data of Ishii and Hanami [4]. This was obtained for a horseshoe-vortex—like flow in a T junction duct. The authors argue that this is equivalent to a very large diameter cylinder i.e., $R_D \approx \infty$. This cannot be the case. The flow that was investigated must scale on local, measurable flow variables i.e., the duct dimensions and the upstream boundary-layer parameters. A Reynolds number based on a hypothetical cylinder of infinite diameter is not a relevant variable. The flow is simply a three-dimensional duct flow and cannot be considered to be equivalent to the cylinder/wall flows of the other investigators. Thus it cannot be used in any determination of a criterion for vortex number.

Table 2 shows, for the data sets other than that of [4], the values of l/D and s/D and H, where l is the cylinder height, s is the separation distance upstream of the front cylinder stagnation point, and H is the upstream boundary layer form parameter, together with the number of vortices N.

Table 2

Source	l/D	s/D	H	N
Baker [3]	4.76	0.49	1.37	4
Pierce et al. [11]	1.80	0.40	1.31	2
Present LDV results	1.80	0.40	1.31	2
Eckerle and Langsten [13]	0.62*	0.40	1.35	2
Abid and Schmitt [14]	2.11	0.44	?	4

* l taken as half duct height.

[2] Department of Civil Engineering, Nottingham University Nottingham, U.K.

It can be seen from Table 2 that N is a simple increasing function of s/D i.e., the dimensionless separation distance. This seems very reasonable—the larger the value of s/D the more space exists for the vortex system to develop. s/D is in turn a function of l/D, decreasing as l/D falls below (1.0) (Baker [17]). The difference between s/D for the results of the authors and Baker [3] can probably be accounted for from the difference in H values (the results of [3] are slightly closer to separation) and also because the results of [17] suggest that s/D peaks at $R_\theta \approx 0.75 \times 10^4$, which is approximately the value used in [3]. From Table 1, one would thus expect s/D to be greater than the present results.

Thus it would seem from this rather limited dataset that for s/D less than approximately 0.43, $N = 2$ and for s/D above this value, $N = 4$. Such a hypotheses also casts some light on the supersonic data of [5], where the number of vortices in general seems to increase as s/D increases (s/D in this case is fixed by the bow shock position). However, this being said, a word of warning is necessary. The recent data of Devenport and Simpson [18], show substantial quasi-periodic unsteadiness within a turbulent horseshoe vortex system. Whether this is, in general the case is not clear. However, if some of the datasets in Tables 1 and 2 are affected by such unsteadiness, then the definition of vortex number becomes extremely difficult. The writer can only echo the author's remarks that further study is required.

Additional References

17 Baker, C. J., "The Position of Points of Maximum and Minimum Shear Stress Upstream of Cylinders Mounted Normal to Flat Plates," *Journal of Wind Engineering and Industrial Aerodynamics*, Vol. 18, 1985, pp. 263-274.

18 Devenport, W., and Simpson, R., "Time Dependent and Time Averaged Turbulence Structure Near the Nose of a Wing Body Junction," *Journal of Fluid Mechanics*, Vol. 210, 1990, pp. 23-55.

Authors' Closure

The authors thank Professor Baker for his thoughtful and informative comments.

The principal objective of the paper was to document that for the particular body shape and low speed, turbulent flow conditions of the experiment, mean velocity measurements in the upstream symmetry plane showed clearly only a single vortex structure, and the computed vorticity field suggested a two-vortex flow model existed. This is in contrast to the four-vortex model sketched in most earlier publications for low speed turbulent junction vortex flows, and initially based on surface flow visualizations only.

The correlation of number of vortices offered by Professor Baker appears to be well thought out. While the flow visualizations for the Pierce and Tree, and Pierce et al. did not